Computational and experimental studies of selected magnesium and ferrous sulfate hydrates: implications for the characterisation of extreme and extraterrestrial environments

Submitted by Johannes Michael Meusburger
to the University of Exeter as a thesis for the degree of
Doctor of Philosophy in Mining and Minerals Engineering, January 2023.

Abstract

Magnesium sulfate hydrates are considered important rock-forming minerals on the outer three Galilean moons of Jupiter (i.e., Europa, Ganymede, Callisto) and, alongside ferrous sulfate hydrates, are promising candidate minerals for the widespread sulfate deposits that occur in the equatorial region of Mars. In such extraterrestrial environments, these minerals experience extreme high-pressure conditions in the interiour of the Galilean moons and low-temperature conditions on the surface of these moons and Mars. The aim of this thesis is to understand the structural stability, compressibility, and thermal expansion of these compounds in such extreme environments and aid their identification in ongoing and future space missions.

Most magnesium sulfate hydrates lack accurate reference elastic tensors, which hinders their seismological identification in lander missions on the icy moons of the outer solar system, as envisioned for the near future. In this thesis, the accuracy of recent advancements in density functional theory to predict the compressibility and elastic constants of icy satellite candidate minerals (i.e., epsomite ($MgSO_4 \cdot 7H_2O$), gypsum ($CaSO_4 \cdot 2H_2O$), carbon dioxide (CO_2), and benzene (C_6H_6)) was assessed by benchmarking them against experimental reference data from the literature. Key findings are that density functional theory calculations do not yield elastic constants accurate enough to be used as a reference for the seismic exploration of icy moons. However, the bulk compressibility of such materials is very accurately reproduced by density functional theory, which was therefore used to predict the compressibility of the icy satellite candidate minerals starkeyite ($MgSO_4 \cdot 4H_2O$) and cranswickite ($MgSO_4 \cdot 4H_2O$). Knowledge of the compressibility of such minerals is critical to model mantle processes (e.g., salt diaprisim, plate tectonics, subduction) and the density structure of the outer three Galilean moons.

The thermal expansion and structural stability of three sulfate minerals (i.e., rozenite ($FeSO_4 \cdot 4H_2O$), starkeyite, and cranswickite) was characterised for the first time using neutron diffraction. Cranswickite transforms to starkeyite at 330 K, well above the maximum surface temperature of 308 K hitherto reported on Mars. Starkeyite likely undergoes a structural phase transition at around 245 K. The structure of this proposed low-temperature polymorph could not be determined but would be of great interest since the temperature drops below 245 K on equatorial Mars at night-time. Starkeyite was also studied by means of

synchrotron X-ray diffraction but suffered radiation damage. No phase transition was observed in rozenite from 290 – 21 K, which contrasts with Raman data reported in the literature, where sharpening of vibrational modes upon cooling was misinterpreted as mode splitting and evidence for two phase transitions at temperatures relevant to the Martian surface. First-principles phonon frequency calculations provide evidence supporting the absence of vibrational mode splitting. A workflow to obtain reliable reference Raman spectra for space exploration was proposed and an optical centre stick for the simultaneous acquisition of neutron diffraction and Raman spectroscopy data at the HRPD instrument was commissioned. Lastly, the structure of a polymorph of hexahydrite ($MgSO_4 \cdot 6H_2O$), most recently proposed in the literature, was shown to be unambiguously wrong.

Table of Contents

List of Figures

List of Tables

Declaration

I hereby declare that this thesis contains no material which has been accepted for the award of any other degree or diploma at any university or equivalent institution and that, to the best of my knowledge and belief, this thesis contains no material previously published or written by another person, except where due reference is made in the text of the thesis. This thesis includes two original papers published in peer-reviewed journals as well as an unpublished manuscript. In addition, this thesis includes one comment that I co-authored as well as an unpublished technical report on the commissioning of experimental equipment that formed part of my PhD project. The inclusion of co-authors reflects the fact that the work came from active collaboration between researchers and acknowledges input into team-based research. In the case of chapters 3, 4, 5, and 6 my contribution to the work involved the following:

Chapter	Reference	Publication status	Student contribution	Author contribution
3	Meusburger, J. M., Hudson-Edwards, K. A., Tang, C. C., Crane, R. A., & Fortes, A. D. (2021). Elasticity of selected icy satellite candidate materials (CO_2, C_6H_6, $MgSO_4 \cdot 7H_2O$ and $CaSO_4 \cdot 2H_2O$) revisited by dispersion corrected density functional theory. *Icarus*, 114611. https://doi.org/https://doi.org/10.1016/j.icarus.2021.114611	Published	75 %	Supervision: K. A. Hudson-Edwards, A. D. Fortes, C. C. Tang, R. A. Crane Conceptualisation: J. M. Meusburger, A. D. Fortes Data acquisition: J. M. Meusburger Data analysis: J. M. Meusburger Writing - original draft: J. M. Meusburger Writing – review and editing: J. M. Meusburger, A. D. Fortes, K. A. Hudson-Edwards, C. C. Tang, R. A. Crane
4	Meusburger, J. M., Hudson-Edwards, K. A., Tang, C. T., Connolly, E. T., Crane, R. A., & Fortes, A. D. (2022a). Low-temperature crystallography and vibrational properties of rozenite ($FeSO_4 \cdot 4H_2O$), a candidate mineral component of the polyhydrated sulfate deposits on Mars. *American Mineralogist [in Press]*. https://doi.org/10.2138/am-2022-8502	Published	75 %	Supervision: K. A. Hudson-Edwards, A. D. Fortes, C. C. Tang, R. A. Crane Conceptualisation: J. M. Meusburger, A. D. Fortes, K. A. Hudson-Edwards, C. C. Tang, R. A. Crane Data acquisition: J. M. Meusburger, A. D. Fortes, C. C. Tang, E. T. Connolly Data analysis: J. M. Meusburger Writing - original draft: J. M. Meusburger Writing – review and editing: J. M. Meusburger, A. D. Fortes, K. A. Hudson-Edwards, C. C. Tang, E. T. Connolly, R. A. Crane

| 5 | Meusburger, J. M., Hudson-Edwards, K. A., Tang, C. T., Connolly, E. T., Crane, R. A., & Fortes, A. D. (2022b). Phase-transition type negative volume expansion and anisotropic X-ray expansion in magnesium sulfate tetrahydrate. *For Submission to Angewandte Chemie* | unpublished | 75 % | Supervision: K. A. Hudson-Edwards, A. D. Fortes, C. C. Tang, R. A. Crane
Conceptualisation: J. M. Meusburger, A. D. Fortes, K. A. Hudson-Edwards, C. C. Tang, R. A. Crane
Data acquisition: J. M. Meusburger, A. D. Fortes, C. C. Tang, E. T. Connolly, K. A. Hudson-Edwards, R. A. Crane
Data analysis: J. M. Meusburger
Writing - original draft: J. M. Meusburger
Writing – review and editing: J. M. Meusburger, A. D. Fortes, K. A. Hudson-Edwards, C. C. Tang, E. T. Connolly, R. A. Crane |
| 6 | Fortes, A. D., & Meusburger, J. M. (2022). Comment on Mineral Diversity on Europa: Exploration of Phases Formed in the $MgSO_4$–H_2SO_4–H_2O Ternary. *ACS Earth and Space Chemistry, 6*(5), 1407–1410. https://doi.org/10.1021/acsearthspacechem.2c00038 | Published | 50 % | Supervision: A. D. Fortes
Conceptualisation: J. M. Meusburger, A. D. Fortes
Writing - original draft: A. D. Fortes
Writing – review and editing: J. M. Meusburger, A. D. Fortes |

List of Abbreviations

BFGS Broyden-Fletcher-Goldfarb-Shanno

BM3-EOS Birch-Murnaghan 3rd order Equation of State

BVA Bond-valence Analysis

CCD Charged Coupled Device

CCR Close Cycled Refrigerator

DFT Density Functional Theory

DFT - D Dispersion-corrected Density Functional Theory

DFPT Density Functional Perturbation Theory

FSH Ferrous Sulfate Hydrate

GGA Generalised Gradient Approximation

IOW Icy Ocean World

IR Infrared

LDA Local Density Approximation

LinAc Linear Accelerator

MAC Multi Analyser Crystal

MSiD Mean Signed Deviation

MSH Magnesium Sulfate Hydrate

MUD Mean Unsigned Deviation

PSD Position Sensitive Detector

RH Relative Humidity

SCF Self Consistent Field

TOF Time of Flight

1. Introduction

This thesis is concerned with the high-pressure and low-temperature behaviour of selected magnesium and ferrous sulfate hydrates. The aim is to understand their behaviour in extreme environments and aid their identification in ongoing and future space missions using vibrational spectroscopy and seismology.

Magnesium sulfate hydrates are considered important rock-forming minerals on the outer three Galilean moons of Jupiter (i.e., Europa, Ganymede, Callisto) (McCord et al., 1998ab, 2001; McKinnon & Zolensky, 2003). In such settings they may play an important role in controlling salt diaprisim, plate tectonics and subduction (Hogenboom et al., 1997; Johnson et al., 2017). In order to improve modelling of such processes, there is a growing interest in the compressibility and high-pressure stability of these compounds. Furthermore, with the likely deployment of seismic stations on Europa envisioned for the near future (Pappalardo et al., 2013), a campaign of study into the elasticity of potential icy satellite candidate minerals is of paramount importance.

The first objective of this thesis is to computationally explore the accuracy of recent advancements in density functional theory to predict the compressibility and elastic constants of icy satellite candidate minerals by benchmarking them against experimental reference data from the literature.

In addition, magnesium and ferrous sulfate hydrates likely form widespread deposits in the equatorial region of Mars (A. Wang et al., 2016). There is a major interest in identifying sulfate hydrates on the Martian surface for principally two reasons. Firstly, their widespread occurrence above clay-mineral deposits (Roach et al., 2010) indicates a transition in global climate from wetter to dryer conditions starting around 4 billion years ago (Bibring et al., 2006). Due to their apparent role as climatological archives a detailed mineralogical characterization of these sulfate deposits is essential in order to decipher the nature and drivers of changing environmental conditions during the planet's early history. Secondly, magnesium and ferrous sulfate hydrates form extended deposits in the equatorial region of Mars (Bishop et al., 2009; Roach et al., 2010). and might be valuable resources for H_2O, Mg, and S (Barkatt & Okutsu, 2022; Li et al., 2018; Z. Wang et al., 2020), all being critical for a sustained human activity on Mars. Starkeyite ($MgSO_4 \cdot 4H_2O$) and rozenite ($FeSO_4 \cdot 4H_2O$) are considered to be a promising match for infrared-reflectance spectra collected from these

deposits (Carter et al., 2013; A. Wang et al., 2016). In a low-temperature Raman spectroscopy study of rozenite, Chio et al. (2007) report evidence for two phase transitions with at least the first one being well within the range of Martian surface temperatures. The crystal structures of these putative polymorphs, however, have not yet been determined. In addition, the low-temperature behaviour of starkeyite, and its stability with respect to its polymorph cranswickite are completely unknown. The second objective of this thesis is to characterise the behaviour of rozenite, starkeyite and cranswickite at temperatures relevant to the Martian surface.

This introduction begins with a short overview of the mineralogy of magnesium and ferrous sulfate hydrates (section 1.1), followed by a description and justification of the work done towards this thesis (section 1.2).

1.1 Mineralogy of magnesium and ferrous sulfate hydrates

1.1.1 Crystallography

A total of 13 $MgSO_4 \cdot nH_2O$ (MSH) phases with hydration state (n) ranging from 1 to 11 and six $FeSO_4 \cdot nH_2O$ (FSH) (n = 1 – 7) have been either found in nature as minerals or synthesised in the laboratory (Table 1.1). Many of these hydrates form solid solutions with a wide range transition metal compounds with the general formula $MeSO_4 \cdot nH_2O$ (n = 1 – 11 and Me = Fe, Mn, Zn, Ni, Co) (Fortes et al., 2012). The structural details of these hydrates are described below. The bonding and polyhedral connectivity will be discussed with a particular focus on bond valency, a concept that was successfully applied by Hawthorne & Sokolova (2012) to the lower hydrates (i.e., n < 7) of MSHs. In a first approximation, the valance units are assumed to be equally distributed (e.g., S^{6+} distributes its six valance units equally between the four surrounding oxygen atoms). Of course, this can vary depending on the actual bond-lengths (Brese & O'Keeffe, 1991), which will be accounted for later in this discussion.

Mineral name	Chemical formula	Reference
Meridianiite	$MgSO_4 \cdot 11H_2O$	(Fortes et al., 2008)
synthetic	$MgSO_4 \cdot 9H_2O$	(Fortes et al., 2017b)
Epsomite	$MgSO_4 \cdot 7H_2O$	(Fortes et al., 2006)
Melanterite	$FeSO_4 \cdot 7H_2O$	(Anderson et al., 2007)
Hexahydrite	$MgSO_4 \cdot 6H_2O$	(Zalkin et al., 1964)
Ferrohexahydrite	$FeSO_4 \cdot 6H_2O$	(Vlasov & Kuznetsov, 1963)
Pentahydrite	$MgSO_4 \cdot 5H_2O$	(Baur & Rolin, 1972)
siderotil	$FeSO_4 \cdot 5H_2O$	(Jambor & Traill, 1963)
synthetic*	$MgSO_4 \cdot 5H_2O$	(Wang et al., 2018)
Starkeyite	$MgSO_4 \cdot 4H_2O$	(Baur, 1964a)
Cranswickite	$MgSO_4 \cdot 4H_2O$	(Peterson, 2011)
Rozenite	$FeSO_4 \cdot 4H_2O$	(Baur, 1962)
synthetic	$MgSO_4 \cdot 3H_2O$	(Grevel et al., 2012)
synthetic	$MgSO_4 \cdot 2.5H_2O$	(Ma et al., 2009b)
Sanderite	$MgSO_4 \cdot 2H_2O$	(Ma et al. 2009)
synthetic**	$MgSO_4 \cdot H_2O$	(Meusburger et al., 2020)
Kieserite	$MgSO_4 \cdot H_2O$	(Meusburger et al., 2020)
Szomolnokite	$FeSO_4 \cdot H_2O$	(Meusburger et al., 2019)
synthetic**	$FeSO_4 \cdot H_2O$	(Meusburger et al., 2019)

Table 1.1 All MSHs (blue) and FSHs (red) with known crystal structures that were either identified as minerals or produced synthetically. *synthesised by the high-pressure dehydration of epsomite ** high-pressure polymorphs, not recoverable at ambient pressure.

The fundamental structural units that build up all MSHs and FSHs are MeO_6 octahedra and SO_4 tetrahedra (Figure 1.1). The sulfate oxygens do not donate any hydrogen bonds in any of the thus far discovered crystal structures. The reason for this becomes clear from simple bond-valance considerations:
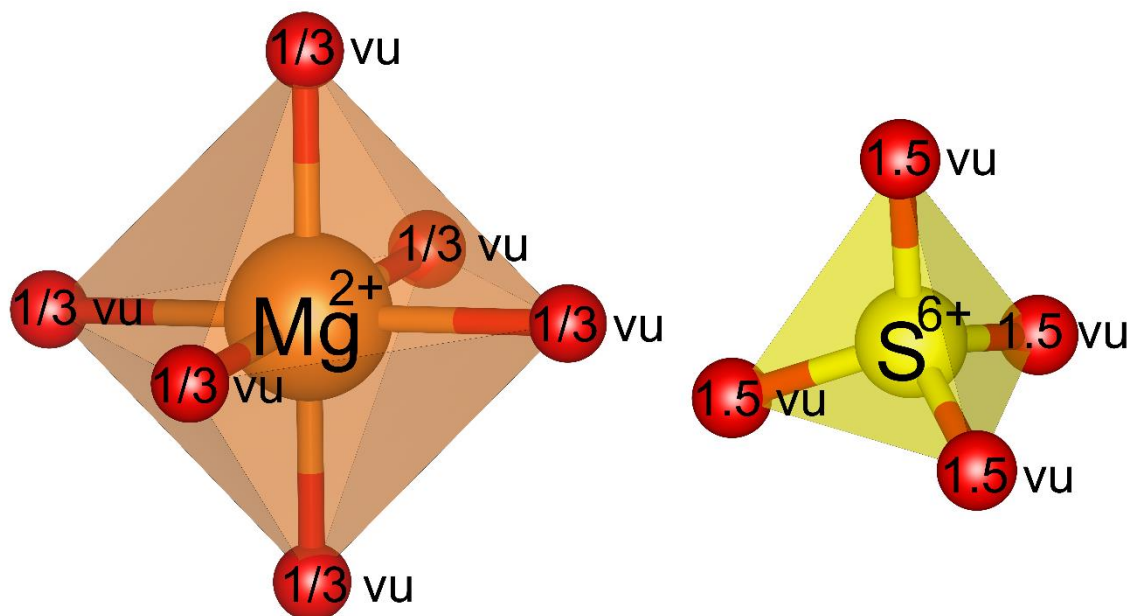
Figure 1.1 Bond-valance in valance units (vu) incident on each of the oxygens from the central cations of the MgO_6 octahedral and SO_4 tetrahedral units. Note that for FSHs the divalent Mg central ion of the octahedral unit is replaced by divalent iron, thus the charge distribution remains unchanged.

The S^{6+} central ion is surrounded by four oxygen anions O^{2-} (Figure 1.1), consequently, 1.5 positive charges are incident on each oxygen.

If just one hydrogen were donated to an oxygen of the SO_4 tetrahedra, forming a hydroxyl group (O – H), 2.5 valance units would be incident on this oxygen, corresponding to a charge oversaturation of 25%. Clearly, the charge oversaturation would be even more pronounced if two hydrogen atoms were donated to the sulfate oxygen, thus explaining the absence of hydroxylated and hydrated oxygens of the sulfate groups in MSHs and FSHs.

The Me cation distributes its two valance units between six oxygens; hence merely ⅓ valance units are incident on each oxygen (Figure 1.1). In a first approximation, if two hydrogen atoms are donated to one of the octahedral oxygens, a total of 2 ⅓ valance units are incident on this oxygen. This corresponds to an oversaturation of just ⅓ valance units. However, the hydrogen atoms are not solely bound to the oxygen of the octahedral unit but also form long-range intermolecular bonds. Consequently, less than two valance units are incident on the oxygen atoms from the two hydrogen atoms, and the oversaturation is smaller than ⅓ valance units. In addition, there is a fundamental relationship between the bond-length and bond-valance (Brown & Altermatt, 1985). Hence the remaining oversaturation is easily compensated for by slightly increasing the distance of the Me – O bond that accepts the hydrogen atoms. A notable example of this mechanism is the mineral kieserite, where the Mg – O bond lengths of the non-hydrated oxygens range from 2.02 – 2.04 Å.
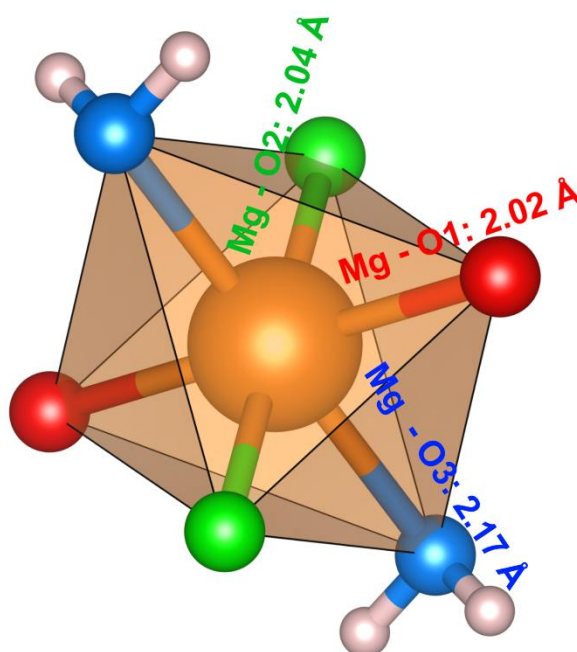
Figure 1.2 Octahedral unit in kieserite, and corresponding Mg - O bond lengths.

In contrast, the distance from the Mg ion to the hydrated oxygen is 2.17 Å (Talla & Wildner, 2019) (Figure 1.2).

By hydrating all oxygens of MeO_6 octahedra, MSHs up to hexahydrite (n = 6) and FSHs up to ferrohexahydrite (n = 6) may be formed (Figure 1.3a). To form higher hydrates, however, interstitial water molecules are necessary (Figure 1.3b) to accommodate the additional water in the crystal structure. MSHs up to n = 11 and FSHs up to n = 7 may be formed this way. Exceptions to this mechanism are pentahydrite ($MgSO_4 \cdot 5H_2O$) and siderotil ($FeSO_4 \cdot 5H_2O$) which feature one interstitial water molecule, although not all oxygens of MeO_6 octahedra are hydrated (Hawthorne & Sokolova, 2012). Notably, although no FSHs with n > 7 were hitherto discovered both meridianiite and $MgSO_4 \cdot 9H_2O$ may incorporate substantial amounts of Fe (Fortes et al., 2012).
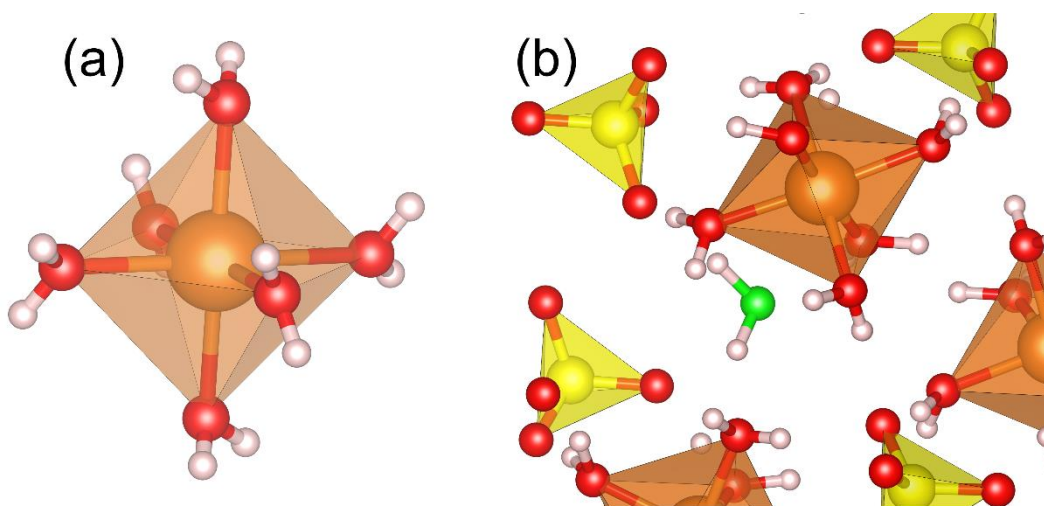
Figure 1.3 (a) fully hydrated $Mg(H_2O)_6$ octahedra. Hydrating the octahedral units allows to build structures up to n = 6. (b) close up view on epsomite (n = 7), in order to achieve hydration states higher than six, interstitial water molecules (green) are necessary.

The formation of the lower hydrates is governed by the undersaturation in charge balance of the non-hydrated MeO_6 and the sulfate oxygens. To achieve charge balance, the MeO_6 and SO_4 units polymerize. For example, a bridging oxygen atom has ⅓ and 1.5 valance units incident from the Me and S cations, respectively. The resulting net charge deficiency is merely ⅙ valance units, which may be easily compensated for by adjusting the bond-lengths. Another mechanism for the oxygen atoms to achieve charge neutrality is the acceptance of hydrogen bonds. This mechanism may dominate to achieve charge neutrality. In the mineral cranswickite, for example, one sulfate oxygen may even compensate for a charge undersaturation of 1.6 valance units by accepting three hydrogen bonds as will be demonstrated in Chapter 5 of this thesis.

Both mechanisms combined give rise to a large diversity of connection schemes observed in the lower hydrates (i.e., n < 6) ranging from 3D frameworks (n = 1, 2), layers (n = 2.5, 3), cyclic dimer units (n = 4), chains (n = 4, 5), isolated dimer units (n = 5) (Figure 1.4).
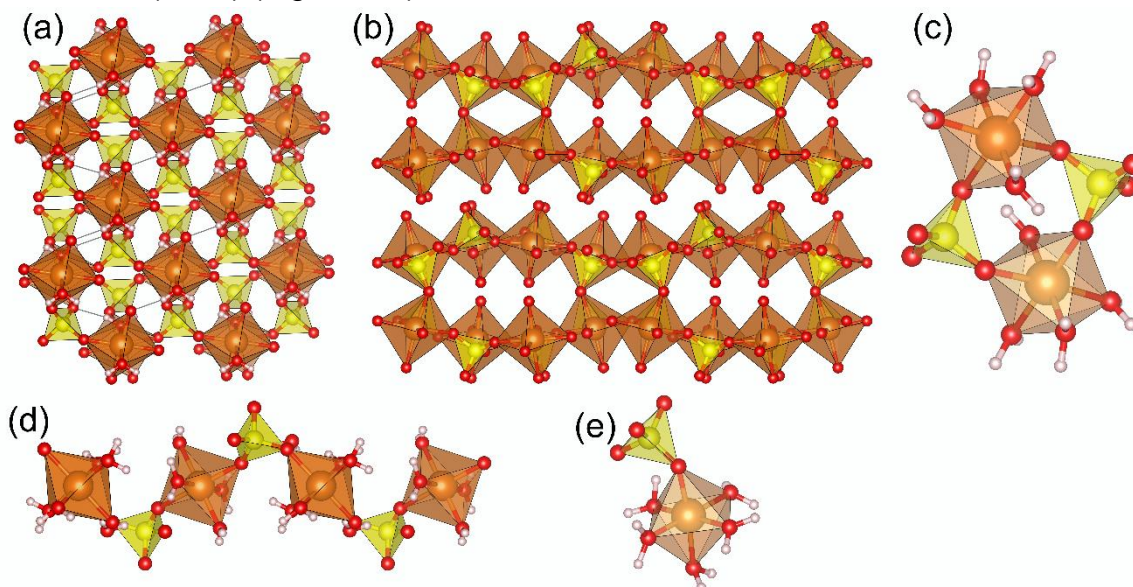
Figure 1.4 Selected examples of the structural diversity found in lower MSHs: (a) 3D framework of kieserite (b) layers in $MgSO_4 \cdot 2.5H_2O$ (c) cyclic dimers in starkeyite (d) chains in pentahydrite (e) isolated dimers of the synthetic polymorph of $MgSO_4 \cdot 5H_2O$. Note that isotypic FSHs have only been discovered for (a), (c) and (d).

1.1.2 High pressure structural stability

The high-pressure behaviour of meridianiite was studied by Fortes et al. (2017b). These authors observed incongruent melting to $MgSO_4 \cdot 9D_2O$ and ice VI at 0.9 GPa and 240 K.

$MgSO_4 \cdot 9D_2O$ itself was studied from 0 to 1 GPa at 240 K (Fortes et al., 2017b). Its compressibility was determined, and no further decomposition was observed.

The compressibility, including its temperature dependence, of epsomite was determined by Fortes et al. (2006) up to 0.45 GPa. Gromnitskaya et al. (2013) studied epsomite up to a pressure of 3 GPa, report four high pressure phases and established their phase boundaries by ultrasonic measurements. Gromnitskaya et al. (2013) also review earlier high-pressure studies of epsomite such as the one by Livshits et al. (1963) and Bridgman (1949), which overall agree reasonably well with their study.

More recently, the crystal structure of the high-pressure "phase V" was determined, which turned out to be a synthetic polymorph of pentahydrite

(MgSO$_4$·5H$_2$O) (W. Wang et al., 2018). The structure of the other high-pressure phases reported by Gromnitskaya et al. (2013) remains to be determined. Importantly, based on an increased background in the neutron diffraction pattern and the appearance of high-pressure ice VII, Gromnitskaya et al. (2013) suggest that the transformation to "phase II" and "phase III" are likely associated with the decomposition of epsomite.

Based on this wide range of evidence for pressure-induced dehydration of both meridianiite and epsomite, there is a considerable interest in the high-pressure behaviour of the lower hydration states. Apart from kieserite, which undergoes a polymorphic phase transition at 2.7 GPa (Meusburger et al., 2020), the high-pressure behaviour of the hydrates with n < 7 remains largely unknown. In our solar system, MSHs may be exposed to pressures as high as 3.45 GPa in the centre of Callisto (Prentice, 1999), hence it is likely that at high-pressure conditions the intermediate and lower hydrates of MSH are the prevalent phases.

Regarding the possible occurrence of FSHs in the interior of icy satellites, from leeching experiments on chondrites, which are believed to constitute the rocky cores of the Galilean moons of Jupiter (McKinnon & Zolensky, 2003), FeSO$_4$ are likely to be a negligible component of the icy mantle (Kargel, 1991). This is also reflected in a much smaller number of high-pressure studies on FSHs as compared to their Mg counterparts. From a thorough search, the only FSH hitherto studied at high-pressure conditions is szomolnokite, which undergoes a structural phase transition at 6.2 GPa (Meusburger et al., 2019).

1.1.3 Variable temperature structural stability

The thermal expansion of meridianiite was determined by Fortes et al. (2008) from 4.2 – 250 K. No phase transition was observed, but interestingly the compound showed negative volume expansions (i.e., volume contraction upon heating) below 55 K. These authors further state that at 274.95 K, meridianiite undergoes incongruent melting to epsomite and brine containing 21.6 wt% MgSO$_4$.

MgSO$_4$·9H$_2$O was never synthesised phase pure, but always as a mixture with either ice or epsomite. In the presence of ice, it slowly transforms to meridianiite at 250 K. The thermal expansion of MgSO$_4$·9H$_2$O was studied from 9 – 260 K by means of high-resolution neutron diffraction with no indication of a polymorphic phase transition (Fortes et al., 2017).

The thermal expansion of epsomite was studied from 1.8 K – 300 K (Fortes et al., 2006), revealing negative linear expansion from 30 – 250 K. No conclusive evidence for a structural phase transition was reported, but these authors state that a very subtle structural distortion upon cooling may not be ruled out with absolute certainty. Epsomite readily transforms to hexahydrite at 298 K and relative humidity conditions lower than 50 – 55 %(Chou & Seal, 2003). At even lower relative humidity of 33 and 3 %, transformations to starkeyite and the synthetic trihydrate were observed, respectively (A. Wang et al., 2016; F. Wang & Zhang, 2011).

The thermal expansion of hexahydrite was just most recently determined by Maynard-Casely et al. (2021) from 180 – 315 K using synchrotron powder diffraction. The volume thermal expansion is positive over the entire temperature range. However, the anisotropy of the thermal expansion was not assessed and is still unknown. Regarding a putative polymorph of hexahydrite reported by Maynard-Casely et al. (2021), their proposed structure is unambiguously wrong, as is outlined in Chapter 6 of this thesis (Fortes & Meusburger, 2022).

The thermal expansion and low-temperature stability of pentahydrite, starkeyite, cranswickite, sanderite, and synthetic $MgSO_4 \cdot 2.5H_2O$ were never characterised, and, therefore, presenting a gap in the scientific literature. The variable temperature behaviour and properties of starkeyite is of interest considering its likely occurrence on Mars, as will be outlined later in this introduction.

Synthetic $MgSO_4 \cdot 5H_2O$, a polymorph of the mineral pentahydrite, was characterized using in-house X-ray diffraction upon heating from 100 – 220 K, after which the diffraction pattern started to change and the sample eventually transformed to epsomite (W. Wang et al., 2018). However, the thermal expansion of synthetic $MgSO_4 \cdot 5H_2O$ was not determined.

$MgSO_4 \cdot 3H_2O$ occurs as a synthetic phase and was studied by Fortes et al. (2010) using single crystal, and powder neutron diffraction from 295 – 8 K. At 245 K it undergoes a structural phase transition. The structure of the low-temperature phase and thermal expansion, however, are yet to be determined (Fortes et al., 2010).

The thermal expansion of kieserite was most recently studied in the 15 – 313 K temperature range (Wildner et al., 2022), with these authors reporting the

absence of a structural phase transition but a very pronounced negative linear thermal expansion over the entire temperature range under investigation.

Wildner et al. (2022) further studied the thermal expansion of other kieserite-type compounds (Me = Ni, Co, Mn, Fe) from 15 to 313 K. From a thorough search of the literature, this study is the only characterisation of the thermal expansion of any FSH. However, the crystal structure of melanterite was studied at room temperature (Baur, 1964b) and 120 K (Fronczek et al., 2001); there was no indications for a structural phase transition upon cooling. In addition, the stability of melanterite, rozenite and szomolnokite, was studied using Raman spectroscopy from room temperature to 8 K (Chio et al., 2007). This study reports that rozenite undergoes two structural phase transitions at 240 – 190 and 140 – 90 K. Szomolnokite and melanterite did not show any indications for a structural phase transition. A low-temperature Mössbauer spectroscopy study, however, revealed that szomolnokite undergoes a magnetic order-disorder transformation at 29.6 K (Alboom et al., 2009).

The temperature-humidity stability of FSH, was extensively studied. At 294 K and 45 % RH, melanterite of end-member composition transforms to rozenite, whereas Cu-bearing melanterite transforms to siderotil (Jambor & Traill, 1963). At an even higher temperatures of 323 K and RH levels of 65 – 30 %, a transformation to szomolnokite was observed (A. Wang et al., 2016).

Regarding the temperature range, MSHs and FSHs are exposed to on the Martian surface, Witzke et al. (2007) suggest 220 – 280 K is typical for the equatorial region, where these hydrates form extended deposits (see next section). In winter, at the poles, temperatures may be as low as 120 K (Bougher et al., 2015). On the surface of the icy satellites of Jupiter, such as Europa (Ashkenazy, 2019), MSHs may be exposed to even lower temperatures, i.e., diurnal and seasonal temperature ranges of 94 – 98 K at equatorial and from 35 – 62 K at polar latitudes. It should be noted that, despite being promising candidate minerals for the Martian sulfate deposits, FSHs are not expected to be rock-forming minerals on the icy satellites of Jupiter.

1.1.4 Occurrence

1.1.4.1 Earth

MSHs are ubiquitous minerals on the surface of the Earth and have been identified on every continent (Mindat, 2022). Extended deposits, however, are mostly limited to subsurface environments (e.g., Strassfurt, Sachsen-Anhalt, Germany (Cadell, 1885)) since MSHs are highly water soluble (Autenrieth & Braune, 1960) and therefore are readily dissolved on the Earth's surface. Subsurface deposits are of considerable economic importance since MSHs are an important fertilizer used in horticulture (Z. Wang et al., 2020). Other rare but notable occurrences of MSHs are in saline sulfate-rich lakes such as Spotted Lake, British Columbia, Canada (Fortes et al., 2017b) where MSHs precipitate from the briny lake water. In terrestrial aqueous environments, it was observed that meridianiite may form if the temperature is sufficiently cold, e.g. at Spotted Lake during the winter months (Cannon, 2012), as inclusions in sea ice in the Lake Saroma coastal lagoon, Japan, or in Antarctic continental ice cores (Elif Genceli et al., 2009).

Interestingly, $MgSO_4 \cdot 9H_2O$ can be produced simply by placing brine sampled from Spotted Lake into the freezer, indicating that it could occur naturally on Earth as a mineral (Fortes et al., 2017b). From the phase diagram it is evident that the stability field of epsomite covers most of the temperature range relevant to aqueous systems on Earth and it is therefore the MSH that typically precipitates (Figure 1.5). At exceptionally high temperatures (e.g., hydrothermal vents (Blažić & Moreau, 2016)) and/or ionic activity, hexahydrite and kieserite may directly precipitate from brine (Autenrieth & Braune, 1960). In addition, pentahydrite, starkeyite, sanderite, and the synthetic $MgSO_4 \cdot 3H_2O$ and $MgSO_4 \cdot 2.5\ H_2O$, may form directly from aqueous solution (Autenrieth & Braune, 1960; von Hodenberg & Kühn, 1967) under such conditions. However, it is noted by these authors that these phases are metastable and often only crystallize in the presence of seed crystals and are, therefore, absent in the phase diagram (Figure 1.5). More recent evidence for the direct precipitation of pentahydrite from the brine of chondritic compositions is given by Thompson et al. (2021).
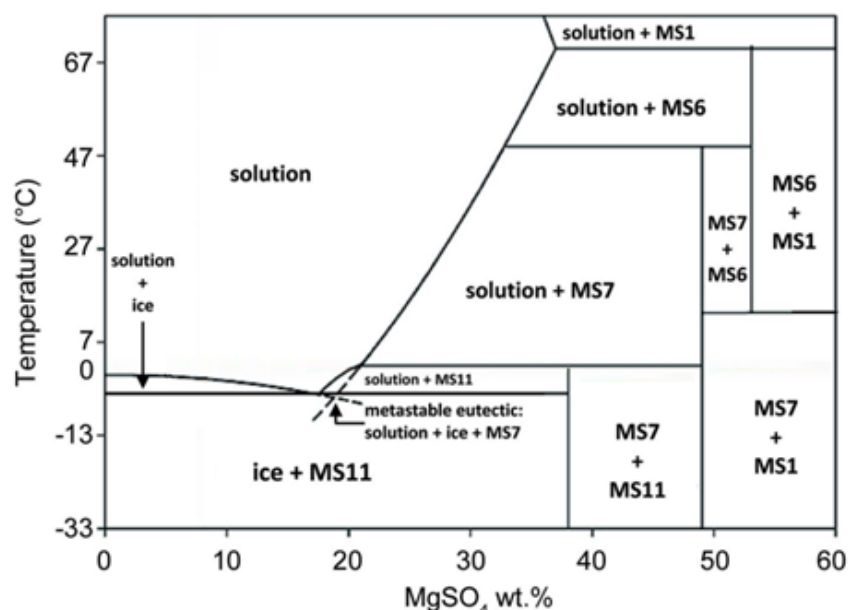
Figure 1.5 Phase diagram for the MgSO$_4$ – H$_2$O system. Modified from Thompson et al. (2021).

FSH typically form as weathering products of sulfide minerals, and, therefore, commonly occur in the vicinity of active and abandoned mines as efflorescence on the primary ore minerals (Jambor et al., 2000). At temperatures that typically prevails in terrestrial aqueous environments, melanterite is the thermodynamically stable phase. Rozenite and szomolnokite may precipitate from solution at temperatures exceeding 329.75 K and 337.6 K, respectively (Fraenckel, 1907).

Both, MSHs and FSHs are sensitive to changes in RH and temperature (A. Wang et al., 2016), and, therefore, readily de- or rehydrate, giving rise to the large diversity of MSHs and FSHs identified as minerals in nature.

1.1.4.2 Mars

Mars is a particularly sulfur-rich planet with an average SO$_3$ content of 6.16%, compared to values of just 0.035% SO$_3$ found in the Earth's crust (Barkatt & Okutsu, 2022). One reason for this discrepancy is that a significant fraction of sulfur-bearing minerals on the Earth's surface dissolve and the constituents are then discharged into the oceans (Barkatt & Okutsu, 2022). On Mars, sulfur typically occurs as sulfide and sulfate minerals, with sulfates being the likely dominant speciation (King & McLennan, 2010). Sulfates have been observed at all latitudes (Figure 1.6), and MSHs, in particular, were identified in both orbiter (Milliken et al., 2010) and rover (Farley et al., 2022; Rapin et al., 2019; Vaniman et al., 2018) missions. Sulfates may be even more common as indicated by

Figure 1.6 since it was most recently demonstrated that as little as 10 wt% of clay minerals obscure the infrared-reflectance signature of MSHs (Sheppard et al., 2022).
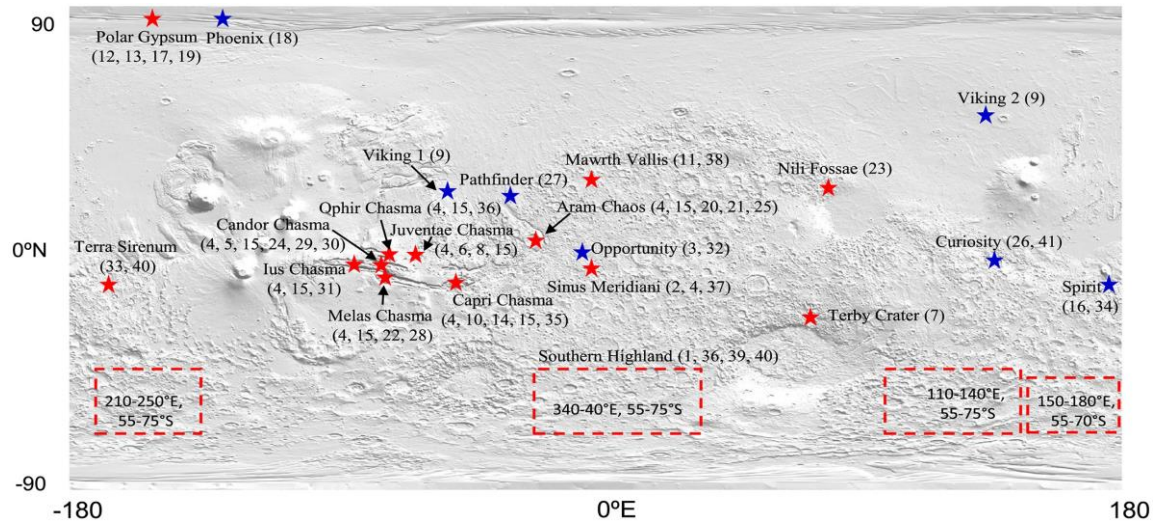
Figure 1.6 Locations where sulfates have been identified on Mars. Red stars indicate observation from orbit, blue stars by rover. Figure from Wang et al. (2016)

Of particular interest for Martian geology are extended sulfate deposits that occur in the equatorial region of Mars and are several kilometres thick (Bishop et al., 2009; Roach et al., 2010). Infrared-reflectance data measured from orbit indicates that these deposits likely consist of alternating layers of monohydrated sulfates (i.e., kieserite and/or szomolnokite) and a polyhydrated sulfate phase (Figure 1.7).
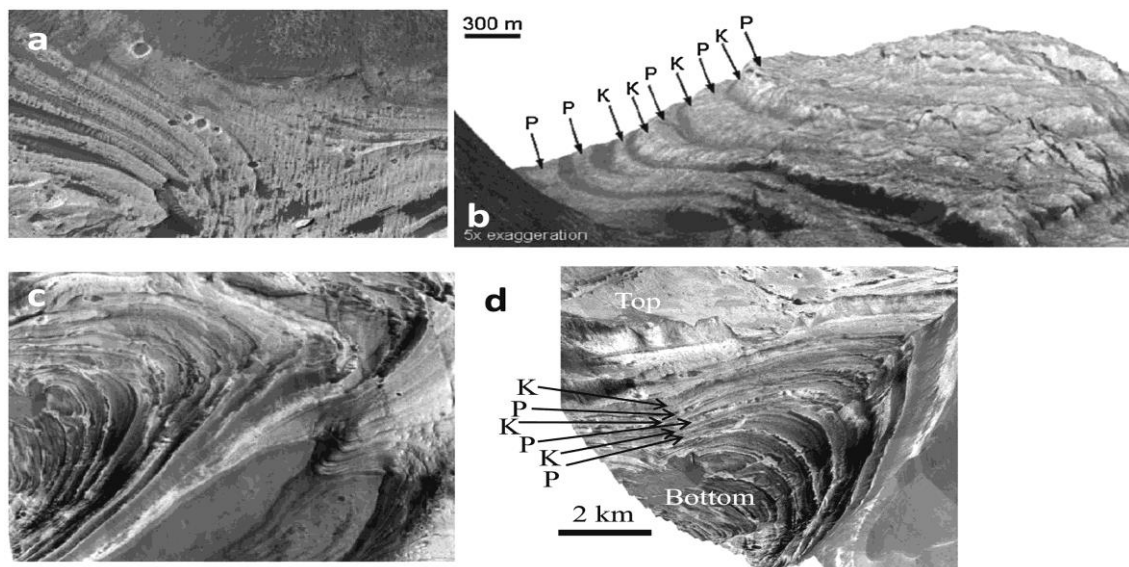
Figure 1.7 Sulfate deposits found in the equatorial region of Mars. P = polyhydrated sulfate phase of unknown hydration state, K = Kieserite. Figure from Wang et al. (2016).

Due to the spectral similarities of MSHs and FSHs, assigning any particular mineral to the spectra collected from the polyhydrated sulfate deposits is challenging (A. Wang et al., 2016). However, it was noted that starkeyite and

its isotypic ferrous counterpart rozenite ($FeSO_4 \cdot 4H_2O$) match the spectral signature very well (Carter et al., 2013; A. Wang et al., 2016). Bishop et al. (2009) report that at most locations szomolnokite matches the spectral signal from the monohydrated phase slightly better than kieserite.

This evidence for a MSHs and/or FSH-rich mineralogy in these deposits agrees well with the hypothesis that they formed by the evaporation of fluids involved in the aqueous alteration of Martian basalt (Tosca et al., 2005). Since basalt is rich in iron and magnesium, one would expect the weathering product to be an iron or magnesium-bearing sulfate (Bibring et al., 2005) or likely a sulfate mineral of intermediate composition.

Interestingly, these deposits are associated with a transition in stratigraphy from a clay-bearing to a sulfate-bearing unit. While clay minerals exhibit a low solubility and readily precipitate, many sulfate minerals are highly soluble and require very high ionic concentrations to form (Tosca et al., 2011). For this reason, it was suggested that the observed transition in mineralogy reflects a change in the Martian climate from wetter to dryer conditions (Milliken et al., 2010). The Mars rover Curiosity is currently exploring the stratigraphic boundary between clay and sulfate layers. Evolved gas (Smith et al., 2022) and chemical analysis (Rapin et al., 2019) using Curiosity's SAM and ChemCam instruments, as well as infrared-reflectance data collected by CRISM (Milliken et al., 2010), all indicate the presence of MSHs at Gale crater, Curiosity's landing site. However, these minerals are absent in the XRD patterns collected using the CheMin instrument, suggesting they are in the amorphous state (Smith et al., 2022). This is curious since MSHs typically precipitate as crystalline materials from aqueous solutions (Autenrieth & Braune, 1960). Based on these findings by Curiosity there are two possibilities. First of all, some MSHs, such as hexahydrite, readily turn amorphous under low atmospheric pressures. On Mars the atmospheric pressure is 6 mbar of mostly CO_2 (Haberle, 2015).

It is not only hexahydrite that turns amorphous under such conditions, but also some FSHs such as rozenite and melanterite (A. Wang & Zhou, 2014). Hence these minerals might also have turned amorphous and are therefore absent in the CheMin data. Another factor that may contribute to the very high apparent abundance of X-ray amorphous materials (i.e., 15 - 70 wt%, Smith et al. 2018) is that they were detected by CheMin in dry environmental conditions inside its sample chamber (<1% RH Bristow et al. 2015); this may alter the state

of the hydrous phases prior to or during analysis. For example, the dehydration of gypsum to bassanite induced by the dry conditions inside CheMin was observed (Vaniman et al., 2018). Laboratory experiments revealed that hexahydrite ($MgSO_4 \cdot 6H_2O$) and starkeyite ($MgSO_4 \cdot 4H_2O$) turn amorphous (Vaniman et al., 2004), whereas kieserite ($MgSO_4 \cdot H_2O$) appears to be stable under such dry conditions (Chipera & Vaniman, 2007). Based on these laboratory experiments, Vaniman et al. (2018) suggested that crystalline MSHs could be amorphized by the low relative humidity (RH) conditions inside CheMin. Hence, from the Curiosity data, not much can be said with absolute certainty about the hydration state and crystallinity of MSHs on Mars, other than that chemical analysis indicates their presence, but they are so far absent in the XRD data.

In early 2021, with the landing of the Perseverance rover, Raman spectroscopic investigations of Martian soil became possible (SuperCam (Wiens et al., 2020) and Sherloc (Bhartia et al., 2021) instruments). Raman spectroscopy has proven very effective in discriminating between various sulfate mineral species (Košek et al., 2017) and thus appears well-suited to identify crystalline and amorphous MSHs and FSHs on the Martian surface. Moreover, both Raman spectrometers analyse the samples *in-situ*, preventing the potential amorphization induced by the dry conditions inside the rover. Importantly, Raman spectra of MSHs were most recently collected by Perseverance (Farley et al., 2022), but no attempt was made to determine crystallinity or hydration state. It will be interesting to see more data from Perseverance over the coming years, which might shed light on the hydration state and crystallinity of MSHs and FSHs on the Martian surface.

1.1.4.3 Icy satellites

MSHs have been identified not only on Mars and Earth, but also on numerous other celestial bodies. An occurrence of the utmost importance is on the surface of the outer three Galilean moons (i.e. Europa, Ganymede, and Callisto), where these minerals were identified by the Galileo near-infrared mapping spectrometer (McCord et al., 1998a, 2001). Crucially on Europa, MSHs occur in disrupted areas (e.g., lineaments, chaotic terrain), which indicates an endogenic origin. Based on these findings, it was proposed that the subsurface ocean likely exhibits a $MgSO_4$-rich chemistry (McCord et al., 1998b). In the particular case of Europa, however, an endogenic origin for the MSHs detected

on Europa's surface is not beyond doubt: Brown & Hand (2013), for example, suggested an exogenic origin of MSHs through the radiolysis of endogenic $MgCl_2$ by sulfur ion bombardment from the neighbouring moon Io.

Nevertheless, MSHs may also be considered as candidate rock-forming minerals in the icy mantles of the two outermost Galilean moons, Ganymede and Callisto (McCord et al., 2001), which both orbit Jupiter at a substantially greater distance from Io. The widespread occurrence of MSHs in the outer solar system is not particularly surprising, considering that they account for a major part of the soluble mass fractions of carbonaceous chondrites (Kargel, 1991), which likely formed the rocky interior of the icy moons of Jupiter and Saturn (Néri et al., 2020).

1.1.5 Relevance for space exploration

As I have outlined in the previous sections, MSHs and FSHs have displayed remarkable structural diversity, complex phase relations and occur at numerous locations throughout the solar system. The following section outlines why the identification of such minerals and differentiation between the various hydration states is important.

Messengers from the past: MSHs and FSHs likely originate from one of the last episodes of aqueous activity involving surface waters. As such, investigating Martian sulfate deposits is critical to understanding the planet's transition from a wet climate with lakes and rivers to today's dry and inhospitable conditions (Bibring et al., 2006; Bristow et al., 2021).

Prime targets for the search for extra-terrestrial life: MSHs and FSHs on Mars are potentially of evaporitic origin and therefore may contain fluid inclusions. These could preserve the chemistry or biosignatures from these early Martian surface waters (François et al., 2016). However, the deposition of the sulfate strata could have also been detrimental to the preservation of organics on the Martian surface. Recently, Bristow et al. (2021) found indications for the destruction of clay minerals likely induced by dense sulfate-rich brine at Gale crater. They hypothesise that the dense sulfate-rich brine could have infiltrated the underlying clay layers, breaking down the clay minerals and thereby destroying potential mineral-organic associations. However, Bristow et al. (2021) also note that the organics could have been re-absorbed onto the surface of

sulfate minerals. In any case, it is critical to be able to identify sulfate minerals on the Martian surface *in-situ*, even if it is just to identify clay minerals not associated with them.

Potential resources for space exploration: Depending on their hydration state, MSHs may contain 7.6 wt% – 17.6 wt% Mg and 13.0 – 62.2 wt% H_2O, which are valuable resources for horticulture (Z. Wang et al., 2020). FSHs equally may be a valuable resource for the extraction of water based on their water content of 11.5 – 45.3 wt%. Most recently, the use of sulfur cement to construct habitats (Figure 1.8) on Mars was proposed (Barkatt & Okutsu, 2022) with MSHs and FSHs containing 10.1 – 23.3 wt% and 11.5 – 18.9 wt% S, respectively. As these authors further noted, such *in-situ* resource utilisation is key for sustainable human activity on Mars. Since MSHs and FSHs form extended deposits in the equatorial region of Mars, they might be valuable resources for the human exploration of Mars. Therefore, it is critical to determine the chemistry and hydration state of these deposits to assess their potential as a resource for H_2O, Mg, and S.
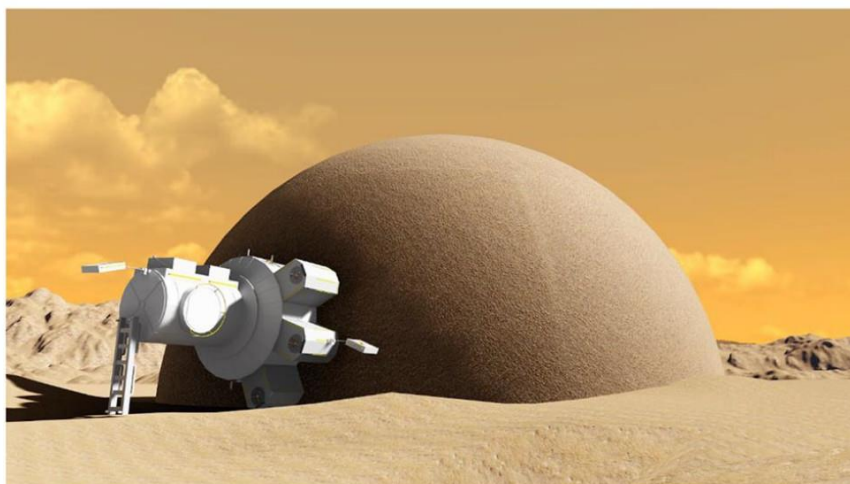
Figure 1.8 Artists rendering of a sulfur cement habitat on Mars. From Barkatt and Okutsu (2022).

As for the icy satellites of Jupiter, MSHs are likely major rock-forming minerals in their icy mantle. Thus, knowledge of their physical properties is critical to model the radial density structure of the satellites and understanding mantle processes (Hogenboom et al., 1995; Johnson et al., 2017; Vance & Brown, 2013). In addition, MSHs may equally serve as a resource on the icy satellites of the outer solar system, but mainly for S and Mg, since water ice is abundant on such celestial bodies.

1.2 Rationale of the thesis and work done

This thesis has involved first-principles simulations of seven crystalline structures (i.e., epsomite ($MgSO_4 \cdot 7H_2O$), starkeyite ($MgSO_4 \cdot 4H_2O$), cranswickite ($MgSO_4 \cdot 4H_2O$), rozenite ($FeSO_4 \cdot 4H_2O$), gypsum ($CaSO_4 \cdot 2H_2O$), carbon dioxide (CO_2), and benzene (C_6H_6)). In addition, the thermal expansion of three sulfate minerals (rozenite, starkeyite, and cranswickite) was for the first time characterised using neutron powder diffraction at HRPD, ISIS Neutron and Muon Source, UK. Furthermore, starkeyite and rozenite were also studied using high-resolution synchrotron X-ray diffraction at I11, Diamond Light Source, UK. Moreover, a contribution was made to a comment clearly outlining why the structure of a polymorph of hexahydrite, most recently proposed in the literature, is unambiguously wrong. Lastly, a contribution was made to the commissioning of an optical centre stick that allows for the simultaneous acquisition of neutron diffraction and Raman spectroscopy data at the HRPD instrument.

Chapter 3: Elasticity of selected icy satellite candidate materials (CO_2, C_6H_6, $MgSO_4 \cdot 7H_2O$ and $CaSO_4 \cdot 2H_2O$) revisited by dispersion corrected density functional theory

Right from the start of the thesis, I wanted to complement my experimental findings with quantum mechanical modelling within the framework of density functional theory (DFT). I also knew that I would face one particular problem: DFT fails to accurately model dispersion forces, which are very important for the loosely packed solids I was going to study. In practice, one needs to apply a correction to standard DFT to obtain accurate results. Due to the repeated postponement of my beam times at Diamond and ISIS during the CoVid pandemic, my supervisors and I decided to use this time for an extensive DFT benchmarking study involving numerous exchange-correlation functionals and dispersion corrections. My motivation was to investigate which combination of exchange-correlation functional and dispersion correction yields the most accurate results in materials where the long-range interactions are dominated by hydrogen bonding or dispersion forces.

I studied the sulfate minerals gypsum and epsomite, which both are experimentally very well characterised over a large temperature and pressure range, a criterion of the utmost importance for a study benchmarking computational predictions against experimental data. Furthermore, we have also

studied CO_2 and C_6H_6, since they are also very well experimentally characterised, and dispersion forces dominate their intermolecular interactions.

The first benchmarking category was the ground-state geometry, knowledge of which is of particular importance to compare my results with the low-temperature structures that my colleagues and I have experimentally determined using neutron diffraction.

Furthermore, we have benchmarked the performance in predicting compressibility and elastic properties. The reason for this is that high-pressure studies are experimentally very demanding. Computationally, however, the behaviour of minerals at a pressure of hundreds of GPa is very easily accessible (Rech & Perottoni, 2020). Compressibility data for abundant mantle minerals is essential to accurately model planetary bodies' radial density structures. This is of great importance for sulfate minerals since they are likely rock-forming minerals in the outer three Galilean moons and thus may be subjected to pressures of up to 3.45 GPa, corresponding to the central pressure of Calisto (Prentice, 1999).

In addition to the bulk elastic properties, the full elastic tensor can also be determined, which, combined with knowledge of the density, allows for the calculation of seismic wave velocities (Jaeken & Cottenier, 2016). Seismic studies are essential for the accurate characterisation of planetary interior structures but require data on the elastic properties of likely constituent minerals. With the potential deployment of seismic stations on icy worlds such as Europa and Titan envisioned for the near future (Lorenz et al., 2018; Pappalardo et al., 2013), a campaign of study into the elasticity of potential icy satellite candidate minerals is of paramount importance. Assessing the role of first-principles computer simulations to this problem is of particular interest for these materials since complex sample handling, phase transitions, and the difficulty of obtaining single crystals often greatly complicate the experimental determination of the full elastic tensor.

Chapter 4: Low-temperature crystallography and vibrational properties of rozenite (FeSO₄·4H₂O), a candidate mineral component of the polyhydrated sulfate deposits on Mars

This study was motivated by low-temperature Raman spectroscopy investigations performed by Chio et al. (2007) on rozenite. Interestingly, these authors report vibrational mode splitting at 240 – 190 K and 140 – 90 K and interpreted this as evidence for two structural phase transitions. Notably, the first transition is well within the temperature range relevant to the Martian surface. As outlined in detail earlier in this introduction, rozenite is a candidate mineral component of the polyhydrated sulfate deposits on the surface and in the subsurface of Mars. Hence if rozenite underwent a phase transition at these temperatures, this new phase would be a promising candidate to occur in the Martian regolith. To investigate these phase transitions and potentially determine the crystal structure of these putative low-temperature polymorphs, high-resolution neutron time-of-flight measurements were carried out from 290 – 21 K. Furthermore, the vibrational properties of rozenite were modelled from first principles to assign the vibrational modes, which is critical for determining if vibrational modes indeed split upon cooling as suggested by Chio et al. (2007).

Lastly, we demonstrated how combining Raman spectroscopy and X-ray diffraction of the same sample material sealed inside a glass capillary and complemented by first-principles calculations yields accurate reference Raman spectra. This workflow appears to be ideally suited for constructing a reliable Raman spectroscopic database for planetary exploration. Such a database is critical to shed light on the geological past and identify resources for the future colonization of planetary bodies throughout the solar system.

Chapter 5: Phase-transition type negative volume expansion and anisotropic X-ray expansion in magnesium sulfate tetrahydrate

Next to rozenite, the isotypic Mg-endmember starkeyite is also considered a promising candidate to form the bulk of the massive equatorial sedimentary sulfate deposits. Like rozenite, it matches the infrared reflectance spectra measured from these deposits very well. In addition, laboratory experiments by Wang et al. (2016) have revealed that starkeyite persists over a wider temperature and humidity range than rozenite. For this reason, we have

characterised of the structural properties of starkeyite under Mars-relevant temperature conditions.

I have measured the thermal expansion of starkeyite using high-resolution synchrotron X-ray diffraction and neutron diffraction. Curiously, the results obtained with both methods are in stark contrast. We identified that the reason for this behaviour is radiation damage, induced by the intense synchrotron X-ray beam. The radiation damage manifests in a volume expansion of the material and a hysteresis in the thermal expansion properties. Synchrotron X-ray induced material expansion was just most recently observed in inorganic compounds (Coates et al., 2021). In this study, we introduced the X-ray expansion tensor r_{ij}, thus laying a solid theoretical foundation for the quantification of this phenomenon, which poses an intriguing avenue for future research in functional materials.

To further investigate the low-temperature stability, we performed DFT calculations on starkeyite and its polymorph cranswickite, a rare mineral on Earth hitherto identified at just two localities (Peterson, 2011; Zayakina., 2019). These calculations suggested that cranswickite is the thermodynamically stable polymorph at low temperatures, indicating that starkeyite could potentially transform into cranswickite under the low-temperature conditions prevailing on present-day Mars.

Motivated by this intriguing computational prediction, we were keen to experimentally investigate the stability of cranswickite. One major obstacle we had to overcome was that cranswickite had never been synthesised in the laboratory, and natural samples are very rare.

I managed to identify a synthesis route and produce sufficient quantities of deuterated cranswickite to carry out a neutron diffraction experiment. To determine its stability field, we have studied the compound from 10 to 340 K using neutron diffraction, and from 0 to 5 GPa using DFT. Although the study of cranswickite was solely motivated by the importance of MSHs for planetary science, cranswickite revealed very interesting thermal expansion properties, which might be of great interest for the material science community.

Chapter 6: Comment on Mineral Diversity on Europa: Exploration of Phases Formed in the MgSO$_4$–H$_2$SO$_4$–H$_2$O Ternary

While I was working on this project, Maynard-Casely et al. (2021) published a paper reporting a new polymorph of hexahydrite. I have identified that the reported structure is unambiguously incorrect. After showing these findings to my ISIS supervisor A. Dominic Fortes, we decided to write a comment highlighting where this error could have been detected at various stages of the analysis, writeup, and submission process and make recommendations to avoid repetition of the mistake. The order of authorship reflects the fact that A. Dominic Fortes contributed most to the comment, including writing of the original draft.

Supplementary 8.1: Technical report on the commissioning of the Raman optical stick

As an ISIS facility development student, I was directly involved with the commissioning and improvement of the *in-situ* Raman spectroscopy equipment developed for use on HRPD. The optical centre stick allows for the simultaneous acquisition of Raman spectra and neutron diffraction data. When combining complementary analytical techniques, acquiring both datasets in the very same experiment is favourable since it is not always possible to replicate the exact same experimental conditions, which may introduce ambiguities and uncertainties in the data interpretation. My main contribution was the development of a Python code that enables the scripting of neutron powder diffraction data and Raman spectrum co-acquisition. Importantly, the code is easily amendable to run all kinds of equipment in parallel with the HRPD instrument and other ISIS instruments controlled by the IBEX software. Lastly, results from the commissioning of the stick are briefly presented.

1.3 References

Alboom, A. van, de Resende, V.G., de Grave, E., and Gómez, J.A.M. (2009) Hyperfine interactions in szomolnokite ($FeSO_4 \cdot H_2O$). Journal of Molecular Structure, 924–926, 448–456.

Anderson, J.L., Peterson, R.C., and Swainson, I.P. (2007) The atomic structure and hydrogen bonding of deuterated melanterite, $FeSO_4 \cdot 7D_2O$. The Canadian Mineralogist, 45, 457–469.

Ashkenazy, Y. (2019) The surface temperature of Europa. Heliyon, 5, e01908.

Autenrieth, H., and Braune, G. (1960) Die Lösungsgleichgewichte des reziproken Salzpaares Na_2Cl_2 + $MgSO_4$ + H_2O bei Sättigung an NaCl unter besonderer Berücksichtigung des metastabilen Bereichs. Kali und Steinsalz , 3, 15–30.

Barkatt, A., and Okutsu, M. (2022) Obtaining elemental sulfur for Martian sulfur concrete. Journal of Chemical Research, 46.

Baur, W.H. (1962) Zur Kristallchemie der Salzhydrate. Die Kristallstrukturen von $MgSO_4.4H_2O$ (leonhardtit) und $FeSO_4.4H_2O$ (rozenit). Acta Crystallographica, 15, 815–826.

——— (1964a) On the crystal chemistry of salt hydrates. II. A neutron diffraction study of $MgSO_4.4H_2O$. Acta Crystallographica, 17, 863–869.

——— (1964b) On the crystal chemistry of salt hydrates. III. The determination of the crystal structure of $FeSO_4 \cdot 7H_2O$ (melanterite). Acta Crystallographica, 17, 1167–1174.

Baur, W.H., and Rolin, J.L. (1972) Salt hydrates. IX. The comparison of the crystal structure of magnesium sulfate pentahydrate with copper sulfate pentahydrate and magnesium chromate pentahydrate. Acta Crystallographica Section B, 28, 1448–1455.

Bhartia, R., Beegle, L.W., DeFlores, L., Abbey, W., Razzell Hollis, J., Uckert, K., Monacelli, B., Edgett, K.S., Kennedy, M.R., Sylvia, M., and others (2021) Perseverance's Scanning Habitable Environments with Raman and Luminescence for Organics and Chemicals (SHERLOC) Investigation. Space Science Reviews, 217, 58.

Bibring, J.-P., Langevin, Y., Mustard, J., Poulet, F., Arvidson, R., Gendrin, A., Gondet, B., Mangold, N., Berthé, M., Gomez, C., and others (2006) Global Mineralogical and Aqueous Mars History Derived from OMEGA/Mars Express Data. Science (New York, N.Y.), 312, 400–404.

Bishop, J.L., Parente, M., Weitz, C.M., Noe Dobrea, E.Z., Roach, L.H., Murchie, S.L., McGuire, P.C., McKeown, N.K., Rossi, C.M., Brown, A.J., and others (2009) Mineralogy of Juventae Chasma: Sulfates in the light-toned mounds, mafic minerals in the bedrock, and hydrated silica and hydroxylated ferric sulfate on the plateau. Journal of Geophysical Research: Planets, 114.

Blažić, L., and Moreau, J. (2016) Discovery of Lower Cretaceous hydrothermal vent complexes in a late rifting setting, southern North Sea: Insights from 3D imaging. Journal of the Geological Society, 174.

Bougher, S.W., Pawlowski, D., Bell, J.M., Nelli, S., McDunn, T., Murphy, J.R., Chizek, M., and Ridley, A. (2015) Mars Global Ionosphere-Thermosphere Model: Solar

cycle, seasonal, and diurnal variations of the Mars upper atmosphere. Journal of Geophysical Research: Planets, 120, 311–342.

Brese, N.E., and O'Keeffe, M. (1991) Bond-valence parameters for solids. Acta Crystallographica Section B, 47, 192–197.

Bridgman, P.W. (1949) Linear Compressions to 30,000 kg/cm^2, including Relatively Incompressible Substances. Proceedings of the American Academy of Arts and Sciences, 77, 189–234.

Bristow, T.F., Bish, D.L., Vaniman, D.T., Morris, R. v, Blake, D.F., Grotzinger, J.P., Rampe, E.B., Crisp, J.A., Achilles, C.N., Ming, D.W., and others (2015) The origin and implications of clay minerals from Yellowknife Bay, Gale crater, Mars. American Mineralogist, 100, 824–836.

Bristow, T.F., Grotzinger, J.P., Rampe, E.B., Cuadros, J., Chipera, S.J., Downs, G.W., Fedo, C.M., Frydenvang, J., McAdam, A.C., Morris, R. v, and others (2021) Brine-driven destruction of clay minerals in Gale crater, Mars. Science, 373, 198–204.

Brown, I.D., and Altermatt, D. (1985) Bond-valence parameters obtained from a systematic analysis of the Inorganic Crystal Structure Database. Acta Crystallographica Section B, 41, 244–247.

Brown, M.E., and Hand, K.P. (2013) Salts and Radiation Products on the Surface of Europa. The Astronomical Journal, 145, 110.

Cadell, H.M. (1885) The salt deposits of Stassfurt. Transactions of the Edinburgh Geological Society, 5, 92–103.

Cannon, K.M. (2012) Spotted Lake: Analog for Hydrated Sulfate Occurrences in the Last Vestiges of Evaporating Martian Paleolakes.

Carter, J., Poulet, F., Bibring, J.-P., Mangold, N., and Murchie, S. (2013) Hydrous minerals on Mars as seen by the CRISM and OMEGA imaging spectrometers: Updated global view. Journal of Geophysical Research: Planets, 118, 831–858.

Chio, C., Sharma, S., and Muenow, D. (2007) The hydrates and deuterates of ferrous sulfate ($FeSO_4$): A Raman spectroscopic study. Journal of Raman Spectroscopy, 38, 87–99.

Chipera, S.J., and Vaniman, D.T. (2007) Experimental stability of magnesium sulfate hydrates that may be present on Mars. Geochimica et Cosmochimica Acta, 71, 241–250.

Chou, I.-M., and Seal, R.R. (2003) Determination of Epsomite-Hexahydrite Equilibria by the Humidity-Buffer Technique at 0.1 MPa with Implications for Phase Equilibria in the System $MgSO_4$-H_2O. Astrobiology, 3, 619–630.

Coates, C.S., Murray, C.A., Boström, H.L.B., Reynolds, E.M., and Goodwin, A.L. (2021) Negative X-ray expansion in cadmium cyanide. Materials Horizons, 8, 1446–1453.

Elif Genceli, F., Horikawa, S., Iizuka, Y., Sakurai, T., Hondoh, T., Kawamura, T., and Witkamp, G.-J. (2009) Meridianiite detected in ice. Journal of Glaciology, 55, 117–122.

Farley, K.A., Stack, K.M., Shuster, D.L., Horgan, B.H.N., Hurowitz, J.A., Tarnas, J.D., Simon, J.I., Sun, V.Z., Scheller, E.L., Moore, K.R., and others (2022) Aqueously

altered igneous rocks sampled on the floor of Jezero crater, Mars. Science, 377, eabo2196.

Fortes, A., Wood, I., and Knight, K. (2008) The crystal structure and thermal expansion tensor of $MgSO_4·11D_2O$ (meridianiite) determined by neutron powder diffraction. Physics and Chemistry of Minerals, 35, 207–221.

Fortes, A.D., and Meusburger, J.M. (2022) Comment on Mineral Diversity on Europa: Exploration of Phases Formed in the $MgSO_4$–H_2SO_4–H_2O Ternary. ACS Earth and Space Chemistry, 6, 1407–1410.

Fortes, A.D., Wood, I.G., Alfredsson, M., Vočadlo, L., and Knight, K.S. (2006) The thermoelastic properties of $MgSO_4·7D_2O$ (epsomite) from powder neutron diffraction and ab initio calculation. European Journal of Mineralogy, 18, 449–462.

Fortes, A.D., Wood, I., and Knight, K. (2008) The crystal structure and thermal expansion tensor of $MgSO_4·11D_2O$ (meridianiite) determined by neutron powder diffraction. Physics and Chemistry of Minerals, 35, 207–221.

Fortes, A.D., Lemée-Cailleau, M.-H., Knight, K.S., and Jura, M. (2010) Magnesium sulfate trihydrate: an elusive mineral on Earth and Mars?

Fortes, A.D., Browning, F., and Wood, I.G. (2012) Cation substitution in synthetic meridianiite ($MgSO_4·11H_2O$) I: X-ray powder diffraction analysis of quenched polycrystalline aggregates. Physics and Chemistry of Minerals, 39, 419–441.

Fortes, A.D., Fernandez-Alonso, F., Tucker, M., and Wood, I.G. (2017a) Isothermal equation of state and high-pressure phase transitions of synthetic meridianiite ($MgSO\ 411D\ 2O$) determined by neutron powder diffraction and quasielastic neutron spectroscopy. Acta Crystallographica Section B, 73, 33–46.

Fortes, A.D., Knight, K.S., and Wood, I.G. (2017b) Structure, thermal expansion and incompressibility of $MgSO_4·9H_2O$, its relationship to meridianiite ($MgSO_4·11H_2O$) and possible natural occurrences. Acta Crystallographica Section B, 73, 47–64.

Fraenckel, F. (1907) Über die Existenzgebiete der Ferrosulfat-Hydrate. Zeitschrift für anorganische Chemie, 55, 223–232.

François, P., Szopa, C., Buch, A., Coll, P., McAdam, A.C., Mahaffy, P.R., Freissinet, C., Glavin, D.P., Navarro-Gonzalez, R., and Cabane, M. (2016) Magnesium sulfate as a key mineral for the detection of organic molecules on Mars using pyrolysis. Journal of Geophysical Research: Planets, 121, 61–74.

Fronczek, F.R., Collins, S.N., and Chan, J.Y. (2001) Refinement of ferrous sulfate heptahydrate (melanterite) with low-temperature CCD data. Acta Crystallographica Section E, 57, i26–i27.

Grevel, K.-D., Majzlan, J., Benisek, A., Dachs, E., Steiger, M., Fortes, A.D., and Marler, B. (2012) Experimentally Determined Standard Thermodynamic Properties of Synthetic $MgSO_4·4H_2O$ (Starkeyite) and $MgSO_4·3H_2O$: A Revised Internally Consistent Thermodynamic Data Set for Magnesium Sulfate Hydrates. Astrobiology, 12, 1042–1054.

Gromnitskaya, E., Yagafarov, O., Lyapin, A., Brazhkin, V., Wood, I., Tucker, M., and Fortes, A. (2013) The high-pressure phase diagram of synthetic epsomite ($MgSO_4·7H_2O$ and $MgSO_4·7D_2O$) from ultrasonic and neutron powder diffraction measurements. Physics and Chemistry of Minerals, 40.

Haberle, R.M. (2015) Solar System/Sun, Atmospheres, Evolution of Atmospheres | Planetary Atmospheres: Mars. Encyclopedia of Atmospheric Sciences: Second Edition, 168–177.

Hawthorne, F., and Sokolova, E. (2012) The role of H_2O in controlling bond topology: I. The [6]$Mg(SO_4)(H_2O)_n$ (n= 0 - 6) structures. Zeitschrift fur Kristallographie, 227, 594–603.

Hogenboom, D.L., Kargel, J.S., Ganasan, J.P., and Lee, L. (1995) Magnesium Sulfate-Water to 400 MPa Using a Novel Piezometer: Densities, Phase Equilibria, and Planetological Implications. Icarus, 115, 258–277.

Hogenboom, D.L., Kargel, J.S., Reiter, M.L., and Khor, Y.N. (1997) Volume Changes Attending Hydration of Quenched Magnesium Sulfate Brine: The Tectonics of Ganymede's Sulci. In Lunar and Planetary Science Conference p. 579.

Jaeken, J.W., and Cottenier, S. (2016) Solving the Christoffel equation: Phase and group velocities. Computer Physics Communications, 207, 445–451.

Jambor, J.L., and Traill, R.J. (1963) On rozenite and siderotil. The Canadian Mineralogist, 7, 751–763.

Jambor, J.L., Nordstrom, D., and Alpers, C. (2000) Metal-sulfate Salts from Sulfide Mineral Oxidation. Reviews in Mineralogy and Geochemistry, 40, 303–350.

Johnson, B.C., Sheppard, R.Y., Pascuzzo, A.C., Fisher, E.A., and Wiggins, S.E. (2017) Porosity and Salt Content Determine if Subduction Can Occur in Europa's Ice Shell. Journal of Geophysical Research: Planets, 122, 2765–2778.

Kargel, J.S. (1991) Brine volcanism and the interior structures of asteroids and icy satellites. Icarus, 94, 368–390.

King, P.L., and McLennan, S.M. (2010) Sulfur on Mars. Elements, 6, 107–112.

Košek, F., Culka, A., Drahota, P., and Jehlička, J. (2017) Applying portable Raman spectrometers for field discrimination of sulfates: Training for successful extraterrestrial detection. Journal of Raman Spectroscopy, 48, 1085–1093.

Li, R., Shi, Y., Shi, L., Alsaedi, M., and Wang, P. (2018) Harvesting Water from Air: Using Anhydrous Salt with Sunlight. Environmental Science & Technology, 52, 5398–5406.

Livshits, L., Genshaft, Y., and Ryabin, Y. (1963) Equilibrium diagram of the crystal hydrates of $MgSO_4$ at high pressures. Russian Journal of Inorganic Chemistry, 8, 676–678.

Lorenz, R.D., Turtle, E.P., Barnes, J.W., Trainer, M.G., Adams, D., Hibbard, K., Sheldon, C.Z., Zacny, K., Peplowski, P.N., Lawrence, D.J., and others (2018) Dragonfly: A rotorcraft lander concept for scientific exploration at titan. Johns Hopkins APL Technical Digest (Applied Physics Laboratory), 34, 374–387.

Ma, H., Bish, D.L., Wang, H.-W., and Chipera, S.J. (2009a) Determination of the crystal structure of sanderite, $MgSO_4 \cdot 2H_2O$, by X-ray powder diffraction and the charge flipping method. American Mineralogist, 94, 622–625.

Ma, H., Bish, D., Wang, H.-W., and Chipera, S. (2009b) Structure determination of the 2.5 hydrate $MgSO_4$ phase by simulated annealing. American Mineralogist , 94, 1071–1074.

Maynard-Casely, H.E., Brand, H.E.A., Wilson, S.A., and Wallwork, K.S. (2021) Mineral Diversity on Europa: Exploration of Phases Formed in the $MgSO_4$–H_2SO_4–H_2O Ternary. ACS Earth and Space Chemistry, 5, 1716–1725.

McCord, T.B., Hansen, G.B., Clark, R.N., Martin, P.D., Hibbitts, C.A., Fanale, F.P., Granahan, J.C., Segura, M., Matson, D.L., Johnson, T. v, and others (1998a) Non-water-ice constituents in the surface material of the icy Galilean satellites from the Galileo near-infrared mapping spectrometer investigation. Journal of Geophysical Research: Planets, 103, 8603–8626.

McCord, T.B., Hansen, G.B., Fanale, F.P., Carlson, R.W., Matson, D.L., Johnson, T. v, Smythe, W.D., Crowley, J.K., Martin, P.D., Ocampo, A., and others (1998b) Salts on Europa's Surface Detected by Galileo's Near Infrared Mapping Spectrometer. Science, 280, 1242 LP – 1245.

McCord, T.B., Hansen, G.B., and Hibbitts, C.A. (2001) Hydrated Salt Minerals on Ganymede's Surface: Evidence of an Ocean Below. Science, 292, 1523.

McKinnon, W.B., and Zolensky, M.E. (2003) Sulfate Content of Europa's Ocean and Shell: Evolutionary Considerations and Some Geological and Astrobiological Implications. Astrobiology, 3, 879–897.

Meusburger, J.M., Ende, M., Talla, D., Wildner, M., and Miletich, R. (2019) Transformation mechanism of the pressure-induced C2/c-to-P$\bar{1}$ transition in ferrous sulfate monohydrate single crystals. Journal of Solid State Chemistry, 277.

Meusburger, J.M., Ende, M., Matzinger, P., Talla, D., Miletich, R., and Wildner, M. (2020) Polymorphism of Mg-sulfate monohydrate kieserite under pressure and its occurrence on giant icy jovian satellites. Icarus, 336, 113459.

Milliken, R.E., Grotzinger, J.P., and Thomson, B.J. (2010) Paleoclimate of Mars as captured by the stratigraphic record in Gale Crater. Geophysical Research Letters, 37, L04201.

Mindat (2022, September 30) Epsomite.

Néri, A., Guyot, F., Reynard, B., and Sotin, C. (2020) A carbonaceous chondrite and cometary origin for icy moons of Jupiter and Saturn. Earth and Planetary Science Letters, 530, 115920.

Pappalardo, R.T., Vance, S., Bagenal, F., Bills, B.G., Blaney, D.L., Blankenship, D.D., Brinckerhoff, W.B., Connerney, J.E.P., Hand, K.P., Hoehler, T.M., and others (2013) Science Potential from a Europa Lander. Astrobiology, 13, 740–773.

Peterson, R.C. (2011) Cranswickite $MgSO_4 \cdot 4H_2O$, a new mineral from Calingasta, Argentina. American Mineralogist, 96, 869–877.

Prentice, A.J.R. (1999) Origin, Bulk Chemical Composition And Physical Structure Of The Galilean Satellites Of Jupiter: A Post-Galileo Analysis. Earth, Moon, and Planets, 87, 11–55.

Rapin, W., Ehlmann, B.L., Dromart, G., Schieber, J., Thomas, N.H., Fischer, W.W., Fox, V.K., Stein, N.T., Nachon, M., Clark, B.C., and others (2019) An interval of high salinity in ancient Gale crater lake on Mars. Nature Geoscience, 12, 889–895.

Rech, G.L., and Perottoni, C.A. (2020) Density functional theory plane-wave/pseudopotential calculations of the equation of state of rhenium in the terapascal regime. Journal of Physics: Conference Series, 1609, 012014.

Roach, L.H., Mustard, J.F., Swayze, G., Milliken, R.E., Bishop, J.L., Murchie, S.L., and Lichtenberg, K. (2010) Hydrated mineral stratigraphy of Ius Chasma, Valles Marineris. Icarus, 206, 253–268.

Sheppard, R.Y., Milliken, R.E., and Robertson, K.M. (2022) Presence of clay minerals can obscure spectral evidence of Mg sulfates: implications for orbital observations of Mars. Icarus, 383, 115083.

Smith, R.J., Rampe, E.B., Horgan, B.H.N., and Dehouck, E. (2018) Deriving Amorphous Component Abundance and Composition of Rocks and Sediments on Earth and Mars. Journal of Geophysical Research: Planets, 123, 2485–2505.

Smith, R.J., McLennan, S.M., Sutter, B., Rampe, E.B., Dehouck, E., Siebach, K.L., Horgan, B.H.N., Sun, V., McAdam, A., Mangold, N., and others (2022) X-Ray Amorphous Sulfur-Bearing Phases in Sedimentary Rocks of Gale Crater, Mars. Journal of Geophysical Research: Planets, 127, e2021JE007128.

Talla, D., and Wildner, M. (2019) Investigation of the kieserite–szomolnokite solid-solution series, $(Mg,Fe)SO_4 \cdot H_2O$, with relevance to Mars: Crystal chemistry, FTIR, and Raman spectroscopy under ambient and martian temperature conditions. American Mineralogist, 104, 1732–1749.

Thompson, S.P., Kennedy, H., Butler, B.M., Day, S.J., Safi, E., and Evans, A. (2021) Laboratory exploration of mineral precipitates from Europa's subsurface ocean. Journal of Applied Crystallography, 54, 1455–1479.

Tosca, N.J., McLennan, S.M., Clark, B.C., Grotzinger, J.P., Hurowitz, J.A., Knoll, A.H., Schröder, C., and Squyres, S.W. (2005) Geochemical modeling of evaporation processes on Mars: Insight from the sedimentary record at Meridiani Planum. Earth and Planetary Science Letters, 240, 122–148.

Tosca, N.J., McLennan, S.M., Lamb, M.P., and Grotzinger, J.P. (2011) Physicochemical properties of concentrated Martian surface waters. Journal of Geophysical Research: Planets, 116, E05004.

Vance, S., and Brown, J.M. (2013) Thermodynamic properties of aqueous $MgSO_4$ to 800MPa at temperatures from −20 to 100°C and concentrations to 2.5molkg−1 from sound speeds, with applications to icy world oceans. Geochimica et Cosmochimica Acta, 110, 176–189.

Vaniman, D.T., Bish, D.L., Chipera, S.J., Fialips, C.I., William Carey, J., and Feldman, W.C. (2004) Magnesium sulphate salts and the history of water on Mars. Nature, 431, 663–665.

Vaniman, D.T., Martínez, G.M., Rampe, E.B., Bristow, T.F., Blake, D.F., Yen, A.S., Ming, D.W., Rapin, W., Meslin, P.-Y., Morookian, J.M., and others (2018) Gypsum, bassanite, and anhydrite at Gale crater, Mars. American Mineralogist, 103, 1011–1020.

Vlasov, V.V., and Kuznetsov, A.V. (1963) Ferrohexahydrite. American Mineralgoist, 48, 433.

von Hodenberg, R., and Kühn, R. (1967) Zur Kentniss der Magnesiumsulfatehydrate und der Effloreszenz des Kieserits von Hartsalzen. Kali und Steinsalz, 4.

Wang, A., and Zhou, Y. (2014) Experimental comparison of the pathways and rates of the dehydration of Al-, Fe-, Mg- and Ca-sulfates under Mars relevant conditions. Icarus, 234, 162–173.

Wang, A., Jolliff, B.L., Liu, Y., and Connor, K. (2016) Setting constraints on the nature and origin of the two major hydrous sulfates on Mars: Monohydrated and polyhydrated sulfates. Journal of Geophysical Research: Planets, 121, 678–694.

Wang, F., and Zhang, Y. (2011) Raman Spectral Investigations on the Phase Transition Behaviors of $MgSO_4 \cdot 7H_2O$ Crystals in Different Efflorescence Processes. Spectroscopy and Spectral Analysis, 31, 700–703.

Wang, W., Fortes, A.D., Dobson, D.P., Howard, C.M., Bowles, J., Hughes, N.J., and Wood, I.G. (2018) Investigation of high-pressure planetary ices by cryo-recovery. II. High-pressure apparatus, examples and a new high-pressure phase of $MgSO_4 \cdot 5H_2O$. Journal of Applied Crystallography, 51, 692–705.

Wang, Z., Hassan, M.U., Nadeem, F., Wu, L., Zhang, F., and Li, X. (2020) Magnesium Fertilization Improves Crop Yield in Most Production Systems: A Meta-Analysis. Frontiers in Plant Science, 10:1727.

Wiens, R.C., Maurice, S., Robinson, S.H., Nelson, A.E., Cais, P., Bernardi, P., Newell, R.T., Clegg, S., Sharma, S.K., Storms, S., and others (2021) The SuperCam Instrument Suite on the NASA Mars 2020 Rover: Body Unit and Combined System Tests. Space Science Reviews, 217, 4.

Wildner, M., Zakharov, B.A., Bogdanov, N.E., Talla, D., Boldyreva, E. v, and Miletich, R. (2022) Crystallography relevant to Mars and Galilean icy moons: crystal behavior of kieserite-type monohydrate sulfates at extraterrestrial conditions down to 15 K. IUCrJ, 9.

Witzke, A., Arnold, G., and Stöffler, D. (2007) Spectral detectability of Ca- and Mg-sulfates in Martian bright soils in the 4–5µm wavelength range. Planetary and Space Science, 55, 429–440.

Zalkin, A., Ruben, H., and Templeton, D.H. (1964) The crystal structure and hydrogen bonding of magnesium sulfate hexahydrate. Acta Crystallographica, 17, 235–240.

Zayakina., N.V. (2019) Cranswickite — a rare tetrahydrate sulfate of magnesium $MgSO_4 \cdot 4H_2O$, the new find in Yakutia. Zapiski RMO (Proceedings of the Russian Mineralogical Society), 148, 49–53.

2. Experimental methods and ab initio simulations

In this chapter, the experimental and computational methods I used in this project will be described. I will start by briefly describing the synthesis of the sample materials. This will be followed by an overview of the experimental methods used in this thesis (i.e., synchrotron and neutron diffraction, Raman spectroscopy). Lastly, I will describe the computational methods and how they were used to predict material properties and aid the interpretation of the experimental data.

2.1 Synthesis

The first point that must be considered when synthesising a sample is which experimental techniques are going to be used for its characterisation. The choice of the analysis techniques can either greatly complicate or simplify the synthesis procedure. For example, studying the samples by powder diffraction allowed me to prepare the crystals by dehydration of the heptahydrates, rather than growing single crystals from aqueous solution, which substantially simplified the synthesis. The use of neutron diffraction, however, introduced two challenges to the sample synthesis. Firstly, the samples must be fully deuterated, which greatly complicated the synthesis procedure since deuterium readily exchanges with protiated hydrogen when getting in contact with atmospheric moisture. Therefore, the synthesis had to be carried out in a helium filled glove bag. Secondly, due to the weak interaction of neutrons with matter, large amounts of sample material (i.e., around ten grams) are typically required to achieve reasonable data collection times. In this thesis rozenite, starkeyite and cranswickite were synthesised. The synthesis of each phase is described in detail in the respective thesis chapters, and thus will here only be briefly summarized.

Principally the synthesis involved the following steps:
> (1) Complete dehydration of reagent $FeSO_4 \cdot 7H_2O$ and $MgSO_4 \cdot 7H_2O$
> (2) Dissolution of anhydrous $MgSO_4$ in D_2O (MSHs) or anhydrous $FeSO_4$ in D_2SO_4 and D_2O (FSHs) until the solution was saturated.

(3) Cooling of the saturated solutions in a fridge readily induced the precipitation of $MgSO_4 \cdot 7D_2O$ and $FeSO_4 \cdot 7D_2O$

(4) Dehydration of $MgSO_4 \cdot 7D_2O$ and $FeSO_4 \cdot 7D_2O$ under controlled relative humidity, temperature, and pressure conditions.

The relative humidity was controlled by placing different saturated salt solutions, each buffering the relative humidity at a characteristic value (Greenspan, 1977), in the synthesis vessels. Carrying out the dehydration in rubber sealed Weck jars allowed helium to diffuse out of the reaction vessel resulting in a reduced atmospheric pressure, which turned out to be critical for the synthesis of cranswickite, and its precursor phase pentahydrite. For a more detailed description of the synthesis setup and procedure I refer to section 8.4. The formation of pentahydrite and cranswickite under reduced atmospheric pressure agrees well with their occurrence in high altitude environments on Earth. Cranswickite was discovered at around 2500 m altitude (~0.75 bar) (Peterson, 2011) and pentahydrite formed at Los Alamos National Laboratories (2300 m altitude ~ 0.77 bar) as a dehydration product of epsomite in dry winter months (Vaniman & Chipera, 2006).

2.2 Synchrotron X-ray and neutron diffraction

2.2.1 Introduction

The vast majority of experimental data presented in this thesis is neutron diffraction data collected at the HRPD instrument (ISIS Neutron and Muon Source, UK) complemented by synchrotron powder diffraction data acquired at the I11 beamline (Diamond Light Source, UK). There are countless excellent general introductions to both neutron and X-ray powder diffraction, such as *Elementary Scattering Theory: For X-ray and Neutron Users* (Sivia, 2011)*, Applications of Neutron Powder Diffraction* (Kisi & Howard, 2008), *Structure Determination from Powder Diffraction* (David et al., 2006), and *Rietveld Refinement* (Dinnebier et al., 2018). For this reason, each technique will only be briefly introduced, and the primary focus will be specifically on the theoretical background and practical execution of powder diffraction experiments at Diamond Light Source's I11 beamline and ISIS Neutron and Muon Source's HRPD instrument.

2.2.2 Historical overview X-ray and neutron diffraction

Diffraction is a phenomenon that occurs when a wave interacts with an aperture, or multiple closely spaced apertures, such as a grating, of comparable dimensions to its wavelength. In crystals, atoms form a three-dimensional periodic diffraction grating (i.e., the crystal lattice), whereby the interatomic distances are of the order of Å (i.e., 10^{-10} m), and therefore of similar dimensions as the wavelength of X-rays (i.e., ~ 0.3 – 2.5 Å typically used in diffraction experiments). This was first recognized by Max Laue and experimentally validated by Paul Knipping and Walter Friedrich in 1912 (Friedrich et al., 1912) by studying a single crystal of $CuSO_4 \cdot 5H_2O$, notably a compound chemically and structurally closely related to the materials studied in this thesis.

Neutrons may equally be used for diffraction experiments if their wavelength is comparable to interatomic distances. The first neutron diffraction experiments were performed in 1936 (Halban & Preiswerk, 1936; Mitchell & Powers, 1936), just four years after its discoverer, James Chadwick, stated when interviewed on the practical use of neutrons, that he is afraid that 'neutrons will not be of any use to anyone' (Kuhn, 1932). As time has proven, surely to Chadwick's delight, his initial assessment of the usefulness of neutrons could not have been more wrong. Neutron diffraction, to name just one of many analytical techniques taking advantage of the unique interaction of neutrons with matter, nowadays is an indispensable tool to probe the magnetic ordering and structure of materials.

2.2.3 Principle

Most information presented in this section has been adapted from *Elementary Scattering Theory: For X-ray and Neutron Users* (Sivia, 2011)*, Applications of Neutron Powder Diffraction* (Kisi & Howard, 2008) and *Structure Analysis From Powder Diffraction Data: Rietveld Refinement in Excel* (Evans & Evans, 2021).

A crystal features a repeating arrangement of atoms forming distinct planes, denoted by the Miller indices hkl, and separated by well-defined distances d_{hkl}. It was a 22-year-old Lawrence Bragg who recognised that the peaks observed in an X-ray diffraction pattern may be described geometrically as

a reflection of the incident wave by an array of such parallel planes. For the waves to interfere constructively, the path differences between adjacent parallel planes must be an integer multiple of the wavelength. The angle between the incident and diffracted wave is 2θ. From Figure 2.1, it is evident that the relationship between the interplanar spacing d_{hkl}, the diffraction angle θ and the wavelength is

$$sin\,\theta = \frac{n\lambda}{2d_{hkl}} \tag{2.1}$$

Rearranging this equation yields the well-known form of Bragg's law

$$n\lambda = 2d_{hkl}\,sin\,\theta \tag{2.2}$$

with n being an integer number corresponding to the order of the Bragg reflection.
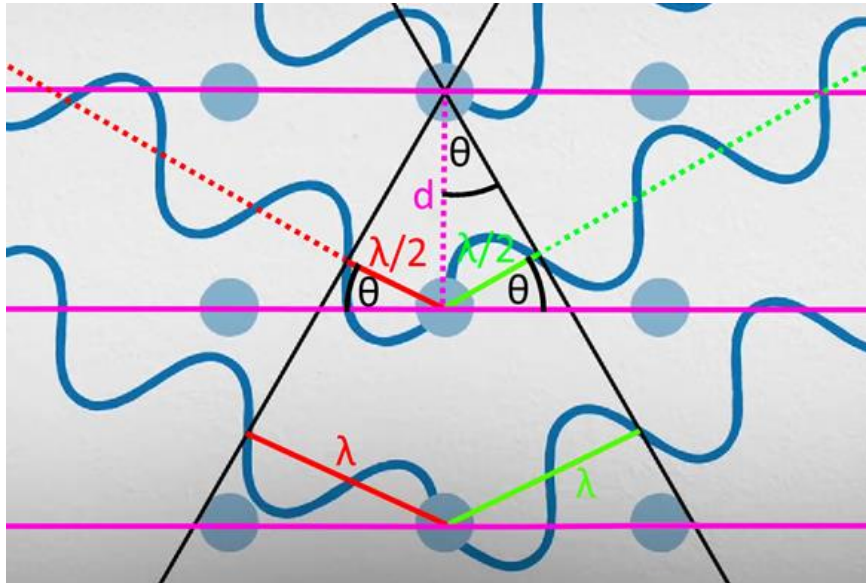
Figure 2.1 Diffraction of the incident wave by parallel planes of the crystal lattice (magenta). For constructive interference to occur, the path difference between adjacent waves must be integer multiples of the wavelength. Modified from Bruker (2019).

The used wavelength λ is known for constant wavelength diffraction experiments, and the angle 2θ at which a Bragg peak is determined in the experiment. If 2θ and λ are known, d_{hkl} is readily obtained from Bragg's law. In neutron time-of-flight experiments, the time-of-flight (t) relates to the wavelength λ via a modified de Broglie equation

$$\lambda = \frac{h\,t}{m\,L} \tag{2.3}$$

with h being the Planks constant, m the mass of the neutron, and L the total neutron flight path.

Substituting λ in Eq. 2.2 with Eq 2.3 then yields

$$d_{hkl} = \frac{h\, t}{2\, m\, L\, sin(\theta)} \tag{2.4}$$

and

$$d_{hkl} = \frac{t}{505.554\, L\, \sin(\theta)} \tag{2.5}$$

when $\frac{h}{2\,m}$ is substituted by the constant 505.554, and units of t (µs), d_{hkl} (Å), and L (m) are used.

Next to the diffraction angle or time-of-flight, also the Bragg peak intensity is usually measured in a diffraction experiment. The intensity is related to the scattering power $f(\lambda, \theta)$ of the elements that constitute the crystal. $f(\lambda, \theta)$ gives the probability that a particle of a specific wavelength is scattered in a certain direction. As mentioned above, this property differs substantially for X-rays and neutrons. In the case of neutron scattering, $f(\lambda, \theta)$ is described by a single isotope-specific parameter, namely the neutron scattering length b

$$b = -f(\lambda, \theta) \tag{2.6}$$

Large values of b denote that the isotope is a strong neutron scatterer. The sign determines if the incident and scattered waves are in phase (constructive interference) or 180° out of phase (destructive interference). There is no simple relationship between the scattering length and the atomic number of an isotope, but the magnitude is a complex interplay between the structure of the nucleus and the spin orientation relative to the neutron. Furthermore, the neutron scattering length does not diminish with increasing scattering angle (Figure 2.2). In the case of X-ray scattering $f(\lambda, \theta)$ is described by the atomic form factor. Atomic form factors decrease monotonically with increasing diffraction angles

(Figure 2.2). Furthermore, atomic form factors depend on the atomic number Z according to

$$f(\lambda, \theta) = Z \, g(\theta) r_e \qquad (2.7)$$

with r_e being the radius of an electron, and $g(Q)$ a herein not further described function modelling the monotonic decay with increasing diffraction angle.
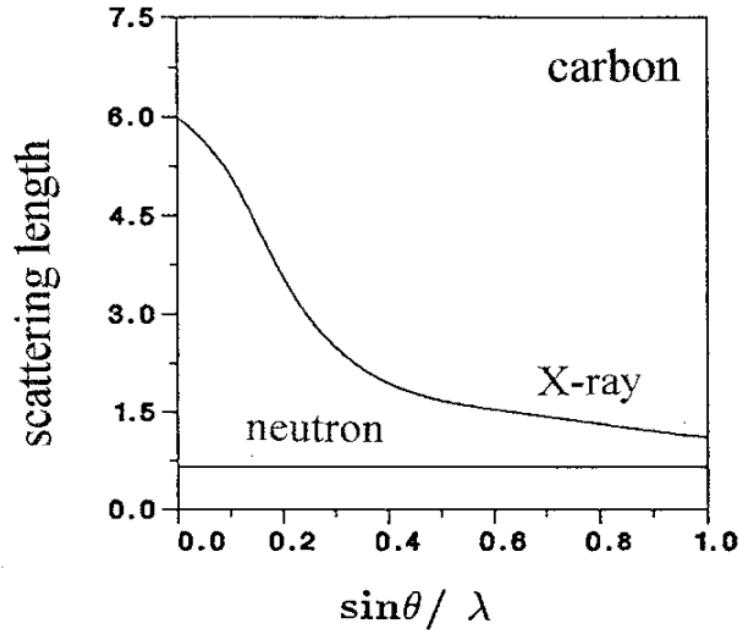
Figure 2.2 Scattering length as a function of diffraction angle. Note the angular dependence of the scattering length for X-rays, whereas the scattering length takes a constant value for neutrons. From Brokmeier (1994).

The intensity of a Bragg peak $I(\mathrm{hkl})$ is proportional to the square of the structure factor $F(\mathrm{hkl})$

$$I(\mathrm{hkl}) = s \times \mathrm{LP} \times m \times \mathrm{Abs} \times |F(\mathrm{hkl})|^2 \qquad (2.8)$$

with s being a global scale factor, LP the Lorentz-Polarisation factor, summarising diffraction geometry dependent variations of the intensity (n.b the polarisation contribution arises from the polarisation of the beam by the monochromator and therefore is not applicable to neutrons), m the multiplicity (i.e., the number of symmetry equivalent reflections for each hkl), and Abs the absorption of X-rays or neutrons which takes place in the specimen itself. For the sake of brevity, other potentially important, but often negligible contributions to the intensity (e.g., preferred orientation, extinction) will not be included in this discussion.

Except for the structure factor $F(\text{hkl})$, all contributions to Eq 2.8 are geometry, symmetry, or chemical composition specific and usually known. The structure factor is

$$F(\text{hkl}) = \sum_{i=1}^{N} t_j f(\lambda, \theta)_i e^{2\pi(hx_i + ky_i + lz_i)} \qquad (2.9)$$

with x_i, y_i and z_i being the atomic coordinates of the ith atom. Since the summation runs over all atoms in the unit-cell N it is evident that the $F(\text{hkl})$, and thus the intensity (eq. 2.8), contains information on the relative arrangements of the atoms in the unit-cell. t_j is the Debye-Waller factor and accounts for the vibration of atoms around their equilibrium position.

2.2.4 Rietveld and Le Bail refinement

Crystal structures refined by the Rietveld method (Rietveld, 1967) and lattice parameters obtained by the Le Bail method (Le Bail, 2005) formed a central part of this thesis. For this reason, the theoretical background of both methods will be briefly summarized. This is followed by a detailed explanation of the refinement strategy.

A prerequisite for using the Rietveld method is a starting model i.e., a crystal structure with fairly accurate lattice parameters, atom coordinates, and displacement parameters. Subsequently, the structural model, peak shape parameters, as well as the parameters stated in eq. 2.8 are used to calculate the intensity for every 2θ value. The calculated intensity is then compared to the observed intensity, and the difference between the two is minimised by refining certain parameters of the structural model or the peak shape. The refinement is a multi-step process in which ideally the agreement between observed and calculated intensity improves with each refinement cycle. The agreement is usually monitored by calculating the R-Factor

$$wRp = \sqrt{\frac{\sum_{i=1}^{N} w_i (I_{obs,i} - I_{calc,i})^2}{\sum_{i=1}^{N} w_i I_{obs,i}^2}} \qquad (2.10)$$

and the main objective of a Rietveld refinement is to vary parameters to decrease the R-factor, and eventually obtain a crystal structure model that is in good agreement with the experimentally determined intensity data. Lastly, it is critical to check that the refined structural model exhibits chemically sensible bond-lengths and angles.

The underlaying concept of the Le Bail method is to use the Rietveld extraction method to obtain $F(\mathrm{hkl})$ even without knowledge of the crystal structure. The Le Bail method is often applied to obtain reflection intensities which then can be used for ab initio structure solution from powder diffraction data. The intensity extraction can be combined with the refinement of non-structural parameters, which allows to obtain good profile and lattice parameters. In addition, this provides an estimate of the best possible R-factor that may be achieved in a subsequent Rietveld refinement. The Le Bail method uses the same agreement R-factors as the Rietveld method (e.g., eq. 2.10) to check the fit quality (Le Bail, 2005). Based on the absence of structural information, the extraction of $F(\mathrm{hkl})$ of partially or completely overlapping peaks is one of the major challenges that must be overcome for a successful application of the Le Bail method.

There are two variations of the Le Bail method implemented in GSAS (Toby, 2001) that will be summarised in the following, each of them varying in the approach used for $F(\mathrm{hkl})$ extraction. Most information presented in the following has been adapted from Toby (2023). In the classical model-independent (referred to as 'Equally weighted Le Bail method' in GSAS) the intensity between overlapping peaks is apportioned according to the multiplicity of each of the $F(\mathrm{hkl})$. Next to the model-independent Le Bail method, GSAS also offers a model-dependent variation of the Le Bail method (referred to as 'Fcalc weighted model-biased Le Bail method' in GSAS), which can be used if a structural model is known. The advantage of the model-dependent Le Bail implementation is that the intensity of overlapping peaks is apportioned according to the structural model, by applying knowledge of the $F(\mathrm{hkl})$, calculated from the structural model. This decomposition method allows extracting of $F(\mathrm{hkl})$ from the observed intensity data more accurately than the classical Le Bail method where the weighting of the $F(\mathrm{hkl})$ is solely based on the multiplicity of the Bragg peak. Since the crystal structure of all compounds studied in this thesis was already known, the model-dependent variation was favoured over the model-independent Le Bail method. In this thesis, the Le Bail method was used to obtain accurate starting

profile parameters and unit-cell parameters for subsequent Rietveld refinements. Based on the improved modelling of the intensity data as compared to the Rietveld method, the model-dependent variation on the Le Bail method typically yields the highest precision for the refinement of lattice parameters (Fortes & Capelli, 2018) and was therefore used to refine the variable temperature lattice parameter data which formed the basis for the analysis of the thermal expansion of rozenite, starkeyite and cranswickite.

2.2.5 Rietveld refinement strategy

Although the Rietveld method is a powerful tool allowing to derive a plethora of structural and sample-dependent information, great care must be taken not to refine too many parameters that are far from their minimum or strongly correlated simultaneously. The GSAS software was used for all Rietveld and Le Bail refinements. A detailed description of the numerous refinable parameters can be found in Larson & Von Dreele (2004). The refinement workflow is outlined below and the wRp at the major refinement steps is stated for rozenite (at 290 K), starkeyite (at 300 K), and cranswickite (at room temperature) for the neutron diffraction data.

Starting crystal structures with fairly accurate lattice parameters, atomic coordinates, and displacement parameter were obtained from the literature (i.e., rozenite (Baur, 1962), starkeyite (Baur, 1964), cranswickite (Peterson, 2011)). It is noteworthy that just the heavy atom structure was reported by Peterson (2011) for cranswickite and starting coordinates for the deuterium atoms had to be obtained prior to the Rietveld refinement. A bond-valence analysis was performed (supplementary 8.5) to identify the donor oxygens and the structure was then examined for sensible donor-acceptor distances. Subsequently, the deuterium atoms were placed along the vector spanned by donor and acceptor oxygen positions at a distance of 0.98 Å from the donor oxygens.

In the first refinement step, only the background, lattice parameter and scale factor were refined, while leaving all other parameters fixed at the values derived by the instrument scientist from NIST silicon SRM640e and CeO_2 SRM674b standards. This resulted in wRp of 0.0820, 0.0722, 0.1453 for rozenite starkeyite and cranswickite, respectively.

After this initial Rietveld refinement, the background was fixed, and accurate lattice parameters and profile parameters were derived in a model-

dependent Le Bail refinement. Time-of-flight neutron diffraction patterns are modelled in GSAS by instrument (i.e., alp, bet-0, bet-1) and sample-dependent (sig-0, sig-1, sig-2, gam-0, gam-1, gam-2) peak broadening parameters. The instrument-dependent broadening parameters were fixed at the values derived by the instrument scientist and sig-0, sig-2 and gam-0 were fixed at zero throughout the entire refinement process. The sample-dependent Gaussian (sig-1, sig-2) and Lorentzian (gam-1) broadening parameters were first refined one by one together with the lattice parameters until convergence was achieved. In the next step, a subset of two out of the three parameters was refined until convergence was achieved. Refinement of all three parameters at once often leads to unstable results. The isotropic Gaussian and Lorentzian broadening typically describe the observed profile already rather well, however, often modelling of the peak shape can be further improved by accounting for anisotropic line broadening which originates from the microstructure of the individual crystallites. To this end, the anisotropic Lorentzian broadening parameters L_{ij} with ij= 11, 22, 33, 12, 13, 23 were refined. Once accurate peak profile and lattice parameters were obtained in the Le Bail refinement, these parameters were fixed and the Rietveld refinement was continued.

Refining only the scale factor and background parameters, while leaving all other parameters fixed at the values derived in the Le Bail refinement resulted in an improved wRp of 0.0818, 0.0418, 0.1029, for rozenite, starkeyite, and cranswickite, respectively. Such good agreement factors without refining any structural parameters are a tribute to the high quality of the used starting models taken from excellent studies in particular by Baur (1964). The higher wRp obtained for cranswickite largely originates from the crudely estimated positions of the deuterium atoms and for rozenite Baur (1962) just approximated the hydrogen atom positions to be equivalent to the positions determined in the isotypic compound starkeyite. Clearly, the structural models of both compounds will benefit from the unconstrained refinement of structural parameters which will be outlined in the following. It is noteworthy that displacement parameters and background coefficients are highly correlated, thus the background was fixed during the refinement of the displacement parameters. Before refining any structural parameters, however, the isotropic displacement parameters for atoms of the same type (i.e., Fe, Mg, O, Ow, D) were constrained to take the same value. The atomic coordinates for each of these groups were then refined

separately until convergence was reached, after which they were all refined simultaneously. This was followed by a refinement of the group-constrained isotropic displacement parameters. This constraint was then lifted, and isotropic displacement parameters were refined for the individual atoms, first for each type of atom and then for all atoms simultaneously. Then atomic positions and individual isotropic displacement parameters were refined simultaneously.

Subsequently, the atomic positions were fixed, and anisotropic displacement parameters were refined, again, first for the individual types of atoms and then for all atoms simultaneously. Then all atoms and displacement parameters were refined simultaneously, followed by a refinement of the profile parameters associated with sample broadening. This yielded excellent wRp of 0.0355, 0.0298, 0.0387 for rozenite, starkeyite and cranswickite, respectively.

Next all parameters but the scale factor were fixed, and the absorption coefficient was refined. The atomic coordinates and displacement parameters were refined first separately and then simultaneously while keeping all other parameters, but the scale factor fixed. Next, the preferred orientation was accounted for using the spherical harmonic model and keeping all other parameters, but the scale factor fixed. Subsequently, the atomic coordinates and displacement parameters were again refined separately and then simultaneously while keeping all other parameters, but the scale factor fixed. For the final refinement step it was attempted to refine all parameters simultaneously. However, in some cases it was necessary to fix the background to avoid unphysical negative eigenvalues of the anisotropic displacement parameter matrix. Additionally, also the sample-dependent profile contributions needed to be fixed in some instances during the final refinement step to reduce the number of refined parameters. The structural (i.e. coordinates, displacement parameters, bond-lengths and angles) and agreement parameters for all structures refined in this thesis are stated either in the main text of chapters 4 and 5 or the supplementary of these chapters. A detailed description of the workflow used for the refinement of the lattice parameters, which were used for the analysis of the thermal expansion may be found in Supplementary 8.4 section.

2.2.6 Diamond Light Source

Most information presented in this section has been adapted from Thompson et al. (2009, 2011), Tartoni et al. (2008), the I11 website (2022), and the Diamond Light Source website (2023). Diamond Light Source is a 3rd generation synchrotron facility located at the Harwell Science and Innovation Campus in Oxfordshire. At Diamond Light Source, very intense beams of light are produced, over a wide energy (=wavelength) range, which allows the investigation the atomic structure and properties of matter at 32 unique beamlines. The following section provides an overview of the inner workings of Diamond Light Source, starting with the various steps involved with the production of synchrotron radiation to the optics that tailor the beam properties and ending with the diffraction and detection process at the I11 High-Resolution X-ray Powder Diffraction Beamline, where the experiments were carried out.

2.2.6.1 Production of synchrotron X-rays

In X-ray tubes used in in-house X-ray diffractometers, the ionisation of mostly core electrons of an anode material (e.g., Ag, Mo, Cu, Co) and subsequent reoccupation by electrons stemming from higher electron shells produces X-rays of a discrete wavelength characteristic for the respective electronic transition (e.g., Cu-Kα_1 = 1.54056 Å). If one strives to create more intense X-ray beams, clearly, the rate at which the ionisation events occur must be increased. In theory, this could be easily achieved by increasing the flux of the ionising radiation incident on the anode, resulting in more characteristic X-ray emission events and a higher flux. However, the problem with this approach is that the ionising radiation heats the anode material to a point where it causes deformation or even melting, resulting in the failure of the anode. Elegant workarounds to aid heat dissipation were developed, such as rotating the anode material (Bouwers, 1937) or, more recently, even using an already molten anode material such as liquid gallium in so-called metal jet anodes (Otendal et al., 2008). Both techniques substantially increased the flux available to in-house X-ray sources. Still, if one wants to increase the X-ray flux even further, an alternative generation pathway that does not involve the ionisation of an anode is necessary. One such pathway is the generation of electromagnetic radiation as "Bremsstrahlung", which translates from German as "braking radiation" and is a continuous spectrum of

electromagnetic radiation produced when charged particles change velocity or direction. The wavelength of Bremsstrahlung may be tuned depending on the amount of change in velocity or direction, thus allowing to tailor the wavelength of the generated electromagnetic radiation to best address a particular scientific problem. For this reason, synchrotron radiation facilities typically do not only produce X-rays, but also feature beamlines exploiting electromagnetic radiation of other energy ranges (e.g., infrared) to probe the structure and dynamics of matter on the atomic level.

In the following, the various steps involved in the generation of synchrotron radiation at Diamond Light source will be briefly described. The electron gun produces the electrons that will eventually be used to create synchrotron radiation via the Bremsstrahlung mechanism. This device works similarly to conventional X-ray tubes in the sense that electrons are extracted from a piece of glowing metal (cathode) by applying a positively charged electric field. The extracted electrons are then guided through a series of chambers with alternating electric fields, commonly referred to as the linear accelerator (LinAc), accelerating the electrons close to the speed of light. Subsequently, the electrons are ejected into the synchrotron, where they are kept on a circular path by bending magnets (Figure 2.3). Since the bending magnets change the path of the electrons, synchrotron radiation is emitted in a direction tangential to the plane of the electron beam. The radiation produced by the bending magnets typically covers a wide range of the electromagnetic spectrum ranging from microwaves to hard X-rays.
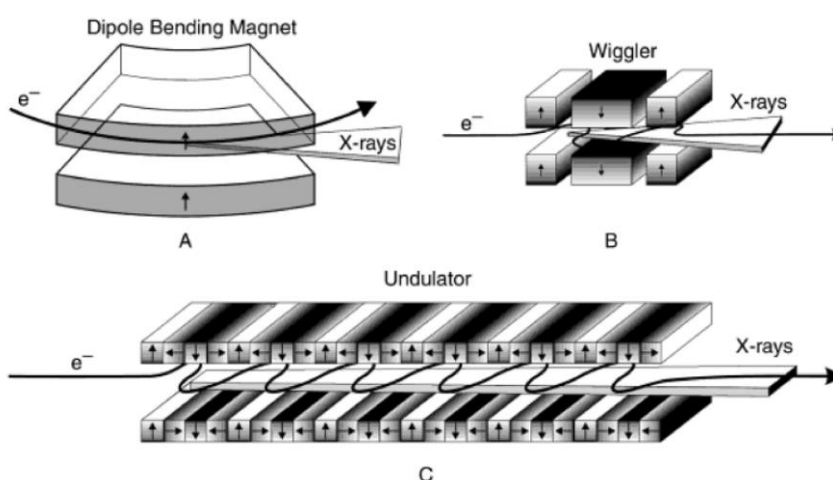
Figure 2.3 (a) Bending magnet insertion device which changes the trajectory of the electron, and therefore produces synchrotron radiation over a wide energy range that is released tangentially to the trajectory of the electron. (b) Wiggler insertion device where the electrons are forced on a wavy trajectory thereby emitting light in the forward direction. (c) Undulator insertion devices work according to the same principle as wigglers, but typically produce a narrower and more focussed spectrum of light. From Dinnebier & Billinge (2008).

However, synchrotron radiation produced by bending magnets is not particularly well focused and brilliant. To produce a beam of such characteristics, so-called undulator insertion devices are commonly used. At I11, the undulator is an array of 90 permanent magnets with a period of 22 mm (Thompson et al., 2009) that force the electrons passing through the insertion device to take an undulating (i.e., wavy) trajectory. With each bend, the electrons produce a spray of X-rays directed in the forward direction, which interferes with the radiation produced at the preceding bend, thus creating a very focused and brilliant beam. The undulator creates synchrotron radiation in the energy range of 5 – 30 keV (Thompson et al., 2009), corresponding to a wavelength range of 2.47968 – 0.41328 Å, and therefore ideally suited for diffraction experiments on crystalline solids.

2.2.6.2 The beamline optics

In the optics hutch, several slits to trim the beam dimensions, and mirrors, to turn the polychromatic (or white) beam into a monochromatic beam are combined to produce a beam perfectly suited for a diffraction experiment. After exiting the undulator insertion device, the first optical element interacting with the beam is a double-crystal-monochromator (Figure 2.4) comprising two liquid nitrogen-cooled silicon crystals cut parallel to the (111) plane. The purpose of the double-crystal-monochromator is to select X-rays of the desired wavelength. The principle of the double-crystal-monochromator becomes readily apparent by looking at Bragg's law (eq. 2.2).
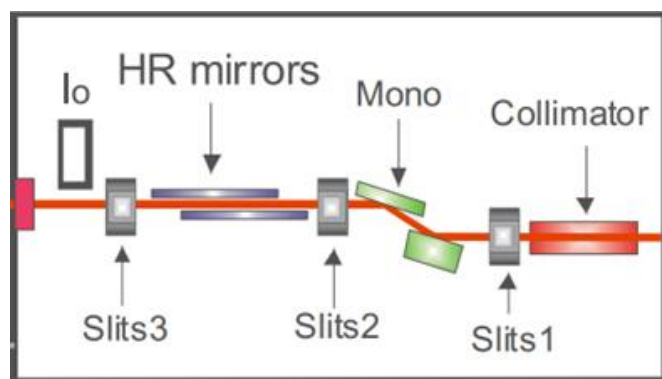
Figure 2.4 Schematic view of the optical hutch. Mono = double crystal monochromator, HR mirror: Harmonic rejection mirror. From Thompson et al. (2009).

The (111) lattice plane of silicon has a well-defined d-spacing value (i.e., 3.135693(5) Å at 295.65 K; NIST, 2015). To select a particular wavelength, one must rotate the monochromator crystal by an angle that satisfies the Bragg condition for this wavelength. From Bragg's law, it is also readily apparent that the monochromator not only selects a single wavelength that satisfies the Bragg condition for a certain rotation angle but also this wavelength's higher order harmonics (n = 1, 3, 5, 7,…). Notably, a silicon crystal merely diffracts the odd harmonics since the even (n = 2, 4, 6,…) harmonics are of zero intensity due to systematic extinction by the *F*-centred silicon lattice.

To obtain a truly monochromatic beam, these higher-order harmonics must be filtered, which is achieved by a pair of so-called harmonic rejection mirrors (Figure 2.4). These are two parallel silicon mirrors, which each have a three-stripe surface (i.e., bare silicon and one stripe each with Rh and Pt deposited coating). Each surface adequately rejects the higher harmonic wavelengths over a specific energy range. This truly monochromatic beam is then directed to the centre of the diffractometer, where the sample is located. The method of sample preparation of this system is now explained.

2.2.6.3 Sample preparation and loading of a capillary

There are two main instrument geometries used for powder diffraction, namely the reflection geometry, where the X-rays are diffracted off a surface of polycrystalline powder loaded in a flat sample holder, and the transmission geometry, where X-rays are diffracted as they pass through the sample loaded in a round glass capillary. At I11, diffraction patterns are recorded in transmission geometry; the exact process of sample preparation for this mode of analysis are explained below.

The sample is ground into a fine powder using a pestle and mortar, after which it is loaded into a capillary. We have used borosilicate glass capillaries since this material is stable over a wide temperature range, produces a low-background signal, and is comparably cheap. Each capillary is sealed at one end and exhibits a funnel on the other end (Figure 2.5). To load powder into the capillary, the funnel is filled with a small amount of powder. A handheld ultrasonic device (e.g., an electric toothbrush) is then brought into contact with the outside of the capillary walls which then vibrates to cause the powder to glide down the capillary tube.
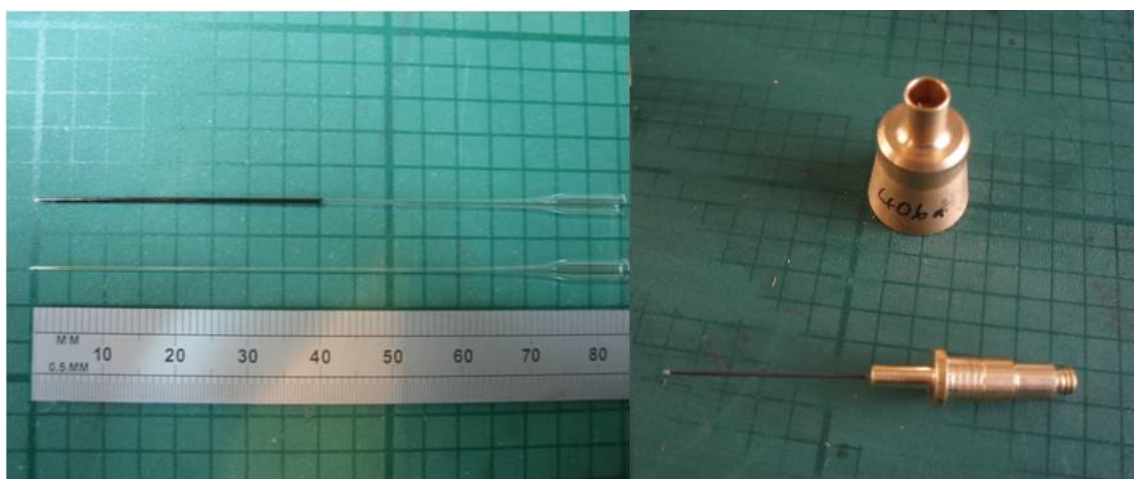
Figure 2.5 (left) The glass capillary is typically filled up to a length of around 4.5 cm. (right) The capillary is cut, placed in a brass pin, and mounted on the magnetic brass holder. Figure from I11 website (2022)

Visual inspection of the capillary is crucial to ensure that the powder is densely packed and has no gaps. After the capillary is filled, it is cut at a length of around 4.5 cm. The capillary is then placed in a brass pin, such that at least 2 cm, but no more than 4 cm (otherwise, the robot sample changer might break the capillary) sticks out of the pin. Lastly, the pin is mounted on a brass holder, which contains an internal magnetic body, allowing it to easily mount it on the sample spinner.

2.2.6.4 Diffraction and detection process at I11

To analyse a sample, the brass holder containing the sample capillary is mounted on the sample spinner so it is perfectly aligned with the focussed and monochromated X-ray beam. Once the beam interacts with the powder in the capillary, the (ideally) randomly oriented crystallites diffract the X-ray beam at discrete angles with varying intensity. The angles can be used to derive information on the unit-cell dimensions and space group symmetry, and the intensity reflects the relative positions of the atoms in the unit-cell. To measure both quantities, I11 has two detectors, namely the position-sensitive detector (PSD) (Thompson et al., 2011) and the multi-analyser crystal detector (MAC) (Tartoni et al., 2008; Thompson et al., 2009) (Figure 2.6).
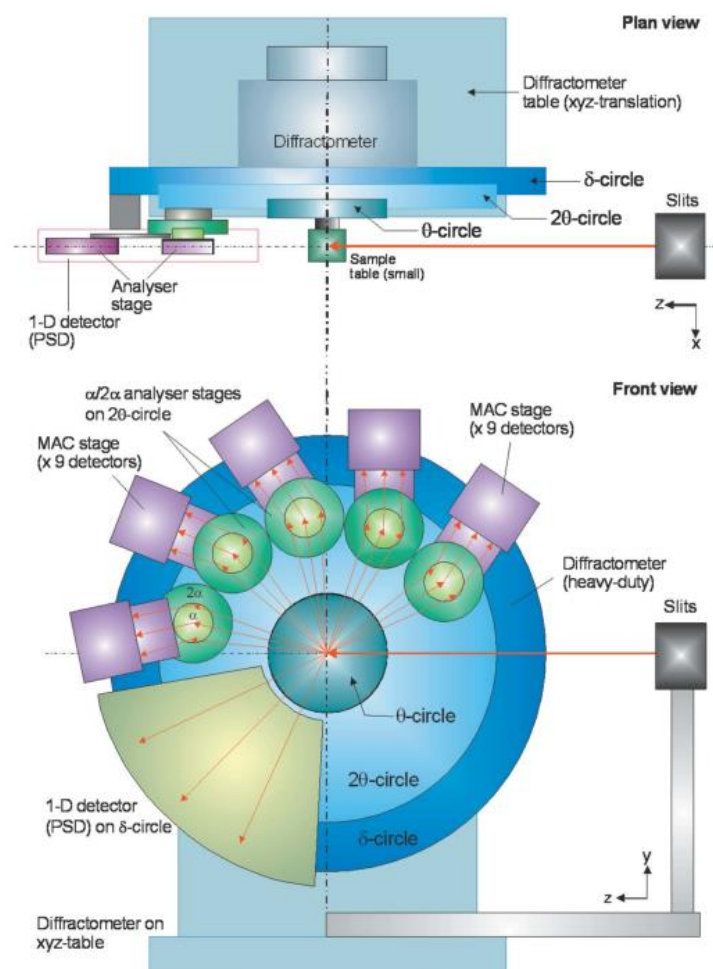
Figure 2.6. Schematic drawing of the I11 diffractometer from Tartoni et al. (2008).

The MAC is the detector of choice if highly accurate lattice parameters and peak resolution are critical, giving a range of applications such as in thermal expansion studies, unit-cell indexing, and subsequent structure solution. However, the high quality of the acquired data comes at the cost of relatively long (i.e., 30 – 60 min) data acquisition times. At I11, the MAC detector comprises five MAC stages (Figure 2.7), each consisting of nine silicon crystals, mounted in 30° increments on the 2θ circle, covering an angular range of 150 °. The nine analyser crystals are stacked on top of each other but with angular offsets of -8, -6, -4, -2, 0, 2, 4, 6, 8 ° to the 2θ position of the MAC arm. The detectors themselves are mounted on the 2α circle, such that each of them fulfills the Bragg conditions of the Si (111) peaks of the analyser crystals. Each analyser crystal thus collects the X-ray beams diffracted by the sample simultaneously. To obtain a diffraction pattern for the 5 – 145 ° angular range, the diffractometer needs to be rotated by just 30 °. The detection module consists of a cerium-doped yttrium aluminium perovskite scintillation crystal, a photomultiplier tube, voltage multiplier and pulse processing board. If an X-ray impinges on the scintillation crystal, electrons are

transferred from the valance to the conduction band and low energetic photons are emitted once the electrons fall back to the valance band. The low-energy photons then enter the photomultiplier, where they interact with the photocathode to produce electrons exploiting the photoelectric effect. These photoelectrons are then multiplied by an array of dynodes, kept at increasingly high voltages to accelerate the electrons moving from one dynode to the next, thus amplifying the signal before the electrons are directed toward the pulse processing board.
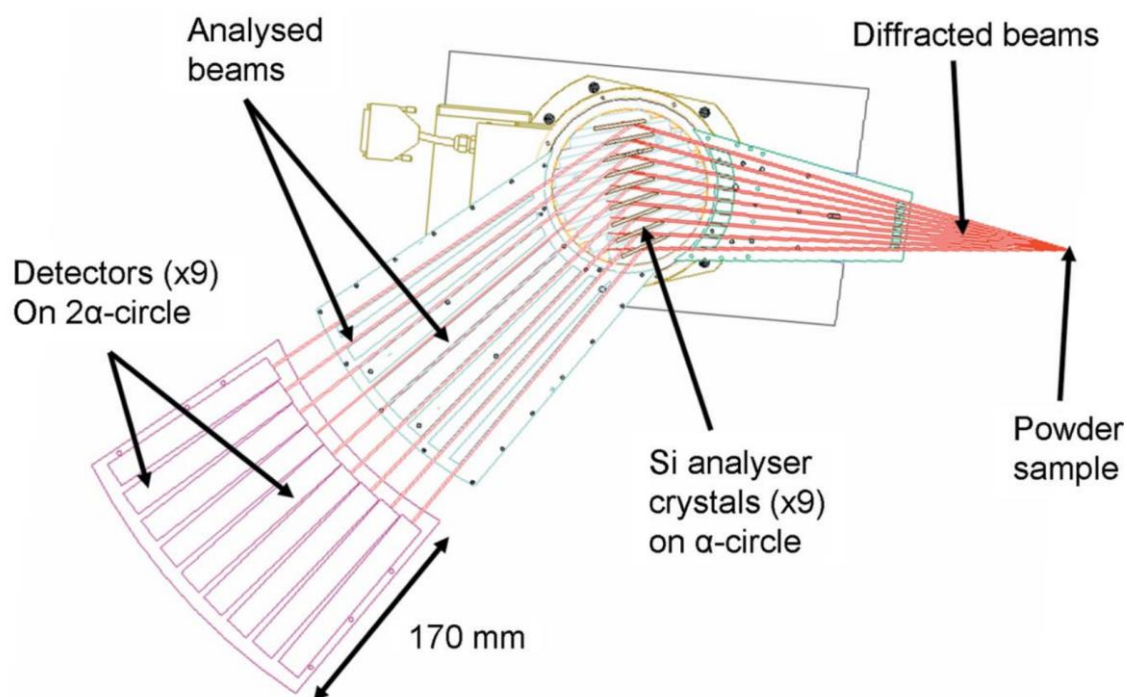
Figure 2.7 Schematic view of a MAC stage from Tartoni et al. (2008).

The PSD is the detector of choice for rapid measurements while still collecting data with high angular resolution. Obvious use cases are measurements where high temporal resolution is critical, such as in-situ crystallisation experiments. A less obvious application, but of increasing importance, is avoiding radiation damage caused by prolonged beam exposure. The typical data acquisition times of the PSD detector range from milliseconds to a few minutes. At I11, the PSD detector comprises 18 MYTHEN-II detector modules covering an angular range of 90 ° (Thompson et al., 2011). Each module is divided into 1280 strips (channels) of silicon diode pitches of 50 μm edge length. X-rays are directly converted into charge in the silicon sensors. If X-rays penetrate a silicon pitch, electron-hole pairs are created and separated by an external bias voltage. The electron moves to the positive and the hole to the negative end of the diode, creating a current which is directed to the readout

electronics. Each of the silicon pitches is connected to the readout electronics which allows the angle of a particular X-ray to be detected. The small size of silicon pitches combined with the large sample detector distance results in a very high angular resolution.

2.2.7 ISIS Neutron and Muon Source

Most information presented in this section has been adapted from Ibberson (2009), Kisi & Howard (2008), and the HRPD website (2022). ISIS Neutron and Muon Source is a pulsed spallation source located next to Diamond Light Source. Muon spectroscopy and various neutron scattering techniques are used to probe the atomic structure and dynamics of materials. At ISIS, bunches (pulses) of protons are directed towards a tungsten metal target, which causes the spalling off of neutrons. This process occurs at two individual target stations, each harbouring a wide range of instruments. In the following, an overview of the inner workings of ISIS is presented, starting with the various steps involved in the production of neutrons over tailoring the beam properties and ending with the diffraction and detection process at the High-Resolution Neutron Powder Diffractometer (HRPD), where the experiments were carried out

2.2.7.1 Production of neutrons

Neutron production at ISIS starts in the ion source. In the first step, hydrogen gas and hot caesium vapour are injected into the ion source. This causes the gas to be ionised forming a so-called discharge plasma and the cations (i.e., Cs^+, H^+) are subsequently attracted towards the cathode. Caesium deposition on the cathode reduces the work function (i.e., minimum energy necessary to remove electrons from a solid). This enables electrons to be donated more easily from the caesium surface to the hydrogen atoms, thus resulting in an increased production of hydrogen anions: H^- (i.e., one proton, two electrons).

The H^- ion pulses are then extracted using a magnet and passed through the Radio Frequency Quadrupole (RFQ) accelerator, where the beam is focussed and shaped using electric fields in the radio frequency energy region produced by four electrodes. Subsequently, discrete pulses of H^- are passed on to the linear accelerator (LinAc).

The LinAc comprises four tanks accelerating the H^- ions, again using radio frequency fields, to 70 meV. 200 μs long pulses are then directed toward the synchrotron, where the final acceleration takes place. At the point of injection into the synchrotron, the H^- ions pass an alumina foil that strips off the electrons and turns them into protons.

In the synchrotron, bending magnets keep the protons on a circular path, while quadrupole magnets keep the beam focused. After orbiting the synchrotron ring approximately 10 000 times, the protons reach their peak energy of 800 meV. Subsequently, 40 pulses a second are extracted and delivered to target station one.

The water-cooled target is made from thick tungsten plates coated with tantalum to avoid corrosion. Every time the proton beam hits the target, high energy neutrons are spalled off the tungsten atoms and directed into 18 individual channels, nine located on each side of the target.

2.2.7.2 From target to instrument: moderator, guide, and choppers

The neutrons produced in the target, are too fast to be used in a neutron diffraction experiment and, therefore, must be thermalized (i.e., slowed down). Target station one features four moderators (2x room temperature water, 1 x liquid methane 110 K, 1 x liquid hydrogen at 20 K), whereby different types of moderators slow down the neutrons to different beam energies. HRPD faces the methane moderator, where neutrons are thermalized by colliding with the hydrogen atoms of methane. The underlying principle is that hydrogen has a very large neutron cross-section and high likelihood of colliding with neutrons, thus causing the incoming neutrons to slow down. It is critical to preserve the sharpness of the pulses and prevent neutrons from the preceding pulse to escape once another pulse enters the moderator. To this end a strongly neutron-absorbing gadolinium foil is inserted into the moderator whereby the foil thickness determines the time threshold upon which neutrons are absorbed. HRPD's resulting flux distribution, peaking around 2 Å, is displayed in Figure 2.8.
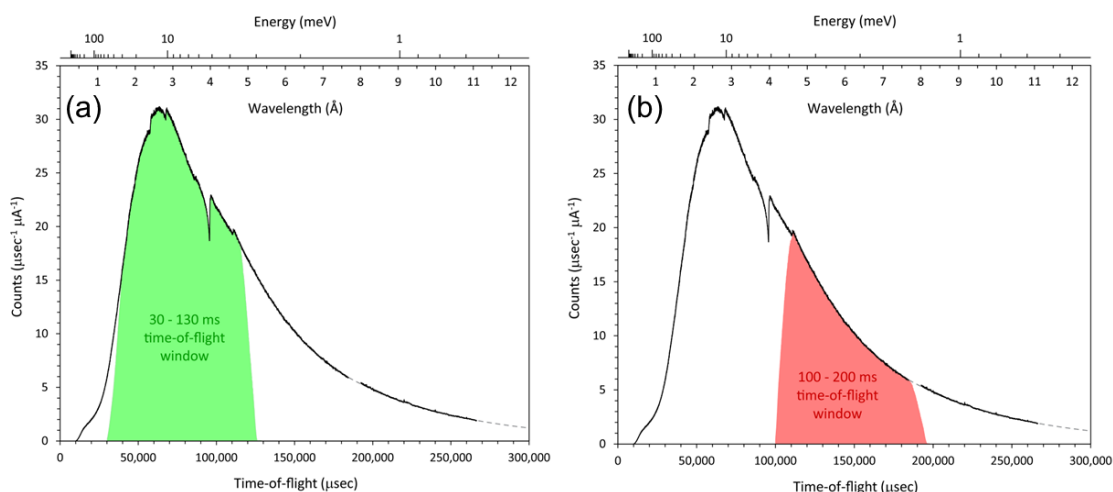
Figure 2.8 Flux distribution of the HRPD instrument. Marked regions denote the d-spacing range in the (a) 30 − 130 ms and (b) 100 − 200 ms time-of-flight window. From the HRPD website (2022).

The flight path at HRPD is ~ 95 m long. Under normal circumstances, the neutron flux would fall rapidly following a simple inverse square law, which would result in an unacceptably low neutron flux impinging on the sample for such a long flight path. To conserve the neutrons as they travel along the flight path, HRPD features a so-called supermirror guide. The supermirror guide comprises [58]Ni-coated glass (chosen for long scattering length, high natural abundance of the isotope and nickel itself, and low neutron absorption), where the neutrons bounce off by total external reflectance from the inside wall. Moreover, the guide is slightly curved (r = 36 km) for the first 60 m of the guide, followed by 33.3 m of a straight section, to reduce the direct line of sight between the target and the instrument (Figure 2.9).
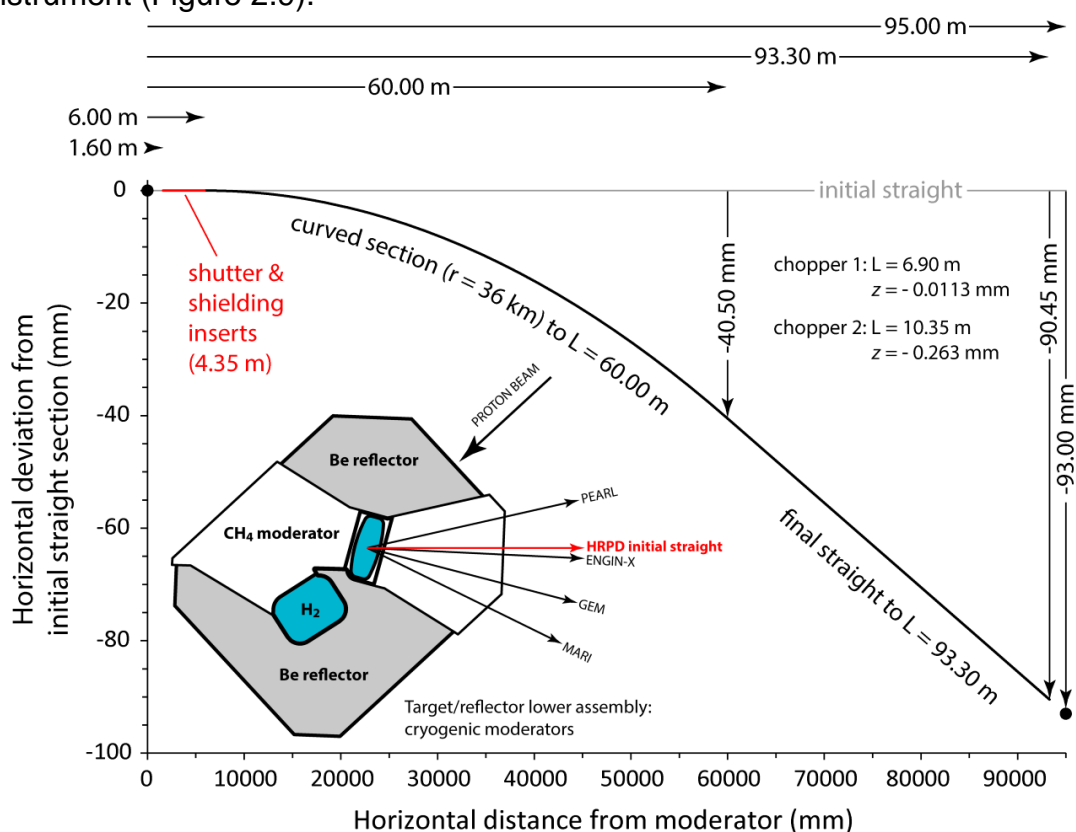
Figure 2.9 Neutron guide at HRPD instrument. From Dominic Fortes (unpublished diagram), included in this thesis with permission of the creator.

This is critical to minimise the potentially harmful effect from γ-radiation and fast neutrons, produced every time when the proton beam hits the target. Furthermore, the guide is ballistic, meaning its cross-section varies along its length, further decreasing transport losses (Figure 2.10). One rather unfortunate side effect of HRPD's long flightpath is, that although the neutrons in each of the pulses can be time sorted, the high repetition rate (40 Hz) of pulse production results in an overlap of the slow neutrons with the fast neutrons of the preceding pulse.
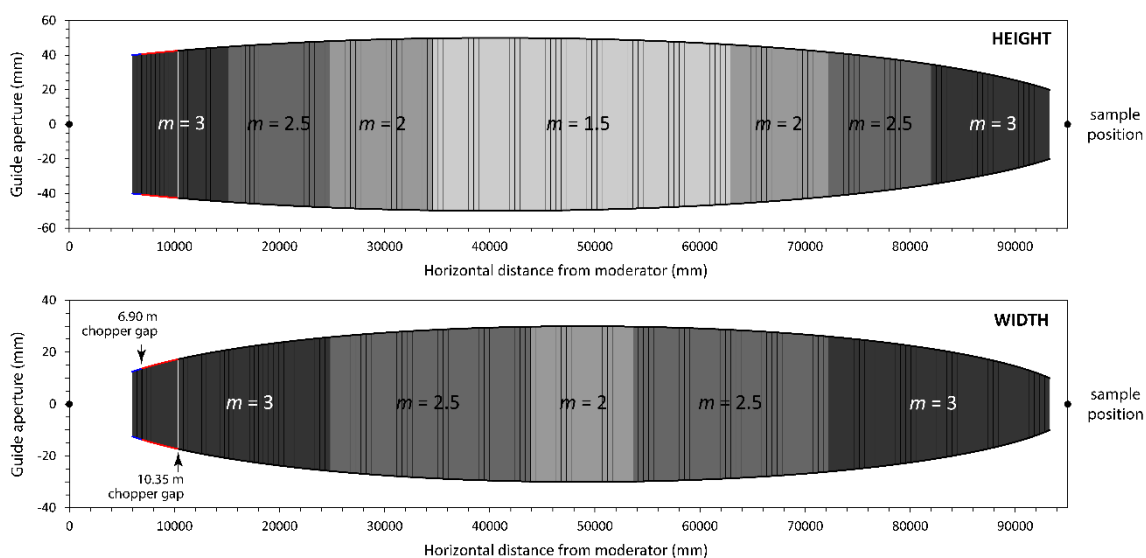
Figure 2.10 Height and width of the neutron guide vary as a function of the path length. m number indicates the grading of the nickel coating. From Dominic Fortes (unpublished diagram), included in this thesis with permission of the creator.

So-called 'choppers' are used to eliminate the time frame overlap of adjacent pulses. Choppers are rotating discs with gaps allowing the beam to pass through. At HRPD they are trimming the 40 Hz pulse rate incident from the target to 10 Hz. Chopping the pulse rate from 40 Hz poses an appreciable sacrifice, considering that by doing so, we dispose of 75% of the flux. Still, it is an absolute necessity to be able to measure 100 ms long TOF windows. For my experiments, I typically used the 30 – 130 and 100 – 200 ms window corresponding to d-spacings of 0.65 – 2.60 Å and 2.15 – 4.00 Å in backscattering, respectively, which are ideally suited to study compounds with unit-cell dimensions typically of the order of 10 Å, such as the one under investigation in this thesis.

Once the chopped pulses exit the supermirror guide, they pass through adjustable jaws made from strongly neutron-absorbing B_4C shielding material, thus collimating the incident beam. Another important property of B_4C is that it is not activated (i.e., made radioactive) by the neutron capture process that may occur when certain materials are exposed to the incident beam. At HRPD, jaw dimensions of 15 x 20 cm are typically used, providing an excellent balance between flux and resolution. The collimated beam exits the jaws, and the neutrons are scattered by the sample and detected by three detector banks.

2.1.7.3 Sample preparation and loading of the aluminium slab cans

I carried out the sample preparation and loading in a helium-filled glove bag to avoid hydrogen-deuterium exchange of the deuterated sample material with moisture from the air. First of all, the sample material is ground to a fine powder using a pestle and mortar. Before the powder can be transferred into the aluminium slab cans (Figure 2.11), one of the openings needs to be covered by a vanadium window (used because of quasi-zero neutron scattering length). After the slab can is filled with the powder, an indium wire is placed in the groove surrounding the slab can opening. Then the second vanadium window is screwed on the sample holder, hereby squeezing the indium wire into the groove to form an impermeable seal. Next, a cartridge heater and thermocouple are inserted into the holes on each side of the slab can. Lastly, all parts of the assembly but the sample cavity are masked by highly neutron-absorbing cadmium and gadolinium sheets to prevent parasitic scattering from the steel and aluminium parts that are otherwise exposed to the neutron beam.
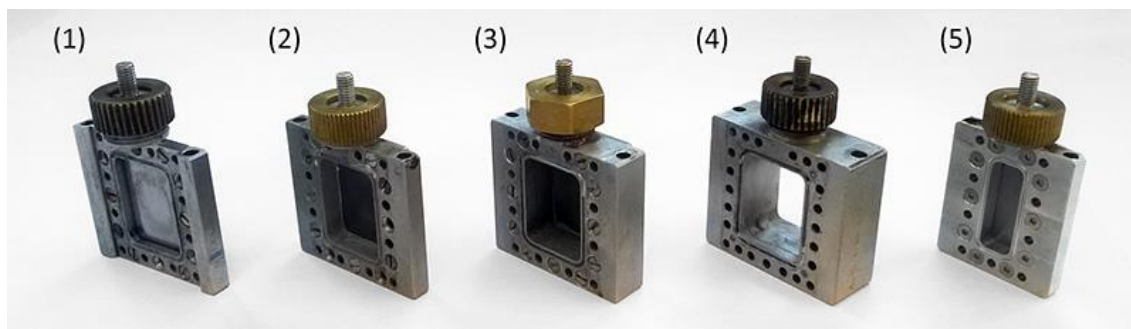
Figure 2.11 Aluminium slab cans at HRPD. From the HRPD website (2022).

2.1.7.4 Diffraction and detection

Once the sample is mounted to the centre stick and the thermocouple and heater are connected to the HRPD readout electronics, the stick is ready to be inserted into close cycled refrigerator (CCR). In a CCR, low temperatures are generated by the mechanical cyclic compression and expansion of gas (e.g., Helium at HRPD). When the collimated beam impinges on the sample in the CCR, the neutrons are scattered in different directions according to their energy (=wavelength). HRPD features four detector banks (low-angle bank: $27.47\,° < 2\theta < 32.23\,°$; 2×10^{-2}, 2 x 90 ° banks: $80.41\,° < 2\theta < 99.59°$; $\Delta d/d \sim 2\times10^{-3}$; and backscattering: $158.46\,° < 2\theta < 176.11\,°$; $\Delta d/d \sim 6\times10^{-4}$) collecting the scattered neutrons (Figure 2.12). Like X-rays, neutrons are uncharged particles. Hence, they must be converted into an electronic signal to be detected. The 90 ° and

backscattering bank use a scintillator coupled to a photomultiplier tube, the underlying principle of detection of which was already explained for the MAC detector at I11. The forward scattering detector, however, is a ^{3}He detector, interacting with neutrons according to the nuclear reaction

$$^3He + n \rightarrow {^1H} + {^3H} \qquad\qquad (2.11)$$

The hydrogen and tritium produced in this nuclear reaction have a very high kinetic energy and further ionise the gas in an avalanche-like reaction. The released electrons are directed toward the anode wire and produce detectable electrical pulses.
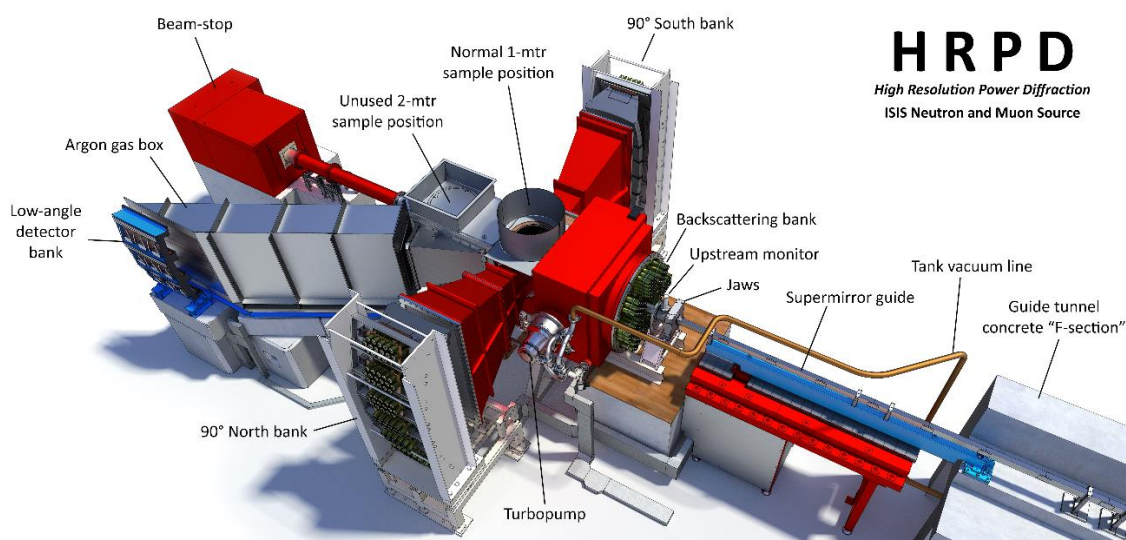
Figure 2.12 Technical drawing of the HRPD instrument, including its three detector banks. From HRPD website (2022).

2.2.8 Neutrons vs X-rays

This last section on diffraction summarises the advantages and disadvantages of using X-rays and neutrons to address the scientific problems tackled in this thesis and beyond.

One major advantage of neutrons over X-rays is the ability to locate deuterium atoms in the crystal structure. This is particularly important since all of the compounds investigated experimentally in this project contained a substantial amount of water of crystallisation. The need for the use of deuterium, however, clearly complicates the sample synthesis and experiment. The sample loading must be carried out in an inert atmosphere, and performing the synthesis with

deuterated water is very costly. Moreover, deuterated materials exhibit largely different Raman-active vibrational frequencies of the modes involving O – H vibrations compared to their protiated counterparts. In detail, the relationship between the frequencies of the O – H and O – D modes may be approximated by a constant scale factor of around 1.34 (Chio et al., 2007), which has practical applications in the assignment of vibrational modes. If one, however, aims to produce reliable reference spectra for the identification of these materials in nature, based on to the natural abundance of hydrogen over deuterium, one needs to know the energy of the O – H rather than the O – D frequencies.

Lastly, it is often assumed that deuterated and protiated materials behave in the same manner, i.e., the results obtained by studying deuterated materials in neutron diffraction experiments are equally applicable to their protiated counterparts. Although this assumption appears to be largely justified, there are a few examples where this assumption has proven to be incorrect, and substantially differing critical temperatures (Grinberg et al., 1967) and pressures (Harshman & Fiory, 2017) of phase transformations were obtained for each of the isotopologues.

Compared to the high flux undulator beamline I11, the flux incident on the sample at HRPD is several orders of magnitude lower, and the interaction of neutrons with the sample is generally weaker as compared to X-rays. Both effects result in longer data collection times but are at least somewhat counteracted by the larger sample volume (i.e., ~4140 mm^3 for 10 mm slab can at HRPD, ~0.96 mm^3 for 0.7 mm capillary at I11) exposed to the beam. Still, the longer data collection times means that fewer diffraction patterns may be acquired or fewer samples may be studied in a given time frame. This is a very critical point for large-scale facilities where every hour of beamtime is valuable and typically awarded on a competitive basis.

However, high flux is not always beneficial but can also induce radiation damage to the sample material, thereby altering the properties under investigation (see chapter 5 of this thesis) or even suppress phase transitions (Coates et al., 2021). Due to the constant flux increase at Synchrotrons around the world, one has to ask the question if the flux is not already saturated for many types of materials.

A few other advantages of the use of neutron diffraction is in the study of materials containing ions with identical or very similar electron configuration and

therefore scattering power (e.g., Al^{3+}/Si^{4+}), the study of magnetic structures, and the non-destructive analysis of large bulk materials (e.g. cultural heritage objects (Festa et al., 2020) and engineering components (Santisteban et al., 2006)).

2.2.9 Bond-valance analysis

Bond-valance analysis (BVA) is a simple yet powerful approach to analyse bonding in minerals. This section is largely based on the comprehensive review of BVA by Brown (2009). Three of the major principles of BVA are the valance sum rule ('*The sum of the bond valences at each atom is equal to the magnitude of the atomic valence*'), the principle of electroneutrality ('*The total valence of the cations is equal to the total valence of the anions*') and the principle of local charge neutrality ('*In an equilibrium condensed phase each ion arranges itself so that it is surrounded by ions of opposite charge, that is, there is no local build-up of charge'*). Since the bond-valence model is a very simple approximation, fulfilling the valence sum rule and the principles of electroneutrality and local charge neutrality alone does not provide sufficient information to predict if a crystal structure represents a thermodynamically stable configuration. At the very least, however, BVA is a simple tool to judge if a crystal structure is reasonable and to identify local valence deficiencies which allows to assign the hydrogen bond donating and potentially even the accepting ions.

Bond valances for individual bonds are computed according to

$$BV = e^{(R_0 - R_i)/U} \tag{2.12}$$

with R_i being the experimentally observed bond-length, R_0 the ion and ligand specific ideal bond-length, and U the universal parameter. R_0 and U are empirical parameters, and numerous values were reported for each of them in the scientific literature. Extensive sets of R_0 values for various cations coordinated by common ligands (e.g., O, F, Cl) were reported by Brown & Altermatt (1985) and Brese & O'Keeffe (1991) and are widely used to this date. A universal constant of 0.37 (Brown & Altermatt, 1985) is often used as U value for all bonds. Once the valance of all bonds that are incident on an ion is calculated the total valance of an ion is simply the sum of the individual bonds surrounding that ion.

BVA for cranswickite and starkeyite (supplementary section 8.5) and rozenite (supplementary section 8.3) using the Brese & O'Keeffe (1991) parameterisation are reported in this thesis. The obtained ionic valances range from 2.206 – 2.231 for Mg, 6.230 – 6.452 for S, 1.749 – 2.239 for O compare very well with values of 1.998 – 2.28 for Mg, 5.548 – 6.186 for S, 1.918 – 2.14 for O as obtained by Hawthorne & Sokolova (2012) (n.b., these authors constrained the valance sum of the bonds incident on the hydrogen atoms to be exactly 1.00) in a comprehensive BVA study of the MSHs with n < 7. The rather large absolute maximum deviations from the ideal ionic values of 0.28 (Mg), 0.452 (S), and 0.14 (O) valence units highlight the limitations of BVA in quantifying bond-valances. Nevertheless, the maximum absolute deviations correspond to relative deviations of 14.00 % (Mg), 7.50 % (S), and 11.95 % (O), a reasonable result considering the simplicity of the approach and the empirical character of the R_0 and U parameters.

BVA may not only be applied to heavy atoms, but also to study hydrogen bonding. Throughout this thesis, the R_0 and U parameterisation following Alig et al. (1994) was used to calculate valences for the hydrogen bonds. BVA is a powerful tool to identify the donor atoms of the hydrogen bonds, since the short covalent O – H bonds exhibit a large valency. Intermolecular hydrogen H⋯O bonds, in comparison, are much weaker rendering it more difficult to locate the acceptor oxygens. In any case, it is of vital importance not only to consider bond-valence calculations but also the geometry of the hydrogen bond when assigning acceptor oxygens. Although BVA alone cannot always be used to identify acceptor oxygens it is still important to include the intermolecular hydrogen bonds into the bond-valence calculation to fulfil the principles of electroneutrality and local charge neutrality. The O1 oxygen in cranswickite, for example, exhibits a deficiency of 0.5 valency units and achieves charge neutrality solely by accepting three strong hydrogen bonds. Admittedly, the valence contribution of even the strongest hydrogen bond studied in this thesis (0.137 valence units) is weak compared to the absolute large deviations of 0.452 valence units of the short-range high-valence S – O bonds from their ideal values.

Nevertheless, it is beneficial to calculate the valences of the H⋯O bonds for several reasons: As above-mentioned the valences obtained from a BVA typically deviate of the order of 10 % from their ideal values. Clearly, this yields larger absolute deviations for short-range high-valence contacts such as S – O

68

but does not justify neglecting long-range low-valence contacts. In particular, since the hydrogen bond is the most important of all directional intermolecular interactions (Steiner, 2002) and as the example of cranswickite demonstrates may be critical to resolve local charge deficiencies. Lastly, BVA provides an estimate of the valence contribution of the individual H···O interactions – regardless of if the inclusion of these contributions reduces the valence sum deviations of the individual ions from their ideal values.

Despite its limitations and considerable deviations of the order of 10 % from the ideal valences, the BVA is a powerful tool and was critical in locating the hydrogen bond donor oxygens of cranswickite (chapter 5, BVA in supplementary 8.5), identifying that the structure presented by Maynard-Casely et al. (2021) is wrong (BVA in supplementary 8.5) and analysing the hydrogen bonding system of rozenite (discussion in chapter 3, BVA in supplementary 8.3).

2.3 Raman spectroscopy

2.3.1 Introduction

Diffraction methods probe the long-range order of crystalline solids and often allow for the determination of their time-averaged crystal structure. However, by virtue of determining time-averaged atomic positions, diffraction methods may create the false impression of atoms being held in static positions through stiff chemical bonds. Yet, they vibrate dynamically with an amplitude that can be of order of 10% of an interatomic distance (Dove, 2011). In order to fully characterise a crystalline solid and its response to extreme conditions, one is interested in both the static and dynamic behaviour of atoms and their energetic properties and interaction with one another. This is where Raman spectroscopy enters the picture since it gives a unique insight into lattice dynamical properties of crystalline solids, provides valuable information on the local structural environment, and as a fingerprint method, is a powerful technique to identify minerals in the field and laboratory.

2.3.2 History

Raman scattering was first discovered in 1928 by Indian physicists Chandrasekhara Venkata Raman and Kariamanikkam Srinivasa Krishnan (Raman & Krishnan, 1928), and independently by Soviet researchers Grigory Landsberg and Leonid Mandelstam (Landsberg & Mandelstam, 1928). Raman and Krishnan, however, published their results earlier and are therefore primarily credited for discovering the Raman effect, culminating in the award of the 1930 Nobel prize in Physics to Raman.

Although the Raman effect has been known for almost 100 years, for many years, there were limitations hindering its applicability to the study of minerals (Nasdala et al., 2004). First, just one out of the order of 10 000 photons undergoes Raman scattering when interacting with a material. Due to the subtleness of the effect, one needs very advanced detectors. Moreover, a strong monochromatic light source, such as a laser, invented in 1960 (Maiman, 1960), is crucial to perform Raman scattering experiments. Lastly, minerals often contain chemical impurities, inclusions, and structural defects, that may give rise to luminescence emissions which can obstruct the Raman bands. Many technological advances were necessary to overcome these problems, but over the last few decades,

Raman spectroscopy has proven to be an indispensable tool for studying minerals. Further evidence of this is that the Perseverance Mars rover relies solely on Raman spectroscopy for mineralogical phase identification (Bhartia et al., 2021; Wiens et al., 2020).

2.3.3 Principle

The following text presents the theoretical background of Raman scattering, starting with classical electrodynamic theory to outline why Raman scattering occurs. The discussion is based on the *Raman spectroscopy: Analytical perspectives in mineralogical research* chapter (Nasdala et al., 2004) of the *Spectroscopic Methods in Mineralogy* book and the excellent lecture series by David Tuschel (Raman applications manager at *Horiba Scientific*, US, (Tuschel, 2012)).

In a Raman scattering experiment, the sample material is irradiated with a laser of wavelengths typically ranging from 400 to 785 nm. The laser light's electric and magnetic field vectors oscillate with a frequency of $4.00 - 7.85 \times 10^{14}$ s^{-1}. The electric field causes the charge carriers (electrons and protons) to oscillate at the frequency of the electric field, thus creating an oscillating dipole moment. This oscillating dipole moment emits radiation that is of the same (Rayleigh scattering), higher (Stokes-type Raman scattering), or lower (Anti-stokes-type Raman scattering) frequency as the electric field induced by the laser. The induced dipole moment μ depends on the polarizability α and the electric field E

$$\mu = \alpha E \tag{2.13}$$

Polarizability is the ease with which the electron cloud may be deformed. Eq 2.13 describes the dipole moment induced by a static electric field. The electric field of the laser light, however, is not static but oscillates sinusoidally

$$E = E_0 \cos(2\pi v t) \tag{2.14}$$

Putting eq. 2.14 into eq. 2.13 then yields following expression for the induced dipole moment

$$\mu = \alpha E_0 \cos(2\pi v t) \qquad (2.15)$$

From eq. 2.15 it is evident that the oscillating nature of the electric field results in an oscillating, and hence time-dependent, dipole moment. To further complicate things, not only the dipole moment varies with time, but also the polarizability itself:

$$\alpha = \alpha_0 + \frac{\partial \alpha}{\partial Q} Q \qquad (2.16)$$

Whereby α_0 is the static polarizability and Q is a normal vibrational coordinate i.e., a linear combination of cartesian displacement coordinates representing the displacement of the nuclei from their equilibrium position. As such eq. 2.16 states that the polarizability, defined as the ease of displacing the electrons with respect to the nuclei, depends on the actual positions of the nuclei.

One more thing that must be taken into account is that the atomic nuclei are not static but rather oscillate around their equilibrium position. Hence the normal vibrational coordinate Q also changes sinusoidally during the vibration

$$Q = Q_0 \cos(2\pi v_{vib} t) \qquad (2.17)$$

with Q_0 being the maximum value of the Q for a vibration. Note that v (eq. 2.14, eq. 2.15), the spatial frequency of the oscillating electric field, and v_{vib}, the spatial frequency of the vibration are different quantities. Accounting for the oscillating electric field and nuclei, and the changes of polarizability during the vibration then finally yields the following expression for the polarizability

$$\alpha = \alpha_0 + \frac{\partial \alpha}{\partial Q} Q_0 \cos(2\pi v_{vib} t) \qquad (2.18)$$

The dipole moment μ (eq. 2.15) may then be expressed as

$$\mu = \left(\alpha_0 + \frac{\partial \alpha}{\partial Q} Q_0 \cos(2\pi v_{vib} t)\right) E_0 \cos(2\pi v t) \qquad (2.19)$$

and after multiplying the terms in brackets, yields

$$\mu = \alpha_0 E_0 \cos(2\pi vt) + \frac{\partial \alpha}{\partial Q} Q_0 E_0 (\cos(2\pi v_{vib} t)) \cos(2\pi vt)) \qquad (2.20)$$

To tidy up things, the trigonometric identity may be applied

$$\cos(A)\cos(B) = \frac{1}{2}\left[\cos(A-B) + \cos(A+B)\right] \qquad (2.21)$$

to eq. 2.20 lastly yielding the dipole moment expressed in the form of

$$\mu = \alpha_0 E_0 \cos(2\pi vt) + \frac{\partial \alpha}{\partial Q} \frac{Q_0 E_0}{2} \left[\cos(2\pi(v-v_{vib})t) + \cos(2\pi v + v_{vib}t)\right] \quad (2.22)$$

The green, red, and blue parts represent Rayleigh, Stokes, and anti-Stokes scattering, respectively. From eq. 2.22 it is evident that for Raman scattering to occur, the change of polarizability as a function of displacement $\frac{\partial \alpha}{\partial Q}$ must be non-zero. Elucidating this on the example of the CO_2 molecule (Figure 2.13), it is evident that the symmetric stretching mode is associated with a change in $\frac{\partial \alpha}{\partial Q}$, and thus is Raman-active. For the bending and anti-symmetric stretching modes $\frac{\partial \alpha}{\partial Q}$ is zero, and thus these modes are Raman-inactive.
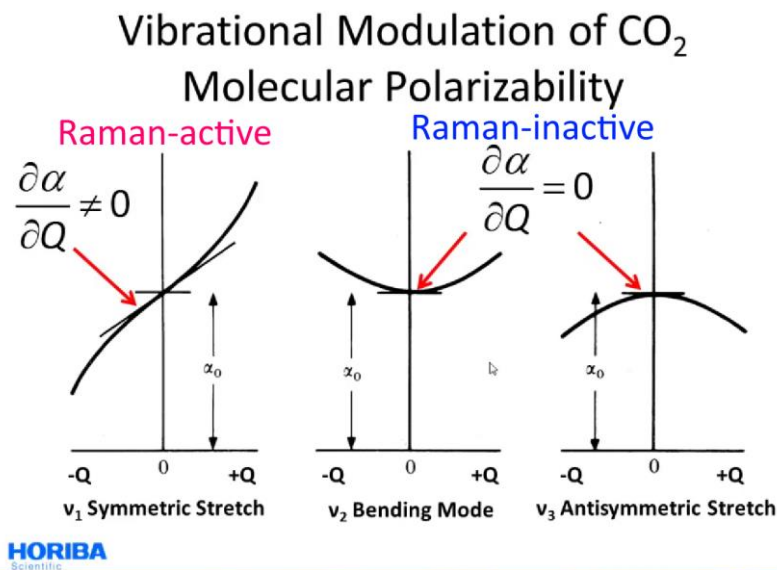
Figure 2.13 Molecular polarizability of CO_2 as a function of the displacement Q. From Tuschel (2012).

The classical electrodynamic theory provides a good explanation for why Raman and Rayleigh scattering occurs. However, a quantum-mechanical description is necessary to understand the likelihood of Stokes and anti-Stokes scattering.

Crystals exhibit vibrational states at a limited number of discrete (quantized) energy levels, but how can these vibrational states be probed? If a crystal is irradiated with a photon of energy matching the energy of a vibrational state, the photon is absorbed, and the vibration is excited. This interaction is called infrared absorption since the vibrational states are typically in the spatial frequency range $30 - 4162$ cm^{-1}, corresponding to the infrared region of the electromagnetic spectrum. If the sample is irradiated with higher energy photons, the system is excited to a virtual energy state but usually recovers to the ground state instantaneously by releasing the vibrational energy in the form of a photon exhibiting the same energy as the incident radiation (Rayleigh scattering). However, there is also a small possibility the system recovers to a higher (Stokes) or lower (anti-Stokes) energy state. As a result of this, the scattered light gains (i.e., blue-shift and anti-Stokes) or loses (i.e., red shift and Stokes) energy corresponding to the difference of the excited state to the ground state (Figure 2.14).
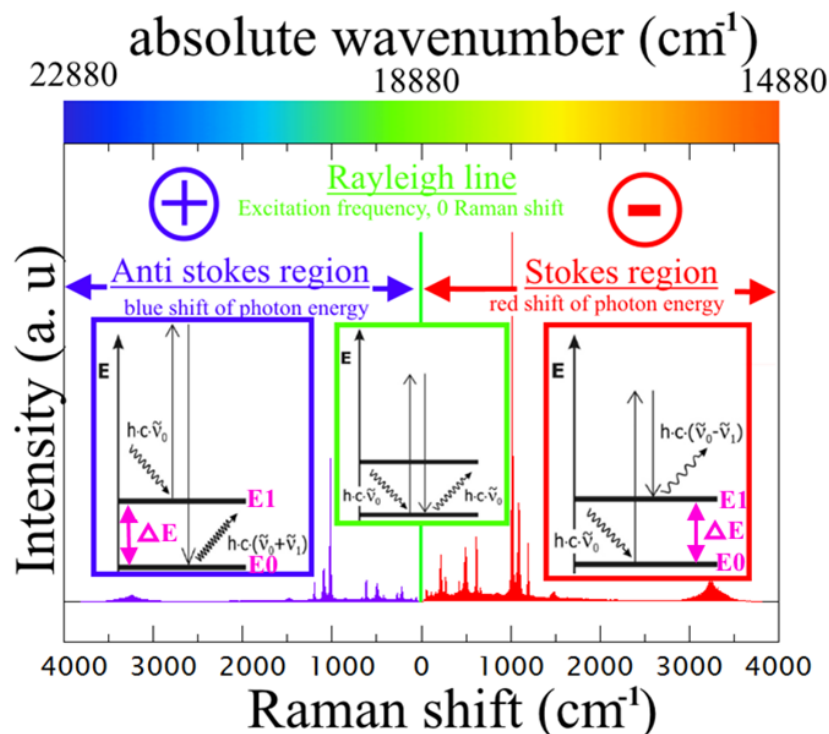
Figure 2.14 Schematic representation of Stokes and anti-Stokes Raman scattering with a green laser.

The system must recover to a lower energy state for anti-Stokes scattering to occur. For this to happen, however, the system must be in a higher vibrational

state in the first place. The population ratio for the first excited (Pv_1) and the ground state (Pv_0) follows the Maxwell-Boltzmann distribution law:

$$\frac{Pv_1}{Pv_0} = e^{-\frac{\Delta E}{k_B T}} \qquad (2.23)$$

At room temperature, a system's vast majority of vibrational units are in the ground-state. Only vibrations with very low spatial frequencies are more likely to be in the excited state and undergo anti-stokes scattering. Figure 2.15 shows that except for experiments carried out at very high temperatures and probing low-frequency vibrations, collecting Stokes-type Raman scattering is beneficial.
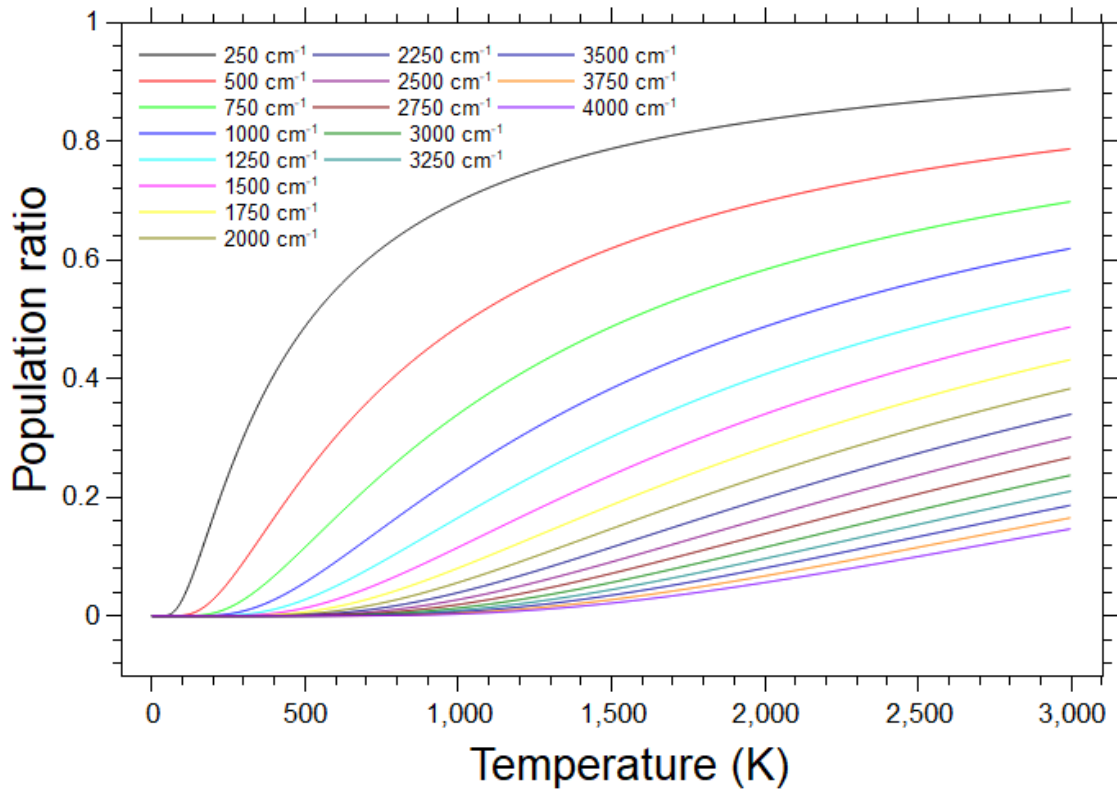
Figure 2.15 Population ratio of the first excited vs. ground state as a function of temperatures in the spatial frequency range (250 - 4000 cm^{-1})

2.3.4 Bwtek I-Raman plus spectrometer

The Raman data presented in this study was collected on a Bwtek i-Raman plus spectrometer and a green laser with a 532 nm wavelength. The system will be briefly explained in the following, and a schematic drawing of the inner workings is displayed in Figure 2.16. The purpose of a Raman spectrometer is to detect Raman scattered light and sort the signal according to its wavelength. The Raman scattered light is directed to the spectrometer via a fibre optics cable. The light passes through an aperture slit, which, among other factors, controls the spectral resolution. The light then passes through a grating, diffracting the polychromatic beam at slightly different angles depending on the photon energy. The higher the number of grooves per mm, the smaller the wavelength range, but the higher the spectral resolution. The dispersed light is then focussed by a concave mirror and reflected onto the CCD detector. Since the grating diffracts the light at slightly different angles depending on the photon energy, the positions photons hit the detector are related to their energy. Each pixel, therefore, measures photons of a certain energy range.
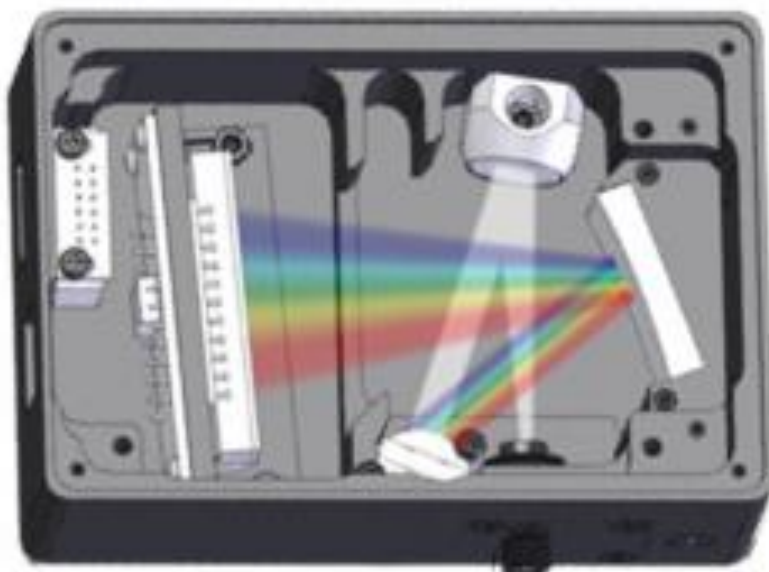
Figure 2.16 Schematic drawing of the inner workings of the Bwtek Raman spectrometer. From the Bwtek website (2022)

2.4 Quantum mechanical modelling

2.4.1 Introduction

The number of citations of a scientific paper is a commonly used measure of its impact on science. Out of the top 100 articles ever published in the scientific literature, twelve are on the subject of density functional theory (DFT), with two papers even making it to the top ten (van Noorden et al., 2014). One of the reasons for this is that there has been a 32-million-fold increase in computational power in the last 32.5 years (Marzari, 2020), therefore making vast computational resources available to a wider community. Likewise, codes for DFT modelling are getting increasingly user-friendly, thus posing a relatively shallow entry barrier for non-experts to perform such calculations. In addition, quantum mechanical modelling within the framework of DFT has become an indispensable tool for predicting the structure and properties of materials. Importantly for my project, DFT has demonstrated to be very successful in aiding the interpretation of experimental data.

In this thesis, DFT has been used to (i) rank polymorphs according to their stability and predict the (ii) elastic and (iii) vibrational properties of minerals likely to occur as rock-forming components on the surface and in the interior of planetary bodies throughout the solar system. The following contains a discussion of the theoretical basis of quantum mechanical materials modelling, emphasizing why the Schrödinger equation cannot be solved for many-electron systems. This is followed by a section on the fundamentals of DFT and, lastly, an overview of how this theory is implemented in the plane-wave DFT codes used in this thesis (CASTEP (Clark et al., 2005) and Quantum ESPRESSO (Giannozzi et al., 2009, 2017)). The discussion is based on the beginner-friendly *Density Functional Theory: A Practical Introduction* book (Sholl & Steckel, 2009) and the more mathematically inclined introduction *Materials modelling using density functional theory: properties and predictions* (Giustino, 2014). In addition, some concepts are influenced by the excellent lecture series *Fireside Chats for Lockdown Times: Introduction to DFT* (Marzari, 2020).

2.4.2 The Schrödinger equation

The Schrödinger equation governs the properties and behaviour of a quantum mechanical system.

The time-independent form of the Schrödinger equation for a single particle is

$$H\phi(\mathbf{r}) = \varepsilon\phi(\mathbf{r}) \qquad (2.24)$$

where ϕ is the wavefunction, which is not an experimentally observable quantity. $|\phi(\mathbf{r})|^2$, however, is the probability of finding the electron at point $\mathbf{r}$. ε are the energy eigenvalues of the state described by $\phi(\mathbf{r})$. The Hamiltonian H is not a quantum mechanical concept but originates from classical mechanics and represents the sum of a system's kinetic and potential energy. The Hamiltonian contains all the information about the system, such as which particles comprise the system, their kinetic energy, and how they interact. In practice, 'solving the Schrödinger equation' means nothing else than plugging in all the information we know about the system via the Hamiltonian and solving for the eigenvalues (=allowed energy values) of the electron. If one wants to model minerals from first-principles, one has to solve the Schrödinger equation for systems involving numerous protons, nuclei, and electrons. In a first approximation, atoms are divided into nuclei (protons and neutrons) and the surrounding electrons rather than building the Hamiltonian treating contributions from protons and neutrons in the core separately. Then the many-body wavefunction ψ is introduced, which depends upon the positions of each electron and nucleus of the system. For a system comprising N electrons with coordinates $\mathbf{r}_1, \mathbf{r}_2, \dots, \mathbf{r}_N$ and M nuclei with coordinates $\mathbf{R}_1, \mathbf{R}_2, \dots, \mathbf{R}_M$ this yields

$$\psi = \psi(\mathbf{r}_1, \mathbf{r}_2, \dots, \mathbf{r}_N; \mathbf{R}_1, \mathbf{R}_2, \dots, \mathbf{R}_M) \qquad (2.25)$$

$|\psi(\mathbf{r}_1, \mathbf{r}_2, \dots, \mathbf{r}_N; \mathbf{R}_1, \mathbf{R}_2, \dots, \mathbf{R}_M)|^2$ then represent the probability of simultaneously locating the first electron at $\mathbf{r}_1$, the second at $\mathbf{r}_2$ as well as finding the first nucleus at $\mathbf{R}_1$, second at $\mathbf{R}_2$, and so forth. The time-independent form of the many-body Schrödinger equation then is

$$H\psi = E_{tot}\psi \tag{2.26}$$

with E_{tot} being the total energy of a system in the state described by the many-body wavefunction ψ.

As mentioned above, to solve this equation, one needs to know the Hamiltonian, which for a many-body system comprising N electrons with coordinates $\mathbf{r}_1, \mathbf{r}_2, ..., \mathbf{r}_N$ and M nuclei with coordinates $\mathbf{R}_1, \mathbf{R}_2, ..., \mathbf{R}_M$ has the following contributions

(i)   the quantum kinetic energy of the electron

$$T_e = -\sum_{i=1} \nabla_i^2 \frac{\hbar^2}{2m_e} \tag{2.27}$$

Where m_e is the electron mass, $\hbar$ is Planck's constant, and the Laplacian ∇_i^2 (i.e., 2nd derivative) is a measure for the curvature of the wavefunction. The summation runs from 1 to the number of electrons N.

(ii)   the quantum kinetic energy of the nucleus

$$T_N = -\sum_{I=1} \nabla_I^2 \frac{\hbar^2}{2M_I} \tag{2.28}$$

where M_I is the mass of the nucleus, and the summation runs from 1 to the number of nuclei M.

The potential energy term includes the Coulomb interaction between all three pairs of charges

(iii)   Coulomb attraction between electrons and nuclei

$$V_{e-N} = -\sum_{i,I} \frac{e^2}{4\pi\epsilon_0} \frac{Z_I}{|\mathbf{r}_i - \mathbf{R}_I|} \tag{2.29}$$

with i and I running from 1 to N and M, respectively. Z_I is the atomic number.

(iv)   Coulomb repulsion between electrons

$$V_{e-e} = \frac{1}{2} \sum_{i \neq j} \frac{e^2}{4\pi\epsilon_0} \frac{1}{|\mathbf{r}_i - \mathbf{r}_j|} \tag{2.30}$$

The summation runs from 1 to N for both indices, whereby $i = j$ is excluded since the very same electron does not repel itself. Lastly, the summation is normalized by ½ to include only one contribution per pair of electrons.

(v)   Coulomb repulsion between nuclei

$$V_{N-N} = \frac{1}{2} \sum_{I \neq J}^{M} \frac{e^2}{4\pi\epsilon_0} \frac{Z_I Z_J}{|\mathbf{R}_I - \mathbf{R}_J|} \tag{2.31}$$

The summation runs from 1 to M, again, for both indices. Z_I and Z_J are the atomic number of the respective nuclei. Substituting eq. $2.27 - 2.31$ for H in eq. 2.26 then yields the many-body Schrödinger equation

$$\left[-\sum_{i=1} \nabla_i^2 \frac{\hbar^2}{2m_e} - \sum_{I=1} \nabla_I^2 \frac{\hbar^2}{2M_I} - \sum_{i,I} \frac{e^2}{4\pi\epsilon_0} \frac{Z_I}{|\mathbf{r}_i - \mathbf{R}_I|} \right.$$
$$\left. + \frac{1}{2}\sum_{i \neq j} \frac{e^2}{4\pi\epsilon_0} \frac{1}{|\mathbf{r}_i - \mathbf{r}_j|} + \frac{1}{2}\sum_{I \neq J}^{N} \frac{e^2}{4\pi\epsilon_0} \frac{Z_I Z_J}{|\mathbf{R}_I - \mathbf{R}_J|} \right] \psi = E_{tot}\psi \tag{2.32}$$

For simplicity, the Schrödinger equation may be expressed in atomic units, thus eliminating all fundamental constants (e.g., mass of the electron, Planck's constant) appearing in eq. 2.32:

$$\left[-\sum_{i=1} \frac{\nabla_i^2}{2} - \sum_{I=1} \frac{\nabla_I^2}{2M_I} - \sum_{i,I} \frac{Z_I}{|\mathbf{r}_i - \mathbf{R}_I|} + \frac{1}{2}\sum_{i \neq j} \frac{1}{|\mathbf{r}_i - \mathbf{r}_j|} + \frac{1}{2}\sum_{I \neq J}^{N} \frac{Z_I Z_J}{|\mathbf{R}_I - \mathbf{R}_J|} \right] \psi = E_{tot}\psi$$
$$\tag{2.33}$$

To be clear, eq. 2.33 is not any easier to solve than eq. 2.32, but it is advantageous to reduce notational clutter before introducing real simplifications to the many-body Schrödinger equation.

2.4.3 The Born-Oppenheimer approximation

The first real simplification can be made by approximating the nuclei as classical objects rather than quantum mechanical ones. This approximation is called the Born-Oppenheimer or Clamped-Nuclei approximation and is based on the fact that protons and neutrons are ~1800 heavier than electrons and, therefore, may be approximated as static in comparison with the fast and light electrons. By virtue of being approximated as static, the nuclei do not exhibit any kinetic energy, thus eliminating this contribution to the Hamiltonian. In addition, the Coulomb repulsion between nuclei takes a constant value. For convenience, the Coulomb repulsion constant can be brought on the right-hand side of the total energy term:

$$E = E_{tot} - \frac{1}{2} \sum_{I \neq J}^{N} \frac{Z_I Z_J}{|\mathbf{R}_I - \mathbf{R}_J|} \tag{2.34}$$

yielding the following simplified Schrödinger equation:

$$\left[-\sum_{i=1} \frac{\nabla_i^2}{2} - \sum_{i,I} \frac{Z_I}{|\mathbf{r}_i - \mathbf{R}_I|} + \frac{1}{2} \sum_{i \neq j} \frac{1}{|\mathbf{r}_i - \mathbf{r}_j|} \right] \psi = E\psi \tag{2.35}$$

So far, the wavefunction depends on the nuclear coordinates $\mathbf{R}_I$ and the electron coordinates $\mathbf{r}_i$. Hence every electron and nuclei add 3 x N and 3 x M, dimensions, respectively, to the Schrödinger equation. The equation may be further simplified by introducing the external potential $V_N(\mathbf{r})$

$$V_N(\mathbf{r}) = \sum_I \frac{Z_I}{|\mathbf{r} - \mathbf{R}_I|} \tag{2.36}$$

which is the Coulomb potential of the nuclei experienced by the electrons and solely depends on the static nuclear positions. In other words, the external

potential defines the energy landscape, shaped by the Coulomb interaction of the static nuclei, that the electrons move in.

This then yields the central equation of electronic structure theory

$$\left[-\sum_{i=1}\frac{\nabla_i^2}{2} - \sum_i V_N(\mathbf{r}_i) + \frac{1}{2}\sum_{i\neq j}\frac{1}{|\mathbf{r}_i - \mathbf{r}_j|}\right]\psi = E\psi \qquad (2.37)$$

It is noteworthy that the wavefunction in eq. 2.35 depends on $\psi(\mathbf{r}_1,\mathbf{r}_2,...,\mathbf{r}_N;\mathbf{R}_1,\mathbf{R}_2,...,\mathbf{R}_M)$, whereas in eq. 2.37 the wavefunction depends only on the electron coordinates $\psi(\mathbf{r}_1,\mathbf{r}_2,...,\mathbf{r}_N)$.

Although introducing the external potential simplifies the Schrödinger equation, it still cannot be solved for a many-electron system. The one-body terms (i.e., kinetic energy and external potential) of the Hamiltonian are relatively easily dealt with; the two-body term (Coulomb electron-electron repulsion), however, prevents the solution of the many-body Schrödinger equation. In summary, although the equation that describes the properties of matter at the subatomic level is known, one cannot solve this equation exactly for systems more complex than a single hydrogen atom. Additional approximations must be made if one wants to solve the Schrödinger equation for many-body systems.

2.4.4 Non-interacting electrons, mean-field approximation, and Hartree potential

The most straightforward way to eliminate the many-body term from the Schrödinger equation is to approximate the electrons as non-interacting. The main benefit of this approximation is that the many-body Schrödinger equation may then be described as the sum of the single-particle Schrödinger equations. Due to the Coulomb repulsion of like-charged electrons, however, approximating the electrons as non-interacting is not realistic and thus does not yield meaningful results for the electronic structure of real systems. The so-called Mean-field approximation tackles this problem by maintaining single-particle description while also taking the electron's Coulomb repulsion into account via the Hartree potential $V_H(\mathbf{r})$

$$V_H(\mathbf{r}) = \int d\mathbf{r}' \frac{n(\mathbf{r}')}{|\mathbf{r} - \mathbf{r}'|} \tag{2.38}$$

Adding the Hartree potential to the single electron wavefunction then yields

$$\left[-\frac{\nabla_i^2}{2} + V_N(\mathbf{r}) + V_H(\mathbf{r}) \right] \phi_i(\mathbf{r}) = \varepsilon_i \phi_i(\mathbf{r}) \tag{2.39}$$

with $\phi_i(\mathbf{r})$ corresponding to the single particle wavefunction and ε_i the eigenvalues (=allowed energy levels) of that wavefunction.

However, eq. 2.39 may still not simply be solved since it contains a circular problem: To solve the Schrödinger equation and obtain the wavefunction, one must know the Hartree potential. To calculate the Hartree potential, the electron density must be known, and to know the electron density, one needs to know the wavefunction. To solve this circular problem, Hartree introduced the self-consistent field method, which will be explained in a separate section in detail. But even if eq. 2.39 is solved using the self-consistent field method; the Mean-field approximation, by virtue of being an approximation from classical physics, does not contain critical quantum-mechanical contributions to the Hamiltonian. Therefore, it is not accurate enough to predict the behavior and properties of materials at the subatomic level.

2.4.5 Fermionic anti-symmetry and the Pauli exclusion principle

Although Hartree made substantial progress towards solving the Schrödinger equation by introducing the Hartree potential and the self-consistent field method, at this stage, he did not yet account for one of the fundamental properties of a quantum mechanical system called total anti-symmetry. All elementary particles are either bosons (integer spin) or fermions (half-integer spin). Electrons are fermions; hence the electronic wavefunction must be totally anti-symmetric

$$\psi(\mathbf{r}_1, \mathbf{r}_2) = -\psi(\mathbf{r}_2, \mathbf{r}_1) \tag{2.40}$$

If any variable (i.e., electron coordinate, spin) are interchanged, the wavefunction must swap sign. A totally antisymmetric wavefunction is constructed as a so-called Slater determinant, here stated for a two-electron system $(\mathbf{r}_1, \mathbf{r}_2)$ that may occupy orbitals α and β.

$$\psi(\mathbf{r}_1, \mathbf{r}_2) = \frac{1}{\sqrt{2}} \begin{Vmatrix} \phi_\alpha(\mathbf{r}_1) & \phi_\beta(\mathbf{r}_1) \\ \phi_\alpha(\mathbf{r}_2) & \phi_\beta(\mathbf{r}_2) \end{Vmatrix} = \frac{1}{\sqrt{2}} \left[\phi_\alpha(\mathbf{r}_1)\phi_\beta(\mathbf{r}_2) - \phi_\beta(\mathbf{r}_1)\phi_\alpha(\mathbf{r}_2) \right] \quad (2.41)$$

For systems of more than two electrons, the Slater determinants prefactor becomes $N!^{-1/2}$. Eq. 2.41 is totally anti-symmetric because if $\mathbf{r}_1$ and $\mathbf{r}_2$ are interchanged, the wavefunction changes sign. Furthermore, if $\mathbf{r}_1$ and $\mathbf{r}_2$ were identical the determinant vanishes. From eq. 2.41 it is evident that it is impossible to find two electrons with same position and spin. This principle is called the Pauli exclusion principle, stating that the individual electron wavefunction can be occupied by two separate electrons, provided they have different spins.

2.4.6 Electron exchange and correlation

From the Pauli exclusion principle, one may directly obtain the two final contributions to the Hamiltonian that were missing in Hartree theory. These are the exchange V_x (=the amount of energy released when two electrons with the same spin swap position) and the correlation V_c (=a measure of how the movement of one electron is influenced by the presence of all the other electrons of the system) potentials. Notably, these two potentials do not have an analog in classical mechanics. To this date, the exact form of V_x and V_c are still unknown and must be approximated.

2.4.7 Density functional theory

2.4.7.1 Hohenberg and Kohn theorems

Density functional theory reduces the problem of solving the many-body Schrödinger equation to the determination of the electron <u>density</u> $n(\mathbf{r})$ (a 3-dimensional function), which minimizes a <u>functional</u> $F[n(\mathbf{r})]$. The core concept of density functional theory was developed by Hohenberg & Kohn (1964) in two theorems:

The ground-state energy from the Schrödinger equation is a unique functional of the electron density $F[n(\mathbf{r})]$.
First Hohenberg-Kohn Theorem

The electron density that minimizes the energy of the overall functional is the true electron density corresponding to the full solution of the Schrödinger equation.
Second Hohenberg-Kohn Theorem

The importance of these theorems cannot be overstated since they provide us with an alternative to the Schrödinger equation expressed in terms of the electron density only! It is also noteworthy that although solving the many-body Schrödinger equation is a problem of fundamental importance for quantum mechanics, the wavefunction is not an experimental observable, but what is observable is the electron density.

Expressing the ground state energy E as a functional of the electron density $F[n(\mathbf{r})]$ yields

$$E = F[n(\mathbf{r})] = \int d\mathbf{r}\, n(\mathbf{r}) V_N(\mathbf{r}) - \sum_i \int d\mathbf{r}\, \phi_i^*(\mathbf{r}) \frac{\nabla^2}{2} \phi_i(\mathbf{r})$$
$$+ E_H[n(\mathbf{r})] + E_{xc}[n(\mathbf{r})] \tag{2.42}$$

The terms are the external potential, kinetic energy, Hartree energy, and exchange correlation energy, respectively. The first three terms include the total energy within the independent electron approximation and potential placed in a Mean-field such that the electrons feel the Coulomb repulsion from all the other electrons in the system (=Hartree), and are relatively easily computable. The

problematic term is the exchange-correlation energy $E_{xc}[n]$, i.e., the difference between the energy obtained using the Hartree model, to the exact ground state energy obtained from the solution of the many-body Schrödinger equation.

2.4.7.2 Kohn-Sham Equations

The Hohenberg and Kohn theorems (Hohenberg & Kohn, 1964) do not state anything about the form of $E_{xc}[n]$ other than it must be a functional of the ground state electron density. If the exact functional form $E_{xc}[n]$ was known, one would obtain the exact ground state energy of the many-body Schrödinger equation. Thus, it is not surprising that considerable effort has been put into finding the exact form of the functional $E_{xc}[n]$, but unfortunately, it is still not known.

Not being discouraged by this, Kohn & Sham (1965) built on the Hohenberg and Kohn theorem and demonstrated how to deal with the $E_{xc}[n]$ term. Naturally, they used the Born-Oppenheimer approximation and treated the nuclei as classical objects. Secondly, the electrons (termed Kohn-Sham electrons to distinguish them from real electrons) were approximated as non-interacting. To compensate for the unphysical approximation of non-interacting electrons at least partially, they used the Mean-field approximation by adding the Hartree potential. Lastly, they introduced the exchange-correlation potential into the equation resulting in the Kohn-Sham equation:

$$\left[-\frac{1}{2}\nabla^2 + V_N(\mathbf{r}) + V_H(\mathbf{r}) + V_{xc}(\mathbf{r}) \right] \phi_i(\mathbf{r}) = \varepsilon_i \phi_i(\mathbf{r}) \qquad (2.43)$$

It is noteworthy that eq. 2.43 is almost identical to the single-particle Schrödinger equation (eq 2.39). ϕ_i is the single particle wave-function of the Kohn-Sham electron i and ε_i are the eigenvalues of that wavefunction. Regarding the physical meaning of the Kohn-Sham wavefunctions, it suffices to say that they are, strictly speaking, just a mathematical tool to build the electron density according to

$$n(\mathbf{r}) = \sum_i |\phi_i(\mathbf{r})|^2 \qquad (2.44)$$

2.4.7.3 Local density approximation

The early 1980s mark the beginning of performing DFT calculations on real materials rather than just model systems. Perdew & Zunger (1981) parameterized an explicit expression $E_{xc}[n]$ by assuming it takes the same value as in the homogenous electron gas. The exchange energy of the electron gas can be determined exactly, and the correlation energy using numerical methods. This approximation is called the local density approximation (LDA) and was successfully applied to a wide range of materials. At first sight, it is rather surprising that such a simple approximation works at all. Meaningful results can be obtained because the LDA correctly models the spherical average of the exchange hole. The exchange hole is the lack of probability of finding one electron in the close vicinity of another because they repel each other. Although LDA does not capture the complex shape of the electron-hole, it correctly captures the spherical average of the charge density surrounding an electron. Despite the successful application of the LDA to predict the properties of numerous materials, there are also some notable examples where this approximation failed to predict the correct ground state (e.g., iron as non-magnetic hexagonal-close-packed, instead of ferromagnetic face-centred-cubic (Sholl & Steckel, 2009)).

2.4.7.4 Generalized Gradient approximation (GGA)

To get more accurate results, the GGA was introduced which, in addition to the local density, considers the gradient of the electron density of the homogenous electron gas to approximate $E_{xc}[n]$. There is a plethora of GGA-type exchange-correlation functionals, and many of them are tailored to a specific use case. This means that some work well for one type of calculation or material but perform rather poorly for others. For this work, I used the standard Perdew-Burke-Enzernhofer (PBE) and Perdew-Burke-Enzernhofer dedicated solid state (PBEsol) functionals (Perdew et al., 1996, 2008), which are both among the most used and tested exchange-correlation functional approximations (n.b. over 157000 citations for Perdew et al. (1996)).

2.4.7.5 The self-consistent field (SCF) method

It was already noted earlier that a self-consistent field method must be used to solve the Kohn-Sham equations. Again, the reason is that some contributions to the Hamiltonian require prior knowledge of the electron density to be calculated. A typical workflow for the self-consistent field method (Figure 2.17) is to calculate the external potential for a set of nuclei, guess a trial electron density, use this electron density to compute the Hartree and exchange-correlation potentials, and combine all of these contributions to solve the Kohn-sham equations. The electron density obtained from the solution of the Kohn-Sham equation is then used to calculate the potentials and again solve the Kohn-Sham equation. If the electron density, computed at the start of the self-consistent field cycle, equals the one obtained from the Kohn-Sham density, the ground-state energy is found, and the calculation is converged. If this is not the case, the Kohn-Sham electron density will be used as the starting point for the next self-consistent field cycle, and this procedure is repeated until convergence is achieved.
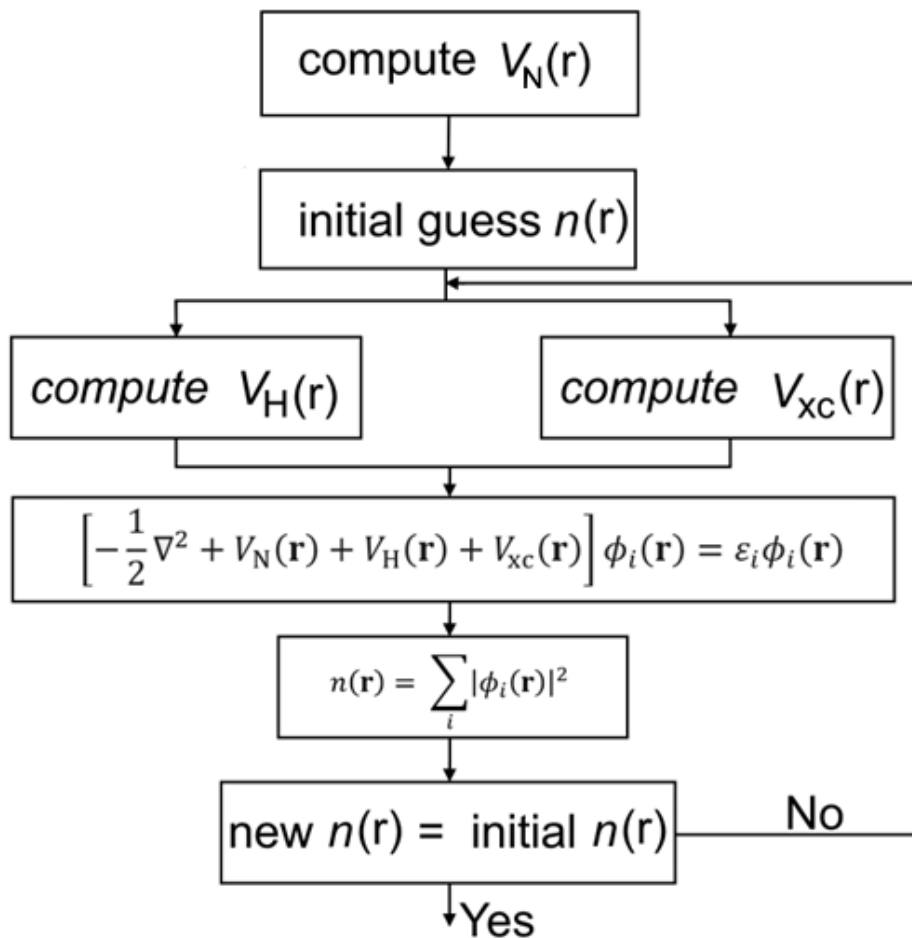
Figure 2.17 Flow chart for solving the Kohn-Sham equations self-consistently. The self-consistent cycles are repeated until the computed electron density at this iteration agrees with the electron density computed in the previous iteration within a predefined convergence tolerance.

2.4.7.6 Dispersion (DFT - D) and self-interaction error (DFT + U) correction

One of the most pronounced failures of standard LDA and GGA-type functionals is the accurate treatment of long-range forces between atoms arising from correlated electronic fluctuations commonly known as London dispersion forces. Dispersion forces between two atoms at a distance x decay as $-1/x^6$, semi-local density functional approximations, however, treat the decay exponentially as e^{-x}. In order to compensate for this shortcoming, considerable effort has been put into the development of numerous dispersion correction methods. Due to their successful application to a large variety of chemical compounds and being implemented as an off-the-shelf option in many popular quantum chemistry codes (e.g. CASTEP, Quantum Espresso) the D2 (Grimme, 2006), TS (Tkatchenko & Scheffler, 2009) and MBD (Ambrosetti et al., 2014) correction schemes were used. At this point it suffices to say that these corrections yielded very accurate ground state geometries for the compounds studied in this thesis. For a detailed description of each of these correction schemes I refer to chapter 3 of this thesis and the excellent review paper by Grimme et al. (2016).

A second common failure of standard LDA and GGA-type functionals is the accurate modelling of strongly correlated systems. This failure stems from the Hartree potential, which includes the electrostatic interaction of each electron with the entire average electron density distribution of the system, including itself. This clearly unphysical interaction is referred to as the self-interaction error and is particularly pronounced for strongly correlated systems (i.e., d and f electrons). For such systems, one cannot simply consider any electron as being influenced by the average electron density distribution, but each electron has a complex influence on its neighbours. There are numerous methods to correct for the self-interaction error, but a particularly effective and computationally cheap correction is the DFT + U method (Timrov et al., 2018, 2021). This method introduces an additional so-called Hubbard U term and splits the electrons in two subsystems. The first subsystem treats the s and p electrons which are well described by the standard LDA and GGA-type exchange-correlation functionals. The second subsystem is concerned with the strongly correlated d and f electrons and includes the additional U term. An appropriate value for the U term can be computed from first principles, which will be demonstrated in detail in chapter 4,

where the DFT + U method was successfully applied to accurately predict the phonon frequencies of rozenite.

2.4.8 Plane-wave DFT

This section describes how the Kohn-Sham equations are solved in practice. So-called plane-wave DFT allows solving the Kohn-Sham equations numerically by representing the wavefunction as a Fourier series of plane waves and then solving for the Fourier coefficients. This approach is particularly well suited for crystals since both plane waves and crystals are periodic. In practice, only one unit-cell must be simulated, which is then repeated periodically in all three dimensions. First of all, plane-wave basis vectors ($\mathbf{b}_1$, $\mathbf{b}_2$, $\mathbf{b}_3$) mutually orthogonal in reciprocal space are chosen

$$\mathbf{b}_1 = 2\pi \frac{\mathbf{a}_2 \times \mathbf{a}_3}{\mathbf{a}_1(\mathbf{a}_2 \times \mathbf{a}_3)} \quad \mathbf{b}_2 = 2\pi \frac{\mathbf{a}_3 \times \mathbf{a}_1}{\mathbf{a}_1(\mathbf{a}_2 \times \mathbf{a}_3)} \quad \mathbf{b}_3 = 2\pi \frac{\mathbf{a}_1 \times \mathbf{a}_2}{\mathbf{a}_1(\mathbf{a}_2 \times \mathbf{a}_3)} \quad (2.45)$$

with $\mathbf{a}_1$, $\mathbf{a}_2$ and $\mathbf{a}_3$ are a crystal's lattice vectors in real space.

According to Bloch's theorem (Bloch, 1929) each crystal orbital with wavevector $\mathbf{k}$ is a product of a periodic function and a plane wave

$$\phi_{\mathbf{k}}(\mathbf{r}) = u_{\mathbf{k}}(\mathbf{r})e^{i\mathbf{k}\cdot\mathbf{r}}$$

$$(2.46)$$

The periodic function $u_{\mathbf{k}}(\mathbf{r})$ is expanded as a Fourier series yielding

$$u_{\mathbf{k}}(\mathbf{r}) = \sum_{\mathbf{G}} c_{\mathbf{k}+\mathbf{G}}e^{i\mathbf{G}\cdot\mathbf{r}}$$

$$(2.47)$$

with each plane wave's reciprocal lattice vector $\mathbf{G}$ being

$$\mathbf{G} = m_1\mathbf{b}_1 + m_2\mathbf{b}_2 + m_3\mathbf{b}_3 \qquad (2.48)$$

Ideally, the summation in eq 2.47 would run over an infinite number of $\mathbf{G}$-vectors. The more $\mathbf{G}$-vectors, the finer details of the wavefunction may be represented by the plane-wave expansion. However, as in every Fourier

expansion, there comes the point where adding increasingly fine details does not improve the modelling of the plane wave anymore but just increases the computational cost. Therefore, a plane-wave kinetic energy cut-off E_{cut} is introduced that truncates the Fourier expansion:

$$E_{cut} = \frac{|\mathbf{G}_{max}|^2}{2} \tag{2.49}$$

This parameter represents the quantum kinetic energy of the plane-wave with the highest $\mathbf{G}$-vector. In practice, this parameter is determined in a convergence test (Figure 2.18).
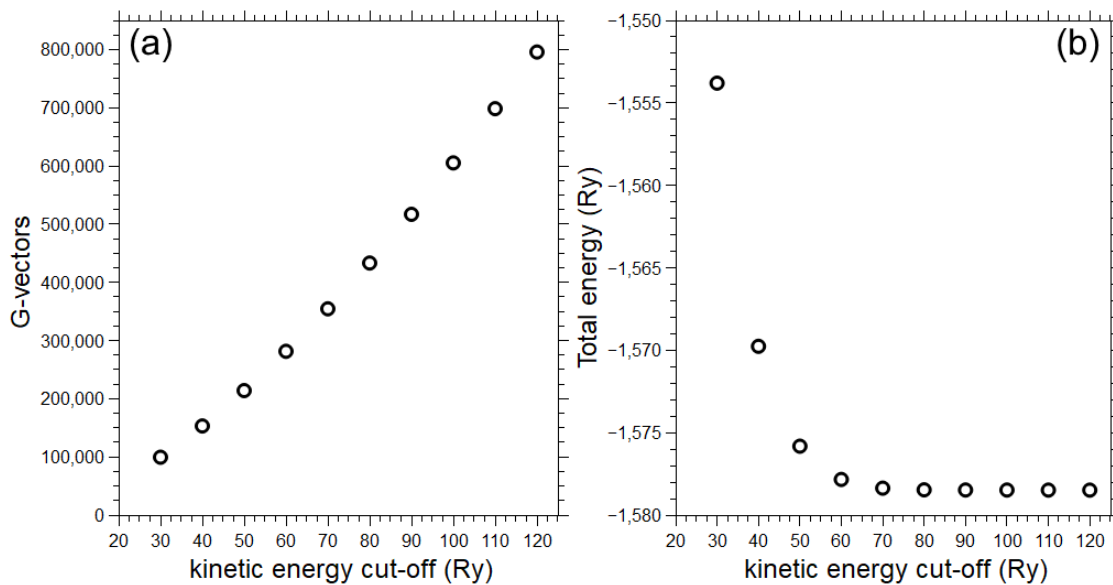
Figure 2.18 (a) number of $\mathbf{G}$-vectors is increasing with increasing kinetic energy cut-off (b) the total energy of the system decreases with increasing cut-off values until 70 Ry. Adding higher energy $\mathbf{G}$-vectors just increases the computational cost but does not improve the accuracy of the calculation.

That is, multiple runs with steadily increasing E_{cut} are performed. The parameter is considered converged if the total energy does not change significantly when E_{cut} is further increased. Clearly, increasing E_{cut} makes the calculation increasingly computationally expensive, therefore, convergence testing is critical to find the threshold upon which a further increase would merely increase the computational cost but not the accuracy of the results.

2.4.8.1 $\mathbf{k}$-points

$\mathbf{k}$ effectively represents the phase of the plane wave and may be represented as $\mathbf{k}$-points in the Brillouin zone. As an example, a $\mathbf{k}$-point ¼ , ½ , 0 means that the phase is repeated every four simulation cells in k_x, every two in

k_y, and every cell in k_z. In practice, the **k**-points are evenly spaced throughout the Brillouin zone on a so-called Monkhorst-Pack grid (Monkhorst & Pack, 1976).

From equation 2.46 and 2.47 it is evident that the energy of every Kohn-Sham orbital varies with **k**. Ideally one would solve the one electron Kohn-Sham equations for an infinite number of **k**-points. However, solutions for the Kohn-Sham equations change very slowly with **k**. Therefore, the Kohn-Sham equations may be solved for a finite set of phases, and as for the **G**-vectors the minimum number of **k**-points necessary to obtain converged results is determined in a convergence test.

2.4.8.2 Pseudopotential

The electrons close to the core have a very high kinetic energy. Therefore, to accurately model them using the plane-wave approach, one would need to use very high kinetic energy cut-offs, making the calculation substantially more computationally expensive. In contrast to the valence electrons, electrons close to the core generally are not involved in chemical bonding, one of the main properties of interest in material simulations. For this reason, the core electrons and nuclei are substituted by a pseudopotential. These pseudopotentials exhibit unphysically smoothed wavefunctions and potentials below the cut-off regions but still get the total energy right. Critically they are constructed in such a way
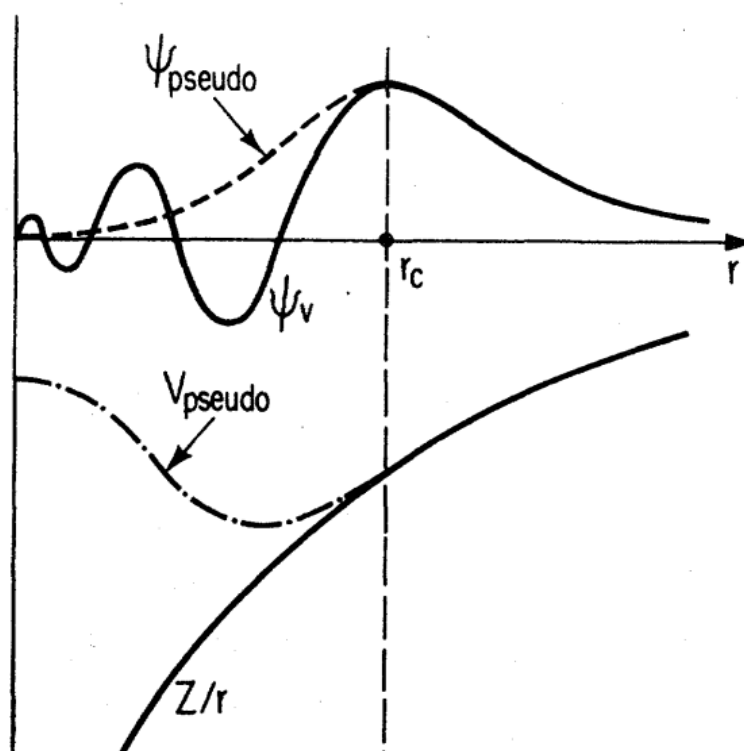
Figure 2.19 Schematic drawing of pseudo wavefunction and potential. From Payne et al. (1992).

that they model the wavefunction and potentials outside of the core region exactly (Figure 2.19).

Three types of pseudopotentials are commonly used in DFT: Norm-conserving, ultrasoft, and projector-augmented wave. I have used ultrasoft pseudopotentials because they allow for lower cut-off energies and thus substantially reduce the computational cost. One might now ask why then not always use ultrasoft pseudopotentials. Well, they are computationally more difficult to handle than norm-conserving pseudopotentials, and therefore some functionalities of DFT codes are not implemented yet in conjunction with ultrasoft pseudopotentials. Moreover, some properties such as nuclear magnetic resonance and X-ray absorption, depend on the core-electron density. Typically, projector-augmented wave pseudopotentials, allowing to reconstruct the core-electron density, are used for such properties.

2.4.8.3 Geometry optimisation

Next to the self-consistent field calculations that yield a system's charge density and ground state energy, it is often useful to compute the ground state geometry. The input geometry used in a DFT calculation is usually an experimentally determined crystal structure. The atomic positions in the experimentally determined structure differ from the ground state equilibrium structure for two reasons. First, the atoms in a crystal oscillate dynamically around their equilibrium position. DFT, in contrast, calculates the static equilibrium geometry. Secondly, although DFT is an exact theory, the exchange-correlation functional used in DFT is approximated. To obtain the equilibrium
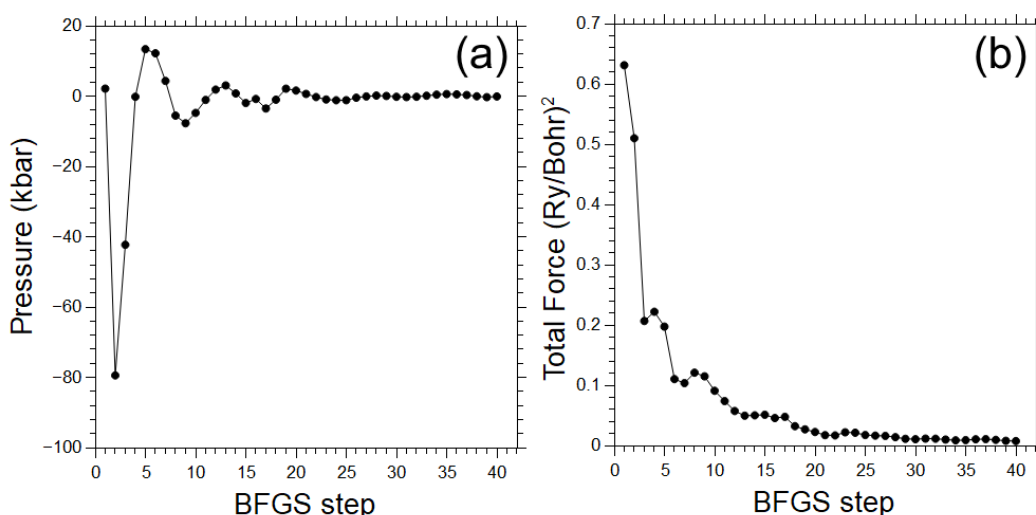
Figure 2.20 Optimisation of (a) the pressure and (b) the total force as a function of optimisation steps using the BFGS algorithm.

ground state structure, both the forces acting on the atoms and the external pressure acting on the cell must be minimised.

To this end, Quantum ESPRESSO and CASTEP use the BFGS algorithm (Pfrommer et al., 1997), minimising the cell pressure and forces acting on the atoms simultaneously (Figure 2.20).

The forces acting on the nuclei in our system may be computed as

$$F_I = -\frac{dU}{d\mathbf{R}_I} \tag{2.50}$$

U being the total potential energy of the nuclei. The problem is that this equation depends on the $3M + 1$ nuclear coordinates, with M being the number of nuclei in the system. The calculation of forces may be simplified by applying the Hellmann-Feynman theorem. This theorem essentially states that to calculate the forces acting on the nuclei, one only needs to know the electron density, which is easily obtained by solving the Kohn-Sham equations self-consistently.

The quantum mechanical stress tensor acting on the cell comprises contributions from the classical electrostatic interaction, kinetic energy, and the exchange-correlation energy

$$\sigma_{ij} = \sigma_{ij}^M + \sigma_{ij}^{kin} + \sigma_{ij}^{xc} \tag{2.51}$$

The stress tensor solely depends on the nuclear coordinates, the electron density, and the Kohn-Sham wavefunctions, and therefore is readily computed. In a geometry optimisation, the forces are typically minimised in any case. In addition, the external pressure acting on the cell can be optimised for any value. Therefore, the response of the structure and total energy to pressures of hundreds of GPa is easily accessible, whereas this task is experimentally very demanding. This allows computing the bulk modulus of compounds (chapter 3 and 5) and the relative stability of polymorphs as a function of pressure by comparing their total energy (chapter 5).

2.4.9 Response properties

Next to equilibrium properties such as the electron density, geometry, and total energy, it is also possible to compute so-called response properties i.e., the response of a system to being perturbed out of its equilibrium state. I have computed two such properties in this thesis: the elastic constants and phonon frequencies.

2.4.9.1 Elastic constants

For the elastic constants, one needs to know how the external pressure acting on the cell responds as the unit-cell is strained from its equilibrium dimensions. To compute the elastic constant, the atoms and unit-cell are first relaxed to the equilibrium ground state. To fully account for each compound's reversible deformation when subjected to any kind of mechanical stress the full elastic tensor needs to be calculated. The elasticity tensor c_{ijkl}, a fourth-rank tensor, combines the inducing property, the tensor of mechanical stress σ_{ij}, with the induced property, the strain tensor ε_{kl}.

$$\sigma_{ij} = c_{ijkl}\varepsilon_{kl} \tag{2.52}$$

The 81 components of the fourth-order elastic tensor c_{ijkl} may be reduced to a maximum of 21 independent elastic constants C_{ij} represented by a symmetric 6 $\times$ 6 matrix. The components of the elastic tensor relate to the elastic constants C_{ij} following the Voigt notation i.e., ii = i for i= 1, 2, 3 and ij =9 i – j otherwise, yielding

$$\sigma_i = C_{ij}\varepsilon_j \tag{2.53}$$

The basic vectors of the Cartesian reference system $\mathbf{e_i}$ with i = 1, 2, 3 are related to the crystallographic lattice vectors $\mathbf{a_1}, \mathbf{a_2}, \mathbf{a_3}$ by $\mathbf{e_2} \;//\; \mathbf{a_2^*}$, $\mathbf{e_3} \;//\; \mathbf{a_3}$ and $\mathbf{e_1} = \mathbf{e_2} \times \mathbf{e_3}$ with the * sign denoting the reciprocal lattice vector.

The number of independent elastic constants increases with decreasing crystal symmetry i.e., a cubic system features three independent elastic constants, whereas a triclinic crystal exhibits a total of 21. In practice, to determine an elastic constant by DFT, the structure is strained in a direction, and the stress tensor for this strained structure is computed. The higher number of

independent elastic constants of low-symmetry compounds also means that more strain patterns in various crystal directions must be applied to obtain the complete set of elastic constants.

For example, the C_{11} elastic constant relates the stress applied parallel to σ_1 with the strain induced parallel ε_1. σ_1 and ε_1. are not constrained to be parallel to the crystallographic *a*-axis, but this is the case for cubic crystals such as CO_2. Therefore, in order to obtain the C_{11} elastic constant for CO_2, the structure was subjected to strain in the direction of the *a*-axis applying six different strain amplitudes ranging from -0.003 to 0.003 and computing the corresponding stress tensor acting on the cell. In order to derive the elastic constants (or a linear combination of elastic constants), the slope of the line was fitted to the stress-strain data (Figure 2.21).
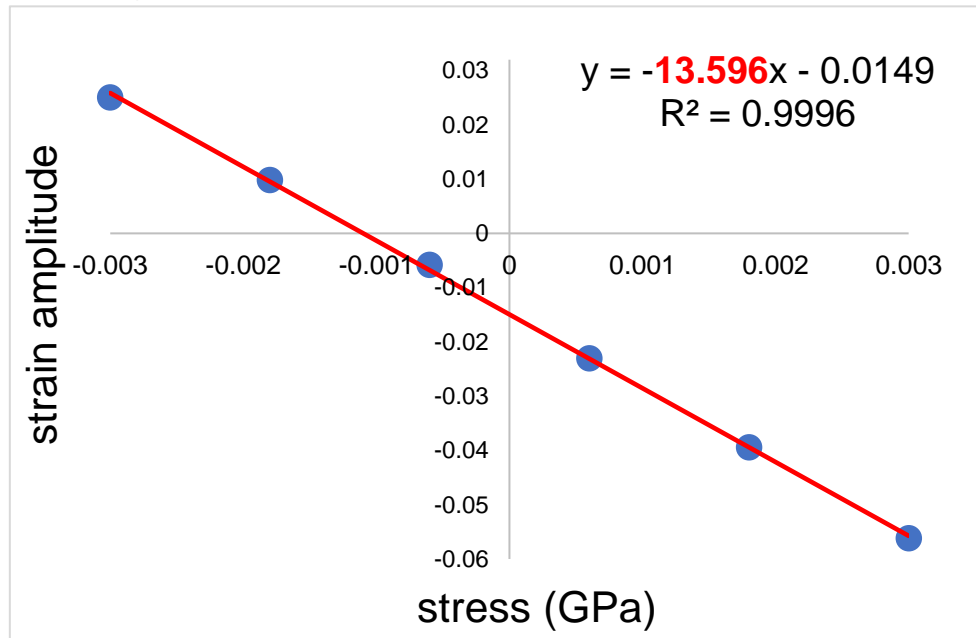
Figure 2.21 Stress-strain relation for solid cubic CO_2 used to determine the C_{11} elastic constant. The elastic constant (C_{11}= 13.596 GPa) may be derived, by determining the slope of the best-fit line to the stress-strain data.

2.4.9.2 Phonons: Density Functional Perturbation Theory

Density functional perturbation theory is a powerful tool for calculating response properties. In particular, phonon frequencies can be readily computed, as I will outline in the following. If a perturbation ΔV of strength λ perturbs the ground state external potential V_0

$$V_\lambda = V_0 + \lambda \Delta V \qquad (2.54)$$

the response of the charge density may be described by a Taylor series expanded to first order by

$$n_\lambda = n_0 + \lambda n_1 \qquad (2.55)$$

λn_1 is the so-called linear response term critical to computing the vibrational frequencies. Essentially, the problem that must be solved is the system's response to the displacement of individual atoms. As mentioned in the geometry optimisation section, the forces acting on the perturbed nuclei can be computed from the electron density using the Hellmann-Feynman theory.

The main benefit of calculating the phonon frequencies is that it allows to assign bands in a Raman or IR spectrum to certain vibrational motions of the atoms in a crystal. This was critical for my thesis project, as will be demonstrated in chapter 4.

2.5 References

Alig, H., Losel, J., & Trömel, M. (1994). Zur Kristallchemie der Wasserstoff–Sauerstoff-Bindungen. Zeitschrift Für Kristallographie - Crystalline Materials, 209(1), 18–21. https://doi.org/doi:10.1524/zkri.1994.209.1.18

Ambrosetti, A., Reilly, A. M., DiStasio, R. A., & Tkatchenko, A. (2014). Long-range correlation energy calculated from coupled atomic response functions. The Journal of Chemical Physics, 140(18), 18A508. https://doi.org/10.1063/1.4865104

Baur, W. H. (1962). Zur Kristallchemie der Salzhydrate. Die Kristallstrukturen von $MgSO_4.4H_2O$ (leonhardtit) und $FeSO_4.4H_2O$ (rozenit). Acta Crystallographica, 15(9), 815–826. https://doi.org/10.1107/S0365110X62002200

Baur, W. H. (1964). On the crystal chemistry of salt hydrates. II. A neutron diffraction study of $MgSO_4.4H_2O$. Acta Crystallographica, 17(7), 863–869. https://doi.org/10.1107/S0365110X64002304

Bhartia, R., Beegle, L. W., DeFlores, L., Abbey, W., Razzell Hollis, J., Uckert, K., Monacelli, B., Edgett, K. S., Kennedy, M. R., Sylvia, M., Aldrich, D., Anderson, M., Asher, S. A., Bailey, Z., Boyd, K., Burton, A. S., Caffrey, M., Calaway, M. J., Calvet, R., … Zan, J. (2021). Perseverance's Scanning Habitable Environments with Raman and Luminescence for Organics and Chemicals (SHERLOC) Investigation. Space Science Reviews, 217(4), 58. https://doi.org/10.1007/s11214-021-00812-z

Bloch, F. (1929). Über die Quantenmechanik der Elektronen in Kristallgittern. Zeitschrift Für Physik, 52(7), 555–600. https://doi.org/10.1007/BF01339455

Bouwers, A. (1937). X-ray tube having a rotary anode (Patent No. US2081789A). United States Patent Office.

Brese, N. E., & O'Keeffe, M. (1991). Bond-valence parameters for solids. Acta Crystallographica Section B, 47(2), 192–197. https://doi.org/10.1107/S0108768190011041

Brown, I. D. (2009). Recent Developments in the Methods and Applications of the Bond Valence Model. Chemical Reviews, 109(12), 6858–6919. https://doi.org/10.1021/cr900053k

Brown, I. D., & Altermatt, D. (1985). Bond-valence parameters obtained from a systematic analysis of the Inorganic Crystal Structure Database. Acta Crystallographica Section B, 41(4), 244–247. https://doi.org/10.1107/S0108768185002063

Bruker. (2019). What is X-ray Diffraction? YouTube. https://www.youtube.com/watch?v=QHMzFUo0NL8&t=27s&ab_channel=Bruker Corporation

Bwtek website. (2022). Bwtek website. https://bwtek.com/spectrometer-introduction/

Chio, C., Sharma, S., & Muenow, D. (2007). The hydrates and deuterates of ferrous sulfate (FeSO4): A Raman spectroscopic study. Journal of Raman Spectroscopy, 38, 87–99. https://doi.org/10.1002/jrs.1623

Clark, S., Segall, M., Pickard, C., Hasnip, P., Probert, M., Refson, K., & Payne, M. (2005). First principles methods using CASTEP. Zeitschrift Für Kristallographie, 220. https://doi.org/10.1524/zkri.220.5.567.65075

Coates, C. S., Murray, C. A., Boström, H. L. B., Reynolds, E. M., & Goodwin, A. L. (2021). Negative X-ray expansion in cadmium cyanide. Materials Horizons, *8*(5), 1446–1453. https://doi.org/10.1039/D0MH01989E

David, W. I. F., Shankland, K., McCusker, L. B., & Bärlocher, C. (2006). *Structure Determination from Powder Diffraction Data*. Oxford University Press. https://doi.org/10.1093/acprof:oso/9780199205530.001.0001

Diamond Light Source website. (2023). Simulations, Animations and Worksheets. https://www.diamond.ac.uk/Public/For-School/Resources/Simulations-and-Worksheets.html

Dinnebier, R. E., & Billinge, S. J. L. (2008). Powder Diffraction. The Royal Society of Chemistry. https://doi.org/10.1039/9781847558237

Dinnebier, R. E., Leineweber, A., & Evans, J. S. O. (2018). Rietveld Refinement. De Gruyter. https://doi.org/10.1515/9783110461381

Dove, M. T. (2011). Introduction to the theory of lattice dynamics.

Evans, J. S. O., & Evans, I. R. (2021). Structure Analysis from Powder Diffraction Data: Rietveld Refinement in Excel. *Journal of Chemical Education*, *98*(2), 495–505. https://doi.org/10.1021/acs.jchemed.0c01016

Festa, G., Romanelli, G., Senesi, R., Arcidiacono, L., Scatigno, C., Parker, S. F., Marques, M. P. M., & Andreani, C. (2020). Neutrons for Cultural Heritage - Techniques, Sensors, and Detection. Sensors, *20*(2). https://doi.org/10.3390/s20020502

Fortes, A. D., & Capelli, S. C. (2018). H/D isotope effect on the molar volume and thermal expansion of benzene. Physical Chemistry Chemical Physics, *20*(24), 16736–16742. https://doi.org/10.1039/C8CP02500B

Friedrich, W., Knipping, P., & Laue, M. (1912). Interferenzerscheinungen bei Röntgenstrahlen. Sitzungsberichte Der Königlich Bayerischen Akademie Der Wissenschaften, Mathematische-Physische Klasse, *42*, 303–322.

Giannozzi, P., Andreussi, O., Brumme, T., Bunau, O., Buongiorno Nardelli, M., Calandra, M., Car, R., Cavazzoni, C., Ceresoli, D., Cococcioni, M., Colonna, N., Carnimeo, I., Dal Corso, A., de Gironcoli, S., Delugas, P., DiStasio, R. A., Ferretti, A., Floris, A., Fratesi, G., … Baroni, S. (2017). Advanced capabilities for materials modelling with Quantum ESPRESSO. Journal of Physics: Condensed Matter, 29(46), 465901. https://doi.org/10.1088/1361-648x/aa8f79

Giannozzi, P., Baroni, S., Bonini, N., Calandra, M., Car, R., Cavazzoni, C., Ceresoli, D., Chiarotti, G. L., Cococcioni, M., Dabo, I., Dal Corso, A., de Gironcoli, S., Fabris, S., Fratesi, G., Gebauer, R., Gerstmann, U., Gougoussis, C., Kokalj, A., Lazzeri, M., … Wentzcovitch, R. M. (2009). QUANTUM ESPRESSO: a modular and open-source software project for quantum simulations of materials. Journal of Physics: Condensed Matter, *21*(39), 395502. https://doi.org/10.1088/0953-8984/21/39/395502

Giustino, F. (2014). *Materials modelling using density functional theory :properties and predictions.*

Greenspan, L. (1977). Humidity Fixed Points of Binary Saturated Aqueous Solutions. Journal of Research of the National Bureau of Standards. Section A, Physics and Chemistry, 81A, 89–96.

Grimme, S. (2006). Semiempirical GGA-type density functional constructed with a long-range dispersion correction. Journal of Computational Chemistry, 27(15), 1787–1799. https://doi.org/10.1002/jcc.20495

Grimme, S., Hansen, A., Brandenburg, J. G., & Bannwarth, C. (2016). Dispersion-Corrected Mean-Field Electronic Structure Methods. Chemical Reviews, 116(9), 5105–5154. https://doi.org/10.1021/acs.chemrev.5b00533

Grinberg, J., Levin, S., Pelah, I., & Wiener, E. (1967). Isotope effect in the high temperature phase transition of KH_2PO_4. Solid State Communications, 5(11), 863–865. https://doi.org/https://doi.org/10.1016/0038-1098(67)90316-X

Halban, H., & Preiswerk, P. (1936). Preuve expérimentale de la diffraction des neutrons. Comptes Rendus de l'Académie Des Sciences, 203, 73–75.

Harshman, D. R., & Fiory, A. T. (2017). On the isotope effect in compressed superconducting H_3S and D_3S. Superconductor Science and Technology, 30(4), 045011. https://doi.org/10.1088/1361-6668/aa5f3c

Hawthorne, F., & Sokolova, E. (2012). The role of H_2O in controlling bond topology: I. The $^{[6]}Mg(SO_4)(H_2O)_n$ (n= 0 - 6) structures. Zeitschrift Fur Kristallographie, 227, 594–603. https://doi.org/10.1524/zkri.2012.1473

Hohenberg, P., & Kohn, W. (1964). Inhomogeneous Electron Gas. Physical Review, 136(3B), B864–B871. https://doi.org/10.1103/PhysRev.136.B864

HRPD website. (2022). Technical information HRPD. https://www.isis.stfc.ac.uk/Pages/Hrpd-technical-information.aspx

I11 website. (2022). I11 capillary sample loading. https://www.diamond.ac.uk/Instruments/Crystallography/I11/status/capillaries.html

Ibberson, R. (2009). Design and performance of the new supermirror guide on HRPD at ISIS. Nuclear Instruments and Methods in Physics Research Section A Accelerators Spectrometers Detectors and Associated Equipment, 600. https://doi.org/10.1016/j.nima.2008.11.066

Kisi, E. H., & Howard, C. J. (2008). Applications of Neutron Powder Diffraction. Oxford University Press. https://doi.org/10.1093/acprof:oso/9780198515944.001.0001

Kohn, W., & Sham, L. J. (1965). Self-Consistent Equations Including Exchange and Correlation Effects. Physical Review, 140(4A), A1133–A1138. https://doi.org/10.1103/PhysRev.140.A1133

Kuhn, F. J. (1932, February 29). Chadwick Calls Neutron "Difficult Catch"; His Find Hailed as Aid in Study of Atom. New York Times, 1–1.

Landsberg, Gr., & Mandelstam, L. (1928). Über die Lichtzerstreuung in Kristallen. Zeitschrift Für Physik, 50(11), 769–780. https://doi.org/10.1007/BF01339412

Larson, A. C., & Von Dreele, R. B. (2004). General Structure Analysis System (GSAS). https://subversion.xray.aps.anl.gov/EXPGUI/gsas/all/GSAS%20Manual.pdf

Le Bail, A. (2005). Whole powder pattern decomposition methods and applications: A retrospection. Powder Diffraction, 20(4), 316–326. https://doi.org/DOI: 10.1154/1.2135315

Maiman, T. H. (1960). Stimulated Optical Radiation in Ruby. Nature, *187*(4736), 493–494. https://doi.org/10.1038/187493a0

Marzari, N. (2020, April 15). Fireside chats for lockdown times - Intro to DFT. Youtube.Com. https://www.youtube.com/watch?v=kYxOWYWxYcQ&t=2689s

Mitchell, D. P., & Powers, P. N. (1936). Bragg reflection of slow neutrons. *Physical Review*, *50*(5), 486.

Monkhorst, H. J., & Pack, J. D. (1976). Special points for Brillouin-zone integrations. Phys. Rev. B, 13(12), 5188–5192. https://doi.org/10.1103/PhysRevB.13.5188

Nasdala, L., Smith, D. C., Kaindl, R., & Ziemann, M. A. (2004). Raman spectroscopy: Analytical perspectives in mineralogical research. In E. Libowitzky & A. Beran (Eds.), Spectroscopic Methods in Mineralogy (Vol. 6). European Mineralogical Union.

NIST. (2015). Certificate: Standard Reference Material 640e. https://www-s.nist.gov/srmors/certificates/640e.pdf

Otendal, M., Tuohimaa, T., Vogt, U., & Hertz, H. M. (2008). A 9 keV electron-impact liquid-gallium-jet x-ray source. Review of Scientific Instruments, *79*(1), 016102. https://doi.org/10.1063/1.2833838

Perdew, Burke, & Ernzerhof. (1996). Generalized Gradient Approximation Made Simple. *Physical Review Letters*, *77 18*, 3865–3868.

Perdew, J. P., Ruzsinszky, A., Csonka, G. I., Vydrov, O. A., Scuseria, G. E., Constantin, L. A., Zhou, X., & Burke, K. (2008). Restoring the Density-Gradient Expansion for Exchange in Solids and Surfaces. Physical Review Letters, 100(13), 136406. https://doi.org/10.1103/PhysRevLett.100.136406

Perdew, J. P., & Zunger, A. (1981). Self-interaction correction to density-functional approximations for many-electron systems. Physical Review B, *23*(10), 5048–5079. https://doi.org/10.1103/PhysRevB.23.5048

Peterson, R. C. (2011). Cranswickite $MgSO_4 \cdot 4H_2O$, a new mineral from Calingasta, Argentina. American Mineralogist, *96*(5–6), 869–877. https://doi.org/https://doi.org/10.2138/am.2011.3673

Raman, C. v, & Krishnan, K. S. (1928). A New Type of Secondary Radiation. Nature, *121*(3048), 501–502. https://doi.org/10.1038/121501c0

Rietveld, H. M. (1967). Line profiles of neutron powder-diffraction peaks for structure refinement. Acta Crystallographica, *22*(1), 151–152. https://doi.org/10.1107/S0365110X67000234

Santisteban, J. R., Daymond, M. R., James, J. A., & Edwards, L. (2006). ENGIN-X: a third-generation neutron strain scanner. Journal of Applied Crystallography, *39*(6), 812–825. https://doi.org/10.1107/S0021889806042245

Sholl, D., & Steckel, J. (2009). Density Functional Theory: A Practical Introduction. https://doi.org/10.1002/9780470447710

Sivia, D. S. (2011). Elementary Scattering Theory: For X-ray and Neutron Users.

Steiner, T. (2002). The Hydrogen Bond in the Solid State. Angewandte Chemie International Edition, *41*(1), 48–76. https://doi.org/https://doi.org/10.1002/1521-3773(20020104)41:1<48::AID-ANIE48>3.0.CO;2-U

Tartoni, N., Thompson, S., Tang, C., Willis, B., Derbyshire, G., Wright, A., Jaye, S., Homer, J., Pizzey, J., & Bell, A. (2008). High-performance X-ray detectors for the new powder diffraction beamline I11 at Diamond. Journal of Synchrotron Radiation, *15*, 43–49. https://doi.org/10.1107/S0909049507046250

Thompson, S. P., Parker, J. E., Marchal, J., Potter, J., Birt, A., Yuan, F., Fearn, R. D., Lennie, A. R., Street, S. R., & Tang, C. C. (2011). Fast X-ray powder diffraction on I11 at Diamond. Journal of Synchrotron Radiation, 18(4), 637–648. https://doi.org/10.1107/S0909049511013641

Thompson, S. P., Parker, J. E., Potter, J., Hill, T. P., Birt, A., Cobb, T. M., Yuan, F., & Tang, C. C. (2009). Beamline I11 at Diamond: A new instrument for high resolution powder diffraction. Review of Scientific Instruments, 80(7), 075107. https://doi.org/10.1063/1.3167217

Timrov, I., Marzari, N., & Cococcioni, M. (2018). Hubbard parameters from density-functional perturbation theory. Physical Review B, 98(8), 85127. https://doi.org/10.1103/PhysRevB.98.085127

Timrov, I., Marzari, N., & Cococcioni, M. (2021). Self-consistent Hubbard parameters from density-functional perturbation theory in the ultrasoft and projector-augmented wave formulations. Physical Review B, 103(4), 45141. https://doi.org/10.1103/PhysRevB.103.045141

Tkatchenko, A., & Scheffler, M. (2009). Accurate Molecular Van Der Waals Interactions from Ground-State Electron Density and Free-Atom Reference Data. Physical Review Letters, 102(7), 73005. https://doi.org/10.1103/PhysRevLett.102.073005

Toby, B. H. (2001). EXPGUI, a graphical user interface for GSAS. *J*ournal of Applied Crystallography, *34*(2), 210–213. https://doi.org/10.1107/S0021889801002242

Toby, B. H. (2023). *Le Bail Intensity Extraction*. https://www.aps.anl.gov/sites/default/files/APS-Uploads/XSD/Powder-Diffraction-Crystallography/6LeBail.pdf

Tuschel, D. (2012). Raman Fundamentals - Electrodynamic Theory. Youtube.Com. https://www.youtube.com/watch?v=_dPzIQEVEtc&ab_channel=DavidTuschel

van Noorden, R., Maher, B., & Nuzzo, R. (2014). The top 100 papers. Nature, 514, 550–553. https://doi.org/10.1038/514550a

Vaniman, D. T., & Chipera, S. J. (2006). Transformations of Mg- and Ca-sulfate hydrates in Mars regolith. American Mineralogist, 91(10), 1628–1642. https://doi.org/doi:10.2138/am.2006.2092

Wiens, R. C., Maurice, S., Robinson, S. H., Nelson, A. E., Cais, P., Bernardi, P., Newell, R. T., Clegg, S., Sharma, S. K., Storms, S., Deming, J., Beckman, D., Ollila, A. M., Gasnault, O., Anderson, R. B., André, Y., Michael Angel, S., Arana, G., Auden, E., … Willis, P. (2020). The SuperCam Instrument Suite on the NASA Mars 2020 Rover: Body Unit and Combined System Tests. Space Science Reviews, *217*(1), 4. https://doi.org/10.1007/s11214-020-00777-5

3. Elasticity of selected icy satellite candidate materials (CO_2, C_6H_6, $MgSO_4 \cdot 7H_2O$ and $CaSO_4 \cdot 2H_2O$) revisited by dispersion corrected density functional theory

This chapter explores the accuracy of recent advancements in density functional theory to model the compressibility and elastic properties of icy satellite candidate minerals by benchmarking them against experimental reference data from the literature. Being able to accurately predict these properties computationally is of great interest for the in-situ detection of such minerals via seismology, as envisioned for the near future for Saturn's moon Titan and Jupiter's moon Europa, as well as to model the density structure and mantle dynamics of icy satellites.

Declaration The contents of this chapter were published in the journal *Icarus* (Meusburger et al., 2021) and are presented in the original format of the journal.
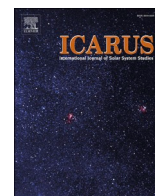
Elasticity of selected icy satellite candidate materials (CO_2, C_6H_6, $MgSO_4 \cdot 7H_2O$ and $CaSO_4 \cdot 2H_2O$) revisited by dispersion corrected density functional theory

Johannes M. Meusburger [a,b,c], Karen A. Hudson-Edwards [a], Chiu C. Tang [b], Rich A. Crane [a], A. Dominic Fortes [c,*]

[a] Camborne School of Mines and Environment and Sustainability Institute, Tremough Campus, University of Exeter, Penryn TR10 9EZ, UK
[b] Diamond Light Source, Harwell Science and Innovation Campus, Fermi Avenue, Didcot OX11 0DE, UK
[c] ISIS Neutron and Muon Source, STFC Rutherford Appleton Laboratory, Harwell Science and Innovation Campus, Chilton, Didcot, Oxfordshire OX11 0QX, UK

A B S T R A C T

Seismic studies are essential for accurate characterisation of planetary interior structures, but are dependent on modelling for interpretation, requiring data on the elastic properties of likely constituent minerals. With the potential deployment of seismic stations on icy worlds such as Europa and Titan envisioned for the near future, a campaign of study into the elasticity of potential icy ocean world minerals is of paramount importance.

In the paper we assess the role of first-principles computer simulations to this problem, in particular focussing on the application of recent advances in simulating dispersion forces in loosely-bonded molecular solids, likely to be the main constituents of icy ocean worlds. This is of particular interest for these kinds of materials, since the complex sample handling, phase transitions and the difficulty of obtaining single crystals often greatly complicates the experimental determination of the full elastic tensor.

We focus on CO_2, C_6H_6, $MgSO_4 \cdot 7H_2O$ and $CaSO_4 \cdot 2H_2O$ as they allow us to benchmark the performance over a wide range of chemical space, structural topologies, crystal symmetries and bonding types, and moreover have accurate experimentally determined unit-cell dimensions, bulk moduli and full elastic tensors for benchmarking purposes.

We demonstrate that the dispersion corrected approaches indeed perform better in modelling the experimental density profiles (mean unsigned differences of only 0.04 g/cm^3 (CO_2), 0.02 g/cm^3 (C_6H_6), 0.003 g/cm^3 ($MgSO_4 \cdot 7H_2O$) and 0.013 g/cm^3 ($CaSO_4 \cdot 2H_2O$)) and may find application in exploring the compressive parameters of candidate materials, which could then be used in rheological models of icy ocean worlds.

Moreover, we have assessed if the elastic constants computed by dispersion corrected density functional theory are accurate enough to be used in a reference data base for the seismic exploration of icy ocean worlds. Despite one approach having demonstrated good accuracy compared with the experimental values in modelling the elasticity of CO_2, we instead find average differences from expected P and S wave velocities of around 10 to 25% for the elastically more complex title compounds. In part these differences are due to the large temperature difference between the experimental elasticity data (typically near 300 K) and our calculations, which were performed in the athermal limit.

1. Introduction

The outer solar system harbours numerous planetary objects of diverse internal and surface structure. The Voyager, Galileo, Cassini and New Horizon missions found indications that some of these objects (e.g. Europa, Ganymede, Callisto, Enceladus, Titan, Triton and Pluto; Nimmo, 2018) may conceal subsurface oceans beneath an icy surface and are thus referred to collectively as icy ocean worlds (IOW). The possibility of sustaining a liquid ocean concealed beneath an icy crust clearly makes them a prime target for the search for extra-terrestrial life.

Present models of the interior of IOW are based on knowledge about their mass, diameter, and low-order gravity-field harmonics as

determined during close flybys in spacecraft missions (Monteux et al., 2018; Nimmo, 2018). In addition, high-resolution images acquired in such spacecraft missions provide insight into the surface geology which in turn may be used to infer IOW's thermal history (e.g. Bland et al., 2012). Unsurprisingly, remote sensing based models are associated with a high degree of uncertainty, making it difficult to constrain key habitability parameters (e.g. depth, ocean pressure, temperature and chemistry) accurately enough to assess the astrobiological potential of these proclaimed subsurface oceans. In order to draw a detailed picture of the internal structure of icy satellites, in situ geophysical exploration methods such as seismology appear to be the method of choice, thus the proposed Europa (Pappalardo et al., 2013) and the recently selected Titan (New Frontiers Dragonfly, Lorenz et al., 2018) lander missions both include a single station seismometer in their proposed scientific payload. Single station seismometers have most recently found application in the successful exploration of the interior of comet 67P/Churyumov–Gerasimenko (Philae mission; Knapmeyer et al., 2017) and Mars (InSight mission), and in the latter case have even enabled determination of both the core radius (Stähler, 2021) and crustal thickness (Drilleau et al., 2021).

Despite recent application on other celestial bodies, seismology has been, first and foremost, a technique to study the Earth and has greatly advanced our knowledge of its interior (e.g. Mohorovičić, 1910; Lehmann, 1936; Stephenson et al., 2021). The successful mineral identification by means of seismology, however, is reliant upon the use of accurate reference elasticity data of promising candidate mineral phases. Due to the difficulties associated with the seismic exploration of celestial bodies, the obvious focus of mineral physicists has been the study of the elastic properties of silicate minerals which account for the bulk of the terrestrial mantle and crust (Ringwood, 1969). Minerals which constitute the icy mantle of IOW are presumed to be various ice polymorphs, chondritic salts (e.g. sulfate and chloride minerals) and acids (e.g. sulfuric acid and its hydrates), and primitive volatiles (e.g. NH_4, CO_2, hydrocarbons, N_2; Fortes and Choukroun, 2010). The elastic properties of many of such phases are poorly constrained or in some instances completely unknown. This current gap in the literature therefore acts as a barrier against the efficacy of a likely future deployment of a seismometer on an IOW.

The determination of elastic constants is further complicated by the pressure and temperature dependency of the elastic tensor, the wide range of pressure (i.e. $\sim$ 0–3.45 GPa; with the upper bound corresponding to Callisto's central pressure assuming a partly differentiated model for the internal structure (Prentice, 1999)) and temperature conditions ($\sim$ 25–450 K, with the upper and lower bound corresponding to the melting temperature of ice VII at $\sim$3.5 GPa (Dubrovinsky and Dubrovinskaia, 2007) and the minimum surface temperature of Pluto and other Kuiper belt objects (Earle et al., 2017), respectively) the candidate phases may be subjected to in the icy mantle. Considering the large number of candidate phases and the complexity of the experiments involved, the exploration of the elastic constants including their pressure and temperature dependency would be a rather ambitious endeavour. Further complicating these experiments are the complex high-pressure high-temperature phase relations involving incongruent melting (e.g. Comodi et al., 2017; Fortes et al., 2017; Gromnitskaya et al., 2013; Wang et al., 2018) and polymorphic phase transitions (e.g. Ende et al., 2020; Meusburger et al., 2019, 2020) as well as the difficult sample handling due to re- or dehydration induced by changes in relative humidity as observed for numerous candidate phases (Wang et al., 2016).

An alternative approach to estimate elastic constants is computation from quantum mechanical first principles, such as within the framework of density functional theory (DFT) (Hohenberg and Kohn, 1964; Kohn and Sham, 1965), as this circumvents the problems associated with sample handling, albeit at the expense of experimental accuracy. One of the major shortcomings of all local and semi-local density functional approximations is the failure to model long-range intermolecular

interactions, commonly referred to as London dispersion forces, accurately (Tkatchenko and Scheffler, 2009). Due to the critical role London dispersion forces play in a plethora of materials, many of them being of technological interest, considerable effort has been put into the development of dispersion correction schemes. The accurate treatment of dispersion forces is regarded as one of the most recent success stories in the field of DFT (Burke, 2012) and has resulted in an improved accuracy for numerous loosely packed solids such as metal organic framework (Formalik et al., 2018), zeolites (Fischer and Angel, 2017) and organic molecular crystals (Winkler and Milman, 2019). Most importantly from a planetary scientist's perspective, the improved modelling of dispersion forces also opens the door for improved accuracy in the computational exploration of the material properties of IOW candidate phases, many of which are dispersion dominated loosely-bonded solids.

In order to test this hypothesis we have assessed the performance of various dispersion correction schemes to model crystal structures and high-pressure behaviour of selected icy satellite candidate phases (i.e. CO_2, C_6H_6, $MgSO_4 \cdot 7H_2O$ and $CaSO_4 \cdot 2H_2O$). These include the D2 scheme (Grimme, 2006), the TS scheme (Tkatchenko and Scheffler, 2009) and the many-body dispersion method with range-separated screening (commonly abbreviated as MBD@rsSCS but named MBD hereafter for the sake of brevity, Ambrosetti et al., 2014) in conjunction with the Perdew–Burke-Ernzerhof (PBE; Perdew et al., 1996) and Perdew–Burke-Ernzerhof dedicated solid state (PBEsol; Perdew et al., 2008) exchange correlation (xc) functionals. The best performing combination of functional and dispersion correction, as well as the PBEsol xc functional, which is regarded as yielding accurate elastic tensor (Winkler and Milman, 2014), will then be applied to compute the full elastic tensor. The results will be evaluated against each other and compared with literature data.

We focus on CO_2, C_6H_6, $MgSO_4 \cdot 7H_2O$ and $CaSO_4 \cdot 2H_2O$ as they allow us to benchmark the performance over a wide range of chemical space, structural topologies, crystal symmetries and bonding types, and moreover have accurate experimentally determined unit-cell dimensions, bulk moduli and full elastic tensors for benchmarking purposes. Finally, we assess the role that dispersion corrected DFT may play in exploring the elasticity of candidate phases. In particular, we want to assess if the elastic constants computed by dispersion corrected DFT are accurate enough to be used in a reference data base for the seismic exploration of IOWs. Such a database would allow for a seismic exploration of IOW (*cf.*, Stähler et al., 2018), ideally casting light on the icy mantle dynamics and chemical fluxes into and out of the ocean, both of them being key parameters in assessing habitability.

2. Methods

2.1. Set up of DFT calculations

A series of plane-wave pseudopotential DFT calculations were carried using the CASTEP code (Clark et al., 2005) version 17.2.1. Input files were generated in the BIOVIA Materials studio software. The calculations were subsequently run according to following geometry optimisation strategy: After initial structural relaxations using a plane-wave cut-off of 800 eV, starting from the experimentally determined

Table 1
Converged basis set parameters and input geometries for all compounds under investigation. [1]the deuterium atoms have been replaced with their light hydrogen counterparts [2]optimisation for $CaSO_4 \bullet 2H_2O$ were carried out using the reduced cell.

Compound	Input geometry	Cut-off energy (eV)	k-points
CO_2	Simon and Peters (1980)	1300	$5 \times 5 \times 5$
C_6H_6	Maynard-Casely et al. (2016)	1300	$4 \times 3 \times 4$
$MgSO_4 \bullet 7H_2O^1$	Fortes et al. (2006)	1300	$2 \times 2 \times 4$
$CaSO_4 \bullet 2H_2O^2$	Comodi et al. (2008)	1300	$5 \times 5 \times 5$

geometries obtained from the literature (Table 1), single point energy calculations for various basis set sampling grids and cut-off energies ranging from 500 to 1400 eV were performed (supplementary material: Fig. s1a-d). Converged basis set parameters (i.e. plane wave cut-off energy and Monkhost-Pack k-points; Monkhorst and Pack, 1976) were derived from these calculations and are reported in Table 1.

The final zero pressure athermal geometry optimisation was then carried out using the converged plane wave basis-set parameters and the generalized-gradient-approximation xc functionals PBE and PBEsol both with and without applying the TS and D2 dispersion corrections. In addition to these optimisations the MBD dispersion correction scheme was used in conjunction with the PBE xc functional. Empirical parameters as used for the various dispersion correction schemes are reported in Section 2.2.

The computationally expensive core-valence electron interactions were modelled using ultra soft pseudopotentials (Vanderbilt, 1990). The Broyden-Fletcher–Goldfarb-Shanno method (Pfrommer et al., 1997), allowing for a simultaneous optimisation of the cell parameters and atomic coordinates, was applied to find the geometry corresponding to the lowest total electronic energy. The optimisations were considered converged when the stresses along any component of the Cartesian stress tensor were less than 0.01 GPa. Additionally, convergence tolerances for the ionic force, ionic displacement and total energy were defined as 0.01 eV/Å, 5×10^{-4} Å and 5×10^{-6} eV/atom, respectively.

2.2. Dispersion corrected DFT

Semi-local exchange correlation functionals such as the PBE and PBEsol xc functionals do not accurately treat long-range forces between atoms arising from correlated electronic fluctuations commonly known as London dispersion forces. By contrast, dispersion forces between two atoms at a distance R decay as $-1/R^6$ (Eisenschitz and London, 1930) semi-local density functional approximations treat the decay exponentially (Ambrosetti et al., 2014).

In order to compensate for this shortcoming, considerable effort has been put into the development of numerous dispersion correction methods. Due to their successful application to a large variety of chemical compounds and being implemented as an off-the-shelf option in many popular quantum chemistry codes (e.g. CASTEP, VASP, Quantum Espresso) we applied the D2 (Grimme, 2006), TS (Tkatchenko and Scheffler, 2009) and MBD (Ambrosetti et al., 2014) correction schemes. For an exhaustive review of other correction schemes the reader is referred to Grimme et al. (2016).

In all of the above mentioned correction schemes the total energy is specified as

$$E_{tot} = E_{KS} + E_{disp} \tag{1}$$

E_{KS} is obtained from Kohn-Sham DFT as specified in Section 2.1, regardless of the combination the dispersion correction is applied to. However, the various dispersion correction schemes differ in how they retrieve the dispersion energy E_{disp}.

Pairwise-additive dispersion correction method such as the TS and D2 methods rely on the summation over C_{6ij}/R_{ij}^6 terms for pairs of atoms (ij) at a distance R_{ij} using interatomic dispersion correction coefficients C_{6ij}

$$E_{disp} = -s_6 \sum_{i,j} \frac{C_{6ij}}{R_{ij}^6} f_{damp}\left(R_{ij}, R_{vdw}\right) \tag{2}$$

f_{damp} denotes a Fermi-type dampening function which was implemented in both schemes to decrease the dispersion energy to zero at small R_{ij}, thus eliminating the singularity inevitably arising from the $-1/R_{ij}^6$ terms at small interatomic distances.

$$f_{damp}\left(R_{ij}, R_{vdw}\right) = \frac{1}{1 + e^{-d\left(\frac{R_{ij}}{s_r R_{vdw}} - 1\right)}} \tag{3}$$

The formalism of D2 and TS (eq. 2) is essentially identical, one major difference, however, is the way each of the dispersion corrections derives the atom specific dispersion correction coefficients C_{6i} and van der Waals radii R_{0i}, which are either determined empirically (D2), or derived by from the ground-state electron density and reference values for the free atoms (TS).

TS and D2 are both semi-empirical i.e. for the implementation of dispersion forces empirical parameters have to be specified, which vary between the xc functionals to which the correction is applied. Next to the atom specific dispersion coefficients (C_{6i}) and van-der Waals radii (R_{0i}), a global scaling factor (s_6), a scaling factor by which the van-der Waals radii are scaled (s_r) and a global factor determining the steepness of the dampening function (d) have to be specified for the D2 correction method. C_{6i} and R_{0i} (already scaled by 1.1) values as reported by Grimme (2006) were used for the PBE + D2 calculations. As for the remaining empirical parameters Grimme (2006) recommended values on the basis of exhaustive benchmarking of 1.10, 0.75 and 20 for the s_6, s_r and d parameter, respectively, to be used for the D2 correction in conjunction with the PBE functional.

For the PBEsol + D2 calculations we followed the approach suggested by Csonka et al. (2008) and fixed the s_6 parameter to unity while rescaling the atom-specific van der Waals radii by 1.42. The values reported for the atom-specific van der Waals radii tabulated in Grimme (2006) were already scaled by 1.10. As pointed out by Tkatchenko and Scheffler (2009), the d parameter relates to the steepness of the dampening term, which is identical for the D2 and TS correction and was hence fixed to a value of 20, independent of the xc functional and dispersion correction.

The global van der Waals scaling factor s_r was set to optimized functional specific values of 1.06 (Al-Saidi et al., 2012) and 0.94 (Tkatchenko and Scheffler, 2009) for the PBEsol + TS and PBE + TS calculations, respectively.

Next to the pairwise additive schemes, the MBD correction (Ambrosetti et al., 2014), which accounts for the many-body nature of dispersion interactions, was employed in conjunction with the PBE xc functional. The MBD scheme obtains the dispersion energy of a system in a three-step process. First, the atomic polarizabilities are obtained using the TS scheme. Second, the short-range atomic polarizabilities are derived by applying a self-consistent screening on the short-range part of the atomic polarizabilities, which are then used to calculate the long-range correlation energy. The s_r parameter was specified as 0.94 as for PBE + TS and a dimensionless range separating parameter β was set to a value of 0.83.

Many-body dispersion correction schemes from the Grimme family such as the D3 (Grimme et al., 2010) and D4 (Caldeweyher et al., 2017) corrections are not implemented in the CASTEP code as of version 19.1 and hence were not considered in this study. Sample input files for each of the calculations can be found in the supplementary data (Section S2).

2.3. Assessment of agreement with experimental values

The performance in replicating experimentally determined unit-cell dimensions and compression behaviour was evaluated for each of the seven distinct combinations (i.e. PBE, PBE + D2, PBE + TS, PBE + MBD, PBEsol, PBEsol + D2 and PBEsol + TS).

The difference between experimental reference (xEXP) and computationally derived (xDFT) values for each parameter was defined as

$$diff_x = xDFT - xEXP \tag{4}$$

For this reason, positive and negative diff$_x$ values represent the over and underestimation, respectively, of the DFT values for a given

quantity.

For the difference assessment the mean signed difference (MSiD) was calculated

$$MSiD = \frac{1}{N} \sum_i^N diff_{x,i} \qquad (5)$$

Despite being useful to identify systematic over or underestimation the MSiD is prone to cancelations (i.e. individual differences will cancel each other out if they are opposite sign). To compensate for this short-coming, the mean unsigned difference (MUD) was calculated for each category under investigation.

$$MUD = \frac{1}{N} \sum_i^N |diff_{x,i}| \qquad (6)$$

2.4. High-pressure calculations, elasticity and acoustic wave propagation

In addition to the zero pressure optimisation, a series of four geometry optimisations at quasi-hydrostatic pressures of 0.5, 1, 1.5 and 2.0 GPa was carried out for each of the seven individual combinations listed in Section 2.1. A third order Birch-Murnaghan Equation of State (BM3-EoS (Birch, 1947)) was fitted to the lattice-parameter data using EOSFIT7-GUI (Gonzalez-Platas et al., 2016). The obtained EoS parameters were evaluated both against each other and against experimentally and computationally derived values from the literature.

The density was interpolated in 0.01 GPa intervals at pressures ranging from 0 to 2.0 GPa using the EoS parameters obtained from fitting the optimized geometries and the experimentally determined literature EoS parameters. Next, we calculated the xDiff, MSiD and MUD with respect to the experimentally determined EoS parameters for each of the seven individual combinations. Moreover, the performance was assessed in terms of relative compressibility. To this end, xDiff, MSiD and MUD were calculated from the V/V_0 data in the above stated pressure intervals and range.

To fully account for each compound's reversible deformation when subjected to any kind of mechanical stress the full elastic tensor was calculated. The elasticity tensor c_{ijkl}, a fourth rank tensor, combines the inducing property, the tensor of mechanical stress σ_{ij}, with the induced property, the strain tensor ε_{kl}

$$\sigma_{ij} = c_{ijkl}\varepsilon_{kl} \qquad (7)$$

The 81 components of the fourth order elastic tensor c_{ijkl} may be reduced to a maximum of 21 independent elastic constants C_{ij}, represented by a symmetric 6 × 6 matrix. The components of the elastic tensor relate to the elastic constants C_{ij}, following the Voigt notation i.e., $ii = i$ for $i = 1, 2, 3$ and $ij = 9 i - j$ otherwise, yielding

$$\sigma_i = C_{ij}\varepsilon_j \qquad (8)$$

The basic vectors of the Cartesian reference system e_i with $i = 1, 2, 3$ are related to the crystallographic lattice vectors a, b, c by $e_2 // b*$, $e_3 // c$ and $e_1 = e_2 \times e_3$ with the * sign denoting the reciprocal lattice vector.

For the computation of the elasticity, we chose the combination that scored most highly on the high-pressure benchmarking as well as the PBEsol xc functional to approximate the xc energy. To this end, the structures were initially relaxed using stricter convergence criteria (i.e. $\sigma_{ij} < 0.002$ GPa, maximum ionic force <0.002 eV/Å, maximum ionic displacement $<1 \times 10^{-4}$ Å, total energy $<1 \times 10^{-6}$ eV/atom) and each structure was subsequently distorted in discrete increments between limiting strain amplitudes of ±0.003, using the minimum number of strain patterns necessary to retrieve a complete set of elastic constants for the respective crystal systems.

Lattice parameters were fixed, but the internal coordinates were allowed to relax during energy minimisation of the strained structures. The Cartesian stress tensor corresponding to each of the strained structures was then calculated. The analysis of the resulting geometries and

computation of the elastic constants was again carried out in Materials Studio. For a more detailed description of the derivation of elastic constants using the stress-strain approach and on the applied strain patterns corresponding to respective crystal systems the reader is referred to Page and Saxe (2002).

The anisotropy of the elasticity was visualised by computing the representation surface of the longitudinal effect of the elastic stiffness (for a definition of the tensor representation surface we refer to Arbeck et al., 2012) using the WinTensor software (Kaminski, 2014).

The computationally determined elastic tensors were compared against experimentally determined literature values by calculating the difference as a percentage with respect to the experimental data for each of the elastic coefficients C_{ij} as well as for acoustic wave velocities in seven crystal directions (i.e., $\langle 100 \rangle$, $\langle 010 \rangle$, $\langle 001 \rangle$, $\langle 110 \rangle$, $\langle 011 \rangle$, $\langle 101 \rangle$, $\langle 111 \rangle$). The transverse and longitudinal polarized shear wave velocities and primary wave velocities were computed using the Christoffel code (Jaeken and Cottenier, 2016) for the computationally and experimentally determined set of elastic constants for each of the crystal directions as stated above. The Christoffel code uses the density and elastic tensor to compute the acoustic wave velocities v of a monochromatic plane wave travelling in direction q for various polarisations p through a crystalline solid according to the Christoffel equation,

$$(\Gamma_{ik} - \rho v^2 \delta_{ik})p_k = 0 \qquad (10)$$

with the Christoffel matrix Γ_{ik} being related to the elastic tensor by

$$\Gamma_{ik} = c_{ijkl} \widehat{q}_j \widehat{q}_l \qquad (11)$$

Thus, the solution of the Christoffel equation is an eigenvalue problem, in which one can solve for the eigenvalues ρv^2 and eigenvectors p for a specified crystal direction q. By virtue of being an eigenvalue problem of a 3 × 3 matrix, the determination of wave motion in a crystalline solid yields three solutions, each corresponding to the wave speed of differently polarized plane waves: one primary wave with longitudinal polarisation and two transverse polarized shear waves. The acoustic wave velocities were sampled for various q with the sampling grid defined in the spherical coordinate system as 180 (θ-axis) × 720 (φ-axis) points evenly spaced over half of the unit sphere.

The Christoffel matrix for each of the crystal systems under investigation as well as a worked example on how to solve the Christoffel equation for acoustic waves propagating in the direction of the principal axis of an orthorhombic crystal are provided in the supplementary material.

3. Results and discussion

3.1. CO₂

CO_2 is one of the most abundant condensed volatiles and has been identified in variety of environments in and outside of the solar system (Minissale et al., 2013). Probably the best known occurrence of solid crystalline CO_2-I (space group $Pa\overline{3}$), colloquially referred to as *dry ice*, is in the southern martian polar region where the temperature drop in winter causes the condensation of CO_2 from the martian atmosphere covering the ice shield with a thick layer of solid CO_2 (Byrne and Ingersoll, 2003). Moreover, solid CO_2 is thought to occur on numerous icy objects in the outer solar system (e.g. Johnson, 1996; McCord et al., 1998a; Prentice, 1993; Cruikshank et al., 2010; Grundy et al., 2006) and has even been identified in the interstellar medium (D'Hendecourt and Jourdain de Muizon, 1989).

By virtue of exhibiting cubic symmetry the CO_2 crystal lattice may be described by a single cell parameter being inversely proportional to density. For this reason, the zero pressure athermal performance was not assessed and will be discussed separately with the high-pressure density profiles.

Despite being subject of numerous studies focussing on the

Table 2

Computationally derived athermal bulk moduli of CO_2 from this study and the literature compared to the experimental values for CO_2. Bulk moduli from speed of sound measurements and inelastic neutron scattering are Voigt-Reuss-Hill averages whereas the ones derived from isothermal compression series are adiabatic. *Speed of sound measured between 88 and 190 K and extrapolated to 0 K. ** EoS parameters as reanalysed and stated by Giordano et al. (2010). RT denotes that the data was acquired at room temperature. N/S denotes that this information is not stated by these authors. [F] indicates that the parameter was fixed during the fitting procedure.

V_0 (Å^3)	K (GPa)	K'	T (K)	EoS	Method	Source
220.81(70)	2.85(15)	7.40(40)	0	BM-3EOS	DFT: PBE	This study
180.73(13)	7.76(20)	9.26(40)	0	BM-3EOS	DFT: PBE + D2	This study
195.58(28)	6.57(23)	5.80(35)	0	BM-3EOS	DFT: PBE + TS	This study
190.54(28)	6.70(31)	5.75(58)	0	BM-3EOS	DFT: PBE + MBD	This study
195.88(1.43)	2.72(47)	11.18(1.82)	0	BM-3EOS	DFT: PBEsol	This study
183.99(41)	4.68(27)	8.87(62)	0	BM-3EOS	DFT: PBEsol+D2	This study
184.60(17)	4.69(11)	8.64(26)	0	BM-3EOS	DFT: PBEsol+TS	This study
157.4(3)	16.5(4)	6.8(1)	0	BM3-EOS	MP2	Li et al. (2013)
147.48	16.6	N/S	0	N/S	DFT:LDA	Gracia et al. (2004)
212.2	3.21	8.10	0	BM-3EOS	DFT: PBE	Bonev et al. (2003)
171.40(44)	10.4(4)	6.8(4)	0	MGD	MGD-Model	Giordano et al. (2010)
171.64	8	N/A	0*	N/A	Speed of sound	Manzhelii et al. (1971)
N/S	8.67	N/A	95	N/A	Inelastic neutron scattering	Powell et al. (1972)
201.98 [F]	3.0 [F]	8.55 [F]	295	N/A	MGD-Model	Giordano et al. (2010)
204(12)	2(1)	9(1)	296	Vinet	WC-anvil cell	Olinger (1982)**
208.6(1.3)	2.93(10)	7.8	296(2)	BM3-EOS	DAC	Liu (1984)
N/S	12.4	N/S	RT	N/S	DAC	Yoo et al. (1999)

exploration of its thermoelastic properties, there are just three studies (i. e. Manzhelii et al., 1971; Powell et al., 1972; Stevenson, 1957) reporting the bulk modulus of CO_2 in the below-room temperature region. Out of these three studies the compressibility reported by Stevenson (1957) is in doubt (Olinger, 1982), leaving compressive parameters as obtained by Manzhelii et al. (1971) from speed of sound measurements in the 80–190 K range and extrapolated to athermal conditions, as well as the full elastic tensor determined by Powell et al. (1972) at 95 K by means of inelastic Neutron scattering, as the only reliable experimentally determined reference data in the below room temperature region. Giordano et al. (2010) experimentally determined the compressibility along various high-tempeature isotherms and combined these data with literature compression data in a Mie-Grüneisen-Debye (MGD) model. The athermal bulk modulus and unit-cell volume as obtained from the MGD fit were in good agreement with the experimentally determined reference data, granting the validity of the model, which was therefore chosen for the performance evaluation of the computed density-pressure profiles.

The density is systematically overestimated, regardless of the functional/dispersion correction applied (Table 2). PBE + D2 demonstrates the best performance, overestimating the zero pressure athermal volume reported by Giordano et al., 2010 by only 5.4%. The PBEsol + D2 ranks second, followed by PBEsol + TS, PBE + MBD, PBE + TS, PBEsol, and lastly PBE being the worst performing approach overestimating the cell volume by 28.8%.

The PBEsol + D2 agrees best with the reference athermal density-pressure profile, closely followed by the PBEsol + TS and PBE + D2, as the top performing combination in the zero-pressure benchmarking category, just on the third place (Fig. 1). When assessing the high-pressure performance in terms of relative compressibility, however, it is apparent that the seemingly excellent performance of the dispersion corrected PBEsol approaches is due to a cancellation of errors, stemming from the overestimation of the cell volume and underestimation of the materials stiffness. In detail, PBEsol + D2 and PBEsol + TS substantially underestimate the material's stiffness ranking ex aequo on 4th rank in the relative compressibility benchmarking category, whereas the top performing combination, PBE + D2, accurately models the relative compression with a MUD of just 1.0% and therefore, may be considered as the top performing combination in the high-pressure category.

As a general trend, even the worst performing dispersion corrected calculations yield a substantial improvement over their non-dispersion corrected counterparts (Fig. 1). It is further noteworthy, that although performing poorly when evaluated against the athermal reference data, the compressibility obtained by the PBE and PBEsol xc functional demonstrates excellent performance when compared to the experimental room temperature pressure profile (Fig. 1) determined by Giordano et al. (2010).

When comparing room temperature compression data for solid CO_2 (Table 2) it should be taken into account that the non-existence of solid CO_2 at standard conditions renders it impossible to experimentally determine V_0 at room temperature, with both K and K' being sensitive to changes in V_0 (Giordano et al., 2010). Comparing their experimental room temperature compression data to earlier studies published by Olinger (1982) and Liu (1984), Giordano et al. (2010) conclude that the data are in good agreement, but the standard deviations in earlier studies are larger due to poor coverage in the low-pressure region and larger scatter of data-points.

Comparing the performance of this studies' best performing combination, PBE + D2, compressive parameters (5.4%, −25.4% and 36.2% difference to the experimental reference values on V_0, K and K' respectively) to earlier DFT studies by Bonev et al. (2003) (i.e. PBE, 23.0%, −69.1%, 19.1% difference to the experimental reference values on V_0, K and K', respectively) and Gracia et al. (2004) (i.e. LDA, − 14.0% and 59.6% difference to the experimental reference values on V_0 and K) reinforces the improved accuracy associated with the implementation of dispersion correction schemes into Kohn-Sham DFT calculations.

Regarding further gain of accuracy by increasing the level of theory, we want to point out that the Post-Hartree-Fock calculations of the second order Møller-Plesset perturbation (MP2) theory type by Li et al. (2013) substantially underestimate the volume and overestimate the stiffness.[1] It is a well-studied phenomenon that MP2 performs badly for dispersion dominated systems (Cybulski and Lytle, 2007), thus explaining the higher accuracy achieved in our calculations.

The elastic constants of CO_2 were computed using the PBEsol and PBE + D2 combinations and then benchmarked against the experimental reference constants reported by Powell et al. (1972) at 95 K. PBE + D2 is in excellent agreement with the reference data, differing by merely 0.0%

---

[1] −8.2%, 58.6% and 0.0% difference to the experimental reference values on V_0, K and K' respectively, compressive parameters by digitizing the volume pressure plot and subsequent equation of state fitting
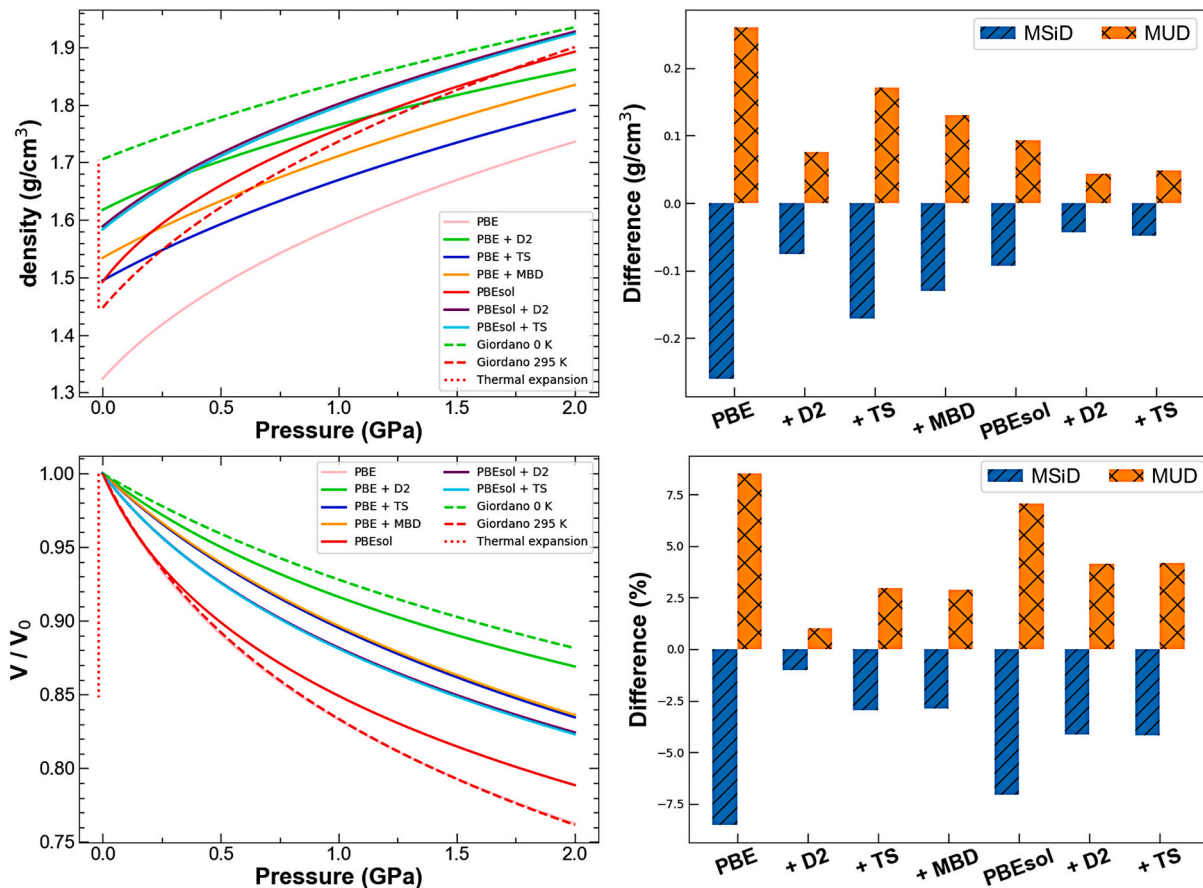
Fig. 1. Density profiles and relative compressibility of CO_2, and their performance assessed in terms of MSiD and MUD. While the dispersion corrected PBEsol approaches yield a low average error on the density, they fail to reproduce the relative compressibility. The dispersion corrected PBE functionals, however, reveal excellent performance for both the density and relative compressibility.

Table 3

Computed elastic constants of CO_2 evaluated against the experimental co-efficients as reported by Powell et al. (1972). Bulk and shear moduli were computed using the Christoffel code whereby the density corresponding to 95 K was interpolated from the 90 and 100 K values as reported by Manzhelii et al. (1971). Temperatures are in K, all other values in GPa. Diff % gives the deviation of the preceding value from the corresponding experimental value in %.

C_{ij}	Exp	PBE + D2	Diff %	PBEsol	Diff %
C_{11}	13.60(6)	13.60(14)	0.0	6.04(18)	−55.6
C_{12}	6.2(1)	5.29(31)	−14.7	0.62(13)	−90.0
C_{44}	5.10(3)	5.23(7)	2.5	2.16(29)	−57.6
K	8.67	8.02	−7.5	2.43	−72.0
G	4.54	4.82	6.2	2.36	−48.0
T	95	0		0	

(C_{11}), −14.7 (C_{12}) and 2.5% (C_{44}), whereas PBEsol largely fails to model the elastic anisotropy underestimating the elastic constants by 55.6 to 90% (Table 3). PBEsol further fails to accurately model the directions of minimum and maximum stiffness (Fig. 2). Both, PBE + D2 and the experimental data show that the <110> and <100> are directions of maximum and minimum stiffness respectively, whereas PBEsol draws an inverted picture with the stiffness reaching a maximum in <100> and a minimum in <110>. This failure to accurately model the elastic anisotropy, clearly, results in an inversion of the maximum and minimum directions of seismic wave velocities as compared to the experimental reference data (Fig. 2). Regarding the absolute accuracy of the computed seismic wave velocities, we note that the agreement between PBE + D2 and the experimental data is striking with a MUD of 1.36% and 3.88% for the P and S waves, respectively. PBEsol completely fails to

reproduce the seismic wave velocities underestimating the P and S wave velocities by 33.68% and 25.15%, respectively.

3.2. C_6H_6

Polycyclic aromatic hydrocarbons are abundant in the universe, contributing an estimated 20–30% to the galactic infrared radiation (Peeters, 2011), and serve as indicator to determine star formation rates (Calzetti, 2011), unarguably a key parameter in understanding a galaxy's formation and evolution. From a topological perspective, polycyclic aromatic hydrocarbons may be described in a simplified manner as fused benzene rings.

Unsurprisingly, considering the cosmic abundance of polycyclic aromatic hydrocarbons, benzene (C_6H_6; space group: *Pbca*) as their fundamental building block has been specifically identified in a large variety of extra-terrestrial settings such as carbonaceous meteorites (Mullie and Reisse, 1987), protoplanetary nebula CRL618 (Cernicharo et al., 2001), and in Titan's atmosphere (Vinatier et al., 2017). The latter occurrence appears to be of special interest from a planetary science perspective, since Vuitton et al. (2008) suggested that the atmospheric benzene, among other aromatics, could condense as it diffuses downwards in Titan's atmosphere covering the surface with a layer of solid benzene. Moreover, Malaska and Hodyss (2014) studied the solubility of hydrocarbons in simulated Titan lake and concluded that Titan's lakes might saturate in benzene from direct airfall over geological timescales and may form hydrocarbon deposits in a similar fashion as terrestrial evaporitic deposits. Seismology has demonstrated to be a powerful (Cornelius and Castagna, 2017), albeit notoriously difficult method (Jones and Davison, 2014), in order to explore terrestrial evaporite
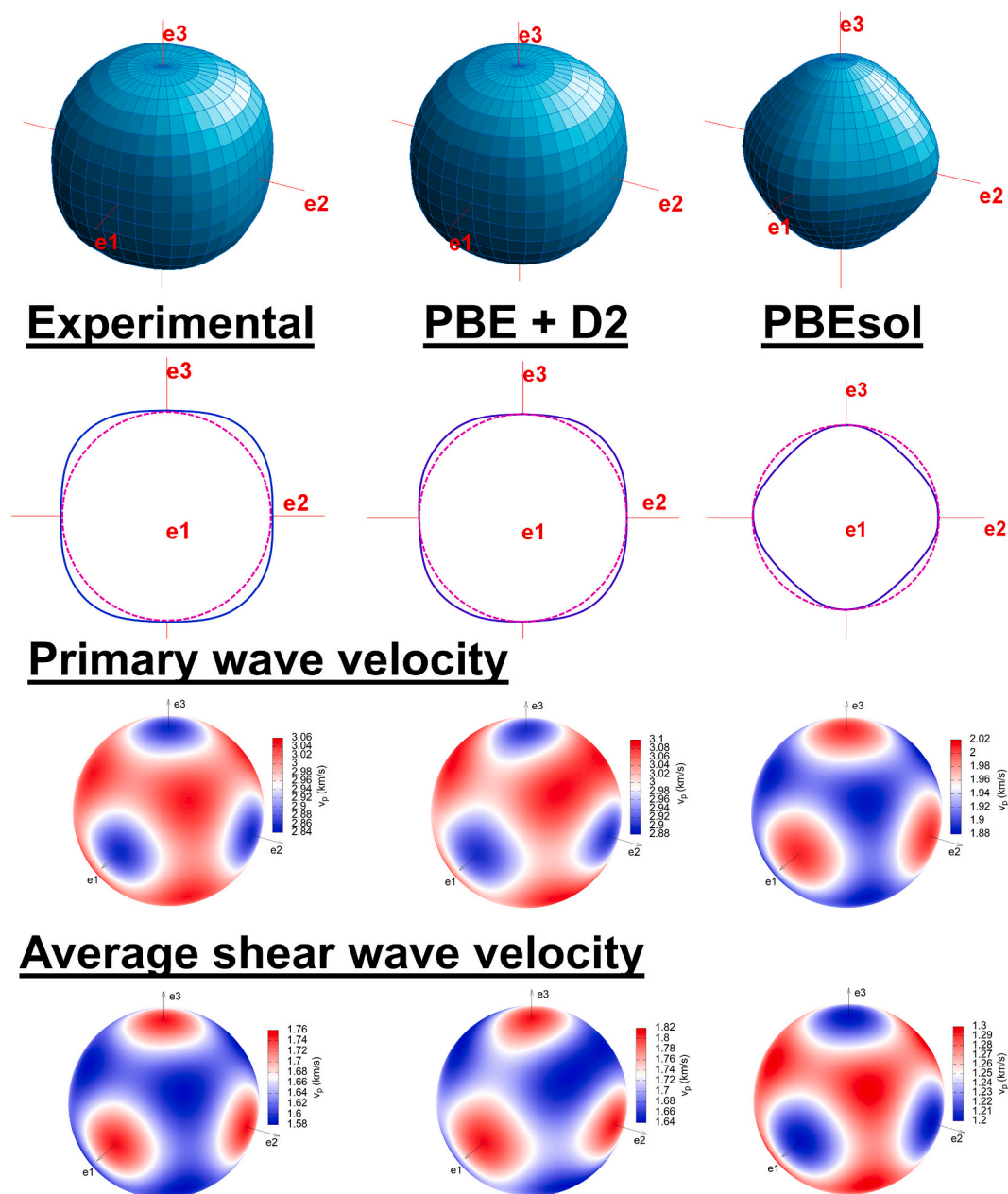
Fig. 2. Representation surfaces of the longitudinal effect of the elastic stiffness of CO_2 clearly demonstrate that PBE + D2 excellently reproduces the materials elasticity, whereas PBEsol fails to do so. From comparing cross-sections along the principal tensor axis (blue) with a circle whose radius corresponds to the magnitude of maximum stiffness (magenta), it becomes apparent that while for the PBE + D2 and experimental tensor the direction of maximum and minimum compressibility are $\langle 110 \rangle$ and $\langle 100 \rangle$ respectively: this is inverted for the PBEsol derived tensor. Naturally, this inversion is also reflected in the seismic wave velocities.

deposits and may also be able to cast light on the mineralogical phase assemblage of these putative hydrocarbon deposits, subject to the condition that the elastic wave velocities of benzene and other candidate materials are accurately known.

The zero pressure athermal unit-cell dimensions were benchmarked against the experimental values determined by Fortes and Capelli (2018) at 10 K by means of high-resolution neutron powder diffraction (Fig. 3). PBE and PBEsol both overestimate the cell volume, whereas the implementation of dispersion corrections results in an underestimation. Again, all dispersion corrected combinations yield a substantial improvement over their non-dispersion corrected counterparts. For PBE the implementation of a dispersion correction reduced the average absolute difference on the lattice parameters by 63%, 88%, 98% for the PBE + D2, PBE + TS and PBE + MBD, respectively.

As for the PBEsol based calculations, implementation of a dispersion corrections improves the performance and reduces the average absolute difference on the lattice parameters by 49% and 51% for the PBEsol + D2 and PBEsol + TS, respectively. Overall, the PBE + MBD is the best performing combination with an MUD of merely 0.014 Å (Fig. 3).

First exploration of the high-pressure behaviour of benzene dates back to pioneering work of Ferche (1891), Heydweiller (1897), Tammann (1903), Meyer (1910), and Bridgman (1914). More recently, pressure-volume data for benzene were reported by Figuière et al. (1978) and Katrusiak et al. (2010). After digitizing and fitting the pressure-volume data reported in Figuière et al. (1978) it was evident that values of ~0.5 as obtained for K' are unrealistically low for such a soft solid as benzene. Fitting of a BM3-EOS to the Katrusiak et al., 2010 data yielded much more realistic EoS parameters $V_0 = 522.43$ Å^3, $K =$
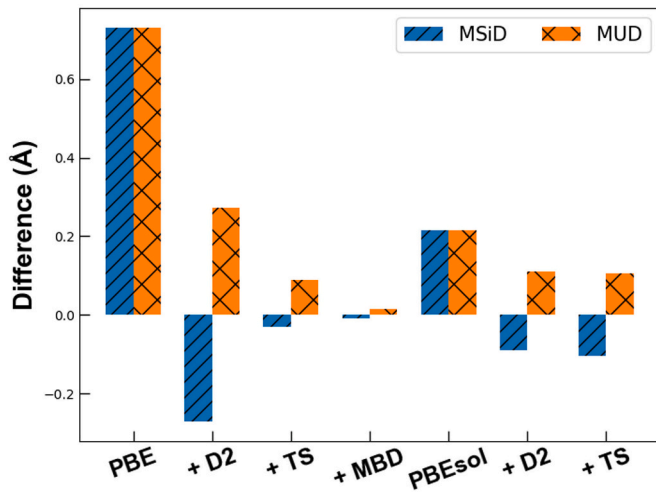
Fig. 3. MSiD (blue) and MUD (orange) of the DFT lattice vectors of C_6H_6 benchmarked against the Fortes and Capelli (2018) values determined at 10 K.

2.32 GPa, $K' = 9.85$ which was used as experimental reference data for our benchmarking purposes as presented in Table 4.

One drawback of benchmarking against the Katrusiak et al. (2010) data is that the compressibility was determined along the 295 K isotherm. Therefore, the effect of temperature will be discussed accordingly in the performance evaluation.

The PBEsol functional comes out on top of both the density profile and relative compressibility benchmark (Fig. 4), which we attribute to a cancellation of the underestimation of the density and stiffness, paired with the benchmarking being carried out against room temperature data. PBE performs poorly in modelling the density profile, but came second in the relative compressibility benchmarking category, once more validating that non-dispersion corrected functional perform very well for room temperature data. We expect the bulk modulus to substantially increase approaching the athermal limit, which is supported by low-temperature bulk moduli of 4.60, 5.85 and 6.28 GPa as obtained at 250, 170 and 138 K in speed of sound measurements (Heseltine et al., 1964; Walmsley, 1968). Comparing the PBE and PBEsol derived bulk moduli of 1.29(2) GPa and 2.51(9) GPa, respectively, to this low-temperature studies it is apparent that both functionals fail to accurately reproduce the stiffness in the low-temperature region. The dispersion corrected PBE yield more realistic bulk moduli ranging from 7.45 to 10.71 GPa. A bulk modulus of 8.2 GPa as derived by Litasov et al., 2019 using the optPBE-vdW approach compares very well to both our dispersion corrected and the experimental low-temperature values.

The elastic constants of C_6H_6 were computed using the PBEsol and

PBE + TS approaches and then benchmarked against the experimental reference determined by Walmsley (1968) at 138 K (Table 5). The stiffness is systematically overestimated by the PBE + TS functional and underestimated by the PBEsol functional. At first sight, the longitudinal effect of the elastic stiffness appears well approximated by both combinations with the maximum direction being along <101> and the local minima parallel to the principal tensor axes. Looking more closely, however, subtle discrepancies become apparent. The experimental data displays an elastic anisotropy along the principal axes with $C_{22} > C_{11} = C_{33}$ resulting in the P waves travelling faster along <010> than <100> and ⟨010⟩. The DFT-derived tensors, however, yield identical values within the limits of errors for respective directions and hence fail to reproduce the anisotropy along the principal tensor axes e_i.

The experimental data further reveals slow shear waves propagating in the <010> and < 100> direction, which are both solely dependent on C_{66} and hence constrained to be equivalent in an orthorhombic crystal by the Christoffel equation, being substantially slower than those travelling in the C_{44} dependent <001> direction (Fig. 5). The DFT calculations, again, failed to reproduce this effect and yielded nearly identical slow shear wave velocities for the principal directions stemming from similar C_{44}/C_{66} ratios of 0.88 and 0.95. These are much lower than a value of 1.7 corresponding to the C_{44}/C_{66} ratio of the experimentally determined elastic constants. PBE + TS and PBEsol bracket the experimental values over- and underestimating the elastic constants by 73% and − 44%, respectively. Naturally, this is also reflected in the seismic wave velocities differing by 23.95% (P, PBE + TS), 24.71% (S, PBE + TS) −25.6% (P, PBEsol), and − 21.6% (S, PBEsol) from the literature reference data. Clearly, benchmarking against lower temperature data, which to our knowledge are not available, would increase and decrease the performance of PBE + TS and PBEsol, respectively.

In general, the elasticity is well approximated, albeit neither approach fully accounts for the elastic anisotropy. Absolute errors on the seismic wave velocities, obtained with either of the functionals, are far from experimental accuracy and hence not suitable for use in a seismic velocities reference data-base.

3.3. $MgSO_4 \cdot 7H_2O$

Remote sensing of the surface of the outer three Galilean moons (i.e. Europa, Ganymede and Callisto) by the *Galileo* near-infrared mapping spectrometer (McCord et al., 1998a, 2001) indicates that epsomite ($MgSO_4 \cdot 7H_2O$; space group: $P2_12_12_1$), among other hydrated minerals, is a promising candidate to partially constitute the non-icy material identified on their surface. As for the origin of $MgSO_4 \cdot 7H_2O$ on the European surface both endogenic (i.e. from brine crystallisation; McCord et al., 1998b) and exogenic (i.e. via the radiolysis of endogenic $MgCl_2$ in conjunction with sulfur ion bombardment from neighbouring Io; Brown and Hand, 2013) processes are being discussed.

The compressibility of epsomite-type $MgSO_4 \cdot 7D_2O$ was determined

Table 4

Computationally derived athermal bulk moduli of C_6H_6 from this study and the literature compared to the experimental values. Bulk moduli from speed of sound measurements are Voigt-Reuss-Hill averages whereas the ones derived from isothermal compression series are adiabatic.

| V_0 (Å^3)	K (GPa)	K′	T (K)	EOS	Method	Source
610.60(58)	1.29(2)	10.83(13)	0	BM-3EOS	DFT: PBE	This study
417.21(27)	10.71(31)	10.46(57)	0	BM-3EOS	DFT: PBE + D2	This study
461.05(10)	9.21(7)	7.12(10)	0	BM-3EOS	DFT: PBE + TS	This study
462.15(25)	7.45(12)	7.97(22)	0	BM-3EOS	DFT: PBE + MBD	This study
502.63(76)	2.51(9)	12.73(44)	0	BM-3EOS	DFT: PBEsol	This study
449.20(31)	8.82(18)	5.22(23)	0	BM-3EOS	DFT: PBEsol+D2	This study
446.02(24)	6.97(11)	7.85(20)	0	BM-3EOS	DFT: PBEsol+TS	This study
484.89	8.2 (1)	6.8 (1)	0	Vinet	DFT:optPBE–vdW	Litasov et al. (2019)
N/A	4.60	N/A	250	N/A	Speed of sound	Heseltine et al. (1964)
N/A	5.85	N/A	170	N/A	Speed of sound	Heseltine et al. (1964)
N/A	6.30	N/A	138	N/A	Speed of sound	Walmsley (1968)
522.43(88)	2.32(10)	9.85(43)	RT	BM-3EOS	Piston + DAC	Katrusiak et al. (2010)

Fig. 4. Density profiles and relative compressibility of C_6H_6 and their performance assessed in terms of MSiD and MUD. We note the excellent agreement between the 10 K density and the PBE + TS and PBE + MBD approaches. Clearly, this is not reflected in the relative compressibility likely due to the benchmarking being carried out against room temperature data.

Table 5

Computed elastic constants of C_6H_6 evaluated against the experimental co-efficients as reported by * Walmsley, 1968 at 138 K. Moreover, the elasticity determined by Heseltine et al., 1964 at 250 K (**) and 170 K (***) is reported for comparison. Bulk and shear moduli were computed using the Christoffel code whereby the densities corresponding to the experimental temperatures of 138 K, 170 K and 250 K were either directly calculated from the experimentally determined unit-cell volume (i.e. 250 K; Fortes and Capelli (2018)) or, if no volume data corresponding to the temperature was available (i.e.138 K and 170 K), interpolated from the two closest data-points as listed in Fortes and Capelli (2018). Temperatures are in K, all other values in GPa. Diff % gives the deviation of the preceding value from the corresponding experimental value in %.

C_{ij}	Exp*	PBEsol	Diff %	PBE + TS	Diff %	Exp**	Exp***
C_{11}	8.61	4.84 (32)	−43.8	13.71(90)	59.2	6.14	8.01
C_{22}	10.01	4.39 (33)	−56.1	13.48 (1.52)	34.7	6.56	9.26
C_{33}	8.63	4.16 (45)	−51.8	13.12(46)	52.0	5.83	7.88
C_{12}	4.15	2.29 (47)	−44.8	7.68(72)	85.1	3.52	3.85
C_{13}	5.10	2.87 (29)	−43.7	10.73(53)	110.4	4.01	4.80
C_{23}	5.38	2.46 (53)	−54.3	7.81(71)	45.2	3.90	5.08
C_{44}	3.56	1.68 (25)	−52.8	5.14(38)	44.4	1.97	3.18
C_{55}	6.13	3.77 (12)	−38.5	10.61(37)	73.1	3.78	5.53
C_{66}	2.10	1.89 (29)	−10.0	5.31(54)	152.9	1.53	1.95
Mean			−44		73		
K	6.28	3.17	−49.5	10.26	63.4	4.60	5.85
G	3.20	1.63	−48.8	4.22	31.9	1.93	2.89
T	138	0		0		250	170

by Fortes et al. (2006) by means of neutron powder diffraction in the temperature range 50–290 K and up to 0.5 GPa. Gromnitskaya et al. (2013) explored the bulk compressibility of $MgSO_4 \cdot 7D_2O$ and $MgSO_4 \cdot 7H_2O$ via speed of sound measurements and demonstrated that the effect of deuteration upon the elastic properties of the isotopologues is small (i.e., hydrogenated $K = 18.8$ GPa, deuterated $K = 21.6$ GPa). For this reason, we suggest that the equation of state as determined by Fortes et al. (2006) along the 50 K isotherm approximates the compressibility of $MgSO_4 \cdot 7H_2O$ close to athermal conditions reasonably well, and therefore chose these data as an experimental reference for our bench-marking purposes.

After benchmarking the DFT derived unit-cell dimensions with respect to the values experimentally determined by Fortes et al. (2006) at a temperature of 2 K (atmospheric pressure), it was apparent that the PBE optimisation yielded an overestimation of all lattice parameters and consequently the cell volume, whereas the other combinations under-estimate this quantity (Fig. 6). The PBE xc functional, in conjunction with the pairwise additive (i.e. D2 and TS) correction schemes, as well as the many body dispersion correction, agree best with the experimentally determined crystal structure. The excellent performance of PBE + TS and PBE + MBD appears to at least partially stem from a cancellation of an overestimation of the *a* and underestimation of *b* lattice parameter, which is reflected in an excellent MSiD but substantially poorer MUD (Fig. 6). The geometries obtained by the non-dispersion corrected PBEsol and the dispersion corrected PBE approaches agree excellently with the experimental reference data (i.e. MUD ranging from 0.039 to 0.050 Å), whereas the non-dispersion corrected PBE and the dispersion corrected PBEsol combinations yield an approximately three fold higher average error (i.e. MUD 0.122–0.155 Å) on the individual lattice pa-rameters and largely over- and underestimated the cell volume, respectively (Fig. 6).

The performance in replicating the density's pressure dependency was evaluated against the along the 50 K isotherm experimentally
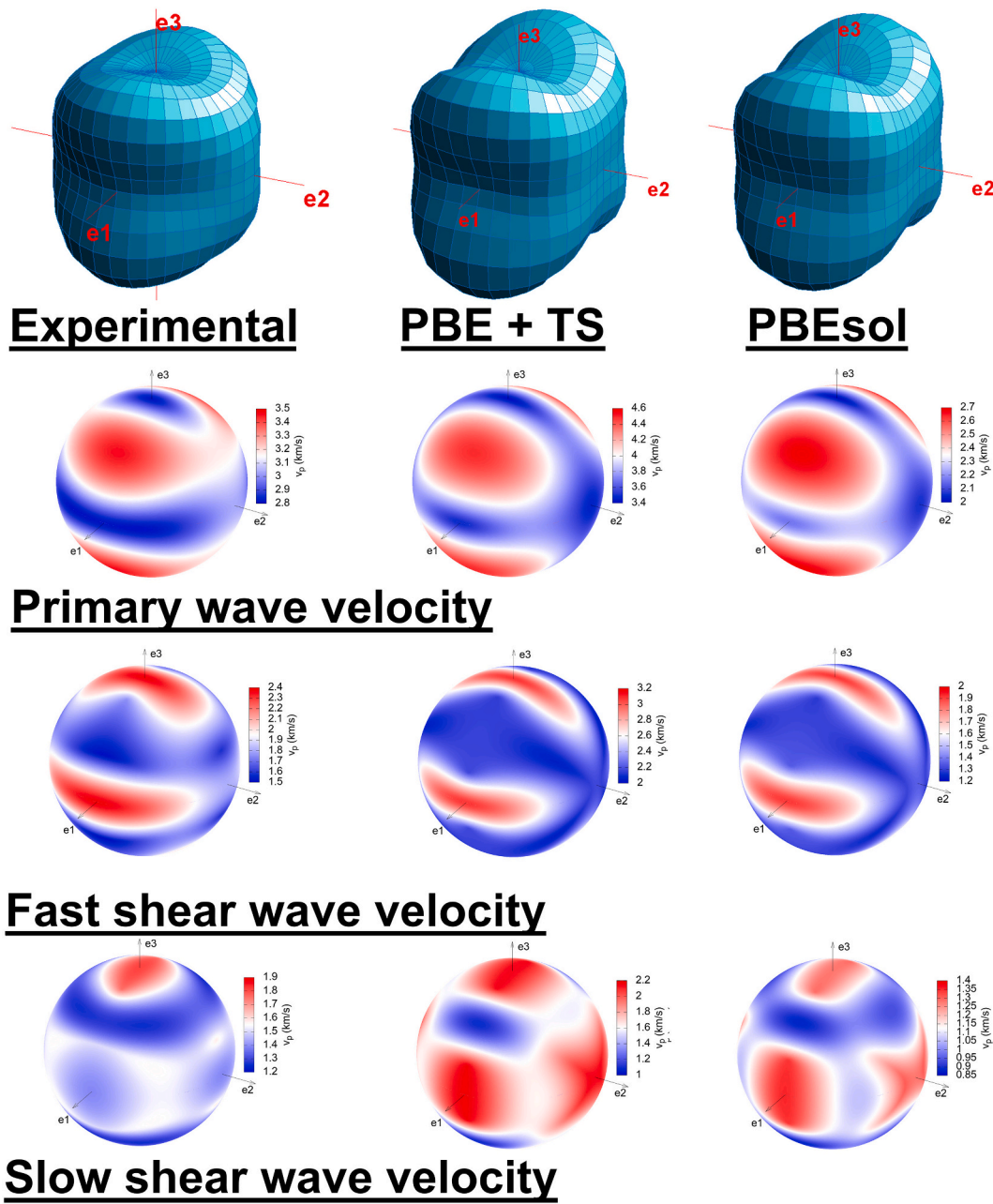
Fig. 5. Representation surfaces of the longitudinal effect of the elastic stiffness of C_6H_6 clearly demonstrates that both the PBEsol and PBE + TS approximate the experimental values (Walmsley, 1968) reasonably well. The anisotropy, however, is not completely accounted for, which is most pronounced in the slow shear wave velocities.

determined EoS parameters as reported by Fortes et al. (2006) (Fig. 7, Table 6). The combinations that came out on top of the zero pressure athermal benchmarking category, i.e. PBE + TS, PBE + D2 and PBEsol, also demonstrated superior performance in approximating the reference density profile. The PBE functional reveals almost identical performance as the PBE + TS approach in the relative compressibility (V/V_0) category, which can at least be partially attributed to a bias of the compressive parameters as reported by Fortes et al. (2006) towards this functional, since they fixed K' to 5.3, a value they have determined by high-pressure geometry optimisations using the PW91 functional. It is well known, that PW91 and PBE produce essentially identical bulk moduli (Mattsson et al., 2006), an observation that is also reflected in our results, with the difference between this studies' PBE and the Fortes et al. (2006) PW91 merely being 0.4%, 6% and 4% on V_0, K and K', respectively. Furthermore, we point out that the PBE xc functional is the

worst performing functional in modelling the experimental density profile (Fig. 7), hence the excellent performance in modelling the relative compressibility likely originates from aforementioned bias and a cancellation of the density and compressibility underestimation. The performance of the PBE + TS in replicating the experimental density profile is excellent, with the MUD just being 0.003 g/cm^3, and was therefore chosen for the computation of the elastic constants.

To our knowledge, three studies (i.e. Alexandrov et al., 1963; Sundara Rao, 1950; Voronkov, 1958) have experimentally determined a complete set of the elastic constants of epsomite. Fortes et al. (2006) evaluated the axial compressibility as determined by means of high-pressure neutron diffraction against values derived from the elastic tensors, reported in the aforementioned studies, and concluded that the elastic tensor values determined by Sundara Rao (1950) and Voronkov (1958) were in doubt, whereas the elastic constants reported by
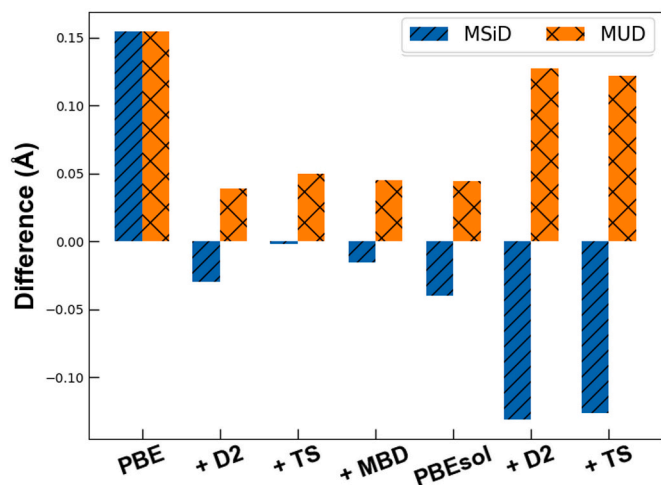
Fig. 6. MSiD (blue) and MUD(orange) of the DFT lattice vectors of MgSO$_4$·7H$_2$O benchmarked against the values determined at 2 K (Fortes et al., 2006) for the deuterated isotopologue.

Alexandrov et al. (1963) revealed satisfactory agreement. For this reason, and due to the lack of reference elastic constants experimentally determined at low-temperatures, values as reported by Alexandrov et al. (1963) were selected for benchmarking purposes. The effect of temperature on epsomite's stiffness (Fortes et al., 2006) is less dramatic than in CO$_2$ or C$_6$H$_6$, but still pronounced and will hence be discussed accordingly.

The computationally derived elastic constants are systematically overestimated by both the PBEsol and PBE + TS approach. The PBE + TS approach performed better with a MUD on the elastic constants of 40.2% compared to 43.0% for the PBEsol functional (Table 7). Regarding the effect of temperature, Stojanoff and Missell (1982) have reported the elastic constants for topologically related α-NiSO$_4$·6H$_2$O to increase on average by 10.2% of upon cooling from 300 K to 4.2 K. Assuming a similar increase for MgSO$_4$·7H$_2$O combined with the systematic overestimation by both PBEsol and PBE + TS, would naturally improve the performance.

Comparing the performance to other studies on hydrated sulfate minerals we note that, Arbeck et al. (2010) obtained MUDs of 11.1% and 12.6% as achieved with the PBEsol xc functional when compared to elastic reference constants experimentally determined for α-NiSO$_4$·6H$_2$O by Stojanoff and Missell (1982) at 300 K and 4.2 K, respectively. We suggest that the better performance achieved by Arbeck et al. (2010) likely originates from the higher symmetry of tetragonal α-NiSO$_4$·6H$_2$O as compared to orthorhombic MgSO$_4$·7H$_2$O, inevitably resulting in a less complex anisotropy of the materials properties (Neumann, 1885).

The compressional anisotropy was further assessed in terms of seismic wave velocities. The relative acoustic velocities as computed from the DFT derived elastic constants appear to be in good agreement, albeit systematically overestimated. In more detail, however, the slow secondary acoustic velocities disagree notably with the experimental data. The wave velocities in direction of the principal axis are well reproduced, in the <110> direction, however, the computed shear waves are overestimated with respect to their axial values (Fig. 8). Lastly, the DFT calculations do not well reproduce the P wave velocity along the principal axis and overestimate the velocity parallel to <100>. This failure clearly stems from the inaccurate modelling of the longitudinal elastic constants as noted above. MUDs on the seismic wave speeds of 18.52% (P, PBE + TS), 24.56% (S, PBE + TS) 19.83 (P, PBEsol), and 25.80% (S, PBEsol) compare very well, and in fact slightly
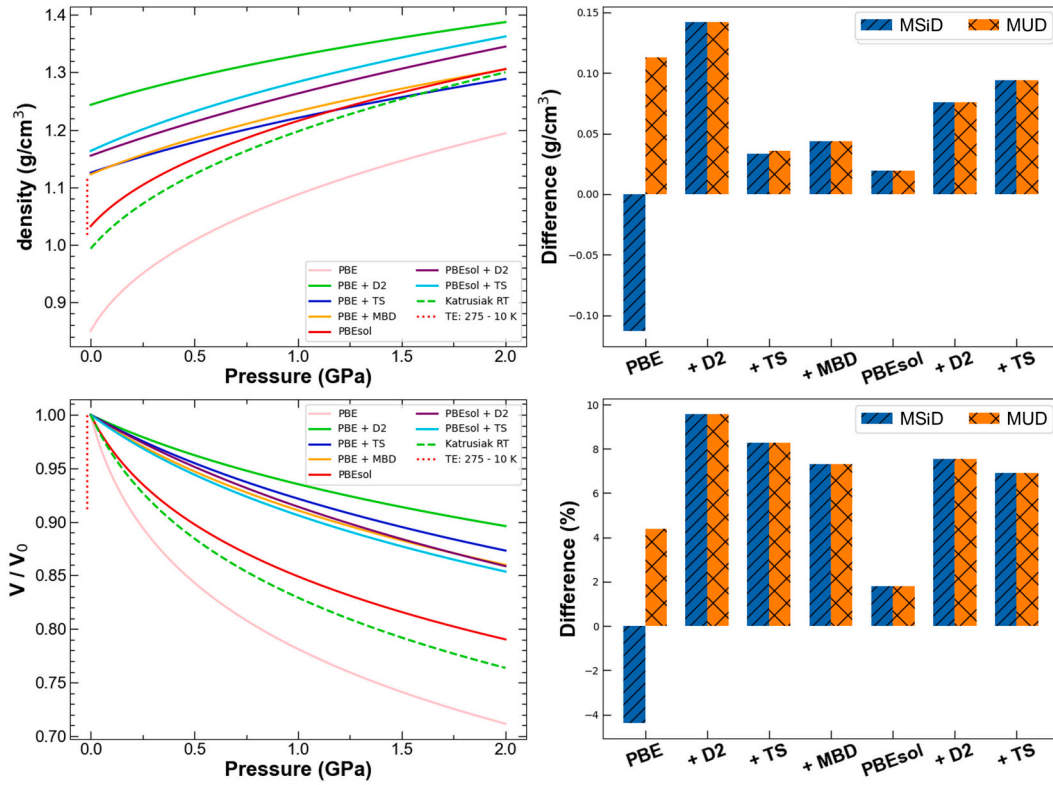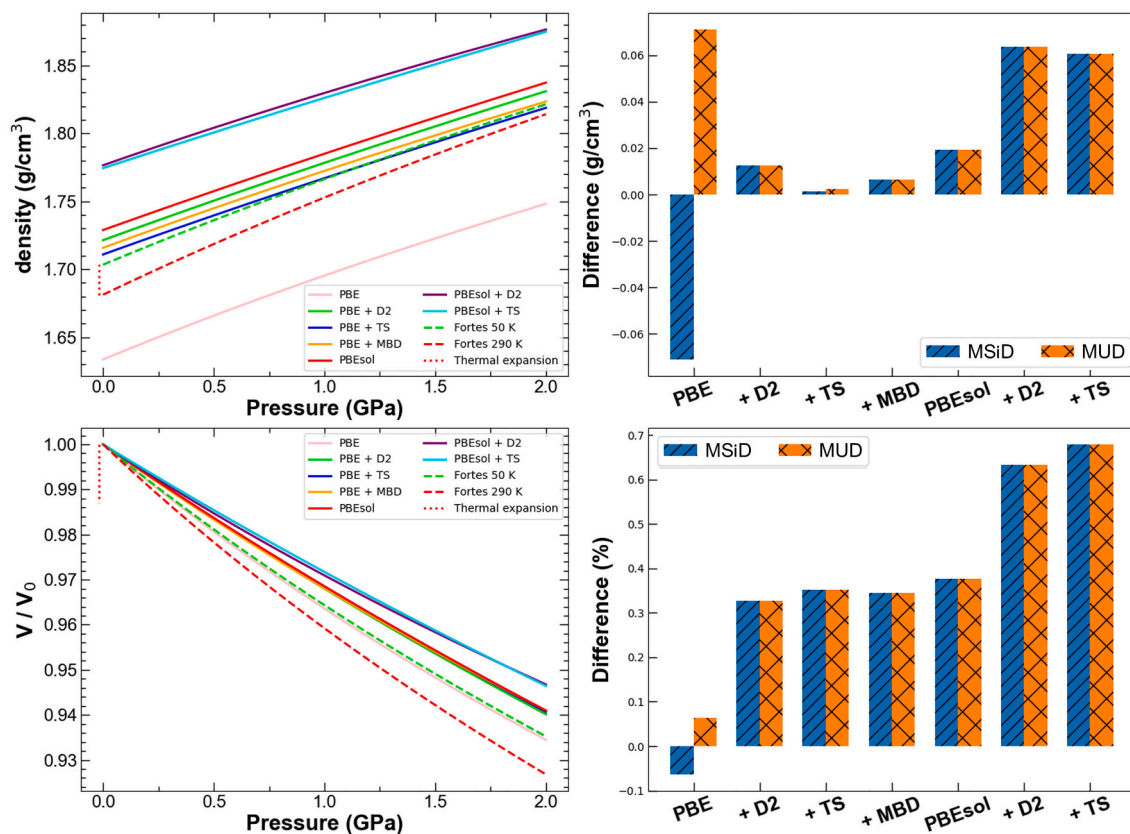

Fig. 7. Density profiles and relative compressibility of MgSO$_4$·7H$_2$O and their performance assessed in terms of MSiD and MUD. We note the excellent performance of the PBE + TS approach in replicating the experimental density pressure profile.

Table 6

Computationally derived athermal bulk moduli of $MgSO_4 \cdot 7H_2O$ from this study and the literature compared to the experimental values. Bulk moduli from speed of sound measurements are Voigt-Reuss-Hill averages whereas the ones derived from isothermal compression series are adiabatic. N/S denotes that this information is not stated by these authors. [F]indicates that the parameter was fixed during the fitting procedure. [D]deuterated isotopologue. RT denotes that the data was acquired at room temperature.

V_0 (Å^3)	K (GPa)	K'	T (K)	EoS	Method	Source
1002.23(28)	24.13(45)	5.94(52)	0	BM-3EOS	DFT: PBE	This study
951.09(10)	29.00(24)	3.60(24)	0	BM-3EOS	DFT: PBE + D2	This study
956.94(7)	29.13(15)	3.80(15	0	BM-3EOS	DFT: PBE + TS	This study
955.05(1.51)	29.25(3.5)	3.15(3.42)	0	BM-3EOS	DFT: PBE + MBD	This study
947.00(33)	29.60(77)	3.46(76)	0	BM-3EOS	DFT: PBEsol	This study
921.59(0.48)	31.02(1.38)	6.00(1.54)	0	BM-3EOS	DFT: PBEsol + D2	This study
922.69(19)	33.26(56)	3.23(55)	0	BM-3EOS	DFT: PBEsol + TS	This study
998.14(51)	23.2(2)	5.3(2)	0	BM-3EOS	DFT: PW91	Fortes et al. (2006)
961.17(7)[D]	25.0(2)	5.3[F]	50	BM-3EOS	NPD + PE-Press	Fortes et al. (2006)
973.80(7)	21.5(1)	5.3[F]	295	BM-3EOS	NPD + PE-Press	Fortes et al. (2006)
N/S	21.6	5.0	RT	N/S	Lever-Piezometer	Bridgman (1949)
N/A	21.6	5.2	295	N/A	Speed of sound	Gromnitskaya et al. (2013)
N/A	18.8[D]	4.2	295	N/A	Speed of sound	Gromnitskaya et al. (2013)
N/A	22.2(7)	N/A	RT	N/A	Speed of sound	Alexandrov et al. (1963)
N/A	28.99	N/A	RT	N/A	Speed of sound	Voronkov (1958)
N/A	43.5	N/A	RT	N/A	Speed of sound	Sundara Rao (1950)

Table 7

Computationally derived elastic constants of $MgSO_4 \cdot 7H_2O$ compared to the experimental data by Alexandrov et al. (1963). Temperatures are in K, all other values in GPa. Diff % gives the deviation of the preceding value from the corresponding experimental value in %.

C_{ij}	Exp	PBEsol	Diff %	PBE + TS	Diff %
C_{11}	32.5(7)	54.84(1.30)	68.7	50.15(72)	54.3
C_{22}	28.8(6)	41.18(6)	43.0	40.83(72)	41.8
C_{33}	31.5(6)	46.27(1.23)	46.9	44.77(1.76)	42.1
C_{12}	17.4(17)	20.31(25)	16.7	19.68(22)	13.1
C_{13}	18.2(18)	24.26(61)	33.3	24.6(59)	35.2
C_{23}	18.2(18)	20.63(30)	13.4	20.97(24)	15.2
C_{44}	7.8(2)	14.11(42)	80.9	13.9(29)	78.2
C_{55}	15.6(3)	21.24(8)	36.2	21.56(17)	38.2
C_{66}	9.0(2)	13.35(28)	48.3	12.97(38)	44.1
Mean			43.0		40.2
K	22.27	28.54	9.5	31.46	41.3
G	9.08	13.99	7.1	14.98	65.0
T	RT	0		0	

exceed the performance achieved for benzene, however, while for benzene PBEsol and PBE + TS are over- and underestimating the wave velocities, respectivly, this quantity is systematically ovestimated for epsomite regardless of the applied combination. Clearly, the accuracy achieved in this study is not sufficient to be used as reference in an elasticity database used for the seismic expoloration icy satellites.

3.4. $CaSO_4 \cdot 2H_2O$

The mineral gypsum ($CaSO_4 \cdot 2H_2O$; space group: $C2/c$) constitutes a major of part of the sulfate fraction of carbonaceous chondrites (Kargel, 1991), which are believed to be the fundamental building blocks to have formed the icy satellites in the outer solar system (Mueller and McKinnon, 1988). Thus it would appear obvious, that $CaSO_4 \cdot 2H_2O$ is a promising candidate to constitute the non-icy materials in the salty crust and mantle of these planetary bodies, however, the mobility of $CaSO_4 \cdot 2H_2O$ is limited by its low solubility. Nevertheless, Kargel et al. (2000) suggested that $CaSO_4 \cdot 2H_2O$ might be leached from the primordial chondritic material in high-temperature environments such as in the vicinity of hydrothermal vents. Due to the high thermal gradient in these environments, $CaSO_4 \cdot 2H_2O$ would re-precipitate as the salty water cools down, potentially forming extensive deposits. If these scenario is true, $CaSO_4 \cdot 2H_2O$ could be an indicator mineral for hydrothermal vents, which support thriving ecosystems on Earth (Corliss et al., 1979) and

may also be present on the Saturnian satellite Enceladus (Waite et al., 2017), under whose presumed ocean conditions life has been demonstrated to persist (Taubner et al., 2018). Moving onwards to less speculative grounds, $CaSO_4 \cdot 2H_2O$ is also an excellent choice for this high-pressure benchmarking study, due to its monoclinic symmetry requiring the determination of 13 independent elastic constants to fully account for its elastic anisotropy making it a sensitive benchmark.

The zero pressure athermal performance was evaluated against the crystal structure as determined by Schofield et al. (1996) at 4.2 K (Fig. 9). The benchmarking reveals that all but the non-dispersion corrected PBE are prone to cancelations as reflected by an excellent MSiD and much poorer MUD. PBE + TS comes out as the top performing functional having a MUD on the lattice parameters of 0.56%, closely followed by the PBEsol, and PBE + MBD combination. The PBE + D2 is the worst performing approach, with its MUD even exceeding the non-dispersion corrected PBE functional. We further note that while PBE based approaches systematically underestimate the lattice parameters, the contrary holds for combinations involving the PBEsol xc functional.

We went on to compare our results to the DFT study of gypsum by Khalkhali et al. (2019) which have applied the PBE, PBE + D2 and PBE + TS combinations also using the Castep code and ultrasoft pseudopotentials. MUDs of 1.640, 1.168 and 0.578% as obtained for PBE, PBE + D2, PBE + TS by Khalkhali et al., 2019 are systematically higher than the ones obtained in this study (i.e. MUD 1.014, 1.069, 0.563%). The reason for this is likely the largely differing choice of the plane wave basis sets i. e., ~0.07 Å^{-1} Brillouin zone sampling and a cut-off = 340 eV compared to ~0.03 Å^{-1} and 1300 eV as used in this study. From the convergence testing (supplementary data) it is obvious, that the Brillouin zone sampling as applied by Khalkhali et al. (2019) is not sufficient to obtain well converged optimisations.

The compressibility of $CaSO_4 \cdot 2H_2O$ has been studied in a piston cylinder experiment by Vaidya et al. (1973), in a time-of-flight neutron powder diffraction experiment involving a Paris-Edinburgh press (Stretton et al., 1997) on the deuterated isotopologue, and in diamond anvil cell experiments by Huang et al. (2000) and Comodi et al. (2008). The compressive parameters as reported by Comodi et al. (2008) and Stretton et al. (1997) are in excellent mutual agreement, but contradict those reported by Huang et al. (2000) and Vaidya et al. (1973). As pointed out by Comodi et al. (2008), the reason for the overestimation of the bulk modulus in the Huang et al. (2000) study likely originates from preferred orientation of the crystallites in the diamond anvil cell powder diffraction experiment. Vaidya et al. (1973) point out that their experiments systematically underestimated bulk moduli for several materials
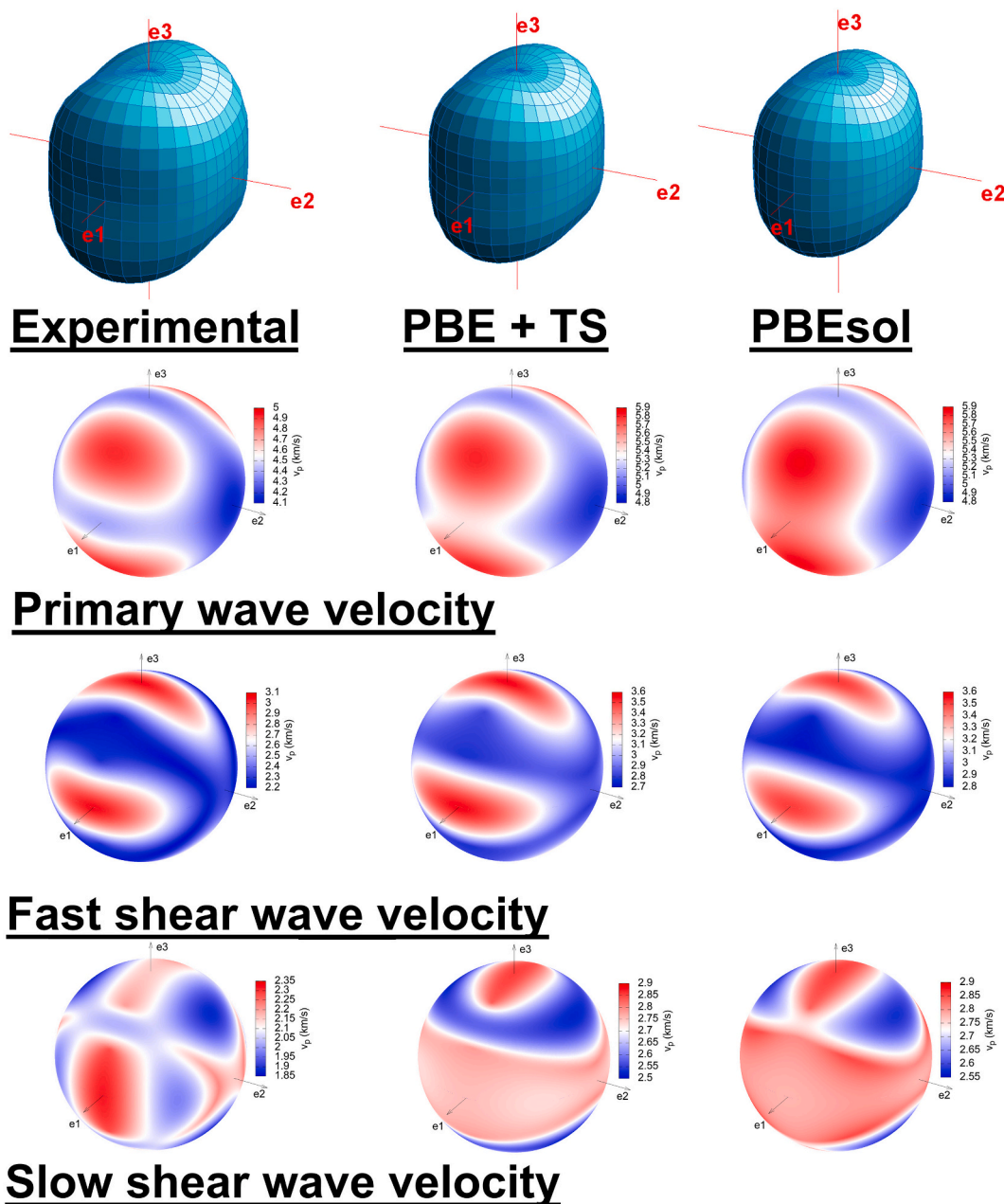
Fig. 8. Representation surfaces of the longitudinal effect of the elastic stiffness of $MgSO_4 \cdot 7H_2O$. Clearly, the overall agreement between theory and experiment is satisfactory. The seismic wave velocities however demonstrates that subtle details such as the Primary wave velocities in <100> and the slow shear wave velocities in <110> are not well reproduced by the DFT calculations.

under investigation, which they attribute the closing of pores of the powder sample during compression, naturally most pronounced at low pressures. We conclude that Comodi et al. (2008) reported the most accurate compressive parameters for $CaSO_4 \cdot 2H_2O$ along the room temperature isotherm. Noteworthy, despite this large body of experimental high-pressure studies, there is not a single low-temperature compression study. For this reason, the Comodi et al. (2008) data set was used as reference for the benchmarking study and the influence of thermal motion onto the compressibility will be discussed accordingly.

With an average density difference of merely 0.013 g/cm³ the PBE + D2 approach agrees best with the experimental reference profile (Fig. 10), and also demonstrates excellent performance in the relative compressibility category, being almost on par with the PBE xc functional. Again, PBE performs very well when benchmarked against room temperature data, albeit systematically overestimating the unit-cell volume. Surprisingly, the inclusion of dispersion corrections in the PBEsol calculations results in poorer performance in both of the high-pressure benchmarking categories. Based on a decrease in volume of just 1.1% upon cooling from room-temperature to 4.2 K (Schofield et al., 1996) and the higher bulk modulus, we expect the temperature to have a substantially lower influence on the elasticity as compared to other title compounds.

Furthermore, our findings were compared to previous DFT high-pressure studies on gypsum by Giacomazzi and Scandolo (2010) and Li and Lee (2018) (Table 8). The latter studied the compressibility of gypsum by applying the revPBE xc functional in conjunction with various dispersion corrections i.e. D2, and the non-local dispersion corrections DF1, DF2 and vv10. The revPBE based calculations systematically underestimate the bulk modulus of gypsum, yielding values of 30.9 GPa (revPBE) and 35.5 GPa (revPBE + D2), as compared to

Fig. 9. MSiD (blue) and MUD (orange) of the DFT lattice vectors of CaSO$_4$·2H$_2$O benchmarked against the values determined at 4.2 K (Schofield et al., 1996) for the deuterated isotopologue.

sufficiently converged and we cannot provide any explanation for the strong disagreement between the two studies.

The elasticity of gypsum has been studied by Haussühl (1965) at 273 and 293 K. It is noteworthy the choice of the crystallographic axis by Haussühl (1965) the *a* and *c* axis are inverted relative to the Comodi et al. (2008) setting, which has been used throughout this study. For this reason, we have transformed the elastic constants as reported by Haussühl (1965) accordingly (i.e., $C_{11} \Leftrightarrow C_{33}$, $C_{23} \Leftrightarrow C_{21}$, ...) for our benchmarking purposes.

Complete sets of elastic constants were computed using the PBEsol and PBE + D2 combinations (Table 9). The large negative values for the coupling constants C_{15} and C_{35} are well reproduced in the DFT calculations. For the small and negative C_{46} coefficient however, we obtain values of approximately the same magnitude but opposite sign. Haussühl (1965) reported a decrease of the magnitude of the C_{46} coefficient upon cooling to 273 K. Extending this trend to lower temperatures one might suggest that the opposite signs observed in theory and experiment might not be a failure of the DFT calculations, but indicate a real change of the sign of the constant C_{46} upon cooling.

The magnitude of the longitudinal elastic constants is well reproduced, but the modelling of the elastic anisotropy clearly is not satisfactory (Fig. 11). In detail, both DFT and the experimental data yield C_{33} to be the stiffest constant (Table 9). As for C_{22} and C_{33}, however, DFT disagrees with the experimental data yielding larger magnitudes for C_{22} than C_{11}. Due to the reference data being collected at temperatures far from 0 K, again, we can merely speculate if this disagreement is a failure of the DFT calculations in reproducing the elasticity or if the relative magnitude of the longitudinal elastic constants indeed changes at lower temperatures. We want to note, that Haussühl (1965) report C_{22} to increase almost twice as much as C_{33} upon cooling, hence we suggest that a real change might at least be in the realm of possibilities.

Obviously, this disagreement in the longitudinal constants as derived by experiment and DFT is also reflected in the anisotropy of the seismic wave propagation (supplementary material: Fig. s2). However, the

43.80 GPa (PBE, this study), 44.18 GPa (PBE + D2, this study) and the experimental value of 44(3) GPa (Comodi et al., 2008). As for the revPBE in conjunction with the non-local dispersion corrections revPBE + DF1, revPBE + DF2 and revPBE + vv10, Li and Lee (2018) report more realistic bulk moduli of 47.7, 43.2 and 40.8 GPa, respectively.

Surprisingly, Giacomazzi and Scandolo (2010) obtained a bulk modulus of 56.7 GPa for gypsum applying the non-dispersion corrected PBE functional. Their results overestimate the bulk modulus by ~30% when compared to both our PBE and the experimentally determined value. The plane wave basis set used in their optimisations appears to be

Fig. 10. Density profiles and relative compressibility of CaSO$_4$·2H$_2$O and their performance assessed in terms of MSiD and MUD. We note the excellent performance of the PBE + D2 in replicating the experimental density pressure profile as well as the relative compressibility.

Table 8

Computationally derived athermal bulk moduli of CaSO$_4$·2H$_2$O from this study and the literature compared to the experimental values. Bulk moduli from speed of sound measurements are Voigt-Reuss-Hill averages whereas the ones derived from isothermal compression series are adiabatic. N/S denotes that this information is not stated by these authors [D] deuterated isotopologue.

V_0 (Å^3)	K (GPa)	K'	T (K)	EOS	Method	Source
508.33(15)	43.80(1.38)	3.13(1.34)	0	BM-3EOS	DFT: PBE	This study
491.55(31)	44.18(3.15)	3.94 (3.15)	0	BM-3EOS	DFT: PBE + D2	This study
488.46(2)	46.49(18)	7.19(20)	0	BM-3EOS	DFT: PBE + TS	This study
482.28(8)	49.36(1.33)	2.81(1.28)	0	BM-3EOS	DFT: PBE + MBD	This study
482.68(13)	46.77(1.51)	5.50(1.58)	0	BM-3EOS	DFT: PBEsol	This study
475.53(16)	49.89(2.12)	4.92(2.17)	0	BM-3EOS	DFT: PBEsol+D2	This study
472.11(4)	50.48(52)	4.59(52)	0	BM-3EOS	DFT: PBEsol+TS	This study
N/S	30.9	N/S	0	BM-3EOS	DFT: revPBE	Li and Lee (2018)
N/S	35.5	N/S	0	BM-3EOS	DFT: revPBE + D2	Li and Lee (2018)
N/S	47.7	N/S	0	BM-3EOS	DFT: revPBE + DF1	Li and Lee (2018)
N/S	43.2	N/S	0	BM-3EOS	DFT: revPBE + DF2	Li and Lee (2018)
N/S	40.8	N/S	0	BM-3EOS	DFT: revPBE +vv10	Li and Lee (2018)
N/S	56.7	2.2	0	Murnaghan	DFT: PBE	Giacomazzi and Scandolo (2010)
494.29(50)	44(3)	3.3(3)	RT	BM-3EOS	DAC	Comodi et al. (2008)
494(3)[D]	45(1)	2.0(2)	RT	BM-3EOS	NPD + PE-Press	Stretton et al. (1997)
495.1(0.6)	52	N/S	RT	N/S	DAC	Huang et al. (2000)
493.56	39.43	8.22	RT	Murnaghan	Piston cylinder	Vaidya et al. (1973)

Table 9

Computed elastic constants of CaSO$_4$·2H$_2$O evaluated against the experimental coefficients as reported by Haussühl (1965). Temperatures are in K, all other values in GPa. Diff % gives the deviation of the preceding value from the corresponding experimental value in %.

C_{ij}	Exp	PBEsol	Diff %	PBE + D2	Diff %
C_{11}	72.5(3)	74.62(91)	2.9	66.79(64)	−7.9
C_{22}	62.7(3)	82.77(73)	32.0	81.89(0.52)	30.6
C_{33}	78.6(3)	90.39(1.22)	15.0	85.23(1.91)	8.4
C_{12}	24.2(2)	29.92(32)	23.6	28.52(22)	17.9
C_{13}	26.9(3)	29.45(52)	9.5	28.80(56)	7.1
C_{23}	41.0(4)	51.34(37)	25.2	50.35(35)	22.8
C_{44}	10.4(3)	19.48(96)	87.3	16.18(1.67)	55.6
C_{55}	26.4(3)	26.56(55)	0.6	26.67(0.2)	1.0
C_{66}	9.1(3)	19.02(96)	109.0	18.33(61)	101.4
C_{15}	−17.4(5)	−10.35(27)	−40.5	−10.41(25)	−40.2
C_{25}	3.1(2)	4.19(27)	35.2	4.57(0.33)	47.4
C_{35}	−7.0(2)	−0.76(22)	−89.1	−0.43(40)	−93.9
C_{46}	−1.6(1)	0.87(36)	−154.4	1.78(30)	−211.3
K	44.22	51.07	15.5	48.49	9.7
G	17.29	21.34	23.4	19.73	14.1
T	273	0		0	

coupling elastic constants arising for monoclinic symmetry complicate the relationship between the elastic constants and seismic wave velocities even in the direction of the principal axes. For this reason, we constrain ourselves to assessing the magnitude of the disagreement between experiment and DFT for each of the crystal directions.

Most recently, Winkler and Milman (2019) have assessed the accuracy of PBE + D2 and PBE + TS in modelling the elastic constants of various low-symmetry dispersion dominated organic compounds. The average differences of the elastic constants (coupling coeffients omitted) relative to the experimental reference data as obtained for gypsum in this study i.e., PBEsol (33.9%) and PBE + D2 (28.1%), compares very well with values of 30.5%, 37.0% and 40.3% as obtained by Winkler and Milman (2019) using the PBE + D2 approach for monoclinic melamine, tolane and aspirin, respectively.

PBEsol and PBE + D2 produce essentially identical seismic wave velocities overestimating the P and S wave velocities by 10.8 and 19.0% (PBEsol), and 9.1 and 15.6% (PBE + D2) yielding a substantial improvement in accuracy over the C$_6$H$_6$ and MgSO$_4$·7H$_2$O calculations. One reason for this might be the less pronounced temperature dependency of the stiffness, but it might also reflect a general trend of increasing accuracy as the degree of intermolecular force domination

diminishes. Moreover, the relatively large error on the elastic constants of gypsum mostly stems from the inaccurate modelling of the smaller elastic constants (Table 9), whereas the theory and experiment agree well for the larger constants. Naturally, the larger constants will dominate the seismic wave velocities resulting in smaller overall errors on this quantity. The differences with respect to the experimental reference appear to be too large in order to be used in a reference database for elastic constants. Next to the obvious interest from a planetary science perspective, an experimental investigation of the elastic properties of gypsum at low-temperatures would be interesting in order to cast light on the origin of apparent discrepancies between theory and experiment as the observed for C_{46} constant and the relative magnitude of the longitudinal elastic constants.

4. Summary, conclusions and outlook

The performance of seven combinations of xc functionals and dispersion corrections (i.e. PBE, PBE + D2, PBE + TS, PBE + MBD, PBEsol, PBEsol + D2, PBEsol + TS) in replicating (i) low-temperature unit-cell shapes and (ii) bulk moduli of CO$_2$, C$_6$H$_6$, MgSO$_4$·7H$_2$O and CaSO$_4$·2H$_2$O was assessed. The best performing approach and the PBEsol xc functional were then used to compute the full elastic tensor, which, again, was benchmarked against experimental reference data.

The unit-cell dimensions close to the ground state were best reproduced by the dispersion corrected PBE schemes (i.e. PBE + D2, PBE + TS and PBE + MBD). PBEsol and PBE systematically overestimated the cell volumes, whereas this property was underestimated by the dispersion corrected PBEsol functional for each of the title compounds with the exception of CO$_2$.

The dispersion corrected PBE functionals further revealed superior performance in modelling the experimental density profiles, especially when benchmarked against experimentally determined equations of state close to the athermal limit (i.e. CO$_2$ and MgSO$_4$·7H$_2$O). This trend is also reflected in the relative compressibility, unless benchmarked against room-temperature compression data (i.e. C$_6$H$_6$ and CaSO$_4$·2H$_2$O), where the non-dispersion corrected PBEsol and PBE xc functionals exceeded, albeit systematically overestimating the density.

The best performing functional for each of the title compounds yielded MUDs of merely 0.04 g/cm^3 (CO$_2$), 0.02 g/cm^3 (C$_6$H$_6$), 0.003 g/cm^3 (MgSO$_4$·7H$_2$O) and 0.013 g/cm^3 (CaSO$_4$·2H$_2$O). We conclude that the bulk compressibility is very well reproduced by dispersion corrected DFT and may find application in exploring the compressive parameters of candidate materials which could then be used in rheological models of
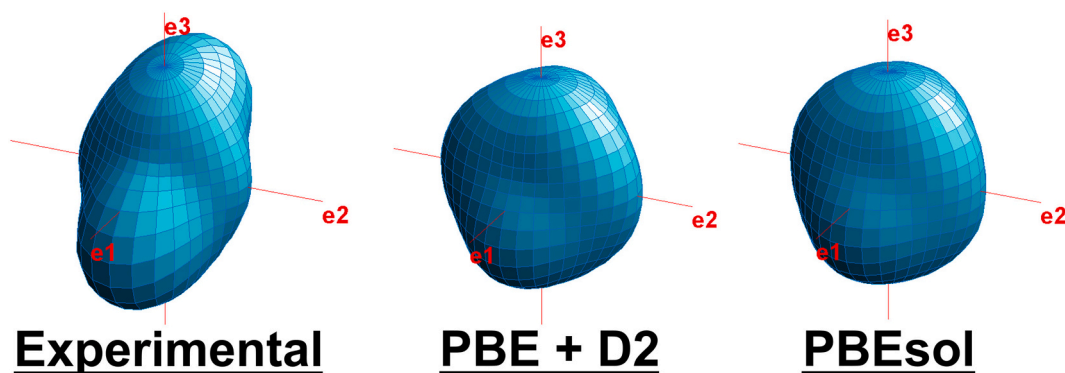
Fig. 11. Representation surfaces of the longitudinal effect of the elastic stiffness of $CaSO_4·2H_2O$. Neither of the DFT approaches reproduces the anisotropy well.

IOWs.

It is noteworthy, that the dispersion corrections yielded superior results for CO_2 and C_6H_6 as compared to hydrogen bonded $MgSO_4·7H_2O$ and $CaSO_4·2H_2O$. This is most evident when comparing $MgSO_4·7H_2O$ and C_6H_6; both exhibit orthorhombic symmetry and therefore require the same number of symmetry-independent lattice parameters and elastic constants to be modelled. Next to dispersion also electrostatic, induction, and exchange-repulsion components contribute to the intermolecular bonding energies (Jeziorski et al., 1994). It has been demonstrated for the water dimer, which may be considered as the prototypical hydrogen bonded system, that the electrostatic and exchange repulsion clearly are the dominating components of the intermolecular interaction (Hoja et al., 2014). As for liquid CO_2 (Yu et al., 2011) and C_6H_6 dimers (Sherrill, 2012) dispersion is the dominating component of intermolecular interaction. Thus, it was not unexpected, that we observed a better performance of dispersion corrections for the dispersion dominated as compared to the hydrogen bonded solids, where other forces are likely dominating the intermolecular interaction.

As for the evaluation of the accuracy of DFT derived elastic tensors the scarcity of experimental elastic constants determined at low temperature is a major limitation, hindering large scale benchmarking studies, which are crucial in order to detect and eventually address systematic failures of the computational exploration of elastic constants using established dispersion correction schemes. Out of the four title compounds, only for benzene and CO_2 could we find complete sets of elastic constants determined at low temperatures, with both compounds exhibiting a dramatic increase in stiffness upon cooling, reinforcing the need for accurate reference data as determined close to athermal conditions.

Lastly, we want to address the question raised in the introduction: Are the elastic constants computed by dispersion corrected DFT accurate enough to be used in a reference data base for the seismic exploration of the icy ocean worlds?

Despite the PBE + D2 approach having demonstrated experimental accuracy in modelling the elasticity of CO_2, clearly, we have to negate this question, based on MUDs of around 10 to 25% on the P and S wave velocities as obtained for the elastically more complex title compounds. Nevertheless, DFT may play a crucial role in determining the elastic properties of candidate materials by providing valid approximations of the elasticity, which can be used as starting values for resonant ultrasound investigations.

Regarding further potential gains in accuracy in the approximation of elastic constants from first principles we note that, Råsander and Moram (2015) observed that the GGA-type PBEsol xc functional surpasses the two hybrid functionals, PBE0 and HSE in performance, thus the use of the computationally more expensive hybrid functionals does not appear to increase the accuracy relative to the GGA-type functionals used in this study. As for the total energy method to computationally derive elastic constants, Caro et al. (2012) note that the stress-strain approach, yields identical results at lower computational cost and should therefore be chosen over the total energy method. Nevertheless, new methods for the computational approximation of elastic constants are emerging. In particular, elastic constants derived from first-principles lattice dynamic calculations, as reported by Wehinger et al. (2016), yielded excellent agreement with experimentally determined elastic constants for the mineral bridgmanite, surpassing in perfomance the widely used stress-strain approach following Page and Saxe (2002), which was applied in this study. We conclude that the lattice dynamics approach might open the possibility to derive more accurate elastic constants and consequently seismic wave velocities from first principles and should therefore be included in future benchmarking studies of icy satellite candidate materials.

A reference data-base of icy satellite candidate materials is still in its infancy and – due to the complex experiments involved – a rather ambitious endeavour, however, the prospect of casting light on internal structure and mantle dynamics of icy ocean worlds to eventually set constraints upon their habitability clearly makes this endeavour worthwhile.

Declaration of Competing Interest

The authors declare that they have no known competing financial interests or personal relationships that could have appeared to influence the work reported in this paper.

Appendix A. Supplementary data

Supplementary data to this article can be found online at https://doi.org/10.1016/j.icarus.2021.114611.

References

Alexandrov, K.S., Rhyzhova, T.V., Rostuntseva, A.I., 1963. Elastic properties of some sulfate heptahydrate crystals. Sov. Phys. Crystallogr. 7, 753–755.

Al-Saidi, W.A., Voora, V.K., Jordan, K.D., 2012. An assessment of the vdW-TS method for extended systems. J. Chem. Theory Comput. 8 (4), 1503–1513. https://doi.org/10.1021/ct200618b.

Ambrosetti, A., Reilly, A.M., DiStasio, R.A., Tkatchenko, A., 2014. Long-range correlation energy calculated from coupled atomic response functions. J. Chem. Phys. 140 (18), 18A508. https://doi.org/10.1063/1.4865104.

Arbeck, D., Haussühl, E., Bayarjagal, L., Winkler, B., Paulsen, N., Haussühl, S., Milman, V., 2010. Piezoelastic properties of retgersite determined by ultrasonic measurements. Eur. Phys. J. B 73, 167–175.

Arbeck, D., Haussühl, E., Winkler, B., Paulsen, N., Haussuhl, S., Milman, V., Gale, J., 2012. Elastic stiffness coefficients of thenardite and their pressure and temperature dependence. Z Kristallogr. 227, 503. https://doi.org/10.1524/zkri.2012.1476.

Birch, F., 1947. Finite elastic strain of cubic crystals. Phys. Rev. 71 (11), 809–824. https://doi.org/10.1103/PhysRev.71.809.

Bland, M.T., Singer, K.N., McKinnon, W.B., Schenk, P.M., 2012. Enceladus' extreme heat flux as revealed by its relaxed craters. Geophys. Res. Lett. 39, L17204 https://doi.org/10.1029/2012GL052736.

Bonev, S.A., Gygi, F., Ogitsu, T., Galli, G., 2003. High-pressure molecular phases of solid carbon dioxide. Phys. Rev. Lett. 91 (6), 65501. https://doi.org/10.1103/PhysRevLett.91.065501.

Bridgman, P.W., 1914. Change of phase under pressure. I. The phase diagram of eleven substances with especial reference to the melting curve. Phys. Rev. 3 (3), 153–203. https://doi.org/10.1103/PhysRev.3.153.

Bridgman, P.W., 1949. Linear compressions to 30.000 Kg/Cm^2, including relatively incompressible subsances. P. Am. Acad. Arts. Sci. 77 (6), 189–234. https://doi.org/10.2307/20023541.

Brown, M.E., Hand, K.P., 2013. Salts and radiation products on the surface of Europa. Astron. J. 145 (4), 110. https://doi.org/10.1088/0004-6256/145/4/110.

Burke, K., 2012. Perspective on density functional theory. J. Chem. Phys. 136, 150901. https://doi.org/10.1063/1.4704546.

Byrne, S., Ingersoll, A.P., 2003. A sublimation model for Martian south polar ice features. Science 299 (5609), 1051–1053. https://doi.org/10.1126/science.1080148.

Caldeweyher, E., Bannwarth, C., Grimme, S., 2017. Extension of the D3 dispersion coefficient model. J. Chem. Phys. 147 (3), 34112. https://doi.org/10.1063/1.4993215.

Calzetti, D., 2011. Polycyclic aromatic hydrocarbons as star formation rate indicators. EAS Publ. Ser. 46, 133–141. https://doi.org/10.1051/eas/1146014.

Caro, M., Schulz, S., O'Reilly, E., 2012. Comparison of stress and total energy methods for calculation of elastic properties of semiconductors. J. Phys. Condens. Mat. 25, 025803. https://doi.org/10.1088/0953-8984/25/2/025803.

Cernicharo, J., Heras, A.M., Tielens, A.G.G.M., Pardo, J.R., Herpin, F., Guélin, M., Waters, L.B.F.M., 2001. Infrared space observatory's discovery of C_4H_2, C_6H_2, and benzene in CRL 618. Astrophys. J. 546 (2), L123–L126. https://doi.org/10.1086/318871.

Clark, S., Segall, M., Pickard, C., Hasnip, P., Probert, M., Refson, K., Payne, M., 2005. First principles methods using CASTEP. Z. Kristallogr. 220 https://doi.org/10.1524/zkri.220.5.567.65075.

Comodi, P., Nazzareni, S., Francesco, P., Speziale, S., 2008. High-pressure behavior of gypsum: a single-crystal X-ray study. Am. Mineral. 93, 1530–1537. https://doi.org/10.2138/am.2008.2917.

Comodi, P., Stagno, V., Zucchini, A., Fei, Y., Prakapenka, V., 2017. The compression behavior of blödite at low and high temperature up to ~10GPa: implications for the stability of hydrous sulfates on icy planetary bodies. Icarus 285, 137–144. https://doi.org/10.1016/j.icarus.2016.11.032.

Corliss, J.B., Dymond, J., Gordon, L.I., Edmond, J.M., von Herzen, R.P., Ballard, R.D., Green, K., Williams, D., Bainbridge, A., Crane, K., van Andel, T.H., 1979. Submarine thermal springs on the Galápagos rift. Science 203 (4385), 1073–1083. https://doi.org/10.1126/science.203.4385.1073.

Cornelius, S., Castagna, J., 2017. Variation in salt-body interval velocities in the deep-water Gulf of Mexico: Keathley Canyon and Walker Ridge areas. Interpretation. 6, 1–40. https://doi.org/10.1190/int-2017-0069.1.

Cruikshank, D.P., et al., 2010. Carbon dioxide on the satellites of Saturn: results from the Cassini VIMS investigation and revisions to the VIMS wavelength scale. Icarus. 206 (2), 561–572. https://doi.org/10.1016/j.icarus.2009.07.012.

Csonka, G.I., Ruzsinszky, A., Perdew, J.P., Grimme, S., 2008. Improved description of stereoelectronic effects in hydrocarbons using semilocal density functional theory. J. Chem. Theory Comput. 4 (6), 888–891. https://doi.org/10.1021/ct800003n.

Cybulski, S.M., Lytle, M.L., 2007. The origin of deficiency of the supermolecule second-order Møller-Plesset approach for evaluating interaction energies. J. Chem. Phys. 127 (14), 141102. https://doi.org/10.1063/1.2795693.

D'Hendecourt, L.B., Jourdain de Muizon, M., 1989. The discovery of interstellar carbon dioxide. Astron. Astrophys. 223, L5–L8.

Drilleau, M., Samuel, H., Rivoldini, A., Panning, M., Lognonné, P., 2021. Bayesian inversion of the Martian structure using geodynamic constraints. Geophys. J. Int. 226 (3), 1615–1644. https://doi.org/10.1093/gji/ggab105.

Dubrovinsky, L., Dubrovinskaia, N., 2007. Melting of ice VII and new high-pressure, high-temperature amorphous ice. Special Paper of the Geological Society of America. 421, 105–113. https://doi.org/10.1130/2007.2421(07).

Earle, A., Binzel, R., Young, L., Stern, S., Ennico, K., Grundy, W., Olkin, C., Weaver, H. A., 2017. Long-term surface temperature modeling of Pluto. Icarus. 287, 37–46. https://doi.org/10.1016/j.icarus.2016.09.036.

Eisenschitz, R., London, F., 1930. Über das Verhältnis der van der Waalsschen Kräfte zu den homöopolaren Bindungskräften. Z. Phys. 60 (7), 491–527. https://doi.org/10.1007/BF01341258.

Ende, M., Kirkkala, T., Loitzenbauer, M., Talla, D., Wildner, M., Miletich, R., 2020. High-pressure behavior of nickel sulfate monohydrate: isothermal compressibility, structural polymorphism, and transition pathway. Inorg. Chem. 59 (9), 6255–6266. https://doi.org/10.1021/acs.inorgchem.0c00370.

Ferche, J., 1891. Ueber einige physikalische Eigenschaften des Benzols. Ann. Phys. 280, 265–287.

Figuière, P., Fuchs, A.H., Ghelfenstein, M., Szwarc, H., 1978. Pressure-volume-temperature relations for crystalline benzene. J. Phys. Chem. Solids 39 (1), 19–24. https://doi.org/10.1016/0022-3697(78)90193-2.

Fischer, M., Angel, R.J., 2017. Accurate structures and energetics of neutral-framework zeotypes from dispersion-corrected DFT calculations. J. Chem. Phys. 146 (17), 174111. https://doi.org/10.1063/1.4981528.

Formalik, F., Fischer, M., Rogacka, J., Firlej, L., Kuchta, B., 2018. Benchmarking of GGA density functionals for modeling structures of nanoporous, rigid and flexible MOFs. J. Chem. Phys. 149 (6), 64110. https://doi.org/10.1063/1.5030493.

Fortes, A.D., Capelli, S.C., 2018. H/D isotope effect on the molar volume and thermal expansion of benzene. Phys. Chem. Chem. Phys. 20 (24), 16736–16742. https://doi.org/10.1039/C8CP02500B.

Fortes, A.D., Choukroun, M., 2010. Phase behaviour of ices and hydrates. Space Sci. Rev. 153 (1), 185–218. https://doi.org/10.1007/s11214-010-9633-3.

Fortes, A.D., Wood, I.G., Alfredsson, M., Vocadlo, L., Knight, K., 2006. The thermoelastic properties of $MgSO_4 \cdot 7D_2O$ (epsomite) from powder neutron diffraction and ab initio calculation. Eur. J. Mineral. 18 (4), 449–462. https://doi.org/10.1127/0935-1221/2006/0018-0449.

Fortes, A.D., Knight, K.S., Wood, I.G., 2017. Structure, thermal expansion and incompressibility of $MgSO_4 \cdot 9H_2O$, its relationship to meridianiite ($MgSO_4 \cdot 11H_2O$) and possible natural occurrences. Acta Crystallogr. B. 73 (1), 47–64. https://doi.org/10.1107/S2052520616018266.

Giacomazzi, L., Scandolo, S., 2010. Gypsum under pressure: a first-principles study. Phys. Rev. B 81 (6), 64103. https://doi.org/10.1103/PhysRevB.81.064103.

Giordano, V.M., Datchi, F., Gorelli, F.A., Bini, R., 2010. Equation of state and anharmonicity of carbon dioxide phase I up to 12 GPa and 800 K. J. Chem. Phys. 133 (14), 144501. https://doi.org/10.1063/1.3495951.

Gonzalez-Platas, J., Alvaro, M., Nestola, F., Angel, R., 2016. EosFit7-GUI: a new graphical user interface for equation of state calculations, analyses and teaching. J. Appl. Crystallogr. 49 (4), 1377–1382. https://doi.org/10.1107/S1600576716008050.

Gracia, L., Marqués, M., Beltrán, A., Pendás, A.M., Recio, J.M., 2004. Bonding and compressibility in molecular and polymeric phases of solid CO2. J. Phys. - Condens. Mat. 16 (14), S1263–S1270. https://doi.org/10.1088/0953-8984/16/14/038.

Grimme, S., 2006. Semiempirical GGA-type density functional constructed with a long-range dispersion correction. J. Comput. Chem. 27 (15), 1787–1799. https://doi.org/10.1002/jcc.20495.

Grimme, S., Antony, J., Ehrlich, S., Krieg, H., 2010. A consistent and accurate ab initio parametrization of density functional dispersion correction (DFT-D) for the 94 elements H-Pu. J. Chem. Phys. 132 (15), 154104. https://doi.org/10.1063/1.3382344.

Grimme, S., Hansen, A., Brandenburg, J.G., Bannwarth, C., 2016. Dispersion-corrected mean-field electronic structure methods. Chem. Rev. 116 (9), 5105–5154. https://doi.org/10.1021/acs.chemrev.5b00533.

Gromnitskaya, E., Yagafarov, O., Lyapin, A., Brazhkin, V., Wood, I.G., Tucker, M., Fortes, A.D., 2013. The high-pressure phase diagram of synthetic epsomite ($MgSO_4 \cdot 7H_2O$ and $MgSO_4 \cdot 7D_2O$) from ultrasonic and neutron powder diffraction measurements. Phys. Chem. Min. 40 (3), 271–285. https://doi.org/10.1007/s00269-013-0567-7.

Grundy, W.M., Young, L.A., Spencer, J.R., Johnson, R.E., Young, E.F., Buie, M.W., 2006. Distributions of H_2O and CO_2 ices on Ariel, Umbriel, Titania, and Oberon from IRTF/SpeX observations. Icarus 184 (2), 543–555. https://doi.org/10.1016/j.icarus.2006.04.016.

Haussühl, S., 1965. Elastische und thermoelastische Eigenschaften von $CaSO_4$ $2H_2O$ (Gips). Z Kristallogr. 122 (3–4), 311–314. https://doi.org/10.1524/zkri.1965.122.3-4.311.

Heseltine, J.C.W., Elliott, D.W., Wilson, O.B., 1964. Elastic constants of single crystal benzene. J. Chem. Phys. 40, 2584–2587. https://doi.org/10.1063/1.1725566.

Heydweiller, A., 1897. Die Erstarrungscontraction für einige organische Verbindungen. Ann. Phys. 297 (7), 527–540. https://doi.org/10.1002/andp.18972970707.

Hohenberg, P., Kohn, W., 1964. Inhomogeneous electron gas. Phys. Rev. 136 (3B), B864–B871. https://doi.org/10.1103/PhysRev.136.B864.

Hoja, J., Sax, A.F., Szalewicz, K., 2014. Is electrostatics sufficient to describe hydrogen-bonding interactions? Chem. Eur. J. 20, 2292–2300. https://doi.org/10.1002/chem.201303528.

Huang, E., Xu, J.-A., Lin, J.-F., Hu, J.-Z., 2000. Pressure-induced phase transitions in gypsum. High Pressure Res. 17 (1), 57–75. https://doi.org/10.1080/08957950008200306.

Jaeken, J., Cottenier, S., 2016. Solving the Christoffel equation: phase and group velocities. Comput. Phys. Commun. 207, 445–451. https://doi.org/10.1016/j.cpc.2016.06.014.

Jeziorski, B., Moszynski, R., Szalewicz, K., 1994. Perturbation theory approach to intermolecular potential energy surfaces of van der Waals complexes. Chem. Rev. 94 (7), 1887–1930. https://doi.org/10.1021/cr00031a008.

Johnson, R.E., 1996. Sputtering of ices in the outer solar system. Rev. Mod. Phys. 68 (1), 305–312. https://doi.org/10.1103/RevModPhys.68.305.

Jones, I., Davison, I., 2014. Seismic imaging in and around salt bodies. Interpretation 2, SL1–SL20. https://doi.org/10.1190/INT-2014-0033.1.

Kaminski, W., 2014. WinTensor (1.5). http://cad4.cpac.washington.edu/WinTensorhome/WinTensor.htm.

Kargel, J.S., 1991. Brine volcanism and the interior structures of asteroids and icy satellites. Icarus 94 (2), 368–390. https://doi.org/10.1016/0019-1035(91)90235-L.

Kargel, J., Kaye, J., Head, J., Marion, G., Sassen, R., Crowley, J., Prieto-Ballesteros, O., Grant, S., Hogenboom, D., 2000. Europa's crust and ocean: origin, composition, and the prospects for life. Icarus 148, 226–265. https://doi.org/10.1006/icar.2000.6471.

Katrusiak, A., Podsiadło, M., Budzianowski, A., 2010. Association CH···π and no van der Waals contacts at the lowest limits of crystalline benzene I and II stability regions. Crys. Growth Des. 10 (8), 3461–3465. https://doi.org/10.1021/cg1002594.

Khalkhali, M., Ma, X., Zhang, H., Liu, Q., 2019. Bulk and surface properties of gypsum: a comparison between classical force fields and dispersion-corrected DFT calculations. Comput. Mater. Sci. 164, 8–16. https://doi.org/10.1016/j.commatsci.2019.03.045.

Knapmeyer, M., Fischer, H.-H., Knollenberg, J., Seidensticker, K., Thiel, K., Arnold, W., Faber, C., Möhlmann, D., 2017. Structure and elastic parameters of the near surface of Abydos site on Comet 67P/Churyumov-Gerasimenko, as obtained by SESAME/CASSE listening to the MUPUS insertion phase. Icarus. 310, 165–193. https://doi.org/10.1016/j.icarus.2017.12.002.

Kohn, W., Sham, L.J., 1965. Self-consistent equations including exchange and correlation effects. Phys. Rev. 140 (4A), A1133–A1138. https://doi.org/10.1103/PhysRev.140.A1133.

Lehmann, I., 1936. P'. Publications Du Bureau Central Seismologique International, Série A. Travaux Scientifique 14, 87–115.

Li, T.-L., Lee, P.-L., 2018. Structural evolution of gypsum under high pressure: single-crystal X-ray experiments revisited. Phys. Chem. Min. 45 (9), 895–906. https://doi.org/10.1007/s00269-018-0971-0.

Li, J., Sode, O., Voth, G.A., Hirata, S., 2013. A solid–solid phase transition in carbon dioxide at high pressures and intermediate temperatures. Nat. Commun. 4 (1), 2647. https://doi.org/10.1038/ncomms3647.

Litasov, K.D., Inerbaev, T.M., Abuova, F.U., Chanyshev, A.D., Dauletbekova, A.K., Akilbekov, A.T., 2019. High-pressure elastic properties of polycyclic aromatic hydrocarbons obtained by first-principles calculations. Geochem. Int. 57 (5), 499–508. https://doi.org/10.1134/S0016702919050069.

Liu, L., 1984. Compression and phase behavior of solid CO_2 to half a megabar. Earth Planet. Sci. Lett. 71 (1), 104–110. https://doi.org/10.1016/0012-821X(84)90056-6.

Lorenz, R.D., Turtle, E.P., Barnes, J.W., Trainer, M.G., Adams, D.S., Hibbard, K., Sheldon, C.Z., Zacny, K., Peplowski, P.N., Lawrence, D.J., Ravine, M.A., McGee, T.G., Sotzen, K., MacKenzie, S.M., Langelaan, J., Schmitz, S., Wolfarth, L.S., Bedini, P.D., 2018. Dragonfly: A rotorcraft lander concept for scientific exploration at titan. Johns Hopkins APL Technical Digest (Appl. Physics Lab.) 34, 374–387.

Malaska, M.J., Hodyss, R., 2014. Dissolution of benzene, naphthalene, and biphenyl in a simulated Titan lake. Icarus 242, 74–81. https://doi.org/10.1016/j.icarus.2014.07.022.

Manzhelii, V.G., Tolkachev, A.M., Bagatskii, M.I., Voitovich, E.I., 1971. Thermal expansion, heat capacity, and compressibility of solid CO_2. Phys. Status. Solidi. B. 44 (1), 39–49. https://doi.org/10.1002/pssb.2220440104.

Mattsson, A., Armiento, R., Schultz, P., Mattsson, T., 2006. Nonequivalence of the generalized gradient approximations PBE and PW91. Phys. Rev. B 73, 195123. https://doi.org/10.1103/PhysRevB.73.195123.

Maynard-Casely, H.E., Hodyss, R., Cable, M.L., Vu, T.H., Rahm, M., 2016. A co-crystal between benzene and ethane: a potential evaporite material for Saturn's moon titan. IUCrJ 3 (3), 192–199. https://doi.org/10.1107/S2052252516002815.

McCord, T.B., Hansen, G.B., Clark, R.N., Martin, P.D., Hibbitts, C.A., Fanale, F.P., Granahan, J.C., Segura, M., Matson, D.L., Johnson, T.V., Carlson, R.W., Smythe, W.D., Danielson, G.E., 1998a. Non-water-ice constituents in the surface material of the icy Galilean satellites from the Galileo near-infrared mapping spectrometer investigation. J. Geophys. Res. Planet. 103 (E4), 8603–8626. https://doi.org/10.1029/98JE00788.

McCord, T.B., Hansen, G.B., Fanale, F.P., Carlson, R.W., Matson, D.L., Johnson, T.V., Smythe, W.D., Crowley, J.K., Martin, P.D., Ocampo, A., Hibbitts, C.A., Granahan, J.C., 1998b. Salts on Europa's Surface Detected by Galileo's Near Infrared Mapping Spectrometer. Science 280 (5367), 1242–1245. https://doi.org/10.1126/science.280.5367.1242.

McCord, Thomas B., Hansen, G.B., Hibbitts, C.A., 2001. Hydrated salt minerals on Ganymede's surface: evidence of an ocean below. Science 292 (5521), 1523. https://doi.org/10.1126/science.1059916.

Meusburger, J.M., Ende, M., Talla, D., Wildner, M., Miletich, R., 2019. Transformation mechanism of the pressure-induced C2/c-to-P1̄ transition in ferrous sulfate monohydrate single crystals. J. Solid State Chem. 277, 240–252. https://doi.org/10.1016/j.jssc.2019.06.004.

Meusburger, Johannes M., Ende, M., Matzinger, P., Talla, D., Miletich, R., Wildner, M., 2020. Polymorphism of Mg-sulfate monohydrate kieserite under pressure and its occurrence on giant icy jovian satellites. Icarus 336, 113459. https://doi.org/10.1016/j.icarus.2019.113459.

Meyer, J., 1910. Die Schmelzwaerme der Eissigsaeure, des Benzols und des Nitrobenzols. Z. Phys. Chem. 72, 225–254.

Minissale, M., Congiu, E., Manicò, G., Pirronello, A., Dulieu, F., 2013. CO_2 formation on interstellar dust grains: a detailed study of the barrier of the CO+O channel. Astron. Astrophys. 559, A49 https://doi.org/10.1051/0004-6361/201321453.

Mohorovičić, A., 1910. Potres od 8. X. 1909 (Earthquake of 8 October 1909). Godišnje izvješće Zagrebačkog meteorološkog opservatorija za godinu 1909 (in Croatian).

Monkhorst, H.J., Pack, J.D., 1976. Special points for Brillouin-zone integrations. Phys. Rev. B 13 (12), 5188–5192. https://doi.org/10.1103/PhysRevB.13.5188.

Monteux, J., Golabek, G.J., Rubie, D.C., Tobie, G., Young, E.D., 2018. Water and the interior structure of terrestrial planets and icy bodies. Space Sci. Rev. 214 (1), 39. https://doi.org/10.1007/s11214-018-0473-x.

Mueller, S., McKinnon, W.B., 1988. Three-layered models of Ganymede and Callisto: compositions, structures, and aspects of evolution. Icarus 76 (3), 437–464. https://doi.org/10.1016/0019-1035(88)90014-0.

Mullie, F., Reisse, J., 1987. Organic matter in carbonaceous chondrites. In: Organic Geo- and Cosmochemistry, pp. 83–117.

Neumann, F.E., 1885. Vorlesungen über die Theorie der Elasticität der festen Körper und des Lichtäthers, gehalten an der Universität Königsberg. B. G, Teubner Leipzig. https://catalog.hathitrust.org/Record/008871677.

Nimmo, F., 2018. Icy satellites: interior structure, dynamics, and evolution. In: Oxford Research Encyclopedia of Planetary Science. https://doi.org/10.1093/acrefore/9780190647926.013.29.

Olinger, B., 1982. The compression of solid CO_2 at 296 K to 10 GPa. J. Chem. Phys. 77 (12), 6255–6258. https://doi.org/10.1063/1.443828.

Page, Y., Saxe, P., 2002. Symmetry-general least-squares extraction of elastic data for strained materials from ab initio calculations of stress. Phys. Rev. B 65, 104104. https://doi.org/10.1103/PhysRevB.65.104104.

Pappalardo, R.T., et al., 2013. Science potential from a Europa Lander. Astrobiology 13 (8), 740–773. https://doi.org/10.1089/ast.2013.1003.

Peeters, E., 2011. Astronomical observations of the PAH emission bands. EAS Publ. Ser. 46, 13–27. https://doi.org/10.1051/eas/1146002.

Perdew, J.P., Burke, K., Ernzerhof, M., 1996. Generalized gradient approximation made simple. Phys. Rev. Lett. 18 (77), 3865–3868.

Perdew, J.P., Ruzsinszky, A., Csonka, G.I., Vydrov, O.A., Scuseria, G.E., Constantin, L.A., Zhou, X., Burke, K., 2008. Restoring the density-gradient expansion for exchange in solids and surfaces. Phys. Rev. Lett. 100 (13), 136406. https://doi.org/10.1103/PhysRevLett.100.136406.

Pfrommer, B.G., Cote, M., Louie, S.G., Cohen, M.L., 1997. Relaxation of crystals with the quasi-Newton method. J. Comput. Phys. 131 (1), 233–240. https://doi.org/10.1006/jcph.1996.5612.

Powell, B.M., Dolling, G., Piseri, L., Martel, P., 1972. Normal modes of solid carbon dioxide. In: Neutron Inelastic Scattering Proceedings of a Symposium on Neutron Inelastic Scattering - Grenoble, 2, p. 207.

Prentice, A.J.R., 1993. The origin and composition of Pluto and Charon: chemically uniform models. Pub. Astron. Soc. Aust. 10 (3), 189–195. https://doi.org/10.1017/S1323358000025649.

Prentice, A.J.R., 1999. Origin, bulk chemical composition and physical structure of the Galilean satellites of Jupiter: a post-Galileo analysis. Earth Moon Planet. 87, 11–55. https://doi.org/10.1023/A:1010692812892.

Råsander, M., Moram, M., 2015. On the accuracy of commonly used density functional approximations in determining the elastic constants of insulators and semiconductors. J. Chem. Phys. 143, 144104 https://doi.org/10.1063/1.4932334.

Ringwood, A.E., 1969. Composition and evolution of the upper mantle. The Earth's Crust and Upper Mantle. 1–17. https://doi.org/10.1029/GM013p0001.

Schofield, P., Knight, K., Stretton, I., 1996. Thermal expansion of gypsum investigated by neutron powder diffraction. Am. Mineral. 81, 847–851. https://doi.org/10.2138/am-1996-7-807.

Sherrill, C., 2012. Energy component analysis of π interactions. Accounts Chem. Res. 46, 1020–1028. https://doi.org/10.1021/ar3001124.

Simon, A., Peters, K., 1980. Single-crystal refinement of the structure of carbon dioxide. Acta Cryst. B. 36 (11), 2750–2751. https://doi.org/10.1107/S0567740880009879.

Stähler, S.C., et al., 2021. Seismic detection of the Martian Core by InSight. In: 52nd Lunar and Planetary Science Conference, Abstract Nr. 1545. Lunar and Planetary Institute.

Stähler, S.C., Panning, M.P., Vance, S.D., Lorenz, R.D., van Driel, M., Nissen-Meyer, T., Kedar, S., 2018. Seismic wave propagation in Icy Ocean worlds. J. Geophys. Res. Planet. 123 (1), 206–232. https://doi.org/10.1002/2017JE005338.

Stephenson, J., Tkalčić, H., Sambridge, M., 2021. Evidence for the innermost inner core: Robust parameter search for radially varying anisotropy using the neighborhood algorithm. J. Geophys. Res. - Sol. Earth 126. https://doi.org/10.1029/2020JB020545 e2020JB020545.

Stevenson, R., 1957. Compressions and solid phases of CO_2, CS_2, COS, O_2, and CO. J. Chem. Phys. 27 (3), 673–675. https://doi.org/10.1063/1.1743812.

Stojanoff, V., Missell, F.P., 1982. Temperature dependence of the elastic constants of α-$NiSO_4$·$6H_2O$. J. Chem. Phys. 77 (2), 939–942. https://doi.org/10.1063/1.443869.

Stretton, I.C., Schofield, P.F., Hull, S., Knight, K.S., 1997. The static compressibility of gypsum. Geophys. Res. Lett. 24 (10), 1267–1270. https://doi.org/10.1029/97GL01066.

Sundara Rao, R.V.G., 1950. Elastic constants of the heptahydrates of magnesium and zinc sulphate. Proc. Indian Acad. Sci. A. 31, 365–370.

Tammann, G., 1903. Kristallisieren und Schmelzen. J. A. Barth, Leipzig, p. 1903.

Taubner, R.-S., et al., 2018. Biological methane production under putative Enceladus-like conditions. Nat. Commun. 9 (1), 748. https://doi.org/10.1038/s41467-018-02876-y.

Tkatchenko, A., Scheffler, M., 2009. Accurate molecular Van Der Waals interactions from ground-state electron density and free-atom reference data. Phys. Rev. Lett. 102 (7), 73005. https://doi.org/10.1103/PhysRevLett.102.073005.

Vaidya, S.N., Bailey, S., Pasternack, T., Kennedy, G.C., 1973. Compressibility of fifteen minerals to 45 kilobars. J. Geophys. Res. 78 (29), 6893–6898. https://doi.org/10.1029/JB078i029p06893.

Vanderbilt, D., 1990. Soft self-consistent pseudopotentials in a generalized eigenvalue formalism. Phys. Rev. B 41 (11), 7892–7895. https://doi.org/10.1103/PhysRevB.41.7892.

Vinatier, S., Schmitt, B., Bézard, B., Rannou, P., Dauphin, C., Kok, R., Jennings, D.E., Flasar, F., 2017. Study of Titan's fall southern stratospheric polar cloud composition with Cassini/CIRS: detection of benzene ice. Icarus 310, 89–104. https://doi.org/10.1016/j.icarus.2017.12.040.

Voronkov, A.A., 1958. The piezoelectric, elastic and dielectric properties of crystals of $MgSO_4$. $7H_2O$. Sov. Phys. –Crystallogr. 3, 722–725.

Vuitton, V., Yelle, R.V., Cui, J., 2008. Formation and distribution of benzene on titan. J. Geophys. Res. 113, E05007 https://doi.org/10.1029/2007JE002997.

Waite, J.H., Glein, C.R., Perryman, R.S., Teolis, B.D., Magee, B.A., Miller, G., Grimes, J., Perry, M.E., Miller, K.E., Bouquet, A., Lunine, J.I., Brockwell, T., Bolton, S.J., 2017. Cassini finds molecular hydrogen in the Enceladus plume: evidence for hydrothermal processes. Science 356 (6334), 155–159. https://doi.org/10.1126/science.aai8703.

Walmsley, S.H., 1968. Excitons, magnons, phonons, molecular crystals. In: Zahlan, A.B. (Ed.), Proceedings of International Symposium. Cambridge University Press, p. 83. Edited by.

Wang, A., Jolliff, B.L., Liu, Y., Connor, K., 2016. Setting constraints on the nature and origin of the two major hydrous sulfates on Mars: monohydrated and polyhydrated sulfates. J. Geophys. Res. Planet. 121 (4), 678–694. https://doi.org/10.1002/2015JE004889.

Wang, W., Fortes, A.D., Dobson, D.P., Howard, C.M., Bowles, J., Hughes, N.J., Wood, I. G., 2018. Investigation of high-pressure planetary ices by cryo-recovery. II. High-pressure apparatus, examples and a new high-pressure phase of $MgSO_4$. $5H_2O$. J. Appl. Crystallogr. 51 (3), 692–705. https://doi.org/10.1107/S1600576718003977.

Wehinger, B., Bosak, A., Nazzareni, S., Antonangeli, D., Mirone, A., Chaplot, S., Mittal, R., Ohtani, E., Shatskiy, A., Saxena, S., Ghose, S., Krisch, M., 2016. Dynamical and elastic properties of $MgSiO_3$ perovskite (bridgmanite). Geophys. Res. Lett. 43, 2568–2575. https://doi.org/10.1002/2016GL067970.

Winkler, B., Milman, V., 2014. Density functional theory based calculations for high pressure research. Z Kristallogr. - Cryst. Mater. 229 (2), 112–122. https://doi.org/10.1515/zkri-2013-1650.

Winkler, B., Milman, V., 2019. Accuracy of dispersion-corrected DFT calculations of elastic tensors of organic molecular structures. Cryst. Growth Des. 20, 206–213. https://doi.org/10.1021/acs.cgd.9b01017.

Yoo, C.S., Cynn, H., Gygi, F., Galli, G., Iota, V., Nicol, M., Carlson, S., Häusermann, D., Mailhiot, C., 1999. Crystal structure of carbon dioxide at high pressure: "Superhard" polymeric carbon dioxide. Phys. Rev. Lett. 83 (26), 5527–5530. https://doi.org/10.1103/PhysRevLett.83.5527.

Yu, K., McDaniel, J., Schmidt, J., 2011. Physically motivated, robust, ab initio force fields for CO_2 and N_2. J. Phys. Chem. B 115, 10054–10063. https://doi.org/10.1021/jp204563n.

4. Low-temperature crystallography and vibrational properties of rozenite (FeSO$_4$·4H$_2$O), a candidate mineral component of the polyhydrated sulfate deposits on Mars

This chapter explores the low-temperature stability and vibrational properties of rozenite, a promising candidate constituent of the polyhydrated sulfate deposits on Mars.

In addition, it presents a combined experimental (XRD and Raman spectroscopy) and theoretical (Density functional theory) workflow to produce accurate reference Raman spectra. This workflow appears to be ideally suited to construct a reliable Raman spectroscopic database for planetary exploration. Such a database is critical to shed light on the geological past and identify resources for the future colonization of planetary bodies throughout the solar system.

Declaration: The contents of this chapter were accepted in the journal *American Mineralogist* (Meusburger et al., 2022), however, still awaits formatting by the journal and publication. Therefore, this chapter is presented in the original format of this thesis.

Low-temperature crystallography and vibrational properties of rozenite ($FeSO_4 \cdot 4H_2O$), a candidate mineral component of the polyhydrated sulfate deposits on Mars

Johannes M. Meusburger[1,2,3], Karen A. Hudson-Edwards[1], Chiu C. Tang[2], Eamonn T. Connolly[2], Rich A. Crane[1], A. Dominic Fortes[3*]

[1] Camborne School of Mines and Environment and Sustainability Institute, Tremough Campus, University of Exeter, Penryn TR10 9EZ, UK
[2] Diamond Light Source, Harwell Science and Innovation Campus, Fermi Avenue, Didcot OX11 0DE, UK
[3] ISIS Neutron and Muon Source, STFC Rutherford Appleton Laboratory, Harwell Science and Innovation Campus, Chilton, Didcot, Oxfordshire, OX11 0QX, UK
*corresponding author

Abstract:

Rozenite ($FeSO_4 \cdot 4H_2O$) is a candidate mineral component of the polyhydrated sulfate deposits on the surface and in the subsurface of Mars. In order to better understand its behavior at temperature conditions prevailing on the Martian surface, and aid its identification in ongoing and future Rover missions, we have carried out a combined experimental and computational study of the mineral's structure and properties. We present neutron powder diffraction data at temperatures ranging from 21 – 290 K, room temperature synchrotron X-ray data and Raman spectra. Moreover, first-principles calculations of the vibrational properties of rozenite were carried out to aid the interpretation of the Raman spectrum. We find, in contrast to a recent Raman spectroscopic study, that there are no phase transitions between 21 and 290 K. We confirm the heavy atom structure reported in the literature (space group $P2_1/n$) to be correct, and present, for the first time, an unconstrained determination of the hydrogen atom positions by means of high-resolution neutron powder diffraction, and report the complete crystal structure at 290 K and 21 K. The anisotropy of the thermal expansion of the lattice vectors is $\alpha_a : \alpha_b : \alpha_c = 1.00 : 2.19 : 1.60$ at 285 K. Subsequent analysis of the thermal expansion tensor reveals highly anisotropic behavior as reflected in negative thermal expansion approximately $\parallel \langle 101 \rangle$ and ratios of the tensor eigenvalues of $\alpha_1 : \alpha_2 : \alpha_3 = -1 : 3.74 : 5.40$ at 285 K. Lastly, we demonstrate how combining Raman spectroscopy and X-ray diffraction of the same sample material sealed inside a capillary with complementary first-principles calculations yields accurate reference Raman spectra. This workflow enables the construction of a reliable Raman spectroscopic database for planetary exploration, which will be invaluable in elucidating the geological past as well as in identifying resources for the future colonization of planetary bodies throughout the solar system.

Keywords: polyhydrated sulfates, Mars, rozenite, negative thermal expansion, Raman spectroscopy, Density Functional Theory, Neutron Diffraction, Synchrotron Diffraction

4.1 Introduction

Ferrous sulfate minerals occur in various hydration states, $FeSO_4 \cdot nH_2O$ with n = 1, 4, 5, 6, 7, most commonly in the vicinity of sulfide ore deposits (Jambor et al., 2000). In such environments, weathering of ore and waste materials releases relatively oxidized forms of iron and sulfur, as well as a wide range of potentially toxic elements, into nearby surface waters (Hudson-Edwards et al., 1999; Nordstrom, 2011), which subsequently precipitate as hydrous ferric and ferrous sulfates. Widespread occurrences of minerals diagnostic to acid mine drainage environments have been identified on the Martian surface using both surface (Klingelhöfer et al., 2004) and orbit-based (Carter et al., 2013) measurements. These findings have been interpreted as evidence for the existence of acidic aquatic environments early in Martian history (Squyres et al., 2004). In detail, it has been proposed that hydrated sulfate minerals on Mars are secondary minerals produced by the evaporation of fluids involved in the aqueous alteration of Martian basalt (Tosca et al., 2005). In the Valles Marineris canyon system, sulfate minerals occur in sandy stratified deposits, typically exposed in canyon walls, and lie stratigraphically above widespread clay-mineral deposits (Roach et al., 2010). This stratigraphic sequence records a transition from neutral-alkaline (clay-forming) to acidic (iron sulfate-forming) aqueous environments indicating a change in global climate from wetter to dryer conditions starting around 3.5 Gya (Bibring et al., 2006). Due to their apparent role as climatological archives, a detailed mineralogical characterization of these sulfate deposits is essential in order to decipher the nature and drivers of changing environmental conditions during the planet's early history. However, attempts to assign any single mineral species to the spectral data acquired for the polyhydrated sulfate deposits have proven to be challenging. This is due to inherent difficulty in differentiating between the diffuse near-IR reflectance spectra of different sulfate phases in the range 0.35 – 5.1 µm (corresponding to the OMEGA spectrometer on-board the Mars Express orbiter (Langevin et al., 2006)) that is typically measured from orbit, i.e., significant spectral similarities occur between sulfates of different chemical composition and degrees of hydration (Bishop et al. 2009).

Numerous studies have been carried out in order to identify candidate minerals for the polyhydrated sulfate phase. If these deposits indeed originate from the alteration of olivine in Martian basalt, the polyhydrated sulfate phase as

its weathering product would likely be an iron- or magnesium-bearing sulfate (Bibring et al., 2005) or a sulfate mineral of intermediate composition. Among the iron sulfates, Carter et al. (2013) noted that rozenite matched the data acquired by OMEGA and CRISM very well. Wang et al. (2016), however, from studies on the phase stability of melanterite ($FeSO_4 \cdot 7H_2O$) under variable temperature and relative humidity conditions, observed that at 323 K, rozenite merely occurs as a transient state and further dehydrates to szomolnokite ($FeSO_4 \cdot H_2O$). Based on this finding they concluded that rozenite is not stable under present day Martian surface conditions. Nevertheless, we note that in the same study, Wang et al. (2016) reported that even after around 2030 hours (number obtained from supporting information (S4) in Wang et al. (2016)) of exposure to relatively dry air (i.e., 33 % relative humidity) rozenite did not reveal any signs of dehydration at temperatures as high as 294 K, which is well above a maximum ground temperature of 280 K measured by the Curiosity rover over the first 100 sols (i.e. Martian days) of data acquisition (Gómez-Elvira et al., 2014). Moreover, rehydration of szomolnokite to rozenite and melanterite was observed at a temperature of 298 K at a relative humidity of 65 % (Mitchell, 1984). Hence, even if temperatures as high as 323 K have prevailed at any point in Martian history (leading to the dehydration of rozenite or melanterite), the process may have been reversed under present day Martian environmental conditions. Thus, rozenite should still be regarded as a promising candidate mineral for the polyhydrated sulfate phase.

In order to unambiguously confirm the absence or presence of rozenite in the Martian polyhydrated sulfate deposits, in-situ analytical techniques such as X-ray diffraction or Raman spectroscopy are needed. Raman spectroscopy in particular has proven very effective in discriminating between various sulfate mineral species (Košek et al., 2017), and thus appears well suited to unravel the mineralogical phase composition of the polyhydrated sulfate phase. Raman spectroscopic investigations of the Martian soil have recently become possible. NASA's Perseverance Rover, landing on the Martian surface in spring 2021, as well as the ESA's Rosalind Franklin Rover, which will likely arrive on Mars in 2023, both feature Raman spectrometers (Rosalind Franklin: The Raman Laser Spectrometer (Rull et al., 2017); Perseverance: SuperCam (Wiens et al., 2020) and SHERLOC (Bhartia et al., 2021)) as part of their scientific payload.

Interestingly, Chio et al. (2007) observed an apparent splitting of Raman-active vibrational modes of rozenite, which they suggested might be indicative of two structural phase transitions (T_{crit1} = 240 – 190 K, T_{crit2} = 140 – 90 K). The first transition is well within the range of temperatures relevant to the Martian surface. Although Raman spectroscopy is a powerful tool for the identification of polymorphic phase transitions, sharpening of closely-spaced vibrational modes at low-temperatures might be erroneously interpreted as splitting due to a phase transition.

With rozenite being one of the most promising candidates for the polyhydrated sulfate phase on the Martian surface, there is an interest in revisiting these putative phase transitions by means of neutron diffraction in order to determine the structural stability of rozenite at temperatures relevant to the Martian surface as well as to solve the crystal structure of any proposed low-temperature polymorphs. For this reason, we have studied herein the structural stability of $FeSO_4 \cdot 4D_2O$ at temperatures ranging from 290 K down to 21 K by means of high-resolution time-of-flight (TOF) neutron diffraction. Furthermore, the samples used for the neutron diffraction have been perdeuterated for the explicit reason of avoiding the large incoherent scattering signal from ordinary ^1H, which produces a substantial background masking weak Bragg peaks. Use of ^2D virtually eliminates this background and allows for rapid acquisition of high-quality data.

Since subtle changes in relative humidity may cause hydrated sulfates to partially or completely re- or dehydrate (Wang et al., 2016), it is entirely possible that the rozenite sample studied by Chio et al. (2007) underwent a transformation in between the initial phase identification by X-ray diffraction and the subsequent measurements of its vibrational properties. In order to confirm that the Raman spectra reported by Chio et al. (2007) indeed corresponds to rozenite, we have carried out Raman spectroscopy and synchrotron X-ray diffraction, which is able to detect the smallest amounts (i.e., 0.1 wt% (Thompson et al., 2009)) of any contaminant phases. Such measurements have been complemented with ab initio calculations in order to further explore the vibrational properties of rozenite. This combined experimental and theoretical approach allows us to cast light on the structural stability of rozenite at Martian surface temperatures and, therefore, will aid the identification of rozenite in future and ongoing Mars missions.

4.2 Methods

4.2.1 Synthesis and phase analysis

$FeSO_4 \cdot 7H_2O$ (Sigma Aldrich ACS reagent grade) was dehydrated under vacuum for 48 hours at 473 K to prepare anhydrous $FeSO_4$. A hot supersaturated solution of $FeSO_4$ in 0.5 M D_2SO_4 (Sigma Aldrich > 99 atom % D) was then cooled to room temperature in order to precipitate fine-grained $FeSO_4 \cdot 7D_2O$. The sealed container was stored for several years, during which time diurnal and seasonal temperature changes resulted in the fine-grained material altering into a fully dense coarse crystalline material. $FeSO_4 \cdot 7D_2O$ crystals were then ground to a powder under helium in order to prevent exchange of ^2D with atmospheric ^1H. The powder was loaded into rubber-sealed glass jars containing a saturated solution of $MgCl_2$ in D_2O (Sigma Aldrich > 99 atom % D), which buffered the relative humidity at 33 % (Greenspan, 1977), and kept at 280 K for 3 days. The sample was then transferred, again under helium, into the sample holder used for the neutron diffraction experiments. This comprised an aluminum frame surrounding a cuboid sample cavity of dimensions 18 × 23 × 10 mm (w × h × d), open at the front and back. The rear opening was first covered with a vanadium foil window sealed by indium wire; powder was then transferred into the sample holder and the front opening was sealed with another vanadium foil window. Gadolinium and cadmium foils were used to mask scattering from various aluminum and steel parts that might be exposed to the incident neutron beam around the edges of the vanadium windows. A cartridge heater, used for temperature control, and a RhFe thermometer were inserted into the aluminum frame of the sample container either side of the sample.

The sample was mounted into a closed cycle refrigerator (CCR) at the High-Resolution Powder Diffraction (HRPD) beamline, ISIS Neutron and Muon Spallation Facility, UK. This instrument allows collection of neutron time-of-flight (TOF) data in various 100 ms-wide 'windows'; those used in this study were 30 – 130 ms and 100 – 200 ms. In HRPD's highest resolution backscattering detectors ($2\theta = 154 – 176°$), these yield diffraction patterns covering d-spacings from 0.65 – 2.60 Å and 2.20 to 3.90 Å, respectively. The latter is often best used for rapid phase identification, even though the incident neutron flux is very low, since Bragg peaks are typically fewer and better dispersed, whilst also being rather more intense than those at shorter d-spacings.

We could thus quickly confirm that the sample was mostly rozenite, but with a few weak Bragg peaks identified as melanterite, indicating that dehydration of the starting material was incomplete. Heating the sample to 305 K for 60 min and then 315 K for a further 20 minutes resulted in the complete transformation of melanterite to rozenite. At 315 K, however, the high temperatures also gave rise to slight further dehydration and the formation of szomolnokite. Therefore, we lowered the temperature again to 305 K and kept the sample at this temperature for a further 12 minutes to ensure the complete transformation from melanterite to rozenite in the final sample material. The diffraction patterns acquired during dehydration of the sample are provided in the supplementary data (Fig. S1). Rietveld refinement of the neutron diffraction pattern acquired at 290 K suggests that the final sample material consists of 93.5(1) wt% rozenite and 6.5(1) wt% szomolnokite.

Protiated $FeSO_4 \cdot 4H_2O$ for the synchrotron X-ray diffraction and Raman analysis was synthesized using the dehydration method stated above. We placed the reagent $FeSO_4 \cdot 7H_2O$ in a rubber sealed glass jar containing a saturated solution of $MgCl_2$ in H_2O for 3 days at around 290 K. Subsequently, the sample was loaded into a borosilicate glass capillary of 0.5 mm diameter. The loaded specimen and the rest of the sample material were used for Raman analysis.

4.2.2 TOF Neutron diffraction and Rietveld refinement

High resolution TOF neutron diffraction data were collected at temperatures ranging from 315 to 21 K upon cooling and warming. After the initial dehydration at 305 and 315 K, the sample was cooled to 290 K. Datasets with long counting times of 3 h 17 min in the 30 – 130 ms and 100 – 200 ms TOF window were then collected to allow crystal structure refinement. In order to characterize the thermal expansion of rozenite, diffraction patterns with shorter counting times of 50 min were collected on cooling in 10 K increments in the 100 – 200 ms TOF window in the temperature range from 290 – 21 K. At the base temperature of 21 K, another dataset for structural refinement was acquired in the 100 – 200 ms TOF window, again, for 3 h 17 min and in 30 – 130 ms window for 4 h 6 min. Lastly, we collected diffraction patterns upon heating from 35 – 285 K in 10 K increments for 37 min each. To ensure good thermal equilibrium between the heated aluminum frame of the sample holder and the powder sample

itself, temperature changes were done at 3 K min^{-1} and a dwell time of 10 minutes after reaching a set-point was used prior to the start of data collection.

The data were time-focused, normalized to the incident spectrum and corrected for instrument efficiency using a V:Nb standard. Diffractometer calibration constants and instrumental peak-profile coefficients were determined using NIST silicon SRM640e and CeO_2 standards.

All refinements were carried out using the Rietveld method (Albinati and Willis, 1982; van Laar and Schenk, 2018) as implemented in the GSAS/EXPGUI software suite (Toby, 2001). The diffraction patterns collected in HRPD's backscattering detector bank at 290 K and 21 K are displayed in Fig. 1 and the refinement parameters are given in Tab. 1 as well as in the CIF. Clearly, the refined structural models are in excellent agreement with the observed intensity data.
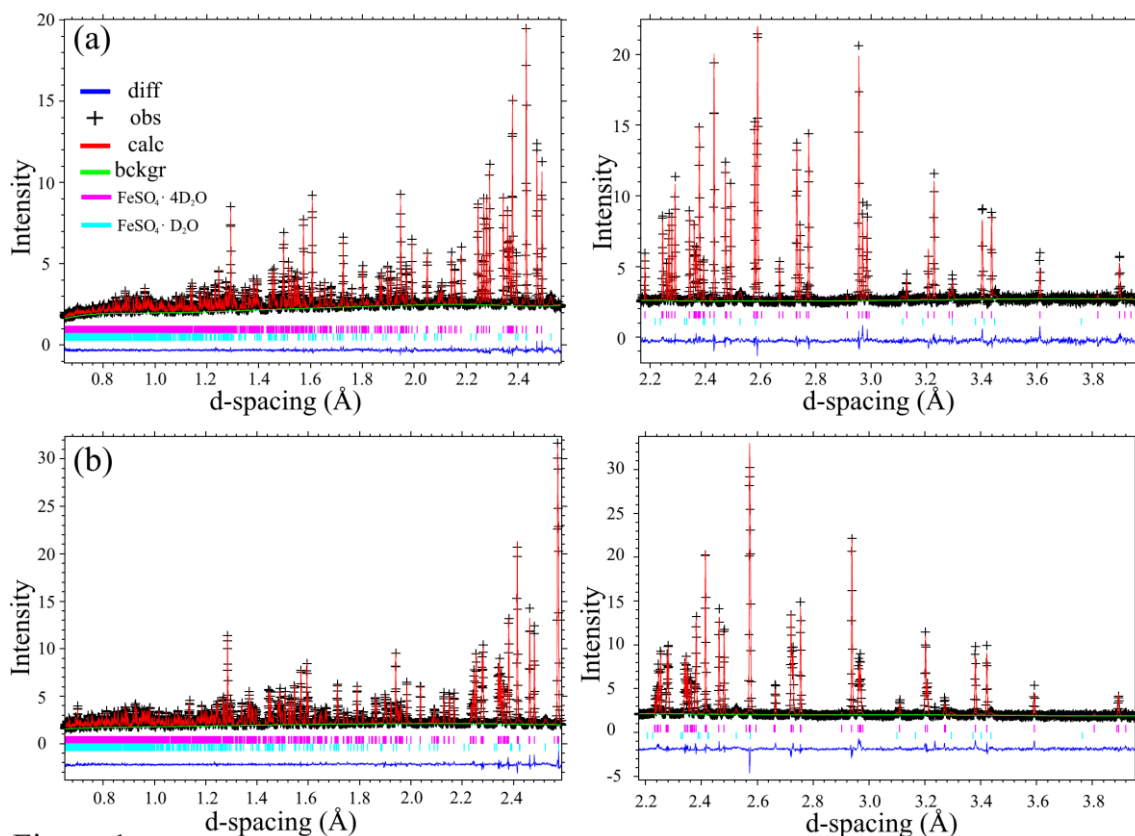
Figure 1

Fig. 1. Neutron diffraction patterns acquired at (a) 290 K and (b) 21 K in the backscattering detector bank collected in the 30 – 130 (left) and 100 – 200 ms (right) TOF window. The observed data plotted as crosses, the red line represents the fitted model, and the blue line the difference profile. The tick marks corresponding to each of the Bragg peaks of $FeSO_4 \cdot 4D_2O$ and $FeSO_4 \cdot D_2O$ are displayed in magenta and cyan, respectively.

Unit-cell parameters were refined from the shorter 100 – 200 ms TOF datasets using initial least-squares cycles of Rietveld refinement, followed by a series of least-squares cycles using the 'F(calc) weighted' method; this workflow typically results in the most precise lattice parameters by virtue of fitting the intensities more accurately. For szomolnokite we used the structure reported by Talla and Wildner (2019) for the refinements and varied the lattice parameters and profile coefficients at each temperature. The small number of weak peaks accessible in the 100 – 200 ms TOF window combined with the low symmetry of szomolnokite precludes us from following the evolution of the lattice parameters accurately as a function of temperature, which are therefore not reported in this study.

Crystal data		
Chemical Formula	$FeSO_4 \cdot 4D_2O$	$FeSO_4 \cdot 4D_2O$
Space group	$P2_1/n$	$P2_1/n$
Temperature	290 K	21 K
a, b, c, β	5.966031(12) Å,	5.942863(15) Å,
	13.609756(31) Å,	13.521390(40) Å,
	7.962529(14) Å,	7.933688(20) Å,
	90.4288(2) °	89.8617(2) °
V	646.509(2)	637.516(2)
Z	4	4
Refinement		
R-factors goodness of fit	Rp = 0.0237, Rwp = 0.0179, χ^2 = 2.190	Rp = 0.0316, Rwp = 0.0257, χ^2 = 5.472
Number of refined parameters	192	182*

Tab. 1. Selected details of the crystal structure refinement of rozenite, for a full description we refer to the CIF. *Number of refined parameters is lower for the measurement at 21 K since the background coefficients had to be fixed for the 30 – 130 ms TOF window.

4.2.3 Synchrotron X-ray diffraction and room temperature Raman spectroscopy

A synchrotron X-ray powder diffraction pattern of the protiated rozenite capillary sample was collected at the I11 instrument, Diamond Light Source, UK using the Multi Analyzing Crystal detectors (Thompson et al., 2009). The experiment was carried out at an ambient temperature of 295 ± 0.5 K. The wavelength of 0.826574(9) Å and a zero-point error of 0.000315(2) ° was determined from a *NIST SRM 640c* silicon standard.

Raman spectra of protiated rozenite were acquired using a *B&WTek i-Raman Plus* spectrometer equipped with a neodymium doped Yttrium-Aluminum-Garnet laser that was frequency-doubled to 532 nm (maximum power of 30 mW as determined by the manufacturer). We collected data over the entire spectral range accessible to the spectrometer (i.e., 65 – 4200 cm^{-1}) with a resolution of smaller than 3.5 cm^{-1} (as determined by the manufacturer at 614 nm) on protiated rozenite powder samples both outside and inside of the very same borosilicate glass capillary that was used for the synchrotron diffraction analysis. The spectra were collected for 53 and 50 seconds and averaged over three acquisitions for the sample outside and inside of the capillary, respectively.

Ab initio vibrational properties from density functional theory (DFT):

We performed Kohn-Sham DFT calculations (Hohenberg and Kohn, 1964; Kohn and Sham, 1965) using ultrasoft pseudopotentials from the *GBRV* library (Garrity et al. 2014). Kinetic energy cut-off values and *k*-point grid density were derived from convergence testing; values of 70 Ry and 840 Ry were adopted for the wave function and charge density cut-offs, respectively and a Monkhorst–Pack (Monkhorst and Pack, 1976) *k*-point grid of 2 × 1 × 2 was applied to sample the Brillouin zone.

The crystal structure as reported by Baur (1962) served as input geometry for an initial relaxation using the PBE functional (Perdew et al., 1996) in conjunction with the D2 dispersion correction (Grimme, 2006). We have demonstrated in our previous work (Meusburger et al., 2021) that the PBE + D2 approach is very well suited to model geometries at temperatures close to the ground state both for dispersion-dominated solids as well as hydrogen-bonded solids such as the one under investigation.

The unit-cell and internal atomic coordinates were relaxed using the Broyden-Fletcher-Goldfarb-Shanno algorithm (Pfrommer et al., 1997), with convergence thresholds 1×10^{-6} Ry, 1×10^{-5} Ry/Bohr, 5×10^{-1} kbar for the total energy, forces, and pressure, respectively. Moreover, we applied a mixing factor of 0.3 and the local Thomas–Fermi charge mixing mode (Raczkowski et al., 2001) in order to achieve convergence in the self-consistent field cycles.

The structure optimized at the DFT + D level served as basis for the self-consistent computation of the Hubbard U by means of Density Functional Perturbation Theory (Timrov et al., 2018). The formulation of the Hubbard model following Dudarev et al. (1998) as well as nonorthogonalized atomic orbitals (Cococcioni and de Gironcoli, 2005; Amadon et al., 2008) as projectors for the strongly localized $3d$ states of Fe^{2+} were used for all DFT + U calculations. We have tested multiple q-meshes and found that a grid of 2 × 1 × 2 is necessary in order to derive Hubbard U values converged to within 0.0007 eV. Subsequently, we used the U value converged with respect to the q-mesh (i.e., 6.9806 eV), and again, computed the U value from this optimized structure. This procedure was repeated three times until the U value (i.e., 6.0156 eV) was identical with respect to the previous iteration.

The geometry obtained from this workflow was then used as input for our phonon calculations at the Γ-point using Density Functional Perturbation Theory in order to compute the Infrared (IR) and Raman spectra of rozenite. The formalism of phonon calculations at the DFT + U level of theory as implemented in Quantum ESPRESSO's ph.x code is presented in detail in Floris et al. (2011, 2020). The open-source Quantum ESPRESSO code suite (Giannozzi et al. 2009, 2017) was used for all ab initio calculations. All files necessary to reproduce our calculations (i.e., input, output, and pseudopotential files) may be accessed on the MaterialsCloudArchive (Meusburger et al., 2022).

4.3 Results and discussion

4.3.1 Complete crystal structure and hydrogen bonding of $FeSO_4 \cdot 4D_2O$ at 290 K

The crystal structure of rozenite was first determined by Baur (1962) and consists of isolated cyclic $[Fe(H_2O)_4SO_4]_2$ units (Fig. 2a) interconnected by a hydrogen bond network (Fig. 2b). $[Fe(H_2O)_4SO_4]_2$ may be further divided into $Fe(H_2O)_4O_2$ octahedral units that engage in corner-sharing of O atoms with the SO_4 tetrahedral units (Fig. 2a).
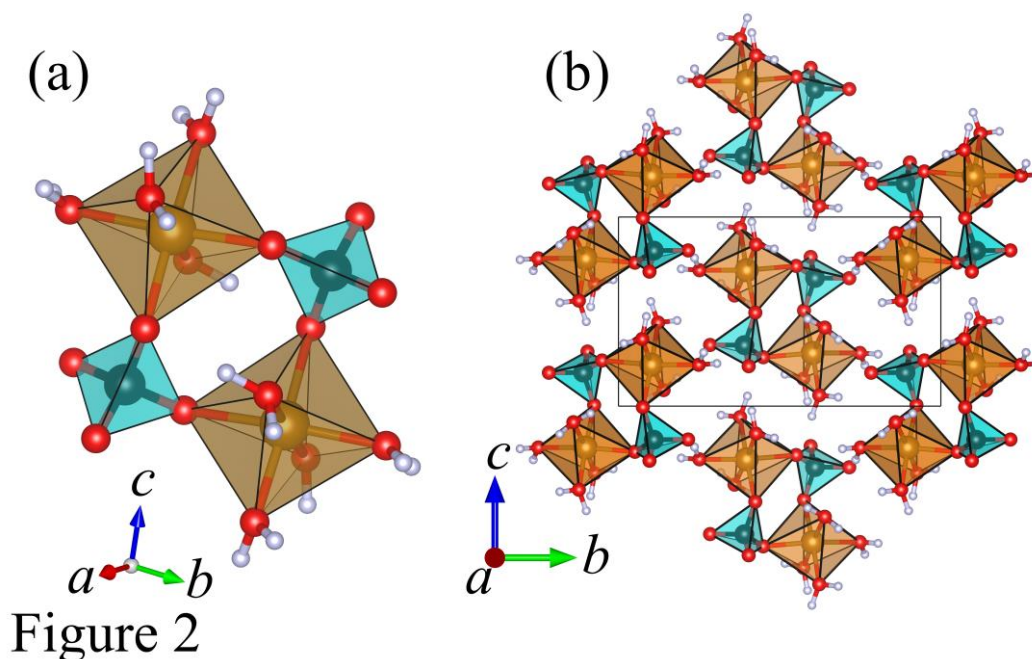
Figure 2

Fig. 2. Crystal structure of rozenite drawn using the VESTA software (Momma and Izumi, 2011). (a) Detailed view of the $[Fe(H_2O)_4SO_4]_2$ units. Note that the non-hydrated oxygens of the $Fe(H_2O)_4O_2$ units form bridges to the SO_4 tetrahedra (orange and cyan, respectively). (b) The $[Fe(H_2O)_4SO_4]_2$ isolated units are linked via a complex network of intermolecular hydrogen bonds.

Considering that the crystal structure of rozenite has not been revisited since its initial determination 60 years ago by means of single crystal X-ray diffraction, the results presented in this study improve the literature data substantially. In contrast to X-ray diffraction, which severely underestimates O – H bond lengths (Baur, 1972), neutron diffraction is particularly well suited to accurately locate the hydrogen atom positions, allowing us to resolve long-standing ambiguities in the hydrogen bonding network of rozenite. In the following section the geometry of the octahedral and tetrahedral units will be discussed and compared to the structure reported by Baur (1962) (Tab. 2).

Source	Baur	This study	Diff*	This study	Diff**
T (K)	RT	290		21	
Fe-O1	2.120(9)	2.121(3)	-0.001	2.130(3)	-0.009
Fe-O2	2.120(9)	2.130(3)	-0.010	2.127(3)	0.003
Fe-Ow1	2.099(11)	2.096(3)	0.003	2.108(3)	-0.011
Fe-Ow2	2.129(11)	2.139(4)	-0.010	2.145(3)	-0.006
Fe-Ow3	2.127(11)	2.114(4)	0.013	2.113(3)	-0.001
Fe-Ow4	2.126(11)	2.097(3)	0.029	2.094(3)	0.003
MSiD[1]			0.004		-0.003
MUD			0.011		0.006
O1-Fe-Ow1	86.2(2.4)	87.44(11)	-1.24	87.44(10)	0.00
O1-Fe-Ow2	95.7(2.4)	95.51(12)	0.19	95.50(11)	0.01
O1-Fe-Ow3	87.0(2.4)	87.13(12)	-0.13	86.88(10)	0.25
O1-Fe-O2	91.9(2.4)	91.00(10)	0.90	90.81(10)	0.19
Ow4-Fe-Ow1	85.5(2.4)	84.73(12)	0.77	84.36(11)	0.37
Ow4-Fe-Ow2	92.5(2.4)	92.31(13)	0.19	92.69(12)	-0.38
Ow4-Fe-Ow3	92.5(2.4)	92.64(13)	-0.14	92.86(11)	-0.22
Ow4-Fe-O2	88.8(2.4)	89.17(12)	-0.37	89.48(11)	-0.31
Ow1-Fe-Ow3	90.7(2.4)	91.97(13)	-1.27	92.47(11)	-0.50
Ow2-Fe-O2	94.0(2.4)	93.10(12)	0.90	93.33(11)	-0.23
Ow2-Fe-Ow3	86.8(2.4)	87.35(13)	-0.55	86.56(11)	0.79
MSiD			-0.068		-0.003
MUD			0.605		0.295
S-O1	1.512(8)	1.487(5)	0.025	1.478(5)	0.009
S-O2	1.492(8)	1.482(5)	0.010	1.485(5)	-0.003
S-O3	1.488(8)	1.468(5)	0.002	1.484(5)	-0.016
S-O4	1.473(8)	1.481(5)	-0.008	1.481(6)	0.000
MSiD			0.012		-0.003
MUD			0.016		0.007
O1-S-O2	109.4(1.1)	108.2(3)	1.2	109.7(4)	-1.5
O1-S-O3	108.3(1.1)	110.4(3)	-2.1	109.9(3)	0.5
O1-S-O4	108.3(1.1)	108.7(3)	-0.4	109.0(3)	-0.3
O2-S-O3	109.7(1.1)	109.3(3)	0.4	108.3(3)	1.0
O2-S-O4	111.8(1.1)	111.2(3)	0.6	111.0(3)	0.2
O3-S-O4	109.3(1.1)	109.0(3)	0.3	108.9(4)	0.1
MSiD			-0.24		0.3
MUD			0.76		0.42

Tab. 2. Bond lengths and angles for the octahedral and tetrahedral units of rozenite as determined in this study at 290 K and 21 K and compared to the values reported by Baur (1962). * refers to the difference between Baur and this study's 290 K structure. ** refers to the difference of this study's 290 K and 21 K structures, thus elucidating the influence of temperature on the respective quantity. The Mean signed difference is defined as $\frac{\sum_i^n x_B - x_T}{n}$ with x_B and x_T being the values as observed by Baur and in this study, respectively for the quantities of interest (i.e., bond-length and angle). Atomic coordinates and displacement parameters for each of the reported structures can be found in Tab. S7 in the supplementary.

Overall, the heavy atom (i.e., Fe, S, O) structure refined from the 290 K dataset is in excellent agreement with the structure reported by Baur (1962). This is reflected by the Mean Unsigned Differences (MUD)[1] of 0.011 Å (Fe – O bonds), 0.605 ° (O – Fe – O angles), 0.016 Å (S – O bonds) and (O – S – O angles) 0.76 ° being either well below or very close to the estimated standard deviations reported by Baur (1962) on the respective quantities.

---

[1] The MUD is defined as $\frac{\sum_i^n |x_B - x_T|}{n}$ with x_B and x_T being the values as observed by Baur and in this study, respectively for the quantities of interest (i.e., bond-length and angle).

Moving on to the hydrogen bond network it is noteworthy that Baur (1962) determined the heavy atom structure of rozenite and did not refine the position of the hydrogen atoms. Instead, he fixed the hydrogen atoms to the positions determined for the isotypic material $MgSO_4 \cdot 4H_2O$ (starkeyite) during the refinement process. As noted above, Baur (1962) determined the hydrogen atom positions by means of X-ray diffraction, which typically yields underestimated bond lengths as well as inaccurate $H - O - H$ angles (Baur, 1972). Baur (1962) counteracted this shortcoming by setting multiple constraints upon the hydrogen bond geometries. Therefore, we present for the first time the complete crystal structure of rozenite with all atomic positions derived from an unconstrained refinement. We assess the differences in the hydrogen bonding network and compare our results to the Baur (1962) study (Tab. 3).

Source	Baur	This study	Diff*	This study	Diff**
T (K)	RT	290		21	
Ow1-H1a	1.010(8)	0.947(5)	0.063	0.965(5)	-0.018
Ow1-H1b	0.962(9)	0.962(4)	0.000	0.972(4)	-0.01
Ow2-H2a	0.933(9)	0.963(5)	-0.03	0.959(4)	0.004
Ow2-H2b	0.958(9)	0.944(5)	0.014	0.975(4)	-0.031
Ow3-H3a	0.955(8)	0.950(5)	0.005	0.949(4)	0.001
Ow3-H3b	0.975(9)	0.943(4)	0.032	0.962(4)	-0.019
Ow4-H4a	0.960(8)	0.953(5)	0.007	0.968(4)	-0.015
Ow4-H4b	0.964(9)	0.973(4)	-0.009	0.960(4)	0.013
MSiD			0.010		-0.009
MUD			0.020		0.014
H1a-Ow1-H1b	105.2(8)	106.0(4)	-0.80	107.8(4)	-1.80
H2a-Ow2-H2b	104.0(8)	105.5(5)	-1.50	107.1(4)	-1.6
H3a-Ow3-H3b	110.2(8)	108.4(4)	1.80	108.1(4)	0.3
H4a-Ow4-H4b	105.1(8)	105.0(4)	0.10	106.9 (4)	-1.90
MSiD			-0.10		-1.25
MUD			1.05		1.40
Ow1-O3	2.855(10)	2.898(4)	-0.043	2.848(4)	0.050
Ow1-O3'	2.790(10)	2.764(4)	0.026	2.744(4)	0.020
Ow2-O4	2.867(10)	2.858(4)	0.009	2.834(4)	0.024
Ow2-O2	3.023(10)	3.015(4)	0.008	2.986(4)	0.029
Ow2-O2'	3.267(10	3.274(4)	-0.007	3.250(4)	0.024
Ow3-O4	2.845(10)	2.836(4)	0.009	2.794(4)	0.042
Ow3-Ow4	3.025(12)	3.059(5)	-0.034	3.029(4)	0.030
Ow3-O1	2.805(10)	2.816(4)	-0.011	2.795(4)	0.021
Ow4-O4	2.837(10)	2.848(4)	-0.011	2.832(4)	0.016
Ow4-O3	2.723(10)	2.733(4)	-0.010	2.718(4)	0.015
MSiD			-0.0064		0.027
MUD			0.0168		0.027
H1a-O3	1.865(6)	1.957(4)	-0.092	1.888(4)	0.069
H1b-O3'	1.834(6)	1.808(4)	0.026	1.776(4)	0.032
H2a-O4	2.201(6)	1.992(5)	0.209	1.967(4)	0.025
H2b-O2	2.417(6)	2.330(5)	0.087	2.249(4)	0.081
H2b-O2'	2.593(6)	2.551(4)	0.042	2.525(4)	0.026
H3a-O4	2.113(6)	2.015(4)	0.098	1.974(4)	0.041
H3a-Ow4	2.345(9)	2.425(5)	-0.080	2.399(4)	0.026
H3b-O1	1.833(6)	1.874(4)	-0.041	1.834(4)	0.040
H4a-O4	1.969(6)	1.948(4)	0.021	1.918(4)	0.093
H4b-O3	1.899(6)	1.764(4)	0.135	1.764(4)	0.000
MSiD			0.041		0.037
MUD			0.083		0.037
O3-Ow1-O3'	104.8(4)	104.90 (11)	-0.10	104.46(10)	0.44
O4-Ow2-O2	144.5(4)	143.43(14)	1.07	142.81(12)	0.62
O4-Ow2-O2'	92.6(3)	93.12(11)	-0.52	93.75(9)	-0.63
O4-Ow3-O1	137.2(4)	136.23(13)	0.97	135.54(11)	0.69
Ow4-Ow3-O1	70.8(3)	70.28(10)	0.52	69.45(8)	0.83
O4-Ow4-O3	117.3(4)	116.68(12)	0.62	118.30(11)	-1.62
MSiD			0.43		0.055
MUD			0.63		0.805
Ow1-H1a-O3	165.8(5)	172.0(4)	-6.2	173.5(4)	-1.60
Ow1-H1b-O3'	171.8(6)	172.5(4)	-0.7	173.1(4)	-0.60
Ow2-H2a-O4	125.7(6)	148.5(4)	-22.8	149.2(3)	-0.70
Ow2-H2b-O2	122.6(6)	129.0(4)	-6.4	131.5(3)	-2.50
Ow2-H2b-O2'	129.6(6)	133.6(4)	-4.0	131.0(3)	2.60
Ow3-H3a-O4	132.3(6)	143.6(3)	-11.3	143.4(3)	0.20
Ow3-H3a-Ow4	127.7(6)	124.0(3)	3.7	123.6(3)	0.40
Ow3-H3b-O1	173.7(5)	175.4(4)	-1.7	176.0(3)	-0.60
Ow4-H4a-O4	149.2(6)	156.7(4)	-7.5	156.4(3)	0.30
Ow4-H4b-O3	141.8(5)	172.6(4)	-30.8	172.2(3)	0.40
MSiD			-8.77		-0.20
MUD			9.51		0.980

Tab. 3. Geometry of the hydrogen bonds of rozenite as determined in this study at 290 K and 21 K, and compared to the values reported by Baur (1962). *refers to the difference between Baur and this study's 290 K structure. ** refers to the difference of this study's 290 K and 21 K structures, thus elucidating the influence of temperature on the respective quantity.

The O ••• O contacts are in excellent agreement (MUD = 0.0168 Å, largest individual difference (LID) = 0.043 Å), which was expected since the distance of donor acceptor oxygens of the hydrogen bonding network is solely determined by the heavy atom positions. Despite the fact that X-ray diffraction (XRD) underestimates O – H bond lengths, the covalent O – H bond distances in our neutron diffraction and the Baur (1962) XRD study agree very well (MUD = 0.020 Å, LID = 0.063 Å). The reason for this is likely that the bond-length constraints for O – H bonds as applied by Baur (1962) are very close to the values we observed in rozenite. Although the constraints used by Baur (1962) yielded H – O distances in close agreement with our refinement, the constrained model fails for the geometry of the H – O – H molecules, as reflected by a large MUD of 1.05 ° and LID of 1.80 °. Moreover, the H ••• O contacts revealed a LID of 0.209 Å. This failure to accurately describe the hydrogen bonding geometry is most pronounced in the O_w – H ••• O angles which exhibit a MUD of 9.51 ° and LID of up to 30.80 °, reinforcing the importance of neutron diffraction data in order to derive accurate geometries for the complete crystal structure.

The hydrogen bonding system in rozenite-type compounds has been subject of intensive discussions (Baur 1962, 1964, 2002; Kellersohn, 1992; Held and Bohaty, 2002; Anderson et al., 2012). Based on a long donor acceptor distance of 3.02 Å Baur (1962) suggested that no intermolecular hydrogen bonding takes place for the Ow2 – H2b ••• O2 contact (Fig. 3a). More recent studies on the rozenite-type compounds $ZnSO_4·4D_2O$ (Anderson et al., 2012), $MnSO_4·4D_2O$ (Held and Bohaty, 2002; Anderson et al., 2012) and $CoSO_4·4D_2O$ (Kellersohn, 1992) interpret H2b to partake in a three-centered interaction (i.e., a bifurcated H-bond, Ow2 – H2b ::: O2/O2') with long donor-acceptor distances of 3.02 Å and 3.26 Å (Fig. 3b). Kellersohn (1992) investigated the Ow2 hydrogen bond system based on bond-valance considerations and noted that exclusion of the two long hydrogen bonds results in the O2 atom exhibiting a deficiency of 0.22 valence units. Our own bond valance calculations (Brown and Altermatt, 1985; Brese and O'Keeffe, 1991; Alig et al., 1994) for rozenite (supplementary information; Tab. S1) yield a deficiency of 0.10 valence units on the O2 atom, reducing to 0.054 if the intermolecular contacts are included in the calculations. Clearly, the long intermolecular hydrogen bonds play a vital role in achieving charge neutrality for the O2 atom and thus should not be neglected when

describing the hydrogen bond network. Supporting this evidence in favor of a three-centered hydrogen bond in rozenite-type compounds, Anderson et al., (2012) suggested, based on an exhaustive comparison with numerous hydrogen bonding systems, that not only the H2b, but also the H3a atom is involved in a three-centered hydrogen bond (Ow3 – H3a ::: O4/Ow4) (Fig. 3c). According to our bond valance calculations the H3a ••• Ow4 contact exhibits a valency of 0.017, making it a weak but non-negligible hydrogen bond. Furthermore, when assessing the geometry of Ow3 – H3a ••• Ow4 contact (i.e., H3a ••• Ow4 = 2.425(5) Å; $\angle$ (Ow3 - H3a ••• Ow4) = 124.0(3) ° at 290 K) it is evident that this bond falls well within even the conservatively defined limits of hydrogen bonding (i.e., H ••• O < 3 Å; $\angle$ (Ow - H ••• O) = 110 ° - 180 °; (Steiner, 2002)). Therefore, based on the large range of evidence in favor of three-centered hydrogen bonding involving the H3a and H2b atoms, we have adopted the hydrogen bonding system proposed by Anderson et al. (2012) (Fig. 3c) for our study.
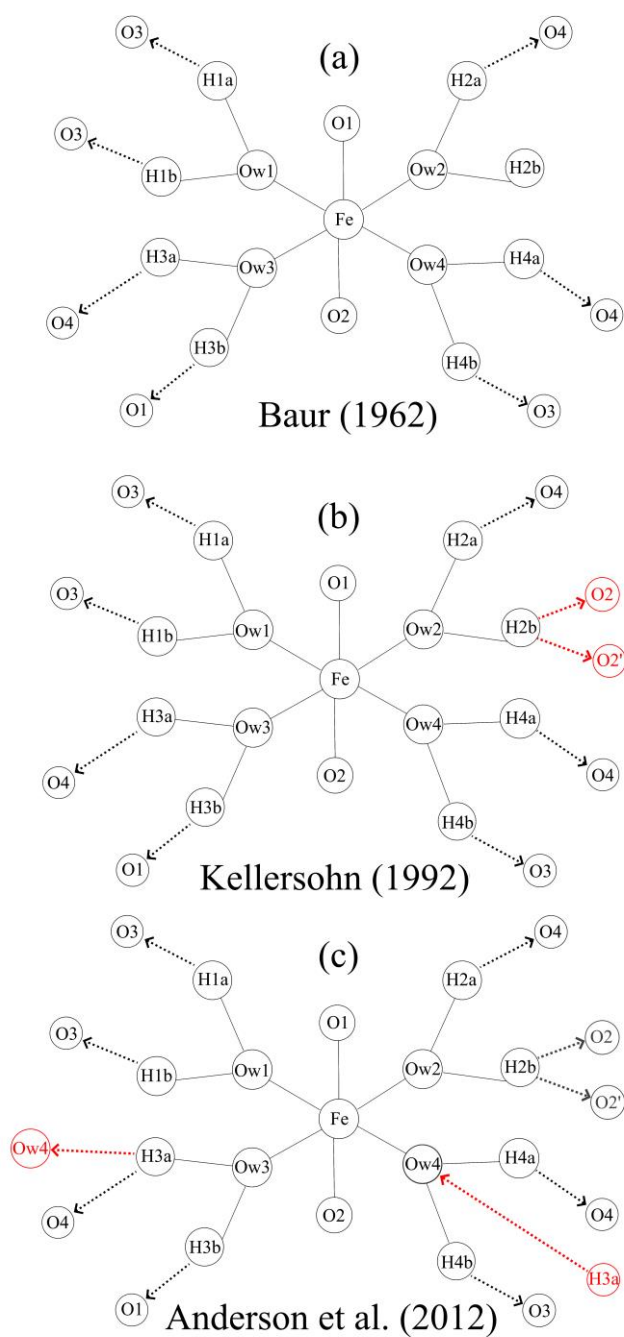
Figure 3

Fig. 3 Interpretation of the hydrogen bond network by (a) Baur (1962), (b) Kellersohn (1992) and (c) Anderson et al. (2012). The changes suggested by these authors with respect to the previous interpretation are marked in red.

4.3.2 Low temperature crystallography, thermal expansion, and absence of phase transition

The powder diffraction data revealed no splitting of Bragg peaks nor appearance of new peaks that might be indicative of a phase transition. Consequently, the refined lattice parameters also varied smoothly (Fig. 4, Tab. S3, Tab. S4). It is noteworthy that the β angle decreased systematically on cooling such that, at ~ 137 K, the unit-cell became metrically orthorhombic. However, β continued to decrease < 90 ° below 137 K and it is important to emphasize that the Laue symmetry of the diffraction pattern retains its monoclinic character throughout the whole temperature range under investigation. Thus, rozenite does not undergo any structural phase transition down to at least 21 K.
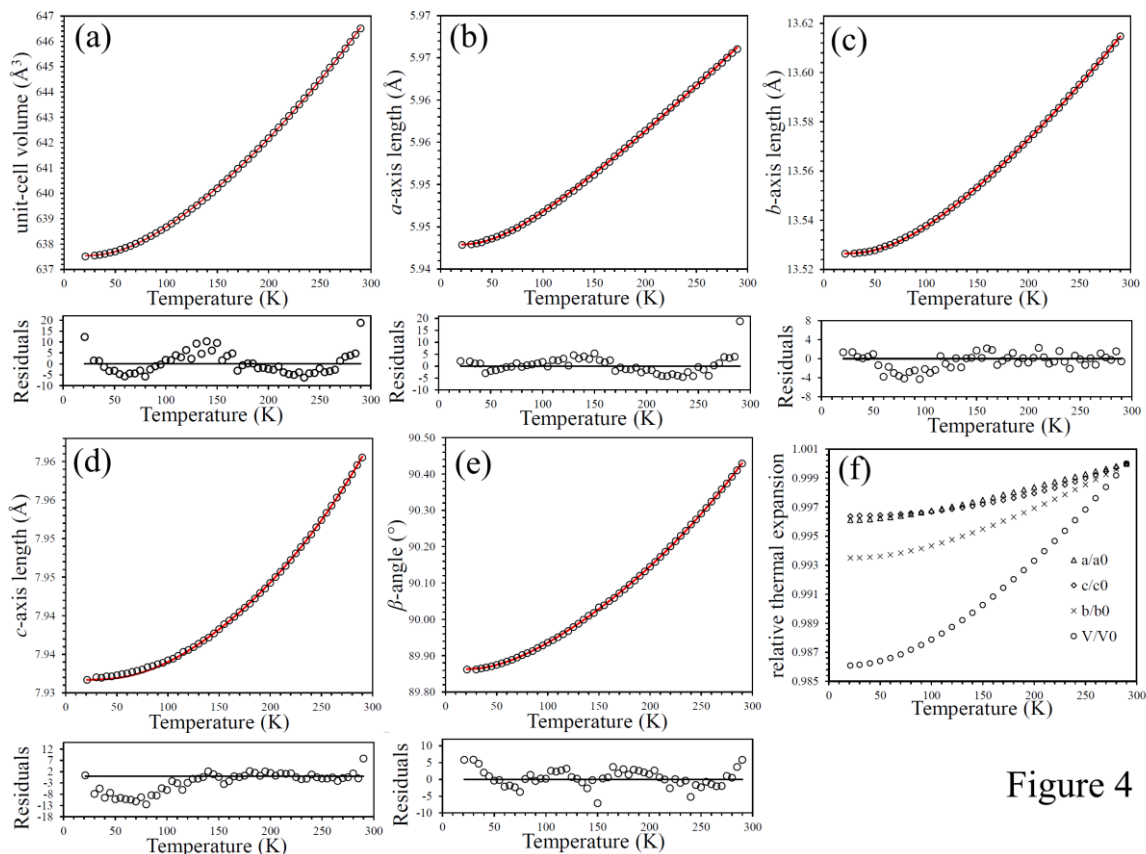
Fig. 4. (a-e) Second-order Debye model fit (red line) to the lattice parameters (black open circle) of rozenite in at temperatures ranging from 290 to 21 K. Error bars are smaller than the symbol size. Residuals are defined as the difference between observed and fitted values divided by the experimental estimated standard deviation determined for each data point. (f) Relative thermal expansion of each of the lattice parameters as a function of temperature. Note the crossover in the evolution of the *a* and *c* axes (T ~ 100 K).

There are various approaches to quantify the temperature dependency of the lattice parameters of crystalline solids, with varying degrees of usefulness and capability for accurate extrapolation. These range from polynomial fits

through to parameterizations based on the classical Einstein model of the internal energy and the more accurate Debye-type model, which is used here.

The Debye model is derived from the Grüneisen relation of the thermoelastic properties.

$$\gamma = \frac{\alpha_V V K_0}{C_V} \tag{1}$$

where γ is the Grüneisen ratio, α_V is the volume thermal expansion coefficient, K_0 is the isothermal bulk modulus, C_V is the isochoric specific heat capacity, and V the unit-cell volume. Equation (1) is integrated with respect to the temperature, whereby γ and K_0 are assumed to be independent of the temperature. This yields the first order approximation to the Grüneisen zero pressure equation of state which expresses the thermal expansion of the crystal as a function of its internal energy $U(T)$ and isothermal bulk modulus K_0

$$V(T) = V_0 \left(1 + \frac{U(T)}{Q} \right) \tag{2}$$

where $Q = (V_0 K_0 / \gamma)$.

$U(T)$ may be derived by the Debye approximation

$$U(T) = 9 N k_B T \left(\frac{T}{\theta_D} \right)^3 \int_0^{\theta_D / T} \frac{x^3}{e^x - 1} dx \tag{3}$$

where N is the number of atoms per formula unit, k_B is Boltzmann's constant, θ_D is the Debye temperature, and $x = \hbar\omega/k_B T$. Note that the zero-point energy of $9 N k_B \theta_D / 8$ is included in Equation (2) via the term V_0.

It was apparent from the residuals obtained from fitting this model to V(T) that the first-order Grüneisen model failed to provide an accurate description of the thermal expansion (see supplementary Fig. S2). Consequently, we fitted a second-order approximation to the Grüneisen zero pressure equation of state (Equation (4)), which introduces the first derivative of the bulk modulus K_0' with respect to pressure via the parameter b

$$V(T) = V_0 \left(1 + \frac{U(T)}{Q - b U(T)} \right) \tag{4}$$

where $b = \frac{1}{2} (K_0' - 1)$.

The sum of squared residuals is thus reduced from 0.32 Å^6 for the first-order fit to 0.014 Å^6 for the second order model.

The value of K_0/γ obtained from the second-order model is 84.5(4) GPa, increased from $K_0 = 58.4(7)$ GPa in the poorer first-order fit. We note that Meusburger et al. (2019) obtained a bulk modulus of 45.2(2) GPa for szomolnokite ($FeSO_4 \cdot H_2O$). It is highly unlikely that rozenite, featuring isolated cyclic $[Fe(H_2O)_4SO_4]_2$ units loosely interconnected by intermolecular hydrogen bonds, exceeds the stiffness of szomolnokite featuring a rigid three dimensional framework structure. Fortes et al. (2006) report a bulk modulus of 21.5(1) GPa for epsomite ($MgSO_4 \cdot 7H_2O$), a mineral featuring isolated $Mg(H_2O)_6$ and SO_4 units loosely interconnected by hydrogen bonds. We should expect, therefore that rozenite will exhibit a compressibility intermediate between these hydrates, implying $\gamma = 1.9 - 4.0$. We further note that an extremely large value for K' of 41.1 as obtained from the second-order Debye fit clearly is unphysical but typical of the case where the complexity of the underlying phonon spectrum is represented by a simple model characterized with a single Debye frequency cut-off. The parameters derived from the second order single Debye fits are given in Tab. 4 and from the first order single Debye model in the supplementary material (Tab. S2). In order to be dimensionally correct, the individual lattice parameters were fitted as a^3, b^3 and c^3.

	a^3	b^3	c^3	β	V
θ_D (K)	240(6)	303(2)	382(4)	381(13)	278(2)
X_0 (cm^3 mol^{-1})	31.5994(6)	372.182(2)	75.1823(4)	13.5290(4)	95.9829(4)
X_0 (Å, Å^3)	5.9428(1)	13.5214(8)	7.9337(5)	934(19)	637.533(3)
Q (x10^4 J cm^{-3})	850(15)	519(3)	1047(12)	1263(26)	811.(3)
K_0/γ (GPa)	269(5)	13.94(7)	139(2)	1617(17)	84.5(4)
K'	12.6	19.92	90.76	146.55	41.11

Tab. 4. Parameters derived from fitting a second order single Debye model upon the lattice parameters of rozenite.

For a more detailed assessment of the thermal expansion of rozenite the orientation and magnitude of the principal axes (Fig. 5a), and components (Fig. 5b) of the thermal expansion tensor were calculated using the Win_strain software (Angel, 2011). Strain tensors were computed incrementally between consecutive data points using the finite Lagrangian strain definition. The reference temperatures correspond to the average of the temperatures of the two data points used to calculate the strains. The thermal expansion tensor is constrained to have the α_2 principal axis parallel to [010], and α_1 and α_3 lying in the (010) plane. The orientation of the crystallographic axes relative to the cartesian reference system as specified by the Institute of Radio Engineers (i.e., X || a^*; Z || c) was used for all calculations.
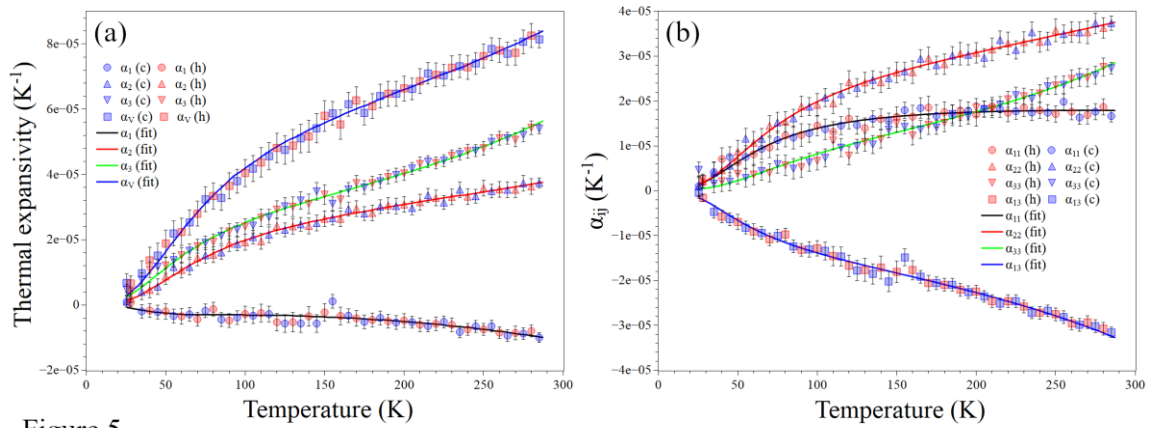
Figure 5

Fig. 5. The evolution of the thermal expansion tensor's principal axes (a), and components (b) of rozenite is continuous over the entire temperature range under investigation. Solid lines represent the 2nd order Debye model fit; red and blue symbols are calculated from the lattice parameter data acquired upon heating and cooling respectively. Error bars were plotted as 3σ. Data plotted in Fig. 5 can be found in the supplementary Tab. S8-11.

Cross-sections through the representation surface of the thermal expansion tensor, evaluated at 285 K (Fig. 6), allow us to understand the relationship to both the monoclinic lattice vectors and the underlying structural elements. The expansion parallel with the *a* and *c* directions of the crystal are similar. The thermal expansion || *b*, however, is substantially larger (i.e., $\alpha_a : \alpha_b : \alpha_c = 1.00 : 2.19 : 1.60$ at 285 K, Tab. S12-13). This behavior may be attributed to a large structural 'void' and the absence of hydrogen bonding between the rigid cyclic dimer units || *b* enabling the structure to undergo greater expansion in this direction upon heating (Fig. 6a).

Mapping of the thermal expansion onto the crystallographic reference frame conceals the true extent of the anisotropy, manifested in the eigenvalues and eigenvectors of the expansion tensor, i.e., the principal thermoelastic strains, $\alpha_1 : \alpha_2 : \alpha_3 = -1.00 : 3.74 : 5.40$ at 285 K. The principal axis α_1, which is approximately oriented parallel to the $\langle 101 \rangle$ direction ($a \angle 40.6(3)$ ° $b \angle 90$ ° $c \angle 49.8(3)$ °), exhibits negative thermal expansion over the entire temperature range under investigation. Contrary to this behavior, α_3, oriented approximately || $\langle 10\bar{1} \rangle$ ($a \angle 49.4(3)$ ° $b \angle 90$ ° $c \angle 139.8(3)$ °) is the true direction of maximum thermal expansion. The stark contrast between the negative thermal expansion approximately || $\langle 101 \rangle$ and the direction of maximum expansion approximately || $\langle 10\bar{1} \rangle$ originates from the evolution of β with temperature. Shrinkage of β, the angle spanning the $\langle 100 \rangle$ and $\langle 001 \rangle$ directions, is mirrored by a simultaneous increase of the complementary angle spanning the $\langle 100 \rangle$ and $\langle 00\bar{1} \rangle$ directions (Fig. 6b). From a structural perspective an angle β close to 90 ° results in adjacent

144

cyclic dimers being almost perfectly stacked on top of each other both in the *a* and *c* direction, despite this is not being a requirement imposed by symmetry. The evolution of β may then be explained as being due to a subtle displacement of the cyclic dimers relative to each other as a function of temperature (Fig. 6b.). Furthermore, the distances between the central atoms of the diagonally opposing $FeO_2(H_2O)_4$ and SO_4 units (Fig. 6b), are increasing upon cooling from 9.91385(3) Å (290 K) to 9.92414(3) Å (21 K) in the ⟨101⟩ direction (i.e., approximately ∥ $α_1$) and shrinking from 9.98531(3) Å (290 K) to 9.90118(3) Å (21 K) in the ⟨10$\bar{1}$⟩ (i.e., approximately ∥ $α_3$). Lastly, the relatively smaller thermal expansion in the *a* than the *c* direction (Fig. 6c) may be attributed to a denser population of the dimer units in this direction.
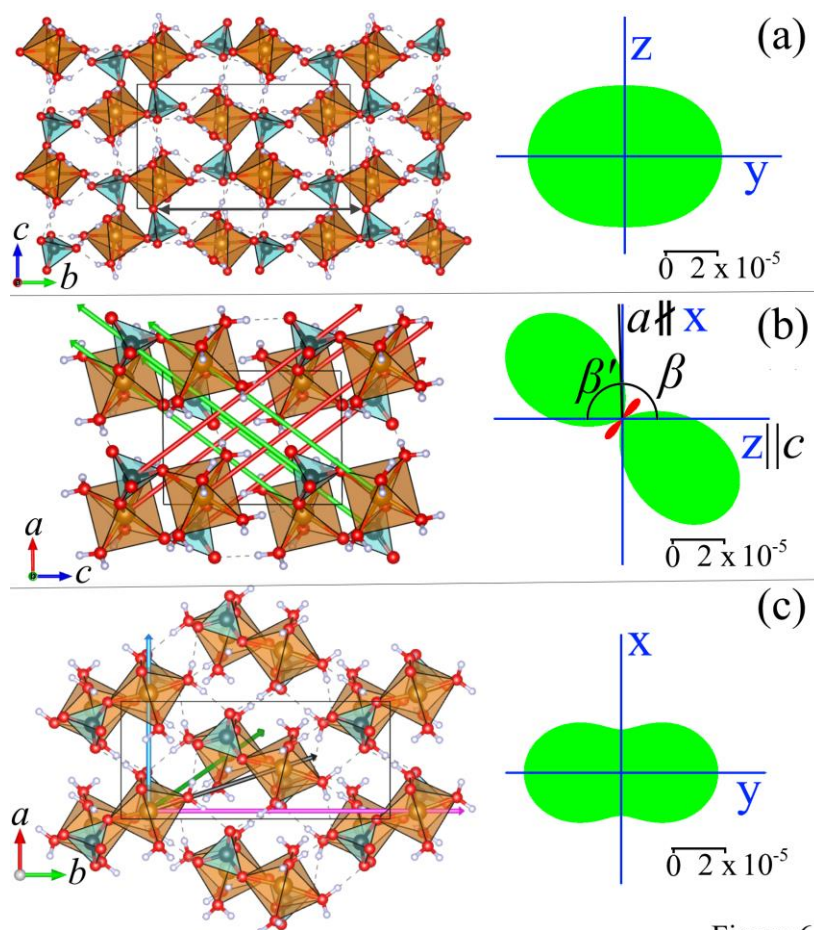
Figure 6

Fig. 6. View of the crystal structure (left) and cross-sections of the thermal expansion tensor for rozenite (green represents positive, red negative values) at 285 K (right). (a) view ∥ *a*: Large 'void' (black arrow: 11.932(5) Å at 290 K and 11.878(5) Å at 21 K) ∥ *b* as well as absence of hydrogen bonding in this direction allows the structure to experience substantial expansion and contraction in this direction as compared to the *c*-direction. (b) view ∥ *b*: Red arrows point ∥ ⟨101⟩ (i.e., the direction of negative thermal expansion, whereas green arrows are oriented ⟨10$\bar{1}$⟩ (i.e., the direction of maximum thermal expansion). The cyclic dimer units are stacked on top of each other and oriented by the angle of β (~90 °). Furthermore, the distance between diagonally opposing Fe and S atoms (connected by the red and green arrows) is increasing upon cooling shrinking in the direction of maximum thermal expansion. (c) view ∥ *c*: arrows point towards to the central atoms of the $FeO_2(H_2O)_4$ units of neighboring $FeO_2(H_2O)_4$ units.

Comparing these findings to other hydrated sulfate minerals it is evident that both large thermoelastic anisotropy and negative linear thermal expansion in particular is a rather common phenomenon in such materials. Negative linear expansion has been observed in epsomite ($MgSO_4 \cdot 7H_2O$) (Fortes et al., 2006), meridianiite ($MgSO_4 \cdot 11H_2O$) (Fortes et al., 2008), and most recently several members of the kieserite group ($M^{2+}SO_4 \cdot H_2O$ with M^{2+} = Mg, Fe, Co, Ni) (Wildner et al., 2022). The negative thermal expansion found in our study is smaller than in $MgSO_4 \cdot 7H_2O$, $MgSO_4 \cdot H_2O$, $FeSO_4 \cdot H_2O$, $CoSO_4 \cdot H_2O$ and of approximately the same magnitude as in $NiSO_4 \cdot H_2O$ and $MgSO_4 \cdot 11H_2O$ (Tab. 5). The volume thermal expansion of rozenite is intermediate between values found in the higher hydrates (e.g., $MgSO_4 \cdot 7H_2O$ and $MgSO_4 \cdot 11H_2O$) and in the lower hydrates (e.g., $FeSO_4 \cdot H_2O$ and $MgSO_4 \cdot H_2O$) (Tab. 5).

Compound	NTE (K^{-1})		T_{ref}	VTE expansion	T_{ref} (K)	Source
$MgSO_4 \cdot 11H_2O$	−1.2(5)	x	50	6.8(4) x 10^{-5}	240	Fortes et al. (2008)
$MgSO_4 \cdot 7H_2O$	−2.0(2)	x	125	10.8(3) x 10^{-5}	290	Fortes et al. (2006)
$FeSO_4 \cdot 4H_2O$	−1.0(2)	x	285	8.2(5) x 10^{-5}	285	This study
$MgSO_4 \cdot H_2O$	−4.4(3)	x	293	3.4(7) x 10^{-5}	293	Wildner et al. (2022)
$FeSO_4 \cdot H_2O$	−1.7(2)	x	293	4.7(5) x 10^{-5}	293	Wildner et al. (2022)
$CoSO_4 \cdot H_2O$	−2.7(2)	x	293	3.3(3) x 10^{-5}	293	Wildner et al. (2022)
$NiSO_4 \cdot H_2O$	−0.8(5)	x	293	3.6(4) x 10^{-5}	293	Wildner et al. (2022)

Tab. 5. Comparison of the negative (NTE) and volume (VTE) thermal expansion of various $M^{2+}SO_4 \cdot nH_2O$.

These trends in the volume thermal expansion reflect the changing degree of polymerization of the $M^{2+}O_x(H_2O)_{6-x}$ and SO_4 units as a function of hydration state, n, changing from isolated polyhedra (n = 6 to 11) through cyclic dimers and chains (n = 3 to 5) to rigid 3D corner-sharing frameworks (n = 1).

4.3.3 Vibrational properties of rozenite and absence of phase transition

Hydrated sulfate minerals may de- or rehydrate under changing relative humidity conditions. Thus, it is possible that a sample or a fraction might transform after its identity and phase purity is confirmed by X-ray diffraction and any subsequent measurements may not reflect the original state. Fig. 7(a, b) displays a comparison of the Raman spectra as observed by Chio et al. (2007) and in this study, both inside and outside the glass capillary. Although the background is increased for the measurement performed through the borosilicate glass, a comparison with data collected outside of the capillary demonstrates that

no additional sharp bands that might be mistaken for Raman-active vibrational modes appear in the spectrum (Fig. 7a).
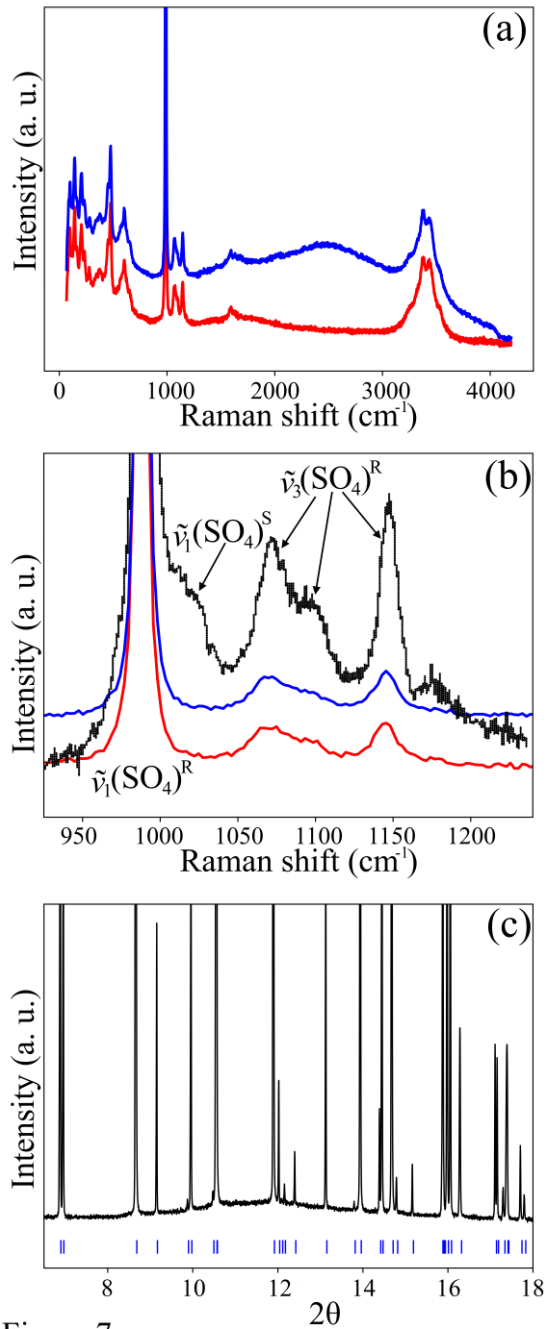
Figure 7

Fig. 7. (a) Raman spectra for rozenite acquired in this study outside (red) and inside (blue) of a borosilicate glass capillary. (b) Selected spectral range for comparison between our data (red and blue curves) and Chio et al. (2007) (black curve). (c) The phase purity of our sample has been confirmed by means of synchrotron X-ray diffraction, suggesting that the shoulder at 1018 cm^{-1} in the Chio et al. (2007) spectrum (black) stems from a contamination of the sample with szomolnokite. $\tilde{v}(SO_4)^R$ and $\tilde{v}(SO_4)^S$ refer to the sulfate stretching modes assigned to rozenite and szomolnokite, respectively. The Raman spectrum reported by Chio et al. (2007) was digitized using the Webplotdigitizer tool (Rohatgi, 2021). The intensity in all graphs was normalized with respect to the maximum intensity.

Synchrotron X-ray diffraction analysis performed on the capillary sample confirms the phase purity of the material (Fig. 7c). As for the data collected by Chio et al. (2007), these authors noted that a shoulder at 1018 cm^{-1} observed in their Raman spectra likely originate from szomolnokite impurities. A comparison of the Raman spectra collected in this study in and outside of the glass capillary shows the absence of the 1018 cm^{-1} band for phase pure rozenite (Fig. 7b), thus confirming this hypothesis. For this reason, acquiring Raman spectra and performing X-ray diffraction on the same capillary, appears to be a suitable workflow in order to produce reliable fingerprint spectra for salt hydrate phases whose hydration state is susceptible to changes in relative humidity.

The neutron diffraction results clearly demonstrate the absence of any structural phase transition down to at least 21 K. This raises the question of how the vibrational mode splitting observed by Chio et al. (2007) may be explained. To understand this problem, we have computed the spatial frequencies of the Raman-active vibrational modes of rozenite from first principles (Fig. 8).

DFT predicts a total of 16 Raman-active vibrational modes in the region of the H_2O stretching modes (Fig. 8a). Therefore, assuming the occurrence of vibrational mode splitting and consequently a structural phase transition is not necessary in order to explain the 10 bands evidenced by Chio et al. (2007) at temperatures lower than 90 K. We further note that our computation suggests that several of the water stretching modes are overlapping; thus merely 10 instead of the total of 16 Raman-active modes are resolvable even at temperatures as low as 8 K.
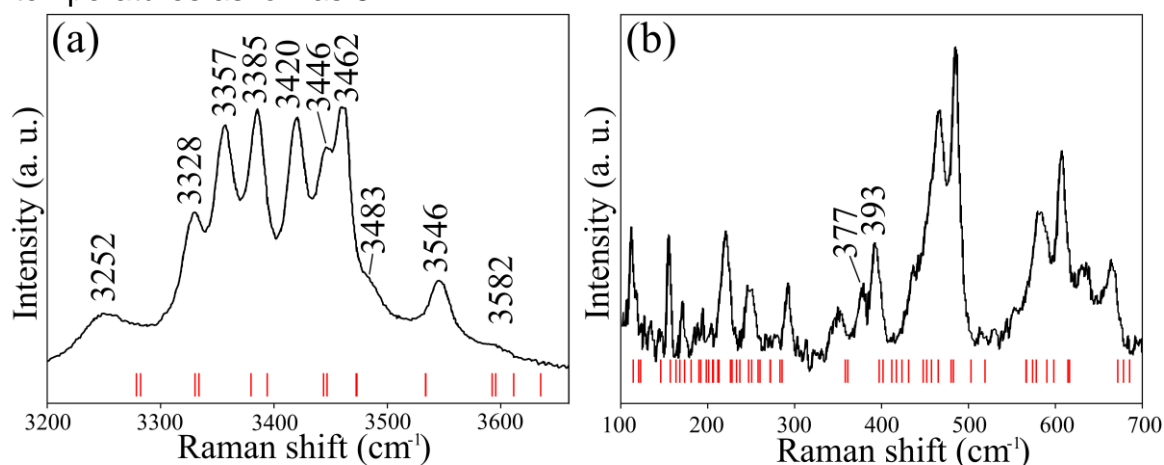
Figure 8

Fig. 8. Spectral region of the (a) water stretching vibration and (b) external modes of the Raman spectrum acquired by Chio et al. (2007) at 8 K. Red markers indicate the Raman-active vibrational mode positions as predicted by DFT. The Raman spectrum reported by Chio et al. (2007) was digitized using the Webplotdigitizer tool (Rohatgi, 2021).

The same holds true for the putative splitting of a mode located in the spectral region of the external vibrations (Fig. 8b) where our ab initio calculations also predict two Raman-active vibrational modes as closely spaced as 2.9 cm^{-1}. Therefore, we conclude that the putative splitting of vibrational modes is a misinterpretation of the sharpening of these modes upon cooling.

Both our DFT calculations as well as group theoretical analysis within the C_{2h} point group using the SAM tool (Kroumova et al., 2003) as implemented in the Bilbao Crystallographic Server (Aroyo et al., 2006) predict a total of 108 Raman active modes ($54A_g + 54B_g$). Since first principle calculations at the Γ-point also yield the frequency of the IR-active modes as well as of the acoustic phonon modes we further note that rozenite exhibits 105 IR active optical modes ($53A_u + 52B_u$) as well as 3 ($A_u + 2B_u$) acoustic phonon modes, totaling to 216 phonon modes of which 213 may be assigned to the optical branch and 3 to the acoustic one. The frequency and symmetry for each of the Raman (Tab. S5) and IR-active (Tab. S6) vibrational modes computed from first principles are provided in the supplementary material. Ruggiero et al. (2015) have also modelled the vibrational properties of rozenite from first principles and curiously reported a total of 213 IR-active vibrational modes (Table S3 in supplementary material of Ruggiero et al. (2015)), at odd with both our first principles calculations as well as our group theoretical analysis. Based on the very low intensity reported for several modes i.e., of the 32 modes in the O – H stretching region 16 exhibit an intensity of less than 5% of the strongest IR active O – H stretching mode, and a total number of 213 IR-active modes which corresponds to the number of optical modes obtained in our study, we believe that Ruggiero et al. (2015) computed the Γ-point frequencies of the complete set of optical vibrational modes but wrongly assigned them all to be IR-active. Comparing the vibrational frequencies of the O – H stretching modes obtained by Ruggiero et al. (2015) (i.e., 3451.2 – 3807.3 cm^{-1}) and the ones computed in our study (3278.7 – 3635.3 cm^{-1}) to the experimental values (3252 – 3582 cm^{-1}), it is evident that our calculations predict the vibrational mode frequencies much more accurately. Ruggiero et al. (2015) computed the vibrational frequencies at a higher level of theory and substantially higher computational cost using the B3LYP hybrid functional, yet again proving the effectiveness of the self-consistent DFT + U approach (Kulik et al., 2006; Timrov et al., 2021) in accurately predicting the material properties of transition metal compounds at a fraction of the computational cost.

4.4 Implications

We have demonstrated, by combining neutron diffraction with ab initio calculation within the framework of DFT, that the known monoclinic phase of rozenite is structurally stable over the entire temperature range it might be exposed to on the Martian surface and does not undergo any structural phase transition down to temperatures of at least 21 K. Rozenite is amongst the most promising candidates for the polyhydrated sulfate phase on the Martian surface. Constraining the low temperature stability and vibrational fingerprint of candidate phases such as rozenite is of vital importance to understand both the climatological history as well as for the future colonization of Mars. Characterization of the stratigraphic sequence (i.e., sulfate vs clay mineral layers) of the polyhydrated sulfate deposits may enable us to decipher the nature, drivers and onset of changing environmental conditions during the planet's early history.

As for the future colonization of Mars, hydrated sulfate minerals may be a valuable resource in the equatorial region where water ice is unstable (Feldman et al., 2004). Therefore, it is not only important to merely delineate between various mineral families, but a detailed mineralogical phase identification, including the mineral's hydration state, is crucial. For instance, 321 mL of water may be extracted from one kg rozenite, whereas complete dehydration of the same amount of the monohydrate yields 106 mL. Moreover, rozenite may be dehydrated to szomolnokite at 315 K, producing 241 mL H_2O/kg, whereas complete desiccation of szomolnokite to anhydrous $FeSO_4$ takes place at much higher temperature (approximately 500 K) (Kanari et al., 2018). In contrast, the dehydration of rozenite to szomolnokite is more efficient process, thus making it a potentially valuable resource for the extraction of water on Mars.

Raman spectroscopy has proven to be a very effective tool in discriminating between the various hydrated mineral species (Košek et al., 2017), but such efficacy relies on an accurate spectral library of the most promising candidate phases. As part of the scientific payload of the Perseverance Rover the first two Raman spectrometer were successfully deployed on the Martian surface (Bhartia et al., 2021; Wiens et al., 2020). The European Space Agency's Rosalind Franklin Rover (Rull et al., 2017), which is expected to land on the Martian surface in 2023, will also rely on Raman spectroscopy for mineralogical phase identification. Accurate vibrational fingerprint data is becoming increasingly important in planetary exploration. In our study, we have

demonstrated that the challenges associated with the sensitivity of the sample material to changing relative humidity conditions may be circumvented by analyzing the sample inside a glass capillary and performing synchrotron X-ray diffraction on the very same capillary. Lastly, we want to highlight the role DFT may play in vibrational mode assignment and interpretation, in particular at low-temperatures where sharpening of vibrational modes might be misinterpreted as mode splitting. This will become even more important in the future as computational resources become cheaper and more readily available, and likewise quantum chemical codes become increasingly user friendly and optimized for high-throughput calculations. Combining such calculations with experimentally determined reference spectra will enable the construction of a reliable Raman spectroscopic database for planetary exploration, which will be invaluable to shed light on the geological past as well as in identifying resources for the future colonization of planetary bodies in the solar system.

4.5 Acknowledgment

4.6 References

Albinati, A., and Willis, B.T.M. (1982) The Rietveld method in neutron and X-ray powder diffraction. Journal of Applied Crystallography, 15, 361–374.

Alig, H., Losel, J., and Trömel, M. (1994) Zur Kristallchemie der Wasserstoff–Sauerstoff-Bindungen. Zeitschrift für Kristallographie - Crystalline Materials, 209, 18–21.

Amadon, B., Jollet, F., and Torrent, M. (2008) γ and β cerium: LDA+U calculations of ground-state parameters. Physical Review B, 77, 155104.

Anderson, J.L., Peterson, R.C., and Swainson, I. (2012) The atomic structure of deuterated boyleite $ZnSO_4 \cdot 4D_2O$, ilesite $MnSO_4 \cdot 4D_2O$, and bianchite $ZnSO_4 \cdot 6D_2O$. American Mineralogist, 97, 1905–1914.

Angel, R.J. (2011) Win_Strain4. Padova.

Aroyo, M.I., Perez-Mato, J.M., Capillas, C., Kroumova, E., Ivantchev, S., Madariaga, G., Kirov, A., and Wondratschek, H. (2006) Bilbao Crystallographic Server: I. Databases and crystallographic computing programs. Zeitschrift für Kristallographie - Crystalline Materials, 221, 15–27.

Baur, W.H. (1962) Zur Kristallchemie der Salzhydrate. Die Kristallstrukturen von $MgSO_4.4H_2O$ (leonhardtit) und $FeSO_4.4H_2O$ (rozenit). Acta Crystallographica, 15, 815–826.

——— (1964) On the crystal chemistry of salt hydrates. II. A neutron diffraction study of $MgSO_4.4H_2O$. Acta Crystallographica, 17, 863–869.

——— (1972) Prediction of hydrogen bonds and hydrogen atom positions in crystalline solids. Acta Crystallographica Section B, 28, 1456–1465.

——— (2002) Zinc(II) sulfate tetrahydrate and magnesium sulfate tetrahydrate. Addendum. Acta Crystallographica Section E, 58, e9–e10.

Bhartia, R., Beegle, L.W., DeFlores, L., Abbey, W., Razzell Hollis, J., Uckert, K., Monacelli, B., Edgett, K.S., Kennedy, M.R., Sylvia, M., and others (2021) Perseverance's Scanning Habitable Environments with Raman and Luminescence for Organics and Chemicals (SHERLOC) Investigation. Space Science Reviews, 217, 58.

Bibring, J.-P., Langevin, Y., Gendrin, A., Gondet, B., Poulet, F., Berthé, M., Soufflot, A., Arvidson, R., Mangold, N., Mustard, J., and others (2005) Mars Surface Diversity as Revealed by the OMEGA/Mars Express Observations. Science, 307, 1576–1581.

Bibring, J.-P., Langevin, Y., Mustard, J., Poulet, F., Arvidson, R., Gendrin, A., Gondet, B., Mangold, N., Berthé, M., Gomez, C., and others (2006) Global Mineralogical and Aqueous Mars History Derived from OMEGA/Mars Express Data. Science (New York, N.Y.), 312, 400–404.

Bishop, J.L., Parente, M., Weitz, C.M., Noe Dobrea, E.Z., Roach, L.H., Murchie, S.L., McGuire, P.C., McKeown, N.K., Rossi, C.M., Brown, A.J., and others (2009) Mineralogy of Juventae Chasma: Sulfates in the light-toned mounds, mafic minerals in the bedrock, and hydrated silica and hydroxylated ferric sulfate on the plateau. Journal of Geophysical Research: Planets, 114.

Brese, N.E., and O'Keeffe, M. (1991) Bond-valence parameters for solids. Acta Crystallographica Section B, 47, 192–197.

Brown, I.D., and Altermatt, D. (1985) Bond-valence parameters obtained from a systematic analysis of the Inorganic Crystal Structure Database. Acta Crystallographica Section B, 41, 244–247.

Carter, J., Poulet, F., Bibring, J.-P., Mangold, N., and Murchie, S. (2013) Hydrous minerals on Mars as seen by the CRISM and OMEGA imaging spectrometers: Updated global view. Journal of Geophysical Research: Planets, 118, 831–858.

Chio, C., Sharma, S., and Muenow, D. (2007) The hydrates and deuterates of ferrous sulfate ($FeSO_4$): A Raman spectroscopic study. Journal of Raman Spectroscopy, 38, 87–99.

Cococcioni, M., and de Gironcoli, S. (2005) Linear response approach to the calculation of the effective interaction parameters in the LDA + U method. Physical Review B, 71, 35105.

Dudarev, S.L., Botton, G.A., Savrasov, S.Y., Humphreys, C.J., and Sutton, A.P. (1998) Electron-energy-loss spectra and the structural stability of nickel oxide: An LSDA+U study. Physical Review B, 57, 1505–1509.

Feldman, W., Mellon, M., Maurice, S., Prettyman, T., Carey, B., Vaniman, D., Bish, D., Claire, F., Chipera, S., Kargel, J., and others (2004) Hydrated states of $MgSO_4$ at equatorial latiudes on Mars. Geophysical Research Letters, 31, L16702-4.

Floris, A., de Gironcoli, S., Gross, E.K.U., and Cococcioni, M. (2011) Vibrational properties of MnO and NiO from DFT + U-based density functional perturbation theory. Physical Review B, 84, 161102.

Floris, A., Timrov, I., Himmetoglu, B., Marzari, N., de Gironcoli, S., and Cococcioni, M. (2020) Hubbard-corrected density functional perturbation theory with ultrasoft pseudopotentials. Physical Review B, 101, 64305.

Fortes, A.D., Wood, I.G., Alfredsson, M., Vočadlo, L., and Knight, K.S. (2006) The thermoelastic properties of $MgSO_4 \cdot 7D_2O$ (epsomite) from powder neutron diffraction and ab initio calculation. European Journal of Mineralogy, 18, 449–462.

Fortes, A.D., Wood, I., and Knight, K. (2008) The crystal structure and thermal expansion tensor of $MgSO_4 \cdot 11D_2O$ (meridianiite) determined by neutron powder diffraction. Physics and Chemistry of Minerals , 35, 207–221.

Garrity, K.F., Bennett, J.W., Rabe, K.M., and Vanderbilt, D. (2014) Pseudopotentials for high-throughput DFT calculations. Computational Materials Science, 81, 446–452.

Giannozzi, P., Baroni, S., Bonini, N., Calandra, M., Car, R., Cavazzoni, C., Ceresoli, D., Chiarotti, G.L., Cococcioni, M., Dabo, I., and others (2009) QUANTUM ESPRESSO: a modular and open-source software project for quantum simulations of materials. Journal of Physics: Condensed Matter, 21, 395502.

Giannozzi, P., Andreussi, O., Brumme, T., Bunau, O., Buongiorno Nardelli, M., Calandra, M., Car, R., Cavazzoni, C., Ceresoli, D., Cococcioni, M., and others (2017) Advanced capabilities for materials modelling with Quantum ESPRESSO. Journal of Physics: Condensed Matter, 29, 465901.

Gómez-Elvira, J., Armiens, C., Carrasco, I., Genzer, M., Gómez, F., Haberle, R., Hamilton, V.E., Harri, A.-M., Kahanpää, H., Kemppinen, O., and others (2014) Curiosity's rover environmental monitoring station: Overview of the first 100 sols. Journal of Geophysical Research: Planets, 119, 1680–1688.

Greenspan, L. (1977) Humidity Fixed Points of Binary Saturated Aqueous Solutions. Journal of Research of the National Bureau of Standards. Section A, Physics and Chemistry, 81A, 89–96.

Grimme, S. (2006) Semiempirical GGA-type density functional constructed with a long-range dispersion correction. Journal of Computational Chemistry, 27, 1787–1799.

Held, P., and Bohaty, L. (2002) Manganese(II) sulfate tetrahydrate (ilesite). Acta Crystallographica Section E, 58, i121–i123.

Hohenberg, P., and Kohn, W. (1964) Inhomogeneous Electron Gas. Physical Review, 136, B864–B871.

Hudson-Edwards, K.A., Schell, C., and Macklin, M.G. (1999) Mineralogy and geochemistry of alluvium contaminated by metal mining in the Rio Tinto area, southwest Spain. Applied Geochemistry, 14, 1015–1030.

Jambor, J., Nordstrom, D., and Alpers, C. (2000) Metal-sulfate Salts from Sulfide Mineral Oxidation. Reviews in Mineralogy and Geochemistry, 40, 303–350.

Kanari, N., Menad, N.-E., Ostrosi, E., Shallari, S., Diot, F., Allain, E., and Yvon, J. (2018) Thermal Behavior of Hydrated Iron Sulfate in Various Atmospheres. Metals, 8.

Kellersohn, T. (1992) Structure of cobalt sulfate tetrahydrate. Acta Crystallographica Section C, 48, 776–779.

Klingelhöfer, G., Morris, R. v, Bernhardt, B., Schröder, C., Rodionov, D.S., de Souza, P.A., Yen, A., Gellert, R., Evlanov, E.N., Zubkov, B., and others (2004) Jarosite and Hematite at Meridiani Planum from Opportunity's Mössbauer Spectrometer. Science, 306, 1740.

Kohn, W., and Sham, L.J. (1965) Self-Consistent Equations Including Exchange and Correlation Effects. Physical Review, 140, A1133–A1138.

Košek, F., Culka, A., Drahota, P., and Jehlička, J. (2017) Applying portable Raman spectrometers for field discrimination of sulfates: Training for successful extraterrestrial detection. Journal of Raman Spectroscopy, 48, 1085–1093.

Kroumova, E., Aroyo, M.I., Perez-Mato, J.M., Kirov, A., Capillas, C., Ivantchev, S., and Wondratschek, H. (2003) Bilbao Crystallographic Server : Useful Databases and Tools for Phase-Transition Studies. Phase Transitions, 76, 155–170.

Kulik, H.J., Cococcioni, M., Scherlis, D.A., and Marzari, N. (2006) Density Functional Theory in Transition-Metal Chemistry: A Self-Consistent Hubbard U Approach. Physical Review Letters, 97, 103001.

Langevin, Y., Poulet, F., Douté, S., Vincendon, M., Bibring, J.-P., Gondet, B., Forget, F., Montmessin, F., and Schmitt, B. (2006) The Vis/NIR OMEGA imaging spectrometer on-board Mars Express.

Meusburger, J.M., Ende, M., Talla, D., Wildner, M., and Miletich, R. (2019) Transformation mechanism of the pressure-induced $C2/c$-to-$P\bar{1}$ transition in ferrous sulfate monohydrate single crystals. Journal of Solid State Chemistry, 277.

Meusburger, J.M., Hudson-Edwards, K.A., Tang, C.C., Crane, R.A., and Fortes, A.D. (2021) Elasticity of selected icy satellite candidate materials (CO_2, C_6H_6, $MgSO_4 \cdot 7H_2O$ and $CaSO_4 \cdot 2H_2O$) revisited by dispersion corrected density functional theory. Icarus, 114611.

Meusburger, J.M., Hudson-Edwards, K.A., Tang, C.T., Connolly, E.T., Crane, R.A., and Fortes, A.D. (2022) Low-temperature crystallography and vibrational properties of rozenite ($FeSO_4 \cdot 4H_2O$), a candidate mineral component of the polyhydrated sulfate deposits on Mars. Materials Cloud Archive.

Mitchell, A.G. (1984) The preparation and characterization of ferrous sulphate hydrates. Journal of Pharmacy and Pharmacology, 36, 506–510.

Momma, K., and Izumi, F. (2011) VESTA3 for three-dimensional visualization of crystal, volumetric and morphology data. Journal of Applied Crystallography, 44, 1272–1276.

Monkhorst, H.J., and Pack, J.D. (1976) Special points for Brillouin-zone integrations. Phys. Rev. B, 13, 5188–5192.

Nordstrom, D. (2011) Mine Waters: Acidic to Circmneutral. Elements, 7.

Perdew, Burke, and Ernzerhof (1996) Generalized Gradient Approximation Made Simple. Physical review letters, 77 18, 3865–3868.

Pfrommer, B.G., Cote, M., Louie, S.G., and Cohen, M.L. (1997) Relaxation of crystals with the quasi-Newton method. Journal of Computational Physics, 131, 233–240.

Raczkowski, D., Canning, A., and Wang, L.W. (2001) Thomas-Fermi charge mixing for obtaining self-consistency in density functional calculations. Physical Review B, 64, 121101.

Roach, L.H., Mustard, J.F., Swayze, G., Milliken, R.E., Bishop, J.L., Murchie, S.L., and Lichtenberg, K. (2010) Hydrated mineral stratigraphy of Ius Chasma, Valles Marineris. Icarus, 206, 253–268.

Rohatgi, A. (2021) Webplotdigitizer: Version 4.5.

Ruggiero, M.T., Bardon, T., Strlič, M., Taday, P.F., and Korter, T.M. (2015) The role of terahertz polariton absorption in the characterization of crystalline iron sulfate hydrates. Physical Chemistry Chemical Physics, 17, 9326–9334.

Rull, F., Maurice, S., Hutchinson, I., Moral, A., Perez, C., Diaz, C., Colombo, M., Belenguer, T., Lopez-Reyes, G., Sansano, A., and others (2017) The Raman Laser Spectrometer for the ExoMars Rover Mission to Mars. Astrobiology, 17, 627–654.

Squyres, S.W., Grotzinger, J.P., Arvidson, R.E., Bell, J.F., Calvin, W., Christensen, P.R., Clark, B.C., Crisp, J.A., Farrand, W.H., Herkenhoff, K.E., and others (2004) In Situ Evidence for an Ancient Aqueous Environment at Meridiani Planum, Mars. Science, 306, 1709.

Steiner, T. (2002) The Hydrogen Bond in the Solid State. Angewandte Chemie International Edition, 41, 48–76.

Talla, D., and Wildner, M. (2019) Investigation of the kieserite–szomolnokite solid-solution series, $(Mg,Fe)SO_4 \cdot H_2O$, with relevance to Mars: Crystal chemistry, FTIR, and Raman spectroscopy under ambient and martian temperature conditions. American Mineralogist, 104, 1732–1749.

Thompson, S.P., Parker, J.E., Potter, J., Hill, T.P., Birt, A., Cobb, T.M., Yuan, F., and Tang, C.C. (2009) Beamline I11 at Diamond: A new instrument for high resolution powder diffraction. Review of Scientific Instruments, 80, 075107.

Timrov, I., Marzari, N., and Cococcioni, M. (2018) Hubbard parameters from density-functional perturbation theory. Physical Review B, 98, 85127.

——— (2021) Self-consistent Hubbard parameters from density-functional perturbation theory in the ultrasoft and projector-augmented wave formulations. Physical Review B, 103, 45141.

Toby, B.H. (2001) EXPGUI, a graphical user interface for GSAS. Journal of Applied Crystallography, 34, 210–213.

Tosca, N.J., McLennan, S.M., Clark, B.C., Grotzinger, J.P., Hurowitz, J.A., Knoll, A.H., Schröder, C., and Squyres, S.W. (2005) Geochemical modeling of evaporation processes on Mars: Insight from the sedimentary record at Meridiani Planum. Earth and Planetary Science Letters, 240, 122–148.

van Laar, B., and Schenk, H. (2018) The development of powder profile refinement at the Reactor Centre Netherlands at Petten. Acta Crystallographica Section A, 74, 88–92.

Wang, A., Jolliff, B.L., Liu, Y., and Connor, K. (2016) Setting constraints on the nature and origin of the two major hydrous sulfates on Mars: Monohydrated and polyhydrated sulfates. Journal of Geophysical Research: Planets, 121, 678–694.

Wiens, R.C., Maurice, S., Robinson, S.H., Nelson, A.E., Cais, P., Bernardi, P., Newell, R.T., Clegg, S., Sharma, S.K., Storms, S., and others (2020) The SuperCam Instrument Suite on the NASA Mars 2020 Rover: Body Unit and Combined System Tests. Space Science Reviews, 217, 4.

Wildner, M., Zakharov, B.A., Bogdanov, N.E., Talla, D., Boldyreva, E. v, and Miletich, R. (2022) Crystallography relevant to Mars and Galilean icy moons: crystal behavior of kieserite-type monohydrate sulfates at extraterrestrial conditions down to 15 K. IUCrJ, 9.

5. Phase-transition type negative volume expansion and anisotropic X-ray expansion in magnesium sulfate tetrahydrate

This chapter reports the thermal expansion of starkeyite and cranswickite as determined by means of synchrotron X-ray and neutron powder diffraction. Starkeyite suffers radiation damage, induced by the intense synchrotron X-ray beam, a phenomenon observed recently in inorganic compounds. The radiation damage was associated with an anisotropic unit-cell expansion. The X-ray expansion tensor r_{ij} is introduced which provides a solid theoretical foundation for the quantification of this phenomenon, which poses an intriguing avenue for future research in functional materials.

Furthermore, the theoretical low-temperature and high-pressure stability of both polymorphs within the framework of density functional theory, and put into context with their likely occurrence as rock-forming minerals in the interior of icy satellites.

Although the study was solely motivated by the importance of MSHs for planetary science, cranswickite and starkeyite revealed very interesting material properties which may be of great interest for the material science community.

Atomic coordinates and displacement parameters of the structures reported in this chapter can be found in Tab. S7 and Tab. S15 of the supplementary section 8.4.

Declaration: The contents of this chapter are intended for submission to *Angewandte Chemie International Edition*. Therefore, this chapter is formatted following to the requirements set out by this journal.

RESEARCH ARTICLE

Phase-transition type negative volume expansion and anisotropic X-ray expansion in magnesium sulfate tetrahydrate

Johannes M. Meusburger[a,b,c], Karen A. Hudson-Edwards*[a], Chiu C. Tang[b], Eamonn T. Connolly[b], Rich A. Crane[a], A. Dominic Fortes*[c]

Abstract: The search for negative thermal expansion materials is a vigorously active field of research, due to their potential application in functional metamaterials that are able to maintain a constant volume over a wide range of temperatures. Using neutron and synchrotron X-ray diffraction data we show here that $MgSO_4.4H_2O$ exhibits a hitherto unique combination of negative expansion characteristics. Firstly, the cranswickite phase of $MgSO_4.4H_2O$ exhibits classical negative linear thermal expansion along its c-axis that is balanced by a similar degree of positive expansion along the a-axis, resulting in a net zero area expansion in the a-c plane. Furthermore, the structure transforms at 330 K to starkeyite-type $MgSO_4.4H_2O$ with a 4.72% volume reduction, which is among the largest known phase-transition type negative expansivities. Finally, irradiation by synchrotron X-rays induces negative linear thermal expansion in starkeyite-type $MgSO_4.4H_2O$. The X-ray induced expansion is strongly anisotropic and we therefore advocate for a tensor description of this property. To this end, we introduce the X-ray expansion tensor r_{ij}, thus laying a solid theoretical foundation for the quantification of this phenomenon, which poses an intriguing avenue for future research in functional materials.

Introduction

Most materials expand upon heating and contract upon cooling, which we describe as 'normal' positive thermal expansion (PTE), but there are a growing number of exceptions where materials exhibit some form of negative thermal expansion (NTE). Similarly, most materials that undergo a solid–solid phase change as a function of temperature transform to a polymorph of lower density; i.e., the material expands on heating through the transition. Here again, there are a select few substances that behave in an atypical fashion, transforming to a denser polymorph on heating. We may thus subdivide NTE into two categories: conventional NTE, due to heating of a single phase and phase-transition type NTE, due to a polymorphic volume reduction[1]. Efforts to understand the mechanisms responsible for both types of NTE (e.g.,[2,3]) depend on the discovery of new materials that exhibit these properties, particularly in combination. This is a vigorously active field of research, the goal being to discover or design a material (or metamaterial) that ideally maintains a constant volume over a large temperature range[4–7]. This is important from the perspective of technological applications; a great many materials exhibit NTE at very low temperatures (e.g., ice[8]), which limits the scope of their use.

[a]   J. M. Meusburger, Prof. K. A. Hudson-Edwards, Dr. R. A. Crane
        Camborne School of Mines and Environment and Sustainability
        Institute, University of Exeter, Tremough Campus, Penryn TR10 9EZ,
        Cornwall, UK, E-mail: k.hudson-edwards@exeter.ac.uk
[b]   J. M. Meusburger, Prof. C. C. Tang, Dr. E. T. Connolly
        Diamond Light Source, Harwell Science and Innovation Campus, Fermi
        Avenue, Didcot OX11 0DE, Oxfordshire, UK
[c]   J. M. Meusburger, Dr. A. D. Fortes
        ISIS Neutron and Muon Source, STFC Rutherford Appleton Laboratory
        Harwell Science and Innovation Campus, Chilton, Didcot OX11 0QX,
        Oxfordshire, UK, Email: dominic.fortes@stfc.ac.uk

Potential applications are widespread ranging from every-day items such as dental fillings[9] and cooker hobs[10] through to high-precision optics[11], artificial muscles[12] and thermally-controlled drug delivery systems[13].

We have carried out systematic studies into the structure and properties of a number of $MgSO_4$ hydrates, which are candidate rock-forming minerals and potentially important environmental markers on Mars[14] and the icy satellites of the outer solar system[15]. As part of this work, we have characterized the behaviour of $MgSO_4·4H_2O$ as a function of temperature using a combined experimental (i.e., neutron and synchrotron powder diffraction) and theoretical (i.e., dispersion corrected density functional theory) approach. Magnesium sulfate tetrahydrate exists as two polymorphs, both of which occur naturally. The mineral starkeyite was structurally characterized 60 years ago using X-rays and neutrons[16,17] and consists of corner-sharing MgO_6 and SO_4 polyhedra arranged into cyclic dimers cross-linked by O–H···O hydrogen bonds. The more recently-discovered form, cranswickite, has only been studied by X-ray powder diffraction methods[18] and is built from the same corner-sharing polyhedral units, but these are arranged into infinite chains. Up to now, cranswickite has never been produced synthetically and the conditions required for its formation have been unclear.

The results, described here, show that this material exhibits a surprising combination of the unusual thermal expansion properties outlined above, including uniaxial NTE that – when combined with a very similar uniaxial PTE along an orthogonal direction – results in a net zero *area* expansion over a wide range of temperatures, and phase-transition type NTE (cranswickite → starkeyite) accompanied by one of the largest volume reductions ever reported. The latter is of particular importance since polymorphic phase transitions have been implicated in processes such as discontinuities of seismic wave propagation[21] which are exploited to probe the Earth's internal structure and composition, as well as deep earthquakes[19], and thus identifying such transitions in rock-forming minerals is of paramount importance for Earth and Planetary science. The phase-transition type NTE presented in this study is the first example where NTE is not only a phenomenon of technological interest but also a naturally occurring process, and based on the very large volume discontinuity associated with the transition, may have implications for the internal structure and dynamics of icy satellites in the outer solar system.

Furthermore, we have observed synchrotron X-ray induced radiation damage in starkeyite. Whilst this is a well-known phenomenon in organic compounds, radiation damage has only recently attracted attention from the inorganic chemistry community as a method for tuning the properties of functional materials[20–22]. Indeed, we demonstrate that irradiating starkeyite with intense synchrotron X-rays has a major influence on its thermal expansion, and even induces negative linear thermal expansion. Furthermore, we found the X-ray induced expansion

to be strongly anisotropic and therefore advocate for a tensor description of this property. To this end, we introduce the X-ray expansion tensor r_{ij}, thus laying a solid theoretical foundation for the quantification of this phenomenon, which poses an intriguing avenue for future research in functional materials.

Results and Discussion

Thermal expansion of cranswickite and starkeyite

The variable temperature lattice parameters of cranswickite (10 – 340 K, Tab. s14-15) and starkeyite (10 – 370 K, Tab. s10-13) measured in 10 K increments were treated following the polynomial extension of the Einstein approximation. Details of the fitting procedure are provided in the supporting information and fitted parameters are stated in Tab. S1 and Tab. S2. Both the experimentally-obtained lattice parameters and the model fits may be used to characterise the thermal expansion and its anisotropy. For a monoclinic crystal, symmetry dictates that only one of the three principal directions of the thermal expansion, which are mutually orthogonal, be aligned with a crystallographic axis, specifically the 2-fold axis of rotational symmetry; the other two directions are free to adopt any orientation, whilst remaining orthogonal to one another, with respect to the crystallographic basis. Hence, we require a tensor description of the thermal expansion, from which we obtain the eigenvalues and eigenvectors, these being the principal magnitudes of the thermal expansion and their direction cosines.

The Win_strain software[23] was used for the thermal expansion calculations and this allowed us to correlate the evolution of thermal expansivity to changes in the crystal structure (see next

Section). The orientation of the unit-cell with respect to the tensor reference system was specified following the Institute of Radio Engineer's convention (i.e., X // a^*, Z // c) and finite Lagrangian strains were computed incrementally between consecutive data points.

The analysis revealed highly anisotropic thermal expansion of the lattice-parameters as reflected by axial ratios of $\alpha_a : \alpha_b : \alpha_c$ of 1.00(6) : 3.84(5) : −1.33(4) at 295 K for cranswickite. Interestingly, the c-axis, displayed negative linear thermal expansion over the entire temperature range under investigation ($\alpha_c = -1.0(8) \times 10^{-6}$ (15 K) to $-3.62(9) \times 10^{-5}$ (335 K)) (Fig. 1ac). The thermal expansion parallel with a is of approximately the same magnitude but opposite sign, already pointing towards a very small, or zero, net expansion of the ac plane. Examination of the ratio of the principal direction magnitudes, $\alpha_1 : \alpha_2 : \alpha_3$ of −1.04(4) : 2.90(4) : 1.00(5) at 295 K reveals that the thermal expansion in the ac plane (i.e., (α_1 and α_3 are both constrained to lie in the ac plane) is zero within one standard deviation. Negative linear thermal expansion is a phenomenon very commonly observed in sulfate hydrates as it was reported for $MgSO_4 \cdot 11H_2O$[24], $MgSO_4 \cdot 7H_2O$[25], and most recently, for the kieserite-type compounds $MeSO_4 \cdot H_2O$[26] as well as $FeSO_4 \cdot 4H_2O$[27]. The magnitude of negative thermal expansion, observed in this study is intermediate between values observed for $MgSO_4 \cdot H_2O$ and $MgSO_4 \cdot 7H_2O$ (Tab. S3). Net zero thermal area expansion, however, is a much rarer phenomenon and hitherto has been
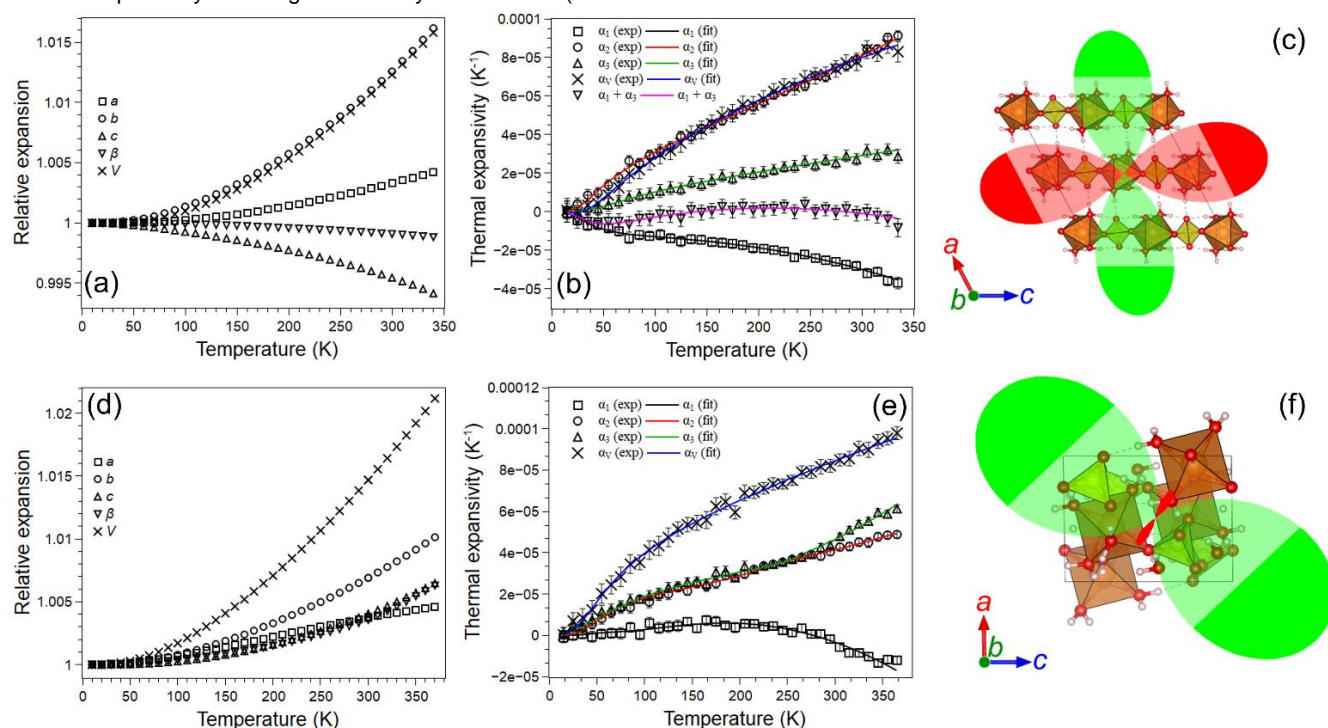
Fig. 1. The relative expansion of the lattice parameters, evolution of the thermal expansion tensor's eigenvalues and cross-section of the thermal expansion in the ac plane of cranswickite (a,b,c) and starkeyite (d,e,f). (b,e) Solid lines represent the Einstein model fit; Error bars were plotted as 3σ. (c,f) green represents positive, red negative thermal expansion. Note that both compounds exhibit positive and negative thermal expansion in this plane, that are in cranswickite even of the same magnitude but opposite sign resulting in a cancellation and consequently net zero area expansion. The coefficients (Tab. S18, Tab. S21) and eigenvalues (Tab. S19, Tab S22) of the thermal expansion tensor as well as the axial expansion (Tab. S20, Tab. S23) are reported in the supplement.

observed only in a few compounds such as $Ag_3[Co(CN)_6]$[28] and the Prussian Blue analogues $(C_3H_5N_2)_2K[Fe(CN)_6]$ and $(C_3H_5N_2)_2K[Co(CN)_6]$[29].

Importantly, we have also observed negative linear thermal expansion in starkeyite, reinforcing the statement, that it is a rather common phenomenon in magnesium sulfate hydrates. The thermal expansion tensor analysis of the lattice parameters obtained from a phase pure sample of starkeyite revealed, that the magnitude of the negative linear thermal expansion decreases with decreasing temperature and persists down to a temperature of 295 K, after which α_1 turns positive (Fig. 1e). At around 245 K we have observed a change in the slope of all three eigenvalues of the thermal expansion tensor. Importantly, the magnitudes of a_3 and α_2 are identical within 3σ from 245 to 15 K, indicating isotropic thermal expansion in the plane spanned by these two eigenvectors. In line with this change in thermal expansivity is the emergence of shoulder of the 212 Bragg peak, unaccounted for by the well-established $P2_1/n$ structural model (Fig. S2, Fig. S3). Clearly, one additional peak does not allow for the indexing of the putative low-temperature phase. The data were acquired with the HRPD instrument, one of the highest resolution neutron diffractometers in the world, and thus we want to stress that the failure of identifying indexable shoulders on additional peaks, is not a limitation of the resolution of the acquired data, but rather a tribute to the subtlety of the underlying effect.

Phase-transition type NTE

While heating the mixed cranswickite/starkeyite sample for 50 minutes at 330 K 1.0(2)% of cranswickite had transformed to starkeyite. The temperature was increased to 340 K in order to speed up and follow the transformation in-situ (Fig. 2a). Although, starkeyite is a common mineral in terrestrial environments and has been known for many decades[16], our observation of this polymorphic phase transition at high temperatures was entirely unexpected. Starkeyite is denser than cranswickite, thus a high temperature cranswickite to starkeyite phase transition clearly violates the density rule[30] i.e., the well-established and intuitive trend of crystals adapting a less dense arrangement of their atoms at higher temperatures. Whilst unexpected, there are an increasing number of precedents for such phase-transition induced NTE[1,5]. Importantly, the phase transition is associated with a volume decrease of 4.72 %, which is substantially larger than the values of 0.1 to 1% that are typically observed for NTE materials[5], and is in fact among the largest hitherto reported; we found that only AgI ($\Delta V/V$ = 5.3%)[31] exhibits a larger NTE. Regarding other compounds with potentially larger NTE, Nakamura et al. (1988)[32] report a volume discontinuity at 85 K in YMn_2 'of about 5%'. Calculating the volume changes from the reported lattice parameter data by means of XRD yields $\Delta V/V$ of only 1.42%, thus giving us reason to believe that the 5% value originates from the dilatometric measurements that were also performed in their study, and often give larger values than crystallographic volume changes derived by diffraction. The reason for this is, that diffraction experiments solely probe the crystallographic unit-cell changes and do not take into account microstructural effects that may enable a denser packing of the sample. On this note, Takenaka et al. (2017)[33] have reported $\Delta V/V$ of 6.7% as obtained by dilatometry compared to a value of 1% by diffraction for $Ca_2RuO_{3.74}$, with the authors further noting that the volume changes obtained by means of dilatometry may
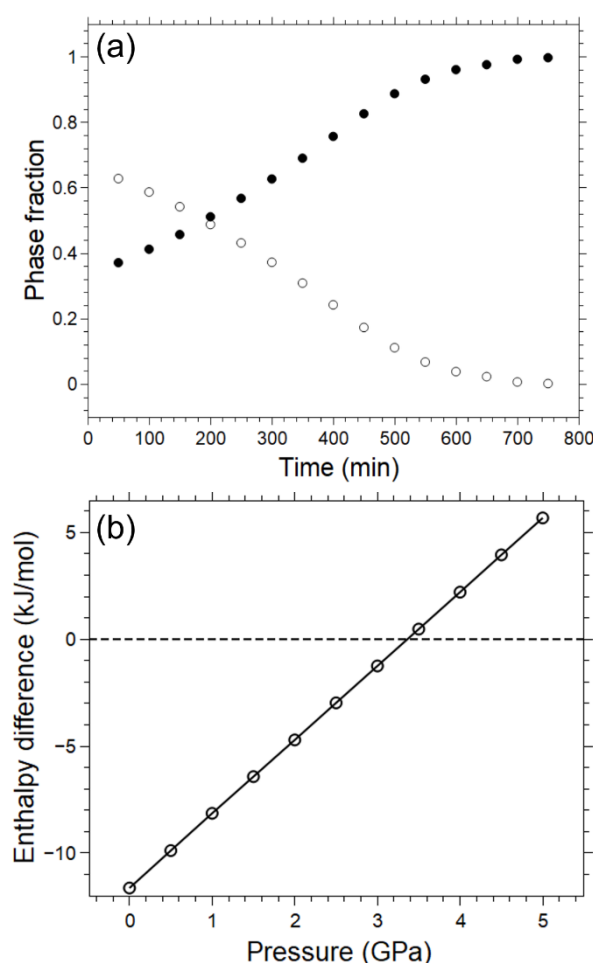
Fig 2. (a) Cranswickite (open circles) to starkeyite (filled circles) transformation at 340 K. Neutron diffraction patterns collected in 50 min intervals. It took a total of 11h 40 min, from the starting phase mixture containing 67.1(1) wt. % cranswickite and 32.9(1) wt. % starkeyite to transform to phase pure starkeyite. (b) Enthalpy difference $\Delta(H_{crans}-H_{stark})$ as obtained from dispersion corrected density functional theory predicts the cranswickite to starkeyite transformation at 3.36 GPa. In addition, the volume pressure data obtained by means of DFT was fitted using a third order Birch-Murnaghan Equation of State yielding following parameters: starkeyite (K = 36.3(4) GPa, K' = 5.1(2); cranswickite (K = 37.2(4) GPa, K' = 5.4(2)).

be up to ten times larger than the crystallographic unit-cell changes.

From an Earth and Planetary science perspective, such large volume discontinuities are of major interest since they may produce large elastic contrasts between rock layers and this affect seismic wave propagation from deep earthquakes. For example, the volume decrease associated with the cranswickite to starkeyite transitions is very close to a value of 5 %, reported for the pressure-induced olivine – wadsleyite transformation, which is the origin of the 410 km seismic discontinuity in Earth's mantle[34]. Clearly, sulfate minerals are of negligible importance for the terrestrial mantle, which is dominated by silicates[35]. On the outer three Galilean moons (i.e., Europa, Ganymede, Callisto) of Jupiter, however, hydrated magnesium sulfate minerals are believed to be major rock forming minerals[36,37]. This is supported by geochemical analysis of primitive chondritic meteorites, the fundamental building block of the rocky cores of the Jovian
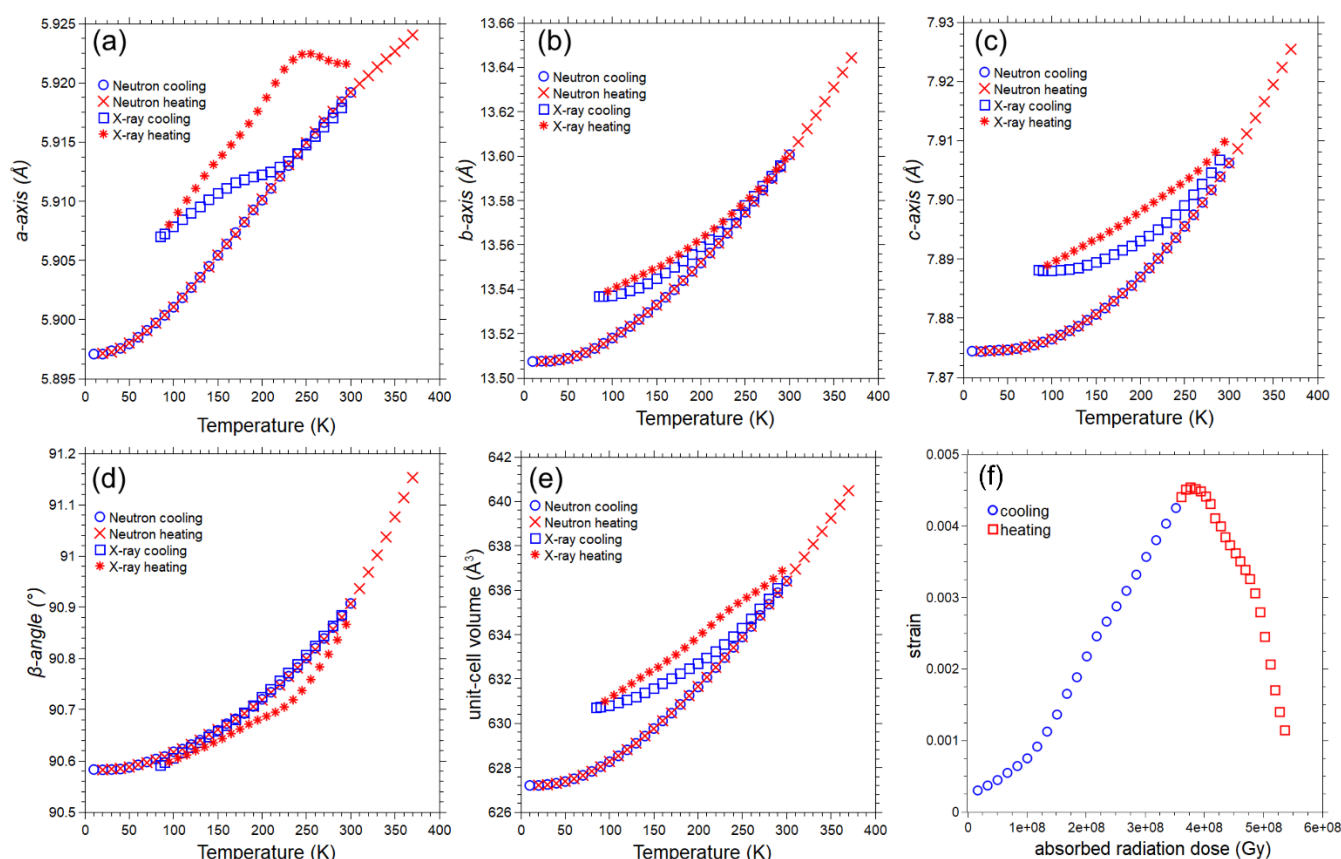
Fig. 3. (a-e) Lattice parameters and unit-cell of starkeyite as determined by neutron and synchrotron X-ray diffraction. (f) Finite Lagrangian strain as a function of Gray (Gy) which corresponds to J/Kg of accumulated dose.

satellites[38], where it is observed that MgSO$_4$ hydrates account for 75 wt. % of their soluble mass fraction[39]. Based on their likely abundance in such environments, it is not surprising that phase transitions in MgSO$_4$ hydrates, for instance the hydration of epsomite to meridianiite, have been implicated in processes such as cryovolcanism on Ganymede[40]. It is noteworthy that the volume decrease associated with the hydration of epsomite is only 3.16 %[40] and therefore substantially smaller than the volume decrease associated with the phase transition induced NTE of cranswickite (i.e, 4.72 %). For this reason, the cranswickite to starkeyite transition has a potential role to play in the structure and dynamics of the icy Jovian satellites, subject to the conditions that cranswickite indeed occurs in such environments. Indications in favour of the existence of cranswickite in the icy mantle of such planetary bodies are the precipitation of pentahydrite, which we have found to be a precursor phase in the formation of cranswickite, from brine of chondritic composition[41] as well as the discovery of cranswickite in terrestrial subsurface environments (i.e., in a borehole core extracted from a depth of 175 m[42]). Studying the relative stability of cranswickite and starkeyite at the pressures to which they might be subjected in the icy mantle of the Galilean moons by means of dispersion corrected density functional theory, demonstrates that cranswickite is the thermodynamically stable polymorph up to a maximum pressure of 3.36 GPa (Fig. 2b), after which a transformation to starkeyite is predicted. The large uncertainties, associated with models of the interior of icy satellites renders it challenging to ascertain at which depth the cranswickite to starkeyite transition might occur in these planetary bodies. However, we have demonstrated that starkeyite

is favoured both at high-temperature as well as high-pressures, both are expected to increase in planetary bodies with increasing depth. The potential seismic exploration of icy moons such as Titan and Europa in the future[43,44] promises to draw a more detailed picture of their internal structures, and might therefore eventually shed light on the potential role of the cranswickite to starkeyite transition in icy mantle dynamics. Lastly, we want to emphasize that although our initial interest in cranswickite originates solely from the importance of MgSO$_4$ hydrates as rock-forming minerals in the outer solar system, the implications of the curious thermal expansion observed in cranswickite are not necessarily restricted to this field. MgSO$_4$ hydrates and their large diverse families of related compounds (i.e., MTO$_4$·nH$_2$O with M = Ni^{2+}, Co^{2+}, Fe^{2+}, Fe^{3+}, Zn^{2+}, Mn^{2+}, Mn^{3+}, Ti^{2+}, V^{2+}; V^{3+}; T = Cr^{6+}, Se^{6+}, P^{5+}, As^{5+}; n = 0 - 11), find widespread applications ranging from fertilizer[45] and thermochemical energy storage[46], over harvesting drinking water from air in water-scarce regions[47] to battery materials[48,49]. Extensive substitution including complete solid solutions were reported for many of these systems (Fortes et al. 2012[50] and references therein), thus opening up the possibility to study both zero area expansion and negative thermal expansion, and the effect of doping with various cations and oxyanions on these phenomena. This is of particular importance since such doping experiments have demonstrated great potential to tailor the material properties of NTE materials[2,51–53]. As noted by Coates and Goodwin (2019)[5], the most exciting area for future research in NTE materials lies in maximising both the temperature range as well as the magnitude of the effect. As such, observing the second largest magnitude of NTE hitherto observed,
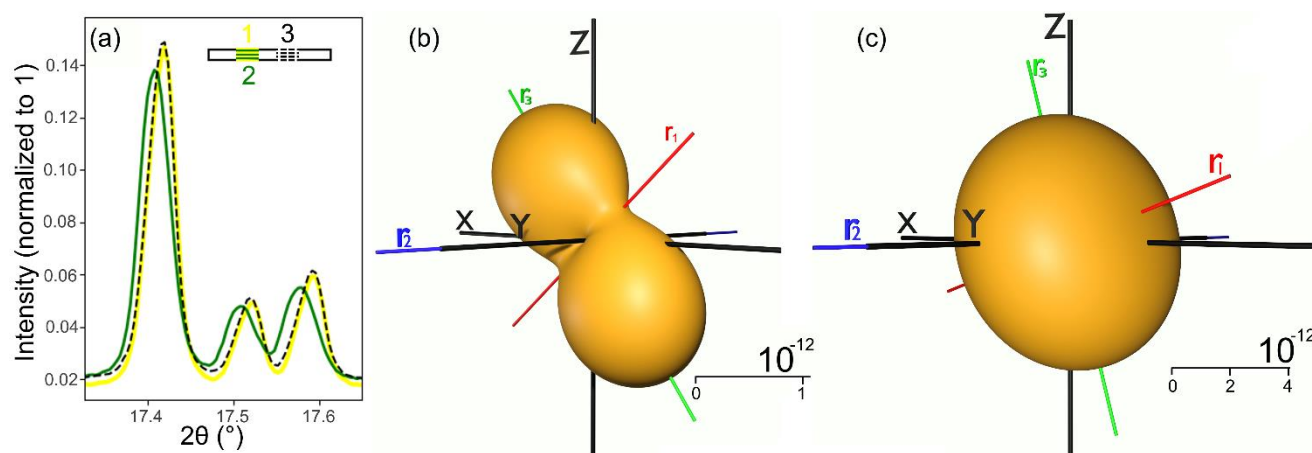
Fig. 4. (a) X-ray expansion of starkeyite. yellow pattern = start of the experiment (V = 636.725(6) Å), green pattern = after 16 hours of irradiation with a synchrotron X-ray beam of 2.5 mm width, clearly demonstrating a Bragg peak shift to higher d-spacing corresponding to positive volume expansion (V = 636.878 (7) Å). Black dashed line = also collected after the 16 hours of irradiation but 5 mm apart from the beam spot ((V = 636.727(6) Å). (b) graphical representation of the X-ray expansion tensor calculated after 16 hours of irradiation and reheating the sample to 295 K clearly demonstrates the anisotropy of X-ray expansion. (c1) representation surface of the X-ray expansion tensor at its maximum value after receiving a radiation dose of 0.37739 GGy.

in a system completely unrelated to previously reported NTE materials, clearly represents an important step towards the latter.

Anisotropic X-ray expansion of starkeyite

The thermal expansion of starkeyite was also measured by means of synchrotron X-ray diffraction (Fig. 3a-e). These results strongly contrast with the thermal expansion determined in the neutron powder diffraction experiment. To assess the difference, we calculated the corresponding finite Lagrangian strain at each temperature point between the neutron and X-ray derived lattice metrics (Fig. 3f). From this analysis it is evident that right from the start of the experiment, there is a subtle but continuous increase in the volumetric strain, reflecting the difference in thermal expansion between the neutron and X-ray irradiated samples. This continues until shortly after the completion of the initial cooling measurements after which the volumetric strain exhibits a decrease as the specimen is warmed back towards room temperature. Unlike the neutron diffraction measurements, where the lattice parameters obtained upon heating and cooling coincide perfectly (Fig. 3a-e. and Fig. S2), there is a pronounced hysteresis in the thermal expansion of starkeyite measured on heating and cooling during irradiation with synchrotron X-rays (Fig. 3a-e). The variations are not smooth but exhibit changes in slope, these being most obvious for the a-axis, which exhibits kinks in the cooling and warming curves at ~ 230 K (Fig. 3a). The most likely explanation for this behaviour is that the sample was damaged by the intense synchrotron radiation, which has a flux more than 8 orders of magnitude higher than the neutron beam used on HRPD, and the structural defects produced by the intense ionizing radiation become annealed out as the sample is heated. In order to test this hypothesis, we took a snapshot measurement of the sample after the experiment and compared it to a snapshot collected at the start of the experiment (Fig. 5a). Clearly, the peaks are systematically broadened and shifted towards lower diffraction angles, corresponding to higher d-spacings and thus positive expansion of the sample induced by the X-ray beam. Translating the capillary sample horizontally by 5 mm (corresponding to twice the beam-width, to a fresh section of the sample), yields a diffraction pattern that perfectly coincides with the pattern collected on the pristine sample at the start of the

experiment, thus serving as proof that the sample was altered by the beam. In order to quantify the X-ray induced volume expansion Coates et al., (2019) propose the σ parameter:

$$\sigma_V = \frac{1}{V}\frac{\Delta V}{\Delta \text{dose}}$$

Similarities between the σ_V parameter and the volumetric thermal expansion coefficient α_V are readily apparent, with the only difference between both parameters is that in σ_V the received radiation dose, rather than temperature is the property inducing strain. Since the compound studied by Coates et al. (2019)[20] exhibits cubic symmetry, the X-ray induced expansion is fully described by a single parameter.

We have observed for the first time that X-ray expansion is an anisotropic property, thus requiring a tensor description in order capture the full extent of the anisotropy of the X-ray expansion in low symmetry compounds such as monoclinic starkeyite. For this purpose, we introduce the X-ray expansion tensor r_{ij}, whereby the letter r is preferred over σ to avoid confusion with the stress tensor σ_{ij}. The X-ray expansion of a monoclinic solid may be described by a symmetrical second rank tensor of the form

$$\begin{matrix} r_{11} & 0 & r_{13} \\ 0 & r_{22} & 0 \\ r_{31} & 0 & r_{33} \end{matrix}$$

The components of the X-ray expansion tensor are related to the Lagrangian strain tensor ε_{ij} by

$$r_{ij} = \frac{\varepsilon_{ij}}{\Delta \text{dose}}$$

with Δdose being the total accumulated dose absorbed by the sample, and details on the dose calculation are provided in the supplementary information. Once the tensor components are known, determining the principal directions of the X-ray expansion tensor (r_1, r_2, and r_3) then is a simple eigenvalue problem of a 3 x 3 matrix. In analogy to the thermal expansion tensor the ratio between the principal axes of the X-ray expansion tensor r_1 : r_2 : r_3 reflects the anisotropy of this property and moreover indicate the directions of maximum and minimum X-ray expansion. The

relationship between the volumetric X-ray expansion r_V and the eigenvalues of the X-ray expansion tensor is $r_V = r_1 + r_2 + r_3$. From the Lagrangian strain tensor calculation it is evident that the strain does not continuously increase as a function of radiation dose (Fig.3f), but rather peaks at 0. 37739 GGy, a radiation dose reached at a temperature of 105 K, with $r_1 : r_2 : r_3$ of 1.000(7) : 1.314(6) : 1.365(6) and a corresponding volumetric X-ray expansion r_V of 12.030 TGy^{-1}. At even higher radiation doses, the strain rather counterintuitively diminishes to a point where it almost vanishes at the end of the experiment after reheating the sample to room temperature. At the end of the experiment when the sample had received the maximum accumulated radiation dose after reheating to 295 K we obtain $r_1 : r_2 : r_3$ of 1.00(13) : 5.13(10) : 15.36(9), thus reflecting a strong increase in the anisotropy of the X-ray expansion with respect to 105 K values (Fig. 4bc). The corresponding r_v value of 2.1221 TGy^{-1} is approximately three order of magnitudes smaller than values of - 2.98 GGy^{-1} and 3.3 GGy^{-1} reported for $Cd(CN)_2$ and protein crystals[20], respectively, and six times smaller than the maximum volumetric X-ray expansion achieved for starkeyite at 105 K. This is also reflected in the relative magnitude of the X-ray expansion tensors determined at the end of the experiment after reheating the sample to room temperature and the maximum value achieved at 105 K (Fig. 5c). As noted earlier, a plausible explanation for this behaviour is the production of structural defects by irradiation, with the defective structure then displaying a substantially different thermal expansion tensor compared with the pristine sample to such an extent that it even induces negative linear thermal expansion // a (Fig. 4a). Upon warming the production of such defects is reduced by a decrease of the acquisition time for each diffraction pattern from 30 to 15 minutes, thus annealing of these defects outpaces their ongoing production to the point where the sample recovers its original properties. As such, we agree with Coates et al. (2019)[20], that radiation effects, indeed might be useful to tune the thermal expansion of materials. In addition to tuning of the thermal expansion properties, synchrotron X-ray have previously been used to both induce[54] and suppress[20] phase transitions and have even been employed to tune the critical temperature of superconductivity[21]. With reference to the extraterrestrial environments mentioned previously, Jupiter's moon Europa is noteworthy for the high flux of ionizing radiation incident on its surface, both from Jupiter's trapped radiation belts and from Galactic Cosmic Rays. The calculated dose rate at 1 m depth below Europa's icy surface is 0.3 Gy yr^{-1} and so the cumulative dose of ~1.5 GGy necessary to produce the maximum volumetric strain in starkeyite would require a period of ~ 5×10^9 yr, or the age of the solar system. However, we recognise that the need for such radiation doses to be sustained over a prolonged period of time (particularly if the structure is able to anneal at a comparable rate) poses a challenge to the application of X-ray irradiation as part of the manufacturing process of functional materials. Nevertheless, X-ray induced effects on the properties of materials have only recently attracted attention from the inorganic chemistry community, and the quest for identifying systems where lower radiation doses are sufficient to tune the properties of functional materials is a promising avenue for future research.

Conclusion

In summary, we have studied the thermal expansion of cranswickite and starkeyite, both showing negative linear thermal expansion. Cranswickite, was produced synthetically, for the first time and, moreover, revealed zero area thermal expansion in the *ac* plane. Furthermore, cranswickite undergoes a first-order phase transition to starkeyite at 330 K accompanied by a volume decrease of 4.72 %, one of the largest values for phase-transition type NTE hitherto observed. By virtue of being a major candidate rock-forming mineral on the outer three Galilean Moons, this transition might play a vital role in the structure and dynamics of their icy mantle. Starkeyite, has displayed discontinuous behaviour of the eigenvalues of the thermal expansion tensor at around 250 K. Importantly, at this temperature, also a shoulder emerges from the 212 Bragg peak, but attempts to index the putative low-temperature structure were unsuccessful. Efforts to grow a single crystal large enough to be used in a neutron diffraction experiment at low-temperatures are underway and if successful clearly would be useful to identify the underlying structural changes associated with discontinuous evolution of the thermal expansion. Lastly, we have observed synchrotron X-ray induced radiation damage, which severely altered the thermal expansion properties of starkeyite, to a point of even inducing negative thermal expansion of the *a*-axis. Notably, this is the first example where such behaviour could be observed in an inorganic compound, and might open up an exciting avenue for future research in functional materials. Regardless if one strives to avoid or exploit radiation damage, a deeper understanding of its impact is crucial also for inorganic compounds, even more so since we have observed Synchrotron X-ray induced radiation damage not just in starkeyite, but also in two other inorganic compounds (i.e., $FeSO_4 \cdot 4H_2O$ and $Ca(NO_3)_2$; unpublished data). We found the X-ray induced expansion to be strongly anisotropic and therefore advocate for a tensor description of X-ray expansion in the form of the X-ray expansion tensor r_{ij}. Lastly, we demonstrate that knowledge of the X-ray expansion tensor as well as the true thermal expansion of the undamaged material as collected in a neutron diffraction experiment is critical to identify and quantify the influence of X-ray radiation, which then may eventually allow to radiation-tune the properties of functional materials.

Acknowledgements

[1]   K. Takenaka, *Front Chem* **2018**, *6*.

[2]   Z.-K. Liu, Y. Wang, S.-L. Shang, *J Phase Equilibria Diffus* **2022**, DOI 10.1007/s11669-022-00942-z.

[3]   E. Liang, Q. Sun, H. Yuan, J. Wang, G. Zeng, Q. Gao, *Front Phys (Beijing)* **2021**, *16*, 53302.

[4]   J. P. Attfield, *Front Chem* **2018**, *6*.

[5]   C. S. Coates, A. L. Goodwin, *Mater Horiz* **2019**, *6*, 211–218.

[6]   R. Chen, Q. Gao, Y. Qiao, J. Guo, L. Er-Jun, *Scr Mater* **2022**, *214*, 114653.

[7]   Q. Li, K. Lin, Z. Liu, L. Hu, Y. Cao, J. Chen, X. Xing, *Chem Rev* **2022**, DOI 10.1021/acs.chemrev.1c00756.

[8]   A. D. Fortes, *Acta Crystallographica Section B* **2018**, *74*, 196–216.

[9]   M. B. Jakubinek, C. O'Neill, C. Felix, R. B. Price, M. A. White, *Dental Materials* **2008**, *24*, 1468–1476.

[10]   W. Pannhorst, *J Non Cryst Solids* **1997**, *219*, 198–204.

[11]   Y.-Y. Zhao, F.-X. Hu, L.-F. Bao, J. Wang, H. Wu, Q.-Z. Huang, R.-R. Wu, Y. Liu, F.-R. Shen, H. Kuang, M. Zhang, W.-L. Zuo, X.-Q. Zheng, J.-R. Sun, B.-G. Shen, *J Am Chem Soc* **2015**, *137*, 1746–1749.

[12]   S. M. Mirvakili, I. W. Hunter, *Advanced Materials* **2018**, *30*, 1704407.

[13]   R. Gatt, L. Mizzi, J. I. Azzopardi, K. M. Azzopardi, D. Attard, A. Casha, J. Briffa, J. N. Grima, *Sci Rep* **2015**, *5*, 8395.

[14]   A. Wang, B. L. Jolliff, Y. Liu, K. Connor, *J Geophys Res Planets* **2016**, *121*, 678–694.

[15]   S. Vance, J. M. Brown, *Geochim Cosmochim Acta* **2013**, *110*, 176–189.

[16]   W. H. Baur, *Acta Crystallogr* **1964**, *17*, 863–869.

[17]   W. H. Baur, *Acta Crystallogr* **1962**, *15*, 815–826.

[18]   R. C. Peterson, *American Mineralogist* **2011**, *96*, 869–877.

[19]   L. Liu, *Physics of the Earth and Planetary Interiors* **1983**, *32*, 226–240.

[20]   C. S. Coates, C. A. Murray, H. L. B. Boström, E. M. Reynolds, A. L. Goodwin, *Mater Horiz* **2021**, *8*, 1446–1453.

[21]   W. Bras, D. A. A. Myles, R. Felici, *Journal of Physics: Condensed Matter* **2021**, *33*, 423002.

[22]   N. E. Bogdanov, B. A. Zakharov, D. Chernyshov, P. Pattison, E. v Boldyreva, *Acta Crystallographica Section B* **2021**, *77*, 365–370.

[23]   R. J. Angel, **2011**.

[24]   A. D. Fortes, I. Wood, K. Knight, *Physics and Chemistry of Minerals* **2008**, *35*, 207–221.

[25]   A. D. Fortes, I. G. Wood, M. Alfredsson, L. Vočadlo, K. S. Knight, *European Journal of Mineralogy* **2006**, *18*, 449–462.

[26]   M. Wildner, B. A. Zakharov, N. E. Bogdanov, D. Talla, E. v Boldyreva, R. Miletich, *IUCrJ* **2022**, *9*, DOI 10.1107/S2052252521012720.

[27]   J. M. Meusburger, K. A. Hudson-Edwards, C. T. Tang, E. T. Connolly, R. A. Crane, A. D. Fortes, **2022**, DOI 10.24435/materialscloud:fd-31.

[28]   A. L. Goodwin, M. Calleja, M. J. Conterio, M. T. Dove, J. S. O. Evans, D. A. Keen, L. Peters, M. G. Tucker, *Science (1979)* **2008**, *319*, 794–797.

[29]   A. E. Phillips, A. L. Goodwin, G. J. Halder, P. D. Southon, C. J. Kepert, *Angewandte Chemie International Edition* **2008**, *47*, 1396–1399.

[30]   G. Tammann, *Aggregatzustaende - Die Zustandsaenderung Der Materie in Abhaengigkeit von Druck Und Temperature*, Verlag Von Leopold Voss, Leipzig, **1922**.

[31]   L. W. Strock, *Zeitschrift für Physikalische Chemie* **1934**, *25B*, 441–459.

[32]   H. Nakamura, H. Wada, K. Yoshimura, M. Shiga, Y. Nakamura,

J. Sakurai, Y. Komura, *Journal of Physics F: Metal Physics* **1988**, *18*, 981–991.

[33] K. Takenaka, Y. Okamoto, T. Shinoda, N. Katayama, Y. Sakai, *Nat Commun* **2017**, *8*, 14102.

[34] J. R. Smyth, D. J. Frost, *Geophys Res Lett* **2002**, *29*, 123-1-123–4.

[35] A. E. Ringwood, *The Earth's Crust and Upper Mantle* **1969**, 1–17.

[36] T. B. McCord, G. B. Hansen, C. A. Hibbitts, *Science (1979)* **2001**, *292*, 1523.

[37] T. B. McCord, G. B. Hansen, F. P. Fanale, R. W. Carlson, D. L. Matson, T. v Johnson, W. D. Smythe, J. K. Crowley, P. D. Martin, A. Ocampo, C. A. Hibbitts, J. C. Granahan, *Science (1979)* **1998**, *280*, 1242 LP – 1245.

[38] W. B. McKinnon, M. E. Zolensky, *Astrobiology* **2003**, *3*, 879–897.

[39] D. L. Hogenboom, J. S. Kargel, J. P. Ganasan, L. Lee, *Icarus* **1995**, *115*, 258–277.

[40] D. ~L. Hogenboom, J. ~S. Kargel, M. ~L. Reiter, Y. ~N. Khor, in *Lunar and Planetary Science Conference*, **1997**, p. 579.

[41] S. P. Thompson, H. Kennedy, B. M. Butler, S. J. Day, E. Safi, A. Evans, *J Appl Crystallogr* **2021**, *54*, 1455–1479.

[42] N. V. Zayakina., *Zapiski RMO (Proceedings of the Russian Mineralogical Society)* **2019**, *148*, 49–53.

[43] R. T. Pappalardo, S. Vance, F. Bagenal, B. G. Bills, D. L. Blaney, D. D. Blankenship, W. B. Brinckerhoff, J. E. P. Connerney, K. P. Hand, T. M. Hoehler, J. S. Leisner, W. S. Kurth, M. A. McGrath, M. T. Mellon, J. M. Moore, G. W. Patterson, L. M. Prockter, D. A. Senske, B. E. Schmidt, E. L. Shock, D. E. Smith, K. M. Soderlund, *Astrobiology* **2013**, *13*, 740–773.

[44] R. D. Lorenz, E. P. Turtle, J. W. Barnes, M. G. Trainer, D. S. Adams, K. E. Hibbard, C. Z. Sheldon, K. Zacny, P. N. Peplowski, D. J. awrence, M. A. Ravine, T. G. McGee, K. S. Sotzen, S. M. MacKenzie, J. W. Langelaan, S. Schmitz, L. S. Wolfarth, P. D. Bedini, *Johns Hopkins APL Technical Digest (Applied Physics Laboratory)* **2018**, *34*, 374–387.

[45] M. Jezek, C.-M. Geilfus, A. Bayer, K.-H. Mühling, *Front Plant Sci* **2015**, *5*, 781.

[46] M. van essen, H. A. Zondag, J. Gores, L. Bleijendaal, M. Bakker, R. Schuitema, W. Helden, Z. He, C. Rindt, *J Sol Energy Eng* **2009**, *131*, 041014.

[47] R. Li, Y. Shi, L. Shi, M. Alsaedi, P. Wang, *Environ Sci Technol* **2018**, *52*, 5398–5406.

[48] N. Marx, L. Croguennec, D. Carlier, L. Bourgeois, P. Kubiak, F. le Cras, C. Delmas, *Chemistry of Materials* **2010**, *22*, 1854–1861.

[49] J. A. Z. Martínez, R. L. Porto, I. E. M. Cortez, T. Brousse, J. A. A. Martínez, L. A. L. Pavón, *J Electrochem Soc* **2018**, *165*, A2349–A2356.

[50] A. D. Fortes, F. Browning, I. G. Wood, *Phys Chem Miner* **2012**, *39*, 419–441.

[51] S. J. Baxter, A. Schneemann, A. D. Ready, P. Wijeratne, A. P. Wilkinson, N. C. Burtch, *J Am Chem Soc* **2019**, *141*, 12849–12854.

[52] N. C. Burtch, *Engineering Precisely Controlled Negative and Zero Thermal Expansion Behaviors in Metal-Organic Frameworks.*, United States, **2019**.

[53] T. Wang, J. Xu, L. Hu, W. Wang, R. Huang, F. Han, Z. Pan, J. Deng, Y. Ren, L. Li, J. Chen, X. Xing, *Appl Phys Lett* **2016**, *109*, 181901.

[54] V. Duffort, V. Caignaert, V. Pralong, B. Raveau, M. R. Suchomel, J. F.

Mitchell, *Solid State Commun* **2014**, *182*, 22–25.

6. Comment on Mineral Diversity on Europa: Exploration of Phases Formed in the MgSO₄–H₂SO₄–H₂O Ternary

This chapter contains a comment, outlining why the crystal structure of MgSO$_4$·6H$_2$O published by Maynard-Casely et al. (2021) is unambiguously incorrect. It is highlighted where this error could have been detected at various stages of the analysis, writeup, and submission process, and recommendations how to avoid this issue in the future. As of the time of the final submission of this thesis (i.e., April 2023) Maynard-Casely et al. (2021) have not replied to this comment.

Declaration The contents of this chapter were published in the journal *ACS Earth and Space Chemistry* (Fortes & Meusburger, 2022) and are presented in the original format of the journal.

Comment

Comment on Mineral Diversity on Europa: Exploration of Phases Formed in the MgSO₄−H₂SO₄−H₂O Ternary

A. Dominic Fortes* and Johannes M. Meusburger

Read Online

ACCESS | 📊 Metrics & More | 📰 Article Recommendations | ⓢ Supporting Information

ABSTRACT: The structure of a new polymorph of $MgSO_4 \cdot 6H_2O$, a potentially important mineral on the surface of Europa, one of Jupiter's icy moons, was reported by Maynard-Casely et al. [Maynard-Casely, H. E.; Brand, H. E.; Wilson, S. A.; Wallwork, K. S. Mineral Diversity on Europa: Exploration of Phases Formed in the $MgSO_4$−H_2SO_4−H_2O Ternary. *ACS Earth Space Chem.* **2021**, *5* (7), 1716−1725. DOI: 10.1021/acsearthspacechem.1c00073]. The reported structure is unambiguously incorrect because the stoichiometry is wrong; the formula unit contains only half of the SO_4^{2-} oxyanions required. We highlight where this error could have been detected at various stages of the analysis, writeup, and submission process and make recommendations to avoid repetition of the mistake.

INTRODUCTION

Maynard-Casely et al.[1] recently reported the results of a study using synchrotron X-rays into the sub-solidus behavior of mixtures containing magnesium sulfate, sulfuric acid, and water, motivated by an interest in the mineralogy of icy planetary bodies in the outer solar system. In the first instance, we thoroughly support this work. Studies of cosmic analogue materials have the potential to shed light on unexpected chemical interactions and identify novel structural motifs while also helping us to interpret remotely sensed or *in situ* data from extraterrestrial phenomena. Our motivation in writing this comment is not to criticize unduly but to recommend methods and tools for authors, reviewers, and editors to avoid the errors that we highlight below.

AREAS OF AGREEMENT

The analysis carried out by Maynard-Casely et al.[1] includes the identification of four unknown crystalline phases, in addition to a number of previously characterized $MgSO_4$ hydrates and water ice. For one of these, unknown 1 (UK1), they provide a structure solution based on their X-ray powder diffraction data and interpret the resulting structural model as a new polymorph of $MgSO_4 \cdot 6H_2O$ or MS6 (the mineral hexahydrite). Their indexing of the unit cell is similar to that of MS6 (i.e., $\Delta a \sim$ 7.6%, $\Delta b \sim -5.3\%$, $\Delta c \sim -0.2\%$, $\Delta \beta \sim 1.6\%$, and $\Delta V \sim 2.1\%$). We have indexed the powder diffraction pattern provided in their Crystallographic Information File (CIF) and obtain the same lattice parameters as Maynard-Casely et al.[1] with a high figure of merit (FoM).

The evidence presented in the paper that this is a distinct phase from MS6 is convincing, and we agree with that specific interpretation. In the first place, both MS6 and UK1 co-exist in one of their samples (Figure 2 of ref 1). Second, the unit-cell volumes for $MgSO_4 \cdot 7H_2O$ and $MgSO_4 \cdot 11H_2O$ agree reasonably well with published data, indicating that instrument calibration is likely not an issue. Some years ago, we determined the lattice

parameters of deuterated MS6 down to 8 K as an accessory phase in samples of $MgSO_4 \cdot 3D_2O$. A comparison of this previously unpublished work[2] with the values of Maynard-Casely et al.[1] (Figure 1) confirms that their results for the known phase of MS6 are accurate, with the absolute difference in
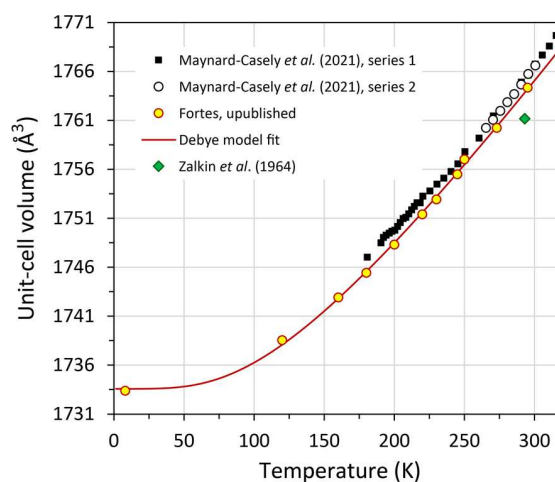
Figure 1. Unit-cell volumes of ordinary protiated MS6 reported by Maynard-Casely et al.[1] (extracted from their Figure 4 by graphical methods) compared to previously unpublished experimental data[2] for deuterated MS6, acquired by neutron powder diffraction and fitted with a Debye-type model of the thermal expansion. The room-T datum from Zalkin et al.[3] is also indicated.

volume potentially being due to deuteration. Third, the Bragg peak intensities of UK1 shown in Figure 6 of ref 1 differ substantially from those of MS6.

It is our view that problems arise in moving beyond basic phase identification and indexing to the structure solution stage. We assert that their final structural model is unambiguously incorrect for the reasons outlined below.

■ PROBLEMATIC STRUCTURE SOLUTION

The authors used the freely available parallel tempering code FOX[4,5] for their structure solution, which is an excellent tool for the job but one that requires careful use. In setting up the solution process, the chances of obtaining a correct solution are increased by the choice of space group, with awareness of the site multiplicities, and, for more complex structures, by providing accurate information on how the atoms may be connected. This could be a Z-matrix for molecular species or a geometric description of the likely coordination polyhedra for inorganic crystals.

Maynard-Casely et al.[1] determined from systematic absences that UK1 is a C-centered monoclinic crystal, adopting either space group $C2/c$ (the same as MS6) or Cc. We note that both $C2/n$ and Cn represent alternative settings with the same absence conditions that were apparently not considered. The authors had by this point already made the assumption that this phase was a polymorph of MS6 and used MgO_6 octahedra and SO_4 tetrahedra to describe the structural motifs in the crystal. We consider this at least to be a reasonable starting point but one that should have been revisited after it became clear that the resulting fit to the data was rather poor. The stated Mg−O bond lengths of 2.2 Å are not correct; typical Mg−O bond lengths in the water-rich $MgSO_4$ hydrates are in the range of 2.0−2.1 Å.[6−9] Longer Mg−O bonds sometimes occur in less hydrated $MgSO_4$ crystals because their polyhedra exhibit an increasing tendency to polymerize, forming corner-sharing dimers or chains.[10] In this case, one may observe MgO_6 polyhedra with greater degrees of distortion as a result of the spread of Mg−O distances between Mg^{2+} and water oxygens ($\sim$2.00−2.05 Å) as well as sulfate oxygens ($\sim$2.05−2.10 Å).[11−14] Hence, Mg−O = 2.2 Å should be considered unlikely unless other structural evidence is obtained to support it.

The authors note that they populated the asymmetric unit with two MgO_6 octahedra and one SO_4 tetrahedron. This provides the correct stoichiometry in space group $C2/c$, where the Mg atoms are on special positions with a multiplicity of 4 and the S atoms occupy general positions with a multiplicity of 8. Loss of the 2-fold axis of rotational symmetry and the center of symmetry in Cc with respect to $C2/c$ results in the multiplicity of the general position being reduced from 8 to 4; space group Cc only has sites of 4-fold multiplicity. This poses no problem for the MgO_6 octahedra, which are already on sites with a multiplicity of 4, but to retain the correct overall stoichiometry, the SO_4 tetrahedra formerly on sites of 8-fold multiplicity must be split in two. Hence, the number of SO_4 tetrahedra included in the asymmetric unit must be doubled. The FOX software will not make this change automatically if a different space-group symbol is entered; one must explicitly click on "Scatterers → Duplicate Scatterer" and then select the item to be copied. Having been unable to obtain a solution in $C2/c$, it appears that Maynard-Casely et al.[1] either failed to recognize the need for duplication of the SO_4 unit or recognized the need but unintentionally omitted the action to achieve it and proceeded to a structure determination in space group Cc without ensuring

that the correct number of SO_4 tetrahedra were included in the asymmetric unit. As a result, the structure presented in the paper does not have the correct stoichiometry. This is readily apparent from examination of Figure 8 of ref 1 and from the CIF, which explicitly lists the site multiplicities; their crystal has the formula sum $MgS_{1/2}O_{16}$, when it would properly be $MgSO_{20}$ if it were indeed a polymorph of MS6. The quality of the final structure refinement is low; wRp = 18.8%, including even the use of eighth-order spherical harmonics, is an extremely poor result. Structure-less profile refinement yields wRp = 4.9% (Pawley method; caption of Figure 6 of ref 1) and wRp = 3.2% (LeBail method; obtained by us using the data provided in the CIF), and one would thus expect a satisfactory Rietveld structure refinement to be close to this or at least <5%.

■ POTENTIAL FOR SPOTTING THE ERROR

We next examine where the error could have been detected and evaluate what steps may be taken to avoid such obviously incorrect crystal structures from being published in the future, paying attention to where assumptions could have been challenged or better working practices could be developed.

The first problem that the authors faced was at the stage of making assumptions about the composition. They naturally assumed that the similarity of the lattice parameters implied a structural and compositional relationship to MS6 without giving due weight to the increase in molar volume and the possibilities afforded by the chemistry of the ternary system with which they were working. The presence of sulfuric acid in the mother liquor and the structural similarity between SO_4 and either HSO_4 and/or H_2SO_4 imply the possibility that crystals could form containing any or all of these units. There are a number of compounds in the Inorganic Crystal Structure Database (ICSD) in which a divalent metal cation is coordinated to HSO_4 and/or H_2SO_4, including $Mg(H_2SO_4) \cdot H_2O$ and $Mg-(HSO_4)_2(H_2SO_4)$.[15−20] Even the notion that such compounds could have formed during their study is not mentioned by the authors, who should certainly have entertained the possibility that the increase in volume and the potential splitting of the sulfate oxyanion into two symmetry inequivalent units was due to the inclusion of HSO_4, $H(SO_4)_2$, or H_2SO_4 in the structure.

The very basic error in the stoichiometry of the structure could have been captured early in the solution process. It should become habitual, after entering the structural motifs in FOX, to visually inspect the unit-cell contents. Clicking the "Display" button and examining only the asymmetric unit allows for a straightforward "head count" of how many MgO_6 and SO_4 polyhedra (for example) are present, even before running the Global Optimization. In the event that the polyhedra are clustered on top of one another, clicking "Parameters → Randomize Configuration" a one or more times will eliminate this problem.

Clearly, in the absence of the correct number of polyhedra, FOX will attempt to move the "wrong" polyhedra to account for the observed electron density at particular locations in the unit cell. Consequently, one would expect to encounter substantial residual features in a Fourier difference map. After running the Global Optimization, one ought to open the "Display" tab, right click in the display window, and select "Fourier maps" to produce a three-dimensional (3D) plot of the difference densities. This is likely to have revealed features indicating a problem with the solution process.

Nevertheless, this incorrect structure was used as the basis for a rigid-body Rietveld refinement. Obtaining a large wRp value,

even with many texture parameters, should have indicated a serious problem. We note that the authors do not report the overall texture coefficient nor do they report the total number of refined parameters. Having completed the refinement, we expect that the authors examined their structure to characterize it relative to MS6, producing figures, tables of atomic coordinates and bond lengths, and a CIF. Any one of these subsequent actions provided an opportunity to count up the number of polyhedra and observe a disparity. Moreover, the imprecision of the atomic coordinates and the large unphysical difference in B_{iso} for the sulfate oxygens act as warning indicators. We are suspicious of the B_{iso} values for the atoms in the MgO_6 octahedra not being refined and do not accept the explanation provided that this step was omitted as a result of the fact that the O atoms have hydrogens attached.

One extremely important aspect of examining the structure should be to ascertain if the bonding between the structural elements is reasonable. In this case, one would be seeking O···O contacts consistent with the formation of O−H···O hydrogen bonds. Considering the ranges of distances and angles found in other water-rich $MgSO_4$ hydrates,[6−14] we expect O···O distances of 2.6−3.0 Å and O···O···O angles in the region of 105°; the exact values will depend upon how strained are the hydrogen bonds, but the approximate values serve as a fair guide for an initial check. With 12 symmetry-inequivalent water molecules, we are seeking 24 potential hydrogen-bonding contacts. Our examination of the structure reported by Maynard-Casely et al.[1] reveals only nine O···O distances and just two pairs of vectors that form an angle that are consistent with ordinary O−H···O hydrogen bonding. There are distances that are too short [O15···O2^a = 2.06(3) Å, O15···O3^a = 2.45(3) Å, and O2^a···O15···O3^a = 56.4(9)°] (a = symmetry code of x, 1 − y, $^1/_2$ + z), while the majority of distances are too long [e.g., O13···O26^b = 3.33(4) Å, O13···O11^c = 3.59(8) Å, and O26^b···O13···O11^c = 70.0(7)°] (b = symmetry code of $^1/_2$ + x, $^1/_2$ − y, z − $^1/_2$, and c = symmetry code of $^1/_2$ + x, $^1/_2$ + y, z). Even a cursory examination of the structure and potential bonding geometry thus reveals serious flaws and a likely incorrect solution.

The final checkpoint for identifying problems comes with the crystallographic information file (CIF),[21,22] which authors will typically deposit as part of their supplementary information. Crystallographic best practice requires the experimentalists to prepare their CIF for publication with care and attention to detail, ensuring that information required for others to understand and reproduce the work is accurately reported. Ideally, a CIF editing tool[23,24] should be used to ensure that syntax is correct at the very least. Prior to submission, the CIF should be evaluated by the CheckCIF utility of the International Union of Crystallography (IUCr);[25] this will highlight issues with the CIF and provide authors with an opportunity to correct the problems or else offer reasons for disregarding the alerts.[26] We can be quite sure that Maynard-Casely et al.[1] did not use the CheckCIF utility because when we submitted their CIF we obtained a syntax error message and the checks were not carried out.

Deleting the incorrectly formatted lines allowed the CheckCIF utility to proceed, and we obtained a report (see the Supporting Information) with 17 A-level alerts, defined as "most likely a serious problem—resolve or explain", 5 C-level alerts, and 11 G-level alerts. Many of these alerts are due to the sparse nature of the CIF, including missing information about the data acquisition and the refinement, which are readily

addressed. However, the CheckCIF report informs us that there is a very short contact distance between S1 and O15 (2.81 Å) and, most telling of all, that the unit cell contains solvent-accessible voids of 86 Å^3. This is a quite considerable amount of void space and reflects the fact that the structure is missing half of its complement of SO_4 tetrahedra. The final page of the report draws the asymmetric unit, showing two MgO_6 octahedra and only one SO_4 tetrahedron. If all of the indicators prior to this point had been missed, the CheckCIF report is at least very clear that there are fundamental problems with the crystal structure.

■ RECOMMENDATIONS

In terms of avoiding these errors in the future, we encourage all authors of crystallographic papers to adopt the best working practice of ensuring that they produce a comprehensive CIF, regardless of whether it is required by a journal for submission or not. This should include use of a CIF editor and the CheckCIF validation utility combined with rigorous error checking to resolve outstanding problems prior to submission. Outside of the core crystallographic journals, the rules concerning adoption of CIF submission and use of CheckCIF as a mandatory step in submission of papers reporting crystal structures are not consistent. Across a range of chemistry journals, we note that the Royal Society of Chemistry of the U.K.,[27] the *European Journal of Chemistry*,[28] the *Canadian Journal of Chemistry*,[29] and the *Australian Journal of Chemistry*[30] each require submission of crystallographic data to the Cambridge Crystallographic Data Centre (CCDC), which, in turn, requires the use of CheckCIF, and most of the author guidelines of these journals offer extensive advice on the content that they expect to appear in the CIF. Despite this, we find recent examples of work (e.g., ref 31) in the aforementioned journals where CIF preparation was extremely poor and CheckCIF validation cannot have been done. Among the family of journals of the American Chemical Society (ACS), only *Crystal Growth & Design*, *Inorganic Chemistry*, *Organic Letters*, *The Journal of Organic Chemistry*, *Organometallics*, and the *Journal of the American Chemical Society* presently mandate the same level of due diligence with regard to CIF checking prior to submission.[32] Because we have observed an increasing number of papers in *ACS Earth and Space Chemistry* that report crystal structures, we advocate for the adoption of a requirement for submission of a comprehensive CIF that has been thoroughly validated. Furthermore, we recommend that any ACS journal in receipt of a crystal structure determined using either X-ray or neutron diffraction methods also follow this practice.

■ ASSOCIATED CONTENT

Ⓢ Supporting Information

The Supporting Information is available free of charge at https://pubs.acs.org/doi/10.1021/acsearthspacechem.2c00038.

IUCr CheckCIF/PLATON report on the CIF supplied in ref 1 (PDF)

■ AUTHOR INFORMATION

Corresponding Author

A. Dominic Fortes − *ISIS Neutron and Muon Source, STFC Rutherford Appleton Laboratory, Harwell Science and Innovation Campus, Didcot, Oxfordshire OX11 0QX, United Kingdom;* ⓘ orcid.org/0000-0001-5907-2285; Email: dominic.fortes@stfc.ac.uk

Author

Johannes M. Meusburger − *ISIS Neutron and Muon Source, STFC Rutherford Appleton Laboratory, Harwell Science and Innovation Campus, Didcot, Oxfordshire OX11 0QX, United Kingdom; Diamond Light Source, Harwell Science and Innovation Campus, Didcot, Oxfordshire OX11 0DE, United Kingdom; Camborne School of Mines and Environment and Sustainability Institute, Tremough Campus, University of Exeter, Penryn, Cornwall TR10 9EZ, United Kingdom*

Complete contact information is available at:
https://pubs.acs.org/10.1021/acsearthspacechem.2c00038

Notes

The authors declare no competing financial interest.

■ REFERENCES

(1) Maynard-Casely, H. E.; Brand, H. E.; Wilson, S. A.; Wallwork, K. S. Mineral diversity on Europa: Exploration of phases formed in the $MgSO_4–H_2SO_4–H_2O$ ternary. *ACS Earth Space Chem.* **2021**, *5*, 1716−1725.

(2) Fortes, A. D.; Knight, K. S. *Thermal Expansion and Phase Transition in Magnesium Sulfate Trihydrate*; Rutherford Appleton Laboratory: Didcot, U.K., 2010; ISIS Experimental Report RB 1010078, https://discovery.ucl.ac.uk/id/eprint/1008249/2/1010078.pdf.

(3) Zalkin, A.; Ruben, H.; Templeton, D. H. The crystal structure and hydrogen bonding of magnesium sulfate hexahydrate. *Acta Crystallogr.* **1964**, *17*, 235−240.

(4) Favre-Nicolin, V.; Černý, R. FOX, free objects for crystallography': A modular approach to *ab initio* structure determination from powder diffraction. *J. Appl. Crystallogr.* **2002**, *35*, 734−743.

(5) Černý, R.; Favre-Nicolin, V.; Rohlíček, J.; Hušák, H. FOX, Current State and Possibilities. *Crystals* **2017**, *7*, 322.

(6) Fortes, A. D.; Wood, I. G.; Alfredsson, M.; Vočadlo, L.; Knight, K. S. The thermoelastic properties of $MgSO_4·7D_2O$ (epsomite) from powder neutron diffraction and *ab initio* calculation. *Eur. J. Min.* **2006**, *18*, 449−462.

(7) Fortes, A. D.; Knight, K. S.; Wood, I. G. Structure, thermal expansion and incompressibility of $MgSO_4·9H_2O$, its relationship to meridianiite ($MgSO_4·11H_2O$) and possible natural occurrences. *Acta Crystallogr., Sect. B: Struct. Sci., Cryst. Eng. Mater.* **2017**, *73*, 47−64.

(8) Fortes, A. D.; Wood, I. G.; Knight, K. S. The crystal structure and thermal expansion tensor of $MgSO_4·11D_2O$ (meridianiite) determined by neutron powder diffraction. *Phys. Chem. Mineral.* **2008**, *35*, 207−221.

(9) Fortes, A.; Wood, I. G.; Gutmann, M. J. $MgSO_4·11H_2O$ and $MgCrO_4·11H_2O$ based on time-of-flight neutron single-crystal Laue data. *Acta Crystallogr., Sect. C: Cryst. Struct. Commun.* **2013**, *69*, 324−329.

(10) Hawthorne, F. C.; Sokolova, E. The role of H_2O in controlling bond topology: I. The $^{[6]}Mg (SO_4)(H_2O)_n$ ($n = 0−11$) structures. *Z. Kristallogr. Cryst. Mater.* **2012**, *227*, 594−603.

(11) Baur, W. H. On the crystal chemistry of salt hydrates. II. A neutron diffraction study of $MgSO_4·4H_2O$. *Acta Crystallogr.* **1964**, *17*, 863−869.

(12) Peterson, R. C. Cranswickite $MgSO_4·4H_2O$, a new mineral from Calingasta, Argentina. *Am. Mineral.* **2011**, *96*, 869−877.

(13) Baur, W. H.; Rolin, J. L. Salt hydrates. IX. The comparison of the crystal structure of magnesium sulfate pentahydrate with copper sulfate pentahydrate and magnesium chromate pentahydrate. *Acta Crystallogr., Sect. B: Struct. Crystallogr. Cryst. Chem.* **1972**, *28*, 1448−1455.

(14) Wang, W.; Fortes, A. D.; Dobson, D. P.; Howard, C. M.; Bowles, J.; Hughes, N. J.; Wood, I. G. Investigation of high-pressure planetary ices by cryo-recovery. II. High-pressure apparatus, examples and a new high-pressure phase of $MgSO_4·5H_2O$. *J. Appl. Crystallogr.* **2018**, *51*, 692−705.

(15) Troyanov, S. I.; Simonov, M. Crystal structure of $Zn(HSO_4)_2$. *Kristallografiya* **1989**, *34*, 233−234.

(16) Troyanov, S. I.; Merinov, B. V.; Verin, I. P.; Kemnitz, E.; Hass, D. Crystal structure of acid magnesium sulfate $Mg-[SO_3(OH)]_2[SO_2(OH)_2]_2$. *Kristallografiya* **1990**, *35*, 852−855.

(17) Worzala, H.; Schneider, M.; Kemnitz, E.; Trojanov, S. I. Über die Bildung und Kristallstruktur von $Mg(HSO_4)_2·H_2O$. *Z. Anorg. Allgem. Chem.* **1991**, *596*, 167−171.

(18) Stiewe, A.; Kemnitz, E.; Troyanov, S. Crystal structures of manganese hydrogen sulfates, $Mn(HSO_4)_2$, $Mn(HSO_4)_2·H_2O$ and $Mn(HSO_4)_2(H_2SO_4)_2$. *Z. Kristallogr. Cryst. Mater.* **1998**, *213*, 654−658.

(19) Morosov, I.; Troyanov, S.; Stiewe, A.; Kemnitz, E. Synthese und Kristallstruktur von Hydrogenselenaten zweiwertiger Metalle—M-$(HSeO_4)_2$ (M= Mg, Mn, Zn) und $M(HSeO_4)_2·H_2O$ (M = Mn, Cd). *Z. Anorg. Allgem. Chem.* **1998**, *624*, 135−140.

(20) Kemnitz, E.; Werner, C.; Stiewe, A.; Worzala, H.; Trojanov, S. Synthese und Struktur von $Zn(HSO_4)_2(H_2SO_4)_2$ und $Cd(HSO_4)_2$. *Z. Naturforsch.* **1996**, *51b*, 14−18.

(21) Hall, S. R.; Allen, F. H.; Brown, I. D. (1991). The Crystallographic Information File (CIF): A new standard archive file for crystallography. *Acta Crystallogr., Sect. A: Found. Crystallogr.* **1991**, *47*, 655−685.

(22) Bernstein, H. J.; Bollinger, J. C.; Brown, I. D.; Gražulis, S.; Hester, J. R.; McMahon, B.; Spadaccini, N.; Westbrook, J. D.; Westrip, S. P. Specification of the Crystallographic Information File format, version 2.0. *J. Appl. Crystallogr.* **2016**, *49*, 277−284.

(23) Westrip, S. P. publCIF: Software for editing, validating and formatting crystallographic information files. *J. Appl. Crystallogr.* **2010**, *43*, 920−925.

(24) Allen, F. H.; Johnson, O.; Shields, G. P.; Smith, B. R.; Towler, M. CIF applications. XV. enCIFer: A program for viewing, editing and visualizing CIFs. *J. Appl. Crystallogr.* **2004**, *37*, 335−338.

(25) Strickland, P. R.; Hoyland, M. A.; McMahon, B. Automated data validation: *checkcif*. In *International Tables for Crystallography*; Hall, S. R., McMahon, B., Eds.; International Union of Crystallography: Chester, U.K., 2006; Vol. *G*, Section 5.7.2.6, pp 561−562, DOI: 10.1107/97809553602060000757.

(26) Spek, A. L. *checkCIF* validation ALERTS: What they mean and how to respond. *Acta Crystallogr., Sect. E: Crystallogr. Commun.* **2020**, *76*, 1−11.

(27) Royal Society of Chemistry. *Author Guidelines, Experimental Reporting Requirements, X-ray Crystallography*; Royal Society of Chemistry: London, U.K., 2022; https://www.rsc.org/journals-books-databases/author-and-reviewer-hub/authors-information/prepare-and-format/experimental-reporting-requirements/#xraycrystallography.

(28) Atlanta Publishing House LLC. *European Journal of Chemistry, Author Guidelines, 4.3.7 Crystallographic Data*; Atlanta Publishing House LLC: Atlanta, GA, 2022; https://www.eurjchem.com/index.php/eurjchem/about/submissions.

(29) Canadian Science Publishing. *Canadian Journal of Chemistry, Author Guidelines, X-ray Structure Analyses*; Canadian Science Publishing: Ottawa, Ontario, Canada, 2022; https://cdnsciencepub.com/journal/cjc/authors.

(30) CSIRO Publishing. *Australian Journal of Chemistry, Author Instructions*; CSIRO Publishing: Clayton South, Victoria, Australia, 2022; https://www.publish.csiro.au/ch/forauthors/authorinstructions.

(31) Maynard-Casely, H. E.; Yevstigneyev, N. S.; Duyker, S. G.; Ennis, C. The crystal structure, thermal expansion and far-IR spectrum of propanal (CH_3CH_2CHO) determined using powder X-ray diffraction, neutron scattering, periodic DFT and synchrotron techniques. *Phys. Chem. Chem. Phys.* **2021**, *24*, 122−128.

(32) American Chemical Society (ACS). *Requirements for Depositing X-ray Crystallographic Data*; ACS: Washington, D.C., 2022; http://pubsapp.acs.org/paragonplus/submission/acs_cif_authguide.pdf.

7. Discussion, conclusions, and future work

7.1 High-pressure behaviour of MSHs

This thesis reports the compression behaviour of starkeyite and cranswickite as predicted by dispersion-corrected DFT and, most importantly, has demonstrated, in an extensive benchmarking study, that such predictions yield highly accurate results. In the following, I want to discuss how the compressibility predicted for starkeyite and cranswickite compares to other MSHs. In detail, I would like to explore if there are any trends in the volume compressibility as a function of hydration state, and if so, what are the underlying reasons for such trends.

To this end, I have compiled the compression data of MSHs as reported in the literature (Table 7.1). To enhance comparability, I have refitted the literature data using a Birch-Murnaghan third order equation of state (BM3-EOS; Birch, 1947). The BM3-EOS describes a material's evolution as a function of applied pressure by three parameters: the zero-pressure volume V_0, the bulk modulus K, and the pressure dependence of the bulk modulus K'. It is well known that K and K' are strongly correlated parameters i.e., one can equally well fit the data by decreasing K and simultaneously increasing K' and vice-versa (Angel, 2000). To account for this correlation of the fitted parameters, I have performed a confidence ellipsoid analysis (Figure 7.1). These ellipsoids are all drawn within the 2σ limit; hence there is a 95.4 % chance that the true values of K and K' lie in the area enclosed by the ellipsoids.

Importantly, the herein presented analysis is the first systematic comparison of the compressibility of MSHs, paying due diligence to the correlation of the fitted equation of state parameters. Interestingly the analysis revealed that $MgSO_4 \cdot 9H_2O$ is the softest of all hitherto studied MSHs. (Fortes et al., 2017b) correctly reported that the bulk modulus K of $MgSO_4 \cdot 9H_2O$ is essentially identical to meridianiite. However, since the compressibility depends on both K and K', the confidence ellipsoid analysis demonstrates that despite the essentially identical bulk moduli, $MgSO_4 \cdot 9H_2O$'s compressibility is significantly smaller than meridianiite's. The analysis further revealed the compressibility of epsomite.at room temperature and meridianiite at 240 K is essentially identical, despite epsomite's 14 % larger bulk modulus (Fortes et al., 2017b). However,

upon cooling, the compressibility of epsomite is increasing (Fortes et al., 2006) (Figure 7.1), indicating that epsomite is likely stiffer than meridianiite at 240 K.

Compound	K [GPa]	K'	T [K]	EOS	Method	Reference
$MgSO_4 \cdot 11D_2O$	19.9(4)	9(1)	240	MILEOS	NPD + gas cell	(Fortes et al. 2017a)
$MgSO_4 \cdot 11D_2O$	20.1(4)	8.7(1.4)	240	BM3-EOS	NPD + gas cell	Refitted this thesis
$MgSO_4 \cdot 11H_2O$	23.1(2)	3.4(3)	0		DFT	Brand, 2009
$\alpha\text{-}MgSO_4 \cdot 9D_2O$	19.5(3)	3.8(4)	240	MILEOS	NPD + P-E press + gas cell	(Fortes et al. 2017b)
$\alpha\text{-}MgSO_4 \cdot 9D_2O$	19.5(3)	3.8(5)	240	BM-3EOS	NPD + P-E press + gas cell	Refitted this thesis
$\alpha\text{-}MgSO_4 \cdot 9H_2O$	24.2(6)	3.7(5)	0	BM-3EOS	DFT (WC)	(Fortes et al. 2017b)
$\alpha\text{-}MgSO_4 \cdot 9H_2O$	24.2(2)	4.1(2)	0	MILEOS	DFT (WC)	(Fortes et al. 2017b)
$MgSO_4 \cdot 7D_2O$	21.5(1)	5.3^y	290	BM-3EOS	NPD + gas cell	(Fortes et al., 2006)
$MgSO_4 \cdot 7D_2O$	25.0(2)	5.3^y	50	BM-3EOS	NPD + gas cell	(Fortes et al., 2006)
$MgSO_4 \cdot 7D_2O$	24.9(7)	6(3.2)	50	BM-3EOS	NPD + gas cell	Refitted this thesis
$MgSO_4 \cdot 7D_2O$	21.4(5)	5.3(1.8)	290	BM-3EOS	NPD + gas cell	Refitted this thesis
$MgSO_4 \cdot 7H_2O$	21.6	5.0	RT	BM-3EOS	Lever piezometer	(Bridgman 1949)
$MgSO_4 \cdot 7H_2O$	23.2(2)	5.3(2)	0	BM-3EOS	DFT (PW91)	(Fortes et al., 2006)
$\alpha\text{-}MgSO_4 \cdot 5H_2O$	33.0 (1)	6.4(1)	0	BM-3EOS	DFT (WC)	(Wang et al. 2018)
$\beta\text{-}MgSO_4 \cdot 5H_2O^x$	31.4(2)	5.4(1)	0	BM-3EOS	DFT (WC)	(Wang et al. 2018)
starkeyite	36.3(4)	5.1(2)	0	BM-3EOS	DFT (PBE+TS)	Determined this thesis
cranswickite	37.2(3)	5.4(1)	0	BM-3EOS	DFT (PBE+TS)	Determined this thesis
$\alpha\text{-} MgSO_4 \cdot H_2O$	48.1(5)	8.1(6)	RT	BM-3EOS	SCXRD + DAC	(Meusburger et al. 2020)
$\alpha\text{-} MgSO_4 \cdot H_2O$	48.3(6)	7.9(7)	RT	BM-3EOS	SCXRD + DAC	Refitted this thesis
$\beta\text{-}MgSO_4 \cdot H_2O$	49.3(5.5)	4.8(1.0)	RT	BM-3EOS	SCXRD + DAC	(Meusburger et al. 2020)
$\beta\text{-}MgSO_4 \cdot H_2O$	49.2(5.4)	4.8(1.0)	RT	BM-3EOS	SCXRD + DAC	Refitted this thesis

Table 7.1 Table Compressibility data on all MSHs, compiled from the literature (black), and refitted(green) to enhance comparability of the data. Data that was for the first time reported in this thesis in red.

The compressibility of starkeyite and cranswickite is intermediate between epsomite and kieserite, reflecting the trend of increasing stiffness with increasing polymerisation of the MgO_6 and SO_4 polyhedra. Interestingly, this analysis revealed that cranswickite is stiffer than starkeyite. On first sight, this observation was rather surprising since starkeyite is the denser polymorph, and one would thus expect it to be stiffer as well. The reason for the observed differences in compressibility likely originates from the connectivity of their fundamental building blocks. Starkeyite features cyclic dimer units interconnected via soft hydrogen bonding. Cranswickite, on the other hand, features rigid infinite chains of alternating MgO_6 and SO_4 polyhedra, posing a greater resistance towards compression.
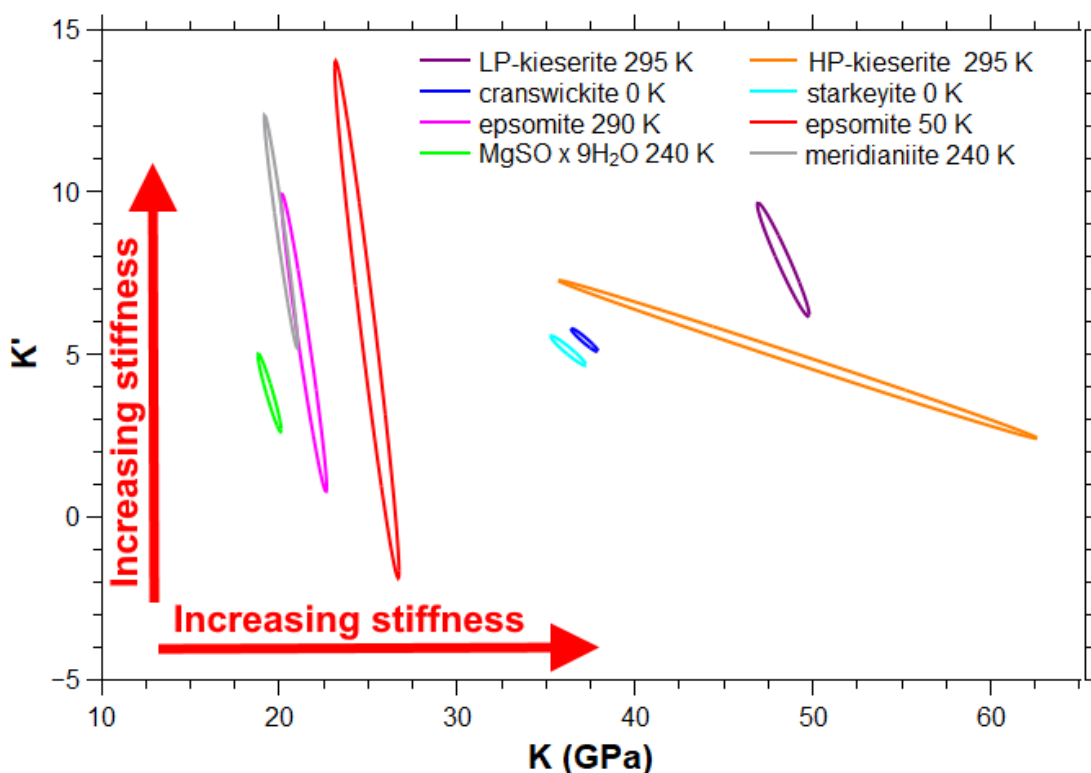
Figure 7.1 Confidence ellipsoids analysis of the compressibility of various MSHs. The ellipsoids are drawn in the 2σ limit in the *K-K'* parameter space.

From an Earth and Planetary Science perspective, the primary motivation to determine the compressibility of a compound is to model the density evolution of rock-forming minerals in planetary bodies. This in turn is critical to model the density structure of such bodies and understand mantle dynamics. The density contrast of rock-forming minerals, for example, is an important factor driving salt diapirism. Salt buried beneath a denser overburden is gravitationally unstable and is therefore ascending, a phenomenon commonly observed in terrestrial salt deposits (Hudec and Jackson, 2007). On the icy moon Europa, the salt content of the ice likely plays a key role in determining if a slab is non-buoyant and, therefore, may even be subducted (Johnson et al., 2017). This is because all MSHs and other candidate salt constituents are substantially denser than ice, thus increasing the overall density of the subducting slabs. In such settings, MSHs might be considered rock-forming minerals up to a pressure of 3.45 GPa (corresponding to the central pressure of Callisto assuming a completely undifferentiated model).

Figure 7.2 displays the density evolution of MSHs to 5 GPa, as well as notable phase transformations of MSHs that were either experimentally observed or computationally predicted.
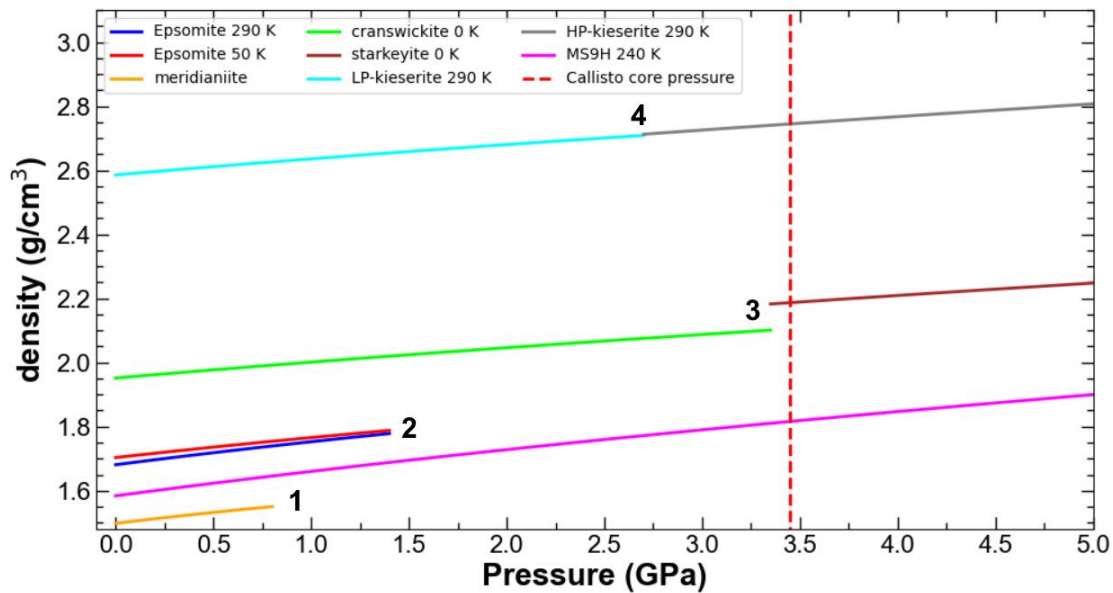
Figure 7.2 (1) Pressure-induced decomposition to MS9H and ice VI at 0.9 GPa (2) Room-temperature transformation of epsomite at 1.4 GPa (3) predicted cranswickite-starkeyite transformation at 3.36 GPa (4) high-pressure transformation of kieserite at 2.7 GPa.

Polymorphic phase transformations at high-pressure were only experimentally observed for kieserite (Meusburger et al., 2020). The transition is second-order in character, and therefore not associated with a volume discontinuity at the transition pressure. The cranswickite-starkeyite transition, for the first time predicted in this thesis, is associated with a density increase of 3.72 %. At 330 K, where the transition occurs at room pressure, we have experimentally determined a density increase of 4.72 %. The DFT-predicted density difference at zero pressure and temperature is merely 3.3 %. Hence, it is likely that the 3.72 % density increase calculated at the transition pressure of 3.36 GPa is also underestimated.

The predicted transition pressure is just within the maximum pressure range MSHs are likely exposed to in the centre of Callisto (i.e, 3.45 GPa; Prentice, 1999). However, one should consider that the phase transition is not only driven by pressure but also temperature, indicating that it could proceed at substantially lower pressures in the icy mantle of the Galilean moons. In models of the interior of Callisto, for example, the temperature is estimated to be approximately 100 – 300 K, depending on the depth and ice/rock ratio (Nagel et al., 2004).

The volume discontinuity of the olivine-wadsleyite transition, accounting for the 410 km discontinuity in velocity seismic waves propagating through the terrestrial mantle, is around 5% (Smyth and Frost, 2002). As for the meridianiite-epsomite transition, which was implicated with rifting of the icy shell, the volume

discontinuity is 3 % (Hogenboom et al., 1997). Based on the large volume discontinuity associated with the cranswickite-starkeyite transitions, it might equally play an important role in the mantle dynamics of icy satellites. Even more so, since both epsomite and meridianiite have revealed pressure-induced dehydration at comparatively low pressures of 0.9 (Fortes et al., 2017b) and 1.6 GPa (Wang et al., 2018), respectively, thus reinforcing the potential role starkeyite and cranswickite might play for the dynamics of the lower icy mantle of the Jovian satellites. To conclude this section, I would like to make following suggestions for future work.

It would be very interesting to

- experimentally validate that the cranswickite-starkeyite transformation occurs at high-pressures, and determine the phase boundary at variable pressure and temperature;
- study the high-pressure behaviour of the intermediate hydrates. An estimate can be readily obtained by means of DFT calculations;
- determine the accurate reference elastic constants for MSHs in preparation for the likely deployment of a seismometer on the surface of Europa;
- benchmark alternative approaches such as elastic constants from lattice dynamics (Wehinger et al., 2016), thermoelastic constants using the Wu-Wentzkovich semi-analytical method (Luo et al., 2021) or molecular dynamics calculations (Li et al., 2022) to obtain more accurate elastic constants from first principles.

7.2 Thermal expansion of MSHs

Compound	α_V	Method	Reference
Ice Ih[D]	15.62 x10^{-5}	NPD	(Fortes et al., 2008)
meridianiite[D]	6.81 x 10^{-5}	NPD	(Fortes et al., 2008)
MgSO$_4$•9D$_2$O	11.0 x10^{-5}	NPD	(Fortes et al., 2017b)
epsomite[D]	8.71 x 10^{-5}	NPD	(Fortes et al., 2006)
hexahydrite	9.24 x 10^{-5}	SXPD	(Maynard-Casely et al. 2021)
pentahydrite[D]	8.85 x 10^{-5}	NPD	This project (unpublished)
Starkeyite[D]	7.33(17) x 10^{-5}	NPD	This thesis
Cranswickite[D]	6.68(29) x 10^{-5}	NPD	This thesis
MgSO$_4$ 3H$_2$O	7.16(28) x 10^{-5}	SXPD	This project (unpublished)
MgSO$_4$ 2.5H$_2$O	5.87(4) x 10^{-5}	SXPD	This project (unpublished)
kieserite	2.8 x 10^{-5}	SCXRD	(Wildner et al., 2022)
α-MgSO$_4$	3.49 x 10^{-5}	NPD	(Fortes et al., 2007)
β-MgSO$_4$	3.95 x 10^{-5}	NPD	(Fortes et al., 2007)

Table 7.2 Thermal expansion of various MSHs at 240 K. [D] deuterated isotopologue studied. NPD: Neutron Powder Diffraction, SXPD: Synchrotron X-ray Powder Diffraction, SCXRD: Single Crystal X-Ray Diffraction. Thermal expansion of pentahydrite, and synthetic MgSO$_4$ 3H$_2$O and MgSO$_4$ 2.5H$_2$O, were also analysed as part of this project, but are not reported in this thesis. Standard deviation is just reported if available in the literature.

The thermal expansion of both polymorphs of MgSO$_4$·4H$_2$O was for the first time determined in this thesis. Like for the compressibility in the preceding section, I will compare their thermal expansion properties to the other MSHs, again looking for trends and possible explanation for these trends. The thermal expansion varies as function of temperature, thus a comparison should be carried out for data collected at the same temperature. I have chosen a reference temperature of 240 K for comparison, since it is below the transformation temperature of MgSO$_4$·9H$_2$O and meridianiite (Fortes et al., 2008; Fortes et al., 2017). In addition, I have included the thermal expansion of ice Ih and anhydrous MgSO$_4$ in the comparison.

The analysis revealed that there is a strong correlation (R^2 = ~90) between the water content of MSHs and their thermal expansion (Figure 7.3). As already noted in the preceding section, MgO$_6$ and SO$_4$ are rigid units, hence the thermal expansion appears to be mainly controlled by the flexible hydrogen-bonded framework. As such the observed correlation was expected. However, there are a few notable deviations from the trend such as meridianiite exhibiting a thermal expansion comparable to the tetrahydrates and the trihydrate, which all feature a substantial degree of MgO$_6$ and SO$_4$ polymerisation. When the thermal expansion of meridianiite was characterised in 2008 (Fortes et al. 2008), data for comparison was limited to epsomite and water ice. Based on this new data on numerous MSHs presented in this thesis it would be worthwhile revisiting the

structure of meridianiite and trying to identify reasons for the deviation from the trend observed in the other compounds of the $MgSO_4 - H_2O$ system. Another pronounced deviation from the trend was observed in kieserite. The reason for this is likely the very large negative linear thermal expansion of kieserite (Wildner et al., 2022) reducing the overall volume expansion, whereas α-$MgSO_4$ and β-$MgSO_4$ exhibit positive expansion in all directions at the reference temperature of 240 K.
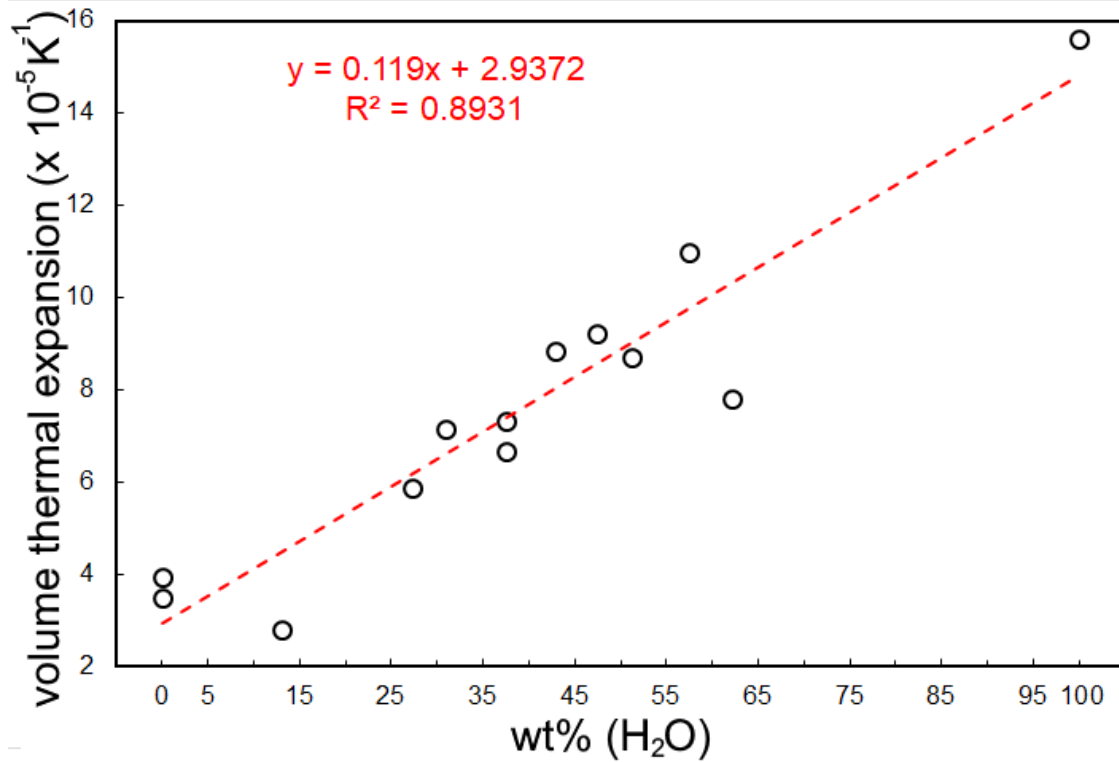
Figure 7.3 Thermal expansion of compounds in the $MgSO_4 - H_2O$ system.

In the icy satellites of the outer solar systems MSHs may be exposed to pressures as high as 3.45 GPa in the centre of Callisto, and 450 K corresponding to the melting point of ice VII at that pressure (Dubrovinsky and Dubrovinskaia ,2007). Wildner et al. (2022) report that the volume decrease in kieserite upon cooling from 293 to 10 K corresponds to a compression of 0.7 GPa. We have obtained comparable results for cranswickite and starkeyite, where cooling from 340 to 10 K corresponds to pressures of 0.6 and 0.7 GPa respectively. This clearly demonstrates that temperature has a pronounced effect on the density of MSHs. Therefore, knowledge of both the compressibility and thermal expansion is critical to model the density evolution of rock forming minerals in the interior of planetary bodies. As for future work it would therefore be of great interest to determine the thermal expansion of other MSHs such as sanderite, and the

synthetic $MgSO_4 \cdot 5H_2O$. Additionally, accurate P-V-T equation of states would enable calculations of the density evolution of MSHs in models of icy satellites.

7.3 Thermal expansion of FSHs

This thesis further reports the thermal expansions of rozenite. In contrast to the MSHs, the thermal expansions of FSHs is largely unknown. Very recently, the thermal expansion of szomolnokite was determined (Wildner et al., 2022), and to the best of my knowledge there are no thermal expansion data for any other FSH reported in the literature. The thermal expansion of rozenite is almost twice as large as szomolnokite's, mirroring the trend of larger thermal expansion for the higher hydrates observed in the MSHs.

Szomolnokite exhibits a 37% larger thermal expansion than isotypic kieserite. Interestingly, Wildner et al. (2022) also studied the thermal expansion of other kieserite-type compounds $MeSO_4 \cdot H_2O$ (Me = Mg, Fe, Co, Ni) and found that their thermal expansion depends on the cation radii of the Me^{2+} central ion of the octahedral unit, and consequently also the molar volume. Intuitively they observed that a larger molar volume results in a larger thermal expansion.

This trend does not hold for the tetrahydrates studied in this thesis, with rozenite and starkeyite displaying virtually identical volume expansion (i.e., at 285 K: α_V (rozenite) = 8.14(9) x 10^{-5} K^{-1}, α_V (starkeyite) = 8.17(12) x 10^{-5} K^{-1}). It is noteworthy, that like the kieserite group also the starkeyite group exhibits numerous isotypic endmembers such as boyleite $ZnSO_4 \cdot 4H_2O$ and ilesite $MnSO_4 \cdot 4H_2O$ (Anderson et al. 2012). The thermal expansion of these compounds, however, has, to the best of my knowledge, never been studied. It would certainly be interesting to find out if these compounds also exhibit the same volume expansion as rozenite and starkeyite.

As a possible explanation for the different thermal expansion of the kieserite group, but virtually identical values for the starkeyite group is the effect of the volume of the MeO_6 units on the unit-cell volume, which is increasingly muted as the hydration state increases (Fortes et al., 2012). This trend is also reflected in the data reported in this thesis, with the MeO_6 polyhedral volume difference between the Mg and Fe endmember being 7.7% in both the starkeyite and kieserite group. The effect of Mg for Fe substitution on the molar volume,

however, is much more pronounced in the kieserite group (2.7%) as compared to the starkeyite group (1.6%).

Substituting the central ion of the MeO_6 does not only change the polyhedral volume, but may also change the thermal expansion properties of this structural unit (Wildner et al., 2022). As for the volume, the influence of this effect upon the molar volume expansion equally is increasingly muted as the hydration state increases. The reason for this is the diminishing contribution of the MeO_6 unit volume to the overall molar volume as more water of crystallisation enters the structure.

I therefore propose that not only the unit-cell volume, but also the thermal expansion will show ever steeper dependencies of the ionic radii of the MeO_6 unit for the 3, 2.5 and 2-hydrate. In addition, based on the virtually identical thermal expansion that was observed for the starkeyite group, it is likely that this behaviour will also be observed in the higher hydrates, since their volume expansion is also largely controlled by the hydrogen bond network.

As a final note on the FSHs, I want to point out that it is curious that 13 MSHs were discovered hitherto, compared to only six FSHs. MSHs and FSHs form mostly isotypic compounds and I cannot think of any obvious reason, why there should not be for example a cranswickite-type $FeSO_4 \cdot 4H_2O$ or sanderite-type $FeSO_4 \cdot 2H_2O$. In my opinion, the reason such compounds where not yet reported is that the FSHs are not as well characterized at variable temperature, pressure and relative humidity conditions as their magnesium counterparts.

- Therefore, it would clearly be interesting to close this gap in literature, and look for other FSHs, both in the laboratory by varying environmental conditions, but also in terrestrial and extra-terrestrial salt deposits using portable XRD or Raman spectroscopy. Since FSHs are also sensitive to changes in temperature and relative humidity, analysing them in the field would prevent any possible transformations that might occur during transport and subsequent analysis in the laboratory. This approach was already successfully applied to MSHs. Cranswickite, for example, was discovered using a portable XRD (Peterson, 2011), and described as a mineral a decade before the conditions for its formation were determined in the laboratory (Meusburger et al., 2022).

- Furthermore, it would be of great interest to study the thermal expansion properties of FSHs and other isotypic transition metal sulfate hydrates. This would allow to investigate trends in the thermal expansion as a function of chemical composition and/or hydration state.

7.4 The polyhydrated sulfate deposits on Mars

Throughout this thesis I have repeatedly referred to the importance of studying promising candidate minerals to constitute the polyhydrated sulfate deposits on Mars. In the following, I will outline how this thesis has advanced our knowledge of the candidate constituents starkeyite and rozenite, the implications this has for the mineralogy of the polyhydrated sulfate deposits, and what open questions remain to be answered.

Interestingly, this thesis has provided indications, both from experimental and theoretical side, that starkeyite is not stable at low-temperature conditions, such as that prevailing on present day Mars. First of all, the DFT calculations, carried out within the static approximation, have revealed that cranswickite is the thermodynamically stable polymorph. Experimentally, we have observed that cranswickite transforms at 330 K, well above the maximum surface temperature of 308 K hitherto reported on Mars (NASA website, 2007). Nevertheless, it would be interesting to explore the long-term stability of cranswickite and starkeyite at variable temperatures to investigate if the cranswickite-starkeyite transition may proceed at lower temperatures, or if even the reverse transformation from starkeyite to cranswickite may be observed under such conditions.

Furthermore, it would be worthwhile to revisit the phase transition likely occurring in starkeyite at 245 K by means of single crystal neutron diffraction. Once solved, the structure of the proposed low-temperature polymorph could be used to investigate its relative stability with respect to cranswickite using *ab initio* calculations. However, the excellent modelling of the 10 K diffraction data using the conventional starkeyite structure gives me reason to believe that the structural and consequently total energy differences between starkeyite and its putative low-temperature polymorph are very subtle.

To obtain more accurate results on the relative stability of cranswickite and starkeyite, more advanced computational studies of the relative stability of the polymorphs would be of great interest. For example, the Gibbs free energy as a

function of temperature, rather than just the enthalpy differences within the static approximation as reported in this study, could be computed by means of DFT. Such calculations are computationally very, but not prohibitively, demanding since they require to compute the complete phonon density of states at variable pressures (Qin et al., 2019).

Based on its likely origin from the alternation of basalt, the polyhydrated sulfate phase is likely a $(Mg_xFe_{1-x})SO_4 \cdot nH_2O$ of intermediate composition, hence it would also be worthwhile to quantify the variable temperature behaviour and stability of intermediate members of the solid solution – even more so since rozenite does not appear to undergo a structural phase transition at low-temperatures. In detail it would be interesting to find out at which iron content the transition is suppressed. Furthermore, *ab initio* studies of a potential cranswickite-type $FeSO_4 \cdot 4H_2O$ would be of great interest, again with a particular focus on how Mg for Fe substitution influences the relative stability of the structure type.

In summary, this thesis has revealed a complex low-temperature behaviour of the tetrahydrates. Additional crystallographic and thermodynamic investigations of $(Mg_xFe_{1-x})SO_4 \cdot 4H_2O$, however, are critical to set constraints upon its stability under Martian surface conditions. Importantly, the Curiosity rover is just about to enter a polyhydrated sulfate-bearing unit (as determined by infrared reflectance data collected from orbit (Milliken et al., 2010)), at Gale crater and will investigate the mineralogy of this strata using XRD. Equally important, the Perseverance rover has most recently detected MSHs at Gale crater (Farley et al. 2022), but no efforts to determine crystallinity or hydration state were undertaken. The reason for this is likely, that the deep-UV Raman reference spectra of just two MSHs were so far determined, and both were assigned only tentatively (Razzell Hollis et al., 2021). To conclude, the coming years promise to provide important *in-situ* data on the current state of MSHs and FSHs exposed to present-day Martian atmospheric conditions. Experimental studies play a vital role to support such space missions, be it by exploring the variable temperature, pressure or humidity stability of candidate phases, or by providing accurate spectroscopic or seismic reference data to enable the identification of these minerals in ongoing and future space missions.

7.5 References

Anderson, J.L., Peterson, R.C., and Swainson, I. (2012) The atomic structure of deuterated boyleite $ZnSO_4 \cdot 4D_2O$, ilesite $MnSO_4 \cdot 4D_2O$, and bianchite $ZnSO_4 \cdot 6D_2O$. American Mineralogist, 97, 1905–1914.

Angel, R.J. (2000) Equations of State. Reviews in Mineralogy and Geochemistry, 41, 35–59.

Birch, F. (1947) Finite Elastic Strain of Cubic Crystals. Physical Review, 71, 809–824.

Bridgman, P.W. (1949) Linear Compressions to 30,000 kg/cm^2, including Relatively Incompressible Substances. Proceedings of the American Academy of Arts and Sciences, 77, 189–234.

Dubrovinsky, L., and Dubrovinskaia, N. (2007) Melting of ice VII and new high-pressure, high-temperature amorphous ice. Special Paper of the Geological Society of America, 421, 105–113.

Farley, K.A., Stack, K.M., Shuster, D.L., Horgan, B.H.N., Hurowitz, J.A., Tarnas, J.D., Simon, J.I., Sun, V.Z., Scheller, E.L., Moore, K.R., and others (2022) Aqueously altered igneous rocks sampled on the floor of Jezero crater, Mars. Science, 377, eabo2196.

Fortes, A., Wood, I., and Knight, K. (2008) The crystal structure and thermal expansion tensor of $MgSO_4 \cdot 11D_2O$ (meridianiite) determined by neutron powder diffraction. Physics and Chemistry of Minerals, 35, 207–221.

Fortes, A.D., Wood, I.G., Alfredsson, M., Vočadlo, L., and Knight, K.S. (2006) The thermoelastic properties of $MgSO_4 \cdot 7D_2O$ (epsomite) from powder neutron diffraction and ab initio calculation. European Journal of Mineralogy, 18, 449–462.

Fortes, A.D., Wood, I.G., Vočadlo, L., Brand, H.E.A., and Knight, K.S. (2007) Crystal structures and thermal expansion of α-$MgSO_4$ and β-$MgSO_4$ from 4.2 to 300K by neutron powder diffraction. Journal of Applied Crystallography, 40, 761–770.

Fortes, A.D., Browning, F., and Wood, I.G. (2012) Cation substitution in synthetic meridianiite ($MgSO_4 \cdot 11H_2O$) II: variation in unit-cell parameters determined from X-ray powder diffraction data. Physics and Chemistry of Minerals, 39, 443–454.

Fortes, A.D., Fernandez-Alonso, F., Tucker, M., and Wood, I.G. (2017a) Isothermal equation of state and high-pressure phase transitions of synthetic meridianiite ($MgSO_411 \cdot D_2O$) determined by neutron powder diffraction and quasielastic neutron spectroscopy. Acta Crystallographica Section B, 73, 33–46.

Fortes, A.D., Knight, K.S., and Wood, I.G. (2017b) Structure, thermal expansion and incompressibility of $MgSO_4 \cdot 9H_2O$, its relationship to meridianiite ($MgSO_4 \cdot 11H_2O$) and possible natural occurrences. Acta Crystallographica Section B, 73, 47–64.

Hogenboom, D.L., Kargel, J.S., Reiter, M.L., and Khor, Y.N. (1997) Volume Changes Attending Hydration of Quenched Magnesium Sulfate Brine: The Tectonics of Ganymede's Sulci. In Lunar and Planetary Science Conference p. 579.

Hudec, M.R., and Jackson, M.P.A. (2007) Terra infirma: Understanding salt tectonics. Earth-Science Reviews, 82, 1–28.

Johnson, B.C., Sheppard, R.Y., Pascuzzo, A.C., Fisher, E.A., and Wiggins, S.E. (2017) Porosity and Salt Content Determine if Subduction Can Occur in Europa's Ice Shell. Journal of Geophysical Research: Planets, 122, 2765–2778.

Li, Y., Vočadlo, L., and Brodholt, J.P. (2022) ElasT: A toolkit for thermoelastic calculations. Computer Physics Communications, 273, 108280.

Luo, C., Deng, X., Wang, W., Shukla, G., Wu, Z., and Wentzcovitch, R.M. (2021) cij: A Python code for quasiharmonic thermoelasticity. Computer Physics Communications, 267, 108067.

Maynard-Casely, H.E., Brand, H.E.A., Wilson, S.A., and Wallwork, K.S. (2021) Mineral Diversity on Europa: Exploration of Phases Formed in the $MgSO_4$–H_2SO_4–H_2O Ternary. ACS Earth and Space Chemistry, 5, 1716–1725.

Meusburger, J.M., Ende, M., Matzinger, P., Talla, D., Miletich, R., and Wildner, M. (2020) Polymorphism of Mg-sulfate monohydrate kieserite under pressure and its occurrence on giant icy jovian satellites. Icarus, 336, 113459.

Meusburger, J.M., Hudson-Edwards, K.A., Tang, C.T., Connolly, E.T., Crane, R.A., and Fortes, A.D. (2022) Phase-transition type negative volume expansion and anisotropic X-ray expansion in magnesium sulfate tetrahydrate. for submission to Angewandte Chemie [in preparation].

Milliken, R.E., Grotzinger, J.P., and Thomson, B.J. (2010) Paleoclimate of Mars as captured by the stratigraphic record in Gale Crater. Geophysical Research Letters, 37, L04201.

Nagel, K., Breuer, D., and Spohn, T. (2004) A model for the interior structure, evolution, and differentiation of Callisto. Icarus, 169, 402–412.

NASA website (2007). Extreme Planet Takes Its Toll. https://www.nasa.gov/mission_pages/mer/mars_mer_feature_20070612.html

Peterson, R.C. (2011) Cranswickite $MgSO_4 \cdot 4H_2O$, a new mineral from Calingasta, Argentina. American Mineralogist, 96, 869–877.

Prentice, A.J.R. (1999) Origin, Bulk Chemical Composition And Physical Structure Of The Galilean Satellites Of Jupiter: A Post-Galileo Analysis. Earth, Moon, and Planets, 87, 11–55.

Qin, T., Zhang, Q., Wentzcovitch, R.M., and Umemoto, K. (2019) qha: A Python package for quasiharmonic free energy calculation for multi-configuration systems. Computer Physics Communications, 237, 199–207.

Razzell Hollis, J., Abbey, W., Beegle, L.W., Bhartia, R., Ehlmann, B.L., Miura, J., Monacelli, B., Moore, K., Nordman, A., Scheller, E., and others (2021) A deep-ultraviolet Raman and Fluorescence spectral library of 62 minerals for the SHERLOC instrument onboard Mars 2020. Planetary and Space Science, 209, 105356.

Smyth, J.R., and Frost, D.J. (2002) The effect of water on the 410-km discontinuity: An experimental study. Geophysical Research Letters, 29, 123-1-123–4.

Wang, W., Fortes, A.D., Dobson, D.P., Howard, C.M., Bowles, J., Hughes, N.J., and Wood, I.G. (2018) Investigation of high-pressure planetary ices by cryo-recovery. II. High-pressure apparatus, examples and a new high-pressure phase of $MgSO_4 \cdot 5H_2O$. Journal of Applied Crystallography, 51, 692–705.

Wehinger, B., Bosak, A., Nazzareni, S., Antonangeli, D., Mirone, A., Chaplot, S.L., Mittal, R., Ohtani, E., Shatskiy, A., Saxena, S., and others (2016) Dynamical and elastic properties of $MgSiO_3$ perovskite (bridgmanite). Geophysical Research Letters, 43, 2568–2575.

Wildner, M., Zakharov, B.A., Bogdanov, N.E., Talla, D., Boldyreva, E. v, and Miletich, R. (2022) Crystallography relevant to Mars and Galilean icy moons: crystal behavior of kieserite-type monohydrate sulfates at extraterrestrial conditions down to 15 K. IUCrJ, 9.

8. Supplementary

8.1 Technical report on the Raman optical centre stick at the HRPD beamline

8.1.1 Case for performing simultaneous neutron diffraction and Raman spectroscopy

Diffraction methods probe the long-range order of crystalline solids and often allow for the determination of their complete time-averaged crystal structure. However, by virtue of determining time-averaged atomic positions, diffraction methods may create the false impression of atoms being held in static positions through stiff chemical bonds, yet they are vibrating dynamically with an amplitude that can be of order of 10% (Dove, 2011) of an interatomic distance. In order to fully characterize a crystalline solid and its response to extreme conditions one is interested in both the static and dynamic behaviour of atoms and their energetic properties and interaction with one another. This is where Raman spectroscopy enters the picture, since it gives a unique insight into lattice dynamical properties of crystalline solids and moreover provides valuable information on the local structural environment.

When combining complementary analytical techniques, it is favourable to acquire both datasets in the very same experiment since it is not always possible to replicate the exact same experimental conditions which may introduce ambiguities and uncertainties in the data interpretation.

Furthermore, the identification of polymorphic phase transitions as well as a*b-initio* structure solution from powder diffraction data are HRPD's core application areas. Phase transitions are often manifested in vibrational mode splitting if they are accompanied by changes in short-range order (site symmetry) and hence can be probed by means of Raman spectroscopy. This allows us to crosscheck the phase boundaries determined by each of the applied methods as well as the structure solutions obtained from the powder diffraction data.

8.1.2 The Raman optical stick

As an ISIS facility development student, I was directly involved with the commissioning and improvement of the in-situ Raman spectroscopy equipment developed for use on HRPD. The optical centre stick (Figure 1) allows for the simultaneous acquisition of Raman and Neutron diffraction data.

The stick comprises a 106 cm^{-1} long aluminum cone that is evacuated in order to prevent scattering from air molecules. At the top of the stick there is a holder for the lens that focusses the laser beam on the sample, sealed in the optical chamber. Aluminium slab cans, for the acquisition of neutron diffraction data may be attached to the optical chamber. The optical centre stick can be inserted into the top loading CCR at the HRPD instrument, and with the use of a spacer, at the SXD instrument. For data acquisition we used B&WTek i-Raman plus spectrometers with lasers of 532 nm and 785 nm wavelength. The laser is connected to the lens and then focused onto the sample in the optical chamber. Raman scattering is detected in backscattering, passing through the optical stick, lens and lastly through a fibre optic cable guiding the photons to the CCD detector.

8.1.3 A python code for simultaneous acquisition of neutron and Raman data

My main contribution was the development of a Python code that enables scripting of both neutron powder diffraction data and Raman spectrum co-acquisition. In order to enable a simultaneous acquisition of both datasets, I had to interface the Raman spectrometer with the IBEX software (Akeroyd et al., 2018) that controls the HRPD instrument. In order to obtain a simultaneous acquisition of Raman and HRPD data, the spectrometer needs to be notified once HRPD starts to acquire data.

Every time HRPD starts a new run, the run number is updated on HRPD's IBEX website in real-time. I have written a code that retrieves the run number from the IBEX website periodically. The frequency of the run number retrieval can be adjusted to any value in the script. Due to the relatively longer acquisition time of the neutron data, as compared to the short measurement times of the Raman spectra, it is typically sufficient to retrieve the run number every minute.

The IBEX website stores the run information not simply in the website's source code, but this information is rendered on the client's side using JavaScript.

In order to overcome this problem, I used the requests-HTML python library (https://requests.readthedocs.io/projects/requests-html/), featuring a headless browser with full JavaScript support to load the website and retrieve the run number.
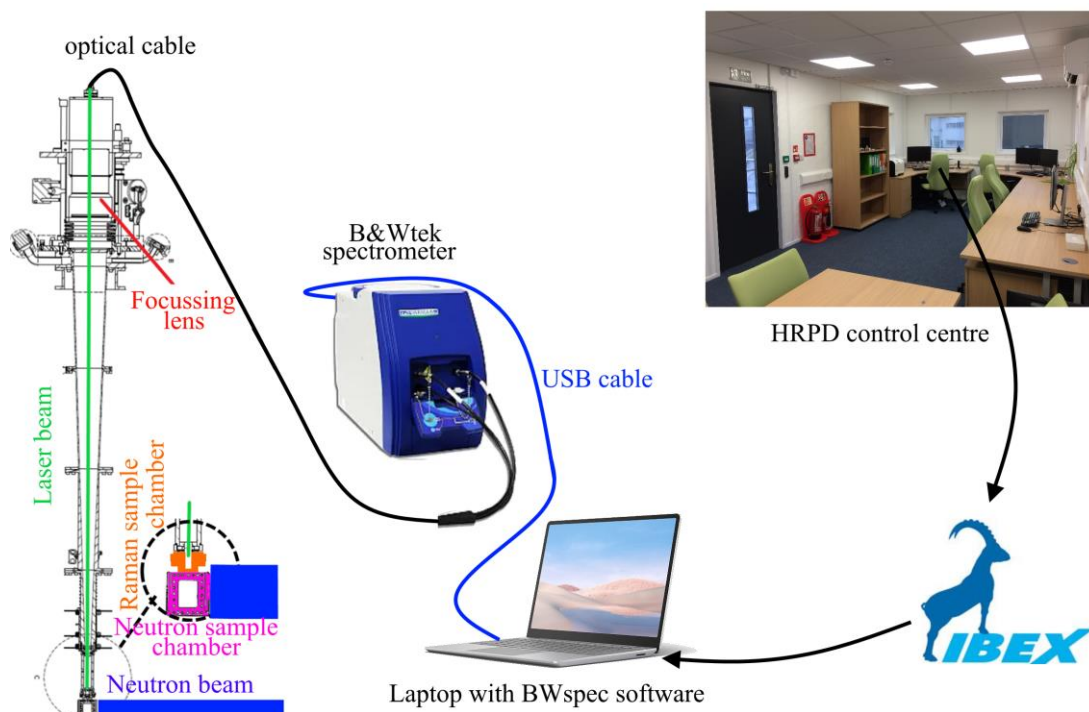
Figure 1. Step 1. A new run is initiated in the HRPD control centre, and the run number updated on ISIS in real time. Step 2. The laptop driving the Raman spectrometer, retrieves the run number ever minute, using my script. Step 3. Once the run number changes with respect to the previous iteration, the Raman data collection is initiated.

Once a new run is started, and the new run number is updated on IBEX, the code initiates a Raman measurement after a dwell time of 10 minutes in order to ensure thermal equilibrium. For the data-acquisition the Raman spectrometer is using the BwSpec software. The code is able to control the keyboard and mouse to start the measurement and save the Raman spectrum as a CSV file. The performance of the python script was tested (Figure 2) and will be briefly summarized in the following Raman and neutron diffraction data simultaneously acquired from 200 – 40 K in 10 K increments, followed by a 10-hour soak at the base temperature. Then data was collected from 30 – 75 K upon heating. The code finished the Raman data acquisition before the end of each neutron diffraction run, for each data point (Figure 2). Importantly, this workflow is clearly transferable to run all kinds of different equipment in parallel with the HRPD instrument, but also other ISIS instruments that are controlled by the IBEX software. Lastly, I want to point out that next to the code development, I also worked on the technical challenges associated with laser alignment and

188

focussing, and the practical problems of loading air- and temperature-sensitive samples into the newly developed diffraction and optical sample holders.
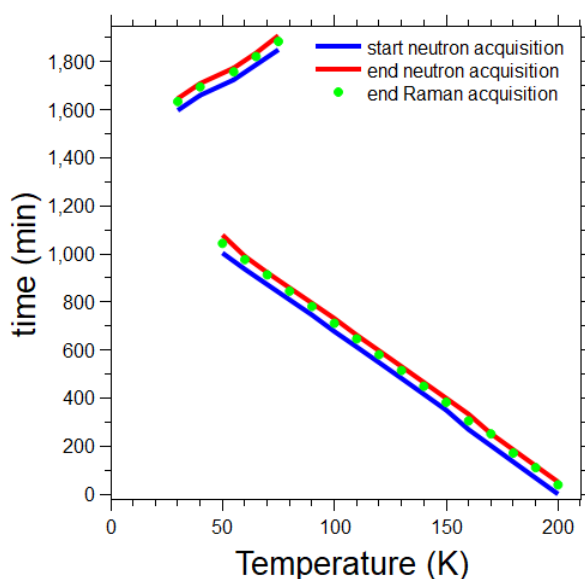
Figure 2. Test run for the simultaneous acquisition of Raman spectra and neutron diffraction data. Note that for all temperature points, the Raman data acquisition ended before completion of the neutron run.

Due to the still ongoing shutdown of target station one, we did not have a chance yet to test these improvements, and for this reason will be included in the final commissioning report, rather than included in this thesis.

8.1.4 Ca(NO$_3$)$_2$ – A commissioning example

For the commissioning of the stick we have characterised the low-temperature behaviour of Ca(NO$_3$)$_2$ down to 50 K by coupled high resolution neutron powder diffraction and Raman spectroscopy on the HRPD instrument. In this temperature range two structural phase transitions had already been identified both by means of heat capacity (Shomate & Kelley, 1944) and vibrational spectroscopy (Brooker, 1976) measurements. Ca(NO$_3$)$_2$ undergoes a series of phase transitions: α ($Pa\bar{3}$) $\rightarrow$ β ($Pbca$) $\rightarrow$ γ (Pc) $\rightarrow$ δ ($P2_1ab$). It is noteworthy that at 80 K both the δ and γ phase coexist suggesting that the phase transition proceeds sluggishly and is thermodynamically first order. The phase transitions are apparent both in the neutron diffraction and Raman spectroscopy dataset (Figure 3a, 3b). The herein reported critical temperatures of transformation are in excellent agreement with the phase boundaries by Shomate & Kelley (1944) and the vibrational mode splitting matches the fingerprint of the phase transitions reported by Brooker (1976) (Figure 3c).
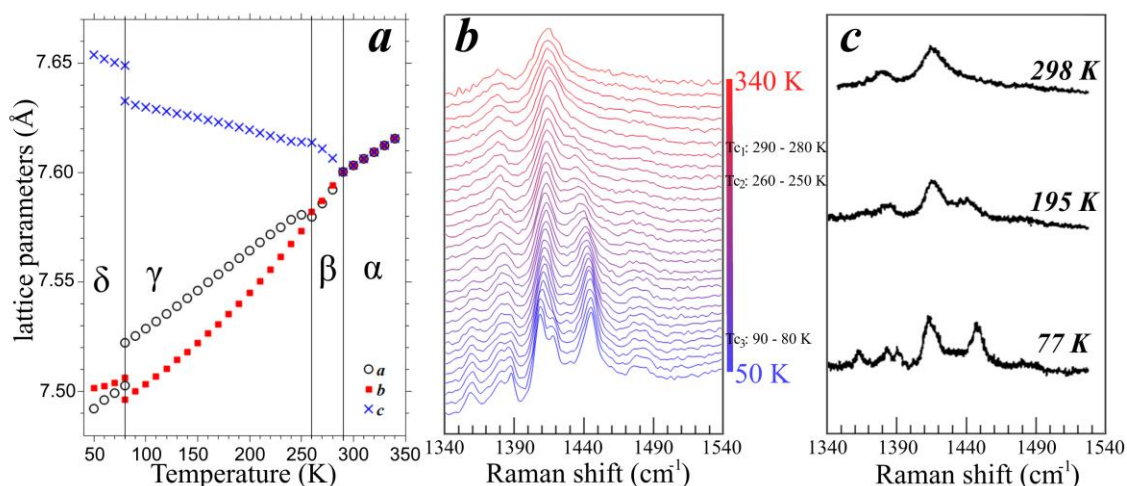
Figure 3 (a) Lattice parameter from Neutron powder diffraction (b) simultaneously acquired Raman spectra (c) Raman spectra by Brooker (1976) for comparison.

Lastly, we observed a previously unreported *β* phase of *Pbca* symmetry.

8.1.5 References

Akeroyd, F. A., Baker, K. V. L., Clarke, M. J., Holt, J. R., Howells, G. D., Keymer, D. P., Löhnert, T., Moreton-Smith, C. M., Oram, D. E., Potter, A., Rey, I. H., Willemsen, T. A., & Woods, K. (2018). IBEX - an EPICS based control system for the ISIS pulsed neutron and muon source. Journal of Physics: Conference Series, 1021, 012019. https://doi.org/10.1088/1742-6596/1021/1/012019

Brooker, M. H. (1976). Raman and i.r. spectra of zinc, cadmium and calcium nitrate: A study of the low temperature phase transitions in calcium nitrate. Spectrochimica Acta Part A: Molecular Spectroscopy, 32(2), 369–377. https://doi.org/https://doi.org/10.1016/0584-8539(76)80090-6

Dove, M. T. (2011). Introduction to the theory of lattice dynamics.

Shomate, C. H., & Kelley, K. K. (1944). The Specific Heats at Low Temperatures of Nitrates of Magnesium, Calcium, Barium and Aluminum1. Journal of the American Chemical Society, 66(9), 1490–1492. https://doi.org/10.1021/ja01237a021

8.2 Supplementary: Elasticity of selected icy satellite candidate materials (CO_2, C_6H_6, $MgSO_4 \cdot 7H_2O$ and $CaSO_4 \cdot 2H_2O$) revisited by dispersion corrected density functional theory

Electronic Supplementary Information

Contents

S1. Convergence testing

Compound	Input geometry	Cut-off energy (eV)	k-points
CO_2	(Simon & Peters, 1980)	1300	5 x 5 x 5
C_6H_6	(Maynard-Casely et al., 2016)	1300	4 x 3 x 4
$MgSO_4 \cdot 7H_2O$[1]	Fortes et al., 2006	1300	2 x 4 x 4
$CaSO_4 \cdot 2H_2O$[2]	(Comodi et al., 2008)	1300	5 x 5 x 5

Tab. 1 Converged basis set parameters and input geometries for all compounds under investigation. [1]the deuterium atoms have been replaced with their hydrogenated counterparts [2]optimisation for $CaSO_4 \cdot 2H_2O$ were carried out using the reduced cell.

Single point en ergy runs at cut-off energies ranging from 500 to 1400 and variable k-point spacing were carried out for each of the title compounds (Fig. s1a-d). It is evident that the parameters values reported in Tab. 1. yield well converged results and denser k-point sampling and higher cut-offs does not further improve the calculation.
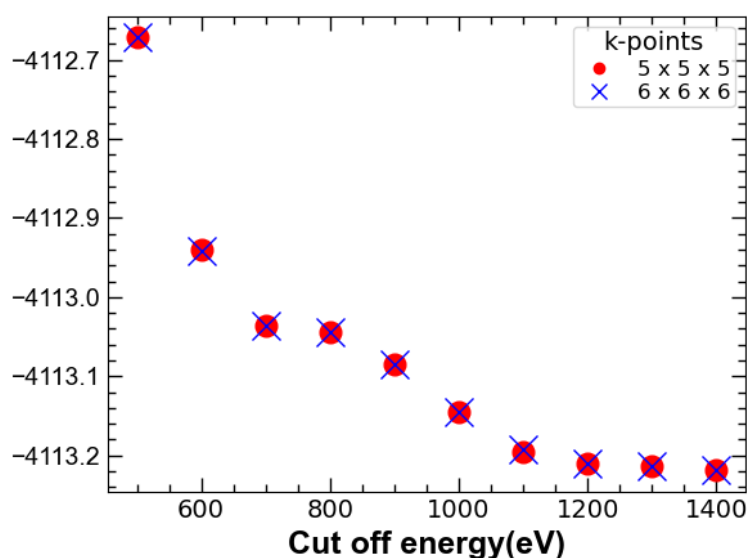
Fig. s1a. Single point energy runs for CO_2 at various cut-off energies and k-point spacing
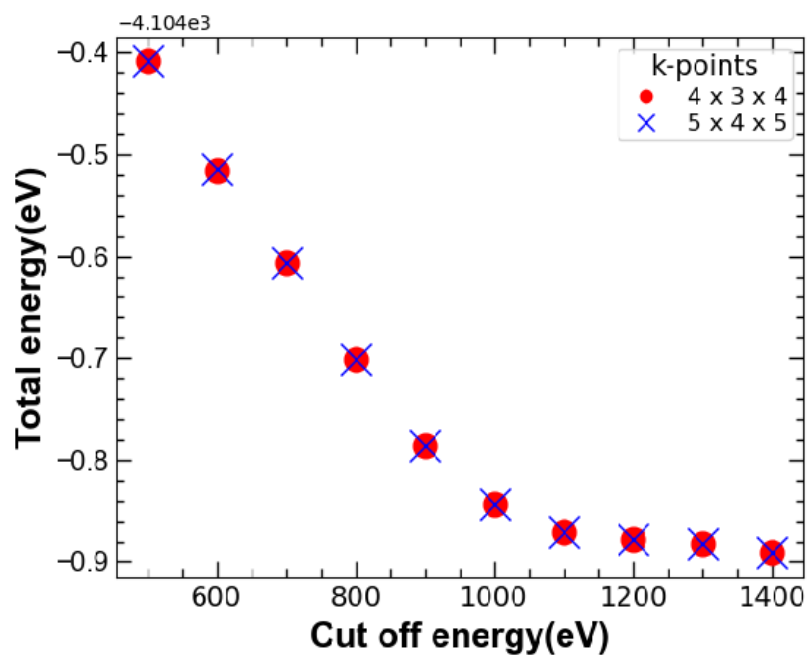
Fig. s1b. Single point energy runs for C_6H_6 at various cut-off energies and k-point spacing.
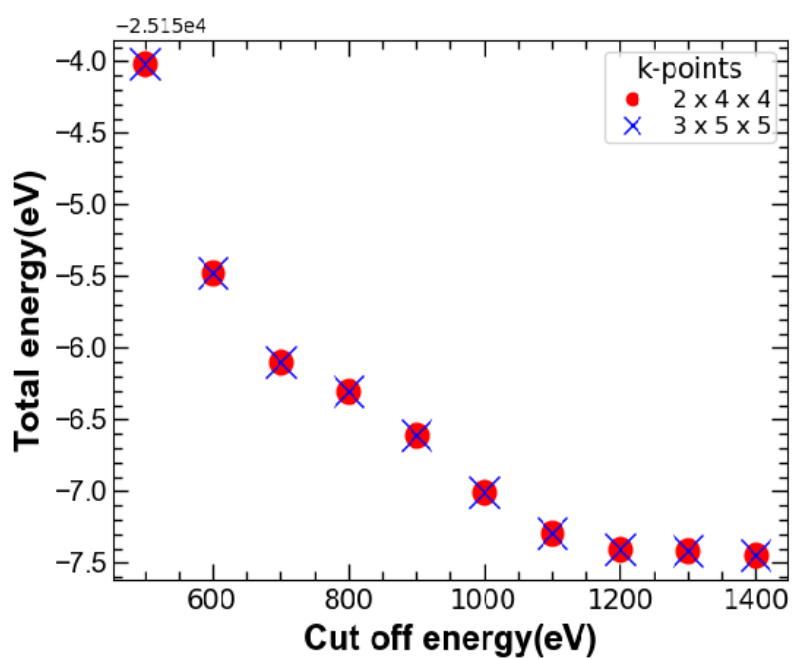
Fig. s1c. Single point energy runs for epsomite at various cut-off energies and k-point spacing.

193
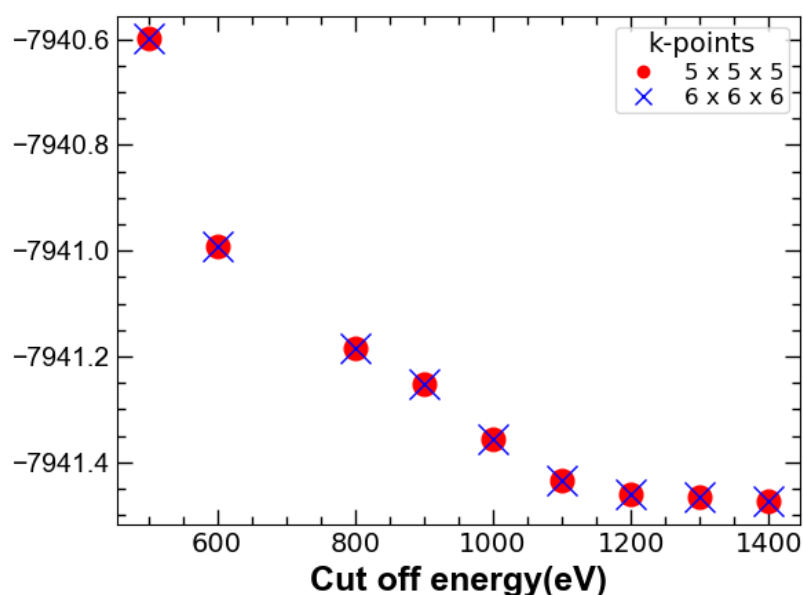
Fig. s1d. Single point energy runs for gypsum at various cut-off energies and k-point spacing.

S2. Sample input files

PBE

.param file

task : GeometryOptimization

comment : CASTEP calculation from Materials Studio

xc_functional : PBE

spin_polarized : false

opt_strategy : Default

page_wvfns :   0

cut_off_energy :   1300.000000000000000

grid_scale :   2.000000000000000

fine_grid_scale :   3.000000000000000

finite_basis_corr :   2

finite_basis_npoints :   3

elec_energy_tol :   5.000000000000000e-007

max_scf_cycles :   100

fix_occupancy : true

metals_method : dm

mixing_scheme : Pulay

mix_charge_amp :   0.500000000000000

mix_charge_gmax :   1.500000000000000

mix_history_length :   20

nextra_bands : 0

num_dump_cycles : 0

geom_energy_tol :   5.000000000000000e-006

geom_force_tol :   0.010000000000000

geom_stress_tol :   0.010000000000000

geom_disp_tol :   5.000000000000000e-004

geom_max_iter :   100

geom_method : BFGS

fixed_npw : false

geom_modulus_est :   25.000000000000000 GPa

calculate_ELF : false

calculate_stress : true

popn_calculate : false

calculate_hirshfeld : false

calculate_densdiff : false

pdos_calculate_weights : false

PBE+D2

task : GeometryOptimization

comment : CASTEP calculation from Materials Studio

xc_functional : PBE

sedc_apply : true

sedc_scheme : G06

sedc_s6_g06 :   0.750000000000000

sedc_d_g06 :   20.000000000000000

spin_polarized : false

opt_strategy : Default

page_wvfns :   0

cut_off_energy :   1.300000000000000e+003

grid_scale :   2.000000000000000

fine_grid_scale :   3.000000000000000

finite_basis_corr :   2

finite_basis_npoints :   3

elec_energy_tol :   5.000000000000000e-007

max_scf_cycles :   100

fix_occupancy : true

metals_method : dm

mixing_scheme : Pulay

mix_charge_amp :   0.500000000000000

mix_charge_gmax :   1.500000000000000

mix_history_length :   20

nextra_bands : 0

num_dump_cycles : 0

geom_energy_tol :   5.000000000000000e-006

geom_force_tol :   0.010000000000000

geom_stress_tol :   0.010000000000000

geom_disp_tol :   5.000000000000000e-004

geom_max_iter :   500

geom_method : BFGS

fixed_npw : false

geom_modulus_est :   25.000000000000000 GPa

calculate_ELF : false

calculate_stress : true

popn_calculate : false

calculate_hirshfeld : false

calculate_densdiff : false

pdos_calculate_weights : false

write_cif_structure: true

write_cell_structure: true

Dispersion correction parameters as specified in the .cell file

%BLOCK SEDC_CUSTOM_PARAMS

   H   C6:1.4509976437   R0:1.0010000467

   C   C6:18.1374704688   R0:1.4520000219

   O   C6:7.2549880640   R0:1.3420000076

  Mg   C6:59.1799754678   R0:1.3639999628

```
    S    C6:57.7289792141    R0:1.6829999685
    Ca    C6:111.9341054414    R0:1.4739999771
%ENDBLOCK SEDC_CUSTOM_PARAMS
```

PBE+TS

task : GeometryOptimization

comment : CASTEP calculation from Materials Studio

xc_functional : PBE

sedc_apply : true

sedc_scheme : TS

sedc_sr_ts :   0.940000000000000

sedc_d_ts :   20.000000000000000

spin_polarized : false

opt_strategy : Default

page_wvfns :   0

cut_off_energy :   1.300000000000000e+003

grid_scale :   2.000000000000000

fine_grid_scale :   3.000000000000000

finite_basis_corr :   2

finite_basis_npoints :   3

elec_energy_tol :   5.000000000000000e-007

max_scf_cycles :   100

fix_occupancy : true

metals_method : dm

mixing_scheme : Pulay

mix_charge_amp :   0.500000000000000

mix_charge_gmax :   1.500000000000000

mix_history_length :   20

nextra_bands : 0

num_dump_cycles : 0

geom_energy_tol :   5.000000000000000e-006

geom_force_tol :   0.010000000000000

geom_stress_tol :   0.010000000000000

geom_disp_tol :   5.000000000000000e-004

geom_max_iter :   500

geom_method : BFGS

fixed_npw : false

geom_modulus_est :   25.000000000000000 GPa

calculate_ELF : false

calculate_stress : true

popn_calculate : false

calculate_hirshfeld : false

calculate_densdiff : false

pdos_calculate_weights : false

write_cif_structure: true

write_cell_structure: true

Dispersion correction parameters as specified in the .cell file


```
%BLOCK SEDC_CUSTOM_PARAMS
    H    C6:3.8839237690     R0:1.6404492855   alpha:0.6668310761
    C    C6:27.8447437286     R0:1.8997460604   alpha:1.7782162428
    O    C6:9.3214168549     R0:1.6880753040   alpha:0.8001973033
   Mg    C6:374.6492614746     R0:2.2595865726   alpha:10.5211124420
    S    C6:80.0685806274     R0:2.0426239967   alpha:2.9044198990
   Ca    C6:1327.1068115234     R0:2.4606740475   alpha:23.7095489502
%ENDBLOCK SEDC_CUSTOM_PARAMS
```

PBE+MBD

It is noteworthy that the output geometry of the PBE+TS calculation served as input geometry for the PBE+MBD optimisations.

task : GeometryOptimization

comment : CASTEP calculation from Materials Studio

xc_functional : PBE

sedc_apply : true

sedc_scheme : mbd*

spin_polarized : false

opt_strategy : Default

page_wvfns :   0

cut_off_energy :   1.300000000000000e+003

grid_scale :   2.000000000000000

fine_grid_scale :   3.000000000000000

finite_basis_corr :   2

finite_basis_npoints :   3

elec_energy_tol :   5.000000000000000e-007

max_scf_cycles :   100

fix_occupancy : true

metals_method : dm

mixing_scheme : Pulay

mix_charge_amp :   0.500000000000000

mix_charge_gmax :   1.500000000000000

mix_history_length :   20

nextra_bands : 0

num_dump_cycles : 0

geom_energy_tol :   5.000000000000000e-006

geom_force_tol :   0.010000000000000

geom_stress_tol :   0.010000000000000

geom_disp_tol :   5.000000000000000e-004

geom_max_iter :   500

geom_method : BFGS

fixed_npw : false

geom_modulus_est :   10.000000000000000 GPa

calculate_ELF : false

calculate_stress : true

popn_calculate : false

calculate_hirshfeld : false

calculate_densdiff : false

pdos_calculate_weights : false

write_cif_structure: true

write_cell_structure: true

PBEsol

task : GeometryOptimization

comment : CASTEP calculation from Materials Studio

xc_functional : PBEsol

spin_polarized : false

opt_strategy : Default

page_wvfns :   0

cut_off_energy :   1300.000000000000000

grid_scale :   2.000000000000000

fine_grid_scale :   3.000000000000000

finite_basis_corr :   2

finite_basis_npoints :   3

elec_energy_tol :   5.000000000000000e-007

max_scf_cycles :   100

fix_occupancy : true

metals_method : dm

mixing_scheme : Pulay

mix_charge_amp :   0.500000000000000

mix_charge_gmax :   1.500000000000000

mix_history_length :   20

nextra_bands : 0

num_dump_cycles : 0

geom_energy_tol :   5.000000000000000e-006

geom_force_tol :   0.010000000000000

geom_stress_tol :   0.010000000000000

geom_disp_tol :   5.000000000000000e-004

geom_max_iter :   100

geom_method : BFGS

fixed_npw : false

geom_modulus_est :   25.000000000000000 GPa

calculate_ELF : false

calculate_stress : true

popn_calculate : false

calculate_hirshfeld : false

calculate_densdiff : false

pdos_calculate_weights : false

write_cif_structure: true

write_cell_structure: true

PBEsol+D2

task : GeometryOptimization

comment : CASTEP calculation from Materials Studio

xc_functional : PBESOL

sedc_apply : true

sedc_scheme : G06

sedc_s6_g06 :   1.000000000000000

sedc_d_g06 :   20.000000000000000

spin_polarized : false

opt_strategy : Default

page_wvfns :   0

cut_off_energy :   1.300000000000000e+003

grid_scale :   2.000000000000000

fine_grid_scale :   3.000000000000000

finite_basis_corr :   2

finite_basis_npoints :   3

elec_energy_tol :   5.000000000000000e-007

max_scf_cycles :   100

fix_occupancy : true

metals_method : dm

mixing_scheme : Pulay

mix_charge_amp :   0.500000000000000

mix_charge_gmax :   1.500000000000000

mix_history_length :   20

nextra_bands : 0

num_dump_cycles : 0

geom_energy_tol :   5.000000000000000e-006

geom_force_tol :   0.010000000000000

geom_stress_tol :   0.010000000000000

geom_disp_tol :   5.000000000000000e-004

geom_max_iter :   200

geom_method : BFGS

fixed_npw : false

geom_modulus_est :   25.000000000000000 GPa

calculate_ELF : false

calculate_stress : true

popn_calculate : false

calculate_hirshfeld : false

calculate_densdiff : false

pdos_calculate_weights : false

write_cif_structure: true

write_cell_structure: true

Dispersion correction parameters as specified in the .cell file

%BLOCK SEDC_CUSTOM_PARAMS
      H   C6:1.4509976437   R0:1.29220006029
      C   C6:18.1374704688   R0:1.8744000282
      O   C6:7.2549880640   R0:1.732400009817
     Mg   C6:59.1799754678   R0:1.76079995198
      S   C6:57.7289792141   R0:2.17259995934
     Ca   C6:111.9341054414   R0:1.90279997044
%ENDBLOCK SEDC_CUSTOM_PARAMS

PBEsol+TS

task : GeometryOptimization

comment : CASTEP calculation from Materials Studio

xc_functional : PBESOL

sedc_apply : true

sedc_scheme : TS

sedc_sr_ts :   1.060000000000000

sedc_d_ts :   20.000000000000000

spin_polarized : false

opt_strategy : Default

page_wvfns :   0

cut_off_energy :   1.300000000000000e+003

grid_scale :   2.000000000000000

fine_grid_scale :   3.000000000000000

finite_basis_corr :   2

finite_basis_npoints :   3

elec_energy_tol :   5.000000000000000e-007

max_scf_cycles :   100

fix_occupancy : true

metals_method : dm

mixing_scheme : Pulay

mix_charge_amp :   0.500000000000000

mix_charge_gmax :   1.500000000000000

mix_history_length :   20

nextra_bands : 0

num_dump_cycles : 0

geom_energy_tol :   5.000000000000000e-006

geom_force_tol :   0.010000000000000

geom_stress_tol :   0.010000000000000

geom_disp_tol :   5.000000000000000e-004

geom_max_iter :   200

geom_method : BFGS

fixed_npw : false

geom_modulus_est :   25.000000000000000 GPa

calculate_ELF : false

calculate_stress : true

popn_calculate : false

calculate_hirshfeld : false

calculate_densdiff : false

pdos_calculate_weights : false

write_cif_structure: true

write_cell_structure: true

Dispersion correction parameters as specified in the .cell file

%BLOCK SEDC_CUSTOM_PARAMS
    H   C6:3.8839237690   R0:1.6404492855 alpha:0.6668310761

C   C6:27.8447437286   R0:1.8997460604   alpha:1.7782162428

O   C6:9.3214168549   R0:1.6880753040   alpha:0.8001973033

Mg   C6:374.6492614746   R0:2.2595865726   alpha:10.5211124420

S   C6:80.0685806274   R0:2.0426239967   alpha:2.9044198990

Ca   C6:1327.1068115234   R0:2.4606740475   alpha:23.7095489502

%ENDBLOCK SEDC_CUSTOM_PARAMS

S3. EoS-Fit7 input files

CO_2

CO2 PBE

system, cubic

FORMAT 1 P A

-0.0010, 6.043934

0.5000 , 5.817703

1.0010, 5.684635

1.5028, 5.595017

1.9966, 5.522587

CO2 PBE+D2

system, cubic

FORMAT 1 P A

-0.0016, 5.653765

0.5013, 5.558910

0.9990, 5.491215

1.4939, 5.439106

1.9987, 5.395771

CO2 PBE+TS

system, cubic

FORMAT 1 P A

0.0097, 5.801235

0.5040, 5.683074

1.0026, 5.594796

1.4975, 5.522820

2.0058, 5.465015

CO2 PBE+MBD

system, cubic

FORMAT 1 P A

-0.0037, 5.754980

0.5084, 5.635544

1.0031, 5.547191

1.5081, 5.478632

1.9935, 5.425206

CO2 PBEsol

system, cubic

FORMAT 1 P A

0.0089, 5.797931

0.5078, 5.608105

0.9996, 5.496378

1.4945, 5.425145

1.9978, 5.366362

CO2 PBEsol+D2

system, cubic

FORMAT 1 P A

0.0010, 5.688195

0.4975, 5.542284

1.0090, 5.454335

1.4972, 5.386934

2.0031, 5.332595

CO2 PBEsol+TS

system, cubic

FORMAT 1 P A

-0.0023, 5.695043

0.4944, 5.550551

0.9917, 5.459476

1.5059, 5.390771

1.9932, 5.336641

C$_6$H$_6$

Benzene PBE

system, orthorhombic

FORMAT 1 P A B C

-0.0002, 8.079146 , 10.071134 , 7.505618

0.4981, 7.512034 , 9.719862 , 7.054056

0.9995 , 7.431872 , 9.485905 , 6.768520

1.4991, 7.321712 , 9.325538 , 6.628962

1.9942, 7.225934 , 9.198581 , 6.540469

Benzene PBE+D2

system, orthorhombic

FORMAT 1 P A B C

0.0007, 7.116619 , 9.070820 , 6.461131

0.5045, 7.045024 , 8.990141 , 6.340295

0.9999 , 7.024325 , 8.878764 , 6.254941

1.5002, 6.974685 , 8.808411 , 6.205882

2.0048 , 6.940125 , 8.746427 , 6.158690

Benzene PBE+TS

system, orthorhombic

FORMAT 1 P A B C

-0.0016, 7.370602 , 9.209387, 6.793223

0.4971, 7.223770 , 9.109777 , 6.691858

0.9976, 7.130477 , 9.033106, 6.599092

1.4971, 7.055969 , 8.971627 , 6.520447

1.9998, 6.993486, 8.919834 , 6.454503

Benzene PBE_MBD

system, orthorhombic

FORMAT 1 P A B C

-0.0024 , 7.332779 , 9.393886 , 6.710093

0.4988 , 7.206044 , 9.208799 , 6.599839

1.0019 , 7.155862, 9.068833 , 6.483801

1.4968, 7.083064 , 9.008336, 6.394846

1.9958 , 7.028885 , 8.939748 , 6.326397

Benzene PBEsol

system, orthorhombic

FORMAT 1 P A B C

0.0007, 7.467660, 9.730824 , 6.912804

0.4934, 7.284494, 9.344396 , 6.638818

1.0016 , 7.177061 , 9.144841, 6.499538

1.5045 , 7.102016 , 9.025035, 6.396184

1.9950, 7.042937 , 8.932411 , 6.316777

Benzene PBEsol + D2

system, orthorhombic

FORMAT 1 P A B C

-0.0009 , 7.215634 , 9.234918 , 6.740412

0.5047 , 7.139696 , 9.098774 , 6.577974

1.0005 , 7.074017 , 9.004113 , 6.447824

1.5031 , 7.020232, 8.854938 , 6.384022

1.9950, 6.976577 , 8.781792 , 6.298872

Benzene PBEsol + TS

system, orthorhombic

FORMAT 1 P A B C

-0.0017 , 7.170292 , 9.268309, 6.712339

0.4944 , 7.097204 , 9.086285 , 6.534455

1.0039, 7.041775, 8.949367, 6.412439

 1.4987 , 6.994291 , 8.850277 , 6.319295

 2.0017, 6.954961 , 8.782632 , 6.233514

MgSO₄•7H₂O

Epsomite PBE

system, orthorhombic

FORMAT 1 P A B C

0.0042, 12.088032, 12.140280 , 6.828839

0.4976, 12.022317, 12.040046 , 6.788703

1.0022, 11.968778 , 11.948713 , 6.753645

1.5076, 11.923468 , 11.858073 , 6.719985

2.0067, 11.878078, 11.781654 ,   6.690913

Epsomite PBE + D2

system, orthorhombic

FORMAT 1 P A B C

0.0025, 11.911623 , 11.861904 , 6.730894

0.5020, 11.864240 , 11.774256 , 6.694453

0.9999, 11.810378 , 11.702694 , 6.661825

1.5051, 11.761708 , 11.633951 , 6.626925

1.9991, 11.713242, 11.570844, 6.597551

Epsomite PBE+TS

system, orthorhombic

FORMAT 1 P A B C

0.0026 , 11.969733 , 11.901343 , 6.716997

0.4994 , 11.920587 , 11.807613 , 6.686450

0.9969, 11.873550 , 11.733085 , 6.651124

1.4977, 11.823811 , 11.660743 , 6.622262

1.9990, 11.771826 , 11.591276 , 6.597127

Epsomite PBE MBD

system, orthorhombic

FORMAT 1 P A B C

-0.0030, 11.942675, 11.876994 ,   6.727911

0.4998 , 11.923062 , 11.798260 , 6.688873

1.0081, 11.849301 , 11.712469 , 6.654607

1.5054,   11.803442 , 11.635673 , 6.626641

2.0068,   11.758272 , 11.566243, 6.601145

Epsomite PBEsol
system, orthorhombic
FORMAT 1 P A B C
-0.0025, 11.904184 , 11.862589 , 6.705788
0.5007,   11.850711 , 11.786154 , 6.671731
1.0063 , 11.793449 , 11.705495 , 6.640750
1.5019 , 11.745258 ,   11.637111 , 6.612177
2.0051, 11.701656 , 11.564760   , 6.583870

Epsomite PBEsol+D2
system, orthorhombic
FORMAT 1 P A B C
0.0002 , 11.853258 , 11.706032 , 6.640369
0.5016 , 11.794150 , 11.647396 , 6.609480
1.0022   , 11.744244 , 11.568822 , 6.582916
1.4983 , 11.702098 , 11.499277 , 6.563584
1.9977, 11.658474, 11.440811, 6.542156

Epsomite PBEsol+TS
system, orthorhombic
FORMAT 1 P A B C
-0.0041, 11.822771   , 11.747714 ,   6.644040
0.4961   , 11.775021 , 11.676176 , 6.614466
1.0078   , 11.731255 ,   11.595677   , 6.588234
1.4999 , 11.687659 , 11.536539 , 6.561818
 1.9966, 11.637409 , 11.473170 , 6.540642

CaSO$_4$•2H$_2$O

gypsum PBE
system, monoclinic
FORMAT 1 P A B C Beta
0.0062,   6.41640, 15.20750, 5.71840, 114.3760

0.4990 , 6.39300, 15.13600 , 5.70910 ,114.4883

0.9963, 6.36650, 15.09560, 5.69220, 114.6666

1.5050, 6.34210 15.05770 5.67790, 114.8266

1.9965, 6.32160 , 15.00580, 5.66410, 114.9722

gypsum PBE+D2

system, monoclinic

FORMAT 1 P A B C Beta

-0.0071, 6.40410, 14.95130, 5.67730, 115.2940

0.5059, 6.37710, 14.91850 , 5.66450, 115.4965

1.0021, 6.35050, 14.88580, 5.64880, 115.8007

1.5032, 6.32710, 14.85390 , 5.63400, 115.9579

2.0042, 6.30170 , 14.83930, 5.61730 , 116.1595

gypsum PBE+TS

system, monoclinic

FORMAT 1 P A B C Beta

0.0029, 6.32550, 15.05060 , 5.64320 , 114.6152

0.5017, 6.30350, 15.01750 , 5.62740, 114.8396

0.9959, 6.28240, 14.97750, 5.61300, 114.9661

1.4972, 6.26250 , 14.94500, 5.59770, 115.0862

2.0031, 6.24270 , 14.91610 , 5.58550 , 115.2518

gypsum PBE+MBD

system, monoclinic

FORMAT 1 P A B C Beta

0.0017, 6.27520 ,14.90970 , 5.69450, 115.1637

0.4962, 6.25560, 14.85710, 5.68470 ,115.3047

0.9981, 6.23230, 14.83960, 5.66490 , 115.5205

1.4976, 6.21260 ,14.79240 , 5.65380 , 115.6323

1.9960, 6.19070 ,14.77240 , 5.63800, 115.8137

gypsum PBEsol

system, monoclinic

FORMAT 1 P A B C Beta

-0.0005, 6.31030, 14.93700, 5.64610, 114.8911

0.4994,   6.28390, 14.90210, 5.63190, 115.1061

0.9990, 6.26110, 14.87360, 5.61770, 115.2735

1.5010, 6.23920, 14.83070, 5.60680, 115.3931

1.9950, 6.21970 ,14.80360 ,5.59220 , 115.5703

gypsum PBEsol+D2

system, monoclinic

FORMAT 1 P A B C Beta

0.0010,   6.26420, 14.87790 , 5.62240 , 114.8240

0.4952, 6.24010, 14.84130 , 5.61070, 115.0426

1.0038, 6.21860, 14.82020, 5.59590 , 115.2076

1.5063,   6.19880, 14.79120 , 5.58170,   115.3950

1.9987, 6.18080 ,14.76650 , 5.56800 , 115.5705

gypsum PBEsol+TS

system, monoclinic

FORMAT 1 P A B C Beta

0.0060 , 6.25390 , 14.93230 , 5.58760, 115.2190

0.4967 ,   6.23160, 14.90710 , 5.56970 ,115.3523

1.0022 , 6.20780 ,14.88000 , 5.55750, 115.5226

1.5081 , 6.18780, 14.84940 , 5.54460, 115.7055

2.0051 , 6.16960, 14.82690 , 5.53080 , 115.8820

S4. Seismic wave velocities gypsum:

Experimental   PBE + D2   PBEsol

Primary wave velocity

Fast shear wave velocity

Slow shear wave velocity
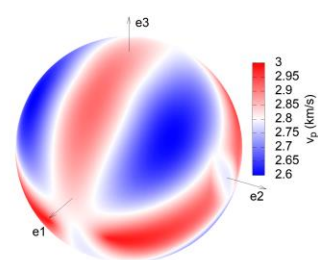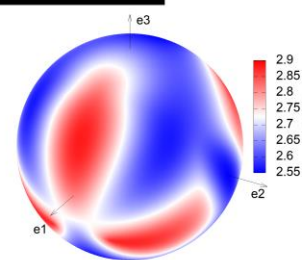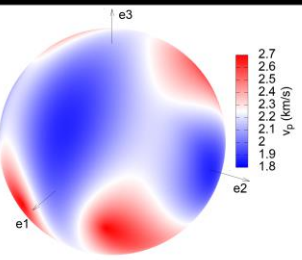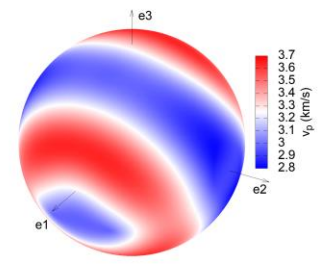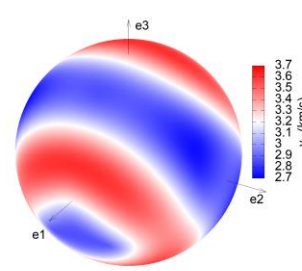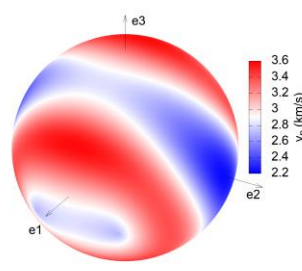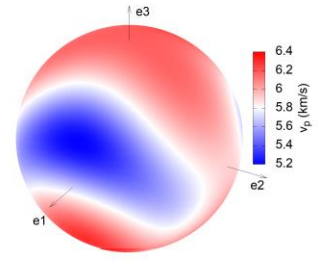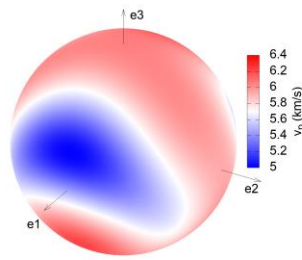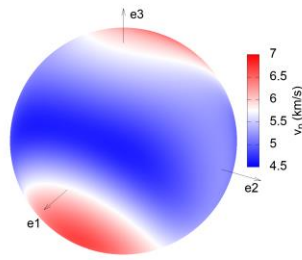
Fig. s2. Seismic wave velocities as obtained for gypsum computed from the experimentally (Haussühl, 1965) and computationally derived elastic constants (this study).

S5. Solving the Christoffel equation:

In the following we will elucidate the relationship between the elastic constants and the seismic wave velocities by solving the Christoffel equation for the main directions.

$$(\Gamma_{ik} - \rho v^2 \delta_{ik}) p_k = 0 \quad \text{(eq. s1)}$$

Here δ_{ik} is the Kronecker delta (1 if i=k, 0 otherwise), thus ρv^2 and p_k are the Christoffel matrix's eigenvalues and eigenvectors, respectively.

$$\begin{bmatrix} \Gamma_{11} - \rho v_1^2 & \Gamma_{12} & \Gamma_{31} \\ \Gamma_{12} & \Gamma_{22} - \rho v_2^2 & \Gamma_{32} \\ \Gamma_{13} & \Gamma_{23} & \Gamma_{33} - \rho v_3^2 \end{bmatrix} \begin{bmatrix} p_1 \\ p_2 \\ p_3 \end{bmatrix} = 0 \quad \text{(eq. s2)}$$

In the most general, triclinic case, 21 independent components C_{ij} must be specified in order to fully account for the elastic anisotropy.

The Christoffel matrix Γ_{ik} is related to the elastic tensor by

$$\Gamma_{ik} = c_{ijkl}\, \hat{q}_j \hat{q}_l \qquad \text{(eq. s3)}$$

The 6 independent Γ_{ik} in direction q are thus:

General case: triclinic symmetry

Tensor notation:

$$\Gamma_{11} = c_{1111}q_1q_1 + c_{1212}q_2q_2 + c_{1313}q_3q_3 + c_{1112}q_1q_2 + c_{1211}q_2q_1$$
$$+ c_{1113}q_1q_3 + c_{1311}q_3q_1 + c_{1213}q_2q_3 + c_{1312}q_3q_2$$

Voigt notation:

$$\Gamma_{11} = C_{11}q_1q_1 + C_{66}q_2q_2 + C_{55}q_3q_3$$
$$+ 2\,(C_{16}q_1q_2 + C_{15}q_1q_3 + C_{56}q_2q_3)$$

Tensor notation:

$$\Gamma_{22} = c_{2121}q_1q_1 + c_{2222}q_2q_2 + c_{2323}q_3q_3 + c_{2122}q_1q_2 + c_{2221}q_2q_1$$
$$+ c_{2123}q_1q_3 + c_{2321}q_3q_1 + c_{2223}q_2q_3 + c_{2322}q_3q_2$$

Voigt notation:

$$\Gamma_{22} = C_{66}q_1q_1 + C_{22}q_2q_2 + C_{44}q_3q_3$$
$$+ 2\,(C_{26}q_1q_2 + C_{46}q_1q_3 + C_{24}q_2q_3)$$

Tensor notation:

$$\Gamma_{33} = c_{3131}q_1q_1 + c_{3232}q_2q_2 + c_{3333}q_3q_3 + c_{3132}q_1q_2 + c_{3231}q_2q_1$$
$$+ c_{3133}q_1q_3 + c_{3331}q_3q_1 + c_{3233}q_2q_3 + c_{3332}q_3q_2$$

Voigt notation:

$$\Gamma_{33} = C_{55}q_1q_1 + C_{44}q_2q_2 + C_{33}q_3q_3$$
$$+ 2\,(C_{45}q_1q_2 + C_{35}q_1q_3 + C_{34}q_2q_3)$$

Tensor notation:

$$\Gamma_{12} = c_{1121}q_1q_1 + c_{1222}q_2q_2 + c_{1323}q_3q_3 + c_{1122}q_1q_2 + c_{1221}q_2q_1$$
$$+ c_{1123}q_1q_3 + c_{1321}q_3q_1 + c_{1223}q_2q_3 + c_{1322}q_3q_2$$

Voigt notation:

$$\Gamma_{12} = C_{16}q_1q_1 + C_{26}q_2q_2 + C_{45}q_3q_3 + q_1q_2(C_{12} + C_{66})$$
$$+ q_1q_3\,(C_{14} + C_{56}) + q_2q_3\,(C_{25} + C_{26})$$

Tensor notation:

$$\Gamma_{13} = c_{1131}q_1q_1 + c_{1232}q_2q_2 + c_{1333}q_3q_3 + c_{1132}q_1q_2 + c_{1231}q_2q_1$$
$$+ c_{1133}q_1q_3 + c_{1331}q_3q_1 + c_{1233}q_2q_3 + c_{1332}q_3q_2$$

Voigt notation:

$$\Gamma_{13} = C_{14}q_1q_1 + C_{56}q_2q_2 + C_{34}q_3q_3 + q_1q_2\,(C_{14} + C_{56})$$
$$+ q_1q_3\,(C_{13} + C_{55}) + q_2q_3\,(C_{36} + C_{45})$$

Tensor notation:

$$\Gamma_{23} = c_{2131}q_1q_1 + c_{2232}q_2q_2 + c_{2333}q_3q_3 + c_{2132}q_1q_2 + c_{2231}q_2q_1$$
$$+ c_{2133}q_1q_3 + c_{2331}q_3q_1 + c_{2233}q_2q_3 + c_{2332}q_3q_2$$

Voigt notation:

$$\Gamma_{23} = C_{56}q_1q_1 + C_{24}q_2q_2 + C_{35}q_3q_3 + q_1q_2\left(C_{25} + C_{46}\right)$$
$$+ q_1q_3\left(C_{36} + C_{45}\right) + q_2q_3\left(C_{23} + C_{44}\right)$$

Monoclinic symmetry

For a monoclinic crystal, like gypsum, the elastic constants C_{14}, C_{24}, C_{34}, C_{45}, C_{62}, C_{63}, C_{64}, C_{65} are zero, hence the components of the coefficients of the Christoffel matrix reduce to:

$$\Gamma_{11} = C_{11}q_1q_1 + C_{66}q_2q_2 + C_{55}q_3q_3 + 2\left(C_{16}q_1q_2 + C_{15}q_1q_3\right)$$
$$\Gamma_{22} = C_{66}q_1q_1 + C_{22}q_2q_2 + C_{44}q_3q_3$$
$$\Gamma_{33} = C_{55}q_1q_1 + C_{44}q_2q_2 + C_{33}q_3q_3 + 2\left(C_{35}q_1q_2\right)$$
$$\Gamma_{12} = C_{16}q_1q_1 + q_1q_2\left(C_{12} + C_{66}\right)$$
$$\Gamma_{13} = q_1q_3\left(C_{13} + C_{55}\right)$$
$$\Gamma_{23} = C_{35}q_3q_3 + q_1q_2\,C_{25} + q_2q_3\left(C_{23} + C_{44}\right)$$

A worked example: Orthorhombic symmetry

For orthorhombic crystals, like epsomite and benzene, the elastic constants C_{14}, C_{24}, C_{34}, C_{45}, C_{62}, C_{63}, C_{64}, C_{65}, C_{16}, C_{15}, C_{25}, C_{35} are zero, hence the coefficients of the Christoffel matrix reduce to:

$$\Gamma_{11} = C_{11}q_1q_1 + C_{66}q_2q_2 + C_{55}q_3q_3$$
$$\Gamma_{22} = C_{66}q_1q_1 + C_{22}q_2q_2 + C_{44}q_3q_3$$
$$\Gamma_{33} = C_{55}q_1q_1 + C_{44}q_2q_2 + C_{33}q_3q_3$$
$$\Gamma_{12} = q_1q_2\left(C_{12} + C_{66}\right)$$
$$\Gamma_{13} = q_1q_3\left(C_{13} + C_{55}\right)$$
$$\Gamma_{23} = q_2q_3\left(C_{23} + C_{44}\right)$$

Solving the Christoffel equation for a direction vector q (1/ 0 / 0) reduces the Christoffel matrix coefficients to

$$\Gamma_{11} = C_{11}$$

$$\Gamma_{22} = C_{66}$$

$$\Gamma_{33} = C_{55}$$

$$\Gamma_{12} = 0$$

$$\Gamma_{13} = 0$$

$$\Gamma_{23} = 0$$

eq. s2 then becomes:

$$\begin{bmatrix} C_{11} - \rho v_1^2 & 0 & 0 \\ 0 & C_{66} - \rho v_2^2 & 0 \\ 0 & 0 & C_{55} - \rho v_3^2 \end{bmatrix} \begin{bmatrix} p_1 \\ p_2 \\ p_3 \end{bmatrix} = 0 \quad (\text{ eq. s3})$$

The eigenvalues are given by the matrix determinant:

$$(C_{11} - \rho v_1^2) \times (C_{66} - \rho v_2^2) \times (C_{55} - \rho v_3^2) = 0 \quad (\text{eq. s4})$$

Clearly, if either factor of this multiplication equals zero the equation is fulfilled, thus yielding three separate equations, from each a eigenvalue of the Christoffel matrix may be retrieved

$$(C_{11} - \rho v_1^2) = 0 \quad (\text{eq. s4a})$$

$$(C_{66} - \rho v_2^2) = 0 \quad (\text{eq. s4b})$$

$$(C_{55} - \rho v_3^2) = 0 \quad (\text{eq. s4c})$$

C_{ij} and ρ are experimentally or computationally derived scalar quantities, thus v is the only unknown and we rearrange for v in order to solve the eigenvalue problem.

$$v_1 = \sqrt{\frac{C_{11}}{\rho}} \qquad v_2 = \sqrt{\frac{C_{66}}{\rho}} \qquad v_3 = \sqrt{\frac{C_{55}}{\rho}}$$

Lastly, we have to assign the velocities to the P wave and the horizontally and vertically polarised S waves by determining the eigenvectors corresponding to each of the eigenvalue solutions.

Let's first consider eigenvalue ρv_1^2

$$\begin{bmatrix} C_{11} - \rho v_1^2 & 0 & 0 \\ 0 & C_{66} - \rho v_1^2 & 0 \\ 0 & 0 & C_{55} - \rho v_1^2 \end{bmatrix} \begin{bmatrix} p_1 \\ p_2 \\ p_3 \end{bmatrix} = 0 \quad \textit{(eq s5)}$$

Again, yielding three separate equations:

$$(C_{11} - \rho v_1^2) \times p_1 = 0 \ \textit{(eq s5a)}$$
$$(C_{66} - \rho v_1^2) \times p_2 = 0 \ \textit{(eq s5b)}$$
$$(C_{55} - \rho v_1^2) \times p_3 = 0 \ \textit{(eq s5c)}$$

Unless $C_{11} = C_{66}$ or $C_{11} = C_{55}$, p_2 and p_3 must equal zero in order to fulfil eq. s5b and eq s5c. p_1 may take any value and was normalized to unity for the sake of simplicity, yielding the eigenvector $\boldsymbol{p}$(1/0/0), corresponding to the eigenvalue solution ρv_1^2, and consequently the seismic wave velocity v_1. Clearly,

the seismic wave that is polarized in the direction of propagation corresponds to the P wave.

$$v_1 = v_P = \sqrt{\frac{C_{11}}{\rho}} \qquad (eq\ s6a)$$

Following the same procedure for v_2 and v_3 it is evident that they correspond to the horizontally $\boldsymbol{p}$(0/1/0) and vertically $\boldsymbol{p}$(0/0/1) polarized shear waves, respectively.

$$v_2 = v_{SH} = \sqrt{\frac{C_{66}}{\rho}} \quad (eq\ s6b)$$

$$v_3 = v_{SV} = \sqrt{\frac{C_{55}}{\rho}} \quad (eq\ s6c)$$

Next to the density, which is a scalar quantity, thus taking a constant value for a material at a given pressure and temperature, the primary wave velocity propagation in (1/0/0) is solely dependent on C_{11}, whereas the horizontally $\boldsymbol{p}$(0/1/0) and vertically polarized shear waves $\boldsymbol{p}$(0/0/1) are dependent on C_{66} and $C_{55,}$ respectively.

Seismic wave velocities in propagation direction $q(0/1/0)$ may be obtained in the same fashion yielding:

$$v_2 = v_P = \sqrt{\frac{C_{22}}{\rho}} \quad ; \quad v_1 = v_{SH} = \sqrt{\frac{C_{66}}{\rho}} \quad ; \quad v_3 = v_{SV} = \sqrt{\frac{C_{44}}{\rho}}$$

and for $q(0/0/1)$, no distinction can be made between horizontally and vertically polarized shear waves. For this reason, the shear waves with polarisation (=eigenvectors) (0/1/0) and (1/0/0) are denoted as v_{S1} and v_{S2}, respectively.

$$v_3 = v_P = \sqrt{\frac{C_{33}}{\rho}} \quad ; \quad v_2 = v_{S1} = \sqrt{\frac{C_{44}}{\rho}} \quad ; \quad v_1 = v_{S2} = \sqrt{\frac{C_{55}}{\rho}}$$

Cubic symmetry

Lastly, the anisotropic elasticity of a cubic material such as CO_2 may be fully accounted for by just 3 independent elastic constants (C_{11}, C_{12} and C_{44}), thus reducing the coefficients of the Christoffel matrix to:

$$\Gamma_{11} = C_{11}q_1q_1 + C_{44}q_2q_2 + C_{44}q_3q_3$$

$$\Gamma_{22} = C_{44}q_1q_1 + C_{11}q_2q_2 + C_{44}q_3q_3$$

$$\Gamma_{33} = C_{44}q_1q_1 + C_{44}q_2q_2 + C_{11}q_3q_3$$

$$\Gamma_{12} = q_1q_2(C_{12} + C_{44})$$

$$\Gamma_{13} = q_1q_3 (C_{12} + C_{44})$$

$$\Gamma_{23} = q_2q_3 (C_{12} + C_{44})$$

8.3 Supplementary: Low-temperature crystallography and vibrational properties of rozenite (FeSO$_4$·4H$_2$O), a candidate mineral component of the polyhydrated sulfate deposits on Mars

Electronic Supplementary Information
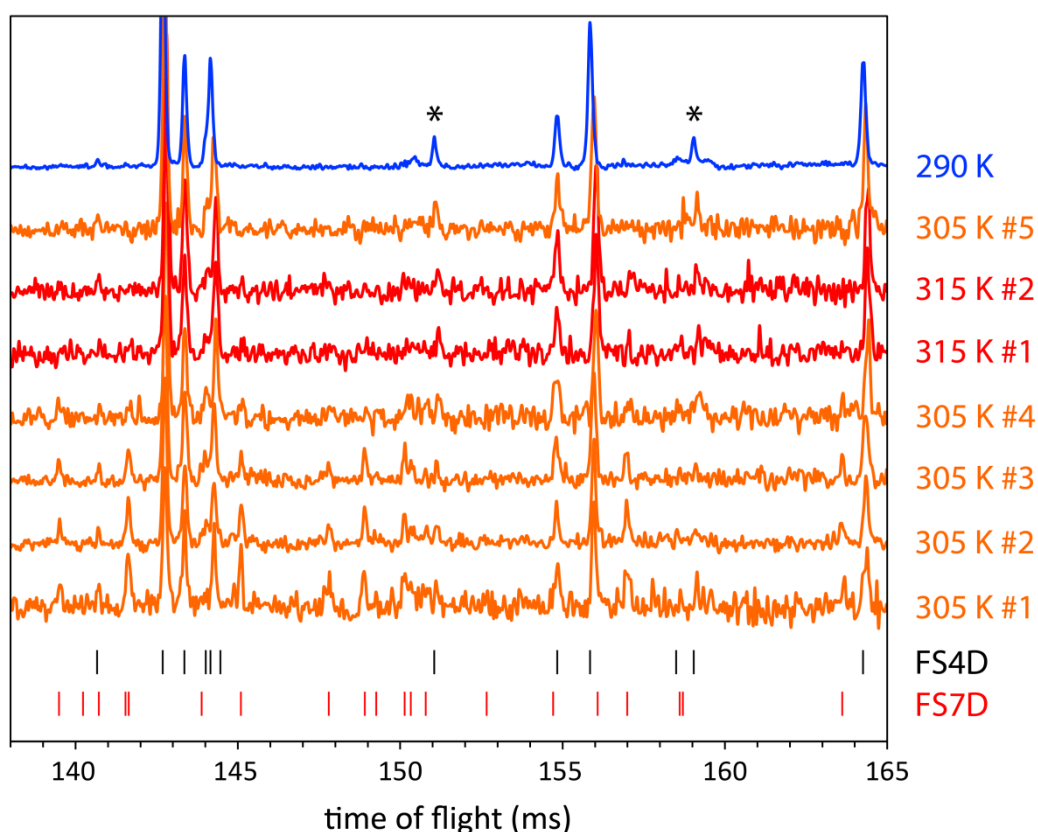
Fig. S1. Stack plot of neutron powder diffraction data collected after the initial sample loading. Data was collected sequentially at 305 K (#1 for 8 min; #2 for 28 m; #3 for 22 m; #4 for 10 m) revealing the presence of a small amount of FeSO$_4$·7D$_2$O (FS7D, red tick marks) in addition to FeSO$_4$·4D$_2$O (FS4D, black tick marks), which represents the bulk of the sample. Data were then collected at 315 K (#1 for 10 min; #2 for another 10 m) to confirm elimination of the FS7D phase. However small peaks from FeSO$_4$·D$_2$O (asterisks) appeared at this temperature, persisting on cooling back to 305 K (#5) and at 290 K.

rozenite - bond valence - without hydrogen								
	O1	O2	O3	O4	Ow1	Ow2	Ow3	Ow4	Σ
Fe - O	0.349	0.341			0.375	0.336	0.361	0.375	2.137
S - O	1.554	1.558	1.600	1.545					6.257
Σ	1.903	1.899	1.600	1.545	0.375	0.336	0.361	0.375	

rozenite - bond valence - with hydrogen								
	O1	O2	O3	O4	Ow1	Ow2	Ow3	Ow4	Σ
Fe - O	0.349	0.341			0.375	0.336	0.361	0.375	2.137
S - O	1.554	1.558	1.600	1.545					6.257
O - H					1.814	1.814	1.841	1.783	7.253
H ⋯ O	0.093	0.048	0.306	0.204				0.017	
Σ	1.996	1.946	1.906	1.749	2.189	2.150	2.202	2.175	

Tab. S1. Bond valance calculations for rozenite excluding (top) and including (bottom) the contribution of the hydrogen atoms. For the Fe – O and S – O bonds a universal parameter of 0.37 as suggested by Brown & Altermatt (1985) was used, whereas the O – H and H ⋯ O values were computed using a more recent universal parameter of 0.404 as derived by Alig et al. (1994) specifically for hydrogen bonds. r_0 values for Fe – O (1.734) and S – O (1.644) were taken from Brese & O'Keeffe (1991) and for O – H (0.914) from Alig et al. (1994). Note that inclusion of the H2b ::: O2/O2' contact substantially improves the bond valance calculation. The Ow atoms are systematically oversaturated by 0.15 – 0.20 valence units, thus the inclusion of the H3a ⋯ Ow4 contact into the calculation does not improve the calculation. However, based on geometrical considerations it is evident that the H3a ⋯ Ow4 contact forms a weak hydrogen bond.
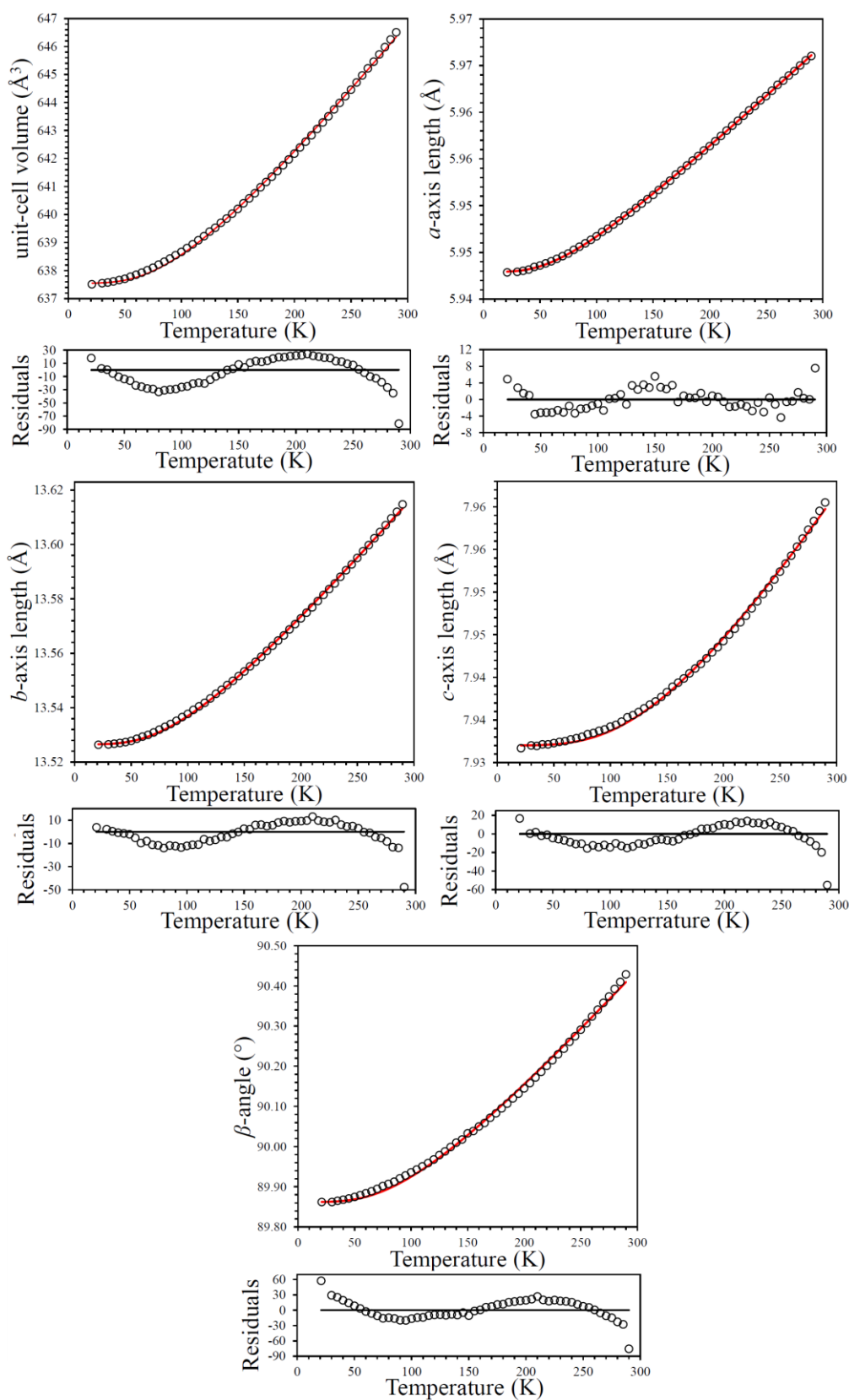
Fig. S2. First order Debye model fit (red line) upon the lattice parameters (black open circle) of rozenite at temperatures ranging from 290 to 21 K. Note the large residuals indicating the poor fit between the modelled and experimental data. Error bars are smaller than the symbol size.

	a^3 (Å^3)	b^3 (Å^3)	c^3 (Å^3)	β	V (Å^3)
θ_D (K)	267(2)	370(6)	610(15)	427(12)	379(8)
X_0 (cm^3 mol^{-1})	31.6002(4)	372.19(2)	75.192(3)	13.5307(3)	95.985(4)
X_0 (Å, Å^3)	5.9429(8)	13.5215(6)	7.9340(3)	89.873(21)	637.55(3)
Q (x10^4 J cm^{-3})	772(3)	404(4)	522(13)	1198(22)	560(7)
K_0/γ (GPa)	244.2(8)	10.9(1)	69(2)	885(16)	58.4(7)

Tab. S2 Parameters derived from fitting a first order single Debye model upon the lattice parameters of rozenite.

T (K)	a (Å)	b (Å)	c (Å)	β (°)	V (Å^3)
290	5.966031(12)	13.609756(31)	7.962529(14)	90.4288(2)	646.509(2)
280	5.965014(25)	13.604674(68)	7.960354(33)	90.3926(4)	645.984(4)
270	5.963939(24)	13.599606(68)	7.958306(33)	90.3580(4)	645.463(4)
260	5.962945(24)	13.594808(67)	7.956294(33)	90.3237(4)	644.967(4)
250	5.961745(24)	13.590061(67)	7.954417(33)	90.2914(4)	644.462(4)
240	5.960692(23)	13.585533(65)	7.952566(32)	90.2607(3)	643.986(4)
230	5.959640(24)	13.580734(69)	7.950936(32)	90.2295(4)	643.514(4)
220	5.958573(26)	13.576474(70)	7.949244(33)	90.2013(4)	643.061(4)
210	5.957480(25)	13.571914(66)	7.947720(32)	90.1724(3)	642.605(4)
200	5.956386(28)	13.567891(69)	7.946274(34)	90.1454(4)	642.181(4)
190	5.955319(29)	13.563782(69)	7.944954(34)	90.1195(4)	641.765(4)
180	5.954314(31)	13.559696(68)	7.943594(35)	90.0955(4)	641.355(4)
170	5.953319(28)	13.555902(63)	7.942473(32)	90.0719(4)	640.978(3)
160	5.952220(28)	13.551914(64)	7.941388(32)	90.0499(4)	640.584(3)
150	5.951150(26)	13.548306(63)	7.940260(32)	90.0329(6)	640.207(3)
140	5.950227(26)	13.544909(66)	7.939180(33)	90.0097(6)	639.860(3)
130	5.949275(27)	13.541560(66)	7.938362(33)	89.9884(6)	639.534(3)
120	5.948406(28)	13.538448(65)	7.937573(34)	89.9680(6)	639.230(3)
110	5.947544(30)	13.535534(67)	7.936811(35)	89.9512(5)	638.938(4)
100	5.946730(30)	13.532723(67)	7.936230(36)	89.9358(5)	638.671(4)
90	5.945970(32)	13.530188(71)	7.935726(38)	89.9208(4)	638.429(4)
80	5.945268(31)	13.528004(68)	7.935337(36)	89.9066(4)	638.219(4)
70	5.944600(30)	13.525946(69)	7.934868(36)	89.8951(4)	638.013(4)
60	5.944048(32)	13.524380(71)	7.934521(37)	89.8843(4)	637.851(4)
50	5.943604(32)	13.522808(74)	7.934297(37)	89.8749(4)	637.711(4)
40	5.943159(30)	13.522054(71)	7.934138(37)	89.8676(4)	637.615(4)
30	5.942915(33)	13.521509(75)	7.934013(38)	89.8622(4)	637.553(4)
21	5.942863(15)	13.521390(40)	7.933688(20)	89.8617(4)	637.516(2)

Tab S3. Unit-cell parameters of rozenite determined upon cooling by means of neutron diffraction.

T (K)	a (Å)	b (Å)	c (Å)	β (°)	V (Å³)
285	5.965567(26)	13.607071(74)	7.961536(35)	90.4097(4)	646.252(4)
275	5.964427(28)	13.602136(76)	7.959341(37)	90.3744(4)	645.719(4)
265	5.963399(26)	13.597331(75)	7.957339(36)	90.3408(4)	645.220(4)
255	5.962329(27)	13.592522(78)	7.955356(37)	90.3069(4)	644.717(4)
245	5.961293(26)	13.587664(77)	7.953491(36)	90.2753(4)	644.226(4)
235	5.960211(27)	13.583157(76)	7.951769(36)	90.2441(4)	643.757(4)
225	5.959095(27)	13.578656(73)	7.950095(35)	90.2145(4)	643.289(4)
215	5.958049(29)	13.574198(75)	7.948476(37)	90.1863(4)	642.835(4)
205	5.956920(30)	13.569922(75)	7.947025(37)	90.1581(4)	642.395(4)
195	5.955903(31)	13.565751(75)	7.945553(37)	90.1323(4)	641.970(4)
185	5.954832(32)	13.561609(73)	7.944251(37)	90.1070(4)	641.554(4)
175	5.953784(33)	13.557784(75)	7.943047(39)	90.0830(4)	641.163(4)
165	5.952678(34)	13.553785(74)	7.941882(39)	90.0594(5)	640.761(4)
155	5.951693(33)	13.550204(74)	7.940904(37)	90.0391(6)	640.407(4)
145	5.950715(31)	13.546632(75)	7.939709(38)	90.0184(7)	640.037(4)
135	5.949765(31)	13.543354(73)	7.938795(37)	89.9988(7)	639.706(4)
125	5.948936(31)	13.540089(75)	7.937936(38)	89.9786(7)	639.394(4)
115	5.947982(31)	13.536813(75)	7.937316(39)	89.9594(6)	639.087(4)
105	5.947203(31)	13.534176(76)	7.936431(40)	89.9427(5)	638.807(4)
95	5.946343(34)	13.531583(74)	7.935903(39)	89.9280(3)	638.550(4)
85	5.945606(37)	13.529043(76)	7.935487(42)	89.9129(4)	638.317(4)
75	5.944876(33)	13.526965(77)	7.935037(40)	89.9017(4)	638.104(4)
65	5.944305(35)	13.525010(78)	7.93472(41)	89.8893(4)	637.925(4)
55	5.943825(37)	13.523563(85)	7.934434(43)	89.8789(5)	637.782(4)
45	5.943449(34)	13.522385(80)	7.934136(40)	89.8709(4)	637.662(4)
35	5.943032(34)	13.521768(78)	7.933968(41)	89.8643(4)	637.574(4)

Tab. S4. Unit-cell parameters of rozenite determined upon heating by means of neutron diffraction.

Mode symmetry	Frequency (cm⁻¹)	Mode symmetry	Frequency (cm⁻¹)
A$_g$	63.55	A$_g$	590.21
B$_g$	71.65	B$_g$	598.23
A$_g$	90.82	A$_g$	614.41
B$_g$	98.75	B$_g$	616.26
A$_g$	99.07	A$_g$	671.79
A$_g$	114.29	B$_g$	678.32
B$_g$	120.61	A$_g$	685.36
B$_g$	122.76	B$_g$	732.51
A$_g$	145.93	A$_g$	746.82
B$_g$	157	B$_g$	752.27
B$_g$	163.46	A$_g$	773.02
A$_g$	167.96	B$_g$	794.41
A$_g$	173.36	A$_g$	805.91
B$_g$	180.99	B$_g$	808.76
B$_g$	189.95	A$_g$	822.09
A$_g$	192	B$_g$	828.89
B$_g$	198.37	B$_g$	840.79
A$_g$	201.07	A$_g$	849.33
A$_g$	205.75	B$_g$	882.62
B$_g$	206.56	A$_g$	897.78
A$_g$	211.67	A$_g$	908.4
B$_g$	212.98	B$_g$	909.93
B$_g$	226.19	B$_g$	942.54
A$_g$	228.06	A$_g$	945.5
A$_g$	233.17	A$_g$	995.73
B$_g$	237.02	B$_g$	997.65
B$_g$	247.07	A$_g$	1035.15
A$_g$	249.98	B$_g$	1039.11
B$_g$	257.95	A$_g$	1164.33
A$_g$	260.18	B$_g$	1188.61
A$_g$	271.78	A$_g$	1567.54
B$_g$	272.13	B$_g$	1579.04
B$_g$	283.17	A$_g$	1598.22
A$_g$	285.63	B$_g$	1603.92
A$_g$	358.26	B$_g$	1608.78
B$_g$	361.16	A$_g$	1611.26
B$_g$	397.28	B$_g$	1660.07
A$_g$	400.2	A$_g$	1660.65
B$_g$	411.81	A$_g$	3278.7
A$_g$	417.08	B$_g$	3282.4
B$_g$	423.51	A$_g$	3330.41
A$_g$	431.16	B$_g$	3333.83
A$_g$	447.93	A$_g$	3379.8
B$_g$	451.98	B$_g$	3394.08
A$_g$	457.45	B$_g$	3443.77
B$_g$	465.19	A$_g$	3444.63
A$_g$	480.06	A$_g$	3472.47

Mode symmetry	Frequency (cm⁻¹)	Mode symmetry	Frequency (cm⁻¹)
B_g	482.66	B_g	3473.16
B_g	502.88	A_g	3533.74
A_g	519.1	B_g	3533.93
A_g	566.21	A_g	3592.42
B_g	566.61	B_g	3595.6
A_g	573.74	A_g	3614.09
B_g	578.02	B_g	3635.25

Tab. S5. Frequency and symmetry of the computed Raman-active vibrational modes.

Mode symmetry	Frequency (cm⁻¹)	Mode symmetry	Frequency (cm⁻¹)
A_u	0	B_u	592.88
B_u	0	A_u	594.08
B_u	0	A_u	615.02
A_u	36.33	B_u	619.7
A_u	59.59	B_u	671.7
B_u	96.61	A_u	674.32
A_u	117.07	B_u	694.4
B_u	133.74	A_u	718.94
A_u	142.6	B_u	755.65
A_u	148.71	A_u	780.14
B_u	150.51	B_u	787.34
B_u	163.05	A_u	793.15
B_u	173.96	A_u	810.18
A_u	181.37	B_u	820.71
A_u	189.63	A_u	834.04
B_u	199.35	B_u	840.34
B_u	204.22	A_u	867.97
B_u	208.65	B_u	882.66
A_u	210.2	A_u	889.03
A_u	219.58	B_u	903.83
B_u	220.99	B_u	910.56
B_u	224.18	A_u	916.24
A_u	226.23	B_u	941.61
B_u	239.48	A_u	944.65
A_u	242.11	A_u	991.31
B_u	243.4	B_u	992.6
A_u	250.61	B_u	1040.96
A_u	260.34	A_u	1042.81
A_u	265.3	A_u	1156.67
B_u	266.62	B_u	1171.02
A_u	273.8	B_u	1554.51
B_u	277.02	A_u	1564.86
B_u	286.49	B_u	1582.68
A_u	302.53	A_u	1587.52
A_u	359.09	A_u	1600.93
B_u	359.93	B_u	1606.18
A_u	403.01	B_u	1611.6

B_u	403.22	A_u	1613.34
B_u	415.38	A_u	3288.4
A_u	418.25	B_u	3308.03
A_u	425.83	B_u	3344.71
B_u	429.31	A_u	3347.71
B_u	432	B_u	3377.25
A_u	441.42	A_u	3382.24
B_u	463.49	B_u	3468.65
A_u	472.3	A_u	3471.16
A_u	478.03	A_u	3472.67
B_u	478.38	B_u	3475.59
A_u	498.3	A_u	3540.06
B_u	506.08	B_u	3548.43
B_u	569.28	A_u	3592.14
A_u	569.44	B_u	3593.5
B_u	574.99	B_u	3611.45
A_u	575.76	A_u	3619.95

Tab. S6. Frequency and symmetry of the computed Infrared-active vibrational modes.

T (K)		290				21		
Fe	x	0.06869(23)	U_{11}	0.0174(7)	x	0.07071(22)	U_{11}	0.0109(6)
	y	0.10246(9)	U_{22}	0.0107(7)	y	0.10235(10)	U_{22}	0.0059(6)
	z	0.21917(17)	U_{33}	0.0166(7)	z	0.21902(17)	U_{33}	0.0045(6)
	U_{eq*}	0.01489	U_{12}	-0.0010(5)	U_{eq}	0.00709	U_{12}	0.0004(5)
			U_{13}	0.0032(5)			U_{13}	0.0013(5)
			U_{23}	0.0011(5)			U_{23}	-0.0010(5)
S	x	0.1995(6)	U_{11}	0.0108(20)	x	0.1966(7)	U_{11}	0.0045(20)
	y	0.10891(31)	U_{22}	0.0212(24)	y	0.10970(35)	U_{22}	0.0159(24)
	z	0.8228(5)	U_{33}	0.0120(22)	z	0.8225(5)	U_{33}	0.0098(23)
	U_{eq}	0.01467	U_{12}	0.0002(18)	U_{eq}	0.01007	U_{12}	-0.0027(18)
			U_{13}	0.0046(16)			U_{13}	0.0062(16)
			U_{23}	0.0004(21)			U_{23}	-0.0009(20)
O1	x	0.0083(4)	U_{11}	0.0208(12)	x	0.00521(34)	U_{11}	0.0033(10)
	y	0.04911(14)	U_{22}	0.0159(12)	y	0.05103(15)	U_{22}	0.0134(11)
	z	0.75906(26)	U_{33}	0.0234(13)	z	0.75856(26)	U_{33}	0.0129(11)
	U_{eq}	0.02002	U_{12}	-0.0018(9)	U_{eq}	0.00989	U_{12}	0.0031(8)
			U_{13}	0.0023(10)			U_{13}	0.0017(8)
			U_{23}	0.0015(10)			U_{23}	-0.0031(9)
O2	x	0.2536(4)	U_{11}	0.0217(12)	x	0.25715(34)	U_{11}	0.0060(11)
	y	0.07597(17)	U_{22}	0.0254(13)	y	0.07558(18)	U_{22}	0.0132(13)
	z	0.99584(25)	U_{33}	0.0168(13)	z	0.99440(27)	U_{33}	0.0113(12)
	U_{eq}	0.0213	U_{12}	-0.0050(10)	U_{eq}	0.01019	U_{12}	-0.0025(8)
			U_{13}	0.0022(9)			U_{13}	0.0013(8)
			U_{23}	-0.0014(9)			U_{23}	0.0036(9)
O3	x	0.39664(35)	U_{11}	0.0185(13)	x	0.39472(34)	U_{11}	0.0117(10)
	y	0.09535(19)	U_{22}	0.0314(13)	y	0.09615(18)	U_{22}	0.0138(11)
	z	0.71601(29)	U_{33}	0.0276(12)	z	0.71128(24)	U_{33}	0.0055(10)
	U_{eq}	0.02581	U_{12}	0.0050(11)	U_{eq}	0.01034	U_{12}	0.0029(10)
			U_{13}	0.0057(9)			U_{13}	-0.0043(7)
			U_{23}	-0.0073(13)			U_{23}	-0.0032(10)
O4	x	0.1337(4)	U_{11}	0.0220(12)	x	0.13344(34)	U_{11}	0.0064(10)
	y	0.21384(15)	U_{22}	0.0122(12)	y	0.21587(16)	U_{22}	0.0118(12)
	z	0.82006(29)	U_{33}	0.0306(13)	z	0.82350(25)	U_{33}	0.0100(11)
	U_{eq}	0.02161	U_{12}	0.0012(9)	U_{eq}	0.0094	U_{12}	0.0019(9)
			U_{13}	0.0022(10)			U_{13}	0.0032(8)
			U_{23}	-0.0015(11)			U_{23}	-0.0029(9)
O1w	x	0.3638(4)	U_{11}	0.0289(16)	x	0.3680(4)	U_{11}	0.0127(13)
	y	0.07329(19)	U_{22}	0.0229(16)	y	0.07361(18)	U_{22}	0.0180(15)
	z	0.3547(4)	U_{33}	0.0213(15)	z	0.35492(32)	U_{33}	0.0031(11)
	U_{eq}	0.0244	U_{12}	0.0152(11)	U_{eq}	0.01125	U_{12}	-0.0010(10)
			U_{13}	-0.0088(12)			U_{13}	0.0007(9)
			U_{23}	-0.0067(13)			U_{23}	0.0012(10)
O2w	x	0.7701(5)	U_{11}	0.0210(16)	x	0.7697(4)	U_{11}	0.0094(13)
	y	0.14040(24)	U_{22}	0.0371(19)	y	0.14000(20)	U_{22}	0.0111(15)
	z	0.0836(4)	U_{33}	0.0264(15)	z	0.08488(32	U_{33}	0.0125(12)
	U_{eq}	0.02818	U_{12}	0.0051(14)	U_{eq}	0.011	U_{12}	0.0035(11)
			U_{13}	-0.0023(12)			U_{13}	-0.0003(10)
			U_{23}	0.0004(12)			U_{23}	0.0001(10)
O3w	x	0.8843(5)	U_{11}	0.0407(18)	x	0.8810(4)	U_{11}	0.0122(12)
	y	0.12369(22)	U_{22}	0.0257(18)	y	0.12287(17)	U_{22}	0.0063(13)
	z	0.44190(35)	U_{33}	0.0262(16)	z	0.44183(28)	U_{33}	0.0021(11)
	U_{eq}	0.0309	U_{12}	0.0206(13	U_{eq}	0.00688	U_{12}	0.0065(9)
			U_{13}	-0.0042(13)			U_{13}	-0.0004(9)
			U_{23}	0.0050(13)			U_{23}	0.0021(9)
O4w	x	0.1834(5)	U_{11}	0.0220(14)	x	0.1854(4)	U_{11}	0.0056(10)
	y	0.24809(19)	U_{22}	0.0191(14)	y	0.24875(17)	U_{22}	0.0107(13)
	z	0.2181(4)	U_{33}	0.0387(17)	z	0.21869(32)	U_{33}	0.0146(12)
	U_{eq}	0.02668	U_{12}	-0.0057(13)	U_{eq}	0.01031	U_{12}	-0.0023(10)
			U_{13}	-0.0074(12)			U_{13}	-0.0017(9)

			U_{23}	-0.0023(13)			U_{23}	0.0001(11)
D1a	x	0.3809(5)	U_{11}	0.0661(22)	x	0.3752(5)	U_{11}	0.0411(16)
	y	0.08628(25)	U_{22}	0.0577(20)	y	0.08645(23)	U_{22}	0.0425(18)
	z	0.4709(4)	U_{33}	0.0540(19)	z	0.4744(4)	U_{33}	0.0253(14)
	U_{eq}	0.05938	U_{12}	0.0218(17)	U_{eq}	0.03626	U_{12}	0.0082(13)
			U_{13}	-0.0215(16)			U_{13}	-0.0091(11)
			U_{23}	-0.0044(18)			U_{23}	0.0006(14)
D1b	x	0.4586(5)	U_{11}	0.0557(18)	x	0.4627(5)	U_{11}	0.0421(17)
	y	0.01785(20)	U_{22}	0.0398(15)	y	0.01660(19)	U_{22}	0.0259(14)
	z	0.33146(35)	U_{33}	0.0500(19)	z	0.3313(4)	U_{33}	0.0369(16)
	U_{eq}	0.04853	U_{12}	0.0128(15)	U_{eq}	0.03496	U_{12}	0.0120(13)
			U_{13}	-0.0038(14)			U_{13}	0.0008(12)
			U_{23}	-0.0027(15)			U_{23}	0.0017(13)
D2a	x	0.6716(5)	U_{11}	0.0482(19)	x	0.6719(5)	U_{11}	0.0251(14)
	y	0.18376(27)	U_{22}	0.0806(25)	y	0.18243(21)	U_{22}	0.0357(17)
	z	0.1438(4)	U_{33}	0.0606(22)	z	0.14848(33)	U_{33}	0.0322(14)
	U_{eq}	0.06309	U_{12}	0.0196(18)	U_{eq}	0.031	U_{12}	0.0008(12)
			U_{13}	0.0080(16)			U_{13}	0.0053(11)
			U_{23}	0.0049(19)			U_{23}	0.0002(13)
D2b	x	0.6766(5)	U_{11}	0.0607(22)	x	0.6770(4)	U_{11}	0.0322(15)
	y	0.09137(29)	U_{22}	0.0978(30)	y	0.08708(23)	U_{22}	0.0370(19)
	z	0.0371(5)	U_{33}	0.0707(23)	z	0.0386(4)	U_{33}	0.0431(17)
	U_{eq}	0.0765	U_{12}	-0.0287(23)	U_{eq}	0.03743	U_{12}	-0.0063(14)
			U_{13}	-0.0186(17)			U_{13}	-0.0047(12)
			U_{23}	0.0217(23)			U_{23}	0.0017(15)
D3a	x	0.7981(5)	U_{11}	0.0472(20)	x	0.7951(5)	U_{11}	0.0348(16)
	y	0.18207(24)	U_{22}	0.0519(21)	y	0.18174(22)	U_{22}	0.0303(16)
	z	0.45213(34)	U_{33}	0.0526(19)	z	0.45270(32)	U_{33}	0.0334(15)
	U_{eq}	0.05057	U_{12}	0.0016(15)	U_{eq}	0.03287	U_{12}	0.0077(13)
			U_{13}	-0.0018(13)			U_{13}	0.0052(12)
			U_{23}	0.0053(15)			U_{23}	-0.0036(12)
D3b	x	0.9199(4)	U_{11}	0.0497(18)	x	0.9184(4)	U_{11}	0.0395(16)
	y	0.10080(23)	U_{22}	0.0530(19)	y	0.10002(21)	U_{22}	0.0290(15)
	z	0.55068(35)	U_{33}	0.0326(15)	z	0.55313(32)	U_{33}	0.0215(14)
	U_{eq}	0.04508	U_{12}	0.0062(14)	U_{eq}	0.02998	U_{12}	0.0034(12)
			U_{13}	0.0043(12)			U_{13}	0.0034(11)
			U_{23}	0.0024(16)			U_{23}	0.0012(13)
D4a	x	0.3147(5)	U_{11}	0.0439(17)	x	0.3184(4)	U_{11}	0.0271(14)
	y	0.26497(19)	U_{22}	0.0425(18)	y	0.26425(18)	U_{22}	0.0325(15)
	z	0.2806(4)	U_{33}	0.0786(23)	z	0.2837(4)	U_{33}	0.0415(15)
	U_{eq}	0.05498	U_{12}	-0.0062(14)	U_{eq}	0.03368	U_{12}	-0.0044(11)
			U_{13}	0.0004(16)			U_{13}	-0.0039(13)
			U_{23}	0.0003(16)			U_{23}	-0.0014(13)
D4b	x	0.5863(5)	U_{11}	0.0466(18)	x	0.5880(4)	U_{11}	0.0248(14)
	y	0.19468(21)	U_{22}	0.0358(15)	y	0.19475(20)	U_{22}	0.0308(14)
	z	0.7265(4)	U_{33}	0.0591(18)	z	0.72560(33)	U_{33}	0.0367(15)
	U_{eq}	0.04711	U_{12}	-0.0047(14)	U_{eq}	0.03077	U_{12}	-0.0084(12)
			U_{13}	0.0151(14)			U_{13}	0.0099(11)
			U_{23}	-0.0075(15)			U_{23}	0.0003(14)

Tab. S7. Positional parameters and anisotropic displacement parameters of the atom sites in $FeSO_4 \cdot 4D_2O$ at 290 K and 21 K. *Value calculated from anisotropic displacement parameters, however, GSAS does not compute the e.s.d for U_{eq}.

T_{ref} (K)	α_{11} (K^{-1})*	α_{22} (K^{-1})*	α_{33} (K^{-1})*	α_{13} (K^{-1})*
28	2.07(1.38)	1.98(1.38)	2.58(1.14)	-1.56(0.84)
40	7.05(2.52)	4.57(2.52)	2.12(2.28)	-5.75(1.41)
50	6.35(2.52)	8.71(2.52)	3.76(2.28)	-6.98(1.71)
60	8.12(2.52)	10.69(2.52)	3.6(2.28)	-9.07(1.71)
70	9.64(2.28)	14.45(2.28)	3.99(2.01)	-10.82(1.41)
80	12.31(2.52)	15.37(2.52)	5.66(2.28)	-9.77(1.41)
90	12.42(2.52)	18.78(2.52)	5.25(2.28)	-13.17(1.41)
100	14.5(2.28)	19.16(2.28)	6.65(2.01)	-12.83(1.71)
110	13.11(2.28)	19.49(2.28)	11.16(2.01)	-14.57(2.13)
120	16.06(2.28)	24.2(2.28)	7.81(2.01)	-16.76(2.4)
130	13.95(2.28)	24.12(2.28)	10.82(2.01)	-17.63(2.55)
140	15.96(2.28)	24.2(2.28)	11.52(2.01)	-17.11(2.55)
150	16.42(2.28)	26.37(2.28)	15.06(2.01)	-18.07(2.4)
160	16.52(2.52)	26.43(2.52)	12.31(2.1)	-17.72(2.13)
170	18.53(2.52)	29.5(2.52)	14.66(2.1)	-20.6(1.71)
180	17.54(2.28)	28.22(2.28)	15.16(2.01)	-20.95(1.41)
190	17.89(2.28)	30.54(2.28)	16.38(2.01)	-22.08(1.41)
200	16.96(2.58)	30.74(2.58)	18.53(2.01)	-22.51(1.41)
210	18.8(2.01)	31.51(2.01)	18.26(2.01)	-24.62(1.41)
220	17.38(2.01)	32.84(2.01)	20.37(1.8)	-24.61(1.41)
230	18.53(2.01)	33.14(2.01)	21.05(1.8)	-25.83(1.41)
240	17.92(1.8)	33.18(1.8)	21.66(2.01)	-27.22(1.41)
250	17.09(1.8)	35.75(1.8)	23.45(2.01)	-27.57(1.41)
260	17.61(1.8)	35.38(1.8)	24.91(2.01)	-29.57(1.41)
270	16.88(2.01)	35.33(2.01)	25.15(2.01)	-29.3(1.41)
280	18.69(1.8)	36.29(1.8)	27.57(2.01)	-30.78(1.41)

Tab. S8. Coefficients of the thermal expansion tensor of rozenite (determined from adjacent datapoints as collected upon heating) as presented in Fig. 5b. T_{ref} = (T_{start} + T_{end})/2 (e.g., Tref = 280 K corresponds to the thermal expansion tensor derived from the unit-cell parameters measured at 275 K and 285 K). * Values reported in these columns were multiplied by 10^6 for the sake of brevity (e.g. α_{11} at 28 K is 2.07 x 10^{-6} K^{-1}).

T_{ref} (K)	α_{11} (K^{-1})*	α_{22} (K^{-1})*	α_{33} (K^{-1})*	α_{13} (K^{-1})*
25.5	1.02(2.13)	0.97(2.31)	4.66(1.77)	-0.39(1.29)
35	4.14(2.28)	4.03(2.28)	1.57(2.01)	-4.71(1.41)
45	7.51(2.28)	5.58(2.28)	2.01(2.01)	-6.37(1.41)
55	7.51(2.52)	11.62(2.28)	2.83(2.01)	-8.20(1.41)
65	9.32(2.28)	11.58(2.28)	4.36(2.01)	-9.42(1.41)
75	11.27(2.1)	15.21(2.28)	5.91(2.01)	-10.03(1.41)
85	11.85(2.52)	16.14(2.01)	4.91(2.28)	-12.39(1.41)
95	12.81(2.01)	18.74(2.01)	6.35(2.01)	-13.09(1.71)
105	13.71(2.28)	20.77(2.01)	7.32(2.01)	-13.44(1.98)
115	14.52(2.01)	21.53(2.28)	9.60(2.01)	-14.66(2.13)
125	14.62(2.01)	22.98(2.01)	9.94(2.53)	-17.8(2.25)
135	16.00(1.8)	24.72(2.01)	10.30(1.01)	-18.58(2.25)
145	15.50(1.8)	25.09(2.28)	13.60(1.80)	-20.25(2.25)
155	17.95(1.8)	26.63(2.01)	14.21(1.53)	-14.84(1.89)
165	18.43(2.28)	29.42(2.01)	13.66(2.01)	-19.21(1.41)
175	16.67(2.52)	27.99(2.01)	14.11(2.53)	-20.6(1.41)
185	16.8(2.28)	30.12(2.01)	17.12(2.01)	-20.95(1.41)
195	17.81(2.01)	30.30(2.28)	16.62(2.80)	-22.61(1.41)
205	18.23(1.8)	29.65(2.01)	18.20(1.80)	-23.57(1.29)
215	18.19(1.8)	33.61(2.01)	19.17(1.80)	-25.22(1.29)
225	17.73(1.8)	31.38(2.01)	21.28(1.80)	-24.61(1.41)
235	17.42(1.8)	35.33(2.28)	20.5(1.01)	-27.22(1.29)
245	17.40(1.8)	33.33(2.01)	23.28(1.80)	-26.78(1.29)
255	19.82(1.8)	34.93(2.01)	23.59(1.01)	-28.19(1.41)
265	16.32(1.53)	35.3(2.28)	25.28(1.01)	-29.91(1.41)
275	17.62(1.8)	37.28(2.28)	25.74(1.01)	-30.17(1.41)
285	16.63(1.29)	37.36(1.59)	27.31(1.29)	-31.56(1.17)

Tab. S9. Coefficients of the thermal expansion tensor of rozenite (determined from adjacent datapoints collected upon cooling) as presented in Fig. 5b. T_{ref} = (T_{start} + T_{end})/2 (e.g., Tref = 285 K corresponds to the thermal expansion tensor derived from the unit-cell parameters measured at 280 K and 290 K). * Values reported in these columns were multiplied by 10^6 for the sake of brevity (e.g. α_{11} at 25.5 K is 1.02 x 10^{-6} K^{-1}).

T_{ref} (K)	a_1 (K^{-1})*	a_2 (K^{-1})*	a_3 (K^{-1})*	a_V (K^{-1})*
25.5	1.0(1.7)	1.0(1.7)	4.7(1.7)	6.7(2.9)
35	-2.0(2.1)	4.0(2.4)	7.7(2.1)	9.7(3.8)
45	-2.2.0(2.1)	5.6(2.4)	11.7(2.1)	15.1(3.8)
55	-3.4.0(2.1)	11.6(2.4)	13.7(2.1)	21.9(3.8)
65	-2.9.0(2.1)	11.6(2.4)	16.6(2.1)	25.3(3.8)
75	-1.8.0(2.1)	15.2(2.4)	19.0(2.1)	32.4(3.8)
85	-4.5.0(2.1)	16.1(2.1)	21.2(2.1)	32.8(3.8)
95	-3.9.0(2.1)	18.7(2.1)	23.1(2.1)	37.9(3.6)
105	-3.3.0(2.4)	20.8(2.1)	24.3(2.4)	41.8(4.0)
115	-2.8.0(2.4)	21.5(2.4)	26.9(2.4)	45.6(4.2)
125	-5.7.0(2.7)	23.0(2.1)	30.2(2.7)	47.5(4.4)
135	-5.7.0(2.7)	24.7(2.1)	32.0(2.7)	51.0(4.4)
145	-5.7.0(2.7)	25.1(2.4)	34.8(2.7)	54.2(4.5)
155	1.1.0(2.1)	26.6(2.1)	31.0(2.1)	58.7(3.6)
165	-3.3.0(2.1)	29.4(2.1)	35.4(2.1)	61.5(3.6)
175	-5.2.0(2.1)	28.0(2.1)	36.0(2.1)	58.8(3.6)
185	-4.0(2.1)	30.1(2.1)	37.9(2.1)	64.0(3.6)
195	-5.4.0(2.1)	30.3(2.4)	39.8(2.1)	64.7(3.8)
205	-5.3.0(1.8)	29.7(2.1)	41.8(1.8)	66.2(3.3)
215	-6.5.0(1.8)	33.6(2.1)	43.9(1.8)	71.0(3.3)
225	-5.2.0(1.8)	31.4(2.1)	44.2(1.8)	70.4(3.3)
235	-8.3.0(1.8)	35.3(2.4)	46.2(1.8)	73.2(3.5)
245	-6.6.0(1.8)	33.3(2.1)	47.3(1.8)	74.0(3.3)
255	-6.5.0(1.8)	34.9(2.1)	50.0(1.8)	78.4(3.5)
265	-9.4.0(1.8)	35.3(2.4)	51.1(1.8)	77.0(3.5)
275	-8.8.0(1.8)	37.3(2.4)	52.1(1.8)	80.6(3.7)
285	-10.0(1.5)	37.4(1.5)	54.0(1.5)	81.4(2.6)

Tab. S10. Principal axes of the thermal expansion tensor of rozenite (determined from adjacent datapoints as collected upon cooling) as presented in Fig. 5a. T_{ref} = (T_{start} + T_{end})/2 (e.g., Tref = 285 K corresponds to the thermal expansion tensor derived from the unit-cell parameters measured at 280 K and 290 K). * Values reported in these columns were multiplied by 10^6 for the sake of brevity (e.g. a_1 at 25.5 K is 1.02 x 10^{-6} K^{-1}).

Tref (K)	a1 (K-1)*	a2 (K-1)*	a3 (K-1)*	av (K-1)*
28	0.7(1.3)	2.0(1.3)	3.9(1.3)	6.6(2.2)
40	-1.7(2.1)	4.6(2.4)	10.8(2.1)	13.7(4.0)
50	-2.0(2.4)	8.7(2.4)	12.1(2.4)	18.8(4.2)
60	-3.5.0(2.4)	10.7(4.4)	15.2(2.4)	22.4(4.2)
70	-4.4.0(2.1)	14.4(9.4)	18.0(2.1)	28.0(3.8)
80	-1.3.0(2.1)	15.4(8.4)	19.3(2.4)	33.4(4.0)
90	-4.8.0(2.1)	18.8(5.4)	22.5(2.4)	36.5(4.0)
100	-2.8.0(2.4)	19.2(9.4)	24.0(2.4)	40.4(4.2)
110	-2.5.0(2.7)	19.5(3.4)	26.7(2.7)	43.7(4.5)
120	-5.3.0(2.7)	24.2(8.4)	29.2(2.7)	48.1(4.5)
130	-5.3.0(2.)	24.1(7.4)	30.1(3.0)	48.9(4.9)
140	-3.5.0(2.)	24.2(7.4)	31.0(3.0)	51.7(4.9)
150	-2.3.0(2.7)	26.4(7.4)	33.8(2.7)	57.9(4.7)
160	-3.4.0(2.7)	26.4(1.4)	32.3(2.7)	55.3(4.5)
170	-4.1.0(2.4)	29.5(3.4)	37.3(2.4)	62.7(4.2)
180	-4.6.0(2.1)	28.2(2.4)	37.3(2.1)	60.9(3.8)
190	-5.0(2.1)	30.5(4.4)	39.2(2.1)	64.7(3.8)
200	-4.8.0(2.1)	30.8(4.4)	40.3(2.1)	66.3(3.8)
210	-6.1.0(1.1)	31.5(3.4)	43.2(2.1)	68.6(3.8)
220	-5.8.0(1.1)	32.8(5.4)	43.5(1.8)	70.5(3.7)
230	-6.1.0(1.1)	33.1(2.4)	45.7(1.8)	72.7(3.7)
240	-7.5.0(1.8)	33.2(3.4)	47.1(2.1)	72.8(3.7)
250	-7.5.0(1.8)	35.8(6.4)	48.0(2.1)	76.3(3.7)
260	-8.5.0(1.8)	35.4(5.4)	51.1(2.1)	78.0(3.7)
270	-8.6.0(1.1)	35.3(4.4)	50.6(2.1)	77.3(3.8)
280	-8.0(1.8)	36.3(8.4)	54.3(2.1)	82.6(3.7)

Tab. S11. Principal axes of the thermal expansion tensor of rozenite (determined from adjacent datapoints as collected upon heating) as presented in Fig. 5a. T_{ref} = (T_{start} + T_{end})/2 (e.g., Tref = 280 K corresponds to the thermal expansion tensor derived from the unit-cell parameters measured at 275 K and 285 K). * Values reported in these columns were multiplied by 10^6 for the sake of brevity (e.g. a_1 at 28 K is 0.7 x 10^{-6} K^{-1}).

T_{ref} (K)	α_a (K^{-1})*	α_b (K^{-1})*	α_c (K^{-1})*
25.5	1.03	0.96	4.64
35	4.11	4.03	1.58
45	7.49	5.58	2.00
55	7.47	11.62	2.82
65	9.29	11.58	4.37
75	11.24	15.22	5.91
85	11.81	16.14	4.90
95	12.78	18.74	6.35
105	13.69	20.77	7.32
115	14.49	21.53	9.60
125	14.61	22.99	9.94
135	16.00	24.73	10.30
145	15.51	25.08	13.60
155	17.98	26.63	14.21
165	18.46	29.43	13.66
175	16.71	27.99	14.11
185	16.88	30.13	17.12
195	17.92	30.29	16.61
205	18.37	29.65	18.20
215	18.35	33.60	19.18
225	17.91	31.38	21.29
235	17.65	35.34	20.50
245	17.67	33.33	23.28
255	20.13	34.93	23.60
265	16.67	35.29	25.29
275	18.02	37.27	25.73
285	17.08	37.35	27.31

Tab. S12. Thermal expansion along the crystallographic axes of rozenite (determined from adjacent datapoints as collected upon cooling). T_{ref} = (T_{start} + T_{end})/2 ((e.g., Tref = 285 K corresponds to the thermal expansion tensor derived from the unit-cell parameters measured at 280 K and 290 K). * Values reported in these columns were multiplied by 10^6 for the sake of brevity (e.g. α_a at 25.5 K is 1.03 x 10^{-6} K^{-1}).

T_{ref} (K)	α_a (K^{-1})*	α_b (K^{-1})*	α_c (K^{-1})*
28	3.22	3.09	4.01
40	7.02	4.56	2.12
50	6.33	8.71	3.76
60	8.08	10.70	3.60
70	9.61	14.45	4.00
80	12.28	15.36	5.67
90	12.40	18.77	5.24
100	14.46	19.16	6.65
110	13.10	19.48	11.15
120	16.04	24.20	7.81
130	13.94	24.11	10.82
140	15.97	24.20	11.51
150	16.43	26.37	15.05
160	16.55	26.43	12.32
170	18.58	29.50	14.67
180	17.60	28.21	15.16
190	17.99	30.54	16.39
200	17.08	30.75	18.53
210	18.95	31.51	18.26
220	17.56	32.84	20.37
230	18.73	33.15	21.06
240	18.15	33.18	21.66
250	17.38	35.75	23.45
260	17.95	35.38	24.93
270	17.24	35.34	25.16
280	19.11	36.28	27.58

Tab. S13. Thermal expansion along the crystallographic axes of rozenite (determined from adjacent datapoints as collected upon heating). T_{ref} = (T_{start} + T_{end})/2 (e.g., Tref = 280 K corresponds to the thermal expansion tensor derived from the unit-cell parameters measured at 275 K and 285 K). * Values reported in these columns were multiplied by 10^6 for the sake of brevity (e.g. α_a at 28 K is 3.22 x 10^{-6} K^{-1}).

8.4 Supplementary: Phase-transition type negative volume expansion and anisotropic X-ray expansion in magnesium sulfate tetrahydrate

Electronic Supplementary Information

Contents

Thermal Expansion Fitting:

The variable temperature lattice parameters of cranswickite (10 - 340 K) and starkeyite (10 – 370 K) measured in 10 K increments were treated following the polynomial extension of the Einstein approximation, which is based on the assumption that all normal modes of vibration in a crystal exhibit the same frequency (Wallace, 1972). Within this approximation, a crystal's expansion is described as Eq (1)

$$V(T) = V_0 + \frac{E}{\left(exp^{(\theta_E/T)} - 1\right)} \qquad (1)$$

whereby $E = 3R\gamma\theta_E/K_T$ with R being the Ideal gas constant, γ the Grüneisen parameter, θ_E the Einstein temperature and K_T the bulk modulus. The expansion of the individual lattice parameters may be fitted following Eq. (2)

$$X(T) = X_0 + \frac{E}{\left(exp^{(\theta_E/T)} - 1\right)} \qquad (2)$$

As might be expected, the rather simple Einstein model describes the evolution of the volume and lattice parameters very poorly (Fig. S4-S13), since the vibrational properties of magnesium sulfates hydrates are characterized by multiple structural units vibrating at different energies (i.e., Raman-active Γ-point frequencies of H_2O = 1509 – 3558 cm^{-1}, SO_4 = 371 – 1215 cm^{-1}, and MgO_6 internal modes and external modes at frequencies < 370 cm^{-1} (Wang et al., 2006)). For this reason, Fortes et al. (2008) suggested to let E vary as a function of temperature according to the simple polynomial

$$E = e_0 + e_1T + e_2T^2 + e_3T^3 \qquad (3)$$

We tested fitting of the individual lattice parameters up to a third-order polynomial expansion of E (Fig S4-S8 cranswickite, Fig S9-S13 and starkeyite). For cranswickite we found that V, b and c only a second-order fit is necessary to accurately model the temperature dependence, whereas for a and β the thermal expansion is well described using a linear dependence on T. For starkeyite, we found that the thermal expansion is well described with a second-order fit upon all lattice-parameters and the cell volume. The parameters derived from this fit are stated in Tab. S1 and Tab. S2, for cranswickite and starkeyite respectively.

Sample Synthesis and Phase Analysis:

Samples of perdeuterated cranswickite ($MgSO_4 \cdot 4D_2O$) were synthesized by dehydration of the heptahydrate under conditions of controlled temperature and humidity and under reduced atmospheric pressure conditions, consistent with the natural occurrence of the mineral in arid high-altitude environments on Earth.

Anhydrous $MgSO_4$ was prepared by dehydrating $MgSO_4 \cdot 7H_2O$ at 673 K for 24 hours. The anhydrous $MgSO_4$ was then dissolved in D_2O under constant heating and stirring to make an oversaturated solution. This solution was placed in a fridge to cool down, after which fine-grained $MgSO_4 \cdot 7D_2O$ precipitated. These crystals were ground and placed in a weighing boat which was then sealed in a glass jar containing $MgCl_2$ dissolved in D_2O to buffer the relative humidity of the atmosphere at around 33 % (Greenspan, 1977) (Fig. S17).

The sealed glass jar was kept in an oven for seven days at 323 K, after which time-of-flight (TOF) neutron powder diffraction measurements were obtained to evaluate the progress of the dehydration. At this point the sample was found to be mostly $MgSO_4 \cdot 5D_2O$ (pentahydrite) with minor cranswickite present in the sample. The sample was then kept at room temperature (285 ± 5 K) for a further six weeks, after which it was placed in an oven for another five days at 33 % RH and 323 K. Phase analysis by means of neutron diffraction revealed the sample was nearly phase pure cranswickite (98.05(8) wt. %) with only a few weak peaks assigned to pentahydrite (Fig. S2).

Deuterated starkeyite was also produced by dehydration of $MgSO_4 \cdot 7D_2O$ in in a container filled with a $MgCl_2/D_2O$ humidity buffer solution, again at 323 K for seven days. The importance difference, however, is that a sealed plastic container (Fig. S18) was used for the synthesis, instead of the glass jar with the rubber gasket used for cranswickite (Fig. S17). This is of crucial, since the rubber gasket allowed Helium to diffuse out of synthesis container, resulting in an under-pressure in the synthesis container, which we found to be crucial for the formation of pentahydrate and the subsequent formation of cranswickite. Protiated starkeyite was synthesised in a similar manner, but using H_2O and $MgSO_4 \cdot 7H_2O$ instead of their deuterated counterparts.

Sample Loading and Data Collection

The TOF neutron powder diffraction measurements were made using the High-Resolution Powder Diffractometer (HRPD) at the ISIS Neutron and Muon Spallation Source (Ibberson, 2009). For measurement at ambient temperature, the cranswickite sample was loaded into a cylindrical vanadium-foil can of internal diameter 8 mm, filled to a depth of ~ 20 mm.

For variable temperature measurements in the range 10 – 340 K (cranswickite) and 10 – 370 K (starkeyite), each of the samples was loaded into an aluminium slab-geometry can with a cuboid internal cavity of dimensions 18 x 23 mm perpendicular to the incident neutron beam and a depth of 10 mm parallel to the beam. These sample holders have thin vanadium foil windows on the front beam-facing side and on the rear, while the exposed aluminium and steel components around the edges of the window are masked with absorbing Gd and Cd foil. The temperature of the slab-geometry cells is controlled by balancing direct heating of the frame from a cartridge heater against a cold bath of helium gas chilled by a cryocooler; the temperature of the frame is monitored with a RhFe thermometer.

For cranswickite, two data-sets with a statistical quality suitable for Rietveld structure refinement were collected at room temperature and at 10 K using the instrument's 30-130 and 100-200 ms TOF windows; these were counted for 4 hr each at both temperatures. In the highest resolution backscattering detectors (2θ = 154 – 176°), these TOF ranges yield time-focussed data covering the *d*-spacings from 0.65 – 2.60 and 2.2 – 4.0 Å, respectively. Diffraction patterns suitable for lattice parameter refinement (50 min counting times) were collected on cooling from 300 to 10 K using only the 30-130 ms TOF window. Subsequently, the sample was reheated to 300 K after which diffraction patterns were acquired, again for 50 min each, between 300 and 330 K. While heating the sample to 340 K, however, the neutron beam tripped, preventing us from collecting data at this temperature. After holding the sample at this temperature for 3.5 hours, without any indications that the beam would be restored, we decided to halt the experiment and keep the sample, still sealed in the sample holder, at room temperature. After 3 days the sample was returned to the beam-line to continue the experiment. Unexpectedly, the sample was found to contain a mixture of cranswickite (68.7(1) wt. %) and starkeyite (31.3(2) wt . %). The coexistence of both polymorphs in the same sample, allowed us to

determine absolute differences in the molar volume and thermal expansion very accurately in the 300 – 340 K temperature range. Finally, at 330 K, we observed the cranswickite to starkeyite transition, that proceeded very slowly (1.1% in 50 min). In order to increase the transformation rate and follow the cranswickite to starkeyite transition in-situ we increased the temperature and collected another 14 diffraction patterns (each for approximately 50 min) until the phase transition was complete. Detailed information on the sample loading and data-analysis procedure as well as histogram plots for the refinement of the room-temperature and 10 K structure are provided (Fig. S5a-b).

For starkeyite, two data-sets suitable for Rietveld refinement were collected at 10 and 300 K in the 30 – 130 and 100 – 200 ms TOF windows. Counting times were 4 h 34 min for each of both TOF windows. Shorter measurements for the purpose of lattice parameter refinement with acquisition times of 25 min were undertaken in the 30 – 130 ms in the temperature ranges 300 – 10 K in 10 K increments upon cooling, and 20 – 370 K upon heating.

For both measurement series, the sample was cooled at a rate of 3 K min^{-1} and after reaching the set-point given 10 minutes to thermally equilibrate prior to the start of the measurement. The data were time-focused, normalized to the incident spectrum and corrected for instrument efficiency using a V:Nb standard. Diffractometer calibration constants and instrumental peak-profile coefficients were determined using NIST silicon SRM640e and CeO_2 SRM674b standards.

For the thermal expansion study of protiated starkeyite, synchrotron powder diffraction measurements were performed on beamline I11 at Diamond Light Source. The powder sample was loaded into a 0.7 mm (diameter) borosilicate glass capillary of ~40 mm in length. Data was collected upon cooling from 290 – 90 K in 10 K increments, followed by a pattern collected at the cryostreams set temperature of 85 K. Afterwards the sample was studied from 95 – 295 K upon heating. Patterns were acquired for 30 and 15 minutes at each temperature point upon heating and cooling, respectively. The multi-analyser crystal detectors (λ = 0.826547(10) Å, 2θ zero-point error = 0.00011(2) °) were used for the variable temperature measurement and the fast position sensitive detector (λ = 0.82656(1) Å, zero-point error refined from the sample) was used to collect snapshots (1 s/pattern) of the material at the start and end of the experiment at various points on the capillary, which therefore allowed to identify

the radiation damage on the sample (Fig 5). Technical descriptions of the synchrotron beamline can be found in Thompson et al. (2009, 2011).

Refinement of Neutron and Synchrotron Diffraction Data

For the refinement of the 10 K and room temperature structure of cranswickite we used the heavy atoms positions reported by Peterson (2011) as the starting model, and placed the deuterium atoms at a 0.98 Å distance of the donor oxygens parallel to the vector spanned by the donor and acceptor oxygens. Peak profile parameters, background, 4th order spherical harmonic texture correction, absorption, unit-cell parameters, DIFA, scale factor as well as the atomic coordinates and anisotropic displacement parameters were refined for both the room temperature as well as the base temperature measurements.

For the refinement of the 10 K and 300 K structure of starkeyite, we used the atomic positions as derived by Baur (1964) from single crystal Neutron diffraction served as starting geometry. Again, profile parameters, background, 4th order spherical harmonic texture correction, absorption, unit-cell parameters, DIFA, scale factor as well as the atomic coordinates and anisotropic displacement parameters were refined.

In order to obtain highly precise and accurate variable temperature lattice parameter DIFA was fixed to the value derived at 10 K and following workflow was used. At each temperature, the pattern was initially refined using the Rietveld method, varying the lattice parameters, background coefficients, scale factors and peak profile coefficients. Subsequently, the patterns were fitted employing the '(calc) weighted' method in GSAS, which is a variation of the LeBail method, typically leading lattice parameters with highest precision, by virtue of an improved fitting of the peak intensities.

To monitor the changes of the phase fractions in the course of the cranswickite to starkeyite transformation at 340 K, the lattice parameters and profile parameters were fixed to the value refined from the first pattern collected at 340 K and merely the scale factor and phase fractions were refined for the 14 patterns subsequently collected until the transformation was complete.

For the variable temperature synchrotron X-ray diffraction experiment of protiated starkeyite, the 300 K Neutron structure was used as basis of the refinement. As for the neutron data, we performed a Rietveld refinement of the lattice parameters, scale factor and background, then fixed the background and

lastly refined the lattice parameters and peak profile parameters using the "(calc) weighted" method as implemented in GSAS.

Dispersion-corrected Density Functional Theory:

Kohn-sham (Hohenberg & Kohn, 1964; Kohn & Sham, 1965) density functional theory calculations were performed in order to aid the understanding of the stability of cranswickite with respect to starkeyite by investigating the difference in total electronic energy. All calculations were carried out using the CASTEP code (Clark et al., 2005) and on-the-fly generated ultrasoft pseudopotentials. Cut off values of 1200 eV for the wavefunction were derived from convergence testing. Monkhorst-Pack k-point grids of 4 x 2 x 3 (starkeyite) and 2 x 4 x 2 were applied to sample the Brillouin zone. Crystal structures as reported in this study (cranswickite) and in the literature (starkeyite, Baur 1964) served as input geometry for the initial geometry relaxations using the PBE (Perdew et al., 1996) exchange-correlation functional in conjunction with the TS pairwise dispersion correction (Tkatchenko & Scheffler, 2009) which is very well suited to model geometries at temperatures close to the ground state both for dispersion-dominated solids as well as hydrogen-bonded solids such as the ones under investigation (Meusburger et al., 2021). For simultaneous relaxation of the unit-cell dimensions as well as the internal atomic coordinates the Broyden-Fletcher-Goldfarb-Shanno algorithm (Pfrommer et al., 1997), with strict convergence thresholds 0.02 GPa, 5×10^{-4}Å, 5×10^{-6} eV/atom for the stress, ionic force, and total energy, respectively was used. The zero-pressure relaxed structure served as input for the high-pressure geometries optimization which were carried out from 0.5 - 5 GPa in increments of 0.5 GPa. All files necessary to reproduce our calculations (i.e., input, output, and pseudopotential files) may be accessed on the MaterialsCloudArchive (Meusburger et al., 2022). Lastly the variable pressure geometries were used to predict the compressibility of both polymorphs. To this end, the volume pressure data was fitted using a third order Birch-Murnaghan Equation of State yielding following parameters: starkeyite (K = 36.3(4) GPa, K' = 5.1(2); cranswickite (K = 37.2(4) GPa, K' = 5.4(2)). We have most recently demonstrated in a benchmarking study (Meusburger et al., 2021) that the DFT+D method applied in this study yields accurate predictions of the compressibility of hydrogen bonded compounds

Dose calculation

In order to calculate the received and absorbed radiation dose in units of Gray (=J/Kg) for the synchrotron measurements, we first have to calculate the photon-energy in joule (J). As the energy used for the I11 experiment was E=15 keV (λ = 0.8265 Å), and 1 eV=1.602177 x 10^{-19} J, each photon therefore delivered 2.40327 x 10^{-15} J. The dimensions of the beam at I11 are 0.8 mm × 2.5 mm (approximated as a uniform uniform top-hat beam) and the photon flux is 1.7 x 10^{13} photons per seconds. The beam cross section (0.8 mm x 2.5 mm) is larger than the illuminated sample cross section (0.68 mm x 2.5 mm; n.b. 0.7 mm (capillary diameter) – 2 x 0.01 (capillary wall thickness)$\rightarrow$ 0.068 mm). This yields a photon flux of 1.4550 x 10^{13} photons/seconds incident on the sample in the capillary. However, before hitting the sample material, the photons pass through the 0.01 mm thick capillary wall, whereby a fraction are attenuated. Using the ABSORB web utility (von Dreele et al., 2013), and taking into account the capillary thickness, composition and density, we calculated that 99.05% of photons pass through the borosilicate glass capillary yielding a photon flux of 1.43132 x 10^{13} photons/second. At a photon energy of 15 keV this corresponds to a 0.034398397 J that is being received by the sample every second. The density of starkeyite as determined by XRD is 2.0074 g/cm^3, but assuming a packing density of 50% for the polycrystalline sample material enclosed in the capillary reduces the density to 1.0037 g/cm^3. The exposed volume (=π x 0.34^2 mm^2 x 2.5 mm) then corresponds to a mass of 9.11286 × 10^{-7} Kg.

Using the exposed mass and received photon energy then yields a **<u>received</u>** 'dose' of 37747.1 J/Kg or Gray (Gy) every second. This received dose rate represents an upper bound for the absorbed dose rate, assuming that 100% of the photons are absorbed by the sample. Clearly this assumption is unrealistic and in order to obtain a more realistic value for the X-ray absorption by the sample, again, we used the ABSORB web utility (von Dreele et al., 2013). We calculate that 24.6861% of the photons are absorbed yielding an **<u>absorbed</u>** dose rate 9318.3 Gy/s, which is the value used for all dose calculations in the accompanying manuscript.

An alternative way to estimate the dose rate is using the Raddose-3D software (Bury et al., 2017). Although Raddose-3D was adapted for capillary samples (Brooks-Bartlett et al., 2017), it assumes that the sample is a single crystal (i.e, 100% packing density), which clearly is an unrealistic assumption for a powdered

sample, thus introducing a large error when calculating an absorbed radiation dose in units of J/Kg. Coates et al. (2021), recognized this shortcoming of the Raddose-3D software, but went on to calculate the dose rate used in their work using Raddose-3D yielding a dose rate of 13407 Gy/s for $Cd(CN)_2$. In order to allow for a comparison of the X-ray expansion with their study, we calculated the received 'dose' rate, absorbed dose rate using the workflow stated above, as well as the dose rate using Raddose-3D for both $MgSO_4 \cdot 4H_2O$ and $Cd(CN)_2$ (Tab. S6).

Tables

	a	*b*	*c*	*β*	*V*
X_0	11.89150(3)	5.11149(2)	12.25434(4)	117.6324(3)	659.894(2)
$θ_D$	270(5)	158(2)	119(3)	137(15)	233(3)
e0	$2.9(2) \times 10^{-2}$	$1.80(8) \times 10^{-2}$	$-2.17(9) \times 10^{-2}$	$-1.9(5) \times 10^{-2}$	3.7(2)
e1	$9.05(7) \times 10^{-5}$	$7.9(1) \times 10^{-5}$	$2.7(3) \times 10^{-5}$	$-1.5(1) \times 10^{-4}$	$2.23(4) \times 10^{-2}$
e2	-	$3.4(4) \times 10^{-8}$	$-1.51(8) \times 10^{-7}$	-	$-8.9(8) \times 10^{-6}$
$χ2$	83.0	247.8	81.5	49.6	185.1

Tab. S1. Parameters derived from fitting the polynomial extension of the Einstein model upon the lattice parameters of cranswickite.

	a	*b*	*c*	*β*	*V*
X_0	5.8971(4)	13.50760(7)	7.87448(3)	90.5844(4)	627.222(4)
$θ_D$	128(7)	205(5)	241(15)	271(7)	176(3)
e0	$7.9(9) \times 10^{-3}$	$6.3(4) \times 10^{-2}$	$1.2(3) \times 10^{-2}$	$6.1(4) \times 10^{-1}$	3.88(2)
e1	$3.1(1) \times 10^{-5}$	$5.9(1.0) \times 10^{-5}$	$7.4(3) \times 10^{-5}$	$-2.4(2) \times 10^{-3}$	$1.25(3) \times 10^{-2}$
e2	$-6.0(2) \times 10^{-8}$	$1.2(2) \times 10^{-7}$	$5.1(1.4) \times 10^{-8}$	$6.5(3) \times 10^{-6}$	$-3.2(6) \times 10^{-6}$
$χ2$	184.0	161	77	946	560

Tab. S2. Parameters derived from fitting the polynomial extension of the Einstein model upon the lattice parameters of starkeyite.

Compound	NTE (K^{-1})	T_{ref} (K)	VTE (K^{-1})	T_{ref} (K)	Source
$MgSO_4 \cdot 11H_2O$	$-1.2(5) \times 10^{-5}$	50	$6.8(4) \times 10^{-5}$	240	Fortes et al. (2008)
$MgSO_4 \cdot 7H_2O$	$-2.0(2) \times 10^{-5}$	125	$10.8(3) \times 10^{-5}$	290	Fortes et al. (2006)
$FeSO_4 \cdot 4H_2O$	$-1.0(2) \times 10^{-5}$	285	$8.2(5) \times 10^{-5}$	285	Meusburger et al. (2022)
$MgSO_4 \cdot 4H_2O$**	$-7.7(3) \times 10^{-6}$	305	$8.2(4) \times 10^{-5}$	305	This study
$MgSO_4 \cdot 4H_2O$*	$-3.19(8) \times 10^{-5}$	305	$8.4(2) \times 10^{-5}$	305	This study
$MgSO_4 \cdot 4H_2O$*	$-2.8(2) \times 10^{-5}$	295	$7.8(8) \times 10^{-5}$	295	This study
$MgSO_4 \cdot H_2O$	$-4.4(3) \times 10^{-5}$	293	$3.4(7) \times 10^{-5}$	293	Wildner et al. (2022)
$FeSO_4 \cdot H_2O$	$-1.7(2) \times 10^{-5}$	293	$4.7(5) \times 10^{-5}$	293	Wildner et al. (2022)
$CoSO_4 \cdot H_2O$	$-2.7(2) \times 10^{-5}$	293	$3.3(3) \times 10^{-5}$	293	Wildner et al. (2022)
$NiSO_4 \cdot H_2O$	$-0.8(5) \times 10^{-5}$	293	$3.6(4) \times 10^{-5}$	293	Wildner et al. (2022)

Tab. S3. Comparison of the negative (NTE) and volume (VTE) thermal expansion of various $MeSO_4 \cdot nH_2O$. *denotes cranswickite ** starkeyite.

Source	Peterson	This study	DIFF	This study	
T (K)	RT	RT		10	
Mg-O2	2.015(5)	2.031(3)	-0.016	2.033(2)	-0.002
Mg-Ow1	2.100(4)	2.063(3)	0.037	2.045(2)	0.018
Mg-Ow2	2.097(3)	2.107(2)	-0.01	2.102(2)	0.005
Mean	2.0708	2.0672	0.0036	2.0601	0.007
DI	0.01798	0.01298		0.0135	
MSiD[1]		0.00367		0.007	
MUD		0.02100		0.008	
O2-Mg-Ow1	94.69(16)	92.39(11)	2.300	92.63(7)	-0.240
O2-Mg-Ow2	93.02(14)	90.55(10)	2.470	90.63(7)	-0.080
Ow1-Mg-Ow2	86.21(11)	89.10(9)	2.890	89.78(7)	-0.680
BAV	16.5332	2.4873	13.855	2.6403	0.038
MSiD		0.6267		-0.33	
MUD		2.5533		0.33	
S-O1	1.521(4)	1.485(4)	0.036	1.485(4)	0.000
S-O2	1.486(5)	1.450(4)	0.036	1.464(4)	-0.014
Mean	1.5034	1.4673	0.0361	1.4719	-0.005
DI	0.01182	0.01207		0.00697	0.007
MSiD		0.036		-0.007	
MUD		0.036		0.007	
O1-S-O1	108.9(3)	108.3(4)	0.6	108.9(4)	0.019
O1-S-O2	112.1(3)	110.03(15)	2.07	109.58(11)	0.010
O1-S-O2'	108.4(2)	108.97(12)	0.57	109.18(8)	0.027
O2-S-O2	107.1(4)	110.5(4)	3.4	110.4(4)	0.019
BAV	4.5007	0.6873	4.016	0.2731	0.2116
MSiD		-0.325		-0.065	
MUD		1.66		0.34	

Tab. S4. Bond lengths and angles for the octahedral and tetrahedral units of cranswickite as determined in this study at room temperature and 10 K and compared to the values reported by Peterson (2011)* refers to the difference between Peterson (2011) and this study's RT structure. ** refers to the difference of this study's RT and 10 K structures, thus elucidating the influence of temperature on the respective quantity. The Mean Signed Difference ($\frac{\sum_i^n x_P - x_T}{n}$) and Mean Unsigned Difference ($\frac{\sum_i^n |x_P - x_T|}{n}$) were calculated with x_P and x_T being the values as observed by Peterson (2011) and in this study, respectively for the quantities of interest.

Source	Peterson	This study	Diff*	This study	Diff**
T (K)	RT	RT		10	
Ow1-H1a	ND	0.963(5)		0.975(3)	-0.012
Ow1-H1b	ND	0.953(4)		0.972(3)	-0.019
Ow2-H2a	ND	0.980(4)		0.978(3)	0.002
Ow2-H2b	ND	0.966(4)		0.973(3)	-0.007
MSiD				-0.009	
MUD				0.010	
H1a-Ow1-H1b	ND	104.4(4)		103.9(3)	0
H2a-Ow2-H2b	ND	108.0(3)		109.3(2)	-1.1
MSiD				-0.55	
MUD				0.55	
Ow1-O1	2.776(6)	2.861(4)	-0.088	2.842(3)	0.022
Ow1-Ow2	2.835(5)	2.804(4)	0.027	2.790(3)	0.018
Ow2-O1	2.776(5)	2.746(4)	0.034	2.725(3)	0.017
Ow2-O1'	2.641(6)	2.731(4)	-0.093	2.721(3)	0.013
MSiD		-0.03		0.0175	
MUD		0.0605		0.0175	
H1a-O1	ND	1.947(4)		1.917(3)	0.031
H1b-Ow2	ND	1.851(4)		1.815(3)	0.039
H2a-O1	ND	1.768(4)		1.747(3)	0.018
H2b-O1'	ND	1.793(4)		1.770(3)	0.023
MSiD				0.278	
MUD				0.278	
O1-Ow1-Ow2	94.92(14)	91.50(9)	3.56	92.57(7)	-1.21
O1-Ow2-O1	115.33(13)	114.78(9)	0.61	114.53(7)	0.19
MSiD		2.085		-0.51	
MUD		2.085		0.70	
Ow1-H1a-O1		157.6(3)		158.1(2)	-0.6
Ow1-H1b-Ow2		178.5(3)		178.3(3)	0.3
Ow2-H2a-O1		176.6(3)		176.9(2)	-0.5
Ow2-H2b-O1		162.9(3)		164.9(2)	-1.8
MSiD				-0.65	
MUD				0.8	

Tab. S5. Bond lengths and angles for the hydrogen bonding system of cranswickite determined in this study at room temperature and 10 K and compared to the values reported by Peterson (2011)* refers to the difference between Peterson (2011) and this study's RT structure. ** refers to the difference of this study's RT and 10 K structures, thus elucidating the influence of temperature on the respective quantity. The Mean Signed Difference ($\frac{\sum_{i}^{n} x_P - x_T}{n}$) and Mean Unsigned Difference ($\frac{\sum_{i}^{n} |x_P - x_T|}{n}$) were calculated with x_P and x_T being the values as observed by Peterson (2011) and in this study, respectively for the quantities of interest.

	Coates et al. (2021)	This study
sample	$Cd(CN)_2$	$MgSO_4$ $4H_2O$
Received dose rate	49122*	37747
Absorbed dose rate manual	37271	9318
Absorbed dose rate Raddose-3D	13407	6154

Tab. S6. Dose rates calculated for $MgSO_4 \cdot 4H_2O$ and $Cd(CN)_2$ using the workflow stated in section 'Dose calculation' (Supplementary material), as well as using the Raddose-3D software. Stated as 38100 Gy/s by Coates et al. (2021).

T (K)		300				10		
Mg	x	0.0677(4)	U_{11}	0.0095(13)	x	0.0739(5)	U_{11}	0.0068(15)
	y	0.10311(18)	U_{22}	0.0182(13)	y	0.10427(22)	U_{22}	0.0103(14)
	z	0.22138(34)	U_{33}	0.0212(14)	z	0.2206(4)	U_{33}	0.0124(15)
	U_{eq^*}	0.0163	U_{12}	-0.0003(10)	U_{eq}	0.00985	U_{12}	0.0026(10)
			U_{13}	-0.0035(11)			U_{13}	-0.0011(12)
			U_{23}	-0.0020(10)			U_{23}	0.0027(11)
S	x	0.1968(8)	U_{11}	0.0154(25)	x	0.1902(10)	U_{11}	0.0137(33)
	y	0.10718(30)	U_{22}	0.0123(23)	y	0.1082(4)	U_{22}	0.0136(28)
	z	0.8247(5)	U_{33}	0.0127(24)	z	0.8265(7)	U_{33}	0.0106(27)
	U_{eq}	0.01344	U_{12}	-0.0038(19)	U_{eq}	0.01259	U_{12}	-0.0049(22)
			U_{13}	0.0049(19)			U_{13}	0.0062(24)
			U_{23}	-0.0045(21)			U_{23}	0.0072(24)
O1	x	0.0047(4)	U_{11}	0.0205(14)	x	0.0038(5)	U_{11}	0.0158(16)
	y	0.04520(17)	U_{22}	0.0210(13)	y	0.04548(18)	U_{22}	0.0097(13)
	z	0.75914(29)	U_{33}	0.0232(14)	z	0.76054(34)	U_{33}	0.0132(15)
	U_{eq}	0.02155	U_{12}	-0.0056(11)	U_{eq}	0.01284	U_{12}	-0.0006(11)
			U_{13}	0.0012(13)			U_{13}	0.0057(13)
			U_{23}	0.0003(11)			U_{23}	0.0005(12)
O2	x	0.2483(4)	U_{11}	0.0244(15)	x	0.2549(5)	U_{11}	0.0123(15)
	y	0.07716(19)	U_{22}	0.0281(15)	y	0.07593(22)	U_{22}	0.0155(15)
	z	0.00336(28)	U_{33}	0.0128(14)	z	0.00125(33)	U_{33}	0.0063(14)
	U_{eq}	0.02182	U_{12}	0.0080(11)	U_{eq}	0.01135	U_{12}	0.0015(10)
			U_{13}	-0.0016(11)			U_{13}	-0.0012(12)
			U_{23}	0.0029(11)			U_{23}	0.0044(11)
O3	x	0.3979(4)	U_{11}	0.0223(14)	x	0.3977(5)	U_{11}	0.0118(16)
	y	0.09093(19)	U_{22}	0.0213(13)	y	0.09177(20)	U_{22}	0.0089(13)
	z	0.72363(30)	U_{33}	0.0202(14)	z	0.71794(34)	U_{33}	0.0140(15)
	U_{eq}	0.02124	U_{12}	0.0026(12)	U_{eq}	0.01157	U_{12}	-0.0003(11)
			U_{13}	0.0053(11)			U_{13}	-0.0001(11)
			U_{23}	-0.0052(12)			U_{23}	-0.0036(13)
O4	x	0.1299(4)	U_{11}	0.0209(14)	x	0.1311(5)	U_{11}	0.0131(16)
	y	0.21057(16)	U_{22}	0.0131(12)	y	0.21298(17)	U_{22}	0.0073(13)
	z	0.81487(32)	U_{33}	0.0293(16)	z	0.8179(4)	U_{33}	0.0149(15)
	U_{eq}	0.02114	U_{12}	-0.0014(11)	U_{eq}	0.01173	U_{12}	0.0021(11)
			U_{13}	-0.0018(11)			U_{13}	0.0049(13)
			U_{23}	0.0001(12)			U_{23}	0.0039(12)
O1w	x	0.3584(5)	U_{11}	0.0283(17)	x	0.3621(6)	U_{11}	0.0123(17)
	y	0.07482(22)	U_{22}	0.0264(18)	y	0.07459(23)	U_{22}	0.0184(17)
	z	0.3572(4)	U_{33}	0.0189(17)	z	0.3566(4)	U_{33}	0.0078(15)
	U_{eq}	0.02455	U_{12}	0.0171(13)	U_{eq}	0.01281	U_{12}	0.0029(12)
			U_{13}	-0.0014(13)			U_{13}	0.0017(14)
			U_{23}	-0.0067(13)			U_{23}	0.0026(13)
O2w	x	0.7768(5)	U_{11}	0.0234(19)	x	0.7764(6)	U_{11}	0.0208(21)
	y	0.13948(26)	U_{22}	0.0344(21)	y	0.13994(25)	U_{22}	0.0143(18)
	z	0.0915(4)	U_{33}	0.0328(19)	z	0.0914(4)	U_{33}	0.0134(16)
	U_{eq}	0.03022	U_{12}	0.0073(15)	U_{eq}	0.01618	U_{12}	-0.0012(13)
			U_{13}	-0.0026(16)			U_{13}	-0.0009(14)
			U_{23}	-0.0066(15)			U_{23}	-0.0018(13)
O3w	x	0.8916(6)	U_{11}	0.0360(22)	x	0.8896(5)	U_{11}	0.0112(18)
	y	0.12746(26)	U_{22}	0.0389(20)	y	0.12837(26)	U_{22}	0.0200(17)
	z	0.4411(4)	U_{33}	0.0256(20)	z	0.4427(4)	U_{33}	0.0073(16)
	U_{eq}	0.03345	U_{12}	0.0203(14)	U_{eq}	0.01284	U_{12}	0.0024(13)
			U_{13}	0.0025(16)			U_{13}	0.0010(13)
			U_{23}	0.0065(15)			U_{23}	0.0025(13)
O4w	x	0.1767(6)	U_{11}	0.0271(18)	x	0.1778(6)	U_{11}	0.0148(17)
	y	0.24783(21)	U_{22}	0.0136(14)	y	0.24778(22)	U_{22}	0.0063(14)
	z	0.2219(4)	U_{33}	0.0357(17)	z	0.2203(4)	U_{33}	0.0210(17)
	U_{eq}	0.02554	U_{12}	-0.0010(13)	U_{eq}	0.01405	U_{12}	-0.0017(14)
			U_{13}	-0.0067(14)			U_{13}	-0.0016(14)

			U_{23}	-0.0024(14)			U_{23}	0.0042(15)
D1a	x	0.3716(5)	U_{11}	0.0418(18)	x	0.3711(6)	U_{11}	0.0263(20)
	y	0.08512(23)	U_{22}	0.0552(20)	y	0.08581(23)	U_{22}	0.0317(18)
	z	0.4767(4)	U_{33}	0.0410(19)	z	0.4781(5)	U_{33}	0.0270(17)
	U_{eq}	0.04612	U_{12}	0.0090(15)	U_{eq}	0.02835	U_{12}	0.0086(14)
			U_{13}	-0.0121(15)			U_{13}	-0.0023(14)
			U_{23}	-0.0103(17)			U_{23}	-0.0035(16)
D1b	x	0.4553(5)	U_{11}	0.0368(17)	x	0.4631(6)	U_{11}	0.0288(19)
	y	0.02214(22)	U_{22}	0.0471(18)	y	0.02035(25)	U_{22}	0.0353(18)
	z	0.3282(4)	U_{33}	0.0412(17)	z	0.3277(4)	U_{33}	0.0280(18)
	U_{eq}	0.0417	U_{12}	0.0097(15)	U_{eq}	0.03073	U_{12}	0.0124(15)
			U_{13}	-0.0005(14)			U_{13}	-0.0065(17)
			U_{23}	0.0053(16)			U_{23}	-0.0036(16)
D2a	x	0.6837(6)	U_{11}	0.0481(24)	x	0.6813(6)	U_{11}	0.0275(21)
	y	0.18741(27)	U_{22}	0.0735(25)	y	0.18860(24)	U_{22}	0.0324(19)
	z	0.1428(4)	U_{33}	0.0540(22)	z	0.1477(4)	U_{33}	0.0324(19)
	U_{eq}	0.05854	U_{12}	0.0197(19)	U_{eq}	0.03073	U_{12}	0.0046(14)
			U_{13}	0.0003(17)			U_{13}	0.0023(16)
			U_{23}	0.0090(20)			U_{23}	0.0009(15)
D2b	x	0.6781(6)	U_{11}	0.0640(25)	x	0.6735(6)	U_{11}	0.0287(19)
	y	0.09457(31)	U_{22}	0.0766(27)	y	0.09183(26)	U_{22}	0.0381(19)
	z	0.0389(4)	U_{33}	0.0659(25)	z	0.0411(4)	U_{33}	0.0357(20)
	U_{eq}	0.06915	U_{12}	-0.0163(21)	U_{eq}	0.03413	U_{12}	-0.0076(16)
			U_{13}	-0.0265(18)			U_{13}	0.0057(17)
			U_{23}	0.0118(21)			U_{23}	-0.0073(17)
D3a	x	0.8011(6)	U_{11}	0.0552(22)	x	0.7950(6)	U_{11}	0.0384(22)
	y	0.18356(25)	U_{22}	0.0483(20)	y	0.18345(26)	U_{22}	0.0308(18)
	z	0.4534(4)	U_{33}	0.0451(19)	z	0.4537(4)	U_{33}	0.0318(20)
	U_{eq}	0.0494	U_{12}	0.0130(16)	U_{eq}	0.03358	U_{12}	0.0177(15)
			U_{13}	0.0107(16)			U_{13}	0.0139(18)
			U_{23}	-0.0033(15)			U_{23}	0.0020(14)
D3b	x	0.9153(5)	U_{11}	0.0426(20)	x	0.9155(5)	U_{11}	0.0270(20)
	y	0.09892(24)	U_{22}	0.0546(21)	y	0.09738(23)	U_{22}	0.0238(17)
	z	0.5486(4)	U_{33}	0.0315(18)	z	0.5503(4)	U_{33}	0.0201(16)
	U_{eq}	0.04292	U_{12}	0.0036(15)	U_{eq}	0.02362	U_{12}	-0.0028(14)
			U_{13}	0.0013(14)			U_{13}	-0.0006(13)
			U_{23}	0.0009(16)			U_{23}	-0.0005(14)
D4a	x	0.3153(6)	U_{11}	0.0395(19)	x	0.3175(6)	U_{11}	0.0255(19)
	y	0.26476(19)	U_{22}	0.0365(17)	y	0.26431(21)	U_{22}	0.0286(17)
	z	0.2781(4)	U_{33}	0.0537(18)	z	0.2782(5)	U_{33}	0.0355(19)
	U_{eq}	0.04332	U_{12}	-0.0066(14)	U_{eq}	0.0299	U_{12}	-0.0029(14)
			U_{13}	-0.0081(16)			U_{13}	-0.0008(17)
			U_{23}	-0.0013(14)			U_{23}	-0.0010(14)
D4b	x	0.5808(5)	U_{11}	0.0394(18)	x	0.5818(6)	U_{11}	0.0348(21)
	y	0.19534(21)	U_{22}	0.0328(16)	y	0.19382(24)	U_{22}	0.0264(18)
	z	0.72734(34)	U_{33}	0.0441(18)	z	0.7246(4)	U_{33}	0.0312(19)
	U_{eq}	0.03868	U_{12}	-0.0007(14)	U_{eq}	0.03076	U_{12}	-0.0036(14)
			U_{13}	0.0067(14)			U_{13}	0.0018(15)
			U_{23}	-0.0022(13)			U_{23}	0.0007(13)

Tab. S7 Positional parameters and anisotropic displacement parameters of the atom sites in stakeyite-type $MgSO_4 \cdot 4D_2O$ at 300 K and 21 K. *Value calculated from anisotropic displacement parameters, however, GSAS does not compute the e.s.d for U_{eq}.

Source	Baur	This study	Diff*	This study	Diff**
T (K)	RT	300		10	
Mg-O1	2.082(4)	2.068(4)	0.012	2.080(4)	-0.012
Mg-O2	2.083(5)	2.073(4)	0.01	2.075(5)	-0.002
Mg-Ow1	2.052(8)	2.050(4)	0.002	2.039(5)	0.011
Mg-Ow2	2.087(5)	2.051(4)	0.036	2.076(5)	-0.025
Mg-Ow3	2.072(5)	2.067(5)	0.005	2.094(5)	-0.027
Mg-Ow4	2.072(4)	2.071(4)	0.001	2.033(5)	0.038
MSiD[1]		0.011		-0.003	
MUD		0.011		0.019	
O1-Mg-Ow1	87.53(19)	87.20(15)	0.33	87.38(17)	-0.18
O1-Mg-Ow2	94.76(18)	95.69(16)	-0.93	94.30(18)	1.39
O1-Mg-Ow3	89.38(18)	89.19(16)	0.19	88.56(17)	0.63
O1-Mg-O2	90.54(17)	90.35(14)	0.19	89.75(17)	0.6
Ow4-Mg-Ow1	86.10(20)	85.32(16)	0.78	86.47(18)	-1.15
Ow4-Mg-Ow2	91.60(20)	91.77(17)	-0.17	91.79(18)	-0.02
Ow4-Mg-Ow3	89.90(30)	85.32(16)	4.58	90.67(18)	-5.35
Ow4-Mg-O2	90.18(19)	89.93(16)	0.25	90.99(18)	-1.06
Ow1-Mg-Ow3	91.10(30)	91.15(17)	-0.05	91.65(18	-0.5
Ow2-Mg-O2	93.70(30)	93.71(16)	-0.01	94.26(18)	-0.55
Ow2-Mg-Ow3	86.50(30)	87.22(16)	-0.72	85.98(17)	1.24
MSiD		0.404		-0.450	
MUD		0.745		1.152	
S-O1	1.480(4)	1.501(6)	-0.021	1.478(7)	0.023
S-O2	1.468(4)	1.497(5)	-0.029	1.489(7)	0.008
S-O3	1.478(6)	1.461(6)	0.017	1.516(7)	-0.055
S-O4	1.466(4)	1.463(5)	0.003	1.459(6)	0.004
MSiD		-0.0075		-0.005	
MUD		0.0175		0.0225	
O1-S-O2	109.1(3)	108.3(3)	0.79	109.8(4)	-1.5
O1-S-O3	109.4(3)	110.2(3)	-0.77	108.6(4)	1.6
O1-S-O4	108.4(3)	108.6(4)	-0.16	111.3(5)	-2.7
O2-S-O3	108.9(3)	108.6(4)	0.33	106.1(4)	2.5
O2-S-O4	112.0(3)	111.3(3)	0.73	112.7(4)	-1.4
O3-S-O4	108.9(3)	109.8(4)	-0.92	108.0(4)	1.8
MSiD		-0.0167		0.05	
MUD		0.617		1.917	

Tab. S8. Bond lengths and angles for the octahedral and tetrahedral units of starkeyite as determined in this study at 300 K and 10 K and compared to the values reported by Baur (1964). * refers to the difference between Baur and this study's 300 K structure. ** refers to the difference of this study's 300 K and 10 K structures, thus elucidating the influence of temperature on the respective quantity. The Mean signed difference is defined as $\frac{\sum_i^n x_B - x_T}{n}$ with x_B and x_T being the values as observed by Baur and in this study, respectively for the quantities of interest (i.e., bond-length and angle).

Source	Baur	This study	Diff*	This study	Diff**
T (K)	RT	300		10	
Ow1-H1a	0.969(10)	0.957(5)	0.012	0.970(6)	-0.013
Ow1-H1b	0.951 (13)	0.948(5)	0.003	0.973(5)	-0.025
Ow2-H2a	0.968(15)	0.949(5)	0.019	0.974(5)	-0.025
Ow2-H2b	0.931 (17)	0.938(5)	-0.007	0.971(5)	-0.033
Ow3-H3a	0.952 (13)	0.938(5)	0.014	0.934(5)	0.004
Ow3-H3b	0.989(10)	0.943(5)	0.046	0.956(5)	-0.013
Ow4-H4a	0.958 (13)	0.955(5)	0.003	0.964(5)	-0.009
Ow4-H4b	0.981 (10)	0.960(5)	0.021	0.972(5)	-0.012
MSiD		0.0139		-0.0158	
MUD		0.0156		0.01675	
H1a-Ow1-H1b	110.4(8)	108.0(4)	2.4	108.7(5)	-0.7
H2a-Ow2-H2b	111.0(1.5)	106.0(5)	5	106.1(5)	-0.1
H3a-Ow3-H3b	108.7(1.0)	108.6(5)	0.1	110.9(5)	-2.3
H4a-Ow4-H4b	108.5(1.0)	106.8(4)	1.6	106.9(4)	-0.1
MSiD		2.275		-0.8	
MUD		2.275		0.8	
Ow1-O3	2.884(5)	2.911(4)	-0.027	2.860(5)	0.051
Ow1-O3'	2.754(5)	2.757(4)	-0.003	2.723(5)	0.034
Ow2-O4	2.835(5)	2.843(5)	-0.008	2.810(5)	0.033
Ow2-O2	3.042(5)	3.043(5)	-0.001	3.011(5)	0.032
Ow2-O2'	3.282(6)	3.305(4)	-0.023	3.266(5)	0.039
Ow3-O4	2.860(6)	2.863(5)	-0.003	2.802(5)	0.061
Ow3-Ow4	3.080(7)	3.084(5)	-0.004	3.032(5)	0.052
Ow3-O1	2.831(5)	2.823(4)	0.008	2.817(5)	0.006
Ow4-O4	2.734(5)	2.827(5)	-0.093	2.824(5)	0.003
Ow4-O3	2.884(5)	2.745(5)	0.139	2.725(5)	0.02
MSiD		-0.0015		0.0331	
MUD		0.0309		0.0331	
H1a-O3	1.919 (10)	1.958(4)	-0.039	1.895(5)	0.063
H1b-O3'	1.818 12)	1.816(4)	0.002	1.761(5)	0.055
H2a-O4	1.948 (15)	1.973(5)	-0.025	1.913(5)	0.06
H2b-O2	2.388 (18)	2.400(5)	-0.012	2.330(5)	0.07
H2b-O2'	2.588 (16)	2.566(5)	0.022	2.494(5)	0.072
H3a-O4	2.063 (12)	2.065(5)	-0.002	2.003(5)	0.062
H3a-Ow4	2.419 (14)	2.443(5)	-0.024	2.404(5)	0.039
H3b-O1	1.901 (11)	1.886(4	0.015	1.867(5)	0.019
H4a-O4	1.919 (10)	1.910(5)	0.009	1.897(5)	0.013
H4b-O3	1.753 (10)	1.786(4)	-0.033	1.755(5)	0.031
MSiD		-0.0087		0.0484	
MUD		0.0183		0.0484	
O3-Ow1-O3'	105.2(2)	104.96(12)	0.24	104.38(13)	0.58
O4-Ow2-O2	146.8(2)	146.44(14)	0.36	145.11(15	1.33
O4-Ow2-O2'	91.8(2)	90.98(11)	0.82	91.87(13)	-0.89
O4-Ow3-O1	137.5(2)	137.28(15)	0.22	137.71(15)	-0.43
Ow4-Ow3-O1	70.8(2)	70.82(11)	-0.02	71.05(11)	-0.23
O4-Ow4-O3	114.3(2)	114.01(13)	0.29	115.13(14)	-1.12
MSiD		0.318		-0.127	
MUD		0.325		0.763	
Ow1-H1a-O3	173.6(8)	173.9(4)	-0.3	173.3(4)	0.6
Ow1-H1b-O3'	167.6 (1.1)	171.0(4)	-3.4	169.5(4)	1.5
Ow2-H2a-O4	151.3 (1.1)	151.6(4)	-0.3	151.9(4)	-0.3
Ow2-H2b-O2	127.1 (1.4)	125.6(4)	1.5	126.6(4)	-1

Ow2-H2b-O2'	131.7 (1.6)	135.9(4)	-4.2	136.3(4)	-0.4
Ow3-H3a-O4	140.2 (1.0)	142.0(4	-1.8	142.3(4)	-0.3
Ow3-H3a-Ow4	126.4 (1.0)	125.5(4)	0.9	124.5(4)	1
Ow3-H3b-O1	162.9 (1.5)	172.2(4)	-9.3	172.3(4)	-0.1
Ow4-H4a-O4	177.7 (9)	160.3(4)	17.4	160.5(5	-0.2
Ow4-H4b-O3	173.6(8)	176.4(4)	-2.8	175.5(4)	0.9
MSiD		-0.23		0.17	
MUD		4.19		0.63	

Tab. S9. Geometry of the hydrogen bonds of starkeyite as determined in this study at 300 K and 10 K, and compared to the values reported by Baur (1964). *refers to the difference between Baur and this study's 300 K structure. ** refers to the difference of this study's 300 K and 10 K structures, thus elucidating the influence of temperature on the respective quantity.

T (K)	a (Å)	b (Å)	c (Å)	β (°)	V (Å^3)
300	5.919189(19)	13.600665(45)	7.906210(21)	90.9073(3)	636.409(2)
290	5.918398(28)	13.595165(68)	7.903924(31)	90.8829(4)	635.887(3)
280	5.917470(29)	13.589954(69)	7.901689(31)	90.8600(4)	635.368(3)
270	5.916645(28)	13.584690(67)	7.899567(30)	90.8390(4)	634.866(3)
260	5.915721(29)	13.579612(66)	7.897475(30)	90.8200(4)	634.364(3)
250	5.914883(18)	13.574690(42)	7.895504(19)	90.8004(3)	633.890(2)
240	5.914018(29)	13.569963(65)	7.893592(29)	90.7821(4)	633.425(3)
230	5.913002(29)	13.565264(67)	7.891860(30)	90.7653(4)	632.961(3)
220	5.912096(29)	13.560709(67)	7.890075(30)	90.7489(4)	632.511(3)
210	5.911077(30)	13.556372(69)	7.888463(31)	90.7339(4)	632.072(4)
200	5.910087(33)	13.551827(75)	7.886968(34)	90.7202(5)	631.637(4)
190	5.909265(30)	13.548097(70)	7.885518(32)	90.7063(4)	631.261(4)
180	5.908235(34)	13.543899(78)	7.884218(35)	90.6924(5)	630.853(4)
170	5.907352(33)	13.539756(77)	7.882859(35)	90.6820(5)	630.459(4)
160	5.906379(33)	13.536380(76)	7.881700(34)	90.6726(5)	630.106(4)
150	5.905428(20)	13.532984(47)	7.880630(21)	90.6596(3)	629.763(4)
140	5.904503(32)	13.529509(76)	7.879651(34)	90.6513(5)	629.425(4)
130	5.903578(33)	13.526384(78)	7.878624(35)	90.6404(5)	629.101(4)
120	5.902699(38)	13.523249(90)	7.877877(39)	90.6319(6)	628.803(4)
110	5.901836(36)	13.520618(86)	7.877141(37)	90.6229(6)	628.531(4)
100	5.901040(35)	13.518029(85)	7.876459(37)	90.6178(5)	628.271(4)
90	5.900358(35)	13.515666(84)	7.875950(37)	90.6084(5)	628.050(4)
80	5.899714(35)	13.513341(84)	7.875440(38)	90.6036(6)	627.833(4)
70	5.899090(34)	13.511451(82)	7.875134(37)	90.5977(5)	627.656(4)
60	5.898505(36)	13.509974(85)	7.874849(38)	90.5922(6)	627.503(4)
50	5.897943(35)	13.508880(84)	7.874636(38)	90.5873(6)	627.376(4)
40	5.897565(34)	13.508149(81)	7.874598(38)	90.5840(6)	627.299(4)
30	5.897368(34)	13.507586(82)	7.874522(38)	90.5831(5)	627.246(4)
20	5.897087(34)	13.507583(81)	7.874349(38)	90.5825(6)	627.202(4)
10	5.897085(24)	13.507440(57)	7.874425(27)	90.5831(4)	627.201(3)

Tab. S10. Unit-cell parameters of starkeyite determined upon cooling by means of neutron diffraction.

T (K)	*a* (Å)	*b* (Å)	*c* (Å)	β (°)	V (Å³)
20	5.897144(34)	13.507433(82)	7.874451(38)	90.5823(5)	627.209(4)
30	5.897250(34)	13.507760(82)	7.874407(37)	90.5841(5)	627.232(4)
40	5.897576(33)	13.508175(79)	7.874485(36)	90.5851(5)	627.292(4)
50	5.898015(34)	13.508801(81)	7.874684(37)	90.5879(5)	627.383(4)
60	5.898495(35)	13.510151(84)	7.874737(38)	90.5927(4)	627.501(4)
70	5.899050(34)	13.511536(83)	7.875112(37)	90.5965(5)	627.654(4)
80	5.899691(34)	13.513396(82)	7.875534(36)	90.6017(5)	627.841(4)
90	5.900391(34)	13.515426(82)	7.875955(36)	90.6077(5)	628.043(4)
100	5.901071(34)	13.518115(82)	7.876456(36)	90.6167(5)	628.279(4)
110	5.901898(34)	13.520597(82)	7.877115(36)	90.6234(5)	628.534(4)
120	5.902739(33)	13.523453(80)	7.877840(35)	90.6319(5)	628.814(4)
130	5.903556(32)	13.526461(78)	7.878691(34)	90.6403(5)	629.107(4)
140	5.904426(32)	13.529763(77)	7.879690(34)	90.6514(5)	629.432(4)
150	5.905457(33)	13.532800(78)	7.880610(35)	90.6613(5)	629.756(4)
160	5.906394(32)	13.536391(71)	7.881759(31)	90.6708(5)	630.113(4)
170	5.907204(31)	13.540224(71)	7.882918(32)	90.6822(5)	630.469(4)
180	5.908265(30)	13.543921(70)	7.884161(31)	90.6926(5)	630.853(4)
190	5.909268(30)	13.547794(69)	7.885454(31)	90.7059(4)	631.242(4)
200	5.910191(30)	13.552146(68)	7.886962(31)	90.7186(4)	631.663(4)
210	5.911134(29)	13.556219(67)	7.888516(30)	90.7332(4)	632.076(3)
220	5.912138(29)	13.560753(68)	7.890124(30)	90.7478(4)	632.521(3)
230	5.913089(28)	13.565255(63)	7.891839(28)	90.7646(4)	632.968(3)
240	5.913915(27)	13.569775(64)	7.893645(29)	90.7813(4)	633.410(3)
250	5.914943(18)	13.574619(41)	7.895525(19)	90.7988(3)	633.895(2)
260	5.915851(29)	13.579506(68)	7.897442(30)	90.8170(4)	634.371(3)
270	5.916760(28)	13.584457(66)	7.899512(30)	90.8370(4)	634.863(3)
280	5.917592(28)	13.589806(68)	7.901624(30)	90.8570(4)	635.369(3)
290	5.918439(29)	13.595066(69)	7.903863(31)	90.8803(4)	635.882(4)
300	5.919204(13)	13.600639(30)	7.906222(14)	90.9069(2)	636.410(2)
310	5.919926(29)	13.606465(69)	7.908625(32)	90.9362(4)	636.949(4)
320	5.920608(29)	13.612309(69)	7.911148(32)	90.9682(4)	637.493(4)
330	5.921340(30)	13.618445(71)	7.913844(32)	91.0017(4)	638.070(4)
340	5.922013(28)	13.624563(71)	7.916586(31)	91.0369(4)	638.644(4)
350	5.922664(25)	13.631057(62)	7.919471(28)	91.0760(4)	639.243(3)
360	5.923344(24)	13.637672(61)	7.922373(27)	91.1137(4)	639.853(3)
370	5.924043(25)	13.644325(63)	7.925434(28)	91.1529(4)	640.480(3)

Tab. S11. Unit-cell parameters of starkeyite determined upon heating by means of neutron diffraction.

T (K)	a (Å)	b (Å)	c (Å)	β (°)	V (Å³)
290	5.917851(5)	13.595722(10)	7.906723(6)	90.8839(1)	636.079(1)
280	5.917056(5)	13.590921(10)	7.904620(6)	90.8631(1)	635.603(1)
270	5.916269(5)	13.586287(10)	7.902683(6)	90.8435(1)	635.150(1)
260	5.915483(6)	13.581878(11)	7.900797(7)	90.8246(1)	634.711(1)
250	5.914728(7)	13.577635(13)	7.899083(8)	90.8063(1)	634.297(1)
240	5.914018(7)	13.573483(14)	7.897485(8)	90.7887(1)	633.901(1)
230	5.913372(8)	13.569565(15)	7.896093(9)	90.7720(1)	633.540(1)
220	5.912880(9)	13.565886(16)	7.894901(10)	90.7556(1)	633.222(1)
210	5.912486(10)	13.562355(17)	7.893854(11)	90.7397(1)	632.934(1)
200	5.912235(11)	13.559006(19)	7.892967(12)	90.7240(1)	632.682(1)
190	5.912041(12)	13.555773(20)	7.892203(13)	90.7080(1)	632.451(1)
180	5.911792(13)	13.552778(21)	7.891454(13)	90.6942(2)	632.226(2)
170	5.911534(13)	13.549949(22)	7.890702(14)	90.6803(2)	632.008(2)
160	5.911105(14)	13.547318(23)	7.890007(15)	90.6683(2)	631.786(2)
150	5.910666(15)	13.544820(24)	7.889400(16)	90.6570(2)	631.575(2)
140	5.910107(16)	13.542600(24)	7.888897(16)	90.6460(2)	631.373(2)
130	5.909500(16)	13.540704(25)	7.888516(16)	90.6360(2)	631.190(2)
120	5.908970(17)	13.539263(25)	7.888254(17)	90.6261(2)	631.047(2)
110	5.908411(17)	13.538088(26)	7.888098(17)	90.6156(2)	630.921(2)
100	5.907823(18)	13.537119(27)	7.887991(18)	90.6055(2)	630.806(2)
90	5.907242(18)	13.536648(28)	7.887976(18)	90.5962(2)	630.722(2)
85	5.906991(21)	13.536616(31)	7.888037(21)	90.5903(3)	630.699(2)

Tab. S12. Unit-cell parameters of starkeyite determined upon cooling by means of synchrotron X-ray diffraction.

T (K)	a (Å)	b (Å)	c (Å)	β (°)	V (Å³)
95	5.908006(20)	13.539055(30)	7.888925(20)	90.5977(3)	630.991(2)
105	5.909049(20)	13.541116(29)	7.889716(20)	90.6047(3)	631.262(2)
115	5.910088(20)	13.542953(29)	7.890471(20)	90.6115(3)	631.518(2)
125	5.911077(20)	13.544956(29)	7.891350(20)	90.6198(3)	631.786(2)
135	5.912138(19)	13.546829(28)	7.892169(19)	90.6270(3)	632.052(2)
145	5.913096(19)	13.548752(28)	7.892999(19)	90.6354(3)	632.309(2)
155	5.913895(18)	13.550477(27)	7.893674(19)	90.6435(3)	632.528(2)
165	5.914763(18)	13.552992(26)	7.894600(18)	90.6532(3)	632.812(2)
175	5.915585(18)	13.555520(27)	7.895507(18)	90.6619(3)	633.089(2)
185	5.916554(17)	13.558354(25)	7.896475(17)	90.6714(3)	633.402(2)
195	5.917599(17)	13.561268(25)	7.897516(17)	90.6797(3)	633.732(2)
205	5.918747(18)	13.564190(24)	7.898544(17)	90.6870(3)	634.073(2)
215	5.919981(18)	13.567213(24)	7.899561(16)	90.6950(3)	634.427(2)
225	5.921139(18)	13.570449(22)	7.900586(15)	90.7051(3)	634.784(2)
235	5.921948(18)	13.573955(22)	7.901598(15)	90.7192(3)	635.114(2)
245	5.922408(17)	13.577493(21)	7.902609(14)	90.7372(3)	635.408(2)
255	5.922451(17)	13.581177(20)	7.903682(14)	90.7588(3)	635.668(2)
265	5.922214(15)	13.585045(19)	7.904895(13)	90.7832(3)	635.917(2)
275	5.921886(14)	13.589228(17)	7.906357(12)	90.8081(3)	636.192(2)
285	5.921662(13)	13.593801(16)	7.908017(11)	90.8361(3)	636.511(2)
295	5.921598(12)	13.598698(16)	7.909797(11)	90.8662(3)	636.872(2)

Tab. S13. Unit-cell parameters of starkeyite determined upon heating by means of synchrotron X-ray diffraction.

T (K)	a (Å)	b (Å)	c (Å)	β (°)	V (Å³)
300	11.930467(69)	5.175658(27)	12.198784(63)	117.5242(5)	667.995(4)
290	11.928022(66)	5.171587(25)	12.202119(61)	117.5304(5)	667.477(3)
280	11.925441(66)	5.167678(26)	12.205385(61)	117.5375(4)	666.964(3)
270	11.923236(65)	5.163833(25)	12.208477(59)	117.5444(5)	666.471(3)
260	11.920793(65(	5.160226(26)	12.211470(60)	117.5503(5)	665.996(3)
250	11.918675(66)	5.156590(27)	12.214349(61)	117.5566(5)	665.527(3)
240	11.916311(62)	5.153234(25)	12.216990(58)	117.5626(5)	665.071(3)
230	11.914182(64(	5.149893(26)	12.219787(60)	117.5680(5)	664.640(3)
220	11.912086(64)	5.146690(26)	12.222234(59)	117.5735(5)	664.209(3)
210	11.910090(64)	5.143570(26)	12.224602(59)	117.5781(5)	663.796(3)
200	11.908200(66)	5.140639(27)	12.226848(61)	117.5823(5)	663.409(3)
190	11.906403(67)	5.137840(28)	12.229099(63)	117.5867(5)	663.043(4)
180	11.904656(69)	5.135132(29)	12.231191(64)	117.5922(5)	662.676(4)
170	11.903090(65)	5.132544(27)	12.233166(60)	117.5961(5)	662.339(3)
160	11.901461(68)	5.130124(28)	12.235098(62)	117.6012(5)	662.009(4)
150	11.900008(70)	5.127805(29)	12.236980(65)	117.6051(5)	661.708(4)
140	11.898742(70)	5.125609(29)	12.238708(65)	117.6084(5)	661.428(4)
130	11.897487(70)	5.123613(30)	12.240438(67)	117.6133(5)	661.164(4)

120	11.896453(70)	5.121605(30)	12.242270(66)	117.6162(5)	660.929(4)
110	11.895370(72)	5.119900(31)	12.243909(66)	117.6191(5)	660.720(4)
100	11.894433(70)	5.118310(30)	12.245339(65)	117.6218(5)	660.524(4)
90	11.893562(72)	5.116803(31)	12.246789(68)	117.6230(5)	660.351(4)
80	11.892824(72)	5.115515(31)	12.248235(68)	117.6252(5)	660.209(4)
70	11.892240(72)	5.114170(31)	12.249914(68)	117.6276(5)	660.079(4)
60	11.891788(74)	5.113270(32)	12.251106(69)	117.6284(5)	659.997(4)
50	11.891653(74)	5.112563(32)	12.252176(68)	117.6310(5)	659.940(4)
40	11.891580(73)	5.112069(31)	12.252991(69)	117.6316(5)	659.913(4)
30	11.891437(75)	5.111635(32)	12.253820(71)	117.6320(5)	659.891(4)
20	11.891486(76)	5.111429(33)	12.254331(71)	117.6322(5)	659.893(4)
10	11.891494(66)	5.111388(28)	12.254453(62)	117.6331(5)	659.890(4)

Tab. S14. Unit-cell parameters of cranswickite determined upon cooling by means of neutron diffraction.

T (K)	a (Å)	b (Å)	c (Å)	β (°)	V (Å³)
300	11.930315(81)	5.175523(32)	12.198657(79)	117.5244(6)	667.961(4)
310	11.933108(83)	5.179775(32)	12.194979(80)	117.5178(6)	668.504(4)
320	11.935539(82)	5.184170(32)	12.191400(81)	117.5090(6)	669.065(4)
330	11.938397(85)	5.188869(34)	12.187214(88)	117.5020(6)	669.644(5)
340	11.941144(88)	5.193808(35)	12.182615(92)	117.4931(6)	670.237(5)

Tab. S15. Unit-cell parameters of cranswickite determined upon heating by means of neutron diffraction.

T (K)		RT				10		
Mg	x	0.0	U_{11}	0.0156(18)	x	0.0	U_{11}	0.0135(12)
	y	0.0	U_{22}	0.0083(14)	y	0.0	U_{22}	0.0082(11)
	z	0.5	U_{33}	0.0111(14)	z	0.5	U_{33}	0.0098(11)
	U_{eq*}	0.01241	U_{12}	-0.0013(12)	U_{eq}	0.01136	U_{12}	-0.0005(9)
			U_{13}	0.0043(14)			U_{13}	0.0033(10)
			U_{23}	-0.0016(11)			U_{23}	0.0017(9)
S	x	0.0	U_{11}	0.0121(31)	x	0.0	U_{11}	0.0119(21)
	y	0.3110(9)	U_{22}	0.0093(24)	y	0.3179(9)	U_{22}	0.0147(22)
	z	0.75	U_{33}	0.0136(27)	z	0.75	U_{33}	0.0071(21)
	U_{eq}	0.00968	U_{12}	0.0	U_{eq}	0.01132	U_{12}	0.0
			U_{13}	0.0110(24)			U_{13}	0.0042(19)
			U_{23}	0.0			U_{23}	0.0
O1	x	0.11314(19)	U_{11}	0.0133(13)	x	0.11399(15)	U_{11}	0.0133(8)
	y	0.52090(35)	U_{22}	0.0204(13)	y	0.51325(27)	U_{22}	0.0080(7)
	z	0.29036(18)	U_{33}	0.0183(12)	z	0.29072(14)	U_{33}	0.0102(8)
	U_{eq}	0.01916	U_{12}	0.0037(9)	U_{eq}	0.01175	U_{12}	0.0008(6)
			U_{13}	0.0026(10)			U_{13}	0.0023(7)
			U_{23}	-0.0018(9)			U_{23}	0.0002(6)
O2	x	0.98626(22)	U_{11}	0.0379(16)	x	0.98719(14)	U_{11}	0.0103(8)
	y	0.1512(4)	U_{22}	0.0265(14)	y	0.15443(27)	U_{22}	0.0132(8)
	z	0.64692(18)	U_{33}	0.0165(13)	z	0.64676(14)	U_{33}	0.0166(9)
	U_{eq}	0.02691	U_{12}	0.0043(11)	U_{eq}	0.01368	U_{12}	-0.0007(6)
			U_{13}	0.0127(13)			U_{13}	0.0055(7)
			U_{23}	-0.0070(9)			U_{23}	-0.0012(6)

Site		RT pos		RT ADP		10 K pos		10 K ADP
O1w	x	0.87475(19)	U_{11}	0.0248(15)	x	0.87479(14)	U_{11}	0.0135(8)
	y	0.7172(4)	U_{22}	0.0123(11)	y	0.71879(32)	U_{22}	0.0137(8)
	z	0.49280(21)	U_{33}	0.0203(12)	z	0.49373(14)	U_{33}	0.0106(8)
	U_{eq}	0.01863	U_{12}	-0.0053(10)	U_{eq}	0.01242	U_{12}	-0.0027(7)
			U_{13}	0.0117(11)			U_{13}	0.0060(7)
			U_{23}	-0.0018(10)			U_{23}	-0.0033(7)
O2w	x	0.84963(21)	U_{11}	0.0094(11)	x	0.84830(16)	U_{11}	0.0085(8)
	y	0.2354(4)	U_{22}	0.0203(14)	y	0.23505(30)	U_{22}	0.0164(8)
	z	0.37836(20)	U_{33}	0.0175(12)	z	0.37885(14)	U_{33}	0.0132(9)
	U_{eq}	0.01619	U_{12}	-0.0012(9)	U_{eq}	0.01166	U_{12}	-0.0023(6)
			U_{13}	0.0051(9)			U_{13}	0.0077(7)
			U_{23}	0.0006(10)			U_{23}	-0.0003(7)
D1a	x	0.86747(24)	U_{11}	0.0425(17)	x	0.86730(16)	U_{11}	0.0298(11)
	y	0.6778(4)	U_{22}	0.0429(16)	y	0.67974(34)	U_{22}	0.0319(10)
	z	0.56636(25)	U_{33}	0.0411(14)	z	0.56771(16)	U_{33}	0.0274(10)
	U_{eq}	0.03908	U_{12}	-0.0079(10)	U_{eq}	0.02835	U_{12}	-0.0045(7)
			U_{13}	0.0271(13)			U_{13}	0.0167(9)
			U_{23}	0.0024(11)			U_{23}	0.0046(8)
D1b	x	0.86493(23)	U_{11}	0.0433(17)	x	0.86389(15)	U_{11}	0.0316(10)
	y	0.5545(4)	U_{22}	0.0269(13)	y	0.54932(31)	U_{22}	0.0142(9)
	z	0.45277(21)	U_{33}	0.0391(15)	z	0.45353(15)	U_{33}	0.0301(10)
	U_{eq}	0.03708	U_{12}	-0.0085(11)	U_{eq}	0.02641	U_{12}	-0.0016(7)
			U_{13}	0.0173(14)			U_{13}	0.0115(8)
			U_{23}	-0.0086(11)			U_{23}	-0.0021(7)
D2a	x	0.76387(24)	U_{11}	0.0308(13)	x	0.76291(18)	U_{11}	0.0216(9)
	y	0.1654(4)	U_{22}	0.0312(14)	y	0.16156(31)	U_{22}	0.0276(9)
	z	0.34586(22)	U_{33}	0.0341(13)	z	0.34691(16)	U_{33}	0.0274(10)
	U_{eq}	0.03257	U_{12}	0.0021(10)	U_{eq}	0.02571	U_{12}	-0.0020(8)
			U_{13}	0.0136(11)			U_{13}	-0.0019(7)
			U_{23}	-0.0001(10)			U_{23}	0.0108(8)
D2b	x	0.85937(21)	U_{11}	0.0411(17)	x	0.85946(14)	U_{11}	0.0249(9)
	y	0.3053(4)	U_{22}	0.0334(13)	y	0.30633(32)	U_{22}	0.0301(9)
	z	0.30980(19)	U_{33}	0.0269(14)	z	0.31092(14)	U_{33}	0.0210(10)
	U_{eq}	0.03316	U_{12}	0.0020(10)	U_{eq}	0.02501	U_{12}	0.0025(7)
			U_{13}	0.0173(14)			U_{13}	0.0114(9)
			U_{23}	0.0044(10)			U_{23}	0.0030(7)

Tab. S16. Positional parameters and anisotropic displacement parameters of the atom sites in cranswickite-type $MgSO_4 \cdot 4D_2O$ at room-temperature and 10 K. *Value calculated from anisotropic displacement parameters, however, GSAS does not compute the e.s.d for U_{eq}.

Phase	Starkeyite	Starkeyite	Cranswickite	Cranswickite
Chemical Formula	$MgSO_4 \cdot 4D_2O$	$MgSO_4 \cdot 4D_2O$	$MgSO_4 \cdot 4D_2O$	$MgSO_4 \cdot 4D_2O$
Space group	$P2_1/n$	$P2_1/n$	$C2/c$	$C2/c$
Temperature	300 K	10 K	Room-temperature	10 K
a, b, c, β	5.919182 (32) Å, 13.600510 (71) Å, 7.906208 (41) Å, 90.9070(3) °	5.89700(5) Å, 13.50755(11) Å, 7.87430(7) Å, 90.5868(5)°	11.92820(11) Å, 5.17176(5) Å, 12.20194(11) Å, 117.5305(4) °	11.89132(10) Å, 5.11135(5) Å, 12.25440(10) Å, 117.6339(4) °
V	636.401 (9)	627.187(13)	667.499(15)	659.867(13)
Z	4	4	4	4
Refinement				
R-factors goodness of fit	Rp = 0.0319, wRp = 0.0233, χ^2 = 2.249	Rp = 0.0449, wRp = 0.0337, χ^2 = 8.712	Rp = 0.0466, wRp = 0.0341, χ^2 = 2.494	Rp = 0.0398, wRp = 0.0350, χ^2 = 7.905
Number of refined parameters	176	184	121	104

Tab. S17. Selected details of the crystal structure refinements.

T_{ref} (K)	α_{11} (K^{-1})*	α_{22} (K^{-1})*	α_{33} (K^{-1})*	α_{13} (K^{-1})*
15	0.8(3.6)	0.8(2.6)	-1.0(2.3)	0.5(2.2)
25	-0.2(3.5)	4.0(3.0)	-4.2(2.3)	-0.8(2.2)
35	1.6(3.6)	8.0(3.0)	-6.8(2.4)	-1.7(2.1)
45	1.2(3.2)	9.7(2.8)	-6.6(2.3)	-1.4(2.1)
55	3.5(3.5)	13.8(2.8)	-8.7(2.4)	-0.3(2.2)
65	4.5(3.5)	17.6(2.8)	-9.7(2.3)	-2.8(2.2)
75	7.1(3.5)	26.3(2.8)	-13.7(2.3)	-2.8(2.2)
85	8.2(3.2)	25.2(2.5)	-11.8(2.3)	-2.8(2.2)
95	8.4(3.1)	29.5(2.5)	-11.8(2.3)	-4.0(2.2)
105	10.3(3.6)	31.1(2.6)	-11.7(2.4)	-2.8(2.2)
115	11.8(3.5)	33.3(2.3)	-13.4(2.3)	-3.4(2.1)
125	11.3(3.2)	39.2(2.5)	-15.0(2.4)	-3.6(2.1)
135	15.0(3.1)	39.0(2.5)	-14.1(2.3)	-2.2(2.2)
145	13.6(3.2)	42.9(2.3)	-14.1(2.3)	-3.6(2.2)
155	15.8(3.2)	45.2(2.3)	-15.4(2.3)	-3.8(2.2)
165	18.3(3.1)	47.2(2.3)	-15.8(2.2)	-3.3(2.1)
175	16.7(3.2)	50.4(2.3)	-16.1(2.2)	-4.3(2.2)
185	19.7(3.2)	52.8(2.5)	-17.1(2.3)	-3.5(2.2)
195	19.1(3.3)	54.5(2.5)	-18.4(2.2)	-4.9(2.3)
205	19.7(3.2)	57.0(2.4)	-18.4(2.0)	-5.3(2.2)
215	20.9(3.1)	60.7(2.0)	-19.4(1.9)	-5.4(2.3)
225	22.6(2.9)	62.2(2.0)	-20.0(2.0)	-5.0(1.9)
235	22.8(2.9)	64.9(2.0)	-22.9(1.9)	-5.9(1.6)
245	25.3(3.1)	65.1(2.3)	-21.6(2.0)	-5.6(1.9)
255	23.5(3.1)	70.5(2.1)	-23.6(2.0)	-5.3(2.1)
265	25.9(3.1)	69.9(1.8)	-24.5(1.9)	-6.6(2.2)
275	24.8(3.2)	74.5(2.0)	-25.3(2.0)	-5.4(2.1)
285	28.1(3.1)	75.7(2.0)	-26.8(2.0)	-6.4(2.2)
295	26.1(3.1)	78.8(2.3)	-27.3(2.2)	-7.1(2.1)
305	30.6(3.4)	84.3(2.0)	-30.9(2.2)	-7.9(2.1)
315	28.3(3.3)	84.3(1.8)	-30.5(2.3)	-6.8(2.2)
325	31.1(3.1)	90.4(2.0)	-35.0(2.3)	-8.2(2.1)
335	27.8(3.8)	91.3(2.4)	-36.2(2.8)	-7.8(2.4)

Tab. S18. Coefficients of the thermal expansion tensor of cranswickite. T_{ref} = $(T_{start} + T_{end})/2$ (e.g., Tref = 335 K corresponds to the thermal expansion tensor derived from the unit-cell parameters measured at 330 K and 340 K). * Values reported in these columns were multiplied by 10^6 for the sake of brevity (e.g. a_{11} at 15 K is 0.8 x 10^{-6} K^{-1}).

T_{ref} (K)	α_1 (K^{-1})*	α_2 (K^{-1})*	α_3 (K^{-1})*	α_V (K^{-1})*
15	-1.1(2.1)	0.8(3.3)	9.0(4.8)	0.60(6.19)
25	-4.3(2.7)	4.0(3.0)	1.0(3.3)	-0.40(5.21)
35	-7.1(2.7)	8.5(3.0)	1.9(3.3)	3.30(5.21)
45	-6.9(2.4)	9.7(2.7)	1.4(3.0)	4.20(4.70)
55	-8.7(2.4)	13.8(2.7)	3.5(3.3)	8.60(4.89)
65	-10.3(2.4)	17.6(2.7)	5.1(3.3)	12.4(4.89)
75	-14.1(2.4)	26.3(2.7)	7.5(3.3)	19.7(4.89_
85	-12.2(2.4)	25.2(2.4)	8.6(3.0)	21.6(4.53)
95	-12.6(2.4)	29.5(2.4)	9.2(3.0)	26.1(4.53)
105	-12.0(2.7)	31.1(2.7)	10.7(3.3)	29.8(5.05)
115	-13.8(2.4)	33.3(2.4)	12.2(3.3)	31.7(4.73)
125	-15.5(2.7)	39.2(2.4)	11.8(3.0)	35.5(4.70)
135	-14.3(2.4)	39.0(2.4)	15.2(3.0)	39.9(4.53_
145	-14.6(2.4)	42.9(2.4)	14.1(3.0)	42.5(4.53)
155	-15.8(2.4)	45.2(2.4)	16.2(3.0)	45.6(4.53)
165	-16.1(2.4)	47.2(2.4)	18.6(3.0)	49.7(4.53)
175	-16.7(2.4)	50.4(2.4)	17.3(3.0)	51.0(4.53)
185	-17.4(2.4)	52.8(2.4)	10.0(3.0)	55.4(4.53)
195	-19.0(2.4)	54.5(2.4)	19.7(3.0)	55.2(4.53)
205	-19.1(2.1)	57.0(2.4)	20.4(3.0)	58.3(4.38)
215	-20.1(2.1)	60.7(2.1)	21.7(2.7)	62.3(4.01)
225	-20.6(2.1)	62.2(2.1)	23.2(2.7)	64.8(4.01)
235	-23.6(2.1)	64.9(2.1)	23.5(3.0)	64.8(4.22)
245	-22.3(2.1)	65.1(2.4)	26.0(3.0)	68.8(4.38)
255	-24.2(2.1)	70.5(2.1)	24.1(3.0)	70.4(4.22)
265	-25.4(2.1)	69.9(1.8)	26.7(2.7)	71.2(3.87)
275	-25.9(2.1)	74.5(2.1)	25.4(3.0)	74.0(4.22)
285	-27.5(2.1)	75.7(2.1)	28.9(3.0)	77.1(4.22)
295	-28.2(2.4)	78.8(2.4)	27.1(3.0)	77.7(4.53)
305	-31.9(2.4	84.3(2.1)	31.6(3.3)	84.0(4.59)
315	-31.2(2.4)	84.3(1.8)	39.1(3.0)	82.2(4.24)
325	-36(2.4)	90.4(2.1)	32.1(3.0)	86.5(4.38)
335	-37.1(3.0)	91.3(2.4)	38.7(3.6)	82.9(5.26)

Tab. S19. Principal axes of the thermal expansion tensor of cranswickite as presented in Fig. 1b. T_{ref} = (T_{start} + T_{end})/2 (e.g., Tref = 335 K corresponds to the thermal expansion tensor derived from the unit-cell parameters measured at 330 K and 340 K). * Values reported in these columns were multiplied by 10^6 for the sake of brevity (e.g. a_1 at 15 K is -1.1 x 10^{-6} K^{-1}).

T_{ref} (K)	α_a (K^{-1})*	α_b (K^{-1})*	α_c (K^{-1})*
15	-0.07	0.80	-1.00
25	-0.41	4.03	-4.17
35	1.20	8.49	-6.77
45	0.61	9.66	-6.65
55	1.14	13.83	-8.73
65	3.80	17.60	-9.73
75	4.91	26.30	-13.71
85	6.21	25.18	-11.81
95	7.32	29.45	-11.84
105	7.88	31.06	-11.68
115	9.10	33.30	-13.39
125	8.69	39.21	-14.96
135	10.55	38.96	-14.13
145	10.64	42.84	-14.12
155	12.21	45.22	-15.38
165	13.69	47.17	-15.79
175	13.16	50.42	-16.14
185	14.67	52.73	-17.10
195	15.09	54.48	-18.41
205	15.87	57.02	-18.37
215	16.76	60.66	-19.37
225	17.60	62.23	-20.02
235	17.87	64.88	-22.89
245	19.84	65.12	-21.62
255	17.77	70.51	-23.57
265	20.49	69.90	-24.51
275	18.49	74.46	-25.33
285	21.64	75.64	-26.76
295	20.50	78.72	-27.33
305	23.41	82.16	-30.15
315	20.37	84.85	-29.35
325	23.95	90.64	-34.34
335	23.01	95.18	-37.74

Tab. S20.Thermal expansion along the crystallographic axes of cranswickite. T_{ref} = (T_{start} + T_{end})/2 ((e.g., Tref = 295 K corresponds to the thermal expansion tensor derived from the unit-cell parameters measured at 290K and 300 K). * Values reported in these columns were multiplied by 10^6 for the sake of brevity (e.g. α_a at 15 K is -0.07 x 10^{-6} K^{-1}).

T_{ref} (K)	α_{11} (K^{-1})*	α_{22} (K^{-1})*	α_{33} (K^{-1})*	α_{13} (K^{-1})*
15	0.0(2.0)	1.1(2.3)	-1.0(1.8)	0.5(1.9)
25	4.8(2.3)	0.0(2.5)	2.2(2.1)	-0.5(2.1)
35	3.3(2.3)	4.2(2.8)	1.0(2.3)	-0.8(2.1)
45	6.4(2.6)	5.4(2.5)	0.5(2.3)	-2.9(2.3)
55	9.4(2.8)	8.1(2.8)	2.7(2.0)	-4.3(2.3)
65	9.8(2.5)	10.9(2.5)	3.6(2.0)	-4.8(2.1)
75	10.5(2.5)	14.0(2.8)	3.9(2.3)	-5.2(2.1)
85	10.8(2.3)	17.2(2.8)	6.5(2.0)	-4.2(2.1)
95	11.4(2.5)	17.4(2.5)	6.5(2.0)	-8.2(2.0)
105	13.4(2.8)	19.2(2.5)	8.7(2.0)	-4.5(2.1)
115	14.4(2.6)	19.5(2.8)	9.3(2.0)	-7.9(2.3)
125	14.7(2.5)	23.2(2.5)	9.5(2.0)	-7.5(2.1)
135	15.5(2.3)	23.1(2.3)	13.0(1.8)	-9.5(2.0)
145	15.5(2.1)	25.7(2.1)	12.4(1.3)	-7.3(1.6)
155	15.8(1.9)	25.1(2.1)	13.6(1.3)	-11.4(1.6)
165	16.3(2.3)	24.9(2.5)	14.7(1.8)	-8.2(2.0)
175	14.7(2.5)	30.6(2.5)	17.2(1.5)	-9.1(2.0)
185	17.1(2.0)	31.0(2.5)	16.5(2.0)	-12.1(1.7)
195	13.6(2.3)	27.5(2.3)	18.4(1.8)	-12.1(1.7)
205	16.4(2.0)	33.5(2.3)	19.0(1.5)	-11.9(1.7)
215	16.9(2.0)	32.0(2.0)	20.4(1.8)	-13.1(1.4)
225	15.0(2.0)	33.6(2.3)	22.6(1.5)	-14.3(1.4)
235	16.8(2.1)	34.6(2.3)	21.9(1.5)	-14.6(1.4)
245	14.2(1.8)	34.8(1.9)	24.2(1.3)	-15.9(1.3)
255	13.7(1.8)	36.3(1.5)	25.0(1.3)	-17.0(1.3)
265	15.2(2.3)	37.4(2.0)	26.5(1.5)	-16.5(1.4)
275	13.4(2.0)	38.8(2.0)	26.9(1.5)	-18.2(1.4)
285	15.1(2.0)	38.4(2.0)	28.3(1.8)	-19.9(1.4)
295	12.7(1.8)	40.5(1.8)	28.9(1.6)	-21.2(1.3)
305	11.6(1.6)	42.7(1.9)	30.6(1.3)	-25.1(1.3)
315	10.6(2.0)	43.0(2.0)	31.9(1.8)	-27.8(1.4)
325	11.4(2.1)	45.1(2.0)	34.1(1.8)	-29.1(1.4)
335	10.3(2.3)	44.9(2.3)	34.7(1.8)	-30.5(1.4)
345	9.8(1.8)	47.7(2.0)	36.4(1.8)	-33.9(1.4)
355	10.2(1.8)	48.5(1.8)	36.7(1.5)	-32.7(1.4)
365	10.5(1.8)	48.8(1.8)	38.7(1.5)	-34.0(1.4)

Tab. S21. Coefficients of the thermal expansion tensor of starkeyite. T_{ref} = (T_{start} + T_{end})/2 (e.g., Tref = 335 K corresponds to the thermal expansion tensor derived from the unit-cell parameters measured at 330 K and 340 K). * Values reported in these columns were multiplied by 10^6 for the sake of brevity (e.g. α_{11} at 15 K is 0.0 x 10^{-6} K^{-1}).

T_{ref} (K)	α_1 (K^{-1})*	α_2 (K^{-1})*	α_3 (K^{-1})*	α_V (K^{-1})*
15	-1.2(2.1)	0.3(2.1)	1.1(2.4)	0.2(3.8)
25	0.0(2.4)	2.1(2.1)	4.9(2.4)	7.0(4.0)
35	0.7(2.4)	3.6(2.4)	4.2(2.7)	8.5(4.3)
45	-0.7(2.4)	5.4(2.4)	7.6(2.7)	12.3(4.5)
55	0.6(2.4)	8.1(2.7)	11.5(3.0)	20.2(4.7)
65	1.0(2.4)	10.9(2.4)	12.5(2.7)	24.4(4.3)
75	1.0(2.7)	13.3(2.7)	14.0(2.7)	28.3(4.7)
85	3.9(2.4)	13.4(2.7)	17.2(2.7)	34.5(4.5)
95	3.0(2.4)	17.5(1.8)	17.5(1.8)	35.3(3.5)
105	6.0(2.7)	16.1(2.7)	19.2(2.4)	41.3(4.5)
115	3.6(2.7)	19.5(2.7)	20.2(2.7)	43.3(4.7)
125	4.2(2.7)	20.0(2.7)	23.2(2.4)	47.4(4.5)
135	4.6(2.7)	23.1(2.1)	23.8(2.1)	51.5(3.5)
145	6.4(1.8)	21.4(2.1)	25.7(2.1)	53.6(3.5)
155	3.3(2.1)	25.1(2.1)	26.1(2.1)	54.5(3.6)
165	7.2(2.4)	23.7(2.4)	24.9(2.4)	55.8(4.2)
175	6.8(2.4)	25.1(2.4)	30.6(2.4)	62.5(4.2)
185	4.7(2.1)	29.0(2.1)	31.0(2.4)	64.7(3.8)
195	3.7(2.4)	27.9(1.5)	27.9(1.5)	59.5(3.2)
205	5.7(2.1)	29.7(2.1)	33.5(2.4)	68.9(3.8)
215	5.5(2.1)	31.9(1.5)	31.9(1.5)	69.3(3.0)
225	4.0(1.8)	33.6(1.5)	33.6(1.5)	71.2(2.8)
235	4.5(2.1)	34.4(1.5)	34.4(1.5)	73.3(3.0)
245	2.5(1.8)	35.4(1.2)	35.4(1.2)	73.3(2.5)
255	1.4(1.8)	36.8(1.2)	36.8(1.2)	75.0(2.5)
265	3.4(2.1)	37.8(1.5)	37.8(1.5)	79.0(3.0)
275	0.7(2.1)	39.2(1.5)	39.2(1.5)	79.1(3.0)
285	0.7(2.1)	38.4(2.1)	42.6(1.8)	81.7(3.5)
295	-1.9(1.8)	40.5(1.8)	43.5(1.8)	82.1(3.1)
305	-5.7(1.8)	42.7(1.8)	47.9(1.5)	84.9(3.0)
315	-8.5(2.1)	43.0(2.1)	51.0(1.8)	85.5(3.5)
325	-8.5(2.1)	45.1(2.1)	53.9(1.8)	90.5(3.5)
335	-10.4(2.1)	44.9(2.4)	55.3(1.8)	89.8(3.7)
345	-13.3(1.8)	47.7(2.1)	59.5(1.8)	93.9(3.3)
355	-11.8(1.8)	48.5(1.8)	58.7(1.8)	95.4(3.1)
365	-12.2(1.8)	48.8(1.8)	61.3(1.8)	97.9(3.1)

Tab. S22. Principal axes of the thermal expansion tensor of starkeyite as presented in Fig. 1e. T_{ref} = (T_{start} + T_{end})/2 (e.g., Tref = 335 K corresponds to the thermal expansion tensor derived from the unit-cell parameters measured at 330 K and 340 K). * Values reported in these columns were multiplied by 10^6 for the sake of brevity (e.g. α_1 at 15 K is -1.2 x 10^{-6} K^{-1}).

T_{ref} (K)	α_a (K^{-1})*	α_b (K^{-1})*	α_c (K^{-1})*
15	1.00	-0.05	0.33
25	1.80	2.42	-0.56
35	5.53	3.07	0.99
45	7.44	4.63	2.53
55	8.14	9.99	0.67
65	9.41	10.25	4.76
75	10.87	13.77	5.36
85	11.87	15.02	5.35
95	11.52	19.90	6.36
105	14.01	18.36	8.37
115	14.25	21.12	9.20
125	13.84	22.24	10.80
135	14.74	24.41	12.68
145	17.46	22.45	11.68
155	15.87	26.54	14.58
165	13.71	28.32	14.70
175	17.96	27.30	15.77
185	16.98	28.60	16.40
195	15.62	32.12	19.12
205	15.96	30.05	19.70
215	16.98	33.45	20.38
225	16.09	33.20	21.74
235	13.97	33.32	22.88
245	17.38	35.70	23.82
255	15.35	36.00	24.28
265	15.37	36.46	26.21
275	14.06	39.38	26.74
285	14.31	38.71	28.34
295	12.93	40.99	29.85
305	12.20	42.84	30.39
315	11.52	42.95	31.90
325	12.36	45.08	34.08
335	11.37	44.92	34.65
345	10.99	47.66	36.44
355	11.48	48.53	36.64
365	11.80	48.78	38.64

Tab. S23. Thermal expansion along the crystallographic axes of starkeyite. T_{ref} = (T_{start} + T_{end})/2 (e.g., Tref = 365 K corresponds to the thermal expansion tensor derived from the unit-cell parameters measured at 360 K and 370 K). * Values reported in these columns were multiplied by 10^6 for the sake of brevity (e.g. α_a at 15 K is 1.00 x 10^{-6} K^{-1}).

Figures
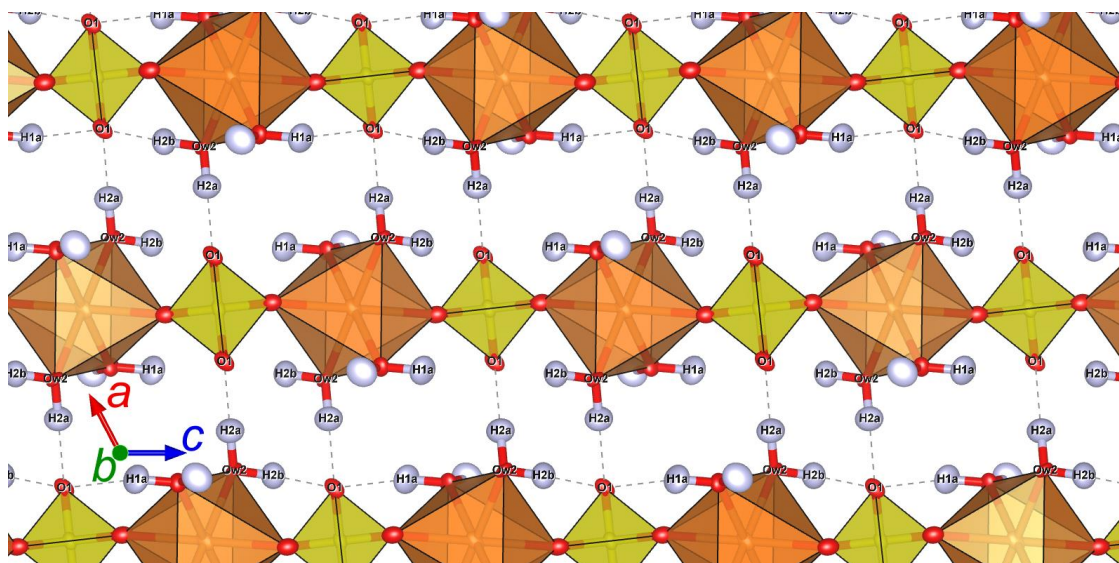
Fig. S1. View on the crystal structure of cranswicktie // *b*. The chains running parallel the c-axis are interconnected by the H2a···O1 hydrogen bond. Additionally, the O1 atom accepts hydrogen bonds from the H2b and H1a atoms, located within the same chain.
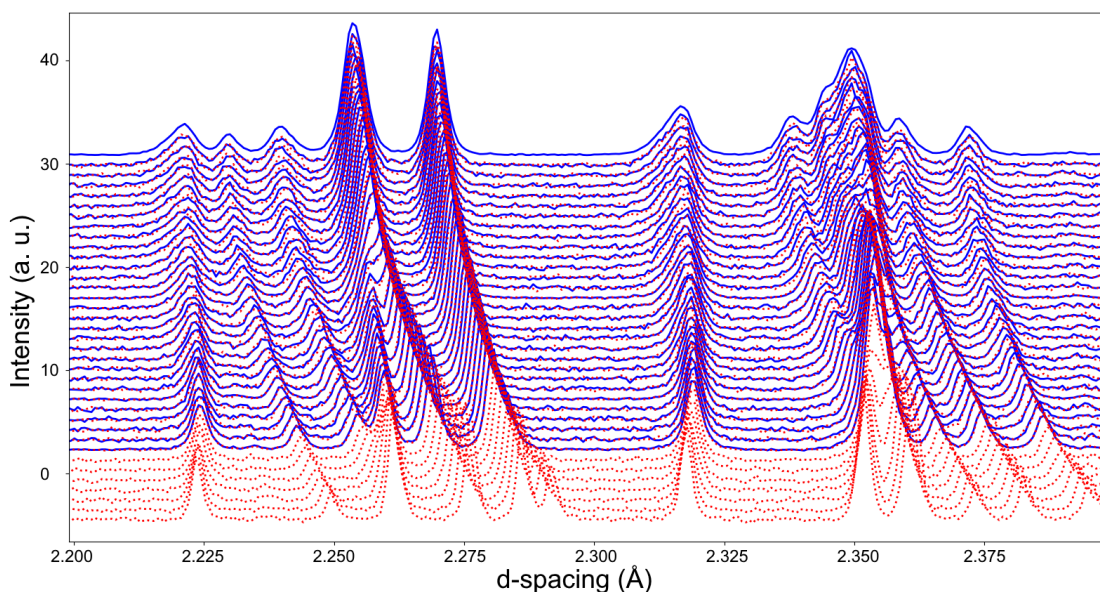
Fig. S2. Neutron diffraction pattern collected upon cooling (blue solid line) and heating (red dotted line) coincide perfectly for starkeyite. Lowermost pattern corresponds to 370 K whereas the uppermost was collected at 10 K and the pattern interval of 10 K. Note that the shoulder emerging at the 212 Bragg peak located between 2.300 and 2.325 Å again merges with the main peak upon heating.
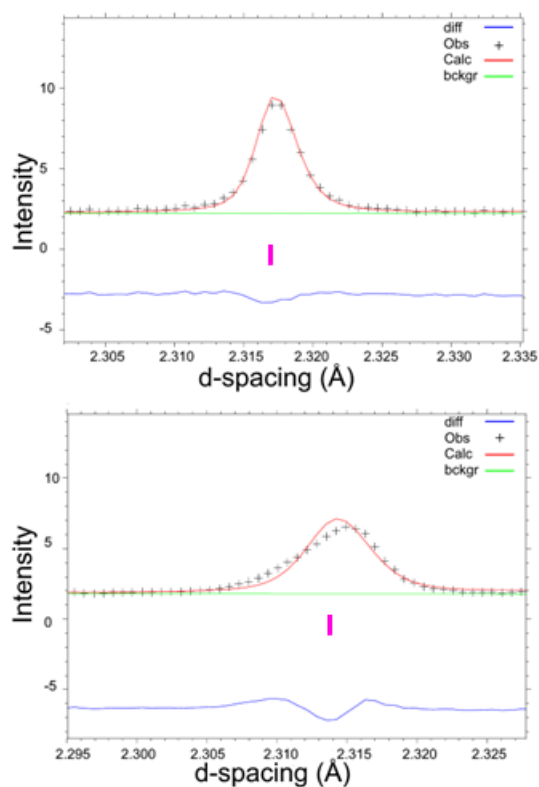
Fig. S3. Rietveld fit of the 212 peak (marked by magenta tick mark) at 300 K (top) and 10 K (bottom). Note the shoulder that is not accounted for by the established structural model of starkeyite (Baur, 1964).
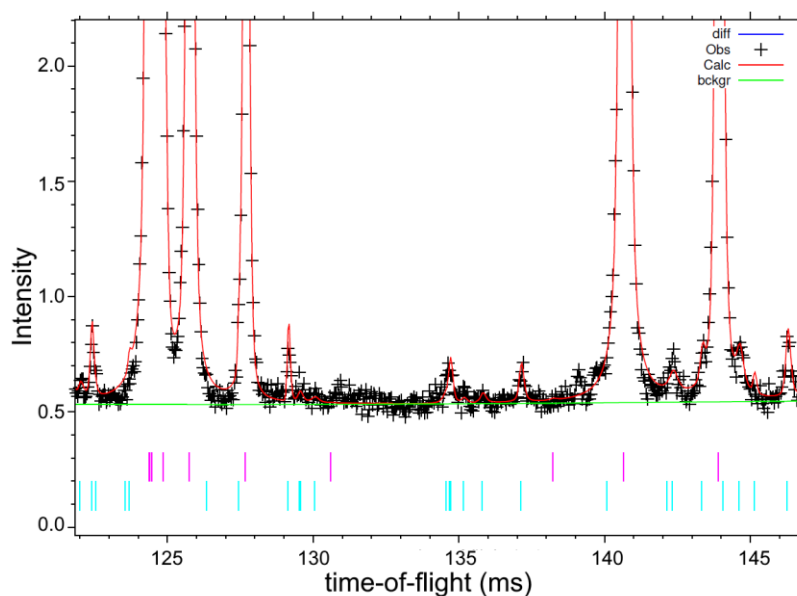
Fig. S4. Four hour soak revealed the presence of a small amount of pentahydrite ($MgSO_4 \cdot 5D_2O$; cyan tick marks) in addition to cranswickite-type $MgSO_4 \cdot 4D_2O$ (magenta tick marks), which represents the vast majority of the sample.
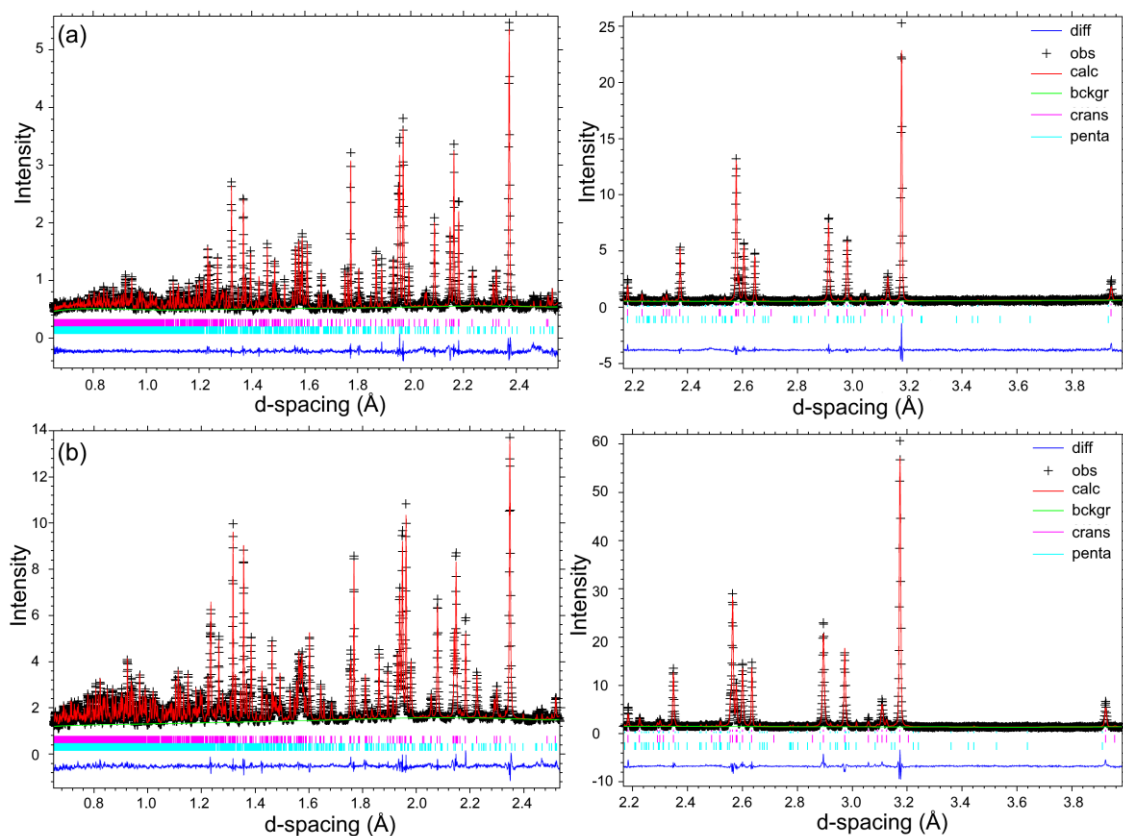
Fig. S5. Neutron diffraction patterns acquired at (a) RT and (b) 10 K in the backscattering detector bank collected in the 30 – 130 (left) and 100 – 200 ms (right) TOF window. The observed data are plotted as crosses, the red line represents the fitted model, and the blue line the difference profile. The tick marks corresponding to each of the Bragg peaks of cranswickite ($MgSO_4 \cdot 4D_2O$) and pentahydrite ($MgSO_4 \cdot 5D_2O$) are displayed in magenta and cyan, respectively.
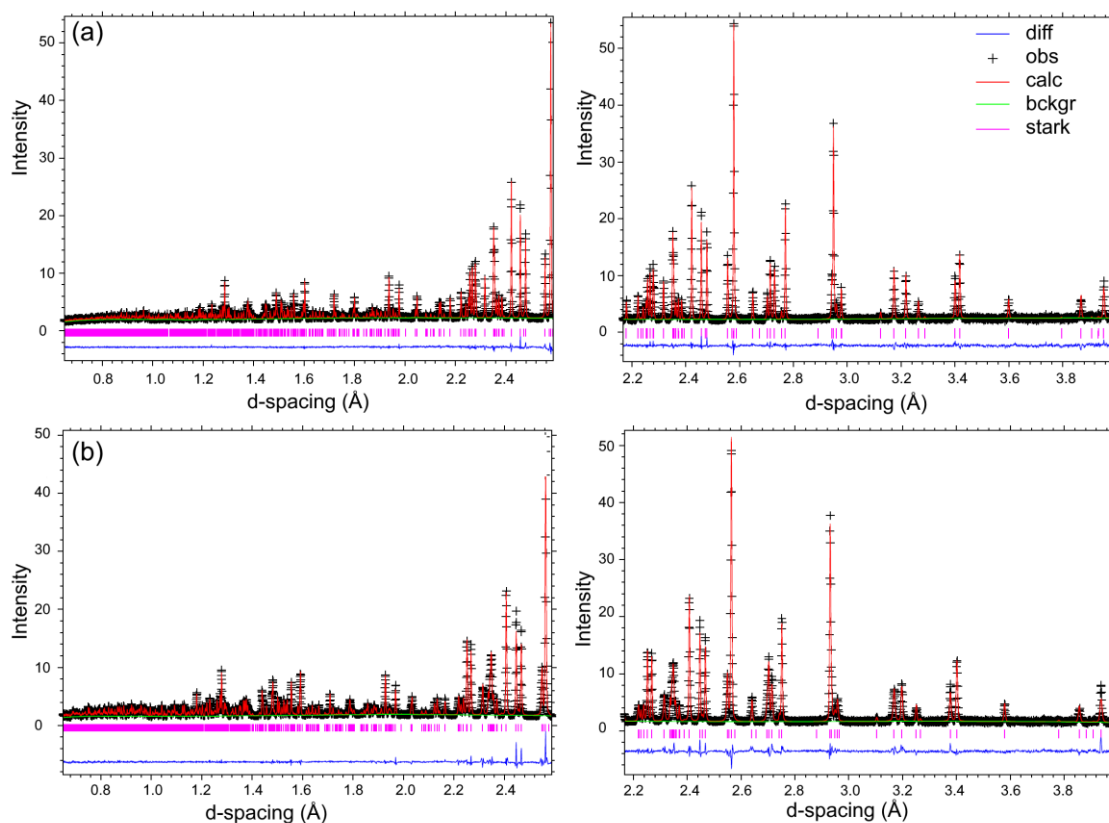
Fig. S6. Neutron diffraction patterns acquired at (a) 300 K and (b) 10 K in the backscattering detector bank collected in the 30 – 130 (left) and 100 – 200 ms (right) TOF window. The observed data are plotted as crosses, the red line represents the fitted model, and the blue line the difference profile. The tick marks corresponding to the Bragg peaks of starkeyite ($MgSO_4 \cdot 4D_2O$) are displayed in magenta.
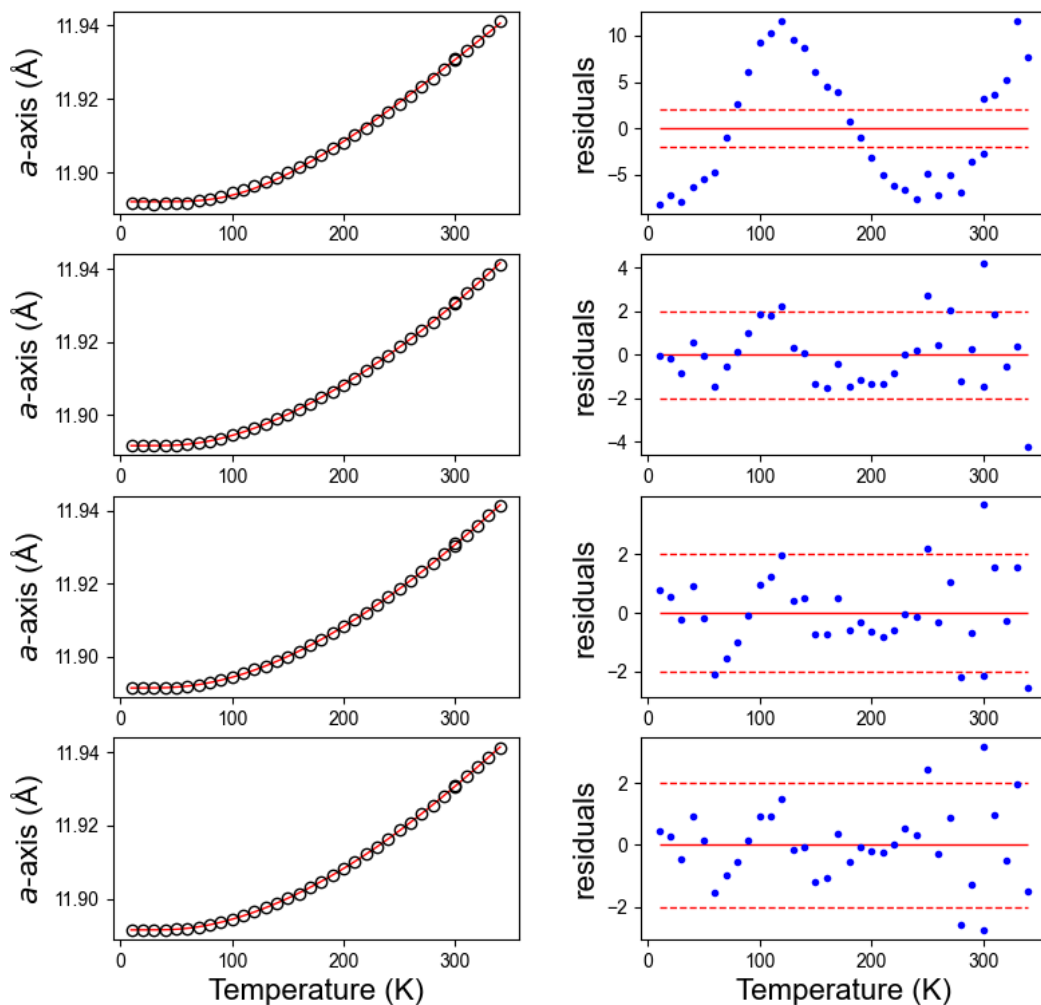
Fig. S7. Classical (χ^2 = 1479.1), linear (χ^2 = 83.0), second-order (χ^2 = 60.1) and third-order (χ^2 = 52.5) Einstein fits upon the *a* lattice parameter of cranswickite (in descending order). Open symbols indicate the measured data-points and the red line the fit. Both, χ^2 as well as the residuals plot, where the red dashed lines represent 2σ, demonstrate that a linear model fits the data well. A further extension would merely introduce unnecessarily large errors on the individual fit parameters without substantially improving the overall fit.
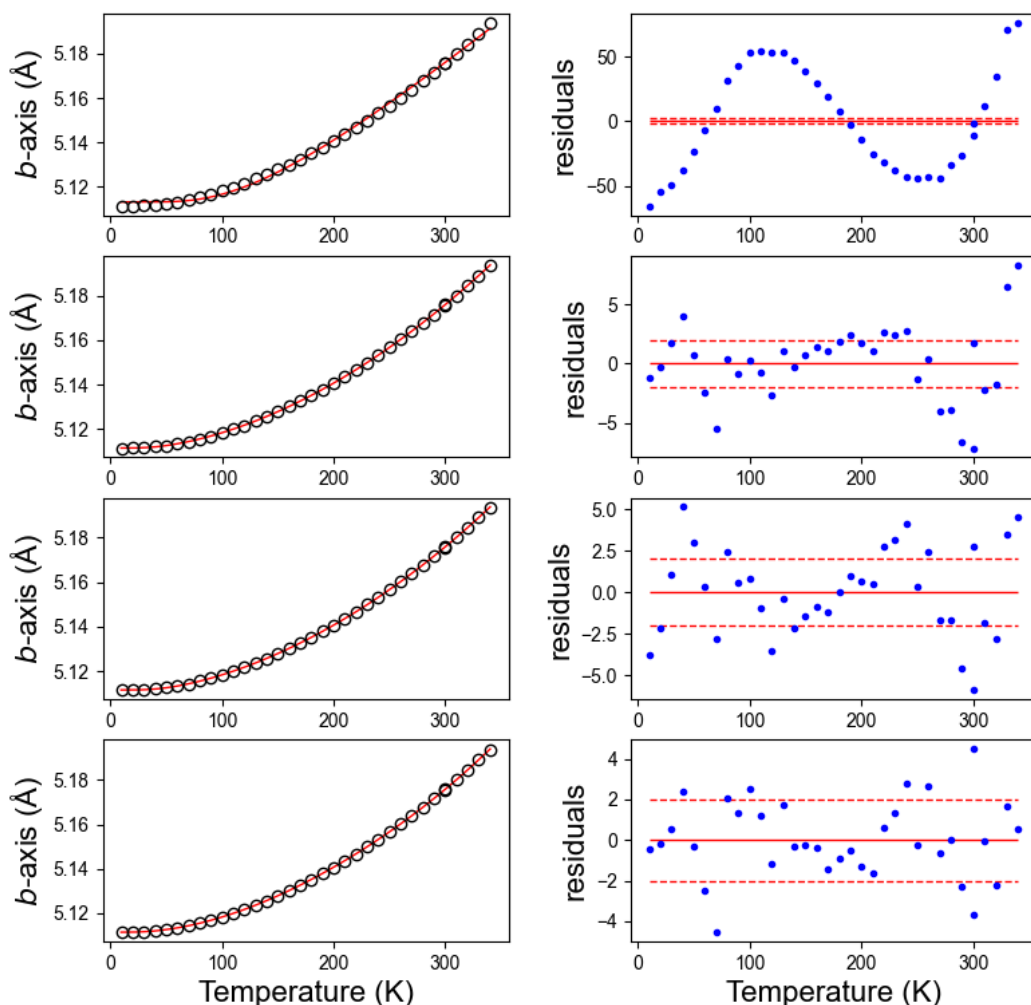
Fig. S8. Classical (χ^2 = 56159.8), linear (χ^2 = 354.8), second-order (χ^2 = 247.8) and third-order (χ^2 = 123.6) Einstein fits upon the b lattice parameter of cranswickite (in descending order). Open symbols indicate the measured data-points and the red line the fit. Although, χ^2 as well as the residuals plot, where the red dashed lines represent 2σ, demonstrate that a third-order model would further improve the fit, the second-order model was preferred, since in the third-order model the e_0 parameter exhibits an e.s.d (σ) exceeding this parameter's value. Nevertheless, also the second-order model yields an excellent description of the thermal evolution of the b-axis.
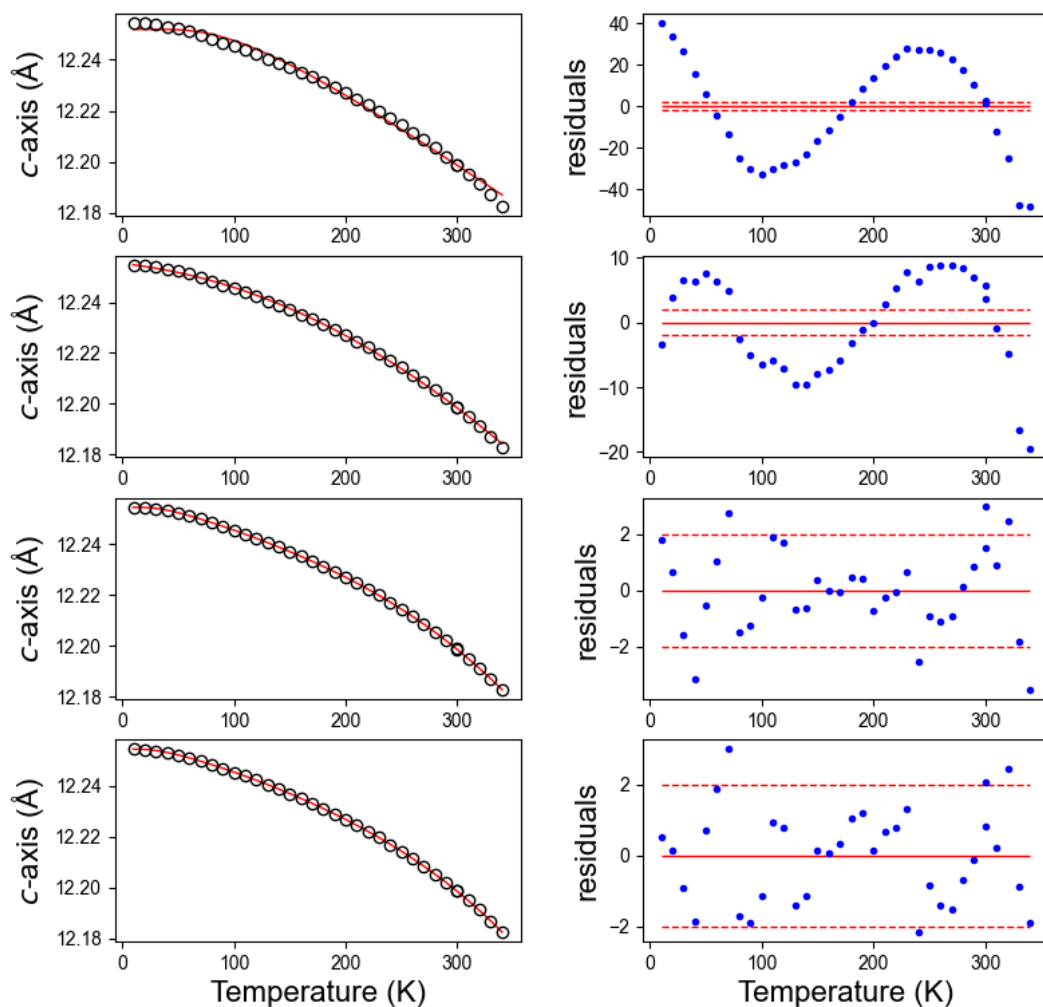
Fig. S9. Classical (χ^2 = 20365.5), linear (χ^2 = 1949.7), second-order (χ^2 = 81.5) and third-order (χ^2 = 60.8) Einstein fits upon the *c*-axis of cranswickite (in descending order). Open symbols indicate the measured data-points and the red line the fit. Both, χ^2 as well as the residuals plot demonstrate that a 2nd order model fits the data well. A further extension to the third order would merely introduce unnecessarily large errors on the individual fit parameters without substantially improving the overall fit.
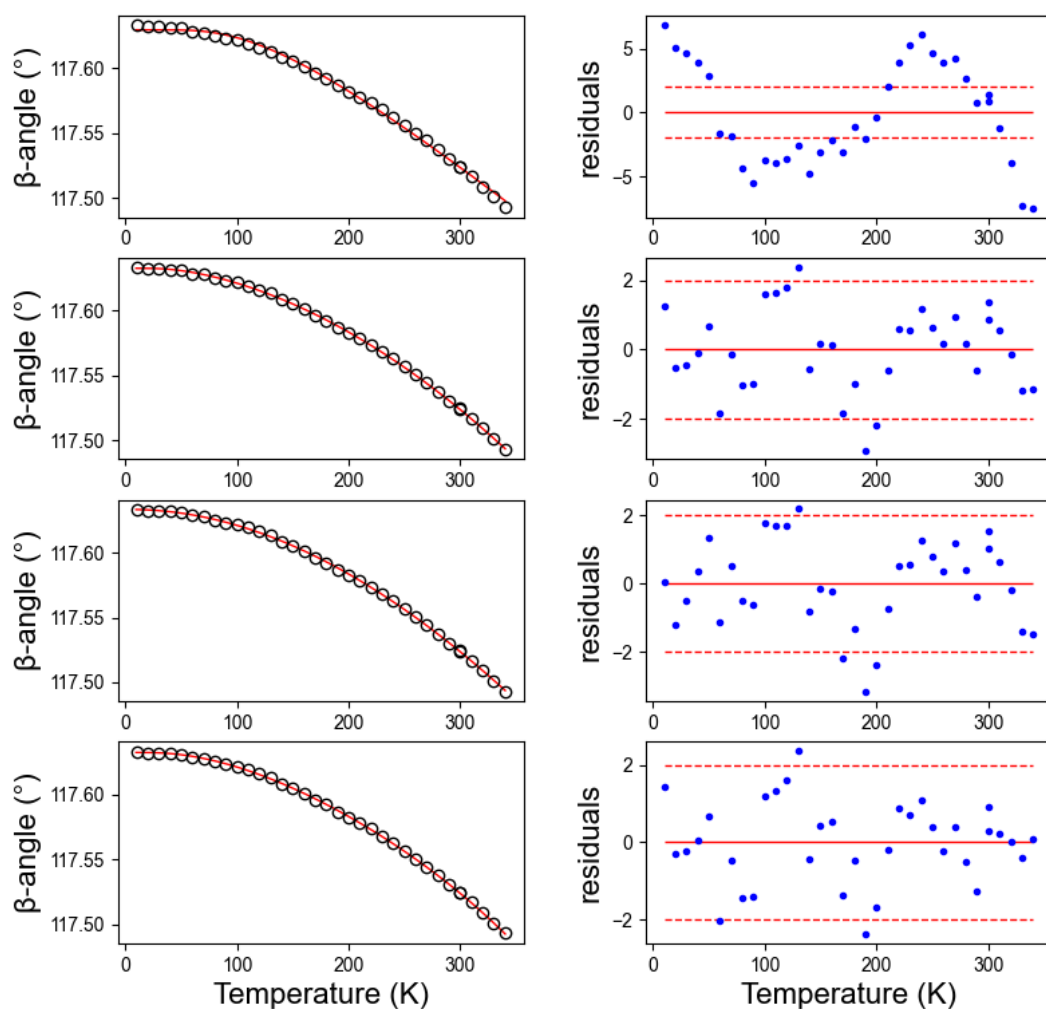
Fig. S10. Classical ($\chi^2 = 550.7$), linear ($\chi^2 = 49.6$), second-order ($\chi^2 = 47.9$) and third-order ($\chi^2 = 39.6$) Einstein fits upon the β lattice parameter of cranswickite (in descending order). Open symbols indicate the measured data-points and the red line the fit. Both, χ^2 as well as the residuals plot, where the red dashed lines represent 2σ, demonstrate that a linear model fits the data well. A further extension would merely introduce unnecessarily large errors on the individual fit parameters without substantially improving the overall fit.
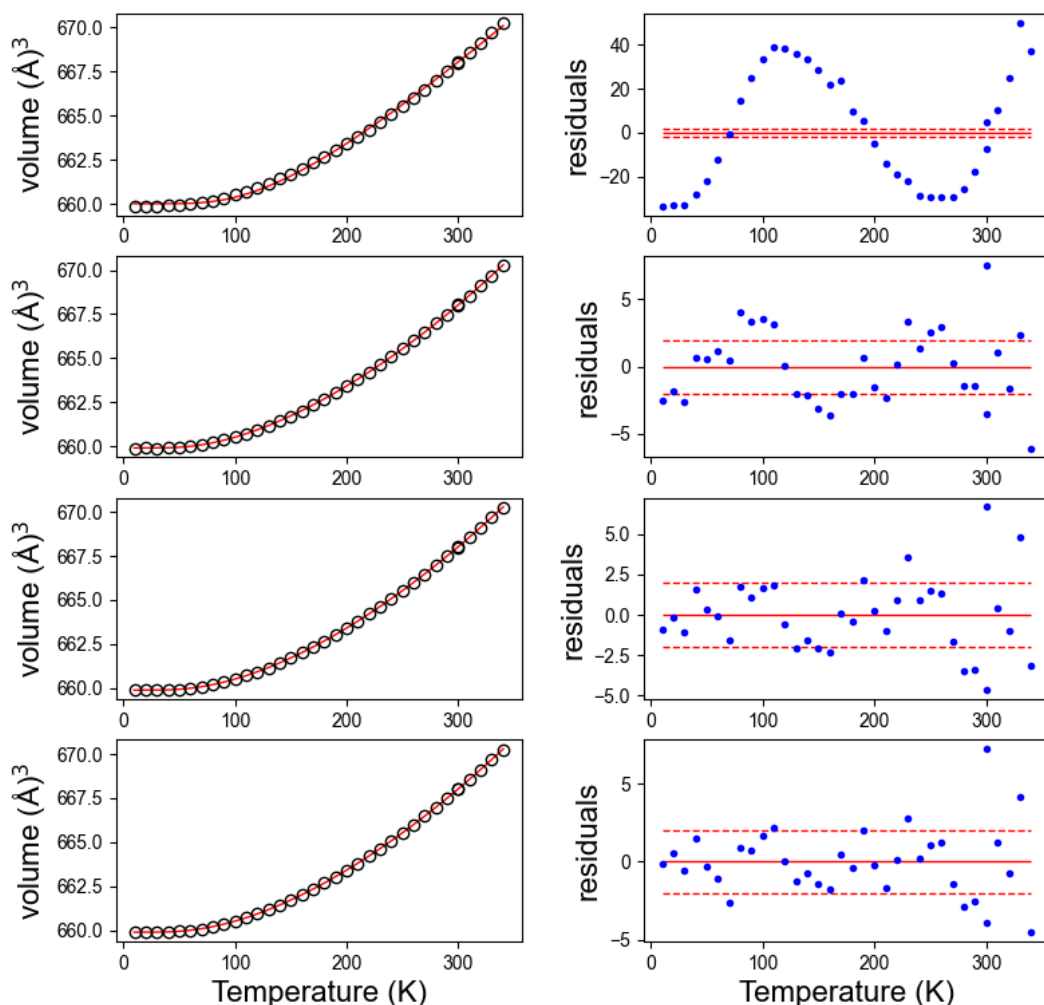
Fig. S11. Classical (χ^2 = 24083), linear (χ^2 = 265), second-order (χ^2 = 185) and third-order (χ^2 = 170) Einstein fits upon the unit-cell volume of cranswickite (in descending order). Open symbols indicate the measured data-points and the red line the fit. Both, χ^2 as well as the residuals plot demonstrate that a 2nd order model fits the data well, where the red dashed lines represent 2σ. A further extension to the third order would merely introduce unnecessarily large errors on the individual fit parameters without substantially improving the overall fit.
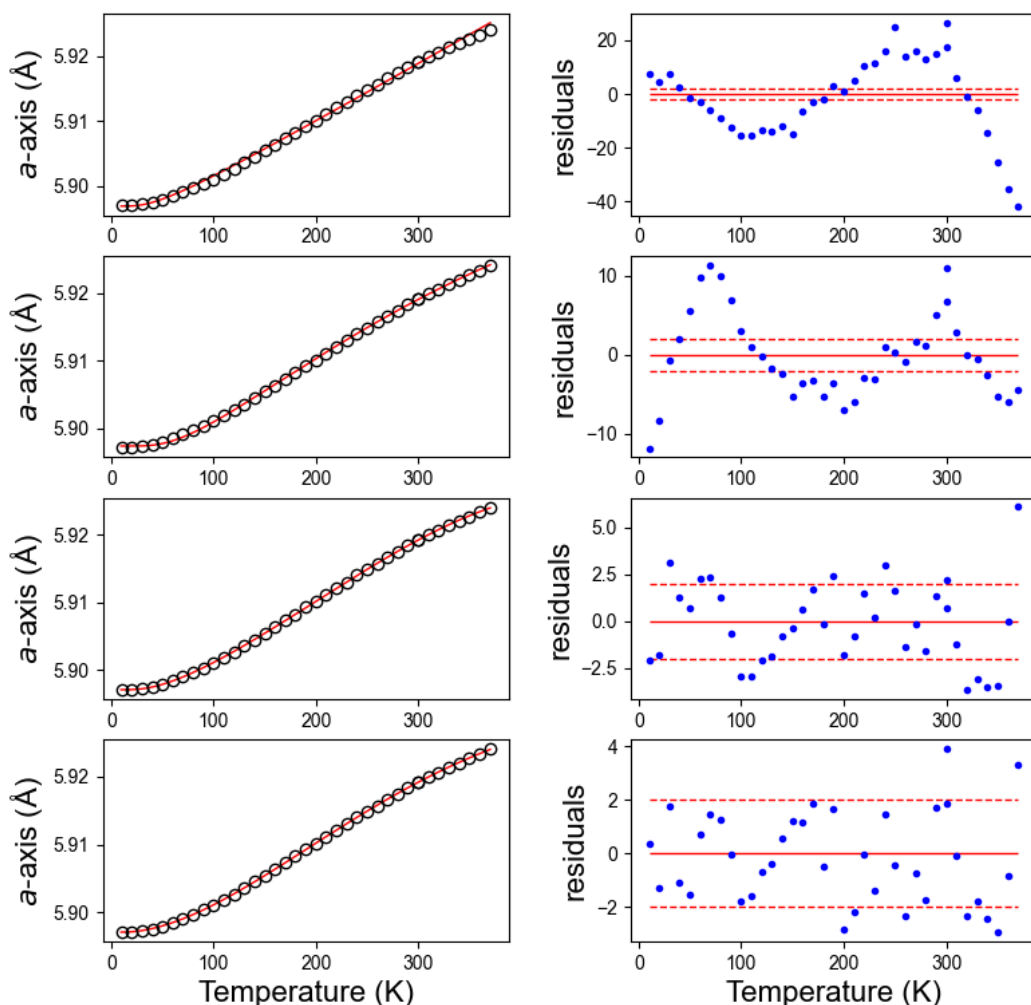
Fig. S12. Classical (χ^2 = 8556.0), linear (χ^2 = 1125.1), second-order (χ^2 = 184.0) and third-order (χ^2 = 111.5) Einstein fits upon the *a* lattice parameter of starkeyite (in descending order). Open symbols indicate the measured data-points and the red line the fit. Although, χ^2 as well as the residuals plot, where the red dashed lines represent 2σ, demonstrate that a third-order model would further improve the fit, the second-order model was preferred, since in the third-order model the e_0 parameter exhibits an e.s.d (σ) exceeding this parameter's value. Nevertheless, also the second-order model yields an excellent description of the thermal evolution of the *b*-axis.
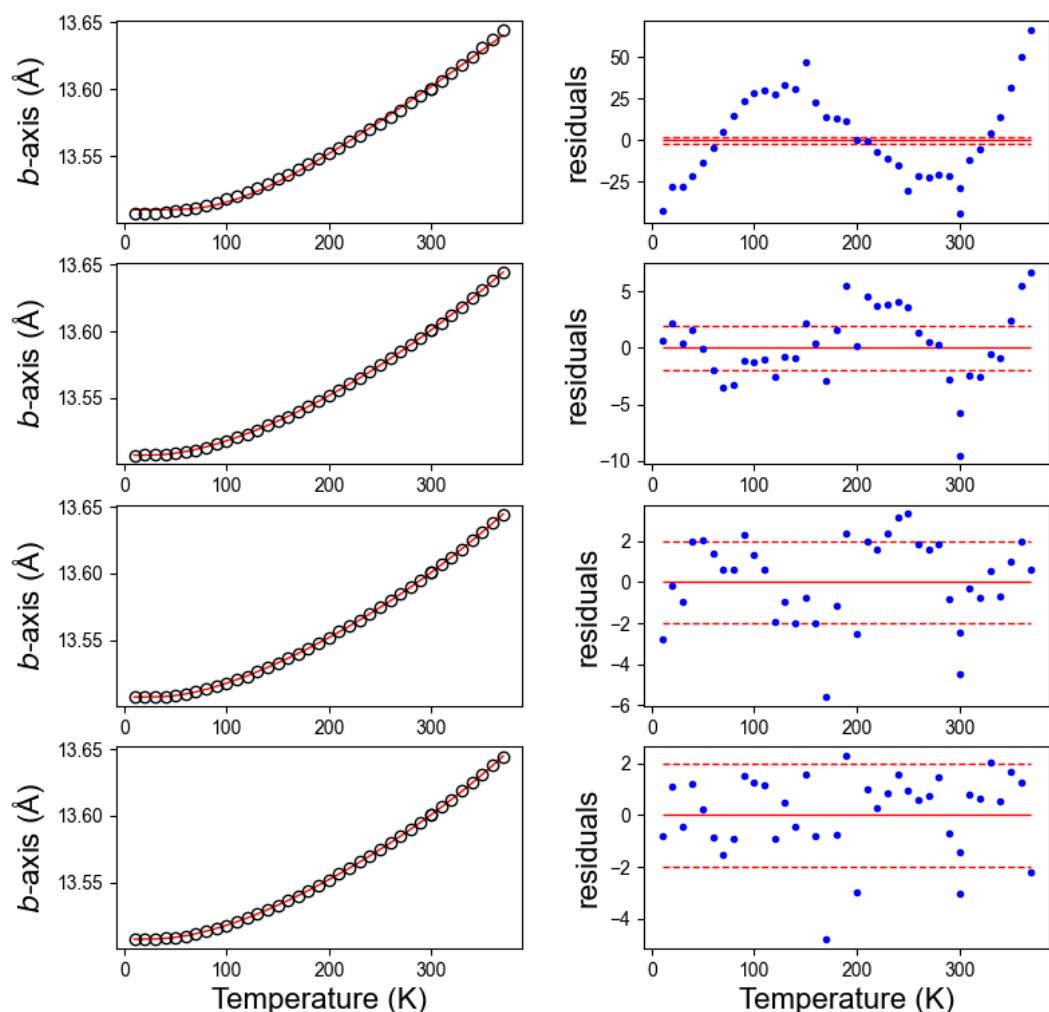
Fig. S13. Classical (χ^2 = 27191), linear (χ^2 = 403), second-order (χ^2 = 161) and third-order (χ^2 = 90) Einstein fits upon the b-axis of starkeyite (in descending order). Open symbols indicate the measured data-points and the red line the fit. Both, χ^2 as well as the residuals plot demonstrate that a 2nd order model fits the data well. A further extension to the third order would merely introduce unnecessarily large errors on the individual fit parameters without substantially improving the overall fit.
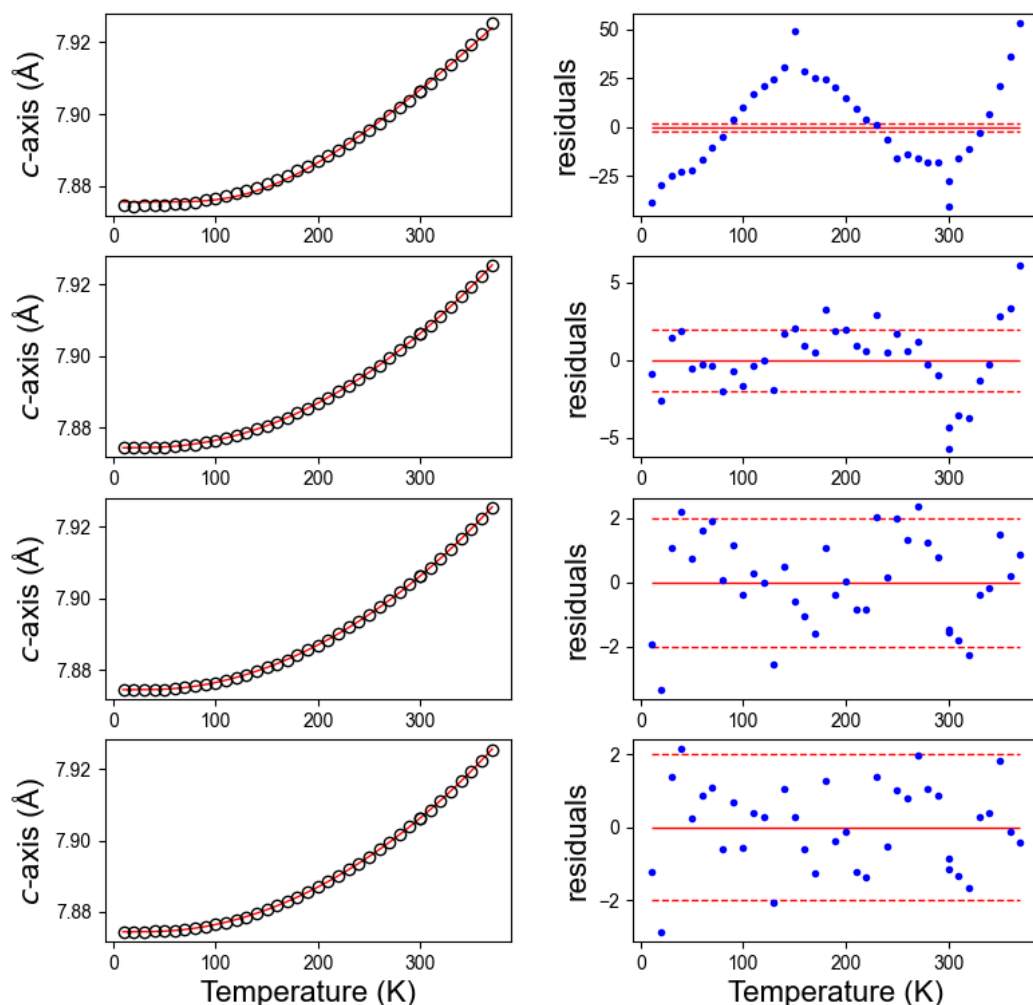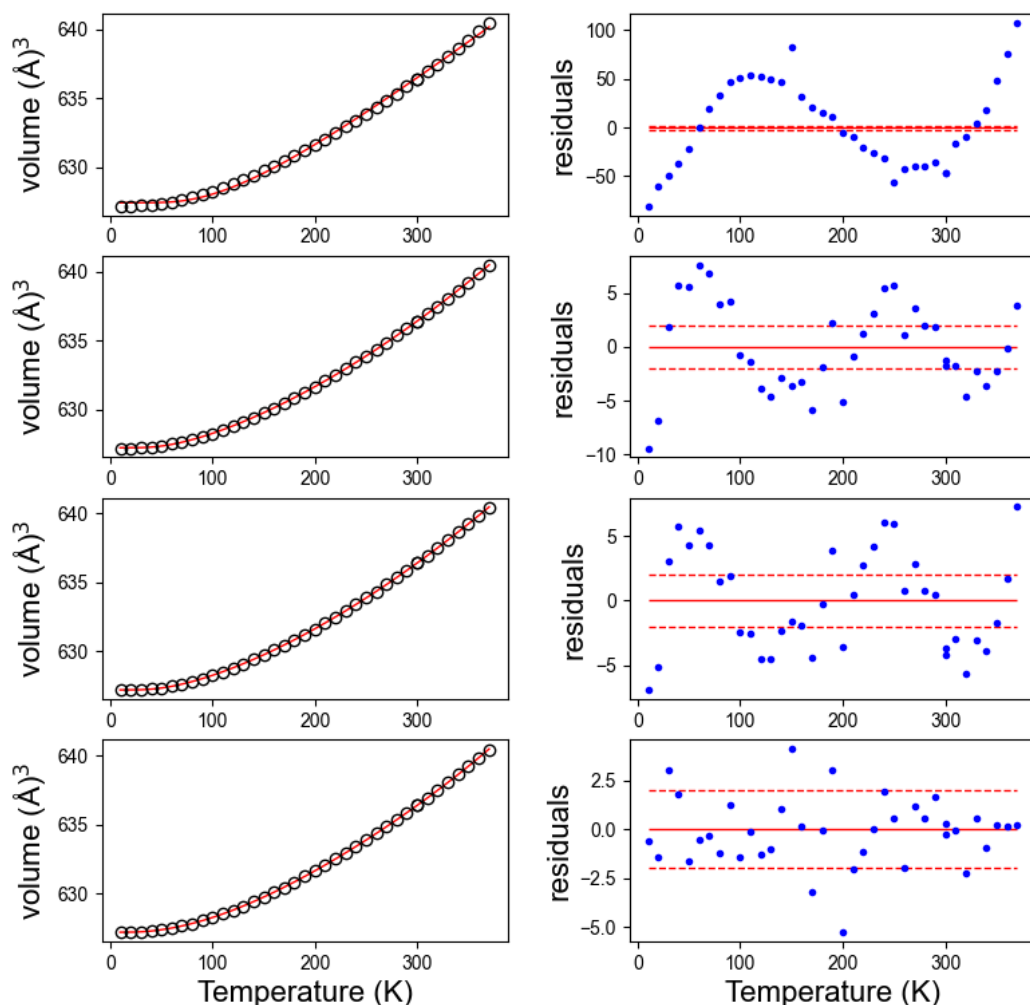
Fig. S14. Classical (χ^2 = 20930), linear (χ^2 = 203), second-order (χ^2 = 77) and third-order (χ^2 = 52) Einstein fits upon the b-axis of starkeyite (in descending order). Open symbols indicate the measured data-points and the red line the fit. Both, χ^2 as well as the residuals plot demonstrate that a 2nd order model fits the data well. A further extension to the third order would merely introduce unnecessarily large errors on the individual fit parameters without substantially improving the overall fit.
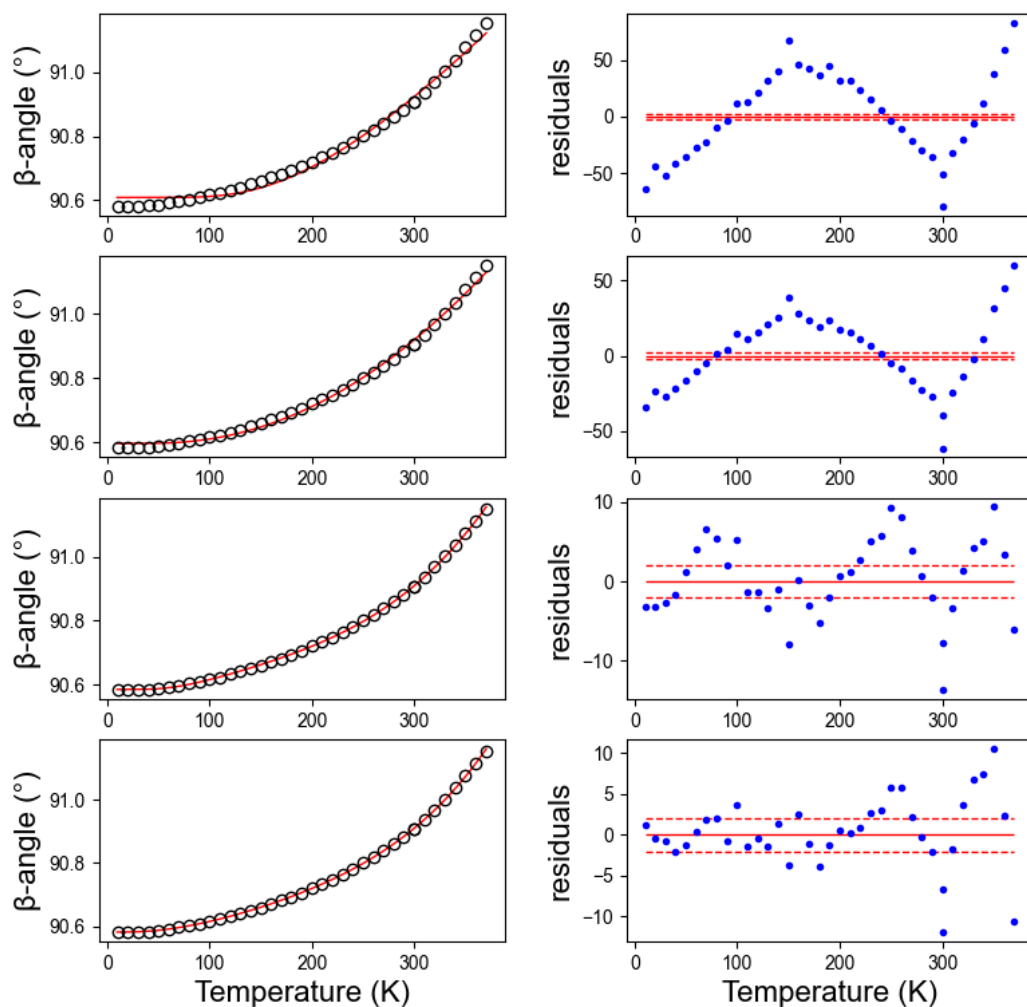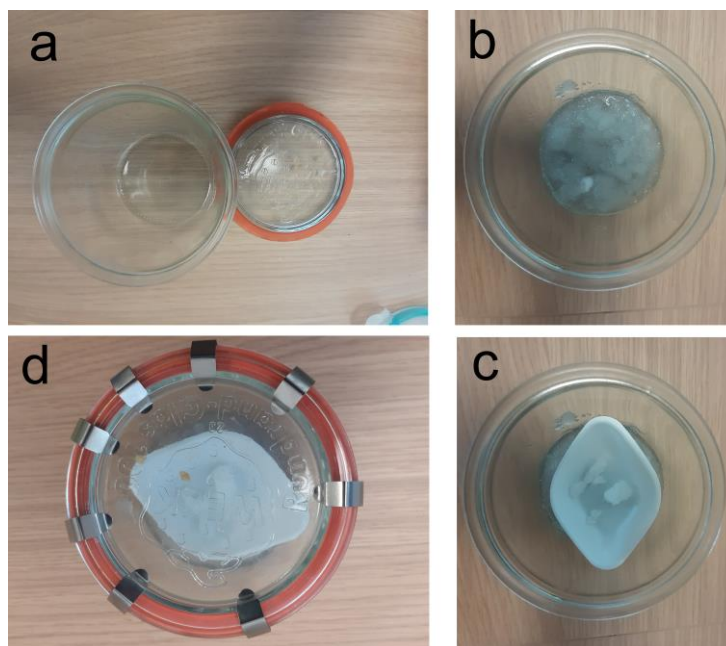
Fig. S15. Classical ($\chi^2 = 56449$), linear ($\chi^2 = 24057$), second-order ($\chi^2 = 946$) and third-order ($\chi^2 = 706$) Einstein fits upon the b-axis of starkeyite (in descending order). Open symbols indicate the measured data-points and the red line the fit. Both, χ^2 as well as the residuals plot demonstrate that a 2nd order model fits the data well. A further extension to the third order would merely introduce unnecessarily large errors on the individual fit parameters without substantially improving the overall fit.

278

Fig. S16. Classical (χ^2 = 75880), linear (χ^2 = 647), second-order (χ^2 = 560) and third-order (χ^2 = 115) Einstein fits upon the b-axis of starkeyite (in descending order). Open symbols indicate the measured data-points and the red line the fit. Both, χ^2 as well as the residuals plot demonstrate that a 2nd order model fits the data well. A further extension to the third order would merely introduce unnecessarily large errors on the individual fit parameters without substantially improving the overall fit.

Fig. S17 (a) Glass jar, rubber gasket and lid as used for the cranswickite synthesis. (b) $MgCl_2/D_2O$ buffer solution placed in the glass jar. (c) Weighing boat is put on top of the humidity buffer solution and filled with $MgSO_4 \cdot 7D_2O$. (d) The jar is closed with the lid and rubber gasket. Note that the loading procedure was carried out in helium atmosphere.
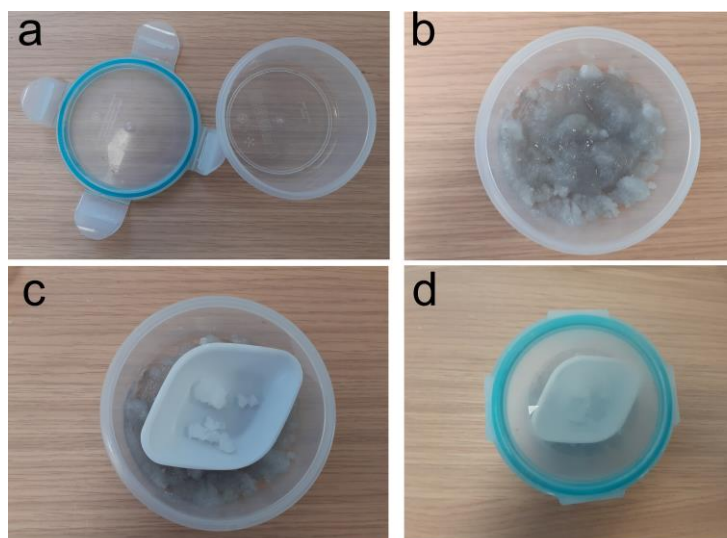
Fig. S18 (a) Plastic container and lid as used for the starkeyite synthesis. (b) For deuterated starkeyite a $MgCl_2/D_2O$ buffer solution is added to the container, for protiated a $MgCl_2/H_2O$ solution. (c) $MgSO_4 \cdot 7D_2O$ or $MgSO_4 \cdot 7H_2O$ is put in the weighing boat and (d) container is closed. Synthesis was not carried out in helium atmosphere for $MgSO_4 \cdot 7H_2O$.

References

Baur, W. H. (1964). On the crystal chemistry of salt hydrates. II. A neutron diffraction study of $MgSO_4.4H_2O$. Acta Crystallographica, *17*(7), 863–869. https://doi.org/10.1107/S0365110X64002304

Brooks-Bartlett, J. C., Batters, R. A., Bury, C. S., Lowe, E. D., Ginn, H. M., Round, A., & Garman, E. F. (2017). Development of tools to automate quantitative analysis of radiation damage in SAXS experiments. Journal of Synchrotron Radiation, 24(1), 63–72. https://doi.org/10.1107/S1600577516015083

Bury, C., Brooks-Bartlett, J., Walsh, S., & Garman, E. (2017). Estimate your dose: RADDOSE-3D. Protein Science, 27. https://doi.org/10.1002/pro.3302

Clark, S., Segall, M., Pickard, C., Hasnip, P., Probert, M., Refson, K., & Payne, M. (2005). First principles methods using CASTEP. Zeitschrift Für Kristallographie, 220. https://doi.org/10.1524/zkri.220.5.567.65075

Coates, C. S., Murray, C. A., Boström, H. L. B., Reynolds, E. M., & Goodwin, A. L. (2021). Negative X-ray expansion in cadmium cyanide. Materials Horizons, *8*(5), 1446–1453. https://doi.org/10.1039/D0MH01989E

Fortes, A. D., Wood, I. G., Alfredsson, M., Vočadlo, L., & Knight, K. S. (2006). The thermoelastic properties of $MgSO_4·7D_2O$ (epsomite) from powder neutron diffraction and ab initio calculation. European Journal of Mineralogy, *18*(4), 449–462. https://doi.org/10.1127/0935-1221/2006/0018-0449

Fortes, A. D., Wood, I., & Knight, K. (2008). The crystal structure and thermal expansion tensor of $MgSO_4·11D_2O$(meridianiite) determined by neutron powder diffraction. Physics and Chemistry of Minerals, *35*, 207–221. https://doi.org/10.1007/s00269-008-0214-x

Greenspan, L. (1977). Humidity Fixed Points of Binary Saturated Aqueous Solutions. Journal of Research of the National Bureau of Standards. Section A, Physics and Chemistry, 81A, 89–96.

Hohenberg, P., & Kohn, W. (1964). Inhomogeneous Electron Gas. *Physical Review*, *136*(3B), B864–B871. https://doi.org/10.1103/PhysRev.136.B864

Ibberson, R. (2009). Design and performance of the new supermirror guide on HRPD at ISIS. Nuclear Instruments and Methods in Physics Research Section A Accelerators Spectrometers Detectors and Associated Equipment, 600. https://doi.org/10.1016/j.nima.2008.11.066

Kohn, W., & Sham, L. J. (1965). Self-Consistent Equations Including Exchange and Correlation Effects. Physical Review, 140(4A), A1133–A1138. https://doi.org/10.1103/PhysRev.140.A1133

Meusburger, J. M., Hudson-Edwards, K. A., Tang, C. C., Crane, R. A., & Fortes, A. D. (2021). Elasticity of selected icy satellite candidate materials (CO_2, C_6H_6, $MgSO_4·7H_2O$ and $CaSO_4·2H_2O$) revisited by dispersion corrected density functional theory. Icarus, 114611. https://doi.org/https://doi.org/10.1016/j.icarus.2021.114611

Meusburger, J. M., Hudson-Edwards, K. A., Tang, C. T., Connolly, E. T., Crane, R. A., & Fortes, A. D. (2022). Low-temperature crystallography and vibrational properties of rozenite ($FeSO_4·4H_2O$), a candidate mineral component of the polyhydrated sulfate deposits on Mars. Materials Cloud Archive. https://doi.org/10.24435/materialscloud:fd-31.

Perdew, Burke, & Ernzerhof. (1996). Generalized Gradient Approximation Made Simple. Physical Review Letters, *77 18*, 3865–3868.

Peterson, R. C. (2011). Cranswickite $MgSO_4 \cdot 4H_2O$, a new mineral from Calingasta, Argentina. American Mineralogist, 96(5–6), 869–877. https://doi.org/https://doi.org/10.2138/am.2011.3673

Pfrommer, B. G., Cote, M., Louie, S. G., & Cohen, M. L. (1997). Relaxation of crystals with the quasi-Newton method. Journal of Computational Physics, 131(1), 233–240. http://inis.iaea.org/search/search.aspx?orig_q=RN:28052322

Thompson, S. P., Parker, J. E., Marchal, J., Potter, J., Birt, A., Yuan, F., Fearn, R. D., Lennie, A. R., Street, S. R., & Tang, C. C. (2011). Fast X-ray powder diffraction on I11 at Diamond. Journal of Synchrotron Radiation, 18(4), 637–648. https://doi.org/10.1107/S0909049511013641

Thompson, S. P., Parker, J. E., Potter, J., Hill, T. P., Birt, A., Cobb, T. M., Yuan, F., & Tang, C. C. (2009). Beamline I11 at Diamond: A new instrument for high resolution powder diffraction. Review of Scientific Instruments, 80(7), 075107. https://doi.org/10.1063/1.3167217

Tkatchenko, A., & Scheffler, M. (2009). Accurate Molecular Van Der Waals Interactions from Ground-State Electron Density and Free-Atom Reference Data. Physical Review Letters, 102(7), 73005. https://doi.org/10.1103/PhysRevLett.102.073005

von Dreele, R. B., Suchomel, M. R., & Toby, B. H. (2013). *ABSORB web utility*. Https://11bm.Xray.Aps.Anl.Gov/Absorb/Absorb.Php. https://11bm.xray.aps.anl.gov/absorb/absorb.php

Wallace, D. C. (1972). Thermodynamics of Crystals (Vol. 51). Wiley.

Wang, A., Freeman, J., Jolliff, B., & Chou, I.-M. (2006). Sulfates on Mars: A systematic Raman spectroscopic study of hydration states of magnesium sulfates. Geochimica et Cosmochimica Acta, 70. https://doi.org/10.1016/j.gca.2006.05.022

Wildner, M., Zakharov, B. A., Bogdanov, N. E., Talla, D., Boldyreva, E. v, & Miletich, R. (2022). Crystallography relevant to Mars and Galilean icy moons: crystal behavior of kieserite-type monohydrate sulfates at extraterrestrial conditions down to 15 K. IUCrJ, 9(2). https://doi.org/10.1107/S2052252521012720

8.5 Supplementary: Additional bond-valence calculations

Cranswickite - bond valence - non hydrogen					
	2 x O1	**2 x O2**	**2 x Ow1**	**2 x Ow2**	**Σ**
Mg - O		0.842	0.736	0.653	**2.231**
S - O	3.074	3.379			**6.452**
Σ	**3.074**	**4.221**	**0.736**	**0.653**	

Cranswickite - bond valence - hydrogen					
	2 x O1	**2 x O2**	**2 x Ow1**	**2 x Ow2**	**Σ**
Mg - O		0.842	0.736	0.653	**2.231**
S - O	3.074	3.379			**6.452**
O - H			3.588	3.457	**7.045**
H ·· O	0.614			0.197	**0.810**
Σ	**3.687**	**4.221**	**4.323**	**4.307**	

Tab. s1. Bond valance calculations for cranswickite excluding (top) and including (bottom) the contribution of the hydrogen atoms (bottom). For the Mg – O and S – O bonds a universal parameter of 0.37 as suggested by Brown & Altermatt (1985) was used, whereas the O – H and H · O values were computed using a more recent universal parameter of 0.404 as derived by Alig et al. (1994) specifically for hydrogen bonds. R_0 values for Mg – O (1.693) and S – O (1.644) were taken from Brese & O'Keeffe (1991) and for O – H (0.914) from Alig et al. (1994). Bond lengths experimentally determined at room temperature by high resolution neutron powder diffraction were used for to calculate the bond valances.

Starkeyite - bond valence - non hydrogen

	O1	O2	O3	O4	Ow1	Ow2	Ow3	Ow4	Σ
Mg - O	0.363	0.358			0.381	0.380	0.364	0.360	**2.206**
S - O	1.472	1.488	1.640	1.631					**6.230**
Σ	**1.835**	**1.846**	**1.640**	**1.631**	**0.381**	**0.380**	**0.364**	**0.360**	

Starkeyite - bond valence - hydrogen

	O1	O2	O3	O4	Ow1	Ow2	Ow3	Ow4	Σ
Mg - O	0.363	0.358			0.381	0.380	0.364	0.360	**2.206**
S - O	1.472	1.488	1.640	1.631					**6.230**
O - H					1.818	1.859	1.873	1.796	**7.347**
H · O	0.090	0.042	0.298	0.216				0.058	**0.704**
Σ	**1.925**	**1.888**	**1.938**	**1.847**	**2.199**	**2.239**	**2.237**	**2.214**	

Tab. s2. Bond valance calculations for starkeyite excluding (top) and includin(bottom) the contribution of the hydrogen atoms (bottom). For the Mg – O and S – O bonds a universal parameter of 0.37 as suggested by Brown & Altermatt (1985) was used, whereas the O – H and H ··O values were computed using a more recent universal parameter of 0.404 as derived by Alig et al. (1994) specifically for hydrogen bonds. R_0 values for Mg – O (1.693) and S – O (1.644) were taken from Brese & O'Keeffe (1991) and for O – H (0.914) from Alig et al. (1994). Bond lengths experimentally determined at 300 K by high resolution neutron powder diffraction were used for to calculate the bond valances.

'MS6H' polymorph - Maynard-Casely et al. (2021) bond valence - non hydrogen

	O11	O12	O13	O14	O15	O16	O21	O22	O23	O24	O25	O26	O1	O2	O3	O4	Σ
Mg1 - O	0.33	0.35	0.33	0.45	0.44	0.44											2.34
Mg2 - O							0.44	0.44	0.33	0.44	0.44	0.44					2.51
S - O													1.93	1.93	1.93	1.93	7.73
Σ	0.33	0.35	0.33	0.45	0.44	0.44	0.44	0.44	0.33	0.44	0.44	0.44	1.93	1.93	1.93	1.93	

Tab. S3. Bond-valence calculation (R_0 parameterisation from Brese & O'Keeffe (1991), U value of 0.37 (Brown & Altermatt, 1985)) of the putative $MgSO_4 \cdot 6H_2O$ polymorph reported by Maynard-Casely et al. (2021). The very large valence sum deviations from the ideal values for the S and Mg2 atoms are noteworthy. Most importantly while setting up this calculation it became obvious that the structure features two independent Mg site but just one S site, although all atoms are on the general site with a multiplicity of 4. From this is follows that the stoichiometry of the compound is wrong, and half of the S atoms are missing.

Acknowledgement